INAUGURAL – DISSERTATION

zur

Erlangung der Doktorwürde

der

Gesamtfakultät für Mathematik,

Ingenieur- und Naturwissenschaften

der

Ruprecht-Karls-Universität

Heidelberg

Vorgelegt von

Truc Lam Pham

aus Frankfurt am Main

Tag der mündlichen Prüfung: 19.07.2024

Design of metal-binding globular β-sheet miniproteins as biosensors and artificial enzymes

(Design von metallbindenden globulären β-Faltblatt-Miniproteinen als Biosensoren und künstliche Enzyme)

1. Gutachterin: Prof. Dr. Franziska Thomas

2. Gutachter: Prof. Dr. Peter Comba

Die vorliegende Arbeit wurde im Zeitraum Dezember 2019 bis Juni 2024 unter Betreuung von Prof. Dr. Franziska Thomas am Organisch-Chemischen Institut und am Centre for Advanced Materials/Institute for Molecular Systems Engineering and Advanced Materials der Ruprecht-Karls-Universität Heidelberg angefertigt. NMR-Messungen von Peptiden wurden in Kollaboration mit Prof. Dr. Michael Kovermann am Fachbereich Chemie der Universität Konstanz durchgeführt. EPR-Messungen wurden in Kollaboration mit dem Arbeitskreis von Prof. Dr. Peter Comba am Anorganisch-Chemischen Institut der Ruprecht-Karls-Universität Heidelberg durchgeführt, hauptsächlich zusammen mit Philipp Baur.

Ein Teil der hier präsentierten Ergebnisse wurde von folgenden Personen im Rahmen ihres Forschungspraktikums und/oder ihrer Bachelorarbeit im Arbeitskreis von Prof. Dr. Franziska Thomas unter meiner Anleitung erhalten:

Guillermo Lozano, Kim Ziebner, Miguel Oliveira, Christine Müller, Jennifer Zilke, Marius Werner, Julius Pampel, Rebeka Papp, Sunnatullo Fazliev, Simon Hans Lilje, Dennis Drescher, Marcos Rafael Conde González, Agi Kishore und Agon Kokollari.

Auszüge aus dieser Arbeit wurden bereits in folgenden **Zeitschriftenartikel** veröffentlicht:

[1] Truc Lam Pham, Michael Kovermann, Franziska Thomas, **Switchable Zinc(II)-Responsive Globular β-Sheet Peptide**, *ACS Synth. Biol.* **2022**, *11*, 254-264. https://pubs.acs.org/doi/10.1021/acssynbio.1c00396

[2] Truc Lam Pham, Jennifer Zilke, Christine Charlotte Müller, Franziska Thomas, **The CSY-protecting group in the microwave-assisted synthesis of aggregation-prone peptides**, *RSC Chem. Biol.* **2022**, *3*, 426-430. https://pubs.rsc.org/en/content/articlelanding/2022/cb/d1cb00252j

[3] Marius Werner, Julius Pampel, Truc Lam Pham, Franziska Thomas, **Late-Stage Functionalisation of Peptides on the Solid Phase by an Iodination-Substitution Approach**, *Chem. Eur. J.* **2022**, *28*, e202201339. https://chemistry-europe.onlinelibrary.wiley.com/doi/10.1002/chem.202201339

[4] Truc Lam Pham, Sunnatullo Fazliev, Philipp Baur, Peter Comba, Franziska Thomas, **An Engineered β-Hairpin Peptide Forming Thermostable Complexes with Zn^{II}, Ni^{II}, and Cu^{II} through a His_3 Site**, *ChemBioChem* **2023**, *24*, e202200588. https://chemistry-europe.onlinelibrary.wiley.com/doi/10.1002/cbic.202200588

[5] Truc Lam Pham, Marcos R. Conde González, Sunnatullo Fazliev, Agi Kishore, Peter Comba, Franziska Thomas, **Relationship of Thermostability and Binding Affinity in Metal-binding WW-Domain Minireceptors**, *ChemBioChem* **2024**, e202300715. https://chemistry-europe.onlinelibrary.wiley.com/doi/full/10.1002/cbic.202300715

[6] Truc Lam Pham, Franziska Thomas, **Design of Functional Globular β-Sheet Miniproteins**, *ChemBioChem* **2024**, e202300745. https://chemistry-europe.onlinelibrary.wiley.com/doi/full/10.1002/cbic.202300745

Copyright der Publikationen:

Falls zutreffend wird vor jedem Kapitel genau angegeben, ob der Inhalt bereits veröffentlicht wurde und die entsprechenden Publikationen zitiert.

Adapted with permission from [1], Copyright 2022, American Chemical Society.

Adapted from Ref. [2] (CC BY-NC 3.0) with permission from the Royal Society of Chemistry.

Adapted with permission from [3] (CC BY-NC 4.0), Copyright 2022, Wiley-VCH GmbH.

Adapted with permission from [4] (CC BY-NC 4.0), Copyright 2022, Wiley-VCH GmbH.

Adapted with permission from [5] (CC BY-NC 4.0), Copyright 2023, Wiley-VCH GmbH.

Adapted with permission from [6] (CC BY-NC 4.0), Copyright 2024, Wiley-VCH GmbH.

Links zu den Lizenzen:

CC BY-NC 3.0: https://creativecommons.org/licenses/by-nc/3.0/

CC BY-NC 4.0: https://creativecommons.org/licenses/by-nc/4.0/

Inhalte der Dissertation wurden vorab durch folgende **Konferenzbeiträge** kommuniziert:

[1] Truc Lam Pham, Sunnatullo Fazliev, Marius Werner, Julius Pampel, Christine Charlotte Müller, Michael Kovermann, Franziska Thomas, **Engineered globular β-sheet peptides as metal ion receptors** (Poster), *36th European/14th International Peptide Symposium* **2022**, Sitges (Spain).

[2] Truc Lam Pham, Marius Werner, Sunnatullo Fazliev, Julius Pampel, Christine Charlotte Müller, Michael Kovermann, Franziska Thomas, **Globular β-sheet peptide metal ion receptors by rational design and late-stage functionalization** (Präsentation), *Hochschule trifft Industrie* **2022**, Biberach an der Riss (Deutschland).

[3] Truc Lam Pham, Franziska Thomas, **Designing functional miniproteins from β-sheet protein folding motifs** (Präsentation), *Hengstberger-Symposium on "Bioelectronics: mimicking and interfacing biological systems"* **2023**, Heidelberg (Deutschland).

[4] Truc Lam Pham, Marius Werner, Sunnatullo Fazliev, Agi Kishore, Marcos Conde González, Julius Pampel, Philipp Baur, Peter Comba, Michael Kovermann, Franziska Thomas, **Designed metal binding globular β-sheet peptides as mini-receptors for bioactive molecules** (Präsentation und Poster), *16th German Peptide Symposium* **2023**, Jena (Deutschland). Posterpreis, 3. Platz.

Weitere Zeitschriftenartikel, die unter Betreuung von Prof. Dr. Franziska Thomas entstanden sind (nicht Teil der Dissertation):

[1] Truc Lam Pham, Franziska Thomas, **Neues zur Synthese von Aminoboronsäuren**, *Nachr. Chem.* **2020**, *68*, 75-79.

[2] Agon Kokollari, Marius Werner, Christina Lindner, Truc Lam Pham, Franziska Thomas, **Rapid On-Resin *N*-Formylation of Peptides as One-Pot Reaction**, *ChemBioChem* **2023**, e202300571.

[3] Marius Werner, Julian. Brinkhofer, Leon Hammermüller, Thomas Heim, Truc Lam Pham, Jonas Huber, Christian Klein, Franziska Thomas, **Peptide Boronic Acids by Late-Stage Hydroboration on the Solid Phase**, *Adv. Sci.* **2024**, 2400640.

[4] Christina Lindner, Anke Friemel, Niklas Schwegler, Lisa Timmermann, Truc Lam Pham, Vanessa Reusche, Michael Kovermann, Franziska Thomas, **Thermostable WW-Domain Scaffold to Design Functional β-Sheet Miniproteins**, *J. Am. Chem. Soc.* **2024**, 10.1021/jacs.4c03498.

„Grau, teurer Freund, ist alle Theorie,

Und grün des Lebens goldner Baum.“

Johann Wolfgang von Goethe, Faust I (1808)

Kurzzusammenfassung

Durch Design wurden in den letzten Jahren eine Vielzahl von Proteinen mit neuartigen Strukturen und Funktionen dargestellt. Allerdings handelt es sich meistens um α-helikale Strukturen, deren Sequenz-Struktur-Beziehung weitgehend verstanden sind. Für globuläre β-Faltblattproteine ist es hingegen nicht der Fall.

Im Rahmen der vorliegenden Arbeit wurden die gut untersuchte WW-Domäne der hPin1 und die β-Haarnadel Trpzip2 als Grundgerüst ausgewählt, um Mini-Metalloproteine für katalytische und biosensorische Anwendungen zu designen. Dazu wurde eine Bindungsstelle aus drei Histidinen auf der Oberfläche der β-Faltblattgerüste eingeführt, sowie zusätzliche Mutationen, um die Stabilität der Peptide zu beeinflussen und zusätzliche Bindungsstellen zu vermeiden.

Die designten WW-Domänen binden selektiv Ni(II), Cu(II) und Zn(II) unter charakteristischen reversiblen Konformationsänderungen. Dabei führte Metallbindung zu einer Erhöhung der Thermostabilität, mit Schmelztemperaturwerten von bis zu 70 °C. Es konnte weiterhin eine positive Korrelation zwischen der Thermostabilität des Apo-Peptids und der Bindungsaffinität beobachtet werden. Die designte β-Haarnadel verhielt sich in ihren Bindungseigenschaften ähnlich wie die WW-Domänen, wies aber eine noch höhere Thermostabilität von bis zu 80 °C, sowie Stabilität gegenüber chaotropen Salzen und organischen Lösungsmitteln auf.

Die Mini-Metalloproteine waren nur gering bis mäßig katalytisch aktiv (Hydrolyse, Phenoloxidation und CuAAC), jedoch sind sie aufgrund ihrer selektiven und reversiblen Konformationsänderung sehr gut für die Biosensorik geeignet. Durch die Einführung einer künstlichen fluoreszierenden Aminosäure mit einer 7-Mercapto-4-Methylcumarin-Seitenkette über eine späte Funktionalisierungsstrategie auf der festen Phase wurde ein iFRET-basierter Metallionensensor entwickelt, der auch bioaktive Moleküle wie Glyphosat oder Pyrophosphat über die Kompetition der Metallbindung oder die direkte Wechselwirkung über die Änderung der FRET-Intensität nachweisen kann. Eine Erweiterung des Analytenspektrums wurde durch das Design eines Rezeptor-Arrays aus Mini-Metalloproteinen erreicht, welches Glyphosat von anderen bioaktiven Molekülen unterscheiden konnte.

Festphasenpeptidsynthese wurde verwendet, um die Miniproteine darzustellen. Jedoch führt die Aminosäure Aspartat, die für Koordinationsstellen und Stabilität wichtig sein kann, während der Synthese zur unerwünschten Aspartimidbildung. Um diese Nebenreaktion zu unterdrücken, wurde die Verwendung der Cyanosulfurylid-Schutzgruppe (CSY) auf die mikrowellengestützte Synthese optimiert. Zuerst wurde der CSY-geschützte Aspartat-Bausteins im Multigramm-Maßstab dargestellt. Die Kupplung des Bausteins erfolgte unter Erhitzen, jedoch musste die Abspaltung der temporären Fmoc-Schutzgruppe durch Piperidin bei Raumtemperatur erfolgen. Die in exzellenter Qualität erhaltenen CSY geschützten Peptide wurden final oxidativ entschützt, wobei ein Zusatz von Hexafluorisopropanol notwendig war.

Abstract

In recent years, numerous proteins with novel structures and functions have been created through design. However, these are mostly α-helical structures whose sequence-structure relationship are largely understood. This is not the case for globular β-sheet proteins.

In the present work, the well-studied WW domain of hPin1 and the β-hairpin Trpzip2 were selected as scaffolds to design mini-metalloproteins for catalytic and biosensory applications. For this purpose, a binding site of three histidines was introduced on the surface of the β-sheets, as well as additional mutations to influence the stability of the peptides and avoid additional binding sites.

The designed WW domains selectively bound Ni(II), Cu(II) and Zn(II) with characteristic reversible conformational changes. Metal binding led to an increase in thermostability, with the metal complexes displaying melting temperatures of up to 70 °C. Furthermore, a positive correlation between the thermostability of the apo-peptide and the binding affinities to the metal ions was observed. The designed β-hairpin behaved similarly to the WW domains in its binding properties but displayed even higher thermostabilities of up to 80 °C, as well as stability towards chaotrophic salts and organic solvents.

The mini-metalloproteins were only slightly to moderately catalytically active (hydrolysis, phenol oxidation and CuAAC), but their selective and reversible conformational change makes them very suitable for biosensing. By introducing an artificial fluorescent amino acid with a 7-mercapto-4-methylcoumarin side chain *via* late-stage functionalization on the solid phase, an iFRET-based metal ion sensor was developed that also detected bioactive molecules such as glyphosate or pyrophosphate through the competition of metal binding or direct interaction *via* the change in FRET intensity. An expansion of the analyte scope was achieved by the design of a receptor array of mini-metalloproteins, which was able to distinguish glyphosate from other bioactive molecules.

Solid phase peptide synthesis was used to synthesize the miniproteins. However, the amino acid aspartate, which may be important for coordination sites and stability, can lead to undesired aspartimide formation during synthesis. To suppress this side reaction, the use of the cyanosulfurylide protecting group (CSY) was optimized for microwave-assisted synthesis. First, the CSY-protected aspartate building block was synthesized on a multi-gram scale. The coupling of the building block was carried out under heating, but the deprotection of the temporary protecting group by piperidine must be carried out at room temperature. The CSY-protected peptides were obtained in excellent quality were finally deprotected under oxidative conditions, which required the addition of hexafluoroisopropanol.

Content

1 Introduction 1

2 State of the art 4

2.1 Sequence, structure and function of natural WW domains 4

2.2 The WW domain of hPin1 as a model system to study protein folding 5

2.3 Design of WW domains 7

2.3.1 *De novo* Design 7

2.3.2 Enhance Thermostability 8

2.3.3 Switchable WW domains 10

2.3.4 Design of WW domain mini-receptors 11

2.4 Sequence, structure and function of β-hairpins 13

2.5 Design of functional β-hairpins 17

2.5.1 Design of β-hairpin mini-receptors and inhibitors 17

2.5.2 Enhance thermostability 20

2.5.3 Switchable β-hairpins 21

2.5.4 β-hairpins as catalyst 24

3 Objectives 28

4 Results and Discussion 30

4.1 Design of metal binding WW domains 30

4.1.1 Design concept of a switchable metal binding WW domain (WW-CA) 30

4.1.2 Influence of Zn(II) on the structure and stability of WW-CA 31

4.1.3 WW-CA is a Zn(II) and pH dependent switch peptide 33

4.1.4 Conformational analysis of WW-CA by NMR spectroscopy 36

4.1.5 Binding of other metal ions to WW-CA and WW-CA-Nle 49

4.1.6 WW-CA is a molten globule 53

4.2 Variants of WW-CA: Increase of thermal stability and suppression of aggregation 58

4.2.1 Design concept 58

4.2.2 Metal ion binding and structural stability 59

4.2.3 Affinity and stoichiometry of metal ion binding 62

4.2.4 Correlation between structural stability and metal binding affinity 65

4.2.5 Structural aspects of Cu(II) binding 68
4.2.6 3D structure prediction indicates predisposition in WW-CA variants 73
4.3 Metal binding tryptophan zipper 76
4.3.1 Design concept of a metal binding tryptophan zipper ($Tz2H_3$) 76
4.3.2 Thermal stability of $Tz2H_3$ metal complexes 76
4.3.3 Stability of $Tz2H_3$ metal complexes under denaturation conditions 79
4.3.4 Metal ion binding affinity of $Tz2H_3$ 83
4.3.5 Coordination geometry of the $Tz2H_3$-Cu(II) complex 85
4.4 Test for catalytic activity of metal binding β-sheet peptides 87
4.4.1 Hydrolysis 87
4.4.2 Phenol oxidation 94
4.4.3 Copper catalysed azide-alkyne cycloaddition 103
4.5 Design of sensors for bioactive molecules 109
4.5.1 Fluorescent labelled WW-CA as sensor for phosphate, pyrophosphate and glyphosate 109
4.5.2 Differential sensing 116
4.6 Aspartimide formation 125
4.6.1 Mechanism of aspartimide formation and prevention strategies 125
4.6.2 Synthesis of Fmoc-Asp(CSY)-OH 127
4.6.3 Microwave assisted synthesis of CSY-protected peptides 127
4.6.4 Oxidative CSY deprotection 131
4.6.5 Structural analysis of CSY protected and native peptides 135
5 Conclusion 138
6 Summary 142
7 Outlook 149
8 Material and Methods 152
8.1 General 152
8.1.1 Reagents and solvents 152
8.1.2 Preparation of buffers and stock solutions, pH measurement 152
8.1.3 Cleaning of glassware for analytical and biochemical experiments 152

8.1.4 Lyophilisation 153
8.1.5 High performance liquid chromatography 153
8.1.6 Mass spectrometry 154
8.1.7 UV/Vis spectroscopy (general settings) 154
8.1.8 Circular dichroism spectroscopy (general settings) 154
8.1.9 Fluorescence spectroscopy (general settings) 155
8.1.10 NMR spectroscopy of small organic molecules 155
8.1.11 IR spectroscopy 155
8.1.12 Melting point measurement 155
8.1.13 Thin layer and column chromatography 155
8.1.14 Software for data analysis and visualization 156
8.2 Peptide synthesis and characterization 156
8.2.1 Automated solid phase peptide synthesis 156
8.2.2 Cleavage and deprotection 156
8.2.3 Peptide purification 157
8.2.4 General handling of peptides 157
8.2.5 Peptide concentration determination using UV/Vis spectroscopy 158
8.2.6 Competitive titration using UV/Vis spectroscopy 158
8.2.7 CD spectra measurement 158
8.2.8 CD titration 159
8.2.9 CD Thermal denaturation 160
8.2.10 Determination of the acidity constant using CD spectroscopy 163
8.2.11 Fluorescence spectra measurement 163
8.2.12 Fluorescence titration 163
8.2.13 Isothermal titration calorimetry 164
8.2.14 NMR spectroscopy of peptides 164
8.2.15 Electron paramagnetic resonance spectroscopy 165
8.2.16 Structure prediction 165
8.3 Assays to determine enzymatic activity 166
8.3.1 Hydrolysis assay 166

8.3.2 Phenol oxidase assay 166
8.3.3 Cu(I)-catalysed azide-alkyne cycloaddition reaction 167
8.4 Sensor design 167
8.4.1 Synthesis of Fmoc-Hse-OH 167
8.4.2 Synthesis of Fmoc-Hse(Dmt)-OH 168
8.4.3 Late-stage functionalisation 169
8.4.4 Differential sensing 169
8.5 Synthesis of aspartate containing peptides 171
8.5.1 Synthesis of Fmoc-Asp(CSY)-O*t*Bu 171
8.5.2 Synthesis of Fmoc-Asp(CSY)-OH 172
8.5.3 Deprotection of Fmoc-Asp(CSY)-OH 173
8.5.4 Deprotection of CSY group containing peptides 174
9 Literature 176
10 Appendix 211
10.1 Abbreviations 211
10.2 Settings of the peptide synthesizer 213
10.3 Details on synthesis and characterisation of peptides 218
10.3.1 WW-CA 218
10.3.2 WW-CA-Nle 219
10.3.3 hPin1$_{WW}$-Nle 220
10.3.4 WW-CA-min 221
10.3.1 WW-CA-ANG 222
10.3.2 Trpzip2 223
10.3.3 Tz2H$_3$ 224
10.3.4 WW-CA(W34Coum) 225
10.3.5 Test peptide 226
10.3.6 WW-ADG 227
10.3.7 WW-PQBP1 230
10.3.8 SH3-NC 233
10.4 Calculation of the cost of the synthesis of Fmoc-Asp(CSY)-OH 236

10.5 Additional NMR spectra 238
10.5.1 Fmoc-Hse-OH 238
10.5.2 Fmoc-Hse(Dmt)-OH DIPEA salt 240
10.5.3 Fmoc-Asp(CSY)-O*t*Bu 244
10.5.4 Fmoc-Asp(CSY)-OH 248
10.5.5 WW-CA-Nle in absence and presence of Zn(II) 252
10.6 Additional FT-IR spectra 253
10.6.1 Fmoc-Hse(Dmt)-OH DIPEA salt 253
10.6.2 Fmoc-Asp(CSY)-O*t*Bu 253
10.6.3 Fmoc-Asp(CSY)-OH 254
10.7 Additional ESI-MS spectra 255
10.7.1 Fmoc-Hse-OH 255
10.7.2 Fmoc-Hse(Dmt)-OH DIPEA salt 256
10.7.3 Fmoc-Asp(CSY)-O*t*Bu 257
10.7.4 Fmoc-Asp(CSY)-OH 258
10.8 Additional CD spectra and CD thermal denaturation profiles 259
10.8.1 WW domains 259
10.8.2 Tryptophan zippers 280
10.9 Additional AlphaFold2 output plots 298
11 Danksagung 301
12 Selbstständigkeitserklärung 304
13 Curriculum Vitae 305

1 Introduction

Proteins, along with RNA, execute the programs encoded in DNA[1-3] and are involved in almost all essential functions of organisms, including provision of structural stability, through the cytoskeleton[4] or collagen,[5] or signalling through receptors and hormones,[6-8] defense through antibodies,[9-10] and catalysis through enzymes.[11-12] These diverse processes can be performed by polymers composed of only 20 amino acid residues, which are connected by amide bonds to form the peptide chains that can be several hundred monomers long and fold into complex three-dimensional structures.[13-14] The analysis of natural proteins has led to a better understanding of the sequence-structure-function relationships and the ongoing unravelling of the protein folding problem.[15-16] Proteins, especially enzymes, have been exploited by humans in technical processes for centuries mainly in food fermentation, before their structures and functions were known.[17-18]

Currently, proteins can be isolated from the source organism or produced in recombinant cells.[19-20] Furthermore, recent advancements in genetic engineering and chemical gene synthesis have made it possible to express proteins with almost any sequence, including non-canonical amino acids.[21-22] This is the basis for numerous advances in the development of therapeutics,[23] biomaterials,[24] enzymes[25] and biosensors.[26] Artificial proteins have the potential of being utilized as components, alongside other artificial biomolecules, to construct customized synthetic cells, which is the ultimate objective of synthetic biology.[18, 27-28]

The field of producing artificial proteins is known as protein design and comprises two main strategies: The first is the Top-Down approach, also known as protein engineering or protein redesign, in which an existing protein is used as a scaffold and mutations are introduced to alter its function.[29-30] If the sequence-structure-function relationship is at least partially understood, mutations can be introduced in a rational manner. However, it is also possible to randomly mutate the entire protein or a part of it, thus, generating a large library, and then use a selection strategy to identify the desired functional proteins. This process is known as directed evolution.[31]

The second strategy is the Bottom-Up approach, also known as *de novo* design.[29, 32] This involves building a protein scaffold from scratch, which requires detailed knowledge of the physical and chemical basis of protein folding and the sequence-structure relationship of the desired scaffold. The process of finding the matching protein sequence to a desired 3D structure is known as the inverse protein folding problem.[33]

Both design approaches can benefit from computational methods.[29, 34] For example, evolutionary information can be obtained through sequence alignments and statistical coupling analysis to aid in scaffold design.[35] Additionally, *de novo* designed active sites can be

incorporated into a suitable protein scaffolds selected from the protein data bank.[36] Significant progress has been made in solving the protein folding problem,[37-38] as well as the inverse folding problem.[39]

So far, the α-helical coiled coil is the only class of peptide scaffold with fully understood sequence-structure relationships.[40-41] This knowledge has led to the *de novo* design of a range of functional coiled coils that cover almost all areas of protein function, including the formation of self-replicating networks.[42-43] In contrast, less research has been conducted on globular β-sheet proteins, albeit significant progress has been made in the field of β-amyloids, where several functional variants have been designed.[44] However, the potential cytotoxicity of β-amyloids hampers their use in *in vivo* applications.[45] Additionally, few *de novo* β-sheet proteins with sensory and enzymatic functions have recently been computationally designed.[46-47]

Despite enormous progress, proteins are still large molecules with complex three-dimensional structures, and in the majority of cases, sequence-structure-function relationships are poorly understood. One way to improve our understanding of sequence-function relationships is to reduce complexity by using miniproteins.[48-49] These are traditionally categorized as a subgroup of peptides due to their size of less than 100 amino acids. For a peptide to be classified as a miniprotein, it must fold independently and cooperatively, adopting a stable three-dimensional structure with at least two secondary structural elements and one hydrophobic core. The structure is primarily stabilized by non-covalent interactions, with potential contributions from metal ion complexation and covalent cross-linking.[48] Miniproteins can be produced by solid-phase peptide synthesis due to their small size. This method allows for the easy introduction of non-canonical amino acids and other artificial modifications.[50-54] It is a useful technique for creating modified miniproteins with specific properties.

WW domains are a natural class of miniproteins of 30 to 40 amino acid residues, comprising a triple-stranded antiparallel β-sheet structure. They contain two conserved tryptophan residues and are domains of larger proteins that are involved in signal transduction. WW domains are not catalytically active but act as protein-protein interaction modules by binding to polyproline-rich sequences. Although the binding motif varies, the overall tertiary structure within this class is highly conserved.[55-56] It has been experimentally proven that WW domains have a high sequence space, meaning that several different sequences can adopt a WW domain-like fold.[57] This was demonstrated by designing several artificial WW domains based on sequence alignments. On average, the sequence homology between the designed and natural WW domains was only 36%.[58-60]

The hPin1 (human protein interacting with never in mitosis A 1) WW domain ($hPin1_{WW}$) is one of the most extensively studied WW-domains. It binds peptides that contain a phosphor-serine or -threonine and proline (pS/pT-P) motif and recruits them to the PPIase-domain of hPin1,

which then isomerizes the target peptide bond.[61] Several groups have resolved the three-dimensional structure of both the whole enzyme and the isolated WW domain using X-ray crystallography or NMR spectroscopy.[62-67] The hPin1$_{WW}$ serves as a model system for various biophysical studies, including the investigation of sequence-dependent stability or the role of hydrogen bonds in peptide folding stability, as well as folding kinetics.[68-69]

Tryptophan zippers are *de novo* designed 12 amino acid β-hairpin peptides that contain two antiparallel β-strands connected by a short loop. The structure is stabilized by four tryptophan residues on one side of the β-sheet, resulting in exceptional thermostability for such a small system.[70] They can be considered as miniproteins due to the presence of a hydrophobic core.[48] Several three-dimensional structures of tryptophan zippers were solved by NMR, and the peptides were used in various biophysical studies as a model systems.[71-73] Trpzip2, within this family, is ideal for peptide design due to its lack of aggregation propensity. It contains only canonical amino acids, and no aspartate, which is prone to aspartimide formation during SPPS.[74]

To convert a protein scaffold into an artificial enzyme or receptor, one option is to introduce a metal binding site. There are already several known *de novo* designed metallopeptides and proteins that have interesting structural aspects, catalytic activity, or sensory function.[75-78] However, it should be noted that most of these are unstructured peptides, α-helical scaffolds or β-amyloids. Functional metal-binding globular β-sheet miniproteins are rare. Therefore, designing them would significantly expand the toolbox of functional and easily accessible components for synthetic biology.

Both miniproteins, hPin1$_{WW}$ and Trpzip2, are ideal candidates for top-down design due to their known 3D structure, robust structure, and well-understood sequence-structure relationship. However, examples of functional miniprotein designs based on hPin1$_{WW}$ and Trpzip2 are rare. The aim of this work is to design metal-binding variants of hPin1$_{WW}$ and Trpzip2, characterize the structure, stability, and binding affinity of these miniproteins, and test their application in homogeneous catalysis and biosensing.

2 State of the art

The major part of Chapter 2 has been published in *ChemBioChem*.[79]

2.1 Sequence, structure and function of natural WW domains

WW domains are triple stranded antiparallel β-sheet miniproteins of 30 to 40 amino acids that are part of larger proteins which are involved in signal transduction (Figure 2-1A). They act as protein-protein interaction modules and recognize proline-rich sequences. The WW domain folds independently without requiring a disulfide bond, metal coordination site or other ligands in order to stabilize the 3D structure. WW domains are named after the two highly conserved Trp residues, which are 20 to 22 amino acids apart. These residues are crucial for the structure and function of the domain.[55-56, 80] There are four groups of WW domains that differ in their preferred ligand motifs, which include polyproline sequences containing Pro-Pro-Xaa-Tyr, Pro-Pro-Leu-Pro, Arg or pSer/pThr-Pro for Group I, II, III and IV, respectively.[55-56, 80-81] It has been reported, that the ligand binding properties of Group II and III are very similar and therefore are considered as one group.[82]

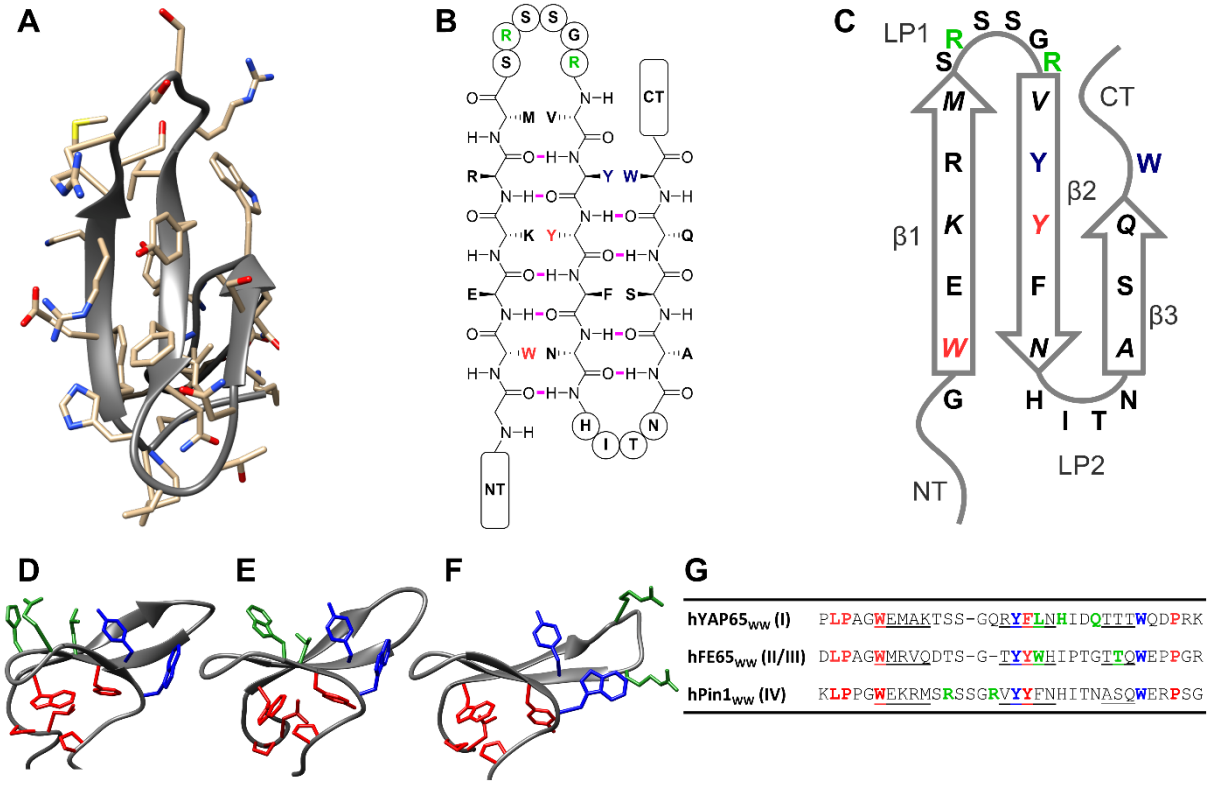

Figure 2-1: A) 3D Structure of a WW domain. As an example, hPin1$_{WW}$ is shown. PDB-ID: 1I6C. B) Schematic representation of the β-sheet peptide backbone of hPin1$_{WW}$ illustrating the backbone, C) Simplified 2D schematic representation of hPin1$_{WW}$. Residues in italics point behind the paper plane. D) 3D structure of hYAP65$_{WW}$ (Group I, PDB-ID: 1K9R), E) hFE65$_{WW}$ (Group II/III, PDB-ID: 2HO2) and F) hPin1$_{WW}$ (Group IV, PDB-ID: 1I8G). G) Sequences of the WW domains, residues belonging to β-strand are underscored. Abbreviations: NT: *N*-terminal region, CT: *C*-terminal region, β: β-strand, LP: loop. Colour code: hydrogen bonds (purple), conserved hydrophobic core (red), conserved proline binding site (blue), group specific residues for ligand recognition (green).

The folding and structure of WW domains rely on cross-strand hydrogen bonds (Figure 2-1B) and a conserved hydrophobic core composed of five amino acids. To enhance clarity, in addition to the classic 3D models, a simplified 2D schematic representation is used in this work (Figure 2-1C). The hydrophobic core includes a Leu and Pro in the *N*-terminal region (NT), a Trp in β-strand 1 (β1), a Phe or Tyr in β-strand 2 (β2), and a Pro in the *C*-terminal region (CT).[67, 83-84] Two loops (LP1 and LP2) link the β-strands and are crucial for ligand binding. Furthermore, the formation of LP1 is the rate-determining step in the folding of the WW domain.[85] Figure 2-1D-F shows three representative WW domains from each group and in Figure 2-1G the sequences are summarized. The hydrophobic core, shown in red, and the Pro binding site, formed by Tyr and Trp, shown in blue, are conserved, while other non-conserved residues on the surface form a second binding pocket and determine the ligand binding specificity, shown in green. Pro is bound in the conserved hydrophobic pocket *via* stacking interaction.[86] In Group I WW domains, a second pocket is formed by Leu in β2 and His and Glu in LP2 (Figure 2-1D).[84] Group II/III WW domains have an additional Trp in β2 that interacts with a Pro residue of the ligand, and a Thr residue in β3 that forms a hydrogen bond with the ligand backbone (Figure 2-1E).[83] Group IV WW domains recognize the negatively charged phosphorylated Ser or Thr residues *via* the two positively charged Arg residues in LP1 (Figure 2-1F).[67]

2.2 The WW domain of hPin1 as a model system to study protein folding

One of the most extensively studied WW domains is part of the human peptidyl-prolyl *cis-trans* isomerase known as 'protein interacting with never in mitosis A 1 (hPin1). The substrate are proteins that contain pSer/pThr-Pro motifs, but non-phosphorylated Ser/Thr-Pro motifs are not recognized by hPin1 and are instead recognized by other enzymes (Scheme 2-1).[61] Isomerization of the Ser-Pro peptide bond switches a protein between two distinct conformations, which is crucial for the protein's activity. Therefore, hPin1 plays a crucial role in various cellular processes, such as cell-cycle regulation, cell growth, neuronal function, immune response, and stress response.[61] Dysregulation of these pathways can lead to several diseases, including Alzheimer's and cancer. Therefore, hPin1 is an interesting drug target and several inhibitors are currently in development.[87-90] The *C*-terminal PPIase domain catalyses the isomerization, while the *N*-terminal Group IV WW domain is responsible for substrate recognition. The interplay between the two domains, also known as the ‘double-check' mechanism, is crucial for the function of hPin1.[63]

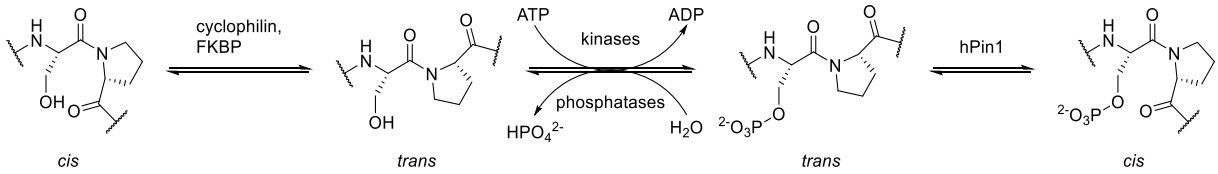

Scheme 2-1: Isomerization of Ser-Pro peptide bonds depending on the phosphorylation state of Ser.

The 3D structure of hPin1, as well as its isolated WW domain ($hPin1_{WW}$), has been analysed by several groups using NMR spectroscopy[65, 67, 91-93] and X-ray crystallography.[63, 66] Additionally, studies on protein folding have been conducted, and the relationship between sequence, structure, and function is well understood.[68] As discussed in the previous chapter, the hydrophobic core is responsible for stability, while the residues on the surface are responsible for ligand binding. The miniprotein $hPin1_{WW}$ is cooperatively folded with a melting temperature (T_m) of 59 °C,[94] which is remarkably stable for a 34-residue protein. A complete alanine scanning was performed to determine the influence of each single residue on folding.[94] As expected, the mutants Trp11Ala, Tyr24Ala and Pro37Ala are unfolded, since the conserved hydrophobic core is disturbed. Trp11 and Tyr24 can be mutated to other aromatic residues without loss of folding, but the stability is reduced by 10 K to 30 K. Interestingly, the mutant Asn26Ala is unable to fold due to the loss of several hydrogen bonds formed by Asn, as shown in Figure 2-2A.[66]

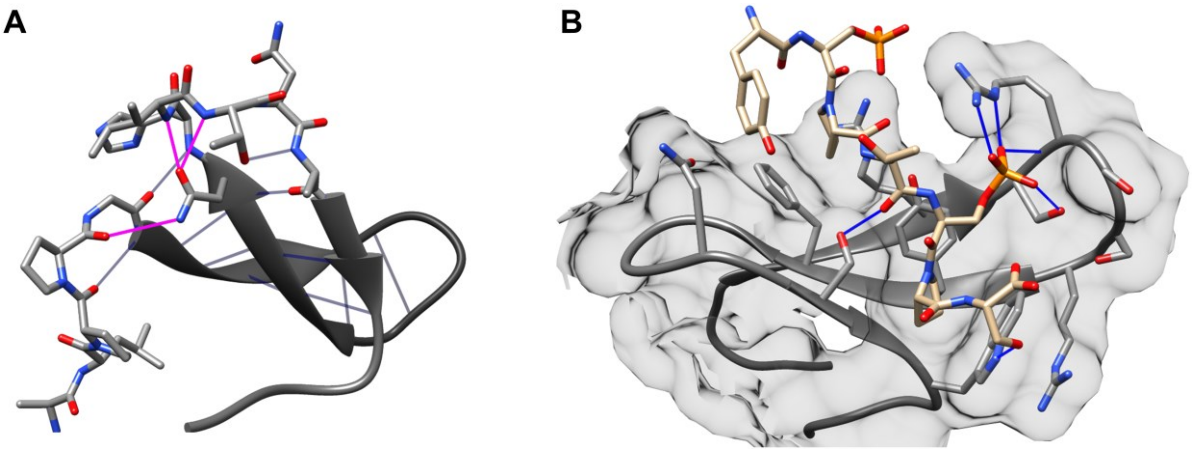

Figure 2-2: A) 3D structure of $hPin1_{WW}$ showing the hydrogen bonds between the peptide backbone of the loop regions with Asn26. B) 3D structure of a $hPin1_{WW}$–ligand complex (Tyr-pSer-Pro-Thr-pSer-Pro-Ser). (PDB-ID: 4GWT and 1F8A).

Mutating Asn26 to Asp destabilises the structure, resulting in a reduction of T_m to 36 °C.[94] This is because deprotonated Asp acts as a hydrogen bond acceptor, but not a donor, and carries a negative charge. Additionally, $hPin1_{WW}$ contains a second, smaller hydrophobic core on the surface of the β-sheet, which is formed by Arg14, Tyr23, and Phe25. Mutations to Ala at these positions led to a significant reduction in T_m by 20 K to 30 K, but the resulting peptides remained folded.[94] The two hydrophobic cores also shield the cross-strand hydrogen bonds from the surrounding water, thereby enhancing their strength.[95-96] The amide bonds in the

backbone have been replaced with ester bonds. Although solvated hydrogen bonds can be eliminated without affecting folding, buried hydrogen bonds are crucial for maintaining the structure. It is important to note that any removal of buried hydrogen bonds will result in a loss of structure. [95-96] Although Trp34 is highly conserved among all WW domains, a mutation at this position does not influence structural stability, indicating its importance for ligand binding but not for folding.[94] The two loops and the *C*-terminus from position 38 onwards are highly tolerant to mutations. The WW domain is connected to the PPIase domain *via* a long, intrinsically disordered loop that starts after position 38 and does not contribute to the WW domain structure. In X-ray crystal structures, this region is not resolved.[63]

LP1 plays a minor role in structural stabilization and is mutation tolerant, but its folding is the rate-determining step of WW domain folding. It is relatively long compared to other WW domains, consisting of six amino acids. Modified hPin1$_{WW}$ containing other LP1 sequences and artificial β-turn mimetics folded more quickly and were more stable than the native peptide but were unable to bind ligands.[97] Therefore, LP1 can be seen as a balance between stability and function, specifically the binding of phosphorylated peptides. Figure 2-2B shows the 3D structure of hPin1 in complex with a representative ligand, which interacts with the surface of hPin1$_{WW}$.[63] Y23 and W34 create a hydrophobic pocket for the ligand's Pro, while the Arg residues in LP1 bind to the phosphate group. Additionally, Phe25 and R14 can interact with the ligand, and the phosphate group interacts with the polar Ser residues and the backbone amides of LP1. The affinity of hPin1$_{WW}$ for several ligands has been reported to be in the µM range.[63]

Due to its small size, hPin1$_{WW}$ can be easily synthesised using solid-phase peptide synthesis, which facilitates the introduction of artificial amino acids.[51] Therefore, hPin1$_{WW}$ was used to study interactions between carbohydrates and aromatic residues. Glycosylated Asn residues and Phe analogues with altered electron density in the benzene ring were introduced at several positions. It was found that placing both in LP1 or LP2 enhances the thermostability of hPin1$_{WW}$. The NMR-derived structures indicate that glycosylation did not significantly perturb the overall structure.[98-99]

2.3 Design of WW domains

2.3.1 *De novo* Design

Mutation tolerance is an essential prerequisite for a scaffold to be useful in design. This has been demonstrated both experimentally and theoretically for the WW domain. A WW domain prototype was designed using a sequence alignment that included 23 WW domains from all three groups. The prototype did not show aggregation tendencies and exhibited a cooperative folding to unfolding transition with a T_m value of 44 °C. Additionally, it adopted a 3D structure typical for a WW domain (Figure 2-3A).[58] The probability of the appearance of a certain amino

acid at a certain position is shown in a simple sequence alignment, assuming independence from other positions, but in a folded and functional protein, residues interact with each other. Therefore, the degree of conservation at a certain position depends on other positions. The statistical coupling analysis method was developed based on these assumptions and applied to design WW domains.[60] A total of 43 designs were made, but only 12 were unfolded. The best hit CC45 (Figure 2-3B) exhibited a cooperative and reversible folding-unfolding transition with a T_m value of 66 °C, which is significantly higher than that of the WW prototype. The NMR-derived structure of CC45, as shown in Figure 2-3C, is typical of a WW domain and is very similar to the WW prototype. It was hypothesized that SCAs do not only contain structural, but also functional information. The designed WW domains were tested against their natural ligands and were found to bind them with similar affinity and specificity as their natural precursors.[59] Despite having only around 36% sequence identity with the natural WW domains, the designed domains were folded and functional.[60] This phenomenon, known as the sequence capacity of a scaffold, was also theoretically calculated for WW domains and found to be high.[57] The ability of multiple sequences to fold into the desired scaffold is a prerequisite in protein design. This allows for the introduction of several mutations while retaining the overall structure.

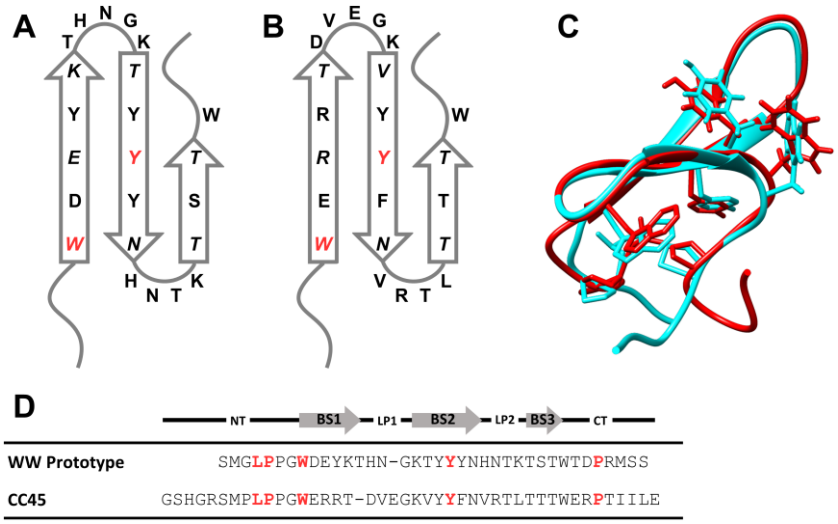

Figure 2-3: *De novo* designed WW domains. A) WW Prototype and B) CC45. C) 3D structural alignment of both WW domains. The side chains of the conserved hydrophobic core and the Pro binding site are presented. WW Prototype (red) and CC45 (cyan). PDB-ID: 1E0M, 1YMZ. D) Sequences of the designed WW domains.

2.3.2 Enhance Thermostability

Several microorganisms have adapted to a broad temperature range and are classified as hyper-thermophilic (>80 °C), thermophilic (80-60 °C), mesophilic (60-15 °C) and psychrophilic (<15 °C).[100] While humans require additional technical help to survive outside a narrow temperature range, these microorganisms have evolved to thrive in diverse environments. Heat stress is a significant issue for many existing organisms as it can cause protein

denaturation and loss of function, ultimately leading to cell death.[101] It is worth noting that some theories suggest thermal vents may be the birthplace of life and that the first organisms were thermophilic.[102] Therefore, it is highly interesting to study the proteins of thermophilic organisms and their adaption mechanism. Beside the fundamental interest, thermostable enzymes are widely used in biotechnological processes.[103] One well-known example is the polymerase chain reaction, which is mediated by the RNA polymerase of *Thermus aquaticus*, a bacteria that lives in hot springs.[104] Additionally, lack of thermostability can be problematic in protein design. When several mutations are introduced to a scaffold, the final construct may not be fully folded and may require repair.[105]

Most native WW domains are mesophilic, and some are thermophilic miniproteins with T_m values ranging from 19 °C to 68 °C.[106-107] Since hPin1$_{WW}$ has a T_m value of 59 °C[94] and is on the border between mesophilic and thermophilic, it was used to design thermostable variants. A common strategy is to cyclise a peptide by connecting the *N*- and *C*-termini if both are in close proximity. In WW domains, this is the case, and additionally, the NT and CT are part of the hydrophobic core. Figure 2-4A shows a cyclised WW domain with a T_m of 72 °C.[108] The NT was elongated by two glycine residues and a cysteine residue, while the CT contained a thioester. Cyclisation was achieved using native chemical ligation. Changes in the number of glycine residues led to destabilisation of the structure. The cyclised hPin1$_{WW}$ remained functional and bound to its natural ligand with similar affinities as the unmodified WW domain.[108] Introducing a cross-strand Trp pair (Figure 2-4B) achieved a further increase in T_m to 75 °C.[109] These Trp pairs are crucial for stabilising the fold of β-hairpins, as discussed later. The variant containing Met15Trp and Val22Trp mutations was thermostable but lost its function and did not interact with the natural ligand.[109] As previously discussed, LP1 is responsible for the folding kinetics of WW domains and also contributes significantly to their stability. The folding speed and thermostability of hPin1$_{WW}$ can be increased by exchanging LP1 with turn mimics, which will be discussed in detail later[97] or β-amino acids.[110] T_m values between 71 °C and 78 °C were achieved. When LP1 of hPin1$_{WW}$ was exchanged with LP1 of the FBP28 WW domain, which is one amino acid shorter, T_m increased to 78 °C (Figure 2-4C).[111] X-ray crystal structure analysis (PDB-ID: 2F21) revealed that the LP1 mutant has a structure that is very similar to the wild-type. As LP1 is responsible for recognizing phosphorylated Ser or Thr, all LP1 variants of hPin1$_{WW}$ were highly thermostable loss-of-function mutants.[97, 111] Combining the cross-strand tryptophan pair and LP1 redesign results in WWst34. This variant is hyperthermostable, with a T_m value of 94 °C, the most stable WW domain up to now (Figure 2-4D).[112] CD and NMR spectroscopic analysis suggest that the structure of WWst34 is similar to that of the wild-type, although the 3D structure has not been resolved.

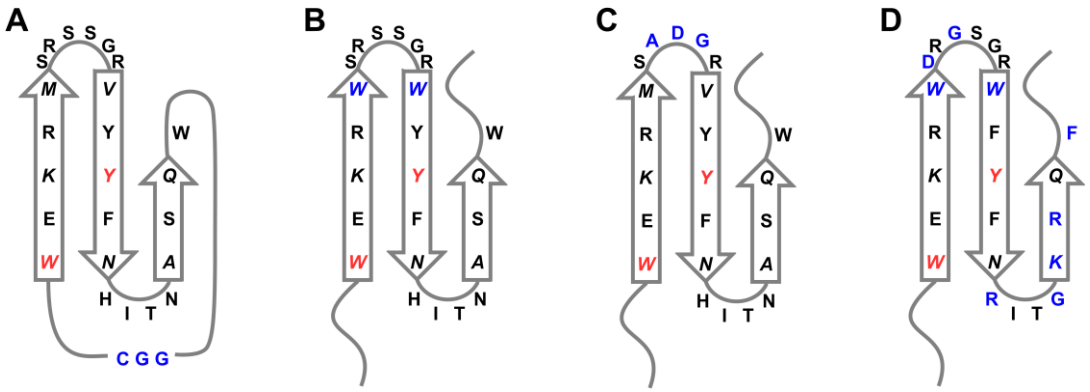

Figure 2-4: Thermostable variants of hPin1$_{WW}$. Mutated residues are shown in blue. A) Cyclisation of the *N*- and *C*-terminus. B) Additional cross-strand Trp/Trp pair. C) Mutate LP1 to that of FBP28$_{WW}$. D) Combining Loop engineering with cross-strand Trp/Trp pair.

2.3.3 Switchable WW domains

Biological function does not always require a rigid scaffold with high stability. Signal transduction, for example, relies on proteins that can adopt different conformations with varying levels of activity, sometimes simply on or off. Additionally, enzymes involved in metabolism are carefully regulated to maintain the concentration of metabolites within the physiological range. The switching can be induced by several mechanisms, including binding of a ligand or metal ions, posttranslational modifications, such as phosphorylation, changes in voltage, mechanical stress, and changes in the environment, such as temperature, ionic strength or pH.[113-119]

Although native WW domains bind to peptide ligands, they mostly maintain their conformation.[65, 67] One approach to induce switchability is to design a protein that is destabilized under certain conditions and therefore is not folded. Folding can then be induced by changing the environment. As previously discussed, the Trp residue in β1 is highly important for the hydrophobic core. If this Trp is mutated to Phe in the WW domain of hYAP, it is only weakly folded. This is because the interaction between Trp in β1 and Tyr in β2 is much stronger than that between Phe and Tyr.[120-121] Ligand binding to the mutant induced folding, and the affinity was weaker than for the wild-type, but in the same order of magnitude. (Figure 2-5A). In addition to the hydrophobic core, LP1 is also important for structural stability. A pH-switchable WW domain, p1-pHSW, was designed by modifying LP1 of a WWst34 variant.[122] This was achieved by introducing a histidine and a lysine residue (Figure 2-5B). At neutral or basic pH, the imidazole side chain was not protonated, and p1-pHSW adopted a WW domain-like structure with a cooperative folding-unfolding transition and a T_m value of 71 °C. Lowering the pH led to protonation of the imidazole side chain of His, which repulsed the also positively charged Lys side chain. The destabilization of LP1 results in the disruption of the entire fold of p1-pHSW, causing T_m to drop below 5 °C.[122]

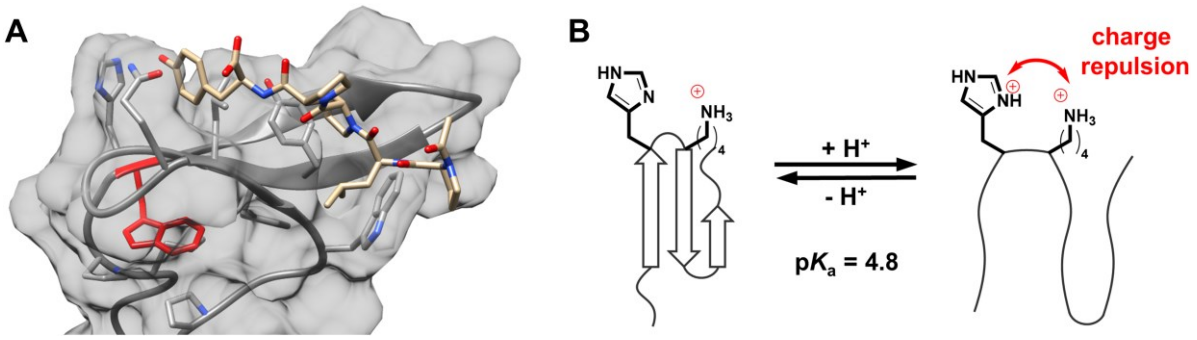

Figure 2-5: Switchable WW domains. A) 3D structure of hYAP65$_{WW}$ bound to its natural polyproline ligand (PDB-ID: 1K9R). In case the conserved Trp in the hydrophobic core (red) is mutated to Phe, the folding of resulting mutant is weakened and induced by ligand binding. B) pH Switchable WW domain p1-pHSW.

2.3.4 Design of WW domain mini-receptors

In a biochemical context, a receptor is a protein that recognises a specific signal, causing conformational changes. This information is then transferred into the cell. Receptors are switchable proteins that must consist of at least two parts: one responsible for signal recognition and a second responsible for signal transduction. Cellular receptors are highly complex molecules, often multi-domain proteins, with a quaternary structure.[123-124] The WW domain, being too small, only fulfils the recognition part, according to this definition.

In the context of biotechnology and sensor design, receptors are defined as the part that is responsible for selective recognition, e.g. binding of an analyte, while the part that converts this binding event into a detectable signal, e.g. change in fluorescence intensity, is called the transducer. The signal is then detected, amplified, processed and visualised by an electronic system. If the receptor is of biological origin, which can be a protein or even a whole cell, the device is called a biosensor.[125-126] According to this more technical definition, native WW domains can be considered miniprotein receptors as they specifically recognise ligands based on their group.

Using display techniques, the affinity of WW domains to their natural ligand could be enhanced or the specificity could be changed to other sequences.[127-130] It was also found that thermostability and binding affinity are uncorrelated. Even uncooperatively folded WW domain variants were able to bind more strongly to ligands than the fully folded native wild-type. Although display techniques have been successfully applied for peptide-ligand interaction in WW domains, they have not been used to generate WW domains that bind to other biomolecules. This is surprising, given that selection techniques are widely used to develop aptamers, RNA or DNA sequences, that bind to small molecules.[131-132]

Currently, only two WW domains have been designed that can recognise biomolecules other than peptides. In one study, a top-down design approach was used to place the DNA binding site of the cold shock protein B from *Bacillus subtilis* onto the surface of the FBP11 WW domain

(Figure 2-6A).[133] To achieve this, two Trp and two Lys residues were introduced on β2, LP2 and β3, and an additional Arg residue was placed at the NT region. It was anticipated that the negatively charged phosphate backbone of the DNA would form salt bridges with the positively charged Lys and Arg residues, while the nucleobases would interact with the indole residues *via* aromatic interactions. To increase stability, LP1 was mutated to Asn-Gly. This sequence is a known strong β-turn inducer, which will be discussed in detail in the next chapter and stabilize the β-sheet. The designed peptide Mut1 (Figure 2-6B) binds single-stranded DNA (ssDNA) with higher affinity than double-stranded DNA (dsDNA), with K_d values of 20 µM and 190 µM, respectively. It was hypothesized that the WW domain Mut1 was too large, resulting in inefficient interaction between the Trp residues and the nucleobases in the grooves of dsDNA. In contrast, the nucleobases in ssDNA are easily accessible. As a control experiment, it was demonstrated that Mut1 was incapable of binding to the natural polyproline ligands of FBP11. Similarly, FBP11 did not bind to single-stranded or double-stranded DNA.[133]

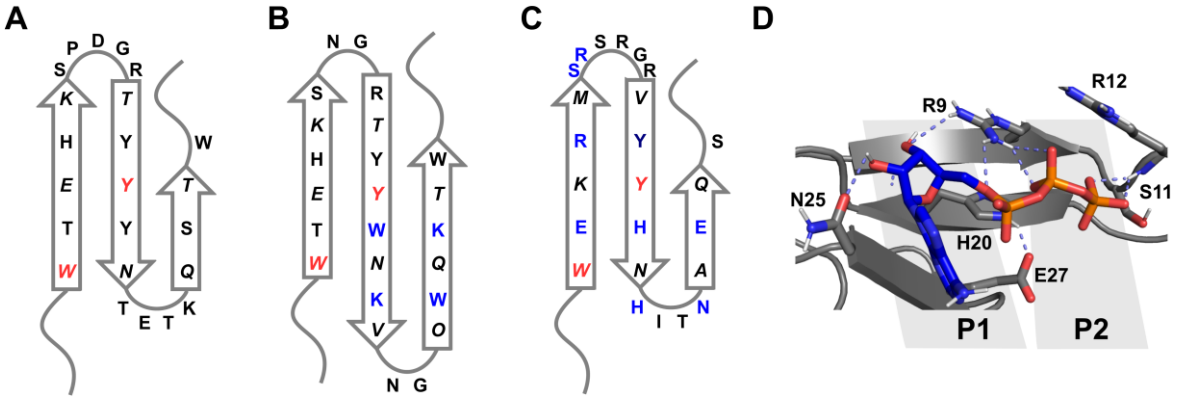

Figure 2-6: WW domains designed to bind DNA and nucleotides. A) Wild-type FBP1$_{WW}$. B) ssDNA binding WW domain based on FBP1$_{WW}$. Residues, that should interact with DNA, are shown in blue. The loops were engineered to increase stability, while the hydrophobic core(red) is left intact. C) ATP binding WW domain WW-2-10. The two ATP binding pockets, are formed by the residues shown in blue. C) 3D computational model of WW-2-10 bound to ATP. The ribose is bound by binding pocket P1, while the triphosphate interacts with Arg residues in P2. Adapted from Ref.[134] (CC BY-NC 3.0) with permission from the Royal Society of Chemistry.

The second design, a ATP binding WW domain, was discovered through a combinatorial approach.[134] To achieve this, hPin1$_{WW}$ was split at LP1 and the resulting *N*- and *C*-terminal fragments were connected to the *C*- and *N*-terminus of peptides that can form an antiparallel coiled coil. The formation of the coiled-coil brings both fragments in close proximity and induces folding. This reconstituted split-hPin1$_{WW}$ is also functional and binds to its natural ligand. A library of 24 combinations was designed by creating four *N*-terminal and six *C*-terminal fragments. The fragments were designed to include polar, aromatic, and charged residues that are expected to interact with different parts of ATP, including the nucleobase, ribose, and organophosphate, respectively. The library was screened for ATP binding, and to ensure selectivity, binding to other organophosphates, cAMP, phosphocholine, and phytate was also

tested. As a final test, the top hit WW-2-10 was synthesized as a full-length sequence and was found to bind to ATP with a K_d value of 14 µM. However, its affinity to all other substrates was 10 to 100 times weaker (Figure 2-6C). Although WW-2-10 was less thermostable than $hPin1_{WW}$, it still exhibits a cooperative folding-unfolding transition with a T_m value of 37 °C. A 3D model of WW-2-10 was generated using Rosetta, and AutoDockVina was used to dock the ATP to the model. Figure 2-6D shows that the triphosphate is bound in a positively charged pocket, while the ribose is bound to a polar pocket *via* hydrogen bonds. These two pockets also explain the selectivity; as other substrates can only interact with one of them.[134]

2.4 Sequence, structure and function of β-hairpins

β-Hairpins are short peptides, typically consisting of 10 to 20 amino acids, that comprise two antiparallel β-strands connected by a turn (Figure 2-7A).[135] The β-sheet is twisted and stabilized by cross-strand hydrogen bonds, as illustrated in Figure 2-7B and C. A simplified 2D representation of the structure, as shown in Figure 2-7D, will be used, similar to the WW domains. In nature, β-hairpins are abundant and often part of larger β-sheet containing proteins. However, unlike WW domains, they are not always able to fold independently and are therefore not considered a domain.[48]

The PDB lists over 49,000 proteins that contain β-hairpins.[136] Therefore, it is not possible to narrow down their natural functions, as each β-hairpin is adapted to the function of the protein to which it belongs. A subset of natural β-hairpins is not part of a larger protein, folded independently and stabilized by up to four disulfide bonds.[137] These hairpins are a component of the innate immune system and function as antimicrobial peptides.

In the early days of β-hairpin design, short peptides were synthesized based on sequences found in β-sheet proteins. However, these peptides were found to be unfolded. Subsequent mutation studies and structural analysis, mostly using NMR spectroscopy, have revealed the rules for designing stable and cooperatively folded β-hairpins step by step.[48, 71-73, 135] In general, amino acids with a high propensity for turn or β-sheet formation in the loop (LP) and the two β-strands (β1 and β2), respectively, are preferred. Additionally, an alternating pattern of hydrophobic and polar amino acids in the β-strands is advantageous. In addition to this broad overview, which generally applies to all types of β-sheet proteins, the proper placement of residues at specific positions in the β-hairpin is crucial.

Initially, the focus was on designing the loop. Statistical analysis revealed that amino acids such as Gly, Pro, Asn, Asp, and Ser are commonly present. Comparison of 3D structures of natural proteins containing β-hairpins led to the development of a X:Y nomenclature, which provides information on the number of amino acids involved in the loop and the hydrogen bond pattern.[135]

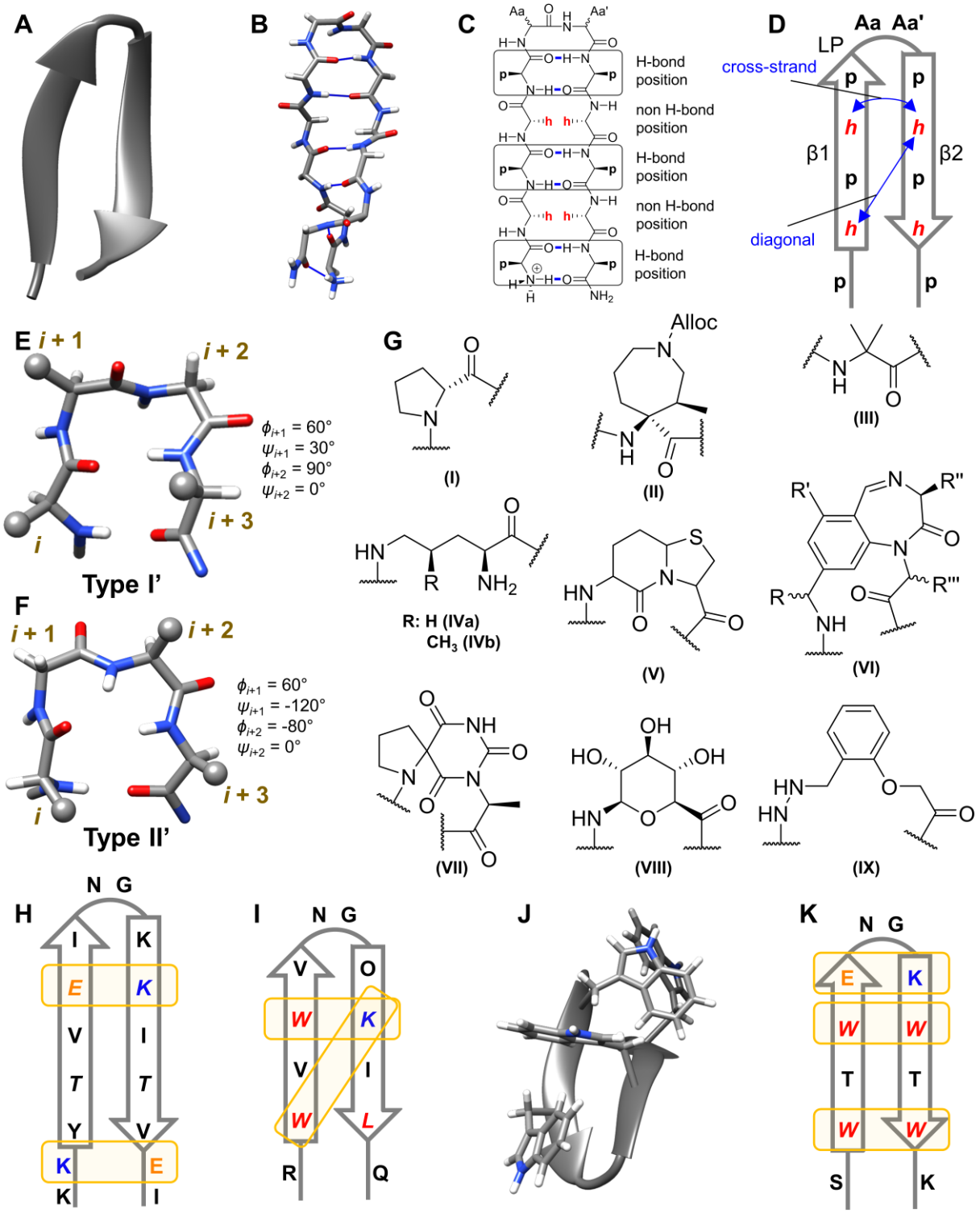

Figure 2-7: General structure of β-hairpins. A) Ribbon diagram of a β-hairpin (Trpzip2, PDB-ID: 1LE1). B) 3D structure of the backbone of Trpzip2 showing the cross-strand hydrogen bonds (blue). C) structural formula of a β-hairpin. D) Simplified two-dimensional schematic representation of a β-hairpin. β: β-strand, LP: loop. Residues in italics point behind the paper plane. E) 3D structure of a representative Type I' β-turn (PDB-ID: 1LE1) and F) Type II' β-turn (PDB-ID: 1LE0). G) Structures of β-turn inducing amino acids and β-turn mimics to place at position *i*+1 (I to III) or which replace both amino acids at position *i*+1 and *i*+2 (IV to IX). H) Two-dimensional representation of a β-hairpin stabilised by two salt bridges (β4) or I) by cation-π interactions. J) 3D model of Trpzip2 (PDB-ID: 1LE1) showing the T-shape geometry of the cross-strand Trp/Trp pairs and K) corresponding schematic representation. Yellow

boxes highlight interacting residues, that stabilize the structure. Positively charged interacting residues are shown in blue, negatively charged in orange and hydrophobic in red. O: L-ornithine.

In general, a loop is defined as an amino acid sequence that connects two secondary structure elements. Therefore, any amino acid that does not belong to an α-helix or β-strand, or any other secondary structure, is considered part of a loop. Due to historical reasons, some define a residue as belonging to a β-sheet if its C=O or N-H is involved in typical hydrogen bonds with a residue located on the neighbouring β-strand.[138] However, others only consider the residue as part of the β-sheet if both its C=O and N-H are involved in hydrogen bonding.[139] The X:Y system combines both definitions, where X is the number of residues in the loop according to the first definition and Y according to the second definition.[140] There are two cases for β-hairpins: The two residues at the end of the antiparallel β-sheet form two hydrogen bonds. In this case, both definitions yield the same number of residues that belong to the loop and X=Y. However, in the other case, only one hydrogen bond is formed between the two residues at the end of the β-sheet. Therefore, in the first definition, they are still counted as part of the β-sheet, but according to the second definition, they belong to the loop and Y=X+2. Applying this system to WW domains shows that LP1 is mostly a 3:5 loop.[111] However, LP1 of $hPin1_{WW}$ is an exception and forms a 4:6 loop, which is important for function.[67] For β-hairpins, 2:2 is the most abundant loop.[135]

This type of nomenclature does not take into account the conformation of the residues. Therefore, a system of "turn" nomenclature has been developed, which cannot be discussed exhaustively, since there are several definitions and recently the classical rules of nomenclature[141] have been challenged by new findings.[142] In short, turns are defined as sequences that reverse the direction of the polypeptide chain. Turns can therefore be seen as a subcategory of loops, and a loop can consist of more than one turn motif. The first residue belonging to the turn is called *i* and the last *i*+*n* and both residues are connected by at least one backbone hydrogen bond (C_i=O···H-N_{i+n} or N_i-H···O=C_{i+n}) or the α-C atoms (α-C_i and α-C_{i+1}) are less than 10 Å (or 7 Å) apart, if no hydrogen bond is observed. Therefore, counting is similar to Y nomenclature and Greek letters are used depending on the number of residues (*n*+1)[141] In β-hairpins and also in natural proteins, the β-turn is the most abundant. It contains four residues and a C_i=O···H-N_{i+3} hydrogen bond. Depending on the conformation of the *i*+1 and *i*+2 residues, 9 subcategories are known, defined by the dihedral angles ϕ_{i+1}, ψ_{i+1} and ϕ_{i+2}, ψ_{i+2} and designated by Roman numbers. The most common β-hairpins are the Type I' and II' β-turns (Figure 2-7E, F). The Type I and II β-turns play a minor role and in their case the signs of all dihedral angles are reversed.[135]

In Type I' β-turns, the most abundant amino acid at *i*+1 is Asn, while at *i*+2 Gly is found. This is reversed in Type II' β-turns (Gly-Asn).[135] The induction of β-turns can also be achieved by non-canonical amino acids and small organic molecules, known as β-turn mimics.[143-144] Since

high stability is required for pharmaceuticals, β-turn mimics have been intensively researched.[145] Placement of D-amino acids, most commonly D-Pro (Figure 2-7G, I), at position *i*+1 induces highly stable Type II' β-turns. At position *i*+2, Gly or L-Pro can be placed.[146-148] A similar effect can be observed when *N*-methylated D-amino acids[149] or quaternary amino acids (Figure 2-7G, II) are used.[150-152] Other non-canonical amino acids that mimic the β-turn at the *i*+1 and *i*+2 positions are α-aminoisobutyric acid (Figure 2-7G, III),[153] δ-linked L-ornithine (Figure 2-7G, IVa)[154] and γ(*R*)-methyl-ornithine (Figure 2-7G, IVb).[155]

In addition to non-canonical amino acids, several small molecules are known that replace both amino acids at the *i*+1 and *i*+2 positions, including thiaprolines (Figure 2-7G, V),[156-157] benzodiazepine (Figure 2-7G, VI)[158-159] spiro compounds (Figure 2-7G, VII)[160] and carbohydrate-based molecules (Figure 2-7G, VIII).[161-162] Several other structures, including light-switchable scaffolds such as azobenzene, will be discussed in more detail later.[143-145] All of the small molecule β-turn mimics presented require multi-step synthesis. A shortcut has been found using a ligation method, which requires only commercially available reagents and standard SPPS methods (Figure 2-7G, IX).[163]

A well-defined turn is not sufficient for the formation of a cooperatively folded β-hairpin. Statistical analysis showed that aromatic and β-branched amino acids, such as Phe, Tyr, Trp and Val, Ile or Thr, are common in β-sheets, but the exact position of the residues is highly important because of side chain interactions across the β-stands. There are two types of positions on a β-sheet, shown in Figure 2-7C.[135] In a hydrogen-bonded position (HBp), the backbone C=O and N-H of the cross-stranded amino acids form hydrogen bonds, whereas in non-hydrogen-bonded positions (nHBp) this is not the case. The distance between two cross-strand residues is different for HBp's and nHBp's and therefore different types of interactions are position dependent.[135]

Furthermore, the amino acid side chains of HBp's point in one direction, outside the paper plane in Figure 2-7C, whereas all the side chains of nHBp's point in the opposite direction. This resulted in two types of side chain-side chain interactions shown in Figure 2-7D: cross-strand and diagonal interactions.[135] Side chains of amino acids on an HBp and an nHBp cannot interact with each other. In general, polar residues are better placed on HBp's and hydrophobic residues on nHBp's. Salt bridges formed between charged residues, such as Glu and Lys, can be placed on nHBp's and HBp's and will stabilise the structure by cross-strand interaction (Figure 2-7H).[164] Uncapped *N*- and *C*-termini can also interact with each other.[165] Cation-π interactions between aromatic amino acids and Lys or Arg are best when placed diagonally to each other at nHBp's (Figure 2-7I).[166-167] Cross-linking of the two β-strands with disulfide bonds is also possible. The two Cys residues should be placed cross-stranded on an nHBp.[168] Interactions between two aliphatic or an aliphatic and an aromatic side chain occur cross-

stranded on HBp's and nHBp's, with the first being preferred.[72-73, 135] The strongest non-covalent stabilisation of β-hairpin can be achieved by placing two aromatic residues cross-strand at nHBp's, with the first nHBp after the loop being the best.[169] The aromatic rings interact edge to face, also called a T-shape (Figure 2-7J). This is preferred over π-stacking. The introduction of two Trp/Trp pairs into a β-hairpin led to the tryptophan zipper family (Figure 2-7K).[70] These small peptides are thermostable with T_m values around 60 to 70 °C and are cooperatively folded. The four Trp residues form a small hydrophobic core and shield the cross-strand hydrogen bonds from the aqueous environment, an effect already discussed for WW domains. Therefore, tryptophan zippers are considered as *de novo* designed miniproteins[48] and have been analysed in detail.[71-73, 121, 135, 170-172] Exchange of Trp to Tyr or Phe reduced the stability.[121, 169, 173-175]

Aggregation has always been a major problem in β-sheet design, as the structures with defined hydrophobic surfaces tend to self-assemble in aqueous solution. Furthermore, cross-strand hydrogen bonds can form between two independent β-sheets, especially, if both are flat. Therefore, twisted β-hairpins are less prone to aggregation.[176] In addition, a positive net charge can prevent aggregation.[73, 177] In general, β-hairpins can tolerate amino acids with low β-sheet propensities to a certain extent,[178] and β-sheets cannot be elongated infinitely. The combination of the two can increase the tendency to aggregate.[179]

2.5 Design of functional β-hairpins

2.5.1 Design of β-hairpin mini-receptors and inhibitors

Since β-hairpins are the first well-studied β-sheet peptides, once the structural features were understood and stably folded peptides were achieved, they were designed to interact with biomolecules. If the target is a small molecule or metal ion, the designed β-hairpin can be considered an artificial mini-receptor, but if the target is a protein, it is often intended to design a peptide drug that inhibits the protein function. There are numerous studies, especially on potential peptide drugs,[144, 180-186] and rather than give an exhaustive list, selected examples and the design principles will be discussed.

Based on β-hairpins containing cross-stranded Trp and Lys residues at the nHBp, a series of nucleotide-binding miniproteins were designed. The first resulting peptide WKWK (Figure 2-8A) recognised nucleoside triphosphates with an affinity of dTTP>GTP>ATP>CTP and K_d values of 0.27, 0.45, 1.4 and 3.7 mM, respectively, while the affinity for nucleoside di- and monophosphates was less pronounced. It was suggested that the two indole residues form a hydrophobic cleft to which the nucleobase is bound, while the positively charged Lys residues interact with the triphosphate group.[187-188] The 3D structure of a similar peptide, KIAβW, in complex with ATP (Figure 2-8B-C) was solved by NMR, supporting the hypothesis. The peptide-ATP complex shows a K_d of 20 µM, which is lower than that of WKWK, but it should

be noted that all experiments were performed at 5 °C instead of 25 °C. Interestingly, ATP binding did not increase the overall stability of the structure, because the cation-π interaction between Trp and Lys was weakened, whereas the aromatic Trp-adenine-Trp interaction increased structural stability.[189] Further mutations were introduced in the hope of increasing the binding affinity. Trp to Phe, Tyr or aliphatic amino acid mutations led to a decrease in binding affinity. The same was observed for the introduction of disulfide bonds, which at least increased peptide stability. In contrast, cross-linking of the β-strands by copper-catalysed azide-alkyne cycloaddition (CuAAC) increased both binding affinity and thermal stability. In addition, this peptide was also stable towards enzymatic degradation.[190] In contrast to nucleotides, the binding of WKWK to an RNA hairpin was much weaker with a K_d value >100 µM. By conjugating an aromatic intercalator (Int) to the *N*-terminus of WKWK (Figure 2-8D), the affinity was increased to a K_d of 3.7 µM. In a control, isolated Int was shown to interact weakly with dsRNA, indicating that the interplay between WKWK and Int is responsible for the strong binding.[191]

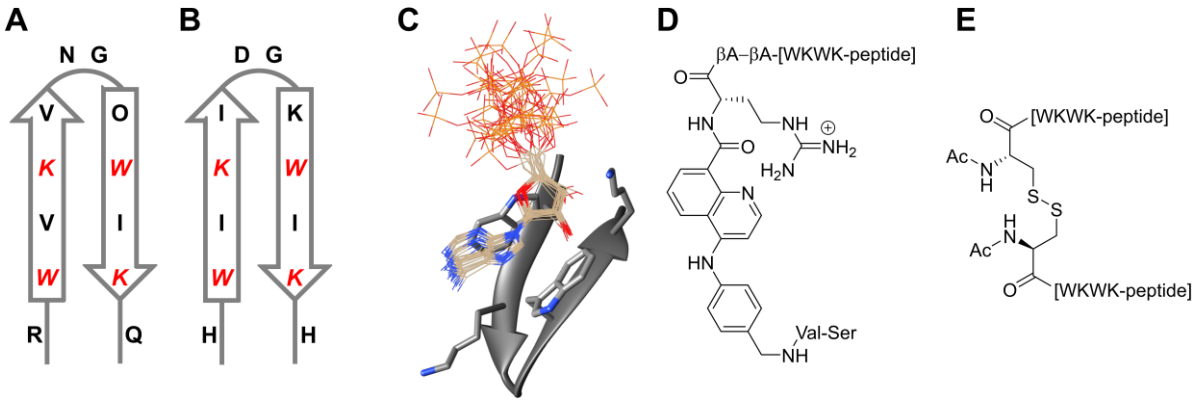

Figure 2-8: Designed β-hairpins that binds to nucleotides and DNA. A) Two-dimensional representation of the nucleotide binding β-hairpin WKWK. B) Two-dimensional representation of KIAβW, a nucleotide-binding β-hairpin. C) NMR structure of the KIAβW-ATP complex.[189] D) WKWK conjugated to an intercalator binds double-stranded RNA. E) DNA-binding peptide $(WKWK)_2$. Dimerization was achieved by additional Csy residues at the *N*-terminus forming disulfide bonds.

Flavin mononucleotide (FMN) could also bind to the Trp-Trp cleft *via* π-π stacking with a K_d of 1.4 mM, but reduction to $FMNH_2$ resulted in an increase in K_d to 25 mM. Binding of FMN to WKWK also decreases the reduction potential by -38 mV compared to free FMN.[192]

Clefts formed by aromatic amino acids are used by many proteins to recognise proline, as discussed in the case of WW domains, but WKWK did not bind PP helices. It was found that a Trpzip peptide, not designed for binding, was able to recognise PP helices. The Pro-binding cleft was formed by two internal Trp residues, Trp5 and Trp12. During binding, Trpzip underwent a conformational change that was not observed when WKWK bound to nucleotides. Therefore, the binding was described as an induced fit mechanism.[193]

To convert WKWK into a DNA-binding peptide, it was dimerised by linking both *N*-termini with disulfide bonds (Figure 2-8E). The dimer $(WKWK)_2$ bound to single-stranded (ssDNA) and double-stranded (dsDNA) DNA with similar K_d values of 3.5 μM and 4.6 μM, respectively, but this changed with salt concentration. Increasing the salt concentration increased the affinity for ssDNA over dsDNA. The explanation was the same as for the DNA binding WW domain. The nucleobases in dsDNA are less accessible than in ssDNA, but at low salt concentration the electrostatic interactions between the positively charged Lys residues and the negatively charged phosphate backbone dominate. At high salt concentrations, electrostatic interactions can be masked and nucleobase binding at the Trp-Trp cleft becomes more important. That the Trp-Trp cleft is responsible for binding was shown by an unfolded mutant containing an Asn to Pro mutation in the loop. The mutant binds to ss and dsDNA with an order of magnitude lower affinity. Interestingly, the D-enantiomer of $(WKWK)_2$ binds ssDNA with the same K_d value, but the affinity for dsDNA was slightly reduced.[194-195]

Binding to nucleic acids may be of interest in a medical context. A β-hairpin was designed to bind to the HIV TAR RNA, inhibiting the binding of TAR to the TAT protein.[196-198] In general, the design strategy is very similar for all β-hairpins intended as drug candidates. A library of cyclic and therefore highly stable and rigid β-hairpins mimicking the epitope of the natural binder is synthesised and subsequently screened for function, the binding affinity to the desired target protein or nucleic acid and the ability to inhibit the natural protein-protein or protein-nucleic acid interaction. Several examples are known, but unfortunately there is currently only one FDA-approved β-hairpin drug, Gramicidin S,[180] which acts as an antimicrobial drug by forming pores in the cell membrane and will be discussed later. β-Hairpins that inhibit protein-protein or protein-nucleic acid interactions are known but not in clinical use[144, 180-186, 199-200] As the design of β-hairpins that bind to nucleic acid has already been discussed, the next example will focus on protein-binding β-hairpins with potential use in cancer therapy.

In cells, growth and proliferation are tightly controlled. The Wnt signalling pathway is of great importance,[201] and one step in this pathway is the interaction of β-catenin with the activating ligand T-cell factor 4 (TCF4). The binding is mediated by a conserved β-catenin binding domain (CBD) of TCF-4, which is a mixed α-β domain. To inhibit the β-catenin-TCF-4 interaction, a CBD from E-cadherin (E-CBD) was used *in vitro*, which has an IC_{50} of 5.4 μM. Unfortunately, E-CBD is a 52-amino acid peptide that cannot cross the cell membrane and therefore cannot be used as a drug. To overcome this limitation, a β-hairpin was designed to mimic the β-sheet of E-CBD. As shown in Figure 2-9A-B, the two β-strands of E-CBD were cyclised through a D-Pro-L-Pro loop and a β-Ala-β-Ala linker. The initial design showed an IC_{50} of 16 μM. Performance was improved by introducing two cross-stranded Cys residues at one of the three positions (A, B, C). The Cys residues could be cross-linked by disulfide formation (ox) or bis-electrophilic linkers (b1 to b7) (Figure 2-9C). Initially, peptide C-b7 showed the best *in vitro*

performance with an IC_{50} of 4.8 µM but failed in the cell-based assay. Finally, A-b6 was the best *in vivo* inhibitor of Wnt signalling, but the IC_{50} determined *in vitro* was 8.5 µM. The key difference between the two peptides is the efficient cellular uptake of A-b6, whereas C-b7 could not cross the cell membrane and therefore remained inactive *in vivo*.[202]

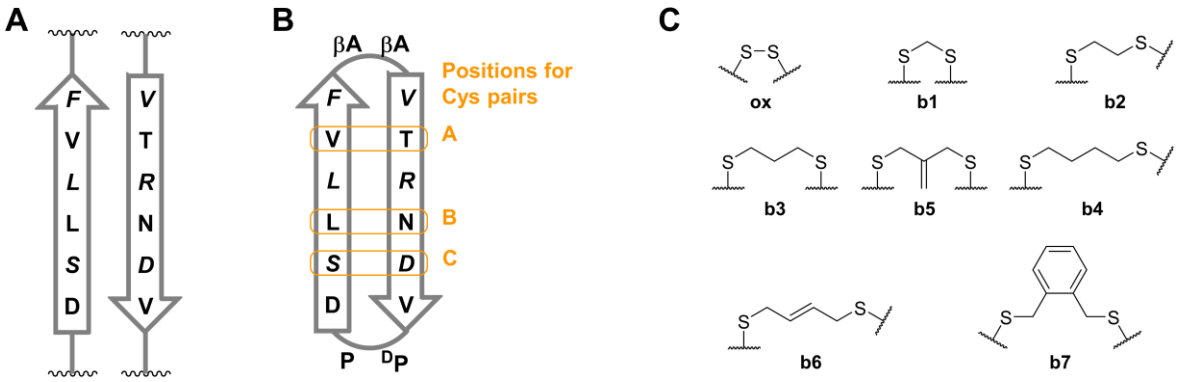

Figure 2-9: Inhibitor of the β-catenin-TCF-4 interaction based on β-hairpin peptides. A) Antiparallel β-sheet of E-CBD. B) Two-dimensional representation of the cyclic β-hairpin peptidomimetics of E-CBD. Positions for cross-linking to stabilise the secondary structure are highlighted in yellow. C) Cross-links to stabilise the structure of the β-hairpin peptidomimetics of E-CBD.

2.5.2 Enhance thermostability

An early strategy to enhance the thermostability of a protein scaffold is to introduce a metal-binding site at a position on the surface of the protein that ideally does not disrupt the protein structure and led to cross-linking of two parts of the protein.[203-205] Interestingly this strategy has not been applied to WW domains so far, but an example of a metal-ion-binding thermostable β-hairpin (WHC) has been reported.[206] WHC contains a His_2Cys_2 site located on the nHBp (Figure 2-10A). The affinity of the peptide for metal ions followed the Irving-Willimas series (Cu(II) > Ni(II), Zn(II)) as determined by mass spectrometry and competition experiments, but no absolute values were reported. WHC was indeed highly thermostable and T_m could not be determined as the structure did not change significantly at high temperatures, but the main contribution to stability is the chemical cross-linking of the Trp residues *via* Mannich dimerization (Figure 2-10B). This reaction is normally undesirable and occurs during TFA-mediated cleavage after SPPS.[207-208]

In natural proteins, cross-linking is mainly achieved through disulfide bonds. Using computational design, cyclic β-hairpins containing a disulfide bond were designed (Figure 2-10C, (NC_cEE_D1, PDB-ID: 5KX2)), that maintain their conformation at 6 M GdnHCl or 95 °C. No changes in the CD spectra were observed at these extreme conditions.[209]

The combination of disulfide bonds and cross-strand Trp-Trp interactions resulted in a folded and hyperthermostable β-hairpin (T_m = 87 °C) that lacks a loop (Figure 2-10D). By elongation the β-strands and introducing two cross-strand disulfide bonds, T_m could be increased to over 100 °C (Figure 2-10E).[210]

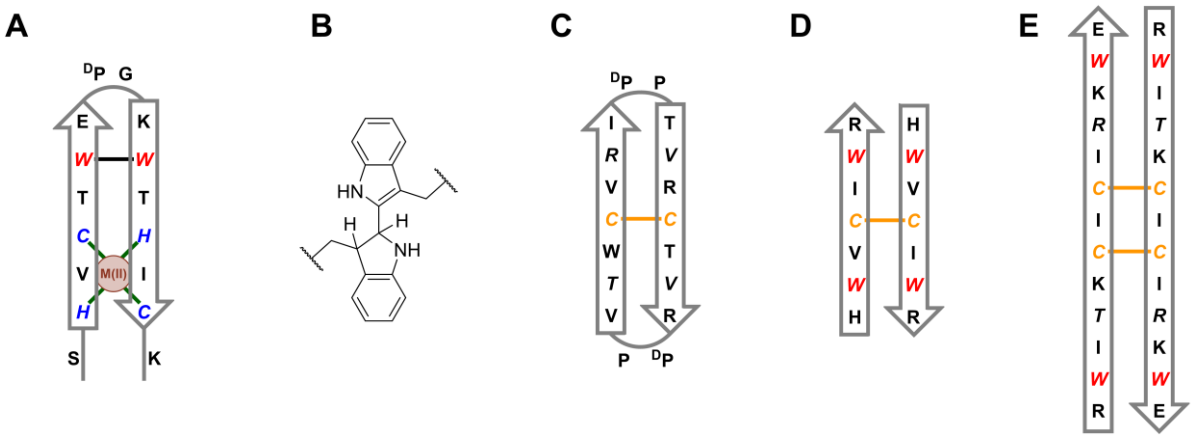

Figure 2-10: Thermostable β-hairpins and cross-linked β-sheets. A) Hyperthermostable metal-binding β-hairpin stabilised by Trp-Trp cross-linking. B) Trp-Trp cross-linking by Mannich dimerization. C) Cyclic β-hairpin stabilised by a cross-strand disulfide bond. D) Thermostable antiparallel β-sheet peptide stabilised by a cross-strand disulfide bond and two cross-strand Trp-Trp interactions. F) Hyperthermostable antiparallel β-sheet peptide stabilised by two cross-strand disulfide bonds and two cross-strand Trp-Trp interactions.

2.5.3 Switchable β-hairpins

As discussed in Chapter 2.3.3, conformational switching is of great importance for biological function. β-Hairpins have been used to pioneer photoswitchable peptides. Replacing the loop with a photoswitchable β-turn mimic is the simplest way to proceed. Figure 2-11A-C shows three examples of photoswitches, an azobenzene, a stilbene and a diarylethene. Only the *Z*-configuration of the photoswitch allows the formation of the β-hairpin structure. To date, several photoswitchable β-hairpins have been reported,[116, 211] and a medically relevant example will be discussed in detail.

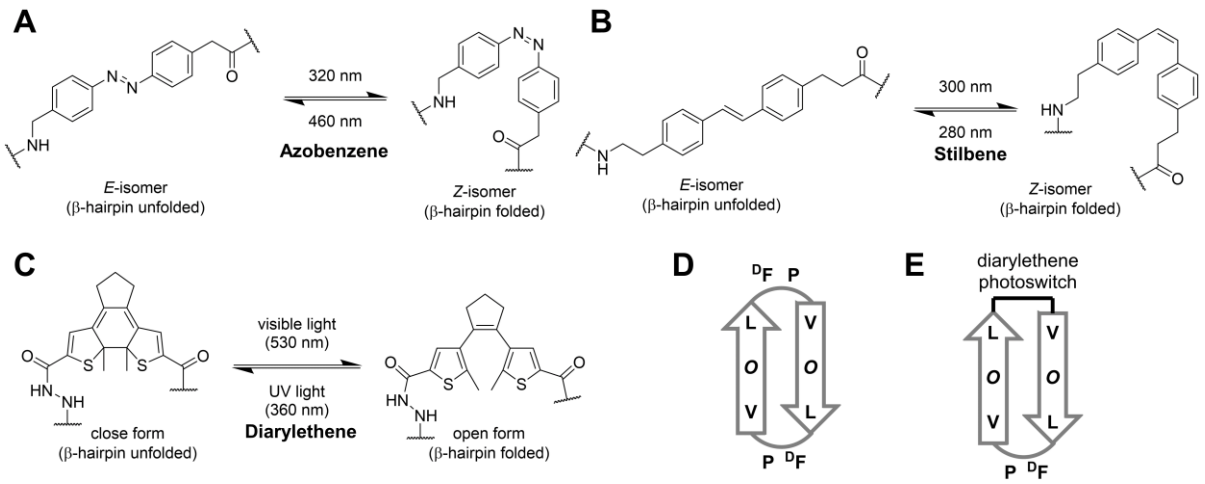

Figure 2-11: Photoswitchable β-hairpins. Structure of photoswitchable β-turn mimics based on A) azobenzene, B) stilbene or C) diarylethene. D) Two-dimensional representation of Gramicidin S, a cyclic antimicrobial β-hairpin peptide. E) Photoswitchable Gramicidin S variant containing a photoswitchable diarylethene based β-turn mimic.

Tremendous progress has been made in the field of in-body light delivery, allowing for localized activation of photopharmaceuticals.[212-213] This may be of interest for drugs with severe side

effects, such as gramicidin S (GS), the only FDA-approved β-hairpin peptide, which forms pores in cell membranes (Figure 2-11D). Although it is a potent antibiotic, it can only be used topically, as GS has general cytotoxic and haemolytic side effects. To create a photoswitchable peptide, a D-Phe-L-Pro-loop was replaced by a diarylethene moiety (Figure 2-11E). In the closed form, the β-hairpin is unfolded and irradiation with visible light converts the diarylethene to the open form, inducing folding and function. It can be switched off by irradiation with UV light. The unfolded GS were also shown to have fewer side effects. In addition, a library of photocontrolled GS derivatives was synthesised to optimise activity against the target, tumour cells and bacteria, while reducing side effects. Finally, animal experiments were used to test the cytotoxic activity *in vivo*. Photocontrolled GS was injected into cancer-bearing mice and activated locally by irradiating only the tumour tissue. The cytotoxic effect was indeed observed only in the irradiated tissue and haemolysis was reduced, but further studies are needed before clinical use.[214-217]

In cells, protein conformation and function are regulated by post-translational modifications.[218] To mimic this, a switchable β-hairpin, Trpswitch, was designed that contains a Lys and Ser residue on one β-strand at the nHBp's and two Trp on the other β-strand, again at the nHBp's (Figure 2-12A). Without any modification, the peptide is folded, and folding can be enhanced by Lys methylation due to stronger cation-π interaction with the Trp residues. (Figure 2-12B). In contrast, phosphorylation of Ser led to unfolding due to unfavourable anion-π interactions. Substitution of pSer by other negatively charged residues such as pThr, pTyr or Glu also led to unfolding.[219-220]

In addition to the switch between unfolded and folded states, the switch between two different conformations is of interest. Using an ambiguous amino acid sequence that can adopt β-hairpin and α-helix, it was shown that switching depends on the polarity of the environment. In water, the peptide adopts a β-hairpin structure, which is stabilised by the interaction of the aromatic side chains. Addition of lipid micelles switches the conformation to an α-helix, which has a hydrophobic site that interacts with lipids and a hydrophilic site that interacts with water (Figure 2-12C-D).[221-222]

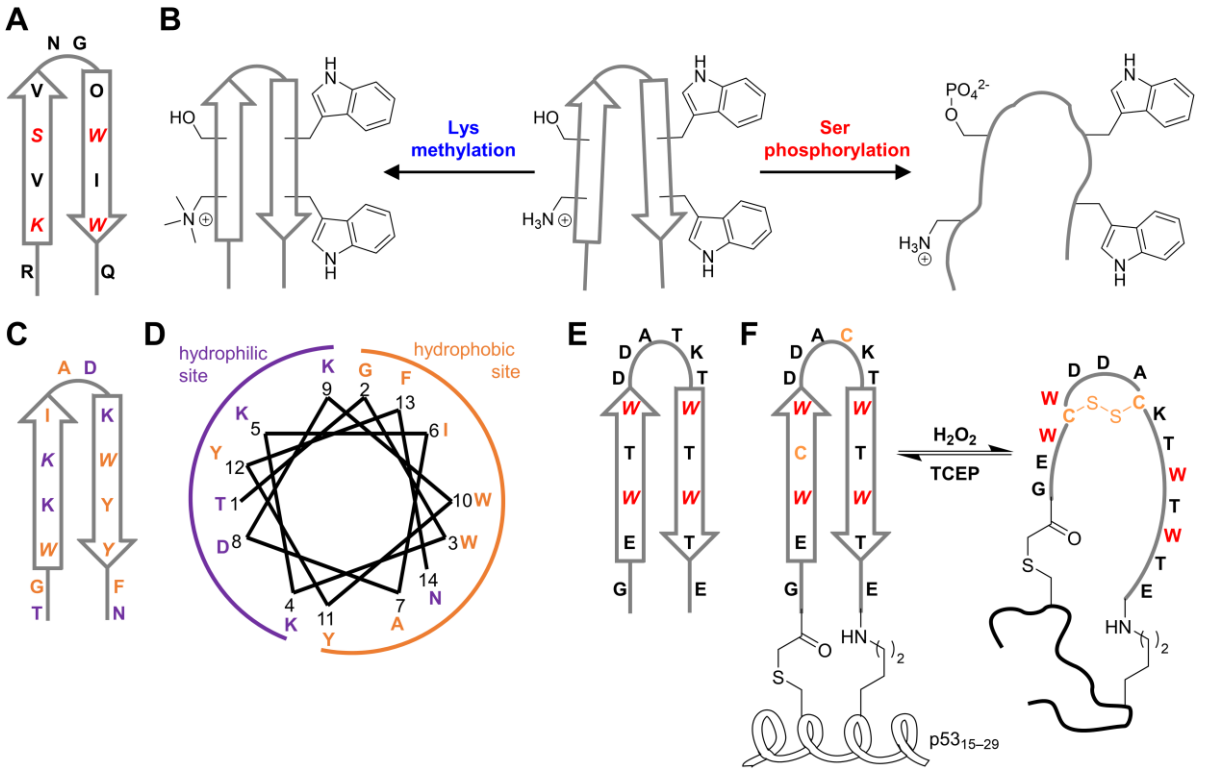

Figure 2-12: Switchable β-hairpins. A) Schematic representation of Trpswitch and B) the corresponding switching mechanism by post-translational modification: methylation of the Lys side chain stabilises the β-hairpin structure, while phosphorylation of the Ser side chain led to unfolding. C) Peptide, that switches between a β-hairpin in aqueous buffer and D) an α-helix in lipid micelles. E) Schematic representation of Trpzip4 and F) Trpzip4 derivate containing two Cys linked to αTMT2. In the reduced state, the β-hairpin is folded and functions as a helix staple for the α-helix. Oxidation led to disulfide bond formation, which disrupts the fold of the whole construct.

The formation and breaking of disulphide bonds is also a way of changing peptide conformation. Therefore, the previous examples in which disulphide bonds are responsible for structural stabilisation can be seen as switchable. However, there is also an example in which disulphide bond formation destroys β-hairpin folding. A functional switch was created by linking a Cys-containing variant of Trpzip4 (Figure 2-12E) to αTMT2, an α-helix derived from p53. Folding of the α-helix is induced by folding of Trpzip4 (Figure 2-12F). One Cys residue was placed in the first β-strand and the other residue in the loop. Oxidation with H_2O_2 led to disulfide formation and disruption of the β-hairpin structure, which subsequently disrupted the folding of αTMT2. The process was reversed using tris(2-carboxyethyl)phosphine (TCEP) as a reducing agent. It was shown that the switch is reversible and that the oxidation and reduction can be performed several times without degrading the peptide. The peptide was then used in a catch-release experiment. Magnetic beads were functionalised with the reduced peptide and gold nanoparticles were coated with hDM2, which can only bind to folded αTMT2. The combination of the two functionalised particles led to the immobilisation of the gold nanoparticles on the surface of the magnetic beads. After the addition of H_2O_2, the release of the gold nanoparticles was observed due to the unfolding of the designed peptide.[223]

2.5.4 β-hairpins as catalyst

Enzymes are one of nature's most powerful tools, combining unsurpassed selectivity with a rate enhancement up to the limit of diffusion. Enzymes are applied in several industrial processes and there is a huge interest in uncovering the mechanism of enzyme activity. The design of artificial enzymes can contribute to this endeavour and furthermore create enzymes which catalysed reactions that do not occur in nature.[36, 224-225] While no catalytic active native or designed WW domain is known, several β-hairpin based enzyme models were designed.

One of the best studied model reactions is the hydrolysis of activated esters (Figure 2-13A). Several α-helical and β-amyloid peptides have been reported as artificial esterases by incorporation of a catalytic triad or a Zn(II)-coordinating His_3 site.[42, 78, 226] Hydrolytically active Trpzip3 variants were designed by mutating T3 and T10 to His at the HBp's (Figure 2-13B).[227] Retention of the D-Pro-Gly loop yielded 3H10H-pG which was folded and exchange of D-Pro to L-Pro yielded 3H10H-pG which was intrinsically disordered. It was expected that the His dyad formed in 3H10H-pG would enhance the hydrolysis of *para*-nitrophenyl acetate, but it turned out that the unstructured peptide was more active. Computational modelling and NMR spectroscopy also suggested that the two His in the folded peptide do not interact with each other, whereas the interactions between the residues in the unfolded peptide remain unclear. However, it should be noted that the rate increase was only moderate compared to free His.[227] By placing the His residues at nHBp's next to Trp residues in a β-hairpin (Figure 2-13C), a peptide was obtained that folded in trifluoroethanol.[228-229] It was hypothesised that His can interact with electron-rich aromatic residues such as Trp or *O*-methyltyrosine in a T-shape interaction, which enhances nucleophilicity. Furthermore, the acyl-His complex formed during hydrolysis is positively charged and can interact with the aromatic side chain in a cation-π interaction (Figure 2-13D). Indeed, trifluoroethanolysis of *p*-nitrophenyl esters was observed ($k_{cat}/k_{uncat} = 9.4 \cdot 10^7$). Catalytic activity was further enhanced by placing three His residues on the nHBp's and leaving one Trp residue ($k_{cat}/k_{uncat} = 2.4 \cdot 10^8$). It was suggested, that a hydrogen-bond network formed between the His residues enhance the activity (Figure 2-13E, F).[228-229] These catalytic activities are difficult to compare with other designed peptides because the reaction was performed in TFE, whereas hydrolysis catalysed by artificial α-helical and β-amyloid enzymes was measured in aqueous buffer.[230-232]

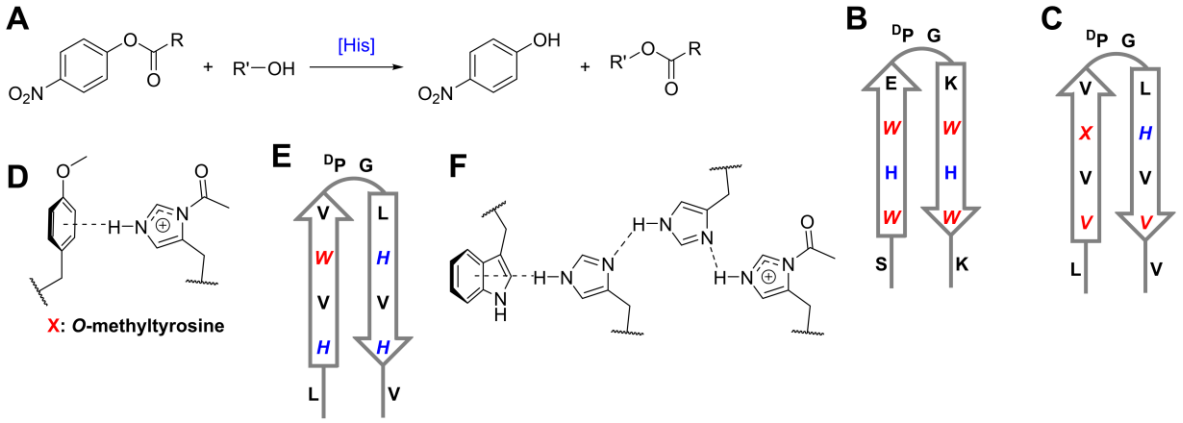

Figure 2-13: Hydrolytic β-hairpins. A) Hydrolase activity was studied using the hydrolysis of *p*-nitrophenyl esters as a model reaction. B) Two-dimensional representation of a hydrolytic active β-hairpin with a His dyad and C) in which His was activated by cation-π interaction with electron-rich aromatic amino acid side chains (X = Trp or *O*-methyltyrosine). D) Cation-π interaction of acylated His and *O*-methyltyrosine, an intermediate in ester hydrolysis. E) Schematic representation of a hydrolytic β-hairpin in which F) His is activated by cation-π interaction and hydrogen bonds between the His residues.

In nature, proteins containing metal cofactors play an important role in catalysis.[233-234] One of the most abundant natural cofactors is heme (Figure 2-14A), which is part of several proteins involved in oxygen transport (haemoglobin, myoglobin), electron transport (cytochrome *c*) and oxygenases (cytochrome P450).[235] Heme-binding β-hairpins have been designed by introducing a His residue that can bind to the central iron. The first designs were highly hydrophobic and only soluble in detergent micelles or artificial lipid membranes (Figure 2-14B).[236] In subsequent designs, two His-containing β-hairpins were linked by an aminoalkylcarboxyl linker between the *N*- and *C*-termini (Figure 2-14C), and the iron centre of the heme was axially coordinated by the two His. It was found that the length of the linker influences the binding affinity and catalytic activity. Short linkers such as Gly show a lower affinity (K_d = 8.9 µM), whereas longer linkers such as amino-octanoic acid increase the affinity (K_d = 0.4 µM). The oxidation of APTS by H_2O_2 was used as a test reaction (Figure 2-14D). The Gly-linked peptide was now more active than the amino-octanoic acid-linked peptide with k_{cat}/K_m of $2.91 \cdot 10^7$ M^{-1} s^{-1} and $1.15 \cdot 10^7$ M^{-1} s^{-1} respectively. Linking three β-hairpins, with the central β-hairpin containing two His residues, led to a construct that bound to two hemes with increased k_{cat}/K_m $4.35 \cdot 10^7$ M^{-1} s^{-1} when calculated for the whole construct. However, as the heme is the active catalyst, the overall activity decreased when the activity per heme was calculated.[237]

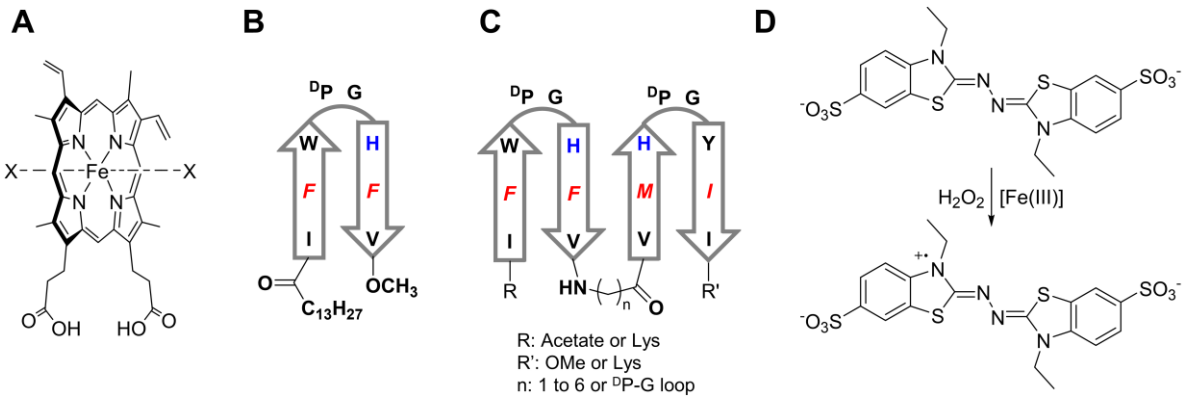

Figure 2-14: β-Hairpin-heme complexes. A) Chemical structure of heme. B) Schematic representation of a hydrophobic β-hairpin, which binds to heme *via* the His side chain (blue). C) Schematic representation of a β-hairpin dimer in which heme is bound in a sandwich-like complex by His residues. The β-hairpin units are connected *via* an aminoalkylcarboxyl linker between the *N*- and *C*-termini. D) Peroxidase activity was studied using the oxidation of ABTS by H_2O_2 as a model reaction.

Water soluble peptides were obtained by introducing Lys residues at the *N*- and *C*-terminus of the peptide (Figure 2-14C). While the affinity of an amino-octanoic acid-linked β-hairpin dimer for heme increased in water (K_d = 39 pM), the catalytic efficiency decreased to $0.73 \cdot 10^3$ M^{-1} s^{-1}. A slight increase in catalytic activity was observed when His was mutated to Cys ($2.75 \cdot 10^3$ M^{-1} s^{-1}), but this mutation reduced the heme binding affinity (K_d = 0.5 µM). A construct containing two His residues in each β-strand was able to bind to two hemes, but the binding affinity (K_d = 1.61 nM) and catalytic efficiency ($k_{cat}/K_m = 0.77 \cdot 10^3$ M^{-1} s^{-1}) were not improved.[238-240]

Beside natural cofactors, β-hairpins connected to artificial cofactors were reported. Conjugation of two β-hairpins at the *N*-terminus to a nickel-diphosphine complex with pendant amines produced a catalyst for electrochemical H_2 production (Figure 2-15A, B).[241-242] Compared to the artificial cofactor alone, the holo-peptide (Figure 2-15C) showed a twofold increase in activity in a water-acetonitrile mixture containing DMF and TFA. Exchanging R to K (Figure 2-15D) reduced the catalytic activity. Interestingly, the length of the β-hairpin plays a crucial role, with shorter β-hairpins (Figure 2-15E) being more active. Furthermore, the length of the linker is also important (Figure 2-15B). In case of n = 0, the free catalyst was almost inactive, and conjugation to peptides could not restore activity.[243]

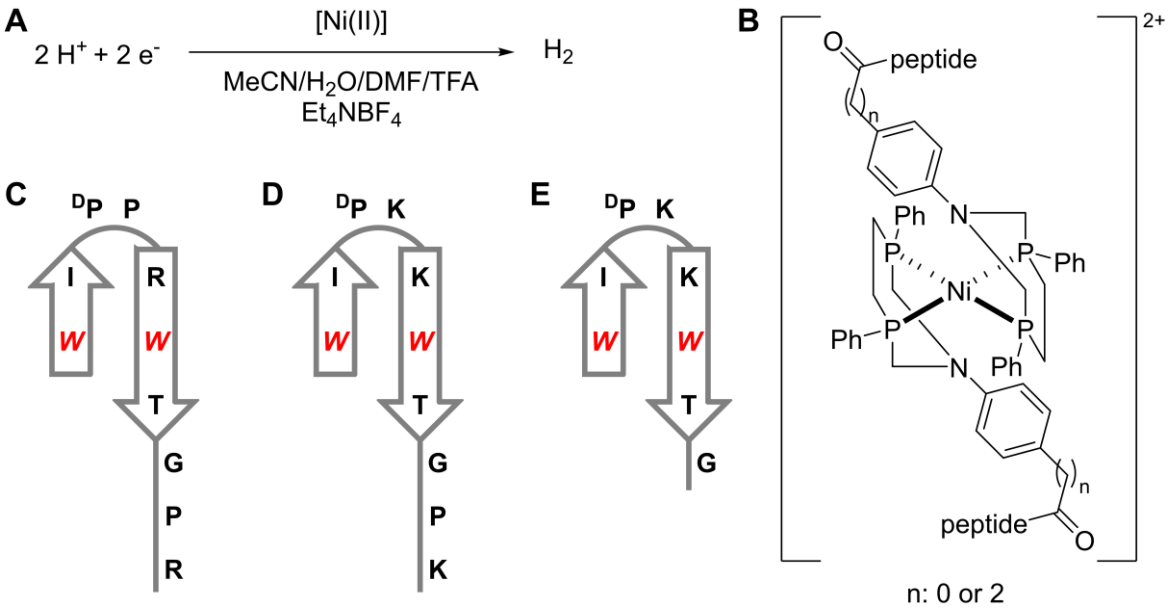

Figure 2-15: Designed β-hairpins linked to artificial Ni(II)-cofactors for electrochemical hydrogen production. A) Reaction equation of the Ni(II) catalysed proton reduction. B) Structure of the nickel-diphosphine complex with pendant amines. C) Schematic representation of the *N*-terminal linked β-hairpin (R10), D) P4K, R5K and R10K mutant of R10 (K10), and E) shortened version of K10 (K8).

3 Objectives

The aim of this work is to add functional globular β-sheet metallo-miniproteins to the synthetic biology toolbox through top-down design of hPin1$_{WW}$ and Trpzip2. The active site of carbonic anhydrase II,[244] which contains three histidine residues, is used as a natural model (Scheme 3-1). Although Zn(II) is bound to install biological function, it is known that other 3d metal ions such as Mn(II), Co(II), Ni(II) and Cu(II) can also bind, as well as Cd(II), Hg(II) and In(III).[245]

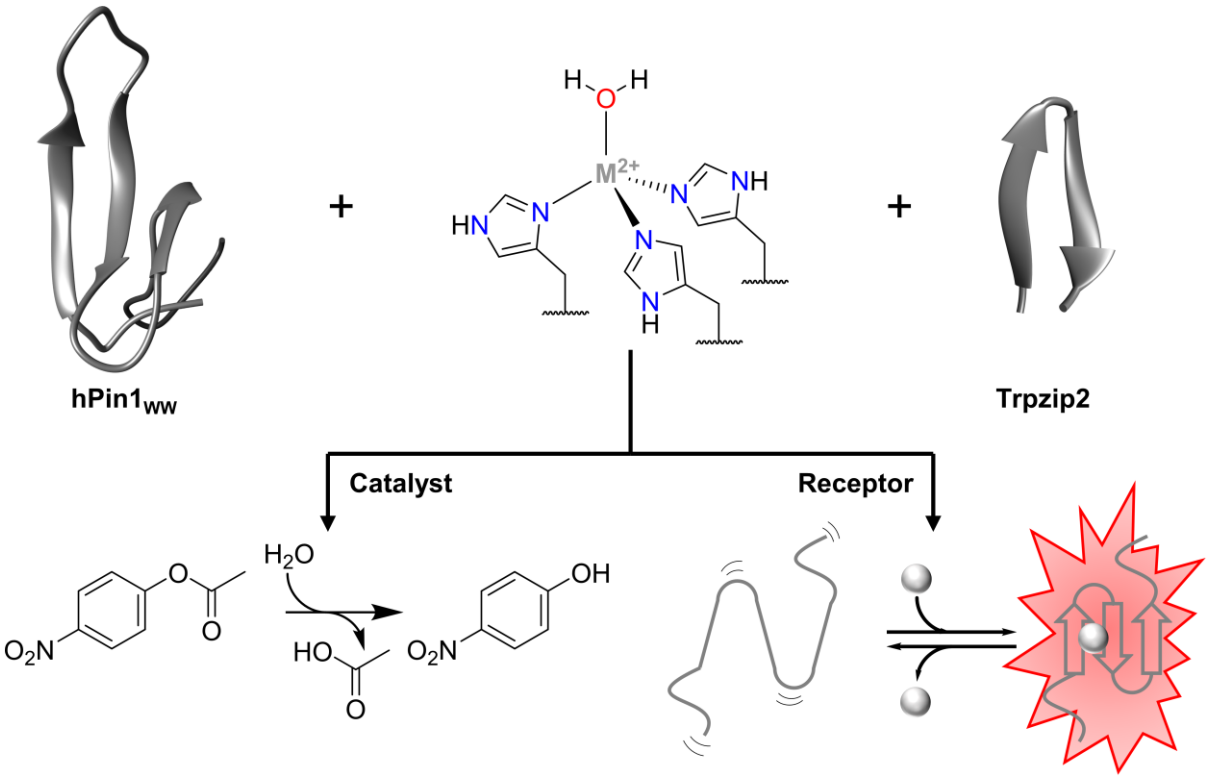

Scheme 3-1: Design of metal binding globular β-sheet miniproteins for catalytic and biosensory application. PDP-ID: 1I6C (hPin1$_{WW}$), 1LE1 (Trpzip2).

The hPin1$_{WW}$ and Trpzip2 variants, which contain a His$_3$ site, will be synthesized using microwave assisted SPPS,[52, 246] purified *via* reversed-phase HPLC,[247-248] and their identity will be verified using MALDI-TOF-MS.[249] The mutation rates for a 34-mer and a 12-mer are approximately 9% and 25%, respectively, which are both very high. It is also possible that additional mutations may be required. Before being applied in catalysis and biosensor design, it is necessary to analyse the structural integrity and metal ion binding affinity of the metallo miniproteins. CD spectroscopy and CD thermal denaturation are the methods of choice to study the secondary structure and thermal stability of peptides.[250-251] Additionally, CD titration will be used to determine the metal ion binding affinity.[252] Fluorescence spectroscopy is a valuable technique to observe structural changes upon metal binding in hPin1$_{WW}$ and Trpzip2, which contain the natural fluorophores tryptophan and tyrosine.[253-254] While CD and fluorescence spectroscopy provide only rough information about secondary structure and the overall conformation, NMR spectroscopy can provide atomic resolution[255-256] and will be

applied to analyse successful candidates in greater detail. The detailed characterization will enhance understanding of how mutations influence the structure of the miniproteins. Currently, only one metal binding tryptophan zipper is known,[206] and there are no reports on metal binding WW domains.

To test the catalytic activity of the designed metallo miniproteins, suitable reactions will be selected and tested based on the metal ion bound. As hCAII is the natural model, it is expected that the Zn(II) complexes might catalyse the well-known hydrolysis of *p*NPA.[257] If successful, other substrates, such as chiral esters,[258] less activated esters,[259] and β-lactam antibiotics,[260] will also be tested. It is important to note that other 3d metals can adopt different oxidation states and may act as redox catalysts, unlike Zn(II). A commonly used test reaction involves the oxidation of phenols to quinones using oxygen from air or hydrogen peroxide as a terminal oxidant.[261-263]

In addition to catalysis, biosensing is also an interesting application.[125] The designed metallo miniproteins can function as sensors, as the binding of metal ions can cause spectroscopically detectable conformational changes. This allows the development of a simple sensing system, especially when there are distinct signals in UV/Vis or fluorescence spectra. The chemical synthesis of miniproteins using SPPS allows the site-selective introduction of fluorescent dyes as a FRET pair.[264-265] This can be used to monitor changes in conformation, which correlate with changes in distances between residues.

4 Results and Discussion

4.1 Design of metal binding WW domains

The major part of Chapter 4.1 has been published in *ACS Synthetic Biology*.[266]

4.1.1 Design concept of a switchable metal binding WW domain (WW-CA)

The independently folding WW domain $hPin1_{WW}$ (Figure 4-1A, B) serves as a starting point for the design of metal binding miniproteins. As discussed in Chapter 2.1, the structure of $hPin1_{WW}$ is stabilised by two hydrophobic cores on each side of the β-sheet. The hydrophobic interactions are stable and permanent. By replacing one of the hydrophobic cores with a metal coordination site, the folding of the WW-domain scaffold should be controllable by the absence or presence of metal ions. By alanine scanning, Jäger *et al*. showed, that mutations in only one residue of the inner hydrophobic core (L7, P8, W11, Y24 and P37) completely destroy the ability of the WW domain to fold, while mutations in the outer hydrophobic core (R14, Y23 and F25) lead to a significant decrease in stability.[94] Therefore, it was reasonable to mutate the outer hydrophobic core in order to obtain a metal-responsive WW domain.

Next, naturally occurring metalloproteins possessing a metal coordination site on the surface of a β-sheet were studied to be used as a model to restructure the surface of $hPin1_{WW}$. A well-known representative is the enzyme human carbonic anhydrase II (hCAII) (crystal structure shown in Figure 4-1C).[244] Three histidines are located on a β-sheet (called His_3 site) and the imidazole side chains coordinate a Zn(II) ion in a tetrahedral geometry with water as fourth ligand. H94 and H96 coordinate Zn(II) *via* Nε and H119 *via* Nδ. Furthermore, Nδ of H94 and H96 form hydrogen bonds to the side chain of Q92 and the backbone of N244, respectively. Nε of H119 forms a hydrogen bond to the side chain of E117. The water molecule also forms hydrogen bonds to two water molecules and T199, which are not shown and very difficult to mimic, but are very important for the function: the catalysis of carbon dioxide hydration.[245] The pK_a of the Zn(II) bound water is reduced to 6.8. After deprotonation the Zn(II) bound hydroxide can nucleophilically attack CO_2. Still, CO_2 is not the only electrophile, that can be targeted. hCAII is known to catalyse other reactions, like ester hydrolysis or hydration of aldehydes and cyanamide.[267] These catalytic aspects are discussed in more detail in Chapter 4.4.1.

The His_3 site of hCAII was “copy-pasted” on the surface of $hPin1_{WW}$. Therefore, R14, Y23 and F25 were mutated to His. Additional mutations (R21Q and N30Q) were introduced to mimic the hydrogen bond pattern and to remove a second coordination site (H27S). The resulting peptide was dubbed WW-CA (schematic representation of the proposed structure in Figure 4-1D). WW-CA was synthesised using standard automated microwave-assisted solid-phase peptide synthesis and purified by HPLC. The identity was verified by MALDI-TOF-MS. Data of peptide characterisation can be found in Chapter 10.3.

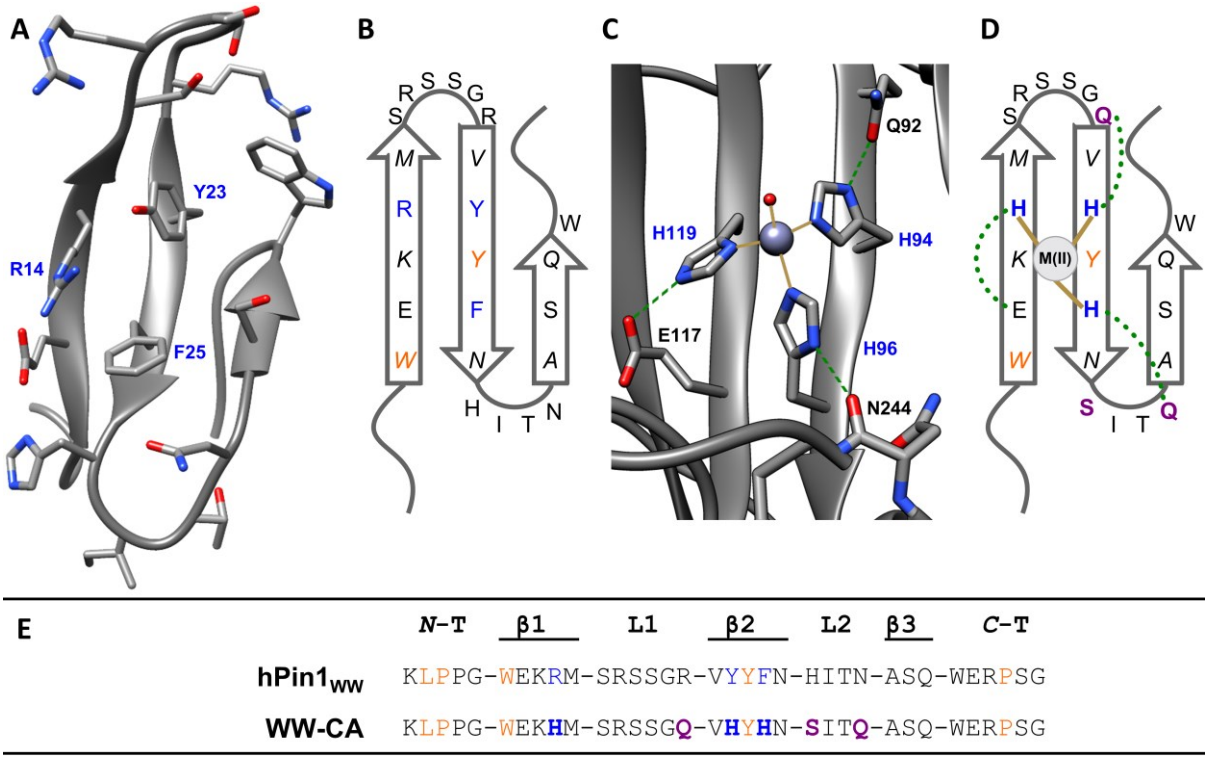

Figure 4-1: A) X-ray crystal structure of hPin1$_{WW}$ (PDB-ID: 4GWT). The residues of the β-sheet surface are highlighted. B) 2D schematic representation of the structure of hPin1$_{WW}$. Italic residues point below the β-sheet, orange: conserved amino acids of the inner hydrophobic core, blue: amino acids of the outer hydrophobic core. C) X-ray crystal structure of the active centre of holo carbonic anhydrase II (PDB-ID: 1CA2). Dotted green lines represent hydrogen bonds, golden lines represent coordinative bonds. D) 2D schematic representation of the anticipated structure of WW-CA. Blue: His$_3$ site, purple: additional mutations.

4.1.2 Influence of Zn(II) on the structure and stability of WW-CA

The structure and conformational changes were analysed by CD spectroscopy. Measurements were performed at pH 7.2 in MOPS-buffered solution. The CD spectrum of the apo-peptide (Figure 4-2) shows only a weak maximum at approximately 227 nm, the characteristic maximum for WW domains, due to the interaction of W11 and Y24. A minimum is observed at 202 nm. The addition of Zn(II) significantly altered the CD spectrum, increasing the intensity of the characteristic maximum and minimum. It can be concluded that the apo and the holo state adopt different conformations. Thermal denaturation experiments were used to analyse the stability of the holo and the apo state (Figure 4-2B). The maximum CD signal was followed over the temperature, which was varied from 0 °C to 98 °C. For WW domains it is common to assume a two-state transition[68] and a detailed discussion on the used equations can be found in Chapter 8.2.9. Furthermore, a known problem in thermal denaturation curve analysis is the description of the pre- and post-transition baselines.[251] It can be assumed, that the pre- and post-transition baselines are either temperature independent and therefore constant values or temperature dependent and are mostly described as linear functions or, in rare cases, parabolic functions.[268] In this work, CD thermal denaturation curves of WW domains were

fitted using two-state models with either assuming the pre- and post-transition baselines to be constant values or linear dependent on temperature change. All fits can be found in the Appendix (Chapter 10.8) and the best fits are shown in the Results and Discussion Chapter.

In the case of apo WW-CA, the signal of the maximum decreased rapidly with increasing temperature until the lower baseline was reached. Fitting a two-state model to the data (Chapter 8.2.9), did not give meaningful results for T_m. No aggregates were observed after the thermal denaturation experiments, but refolding only partially occurred, especially when heating and cooling were repeated (Figure 4-2C and D). In contrast, the WW-CA-Zn(II) complex showed a sigmoidal thermal denaturation profile. In this case, fitting using a two-state model gave a T_m value of 34 °C. The transition was broad, which is typical of WW domains.[94] However, aggregates were observed after thermal denaturation, indicating an irreversible process. In summary, it can be concluded that the apo-peptide shows an uncooperative folding-to-unfolding transition, whereas the unfolding process of the holo-peptide is cooperative.

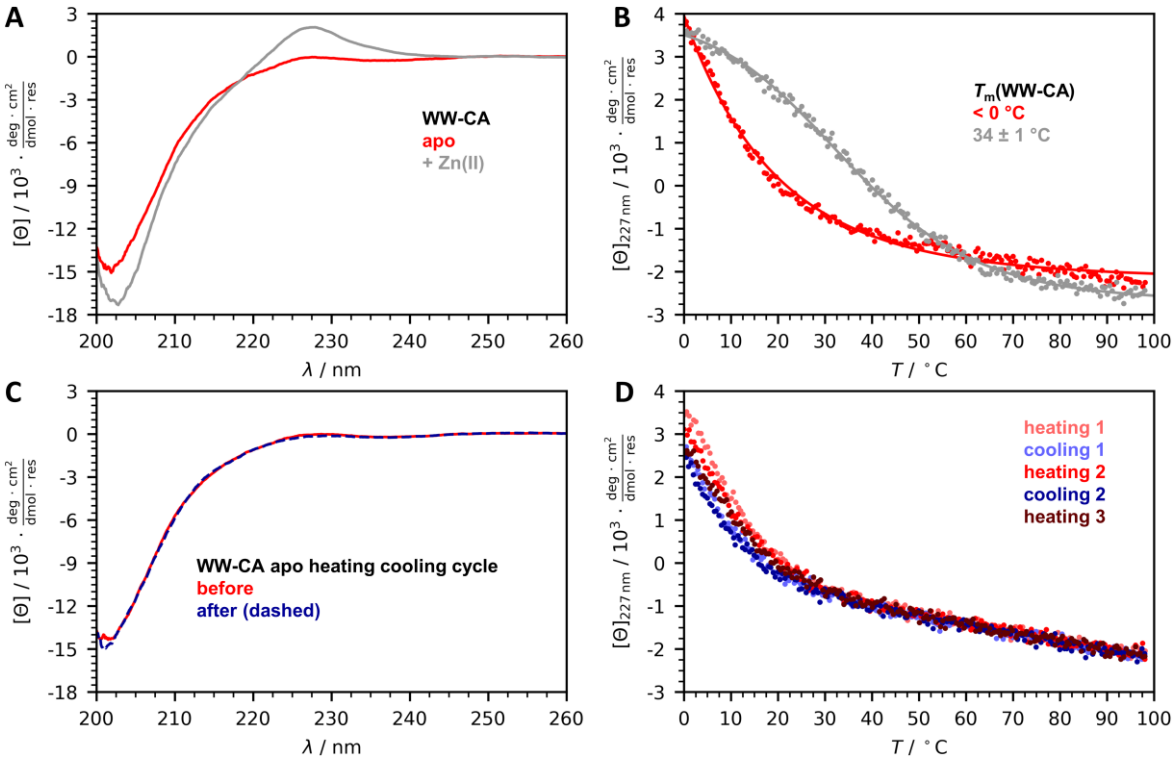

Figure 4-2: CD spectroscopic analysis of WW-CA. A) CD spectra at 20 °C and B) thermal denaturation analysis of WW-CA in presence and absence of Zn(II). C) CD spectra before and after the heating-cooling cycle and D) thermal denaturation and refolding curves of apo WW-CA. Conditions: 100 µM WW-CA, 100 µM $ZnSO_4$ (if present), 10 mM MOPS, 150 mM NaCl, pH 7.2, 1 mm cuvette.

The addition of Zn(II) also increases the ionic strength of the solution, which could affect the structure of WW-CA. Therefore, CD spectra of WW-CA were recorded at different NaCl concentrations. In the case of apo WW-CA, the spectra changed only marginally, but the characteristic maximum in the spectra of holo WW-CA increased with increasing NaCl

concentration (Figure 4-3). However, in the absence of NaCl, the spectra of the holo and apo states differ significantly. The plateau was reached at a NaCl concentration of 150 mM, therefore this concentration was maintained for all experiments. To exclude the possibility that apo WW-CA denatured during NaCl titration or that the order of Zn(II) addition influenced the structure of WW-CA, Zn(II) was added at the end to the apo peptide. The resulting spectrum was similar to that of holo-WW-CA at the same NaCl concentration.

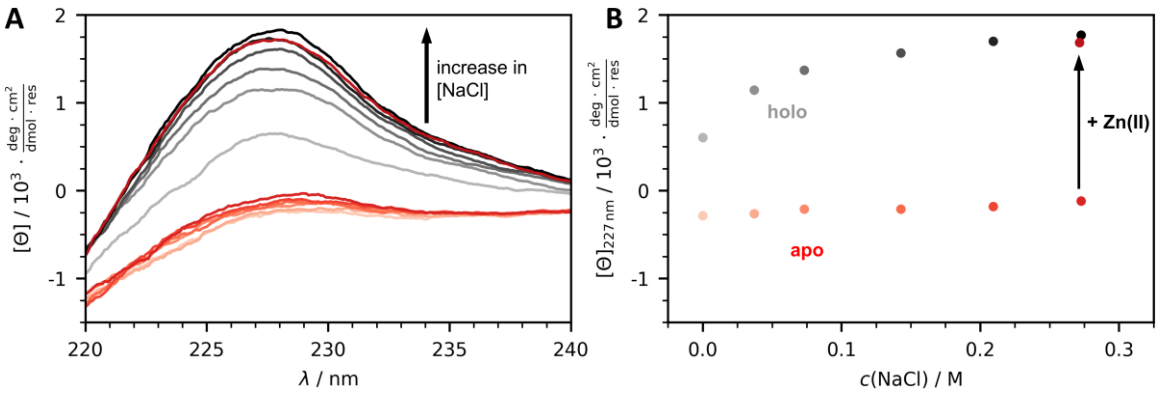

Figure 4-3: A) CD spectra of apo (rec) and holo (grey) WW-CA folding dependent on the NaCl concentration and B) resulting titration curves. Conditions: 10 µM WW-CA, 10 µM $ZnSO_4$ (respectively), 10 mM MOPS, pH 7.2 titrated with 3 M NaCl, 10 mM MOPS, pH 7.2, 1 cm cuvette, 20 °C. In case no Zn(II) was present 10 µL $ZnSO_4$ solution (2 mM) was added after the last titration point.

4.1.3 WW-CA is a Zn(II) and pH dependent switch peptide

Having demonstrated the ability of WW-CA to bind Zn(II) and change its conformation during metal binding, the reversibility of the Zn(II)-induced conformational change was analysed. For several metalloproteins it is known that removal of the metal cofactor leads to irreversible denaturation. The switch experiment was performed by alternately adding stoichiometric amounts of Zn(II) and EDTA to WW-CA. After each addition and 11 min equilibration, CD spectra were recorded (Figure 4-4A). Before Zn(II) was added, the characteristic CD spectrum of apo WW-CA was obtained. Zn(II) addition resulted in the already described increase of the exciton signal at 227 nm. After the addition of EDTA, the CD spectrum was again typical of the apo state. This process was repeated a total of five times without loss of signal intensity (Figure 4-4B), indicating Zn(II) binding being a reversible process and WW-CA being a Zn(II)-dependent switch. WW-CA is assumed to bind Zn(II) *via* the imidazole side chains of the three histidines (Figure 4-4C). Therefore, the Zn(II) binding should be pH sensitive, because the imidazole side chains should be protonated under acidic conditions thus losing the ability to coordinate Zn(II). To see if pH induced switching of WW-CA was possible, the WW-CA-Zn(II) complex was titrated alternately with 2 M HCl and 2 M NaOH. CD spectra were recorded after each titration step (Figure 4-4D). Initially the CD spectrum was typical of the holo peptide, after acidification the exciton signal was depleted. After neutralisation, the CD spectrum returned to its initial form. The pH dependent switching was repeated five times without any sign of

irreversible peptide denaturation. A closer look at the CD spectrum at low pH in the presence of Zn(II) revealed that the characteristic maximum was completely lost compared to the CD spectrum of the apo peptide at pH 7.2, where the exciton coupling signal is weak but visible. The pH switch experiment was therefore also conducted with apo WW-CA (Figure 4-4G).

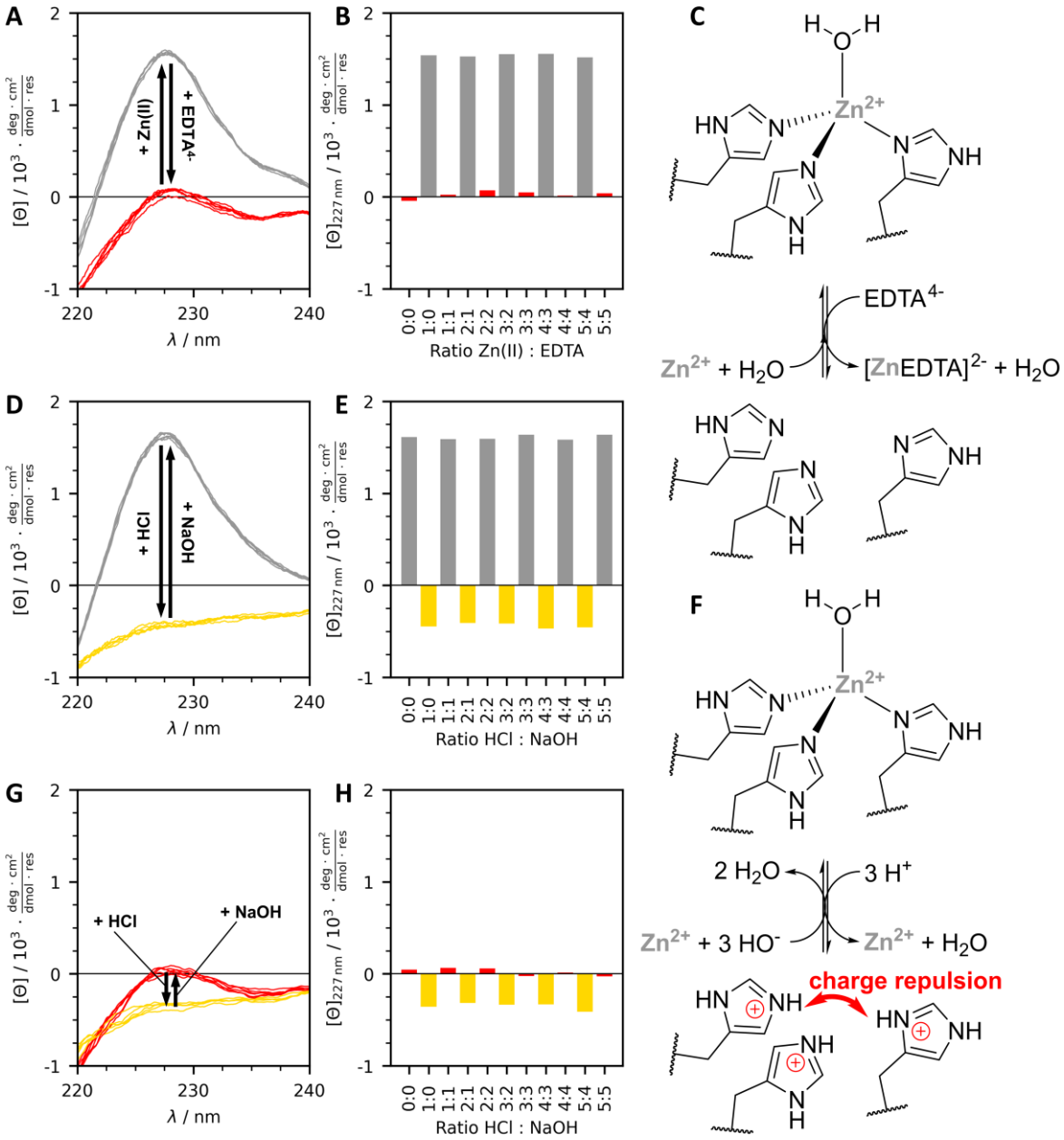

Figure 4-4: Conformational switch experiments. A) Conformational switch of WW-CA by alternate addition of Zn(II) and EDTA, B) corresponding [Θ] values at 227 nm *versus* the molar ratio of added Zn(II) and EDTA. C) Proposed mechanism of the demetallation-metalation reaction. D) Conformational switch of the WW-CA-Zn(II) complex by alternate addition of HCl and NaOH, E) corresponding [Θ] values at 227 nm *versus* the molar ratio of added HCl and NaOH. F) Proposed mechanism of the pH switch reaction. G) Conformational switch of apo WW-CA by alternate addition of HCl and NaOH, H) corresponding [Θ] values at 227 nm *versus* the molar ratio of added HCl and NaOH. Conditions: 10 µM WW-CA, 10 µM $ZnSO_4$ (if present), 10 mM MOPS, 150 mM NaCl, pH 7.2, 1 cm cuvette, 20 °C, titrated with A) 2 mM $ZnSO_4$ or 2 mM Na_2H_2EDTA in 10 mM MOPS, 150 mM NaCl, pH 7.2 or D) and G) 2 M HCl or 2 M NaOH.

At neutral pH, the expected CD spectra for apo WW-CA are visible. Upon acidification, the holo and apo state CD spectra are identical and after neutralisation the weak exciton signal is again visible. As with the holo state, the pH-dependent switching process was repeated five times and was reversible.

To gain more information about the pH dependency, the degree of folding of the WW-CA-Zn(II) complex was studied at different pH (Figure 4-5A) showing that the characteristic maximum in the CD spectra decreased with decreasing pH. Thermal denaturation curves were also recorded at different pH values (Figure 4-5B). Below pH 6, no upper baseline was observed, and the unfolding process was uncooperative. Plotting the signal intensity of the CD maximum against the pH value yields a sigmoidal curve (Figure 4-5C), which was fitted using a modified Henderson-Hasselbalch equation (see Chapter 8.2.10), yielding a pK_a of 6.05. A similar curve was obtained by plotting the T_m values *versus* the pH value. Because T_m could only be measured up to pH 6.2, only the upper half of the curve could be reproduced. These two results suggest that at a pH below 6 the imidazoles are protonated and unable to bind Zn(II), which is also consistent with the reported pK_a values for the His side chain.[269]

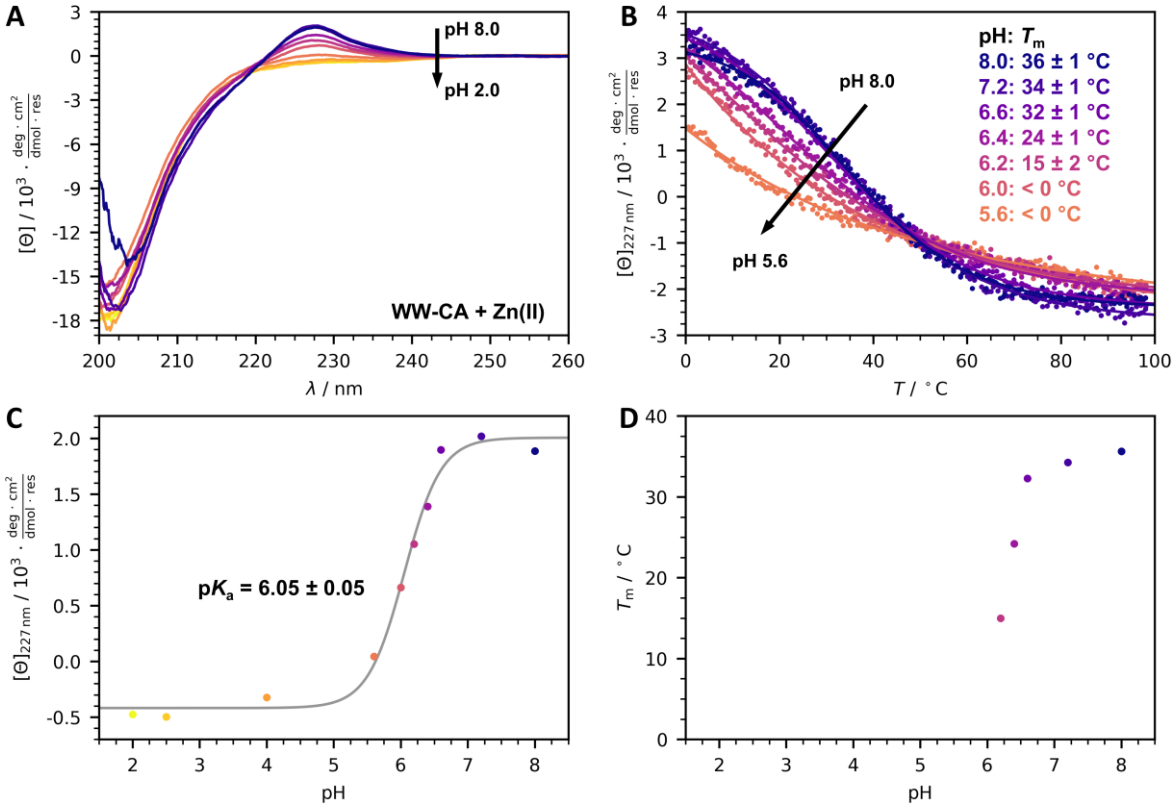

Figure 4-5: pH-Dependence of the structure of the WW-CA-Zn(II) complex. A) CD spectra at different pH values. B) Thermal denaturation curves of WW-CA at different pH values. C) Plot of the CD-signal at 227 nm *versus* the pH value and sigmoidal curve fit to determine the pK_a value. D) Plot of T_m values *versus* pH. Conditions: 100 µM peptide, 100 µM $ZnSO_4$, 10 mM buffer (HEPES: pH 8.0; MOPS: pH 7.2, 6.6; MES: pH 6.4, 6.2, 6.0, 5.6; formate: pH 4.0; hydrogen sulfate: pH 2.5, 2.0), 150 mM NaCl, 1 mm cuvette, 20 °C.

The signal intensity at the characteristic maximum is a measure of the degree of folding.[270] It can therefore be concluded that WW-CA is weakly folded in the apo state and that Zn(II) induces folding. At pH 2 the histidines are protonated and lose their ability to bind Zn(II). In addition, they are positively charged and repel each other, further weakening the folding and completely depleting the exciton signal.

The CD experiments led to four hypotheses concerning WW-CA:

1) WW-CA reversibly changes its conformation depending on Zn(II) availability and pH value. At pH 7.2 two conformations are observed in the absence and presence of Zn(II) (apo and holo state). At pH 2, only a protonated apo conformation (apo+nH$^+$) exists, which cannot interact with Zn(II).

2) The conformations differ in their degree of folding. The holo state is more folded than the apo state and the apo state unfolds further when the pH value is lowered.

3) Furthermore, the folding to unfolding transition is influenced by Zn(II) at a pH higher than the pK_a of the His side chains at approximately 6. While the holo state unfolds cooperatively, the apo and apo+nH$^+$ states unfold non-cooperatively.

4) The incorporated His_3 site is responsible for the Zn(II) binding and the resulting overall conformational change influences the orientation of the aromatic amino acids in the hydrophobic core.

4.1.4 Conformational analysis of WW-CA by NMR spectroscopy

4.1.4.1 Solving the aggregation problem

In order to obtain detailed structural information on the switching process and to further test the four hypotheses (Chapter 4.1.3), 1D and 2D NMR experiments were performed in collaboration with the Kovermann laboratory (University of Konstanz). To perform NMR experiments, it is necessary to work with a peptide concentration of 1 mM. The solution needs to be stable for several days due to the long duration of the two-dimensional experiments. This proved to be a serious problem as buffered WW-CA solutions were not stable, especially in the presence of Zn(II). After 1 d at room temperature, visible aggregates were observed. In addition, the ability to dissolve lyophilized WW-CA in saline buffer is dependent on the batch, with older batches tending to form more aggregates. A safe procedure was to dissolve WW-CA first in pure water, before adding buffer stock solution. If applicable, the metal salt solution should be added last. This procedure was generally applied to all the peptides discussed (see Chapter 8.2.4 for details). The aggregates can be solubilised by adding dilute acid, such as 1 M HCl or even 0.1% TFA in water. HPLC analysis showed the appearance of a new shoulder, which was not present at the beginning (Figure 4-6A). MALDI-TOF-MS revealed a new species with a m/z of +16 compared to the parent peptide, indicating the addition of an oxygen atom,

which arises from the oxidation of methionine to methionine sulfoxide. It is known that the formation of methionine sulfoxide due to oxidation can cause drastic changes in the peptide structure and, hence, in the aggregation behaviour.[271-272] Therefore, a mutant of WW-CA containing norleucine (Met15Nle), a common substitute for Met, was synthesised and dubbed WW-CA-Nle. CD spectroscopic analysis showed that this new peptide behaved similarly to WW-CA (Figure 4-6C, D and E). The CD spectra at pH 7.2 and pH 2.0 as well as the thermal denaturation curves were superimposeable to those of WW-CA and the resulting T_m values for the holo peptide were comparable. Solutions of the WW-CA-Nle-Zn(II) complex were prepared at a concentration of 1 mM, and shown to be stable for 1 d at 10 °C.

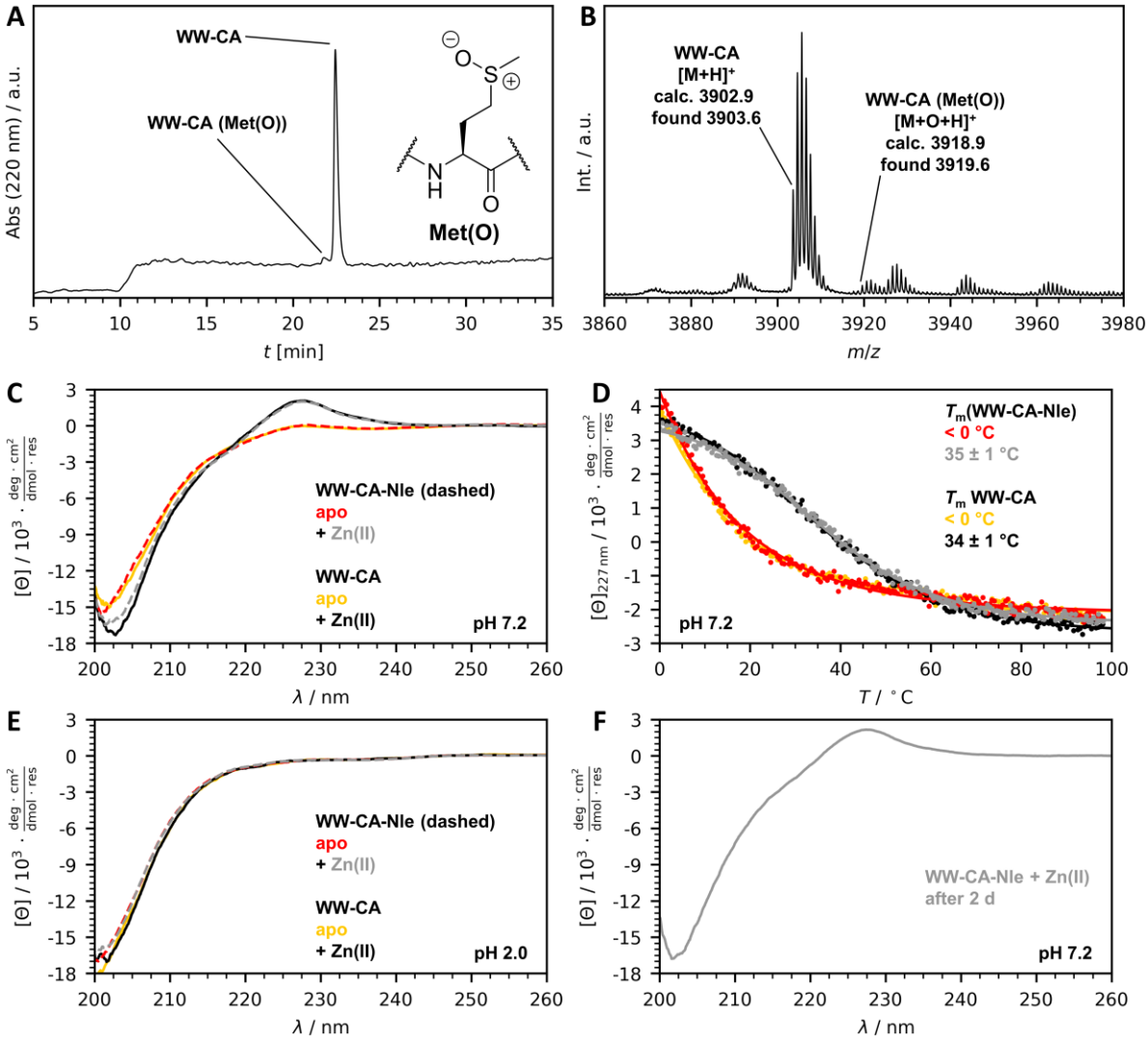

Figure 4-6: A) Chromatogram of matured WW-CA (Gradient 20-40% buffer B in A) and chemical structure of Met(O). B) Formation of Met(O) is proved by MALDI-TOF-MS. C) CD spectra at 20 °C and D) thermal denaturation curves of WW-CA-Nle and WW-CA in presence and absence of Zn(II) at pH 7.2. E) CD spectra at 20 °C of WW-CA-Nle and WW-CA in presence and absence of Zn(II) at pH 2.0. F) CD spectra of WW-CA-Nle-Zn(II) complex at 20 °C after incubation overnight at 10 °C at 1 mM peptide and Zn(II) concentration, followed by ten-fold dilution prior to CD measurement. Conditions: 100 µM peptide, 100 µM $ZnSO_4$ (if present), 10 mM buffer substance (MOPS: pH 7.2, hydrogen sulfate: pH 2.0), 150 mM NaCl, 1 mm cuvette.

The solution was then left for another day at room temperature and diluted to 100 µM for CD measurement (Figure 4-6F). The CD spectrum of the matured WW-CA-Nle-Zn(II) complex was identical to that of the freshly prepared WW-CA-Zn(II) complex.

4.1.4.2 Analysis of conformational changes by 1D NMR

With the new peptide in hand, 1D ^{1}H NMR experiments were performed at pH 7.2 in the presence and absence of Zn(II), showing significant differences in the signal pattern between the holo and apo states (Figure 4-7). Nevertheless, the typical characteristics of a folded peptide, a large dispersion in the NH region, as well as aliphatic signals below 0.7 ppm,[255, 273] only differ slightly between the holo and apo states. Next, the effect of low pH value was analysed. At pH 2, the spectra of the apo peptide differ significantly from those of the apo peptide at pH 7.2, but the addition of Zn(II) at low pH does not change the signal pattern, with both spectra being superimposable.

These observations correlate with the CD experiments and support hypothesis 1): At pH 7.2 the addition of Zn(II) led to a conformational change, which was not observed at pH 2, because of the protonation of the histidine side chains and consequently the inability to coordinate Zn(II). The conformational change of the apo state at acidic pH was also observed in the ^{1}H NMR spectrum. However, information of which residues were involved in Zn(II) binding and which residues are most dynamic during the conformational change could not be drawn from the 1D experiments. Furthermore, the degree of folding and structural stability remained unclear from these NMR data.

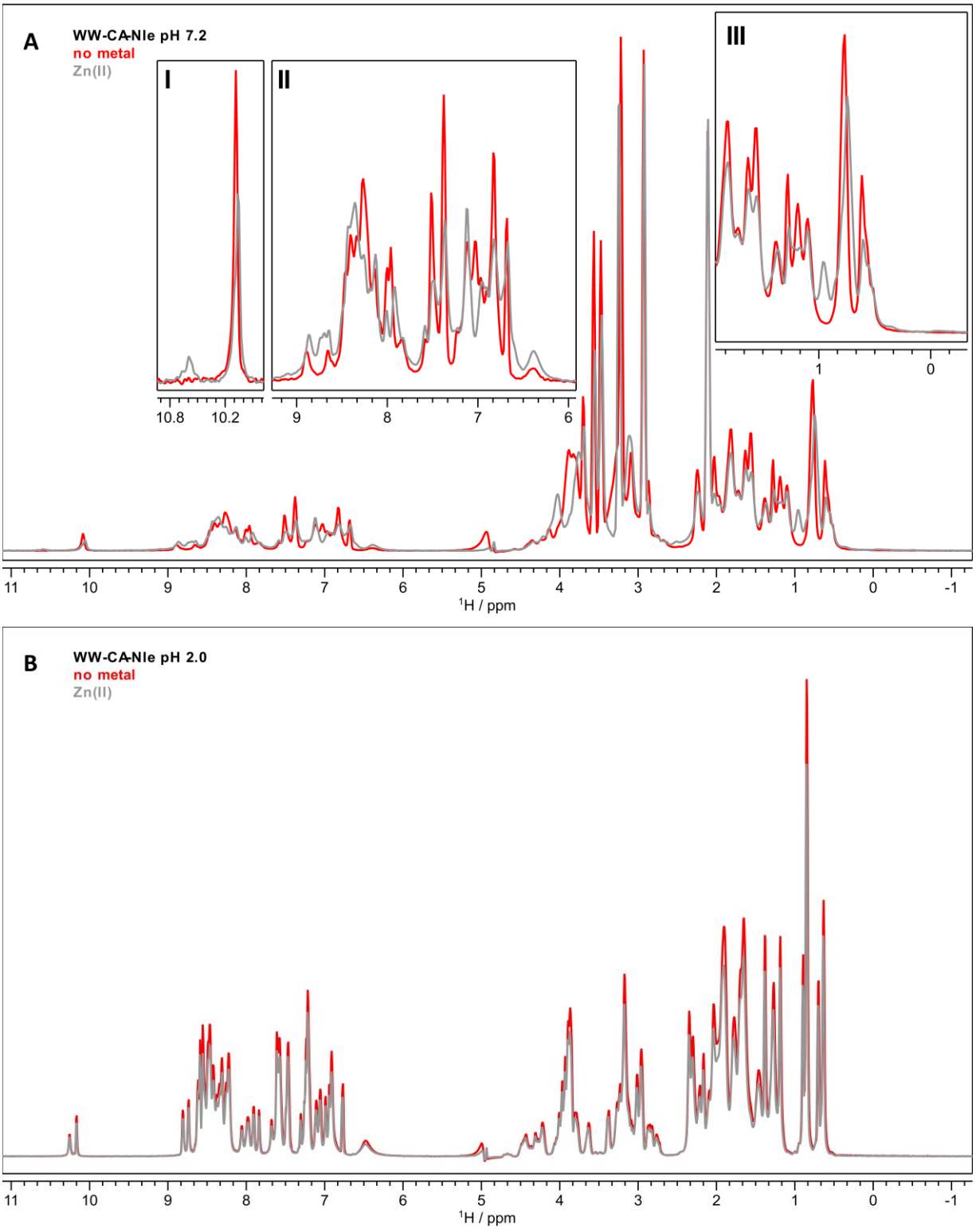

Figure 4-7: 1D ^{1}H NMR (600 MHz, 5% *v/v* D_2O in aqueous buffer containing 150 mM NaCl and A) 10 mM MOPS, pH 7.2 or B) hydrogen sulfate, pH 2) spectra acquired on WW-CA-Nle in absence and presence of $ZnSO_4$ (each 1 mM) at 10 °C.

To gain more insights in the degree of folding of WW-CA-Nle in presence and absence of Zn(II) and at neutral and acidic pH, the diffusion coefficient *D* was determined using pulse-field gradient NMR spectroscopy. As can be seen in Figure 4-8, at pH 7.2 only marginal changes in *D* are observed in the absence ($1.35 \cdot 10^{-10}$ m^2 s^{-1}) and presence ($1.37 \cdot 10^{-10}$ m^2 s^{-1}) of

Zn(II). Decreasing the pH to 2.0 led to a decrease in *D*. The value for the apo-peptide was $1.29 \cdot 10^{-10}$ m^2 s^{-1} which was similar to the holo state ($1.26 \cdot 10^{-10}$ m^2 s^{-1}). A folded peptide should be more compact than an unfolded one and therefore diffuse faster, corresponding to a higher diffusion coefficient. Therefore, these results support hypothesis 2 drawn from the CD data, that the holo conformation has a higher degree of folding than the apo and apo+*n*H$^+$ states. However, it should be noted, that the difference in *D* between apo and holo WW-CA is very small.

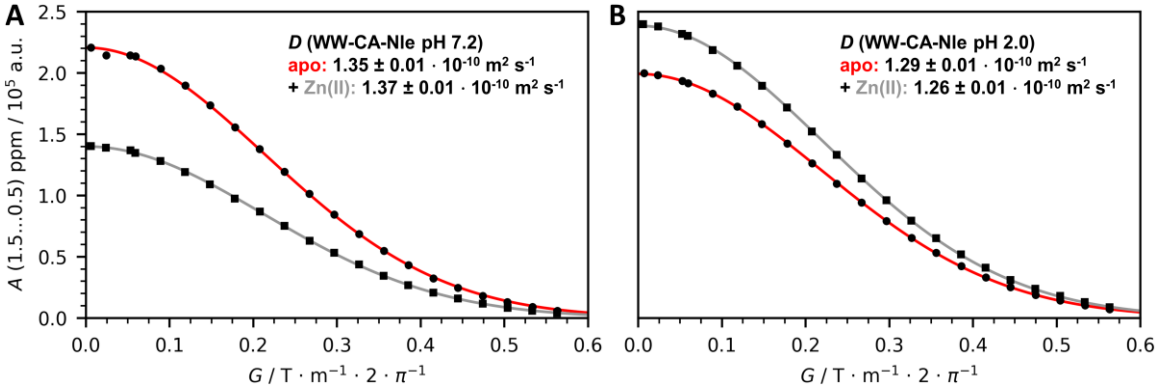

Figure 4-8: Determination of the diffusion coefficient *D* of WW-CA-Nle in presence and absence of Zn(II) at A) pH 7.2 and B) pH 2.0. Conditions: 1 mM peptide, 1 mM $ZnSO_4$ (respectively), 5% *v/v* D_2O in aqueous buffer: 10 mM MOPS, pH 7.2 or hydrogen sulfate, pH 2.0, 150 mM NaCl, 298 K.

Next, 1D ^{1}H NMR experiments were performed at different temperatures (7 to 32 °C) to determine the temperature dependent unfolding transition (Figure 4-9 and Figure 4-10). The maximum temperature was not set above the CD-derived T_m to avoid peptide aggregation. For both the holo and apo states, heating resulted in significant changes in the NMR spectra. In general, the number of signals and the dispersion of chemical shifts decreased, especially in the backbone amide proton region, showing the expected decrease in folding with increasing temperature. To quantify the process, it was assumed that the exchange of amide protons with the solvent increases linearly with increasing temperature, leading to a decrease in the integral. However, if the amide proton is involved in a backbone hydrogen bond, the solvent exchange is slowed down. In contrast, aliphatic protons do not exchange. Therefore, the ratio of the integrals of the backbone amide proton region (A_{NH}, 9.75 to 7.70 ppm) and the aliphatic proton region (A_{CH}, 1.92 to -1.00 ppm) was plotted against temperature (Figure 4-13A). The A_{NH}/A_{CH} of the apo peptide decreases linearly, indicating non-cooperative unfolding, whereas the temperature dependence of the holo peptide shows a curved shape. The closer the temperature is to the CD-derived melting temperature of the WW-CA-Nle-Zn(II) complex (34.8 °C), the more the graphs of the holo and apo peptides converge. This can be explained by the fact that the backbone amide protons of the unfolded holo peptide are exposed and therefore exchange with the solvent at a similar rate as the backbone amide protons of the apo peptide.

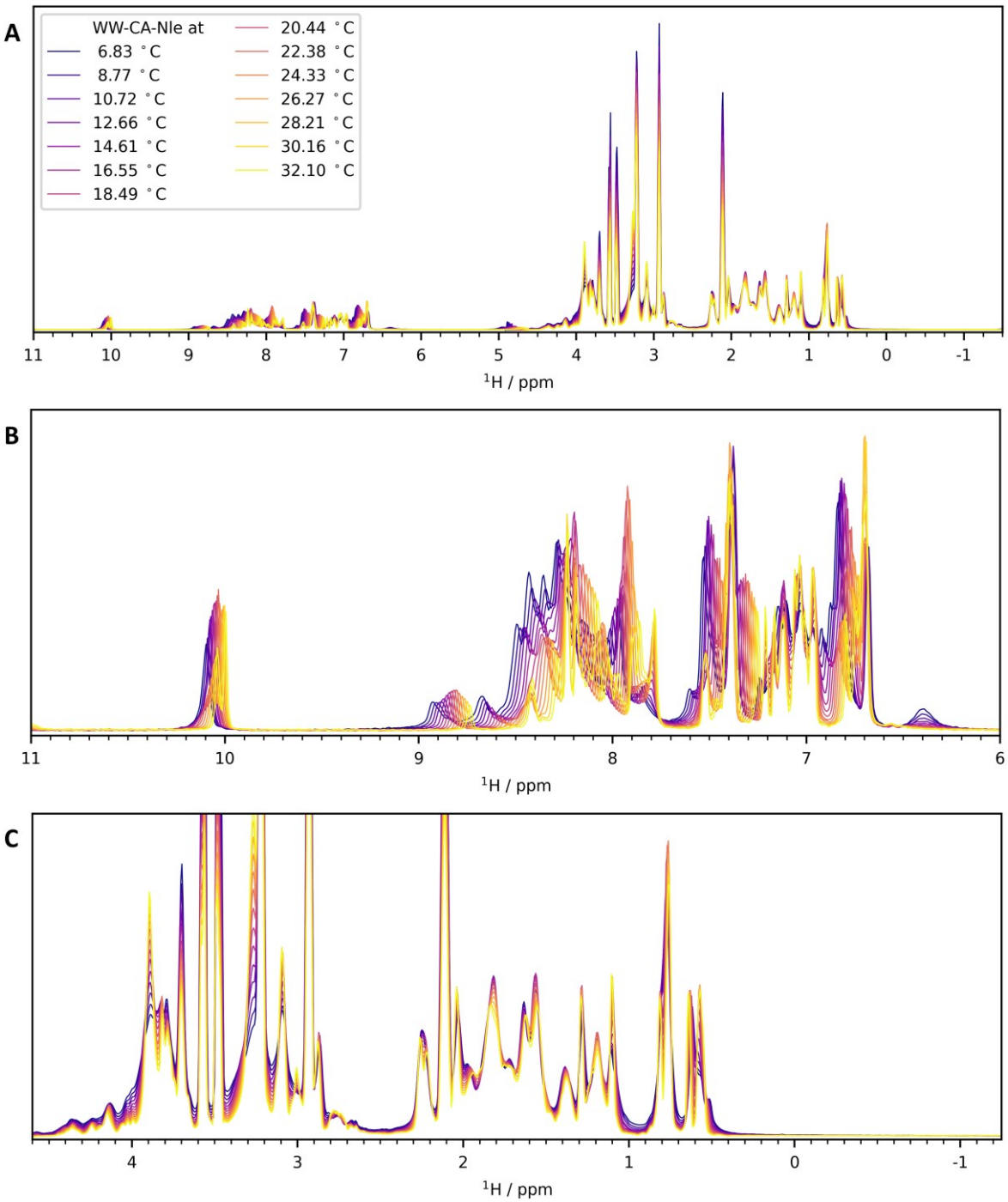

Figure 4-9: 1D ^{1}H NMR (600 MHz, 5% *v/v* D_2O in aqueous buffer: 10 mM MOPS, 150 mM NaCl, pH 7.2) spectra acquired on apo WW-CA-Nle (1 mM) at different temperatures (6.83 to 32.10 °C). A) full spectrum, B) down field and C) upfield zooms.

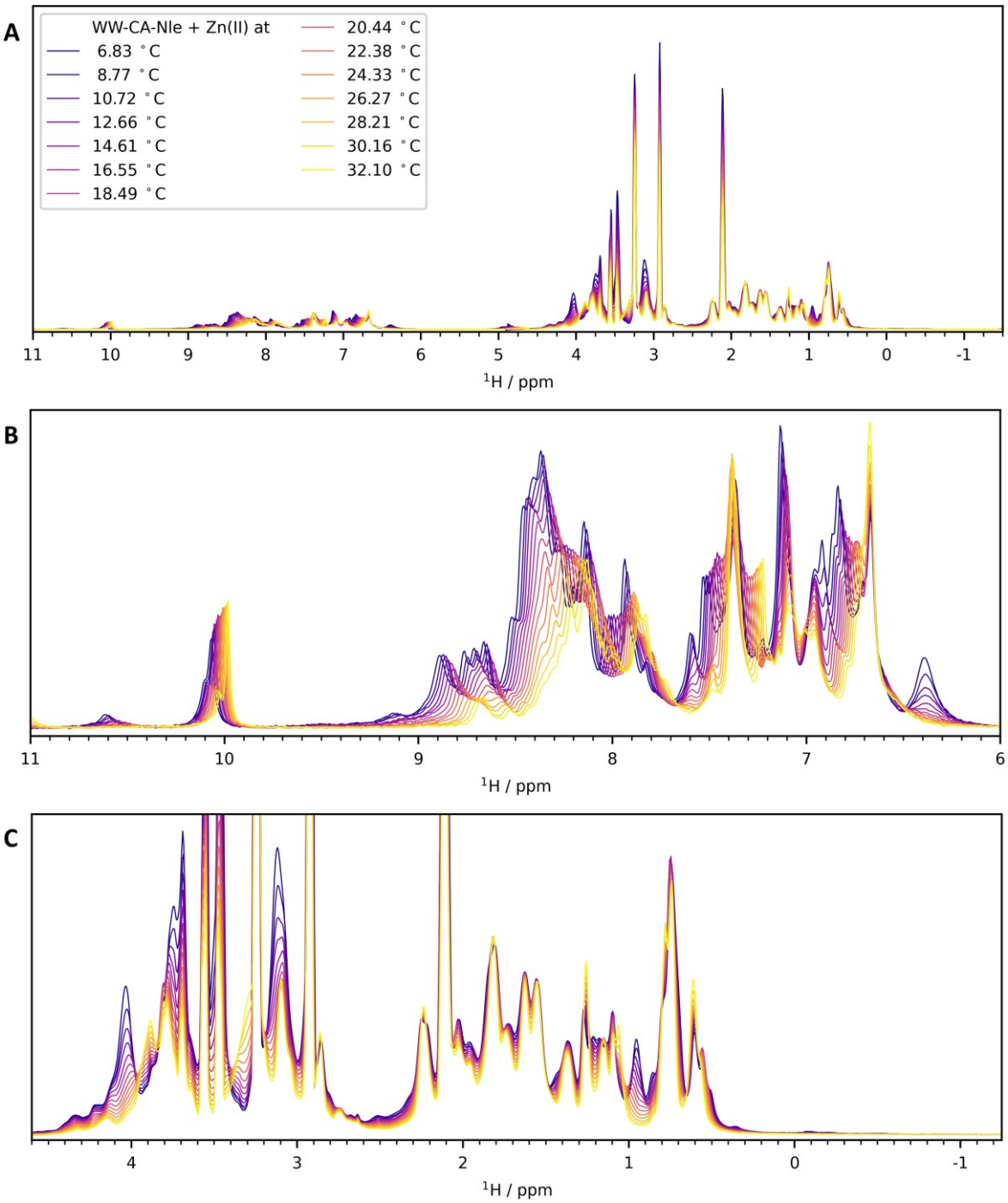

Figure 4-10: 1D ^{1}H NMR (600 MHz, 5% *v/v* D_2O in aqueous buffer: 10 mM MOPS, 150 mM NaCl, pH 7.2) spectra acquired on WW-CA-Nle in presence of $ZnSO_4$ (each 1 mM) at different temperatures (6.83 to 32.10 °C). A) full spectrum, B) downfield and C) upfield zooms.

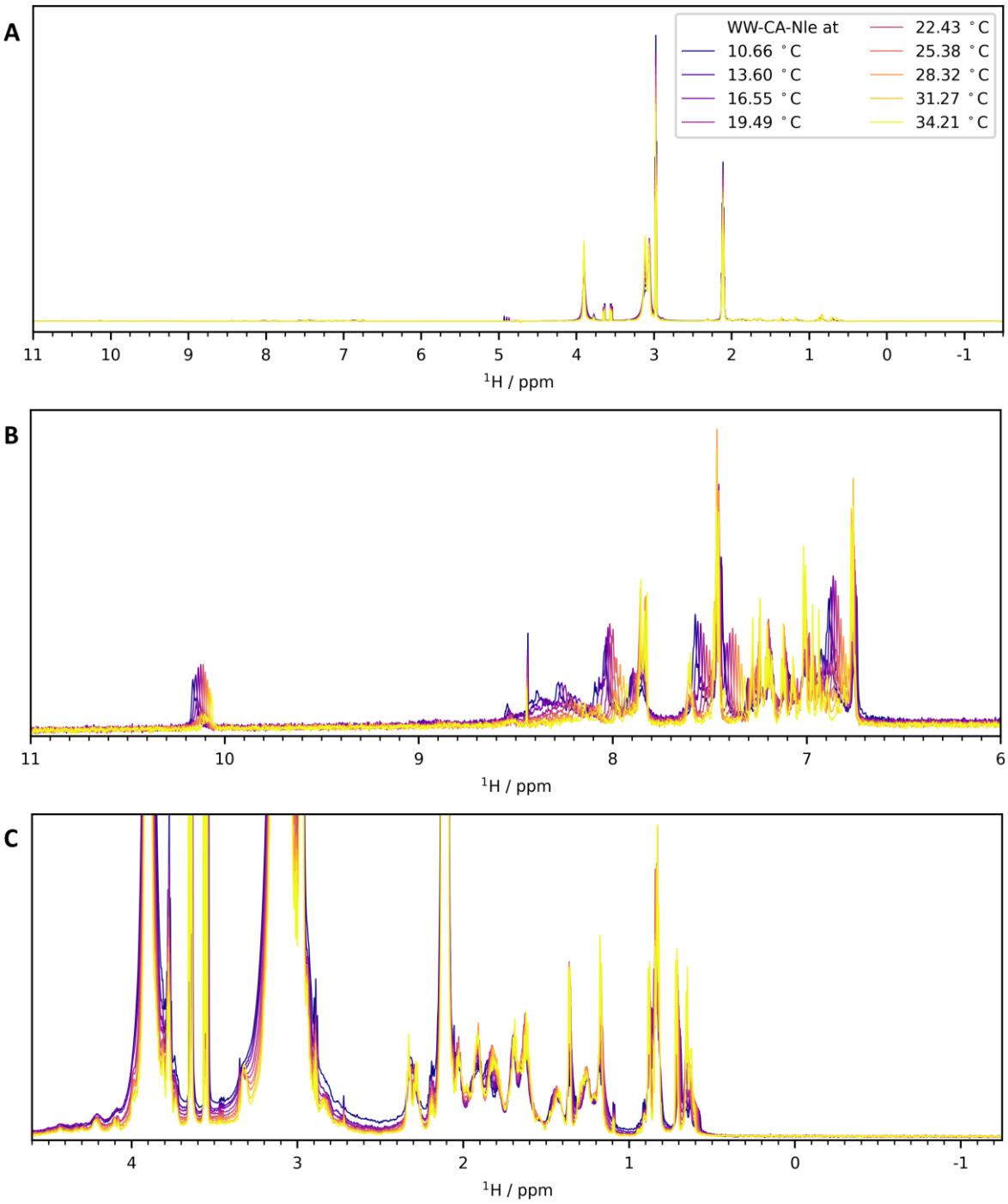

Figure 4-11: 1D ^{1}H NMR (600 MHz, 5% *v/v* D_2O in aqueous buffer: 10 mM MOPS, 150 mM NaCl, pH 7.2) spectra acquired on apo WW-CA-Nle (100 µM) at different temperatures (10.66 to 34.21 °C). A) full spectrum, B) down field and C) upfield zooms.

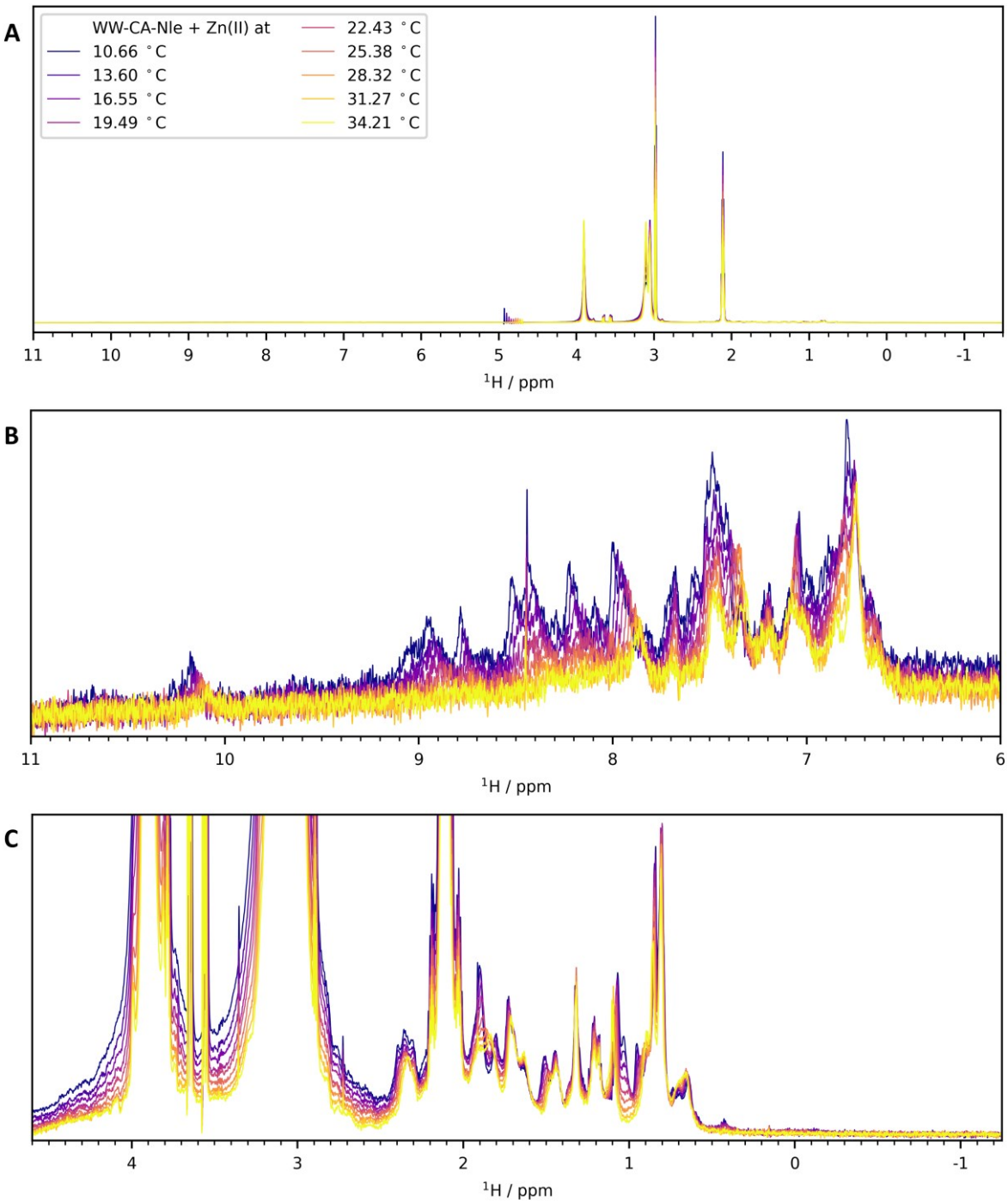

Figure 4-12: 1D ^{1}H NMR (600 MHz, 5% *v/v* D_2O in aqueous buffer: 10 mM MOPS, 150 mM NaCl, pH 7.2) spectra acquired on WW-CA-Nle in presence of $ZnSO_4$ (each 100 µM) at different temperatures (10.66 to 34.21 °C). A) full spectrum, B) down field and C) upfield zooms.

Another method of measuring thermal unfolding by NMR spectroscopy is to calculate the native fraction $f_n = F_n/(F_n + F_{n+u})$ and plot f_n *versus* T.[273] The integral of the high field shifted signals F_n (around 0.6 ppm to 0.3 ppm) is characteristic of the natively folded peptide and the aliphatic region F_{n+u} (around 1 ppm to 0.6 ppm) is populated by signals from both unfolded and folded peptide species. Figure 4-13 shows the temperature dependence of f_n of both apo and holo WW-CA-Nle. Four different combinations of integrals were used to avoid artefacts due to fraudulent selection of integral boundaries. In the case of Figure 4-13C and E,

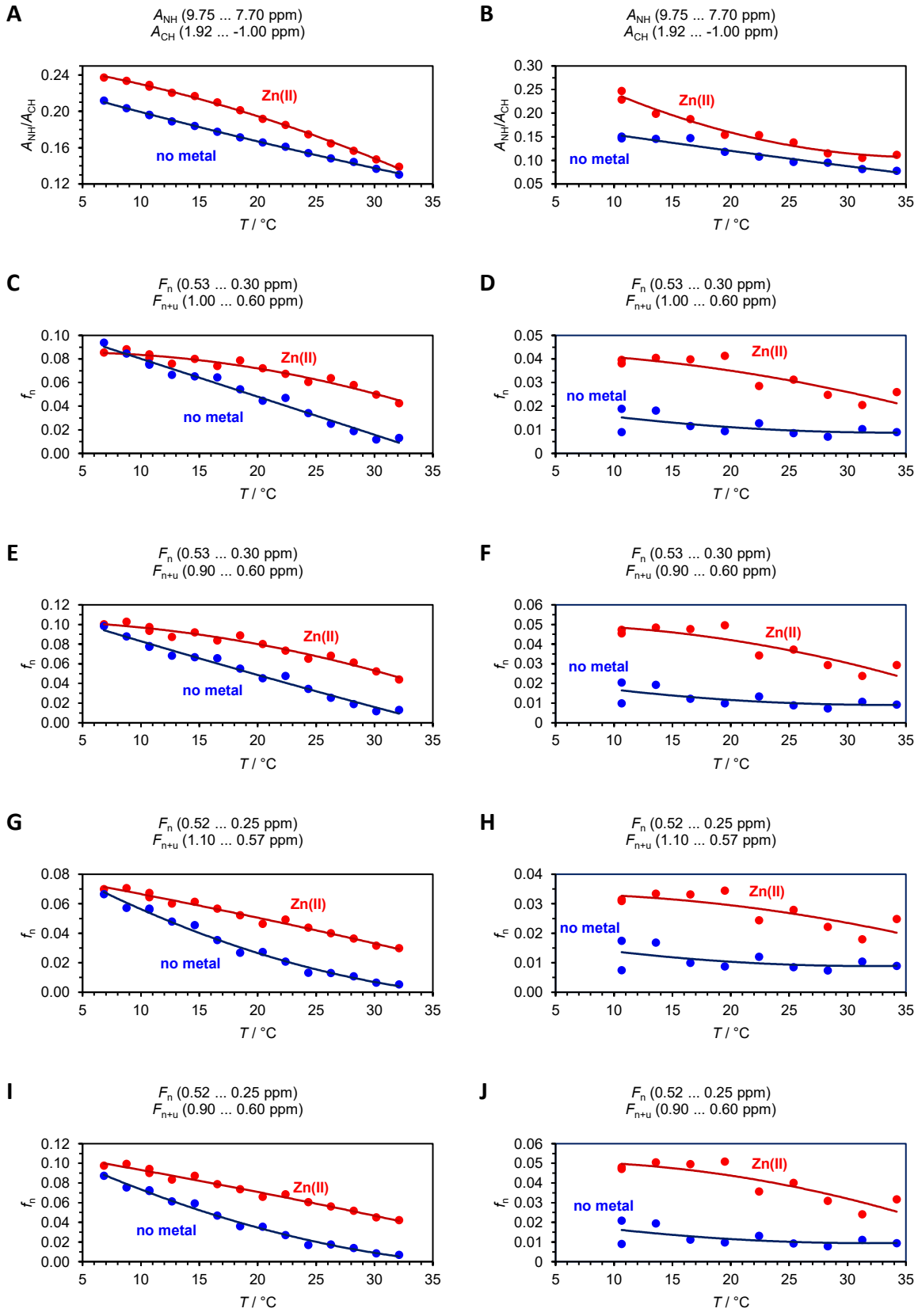

Figure 4-13: Thermal denaturation analysis by NMR. A) and B) A_{NH}/A_{CH} and C) to J) native fraction f_n of WW-CA-Nle in absence and presence of Zn(II) calculated from different integrals of the aliphatic region as a function of T. Peptide concentration: 1 mM (A,C,E,G,I) and 100 µM (B,D,F,H,J). See Figure 4-9 to Figure 4-12 for the corresponding temperature dependent 1D ^{1}H NMR spectra.

the graph in the absence of Zn(II) is linearly decreasing and the graph in the presence of Zn(II) is curved. For G and I it is inverted. However, all graphs show that f_n decreases to a lesser extent in the holo state than in the apo state. In no case a cooperative unfolding of the apo state was observed. To exclude artefacts due to concentration differences, the ^{1}H-NMR experiment was repeated with a peptide concentration of 100 µM, similar to the CD experiments (Figure 4-11 and Figure 4-12). Although the signal-to-noise ratio was lower, changes in the spectra due to temperature increase were detectable and comparable to the measurements at higher concentration. Furthermore, the A_{NH}/A_{CH} or f_n *versus* T plots were also comparable to the experiment at 1 mM peptide concentration (Figure 4-13), although the exact shape of the curves differs. Nevertheless, in all plots the holo peptide unfolds to a lesser extent with increasing temperature than the apo peptide, which is in agreement with all other experimental data.

Cooling the peptide and Zn(II) addition led to an increase in the exciton signal, which is considered to be an indicator of the degree of folding. From these observations one might conclude that the conformation of holo WW-CA is similar to that of apo-WW-CA at low temperatures. However, it should be noted that the exciton signal only indicates the interaction between the Trp and Tyr residues in the hydrophobic core. So far, the CD thermal denaturation curves were collected by following a single wavelength at the characteristic maximum. To gain a more global view of the unfolding process, the CD spectra of holo and apo WW-CA-Nle were recorded from 8 °C to 32 °C. In both cases a loss of intensity was observed at both the maximum and the minimum, but the signal loss was greater in the apo state (Figure 4-14A and B) which is similar to the thermal denaturation curves collected by CD and NMR. In general, the global shape of the spectrum in presence and absence of Zn(II) was different at each temperature. To visualise the changes more clearly, the difference spectra were calculated (Figure 4-14C), which show that the holo state is different from the apo state at each temperature. This is in very good agreement with the NMR experiments. Neither the CD nor the NMR spectra of the holo peptide are similar to a spectrum of the apo peptide at low temperature. It must be assumed that the holo state is inherently different from the apo state and that the induction of folding by Zn(II) is not identical to the induction of folding by cooling.

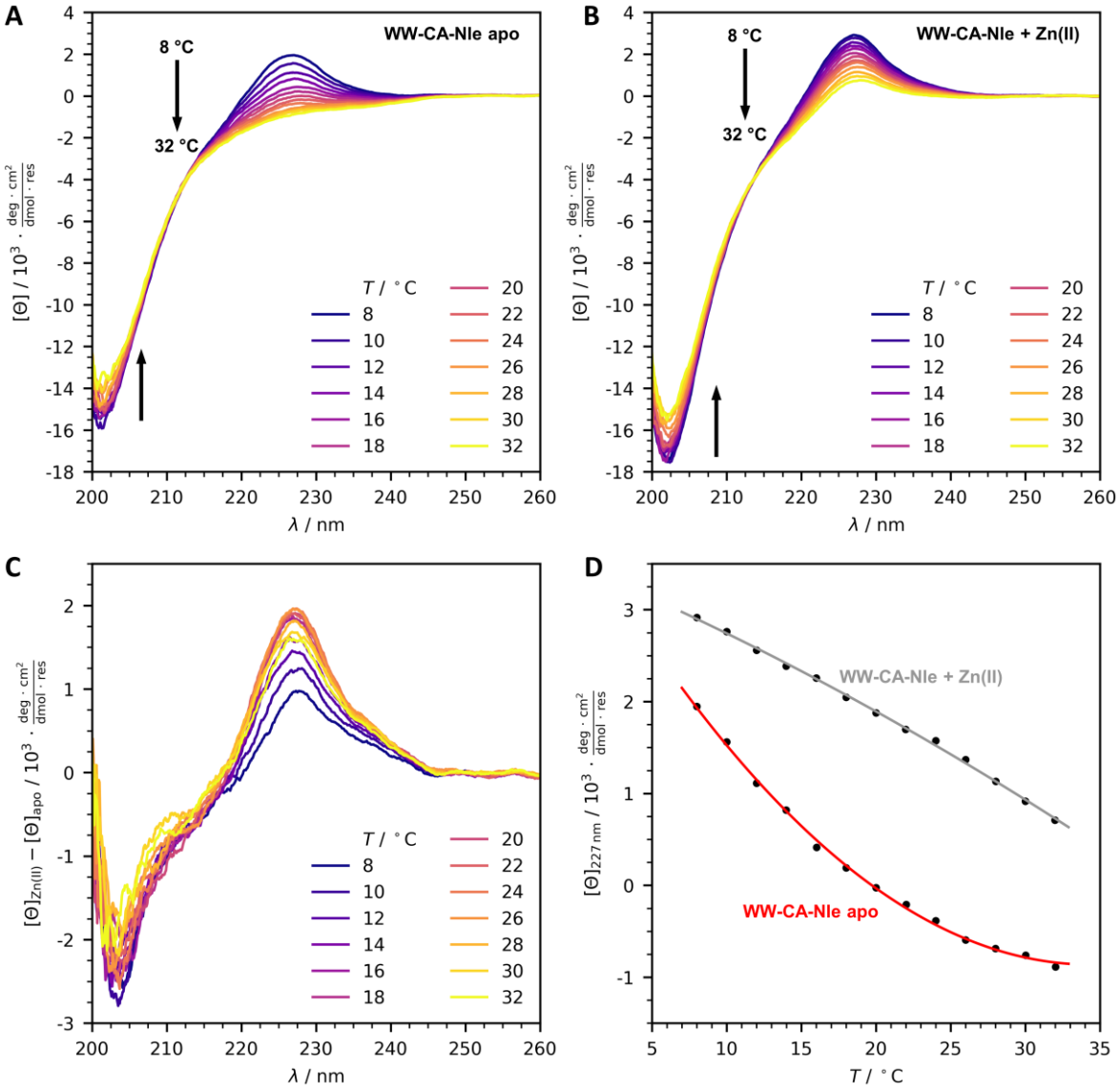

Figure 4-14: CD spectra of A) apo and B) holo WW-CA-Nle at different temperature. C) Difference spectrum. D) Resulting denaturation curve. (100 µM WW-CA, 100 µM $ZnSO_4$ (if present), 10 mM MOPS, 150 mM NaCl, pH 7.2, 1 mm cuvette).

4.1.4.3 2D NMR experiments for amino acid residue resolved analysis

To obtain more resolved information, natural abundance 2D ^{1}H-^{15}N heteronuclear single quantum coherence (HSQC) spectra were collected in the presence and absence of Zn(II). As can be observed in Figure 4-15, the signal patterns of the apo and holo states are different. While the apo state e.g. shows only one signal for the NH of the tryptophan indole side chain, the holo state shows two signals. In the backbone amide region, the dispersion of chemical shifts is higher for the holo state than for the apo state. The region of the glutamine and asparagine side chains is similar, but not superimposable for either state. The total number of resolved signals was 34 for the holo peptide and only 26 for the apo peptide. In agreement with the previous experiments, these observations show that the degree of folding is higher in the holo than in the apo state. Furthermore, these experiments, together with temperature

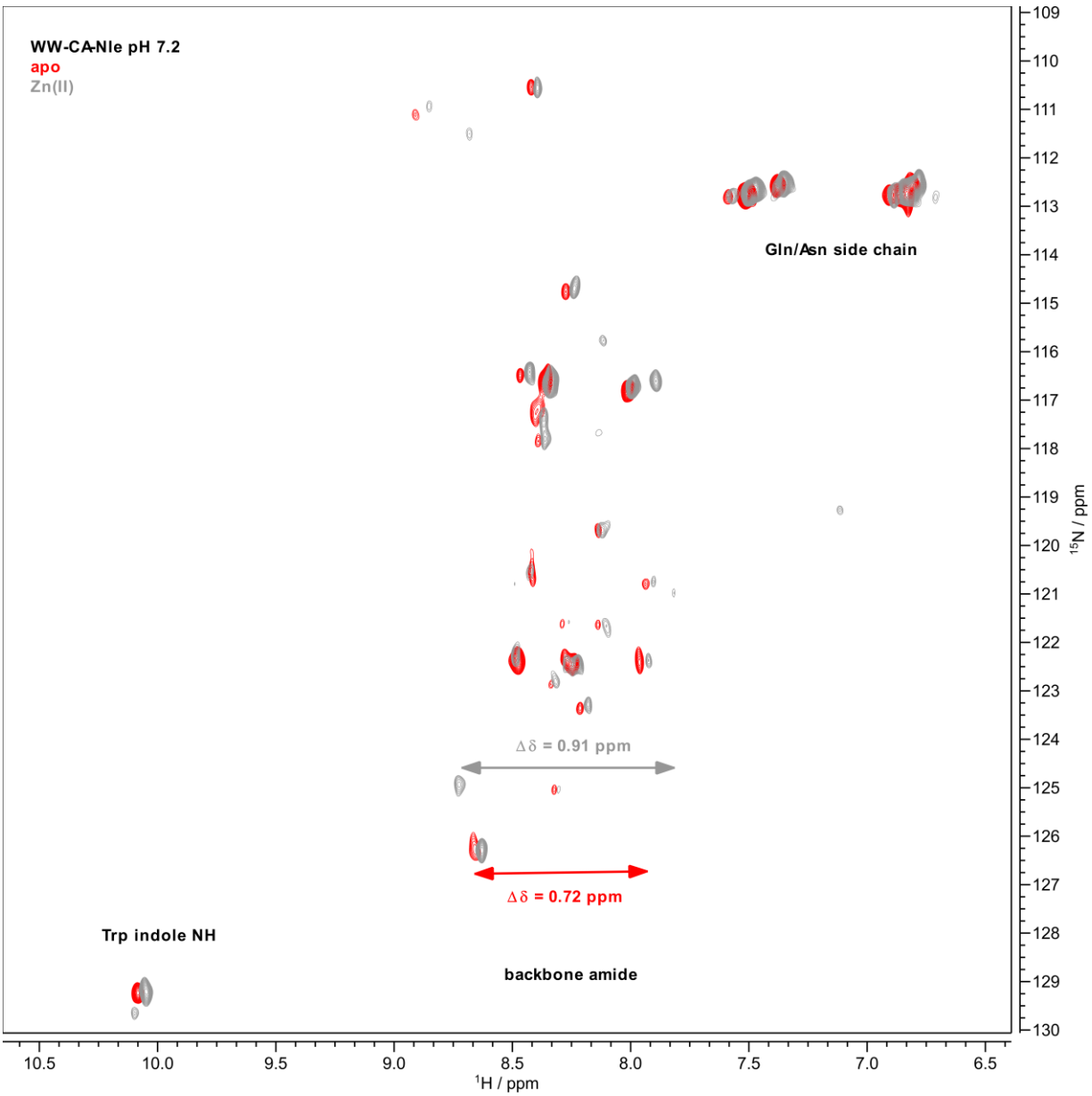

Figure 4-15: 2D ^{1}H-^{15}N HSCQ (800 MHz, 5% *v/v* D_2O in aqueous buffer: 10 mM MOPS, 150 mM NaCl, pH 7.2) spectra acquired on WW-CA-Nle in absence and presence of $ZnSO_4$ (each 1 mM) at 10 °C. The dispersion of chemical shifts Δδ was given for amide backbone protons. Because no full assignment is possible, there are also other possibilities which signals are chosen for the determination of Δδ, (Appendix, Chapter 10.8). Each of these choices show a higher Δδ for the holo state in comparison to the apo state.

dependent NMR and CD analysis, confirm that the conformational change of the peptide does not only affect a few residues, but is a global event. It is very important to note that the apo state is not a fully unfolded peptide, but a loosely folded one. Unfortunately, the NH signals of the histidine residues were insufficiently resolved to confirm Zn(II) binding *via* the imidazole side chain.

To address the latter question, 2D ^{1}H-^{13}C HSQC spectra were recorded to monitor changes in the apo and holo states for the aromatic region as well as for the characteristic β-CH_2 signals of the histidine side chains (Figure 4-16A). Similar to all previous observations, the addition of

Zn(II) led to a significant change in the overall spectrum. All signals in the aromatic regions were assigned to the respective residues using values known from the literature.[274] In the presence of Zn(II) the aromatic signals of W11/W34 and Y24 are shifted and in some cases broadened compared to the apo state. The aromatic signals of the histidine residues (δ2-CH and 1-εCH) disappeared upon addition of Zn(II) and the β-CH_2 signals were shifted. These results are in agreement with the CD data. The exciton signal is caused by the aromatic residues W11 and Y24, and conformational changes in these residues can also be observed in the NMR spectra. Finally, a direct involvement of the His_3 site in the Zn(II) binding process was confirmed. As a final control experiment, 2D ^{1}H-^{13}C HSQC spectra were recorded at pH 2 (Figure 4-16B). As expected, the spectra of the holo and apo state were superimposable. No changes were observed in the aromatic region, in particular no changes in the histidine signals, showing that at pH 2 Zn(II) is not coordinated to WW-CA-Nle.

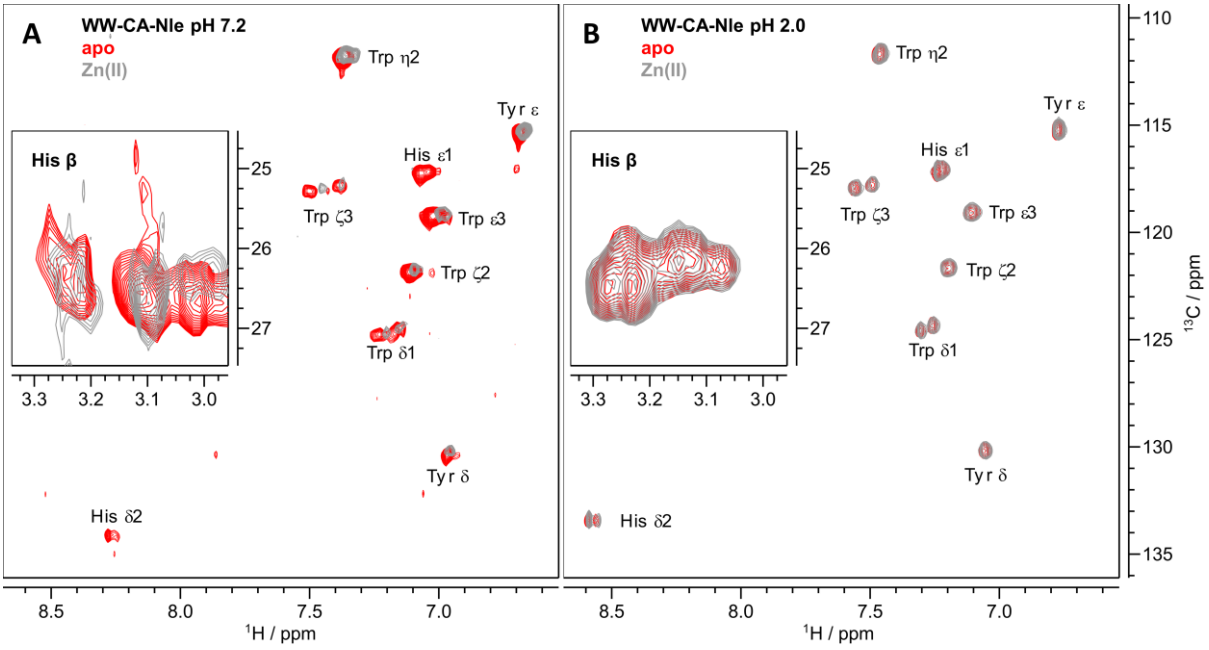

Figure 4-16: A) 2D ^{1}H-^{13}C HSQC spectra of WW-CA-Nle in absence and presence of Zn(II) at pH 7.2 and 10 °C. B) 2D ^{1}H-^{13}C HSQC spectra of WW-CA-Nle in absence and presence of Zn(II) at pH 2.0 and 10 °C. 600 MHz, 1 mM WW-CA-Nle, 1 mM $ZnSO_4$ (if present), 5% D_2O in aqueous buffer, 10 mM MOPS (pH 7.2) or 10 mM hydrogen sulfate (pH 2.0), 150 mM NaCl.

4.1.5 Binding of other metal ions to WW-CA and WW-CA-Nle

Following the detailed characterisation of the Zn(II) binding of WW-CA, the question arises as to how other metal ions affect the structure of WW-CA. Several metal ions were tested and as can be seen in Figure 4-17A to D, Ca(II), Mg(II), Co(II), Mn(II) and Fe(II) did not cause significant changes in the CD spectra and thermal denaturation curves compared to the apo peptide. Differences were observed only in the case of Cu(II) and Ni(II). However, the spectra obtained were also different from those of the Zn(II) complex. The maximum at 227 nm was slightly red-shifted in both cases and a shoulder was present between 220 nm and 210 nm.

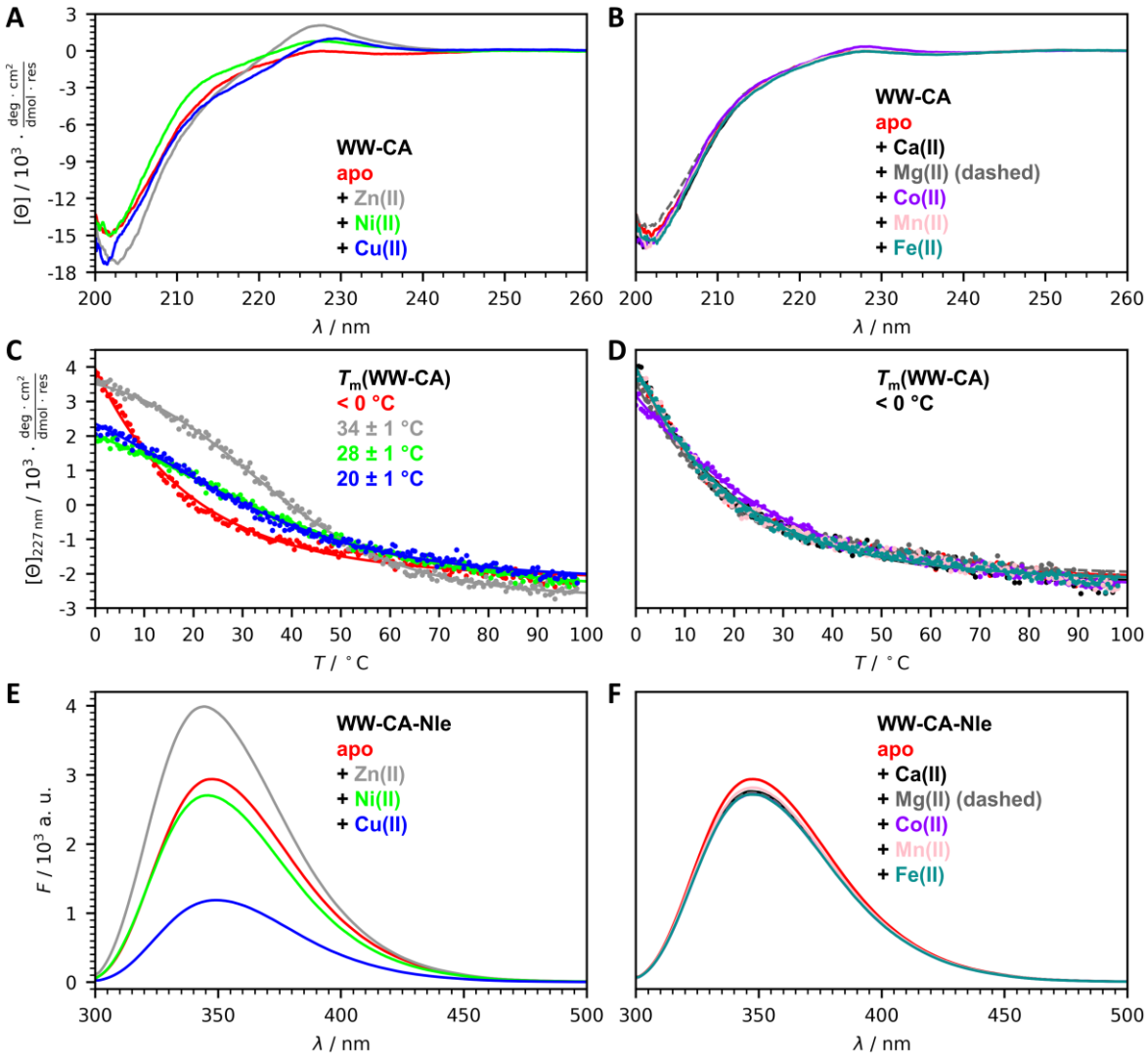

Figure 4-17: Spectroscopic analysis of WW-CA and WW-CA-Nle in presence of different divalent metal ions. A) and B) CD spectra at 20 °C. C) CD thermal denaturation curves in presence of metal ions, that stabilizes the fold of WW-CA (T_m > 0 °C) and D) metal ions that do not stabilize the fold of WW-CA (T_m < 0 °C). Conditions: 100 µM peptide, 100 µM metal salts (if present), 10 mM MOPS, 150 mM NaCl, pH 7.2, 1 mm cuvette. E) Fluorescence spectra of WW-CA-Nle in absence and presence of divalent metal ions that significantly change the tryptophan fluorescence of WW-CA-Nle and F) that do not change the tryptophan fluorescence of WW-CA-Nle. Conditions: 10 µM WW-CA-Nle, 10 µM metal salt (if present), 10 mM MOPS, 150 mM NaCl, pH 7.2, excitation wavelength: 295 nm, room temperature (20 °C to 25 °C).

The thermal denaturation curves of the WW-CA-Cu(II) and Ni(II) complexes show significantly lower signal intensities and very broad transitions with reduced T_m values (WW-CA-Ni(II): 28 °C; WW-CA-Cu(II): 19.8 °C) compared to WW-CA-Zn(II). These results indicate the binding of Ni(II) and Cu(II) to WW-CA, while the other metal ions do not cause any visible changes in the WW-CA conformation. This was further confirmed by fluorescence spectroscopy (Figure 4-17E and F, using WW-CA-Nle). The aromatic residues of tryptophan were excited at 295 nm, and the emission was recorded. The resulting spectra for apo WW-CA-Nle show a maximum around 347 nm. Addition of Zn(II) caused an increase in Trp fluorescence, while Ni(II) resulted

in a slight and Cu(II) a strong quenching of the signal. The fluorescence spectra of all other metals are not significantly different from that of the apo peptide.

Next, the binding affinity of WW-CA to Zn(II) was studied by titrating Zn(II) to apo WW-CA and recording CD spectra. The signal intensity at the characteristic maximum increased with increasing Zn(II) concentration (Figure 4-18A and B), from which a binding isotherm was obtained that represents a typical case of K_d < [WW-CA] (more details in Chapter 8.2.8). Initially, the signal increased strongly until [Zn(II)] ≈ [WW-CA] at which point saturation occurs. Therefore, curve fitting was performed assuming tight binding, which yield a K_d value of 1.2 µM. The binding affinity of WW-CA for Zn(II) is weaker than that of natural Zn(II) binding proteins, which have K_d values in the nM to fM range.[245, 275] However, the K_d is in the same range as other designed Zn(II)-binding peptides containing a His_3 site.[226, 258, 276] During fitting, the value for [WW-CA] was 8.7 ± 0.7 µM, which is close to the true [P] of 10 µM, indicating a 1:1 binding.

In order to determine the K_d value of Ni(II) binding, CD titration was carried out as described for Zn(II), resulting in a saturation binding curve with a dissociation constant of 5 µM (Figure 4-18C and D) and 1:1 binding stoichiometry. In the case of Cu(II), CD titration did not result in saturation of the signal (Figure 4-18E to G). Initially the exciton signal increased until the WW-CA:Cu(II) ratio was 1:1.2. From this point on the signal decreased upon further Cu(II) addition until a ratio of 1:2.5 was reached. Then, a maximum at 233 nm began to rise and the titration was stopped at a ratio of 1:10. Fluorescence titration was therefore carried out (Figure 4-18H and I, using WW-CA-Nle), resulting in a saturation binding curve with a K_d of 0.5 µM and again 1:1 binding stoichiometry. The binding affinity of the metal ions correlates with the trend of the Irving-Williams series. Cu(II) is most strongly bound, followed by Zn(II) and Ni(II). It is interesting to note that the K_d values do not correlate with the T_m values. Although Cu(II) shows the strongest binding, the T_m value was the lowest.

From the CD and fluorescence spectroscopic results it can be concluded that Zn(II), Ni(II) and Cu(II) bind to WW-CA but induce different and therefore easily distinguishable conformational changes, which can be explained by the different geometries preferred by the metal ions. Zn(II), with a d^{10} electron configuration, prefers a tetrahedral, Ni(II), d^8, a square-planar and Cu(II), d^9, a Jahn-Teller distorted octahedral coordination sphere. It should be noted that metal ions in proteins can adopt different coordination geometries, often those that do not correspond to the preferred geometries. In this case, the protein is rigid and forces the metal into a non-ideal geometry. This is known as the entatic state and plays an important role in catalysis and electron transfer processes.[277-279] But in this case, WW-CA should be seen as a flexible ligand, allowing the metal ion to force the peptide into a new conformation. In case of hCAII, X-ray analysis revealed that Cu(II) or Ni(II) binds to the His_3 site with a trigonal-bipyramidal (CuN_3O_2)

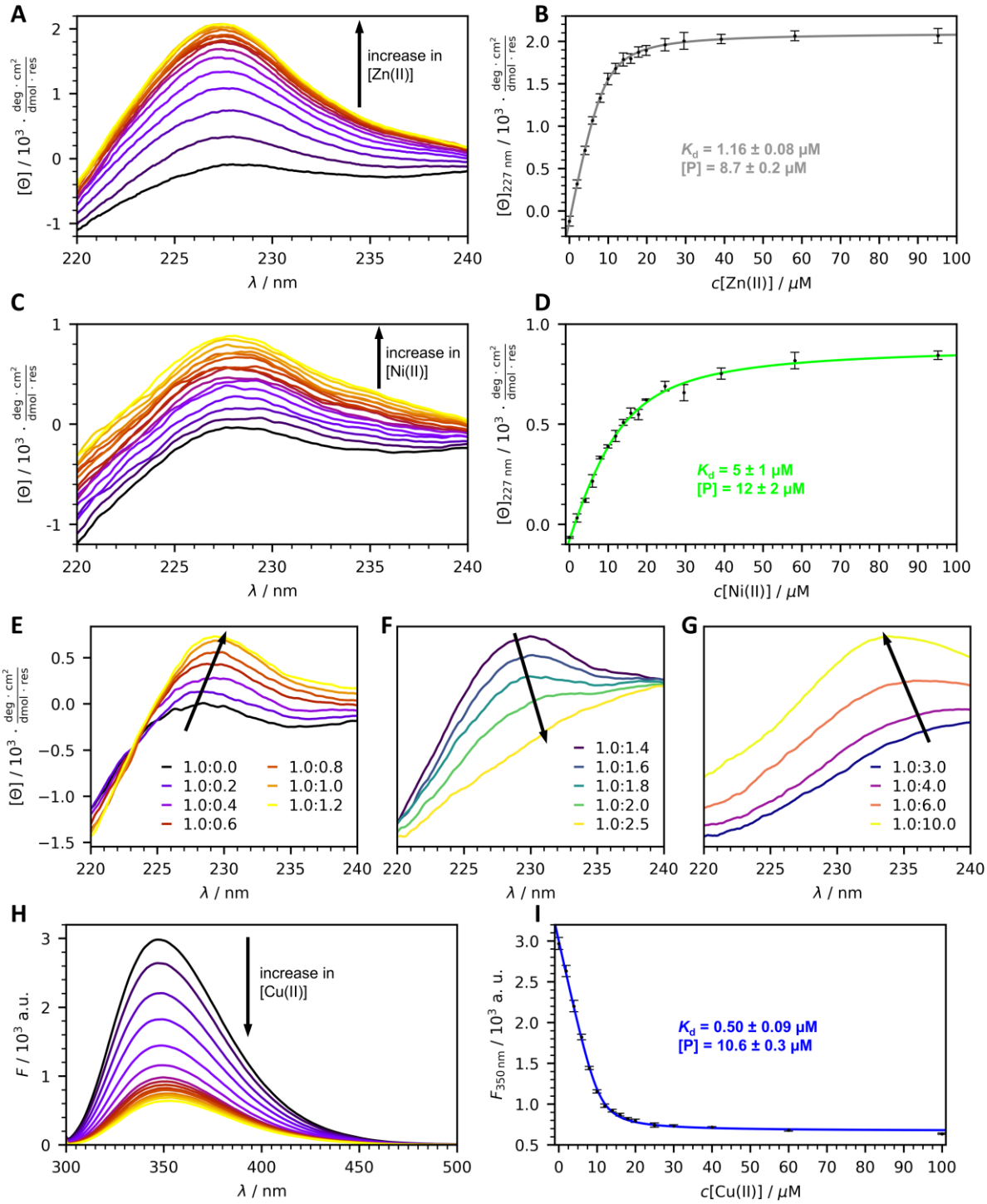

Figure 4-18: Metal ion titration experiments. A) CD spectra of WW-CA at different concentrations of Zn(II) and B) resulting binding isotherm. C) CD spectra of WW-CA at different concentrations of Ni(II) and D) resulting binding isotherm. E-G) CD spectra of WW-CA at different concentrations of Cu(II). Conditions: 10 µM WW-CA, 10 mM MOPS, 150 mM NaCl, pH 7.2 titrated with 2 mM $ZnSO_4$/$NiSO_4$, 10 mM MOPS, 150 mM NaCl, pH 7.2 or 4 mM $CuSO_4$ and 20 mM MOPS, 300 mM NaCl, pH 7.2; 1 cm cuvette, 20 °C. H) Fluorescence spectra of WW-CA at different concentrations of Cu(II) and I) resulting binding isotherm. Conditions: 10 µM peptide, $CuSO_4$ (0-100 µM), 10 mM MOPS, 150 mM NaCl, pH 7.2,10 mm x 2 mm cuvette, λ_{ex} = 295 nm, room temperature (20-25 °C).

or octahedral (NiN_3O_3) coordination geometry, respectively, but the overall conformation of the protein remains unchanged.[280-281] In contrast, the characteristic conformational change of

WW-CA allows discrimination between the metal ions, which is very important for sensory applications.

4.1.6 WW-CA is a molten globule

The NMR experiments correlated well with the CD experiments and all four hypotheses (see chapter 4.1.3) were confirmed. Additional and detailed information about the residues involved was also obtained. WW-CA exists in a weakly folded apo state formed by the interaction of the amino acid residues of the inner hydrophobic core, which fold and unfold non-cooperatively. The apo state can bind Zn(II), Ni(II) and Cu(II) *via* the incorporated His_3 site and the resulting holo state has a better packed inner hydrophobic core and exhibits a cooperative folding-to-unfolding transition. The three-dimensional peptide structure is very sensitive to changes in ionic strength, pH, Zn(II) concentration and temperature. Heating the WW-CA-Zn(II) complex above T_m leads to aggregation, as did solvation of the lyophilised peptide in a buffer solution containing Zn(II). In both cases WW-CA is completely unfolded, indicating the difference between the apo state and the completely unfolded state: in the unfolded state interaction with Zn(II) led to aggregation, while the apo state can bind Zn(II) and form a globular 1:1 complex, as was proved by titration. Therefore, apo-WW-CA is unfolded in lyophilised form, but must adopt a monomeric weakly folded apo state with a preformed His_3 site in solution that can bind to Zn(II).

The switching behaviour is still somewhat special and does not agree with textbook examples. Standard models assume that switchable proteins are completely unfolded and adopt a stable structure upon a certain external trigger, such as metal ions or a change in pH, or exist in at least two different stably folded conformations and switch between them.[282] Neither of these cases applies to WW-CA. Furthermore, the ^1H NMR spectra of the apo and holo states differ less than expected for a switch between two completely different conformations, and in the 2D ^1H-^{15}N HSQC the chemical shift dispersion of the backbone amid protons were less then expected for a fully folded peptide, including the holo state. In order to obtain a better understanding of the degree of folding of WW-CA, the parent peptide $hPin1_{WW}$-Nle, a variant in which the oxidation-sensitive Met is substituted by Nle, was synthesised by SPPS and purified by HPLC (characterisation data in Chapter 10.3) as a reference. In Figure 4-19 the CD spectra and thermal denaturation curves of $hPin1_{WW}$-Nle and WW-CA-Nle are shown. The exciton signal of $hPin1_{WW}$-Nle is much more pronounced than the exciton signal of holo WW-CA-Nle. In addition, the thermal denaturation curve of $hPin1_{WW}$-Nle shows a clear sigmoidal shape with a T_m value 20 K higher than that of holo WW-CA-Nle.

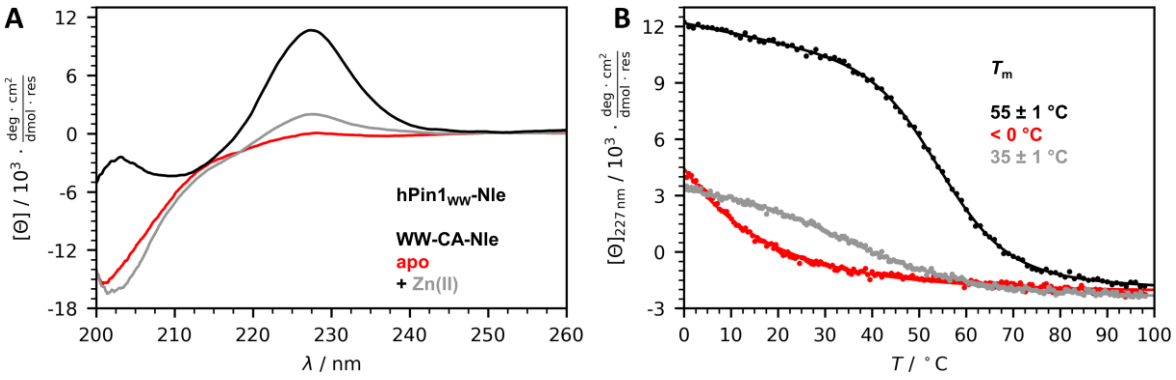

Figure 4-19: A) CD spectra at 20 °C and B) thermal denaturation curves of hPin1$_{WW}$-Nle in comparison to WW-CA-Nle in the apo and holo state. Conditions: 50 µM hPin1$_{WW}$-Nle or 100 µM WW-CA-Nle, 100 µM $ZnSO_4$ (if present), 10 mM MOPS, 150 mM NaCl, pH 7.2, 1 mm cuvette.

The ^{1}H NMR spectrum of hPin1$_{WW}$-Nle confirms that this peptide is well folded (Figure 4-20). The signals are well resolved, with a high dispersion at the NH and aromatic region. Both Trp11 and Trp34 NH are visible at 10.58 ppm and 10.07 ppm, respectively, showing that both residues are surrounded by different chemical environments. Furthermore, upfield shifted methyl signals, characteristic of folded peptides,[283-284] are observed below 0 ppm. Finally, the 2D ^{1}H-^{15}N-HSQC spectrum of hPin1$_{WW}$-Nle is of excellent quality and 36 NH signals are very well resolved with a high dispersion (Figure 4-21). A first glance at the NMR spectra, one would identify even holo WW-CA-Nle as an at least partially disordered peptide, but the CD spectrum showed clear evidence, that secondary structure is present, albeit weaker than in the parent peptide hPin1$_{WW}$-Nle. On one hand, NMR analysis confirmed conformational change after Zn(II) binding and correlates with the CD data, as discussed earlier. On the other hand, NMR and CD spectra seem to indicate a different degree of folding. As discussed earlier, there is a distinct difference in aggregation tendency in presence of Zn(II) between the fully unfolded and the apo state. To explain the observations, including the high sensitivity of WW-CA to its environment and the mobility of its hydrophobic core, WW-CA is assumed to be a molten globule (MG)[285-286] or a marginally stable peptide (MSP).[287] MG states have been reported for both a WW domain mutant[288] and an apo state of a Zn(II)-binding four-helix bundle.[289] A peptide in the MG state is partially folded and most of the secondary structure is present, but the hydrophobic core is not tightly packed and the side chains remain mobile, explaining the low chemical shift dispersion in the NMR spectra, while in the CD spectra signals typical of secondary structure elements are observed.[255] Furthermore, in the fully unfolded state, the His_3 site is not preformed and aggregation can be explained by coordination of His side chains from several peptides to a Zn(II) ion.

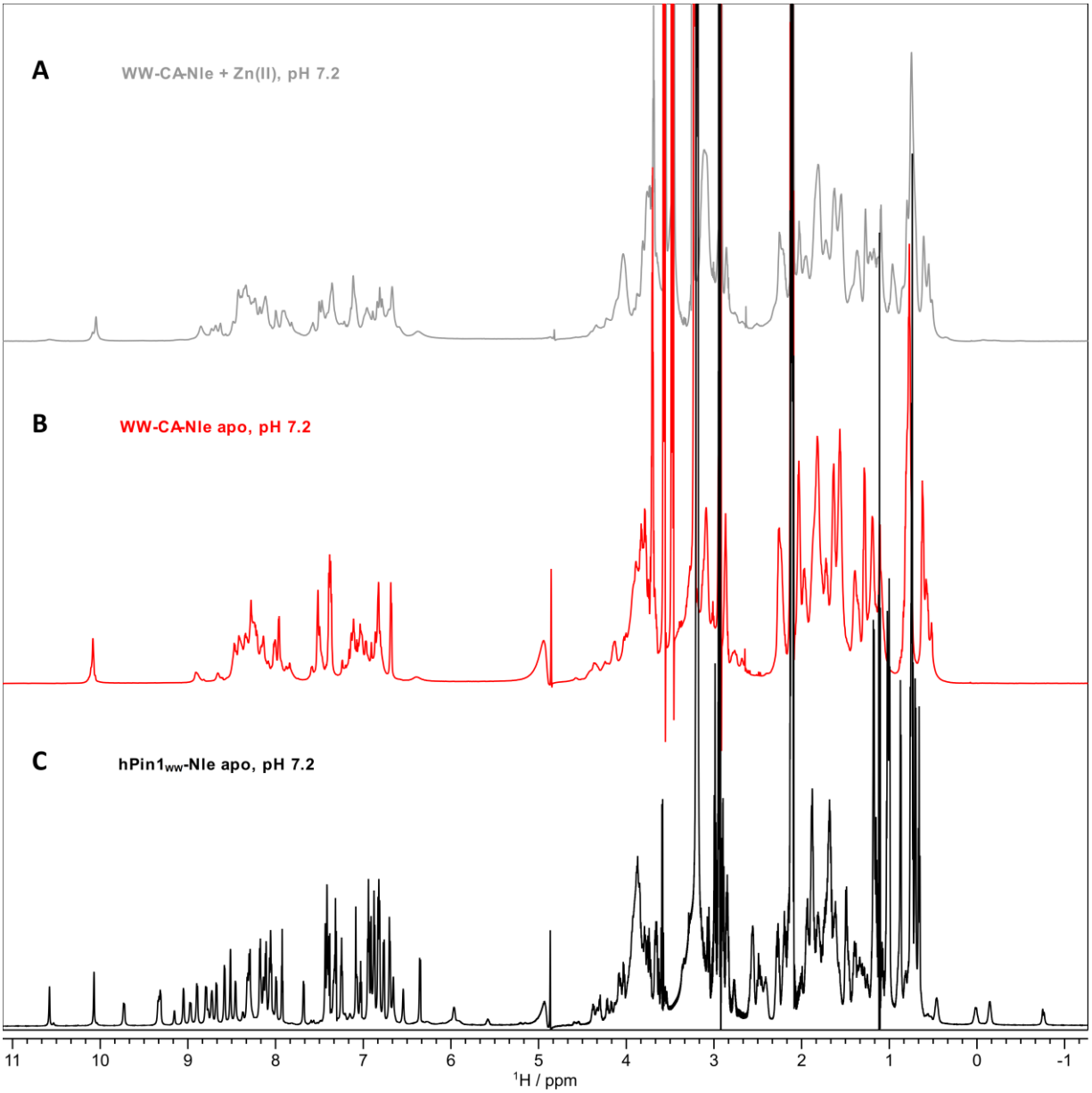

Figure 4-20: Comparison of the 1D ^{1}H NMR spectra of A) holo WW-CA-Nle, B) apo WW-CA-Nle and c) hPin1$_{WW}$-Nle. Conditions: 800 MHz, 1 mM peptide, 1 mM $ZnSO_4$ (if present), 10 mM MOPS, 150 mM NaCl, pH 7.2, 5% *v/v* D_2O, 10 °C.

Similar to MG's, MSP's are intermediate between fully folded and intrinsically disordered peptides with a change in free energy of unfolding Δ*G* between 0 and 12.6 kJ/mol at 25 °C.[287] Since the WW-CA-Zn(II) complex aggregates during thermal denaturation, an accurate determination of the thermodynamic parameters for the unfolding process of WW-CA is not possible. By fitting a two-state folding model to the data (see Chapter 8.2.9), an estimate of Δ*G* of about 2 kJ/mol at 25 °C can be obtained for the holo state. Due to the non-cooperative unfolding of the apo state, Δ*G* should be close to 0 kJ/mol. At first sight, such low stability might be seen as a disadvantage, since a major goal in peptide design is to generate highly stable peptides that can maintain their folding, which is essential for function, even under harsh conditions.

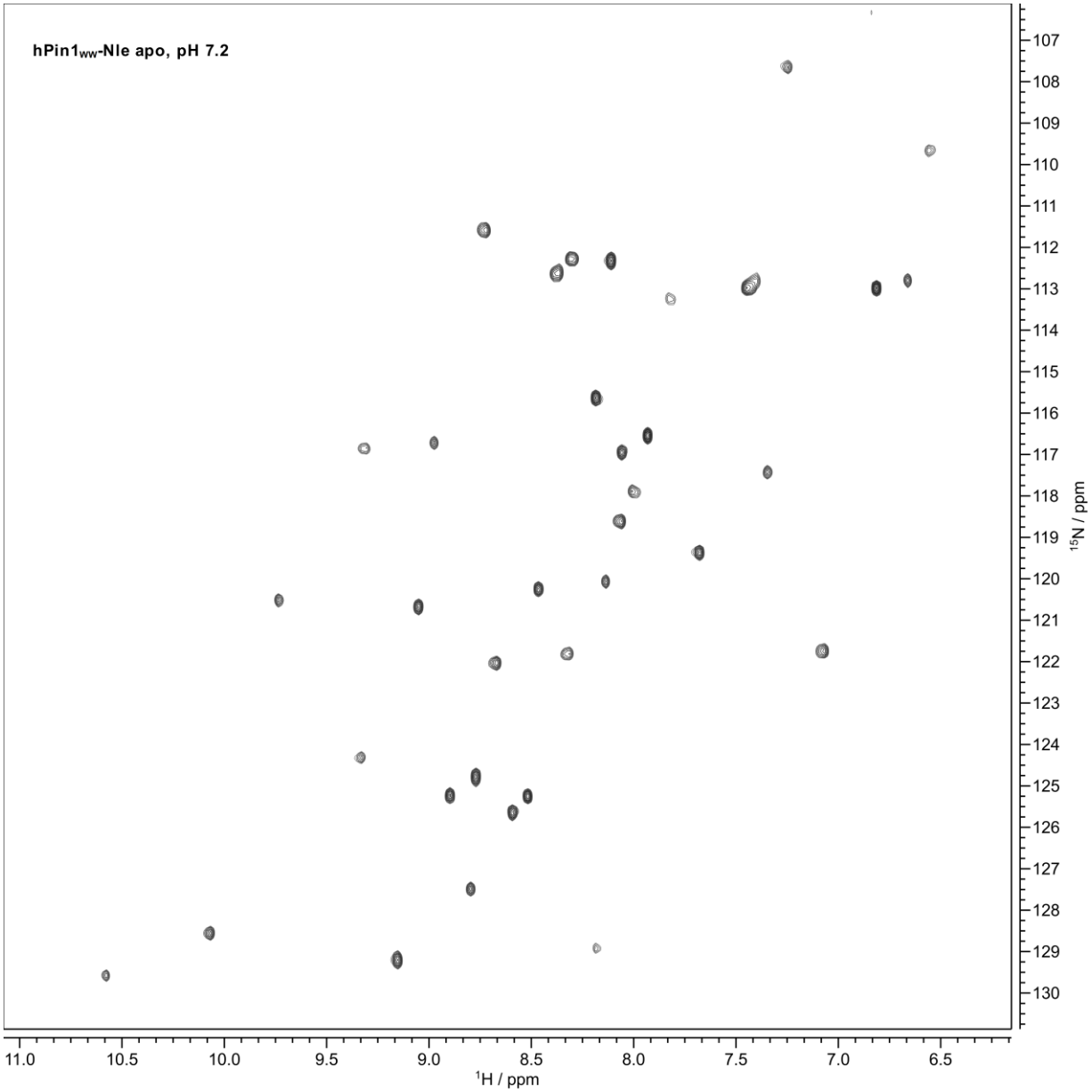

Figure 4-21: 2D ^{1}H-^{15}N HSCQ (800 MHz, 5% *v/v* D_2O in aqueous buffer: 10 mM MOPS, 150 mM NaCl, pH 7.2) spectra acquired on hPin1WW-Nle (1 mM) at 10 °C.

On the other hand, MSPs change conformation even with small environmental changes due to the small differences in free energy between two different states. These conformational changes are easily detected and the MSPs can be used as natural sensors. Therefore, being an MSP is not a disadvantage for WW-CA. In contrast, a stably folded and rigid peptide with a high Δ*G* cannot detect small changes because conformational changes only occur under harsh conditions. Some MSPs are known in nature, such as the temperature-sensitive p53 protein family, which regulate gene expression.[290] It has been suggested that MSPs may be well suited to sensory applications, but no example has been reported to date.[287]

However, further stabilisation would be required if WW-CA was intended for potential intracellular application aside from sensory applications, and with aggregation potential being

a major concern. Naturally, it has to be considered that the cytoplasm is not a diluted aqueous buffer solution, but contains biomacromolecules in a concentration range of 300 mg/L to 400 mg/mL.[291] Macromolecular crowding can have structural stabilising and aggregation inhibiting effects.[292-294] It is known, that crowding can induce the MG state of disordered proteins,[295-296] and stabilise the folding of proteins in the MG state.[297] A similar effect can be achieved by using small, polar, non-toxic and neutral molecules, known as osmolytes, such as glycerol.[298-300] To analyse crowding effects, the CD spectra and thermal denaturation curves of apo and holo WW-CA-Nle containing 300 g/L glycerol were recorded (Figure 4-22). A slight increase in exciton signal was observed for both the apo and holo state. Overall, the shape of the thermal denaturation curves was similar to those in the absence of glycerol. Apo WW-CA still showed a non-cooperative folding to unfolding transition, but fitting a two-state model yielded a melting temperature that was shifted to around 0 °C; however, although this value has to be interpreted carefully, as no upper baseline is observed. In case of the holo state a slight increase in T_m of 1 K is observed. After thermal denaturation and cooling to 20 °C, no aggregates were observed for the holo and the apo peptide. The CD spectra after thermal denaturation were superimposable with the spectra before heating, proving the reversibility of the folding-unfolding process in presence of glycerol. Calculating ΔG at 25 °C for the WW-CA-Nle-Zn(II) complex gives a value of about 2 kJ/mol. These experiments show, that, although crowding did not increase thermal stability, it was able to stabilise the molten globule structure, completely inhibit aggregation and support refolding after thermal denaturation.

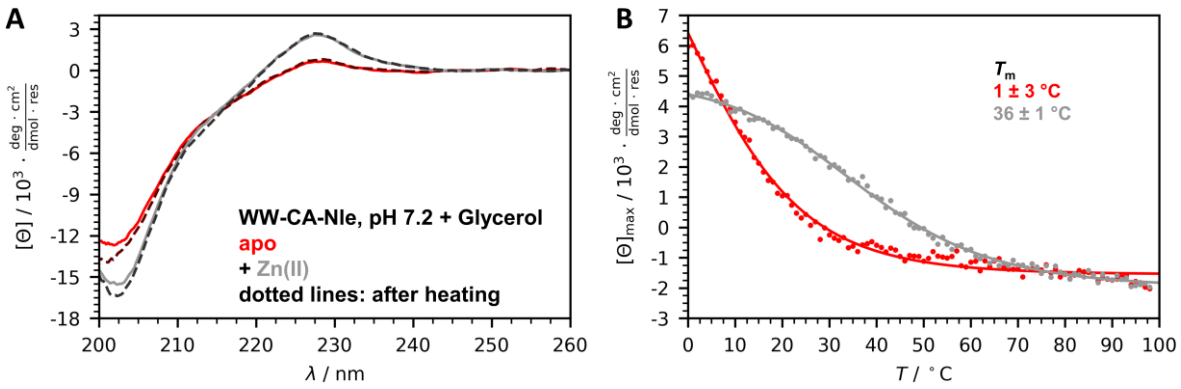

Figure 4-22: Influence of glycerol on WW-CA-Nle. A) CD spectra at 20 °C of WW-CA-Nle in absence and presence of Zn(II) before and after thermal unfolding. B) Corresponding CD thermal denaturation curves. Conditions: 50 µM peptide, 50 µM $ZnSO_4$ (if present), 300 g/L glycerol, 10 mM MOPS, 150 mM NaCl, pH 7.2, 1 mm cuvette.

4.2 Variants of WW-CA: Increase of thermal stability and suppression of aggregation

The major part of Chapter 4.2 has been published in *ChemBioChem*.[301]

4.2.1 Design concept

With WW-CA, a pH and metal-ion selective switchable peptide, was designed. Despite the positive aspects, WW-CA still tend to aggregate. Mutation of Met to Nle reduced this drawback, but still, in case WW-CA, or WW-CA-Nle is heated above its T_m of 34 °C in presence of Zn(II), aggregation occurs. The potential application in biological systems is therefore limited to cells and organisms that can grow at room temperature or below.

To overcome these limitations, more stable variants of WW-CA-Nle have been designed. WW-CA-Nle, a peptide of 34 amino acid residues, contains in total 7 mutations, which corresponds to a mutation rate of 21%. Therefore, in a redesign step, the His_3 site was retained, while all other mutations were reversed, except for the substitution of Met by Nle, as this prevents the formation of Met(O). Furthermore, His27 had to be mutated to avoid ambiguity in metal binding; but this time, Arg had been introduced instead of Ser as it is positively charged and should increase solubility, while reducing the aggregation propensity. The R21Q and N21Q mutations were initially introduced in WW-CA with the intention to form hydrogen bonds to His23 and His25, but there is no evidence that this is the case. Therefore, these mutations had been reversed. The redesigned peptide was named WW-CA-min (Figure 4-23).

In a second redesign step, Loop 1 was altered, to further increase thermal stability. It was reported by Jäger *et al*. that replacement of the SRSSGR loop with the shorter SADGR loop increased the thermal stability of $hPin1_{WW}$ by 18 K to 78 °C.[111] To avoid aspartimide formation during SPPS, which is a serious problem at DG positions,[302] SANGR was chosen as a loop sequence. This peptide was named WW-CA-ANG (Figure 4-23).

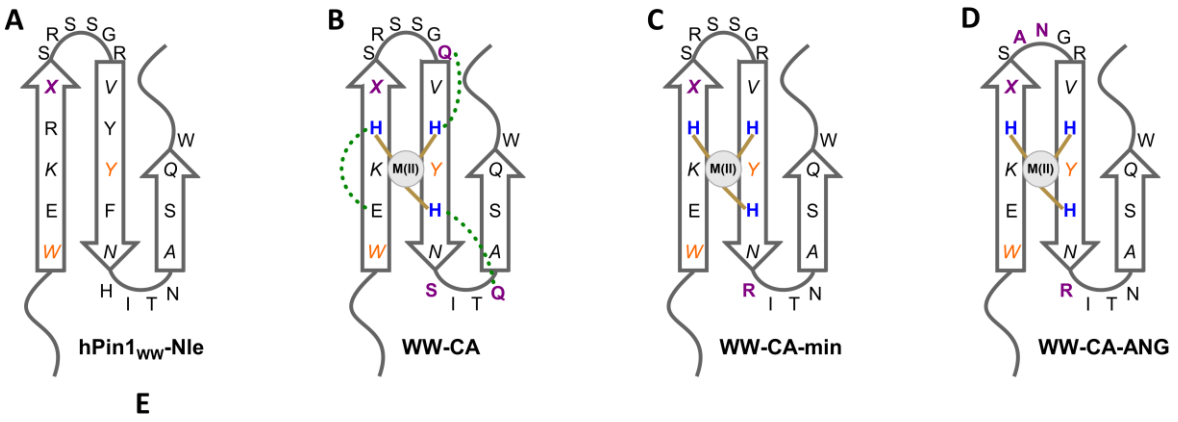

E

	N-T β1 L1 β2 L2 β3 C-T
hPin1$_{ww}$-Nle	KLPPG-WEKRX-SRSSGR-VYYFN-HITN-ASQ-WERPSG
WW-CA-Nle	KLPPG-WEKHX-SRSSGQ-VHYHN-SITQ-ASQ-WERPSG
WW-CA-min	KLPPG-WEKHX-SRSSGR-VHYHN-RITN-ASQ-WERPSG
WW-CA-ANG	KLPPG-WEKHX-S-ANGR-VHYHN-RITN-ASQ-WERPSG

Figure 4-23: Design concept of metal coordinating WW-CA variants. Schematic 2D representations of the structures of A) hPin1$_{ww}$-Nle, B) WW-CA-Nle, C) WW-CA-min, D) WW-CA-ANG. Italic residues point below the β-sheet. Residues depicted in orange are part of the hydrophobic core. Residues depicted in blue highlight the metal binding site. Residues depicted in purple refer to further variations from hPin1$_{ww}$. Potential hydrogen bonds are represented as green dashed and coordinative bonds as brown lines. X symbolizes the non-canonical amino acid norleucine. E) Sequences of the depicted peptides.

4.2.2 Metal ion binding and structural stability

To analyse the structure and metal ion binding properties of the two new peptides, CD spectra and thermal denaturation curves were recorded in the absence and presence of the metal ions Ni(II), Cu(II) and Zn(II) (Figure 4-24).

Two important changes were made from the WW-CA study: 1) The peptide concentration (and corresponding metal ion concentration) was reduced from 100 µM to 50 µM. This was done for two reasons: First, aggregation is a concentration dependent process and it was observed that heating WW-CA-Nle with Zn(II) at only 50 µM concentration reduced the amount of visible aggregates. Second, the 1 mm CD cuvette needs to be filled with at least 200 µL of sample for a reasonable measurement but is still only half full. Previously, 250 µL of sample was prepared in a polypropylene reaction tube and 200 µL was transferred to the cuvette. This is fine for simple spectra measurements, but evaporation could be observed during heating. Although the cuvette is tightly sealed with a PTFE stopper, the water evaporates into the air-filled volume and after cooling droplets of condensed water were observed. With the modified protocol, 500 µL of sample were prepared and the cuvette was filled as much as possible (400 µL to 450 µL depending on the cuvette used). By reducing the concentration, the amount of peptide used for the respective experiment was kept constant. 2) The thermal denaturation curves are recorded at the maximum wavelength determined at 20 °C. In the previous experiments, the

wavelength was always set to 227 nm. The maximum in the CD spectra of the WW domains is very broad and at wavelengths around 227 nm the ellipticity is very similar, so it is common in the literature to use only one wavelength for all (values from 226 nm to 229 nm were reported).[94, 108, 111] To better fit the individual peptides and peptide-metal ion complexes, the CD spectrum was first recorded at 20 °C, then the wavelength of the maximum was determined and the ellipticity at this wavelength was followed during thermal denaturation.

The following trends can be observed for the CD spectra of the three WW-CA peptides in the absence and presence of metal ions (Ni(II), Cu(II), Zn(II)): The intensity of the characteristic exciton at around 227 nm increased from WW-CA-Nle over WW-CA-min to WW-CA-ANG. In the presence of metal ions, individual changes in the CD spectra were observed for all three peptides. It can thus be concluded that all three peptides bind to Zn(II), Ni(II) and Cu(II) under changing their conformation. The presence of metal ions led to an increase in exciton signal intensity of WW-CA-Nle. Additionally, addition of Cu(II) caused a slight redshift of the maximum of the exciton signal. In case of WW-CA-min only the addition of Zn(II) resulted in an increased exciton signal intensity, while Ni(II) and Cu(II) led to a slight decrease of signal intensity. Again, addition of Cu(II) caused a slight redshift of the signal's maximum. The same is true for WW-CA-ANG, but in this case, addition of all metal ions resulted in a decrease of the exciton signal intensity. Upon addition of Ni(II), a shoulder between 210 nm and 220 nm became visible for all three peptides. To a lesser degree, this shoulder was also induced in WW-CA-ANG upon the addition of Zn(II). In case of the addition of Cu(II), a decrease of signal intensity between 210 nm and 220 nm was observed when measuring WW-CA-Nle and WW-CA-min; however, this was not the case for WW-CA-ANG.

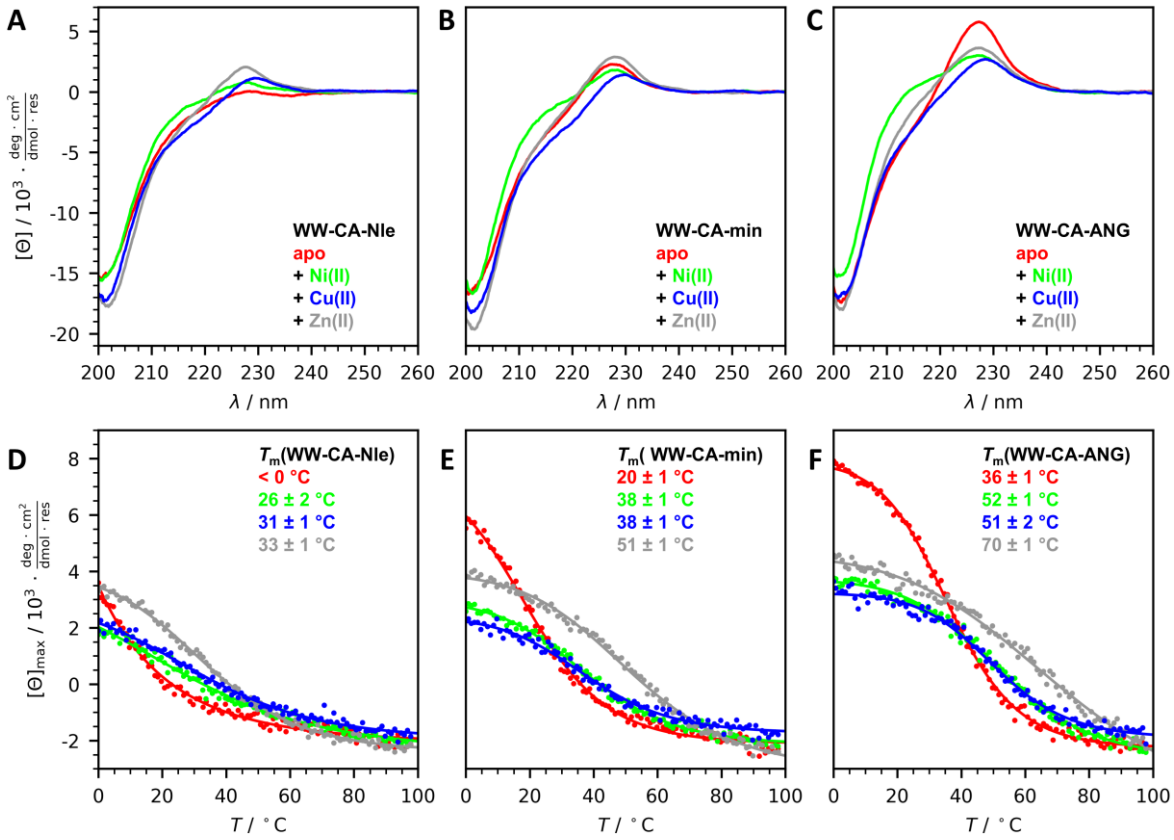

Figure 4-24: CD spectroscopic analysis of WW-CA variants in absence and presence of metal ions. CD spectra of A) WW-CA-Nle, B) WW-CA-min, C) WW-CA-ANG. Thermal denaturation profiles of D) WW-CA-Nle, E) WW-CA-min, F) WW-CA-ANG. Conditions: 50 µM peptide, 50 µM metal salt (if present), 10 mM MOPS, pH 7.2, 150 mM NaCl, 1 mm cuvette. CD spectra were recorded at 20 °C. CD thermal denaturation profiles were recorded from 0 °C to 98 °C.

Analysis of the thermal denaturation experiments revealed the following trends: The thermal denaturation curve of WW-CA-Nle, apo as well as holo, showed the lowest signal intensity of the upper baseline, which represents the folded state. This was followed by WW-CA-min and WW-CA-ANG, with the latter displaying this highest CD signal intensity at the upper baseline. Interestingly, the lower baseline, representing the fully denatured state, was very similar for all peptides, regardless of whether metal ions were present or not. T_m values increased in following order: WW-CA-Nle < WW-CA-min < WW-CA-ANG. Furthermore, in presence of metal ions cooperative folding to unfolding transitions and an increase in T_m values compared to the apo states were observed for all three peptides. Zn(II) increased the T_m value by more than 30 K and Ni(II) and Cu(II) by about 20 K compared to that of the apo states. The WW-CA-ANG-Zn(II) complex showed the highest T_m value of 70 °C and therefore is a thermostable metallo mini-protein. In general, the metal complexes of WW-CA-min and WW-CA-ANG always showed an increased thermostability in comparison to WW-CA, therefore the redesign can be considered as successful.

Moreover, for WW-CA-min and WW-CA-ANG, no aggregation was observed and the thermal unfolding was reversible (CD spectra of peptides after thermal denaturation see Appendix

Chapter 10.8), which was not the case for the WW-CA-Nle-Zn(II) complex, which aggregates upon heating above its T_m. It should also be noted that the changes, lower peptide concentration and monitoring of thermal denaturation at a different wavelength, had an influence on the thermal denaturation profiles of WW-CA-Nle in presence of Cu(II) and Ni(II), while the Zn(II) complex was not affected. For the Ni(II) complex T_m did not change significantly, but for the Cu(II) complex the new thermal denaturation curve had a similar shape to that of WW-CA-Nle-Ni(II) and a similar T_m of 30 °C (old value 19 °C).

The folding-unfolding transition is not only characterised by the midpoint, which is defined as T_m, but also by the steepness of the transition, which is expressed by ΔH, the change in enthalpy of unfolding and ΔC_p, the difference in heat capacity of the unfolded and folded state. Since it is known, that ΔC_p cannot be determined accurately using CD thermal denaturation,[251] it was set to 0 (detailed discussion in Chapter 8.2.9). Therefore, ΔH should not be over-interpreted and should be seen as a measure of the shape of the thermal denaturation curve. With increasing ΔH, the steepness of the transition also increases (values for ΔH can be found in the Appendix, Chapter 10.8). It would be expected that an increase in thermal stability would also be associated with an increase in ΔH, or at least ΔH would not change, simply shifting the curve to higher temperature values. The expectation is met in case of WW-CA-Nle. The Zn(II) complex, which displays the highest T_m, also has the highest ΔH value, followed by Cu(II) and Ni(II). The WW-CA-min complexes exhibit significantly increased thermostability, but the ΔH values hardly differ from the value of the apo state. This is in contrast to WW-CA-ANG, where the apo state has the highest ΔH value. The Cu(II) complex shows a slightly lower value, followed by Ni(II), but both have similar T_m values. Although the WW-CA-ANG-Zn(II) complex has the highest T_m of all, its transition is very broad, which may indicate reduced cooperativity of the unfolding process. Additionally, the ΔH value is significantly lower. A steep transition is more likely to indicate a two-state folding-unfolding process, while a broad transition may indicate a gradual unfolding. Combined with the fact that, in some cases, metal binding leads to a reduction in exciton signal intensity, this indicates that the induced conformational change may result in an unfavourable alteration in the hydrophobic core.

4.2.3 Affinity and stoichiometry of metal ion binding

To further analyses the metal binding properties of the peptides, fluorescence spectra were recorded in the absence and presence of metal ions (Figure 4-25A to C). The tryptophan residues of the peptides were excited at 295 nm and the emission was recorded. As a general trend it was observed that addition of Zn(II) led to a fluorescence enhancement for all three peptides, while addition of Ni(II) resulted in a slight and Cu(II) is a strong fluorescence decrease.

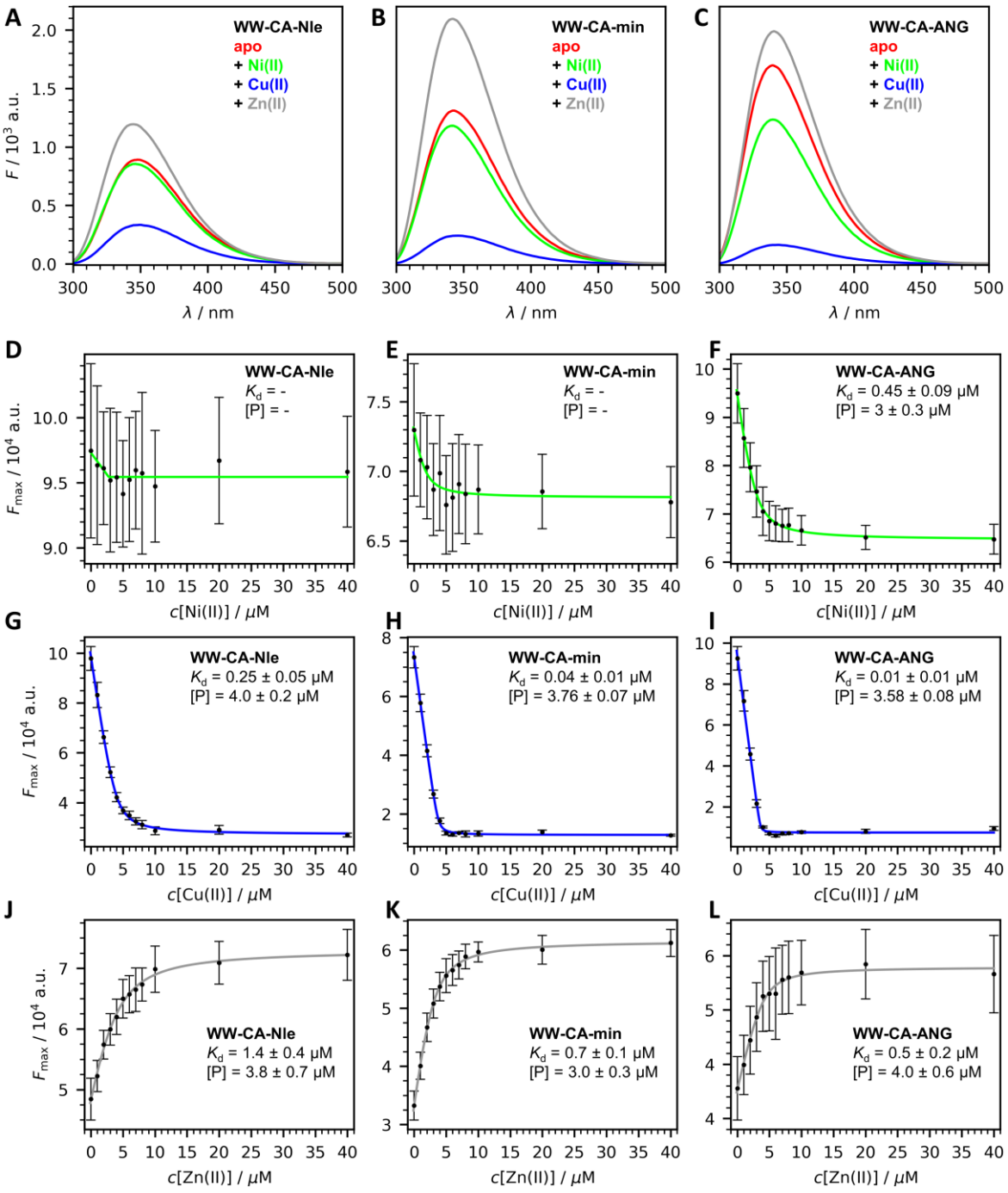

Figure 4-25: Determination of metal binding affinity of the WW-CA variants. Fluorescence spectra of A) WW-CA-Nle, B) WW-CA-min, and C) WW-CA-ANG in absence and presence of metal ions. Conditions: 10 µM peptide, 10 µM metal salt (if present), 10 mM MOPS, pH 7.2, 150 mM NaCl, Trp residues were excited at λ_{ex} = 295 nm, room temperature (20-25 °C), 10 mm x 2 mm cuvette. Saturation binding curves of D) WW-CA-Nle and Ni(II), E) WW-CA-min and Ni(II), F) WW-CA-ANG and Ni(II), G) WW-CA-Nle and Cu(II), H) WW-CA-min and Cu(II), I) WW-CA-ANG and Cu(II), J) WW-CA-Nle and Zn(II), K) WW-CA-min and Zn(II), L) WW-CA-ANG and Zn(II). Conditions: 4 µM peptide, 0-40 µM metal salt, 10 mM MOPS, pH 7.2, 150 mM NaCl, Trp residues were excited at λ_{ex} = 295 nm, room temperature (20-25 °C), 96-well plates.

The change in fluorescence intensity was then used to determine the peptide-metal ion dissociation constants (Figure 4-25D to L). For almost all peptide-metal ion combinations, typical saturation curves were obtained and the fitted value for the peptide concentration

matched the used peptide concentration of 4 µM, suggesting a 1:1 binding. Only the WW-CA-Nle and WW-CA-min Ni(II) complexes could not be analysed using this method (Figure 4-25D and E). Here the change in fluorescence intensity was too low compared to the noise and the fit did not yield meaningful values. Instead, CD titration was performed (Figure 4-26). In addition to the CD titration Ni(II) to WW-CA-Nle and WW-CA-min, the CD titration of Zn(II) to WW-CA is also presented. The obtained K_d of 1.19 µM fits very well with the value determined by fluorescence titration (1.4 µM), marking CD titration a very useful complementary experiment for the determination of K_d values. Titration of WW-CA and WW-CA min with Ni(II) gave saturation binding curves from which K_d values were determined that were in the lower µM to upper nM regime. Additionally, a 1:1 binding stoichiometry was confirmed. In general, the metal ion binding to WW-CA-Nle is the weakest, followed by metal ion binding to WW-CA-min, while WW-CA-ANG binds metal ions the strongest.

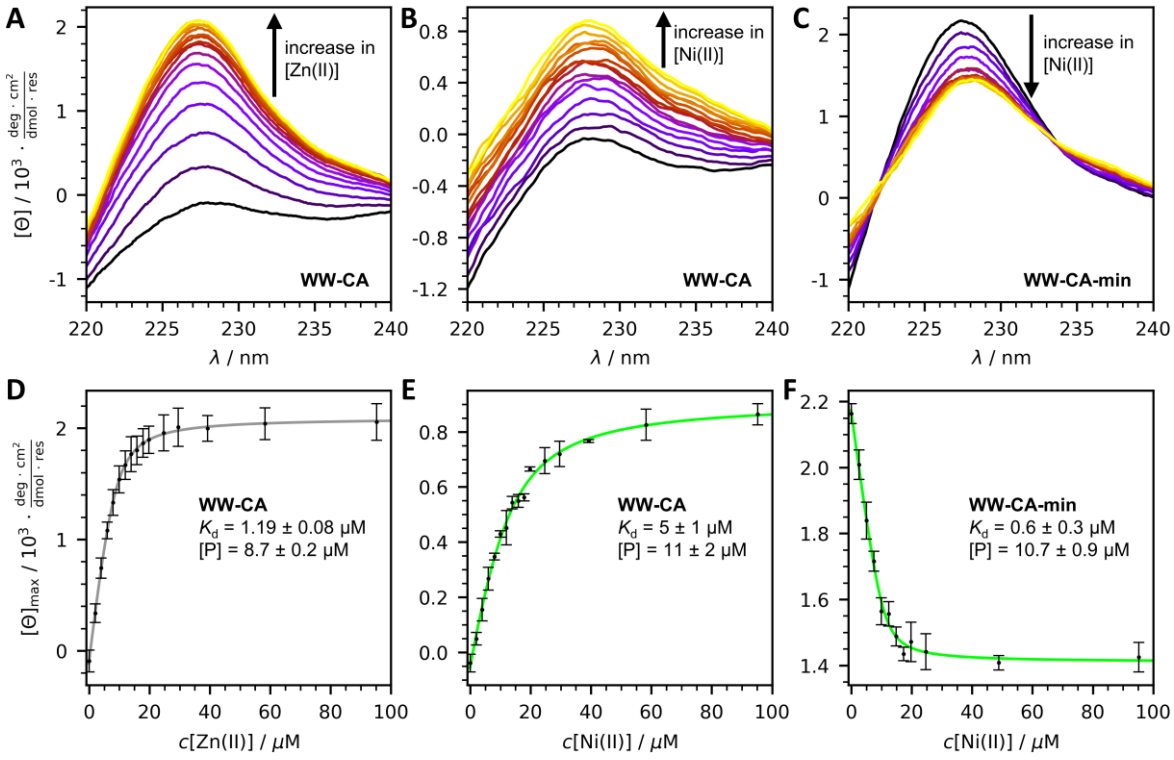

Figure 4-26: CD titration to determine metal ion binding. CD spectra of A) WW-CA titrated with Zn(II), B) WW-CA titrated with Ni(II), C) WW-CA-min titrated with Ni(II). Saturation binding curves of A) WW-CA and Zn(II), B) WW-CA and Ni(II), C) WW-CA-min and Ni(II). Conditions: MOPS-buffered peptide solution (10 µM peptide, 10 mM MOPS, 150 mM NaCl, pH 7.2), in a 1 cm cuvette was titrated with MOPS-buffered Zn(II) or Ni(II) solution (2 mM $ZnSO_4$ or $NiSO_4$,10 mM MOPS, 150 mM NaCl, pH 7.2) at 20 °C. Wavelength at $[\Theta]_{max}$: WW-CA+Zn(II): 228 nm, WW-CA+Ni(II): 228.5 nm, WW-CA-min+Ni(II): 227.5 nm.

For the Cu(II) peptide interaction, the fits of the saturation binding curves determined by fluorescence titration gave K_d values that were more than 20 times lower than the peptide concentration (4 µM), which is outside of the acceptable range.[303] It was not possible to further reduce the peptide concentration, as further decrease of the signal intensity would result in a low signal-to-noise ratio. Therefore, competitive titration in presence of TAMSMB (2-(2-

thiazolylazo)-4-methyl-5-(sulfomethylamino) benzoic acid)[304] was performed (Figure 4-27). The curves show a sigmoidal shape, indicating that all three peptides possess two Cu(II) binding sites. The first Cu(II) binding site reveals a K_d value in the lower nM to upper pM range and the second binding site in the lower µM to upper nM range.

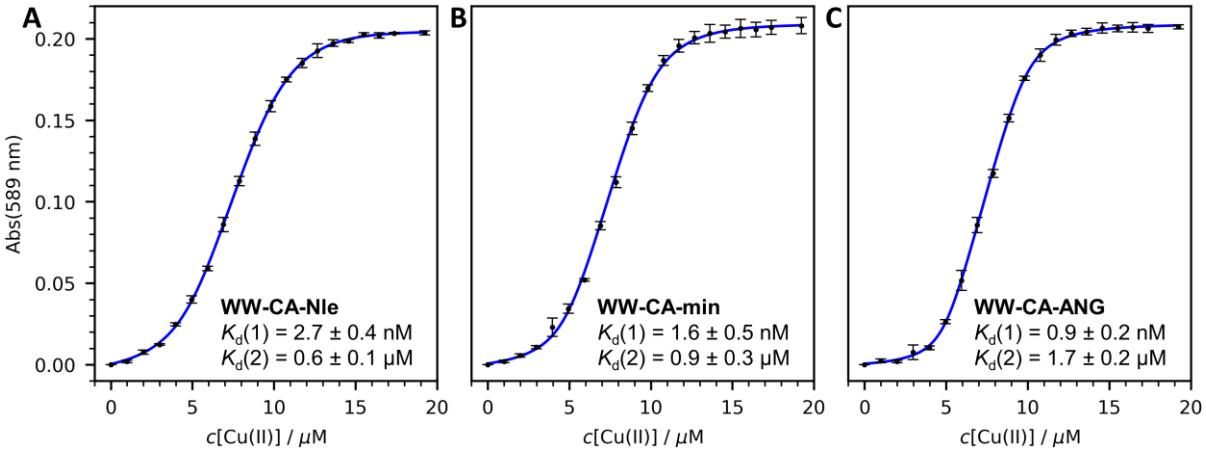

Figure 4-27: Competitive titration to determine the Cu(II) binding affinity to A) WW-CA-Nle, B) WW-CA-min and C) WW-CA-ANG. Conditions: 5 µM peptide, 5 µM TAMSMB, 10 mM MOPS, 150 mM NaCl, pH 7.2, 1 cm cuvette, titrated with 1 mM CuSO4, 10 mM MOPS, 150 mM NaCl, pH 7.2, room temperature (20-25 °C).

Due to the significant difference in affinity of approximately three orders of magnitude between the first and second binding sites, it is likely that the first binding event occurs at the His_3 site, while the second binding is non-specific, as known for Cu(II) ions. This effect is exploited in the biuret test to detect and quantify proteins.[305] For the first binding site, the affinity increases from WW-CA-Nle to WW-CA-min and then to WW-CA-ANG. However, for the second binding site, the opposite is true. Therefore, WW-CA-ANG binds Cu(II) more selectively at the His_3 site than the other two peptides.

The K_d values also showed an easily detectable trend: Regardless of which metal ion was present, the K_d for WW-CA-Nle was always the highest, followed by WW-CA-min and WW-CA-ANG. The metal ions also showed a peptide-independent trend: Ni(II) and Zn(II) bind to the peptides with similar K_d values and Cu(II) binds with the lowest K_d values, which is in accordance to the Irving-Williams series.[306]

4.2.4 Correlation between structural stability and metal binding affinity

When the T_m values of the peptides is compared with the K_d, a correlation is observed: the higher the T_m of the apo state, the lower the K_d, i.e. the higher the binding affinity. WW-CA-Nle, which always binds with the lowest affinity, also has the lowest T_m value of the apo state, whereas WW-CA-ANG, the strongest binder, also denatures at higher temperatures. However, this is only true when comparing different peptides. If the peptide is kept constant and the metal ion is varied, no correlation is observed. All peptide-Zn(II) complexes show the highest T_m

values, but the binding affinity of Zn(II) is similar to that of Ni(II). Cu(II) binds with the highest affinity to each peptide, and the affinity of Ni(II) is orders of magnitude weaker, but the thermal stability of peptide-Cu(II) and Ni(II) complexes was very similar. It should be kept in mind, that a high binding affinity does not have to correlate with a higher thermal stability. In some cases, the binding of metal ions led to destabilization of the protein and T_m value is reduced.[307]

Assuming a positive correlation between the thermostability of the apo state and binding affinity, it can be inferred that thermostable peptides are better folded, resulting in better preorganisation of the His_3 site. To investigate this hypothesis, isothermal titration calorimetry was performed (Figure 4-28), where Zn(II) was titrated to all three WW-CA variants, resulting in thermograms with decreasing heat development upon the addition of Zn(II). Binding isotherms were calculated by integration, from which the thermodynamic parameters of the binding events were determined. The K_d values and Zn(II):peptide stoichiometry obtained agree well with the results of both the CD and fluorescence measurements. The binding affinity increases from WW-CA-Nle to WW-CA-min and finally to WW-CA-ANG, as reflected in the negative ΔG values, which differ only slightly in numerical value. The values for the enthalpy ΔH and the entropy term $-T\Delta S$ are notably different. The WW-CA-Nle-Zn(II) complex released the most heat and had a positive entropy term, which means a decrease in entropy. The WW-CA-min complex releases slightly less heat and had a less positive entropy term. The WW-CA-ANG complex showed the greatest difference, with significantly less heat release and a negative entropy term, indicating an increase in entropy.

The CD spectroscopic data correlates well with these observations. The binding of Zn(II) to WW-CA-Nle is enthalpically favoured, as the peptide is present in a molten globule state and little energy is required for deformation. This led to an induction of peptide folding, resulting in better packing of the hydrophobic core. The increase in the exciton signal is recognisable, and the entropy decreases. A disadvantage here is the poor preorganisation in a molten globule, which results in the lowest overall binding affinity. WW-CA-min is better folded in the apo state, i.e. the degree of preorganisation is higher, which increases the overall affinity. ΔH is slightly weaker, however, as the better folding of the apo state is also accompanied by an increased energy input for the conformational change. The behaviour of WW-CA-ANG is the opposite. The signal intensity of the exciton decreases upon binding of Zn(II), indicating an unfavourable conformational change in the hydrophobic core. This change increased the entropy, but the forced conformational change on a well-folded peptide consumes some of the heat, resulting in a reduced ΔH. The preorganization is improved, but not outstanding, because the increase in affinity from WW-CA-Nle to WW-CA-min is significantly stronger than from WW-CA-min to WW-CA-ANG. A further increase in thermostability may not necessarily lead to a further increase in affinity, as the preorganization is not further improved. In this case, it is also more accurate to speak of predisposition.[308] In cases of preorganization, the ligands are already

arranged in the correct spatial conformation, and the peptide's conformation does not change further during metal binding. In contrast, in predisposition, the ligands are only roughly arranged, and metal binding induces conformational changes that can range from individual bonds to the entire peptide, which was observed in the metal ion binding of all WW-CA variants.

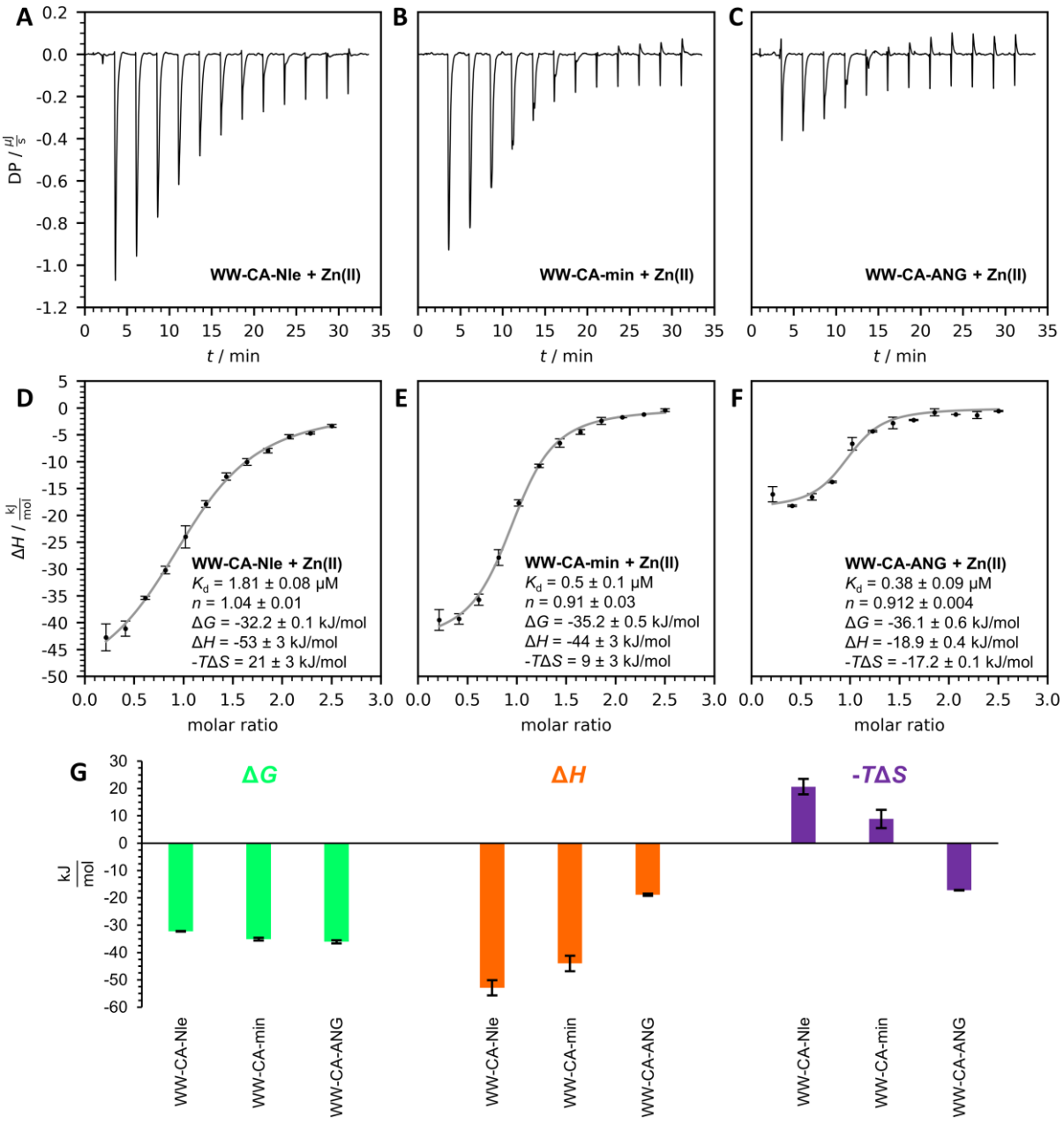

Figure 4-28: ITC analysis of Zn(II) binding to WW-CA variants. Baseline-corrected thermograms of Zn(II) titration to A) WW-CA-Nle, B) WW-CA-min, and C) WW-CA-ANG. ITC binding isotherms of Zn(II) titration to D) WW-CA-Nle, E) WW-CA-min, and F) WW-CA-ANG. A model for a single set of identical binding sites was fitted to the data. The fitted thermodynamic parameters are depicted in the respective diagrams. G) Bar chart representation of the thermodynamic parameters Δ*G*, Δ*H* and -*T*Δ*S* of Zn(II) binding to WW-CA-Nle, WW-CA-min, and WW-CA-ANG. Conditions: 10 µM peptide, 10 mM MOPS, pH 7.2, 150 mM NaCl titrated with 200 µM $ZnSO_4$, 10 mM MOPS, pH 7.2, 150 mM NaCl, 20 °C.

4.2.5 Structural aspects of Cu(II) binding

The unexpected capability of all WW-CA variants to bind two Cu(II) ions is highly interesting, since several Cu(II) containing enzymes are di- or multicopper proteins. To further investigate the Cu(II) binding, CD titration was performed (Figure 4-29). In case of WW-CA, first an increase and red shift of the exciton signal was observed as expected. But then, if the Cu(II):peptide ratio is higher than 1.2, an decrease in signal intensity was observed until a Cu(II):peptide ratio of 2.5 was reached. If the Cu(II) concentration was further increased, the maximum increased again, but was strongly red shifted to 234 nm. The observations for WW-CA-min where slightly different. Here the exciton signal decreased with increasing Cu(II) concentration up to a Cu(II):peptide ratio of 2.5. Then a maximum at 235 nm appeared, which increased as the Cu(II) concentration was further increased. A similar behaviour was observed for WW-CA-ANG. Again, the maximum decreased first, but this time a Cu(II):peptide ratio of 4 was required, before the maximum at 231 nm increased.

These observations are in agreement with the competitive titration experiments. Instead of a simple decrease or increase of signal intensity with a saturation behaviour, the CD spectra changed at higher Cu(II) concentration clearly indicating additional binding and perturbation of the structure, since the spectra at high Cu(II) concentration are not similar to that of a WW domain. WW-CA is only weakly folded and more prone to Cu(II) induced denaturation. In contrast WW-CA-ANG is a stably folded peptide, even in the apo state, and structural perturbation only occurs at high Cu(II) concentration. Therefore, the second Cu(II) binding event is weaker for WW-CA-ANG than for WW-CA-Nle.

Because the WW-CA variants show unexpected Cu(II) binding behaviour which is assumed to be unspecific, the interaction of Cu(II) with the parent peptide hPin1$_{WW}$-Nle was analysed by CD spectroscopy. As shown in Figure 4-30A, addition of Cu(II) led to a decrease in the exciton signal at 227 nm, which is a clear indication for binding, while addition of Ni(II) and Zn(II) did not cause any structural change. Furthermore, the thermal denaturation experiments (Figure 4-30B) revealed that in presence of Cu(II) the thermal stability decreased by 11 K, which is in sharp contrast to all WW-CA variants, where metal ion binding always increased thermal stability. Again, the thermal denaturation curves in presence of Ni(II) and Zn(II) are equivalent to that of the apo peptide. Therefore, hPin1$_{WW}$-Nle binds exclusively to Cu(II), not to Ni(II) and Zn(II), which is very interesting, since hPin1$_{WW}$-Nle is not considered a metal binding peptide and its biological function does not require metal ions.

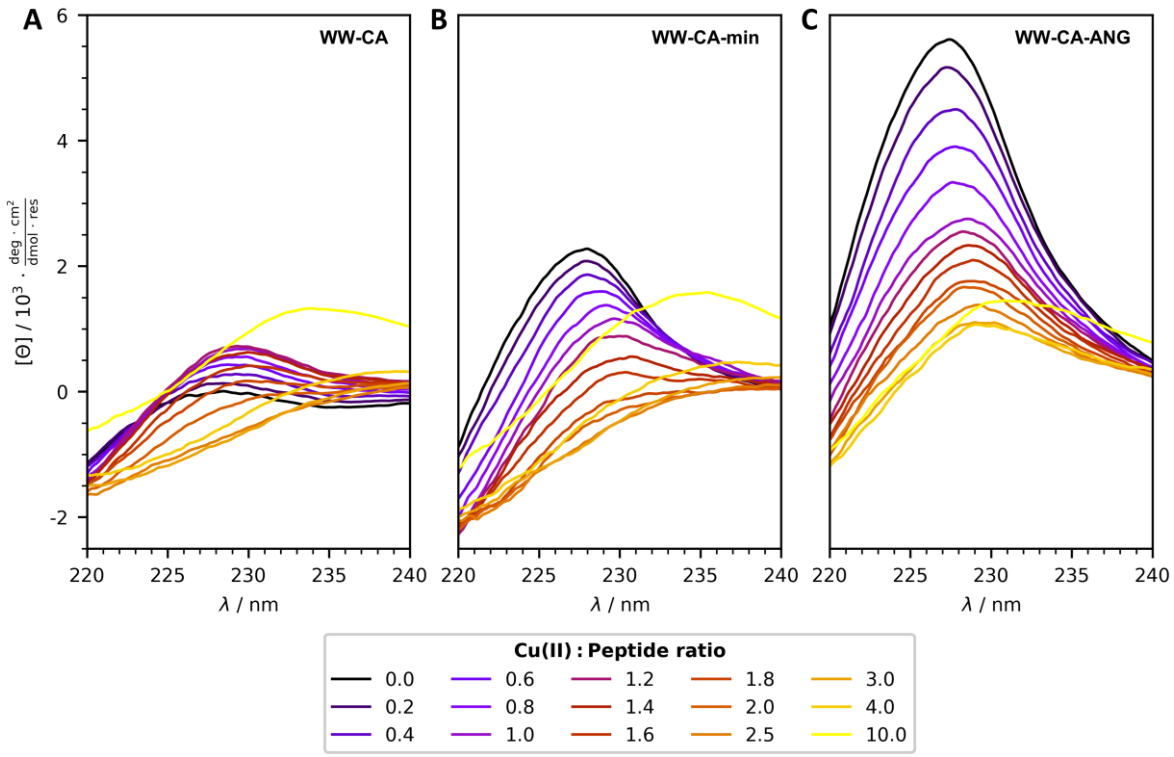

Figure 4-29: CD titration of Cu(II) to A) WW-CA, B) WW-CA-min and C) WW-CA-ANG. Conditions: 10 µM peptide, 10 mM MOPS, pH 7.2, 150 mM NaCl in a 10 mm cuvette is titrated with 2 mM $CuSO_4$ in 10 mM MOPS, pH 7.2, 150 mM NaCl at 20 °C.

Then CD titration was performed to determine the binding affinity. As shown in Figure 4-30C The exciton signal intensity decreased with increasing Cu(II) concentration and a saturation behaviour was observed. In contrast to the WW-CA variants, no further structural deformation was observed. With a T_m of 55 °C in the apo state, which is higher than that of apo WW-CA-ANG (36 °C), $hPin1_{WW}$-Nle is a stably folded peptide and high Cu(II) concentration did not lead to denaturation. Fitting the decrease in exciton signal intensity (Figure 4-30D) yielded a K_d value of 7 µM and a 1:1 stoichiometry. This affinity is much weaker than that of the WW-CA variants. To confirm the binding affinity, fluorescence titration was performed (Figure 4-30E). Cu(II) quenched the Trp fluorescence and again saturation was observed with increasing Cu(II) concentration. Although the binding stoichiometry was confirmed to be 1:1 (Figure 4-30F), the K_d value (1.2 µM) was significantly lower and comparable to the second K_d value of the WW-CA variants.

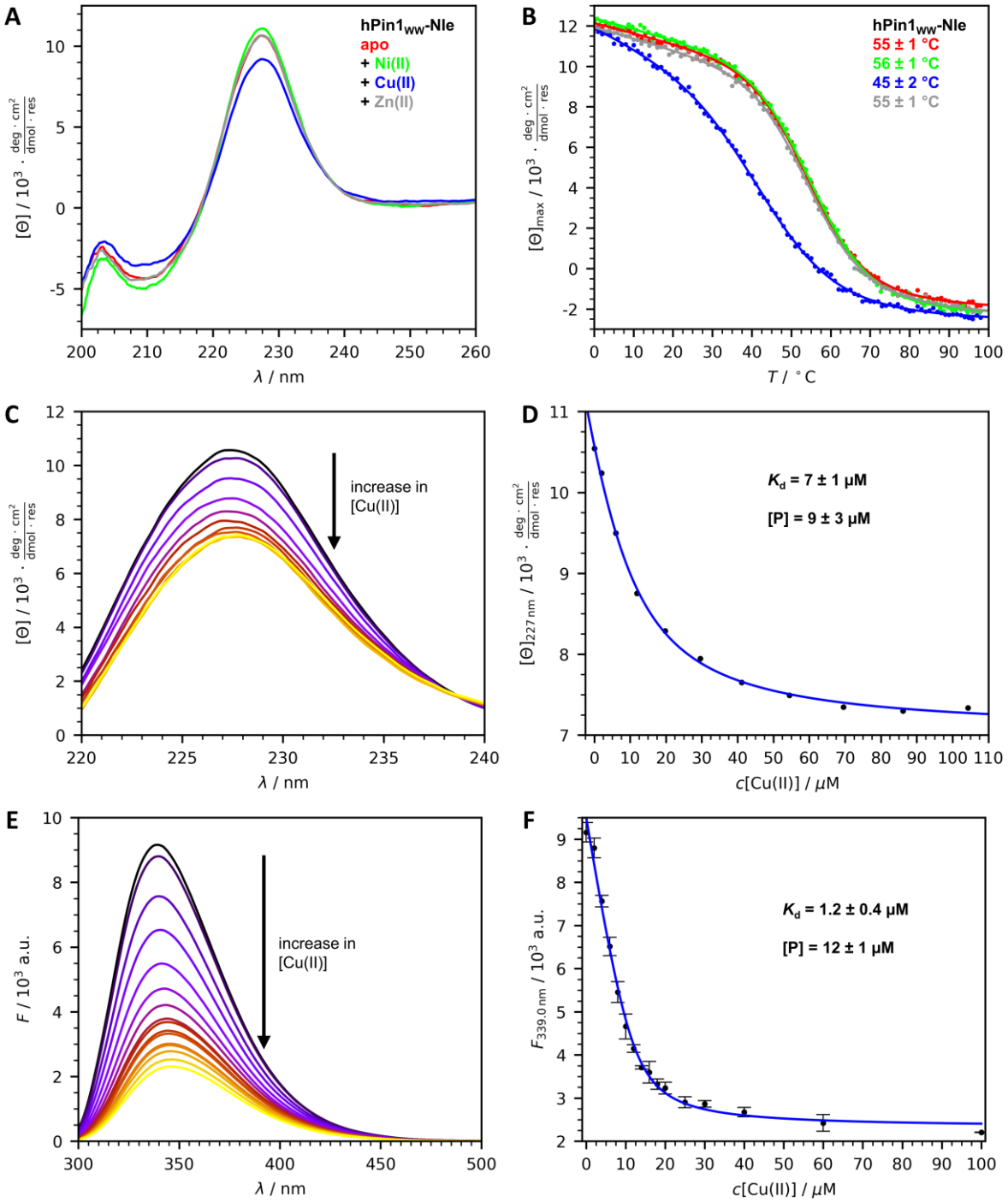

Figure 4-30: Interaction of hPin1$_{WW}$-Nle with metal ions. A) CD spectra and B) thermal denaturation of hPin1$_{WW}$-Nle in absence and presence of metal ions. Conditions: 50 µM peptide, 50 µM metal ions (if present), 10 mM MOPS, pH 7.2, 150 mM NaCl, 1 mm cuvette, spectra were recorded at 20 °C, thermal denaturation curves were recorded from 0-98 °C. C) CD spectra of hPin1$_{WW}$-Nle at different Cu(II) concentrations and D) the saturation binding curve. Conditions: 10 µM peptide, 10 mM MOPS, pH 7.2, 150 mM NaCl in a 10 mm cuvette is titrated with 2 mM $CuSO_4$ in 10 mM MOPS, pH 7.2, 150 mM NaCl at 20 °C. E) Fluorescence spectra of hPin1$_{WW}$-Nle at different Cu(II) concentrations and F) the resulting saturation binding curve. Conditions: 10 µM peptide, $CuSO_4$ (0-100 µM), 10 mM MOPS, pH 7.2, 150 mM NaCl in a 10 mm x 2 mm cuvette, λ_{ex} = 295 nm, room temperature (20-25 °C).

The methods described above demonstrate the global conformational changes of the peptides upon copper binding. EPR spectroscopy was employed to obtain structural information about the geometry and the ligands involved. In contrast to the previous experiments, an excess of peptide was used to ensure complete binding of Cu(II). The spectra were fitted with EasySpin[309] to obtain the *g* and *A* values. Figure 4-31 displays the measured and simulated spectra. All spectra exhibit axial symmetry ($g_z > g_{x,y} > 2.0023$), indicating a tetragonal geometry. Additionally, both WW-CA-Nle and WW-CA-min show the presence of two Cu(II) species, which is not evident in case of WW-CA-ANG, possibly due to the EPR signal of the second species being below the detection limit. From the previous experiments, it was observed that WW-CA-ANG also displayed a second copper binding site, although the affinity was significantly lower compared to the other two peptides. The simulation indicates the presence of a major and a minor species. The ratio for WW-CA-Nle is 1:0.3, while for WW-CA-min it is 1:0.006. These values align with the K_d values obtained from the competitive titration experiments. The first binding site of WW-CA-Nle exhibits weaker affinity for Cu(II) than the first binding site of WW-CA-min. Conversely, the second binding site of WW-CA-Nle exhibits greater affinity than that of WW-CA-min. When the concentration of Cu(II) is lower than that of the peptide, the two species are expected to be in equilibrium, with the higher affinity site being favoured. As a result, the second binding site is more occupied in WW-CA-Nle than in WW-CA-min. In contrast, WW-CA-ANG binds Cu(II) at its first binding site with much higher affinity than the second. It is therefore expected that the minor species will give weaker or no signals in the EPR.

The comparison of the $g_\parallel$ and $A_\parallel$ values in the Blumberg-Peisach plot[310] suggests a tetrahedral $[CuN_3O_n]^{2+}$ structure for the main species of WW-CA-Nle and WW-CA-min, where n can range from 1 to 3. Possible geometries include distorted square planar, square pyramid, or Jahn-Teller distorted octahedron. The His_3 site, in combination with additional water molecules, are the most probable ligands. In contrast, the $g_\parallel$ and $A_\parallel$ values of the minor species of WW-CA-Nle and WW-CA-min suggest a weak planar ligand field. Instead of His, a deprotonated Glu could serve as a ligand, which would further reduce the charge.

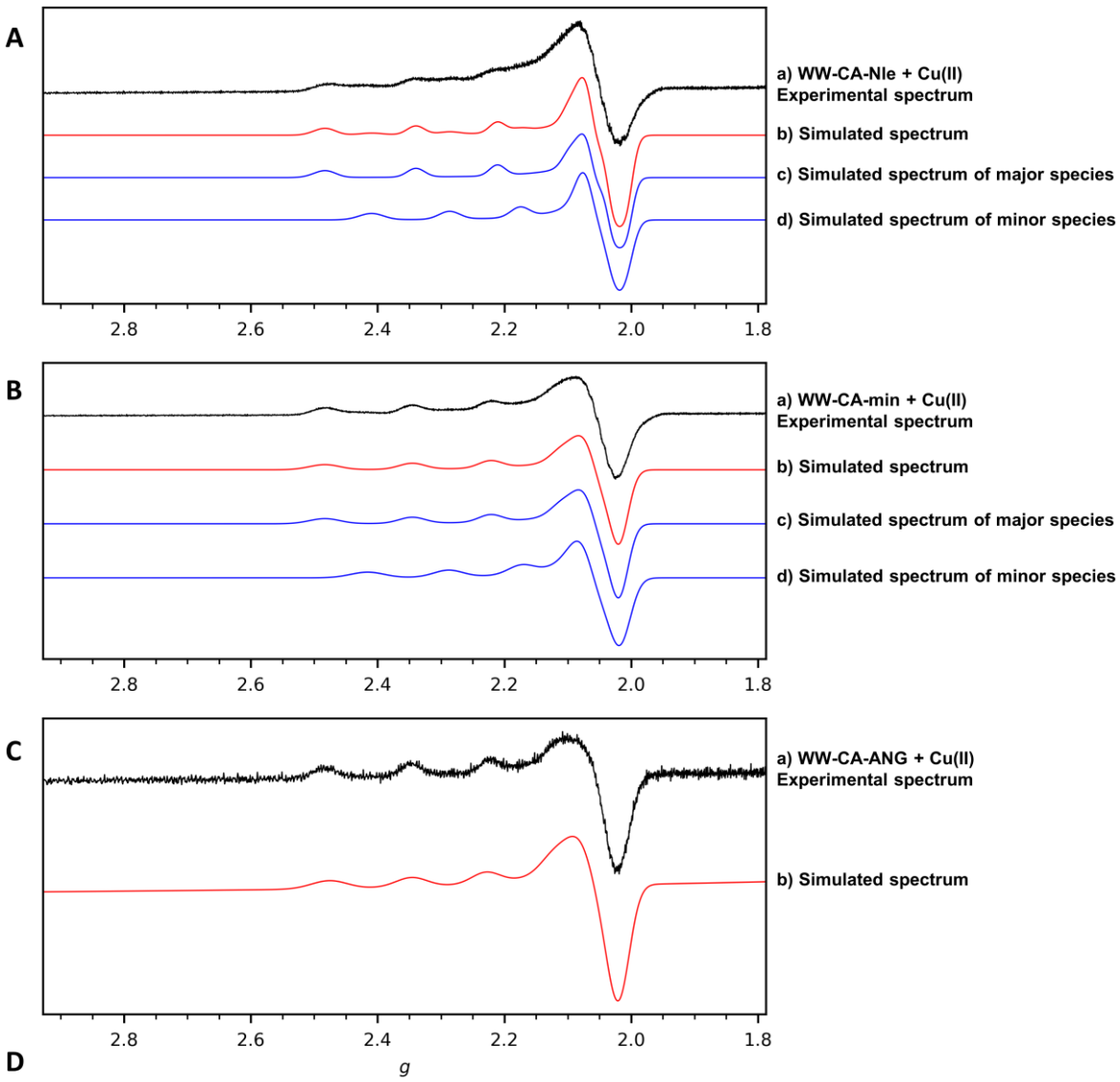

D

		g_x	g_y	g_z	A_x	A_y	A_z
						10^{-3} cm^{-1}	
WW-CA-Nle	Major	2.04	2.07	2.27	0.3	0.2	17.7
	Minor	2.04	2.07	2.23	0.3	0.2	15.7
WW-CA-min	Major	2.05	2.05	2.28	1.4	0.8	17.0
	minor	2.06	2.06	2.23	1.2	1.0	16.1
WW-CA-ANG		2.05	2.05	2.29	0.4	2.4	16.2

Figure 4-31: EPR spectroscopy of the Cu(II) complexes of the WW-CA peptides. A) X-band EPR spectra and simulated spectra of A) WW-CA-Nle, B) WW-CA-min, and C) WW-CA-ANG. The simulated spectra of WW-CA-Nle and WW-CA-min represent weighted average spectra of the major and minor peptide-Cu(II) species. Simulation was performed with EasySpin, D) Overview of the simulated Spin Hamiltonian parameters for WW-CA-Nle, WW-CA-min and WW-CA-ANG. Conditions: 416.67 µM peptide, 400 µM $CuSO_4$, 300 g/L glycerol, 10 mM MOPS, pH 7.2, 150 mM NaCl, below 100 K.

4.2.6 3D structure prediction indicates predisposition in WW-CA variants

The EPR measurements confirm the primary binding of Cu(II) to the designed His_3 site. However, the position of the second, weaker binding site remains unclear. Furthermore, CD spectroscopy and ITC suggest that the His_3 site is predisposed, but not preorganized, for metal ion binding. To gain insight into the structure of the His_3 site and possible locations of the second Cu(II) binding site, 3D models of the apo peptides were created using AlphaFold2.[37, 311] As presented in Figure 4-32A-D, AlphaFold2 predicted the structure of all three WW-CA variants to be typical for a WW domain and thus similar to the structure of $hPin1_{WW}$. A close look at the His_3 site shows that the imidazole side chains are not preorganized for Zn(II) binding, as it is the case in apo hCAII (Figure 4-32E), which is considered as one of the prime examples for a protein containing a preorganized metal binding site.[281] Zn(II) binding to the WW-CA variants would require conformational change of each His residue and, as experimentally proven, additional conformational change of the whole peptide. In contrast, only minimal structural changes occurs after Zn(II) binding in hCAII (Figure 4-32E). The biggest changes between apo and holo hCAII are some water molecules in the active site, that move into their designated place after Zn(II) binding and that play a crucial role in catalysis.[312] Interestingly, removal of Zn(II) from holo hCAII decreases the T_m value from 59 °C to 51 °C,[312] less drastic then in case of the WW-CA variants, where an increase in T_m of 30 K was observed. The excellent preorganization also led to a very high Zn(II) affinity in the upper fM to lower pM range.[313-314] Similar to the WW-CA variants the hydrophobic core of hCAII consist of two Phe and one Trp, among others, and is located directly below the β-sheet, where the His_3 site is located. If the aromatic residues are mutated to aliphatic or polar residues, the His_3 site is distorted from its ideal preorganization and the Zn(II) affinity decreases from 0.8 pM to 29 pM.[313] At the same time, the new conformation show an increase affinity for Cu(II), the K_d value decreases from 17 fM to 2 fM.[313]

In addition to the His_3 site, coordination *via* two His and Glu12 is possible. It is evident that in WW-CA-min and WW-CA-ANG, Glu12 is in close proximity with Arg27 or Arg26, respectively and both residues can form a salt bridge. In WW-CA-Nle, there is a Ser at position 27, which should interact less strong with Glu12. This may explain the higher binding affinity of the second binding site of WW-CA-Nle to Cu(II). In addition, WW-CA-Nle and WW-CA-min have a longer first loop than WW-CA-ANG, which may also contain the second binding site. If Cu(II) binding occurs in the loop, Cu(II) is coordinated by the backbone, as is the case with the biuret test.[305] Binding should be easier in the longer loop. In case of $hPin1_{WW}$-Nle, binding could occur in the first loop or at Glu12 and His27. In case a His_2Glu site is the second binding site for Cu(II), it is questionable, why Zn(II) or Ni(II) does not also bind to this coordination site but clearly showed 1:1 binding in all experiments. His_2Glu sites are known in several Zn(II) containing enzymes, e.g. the metalloprotease thermolysine.[315]

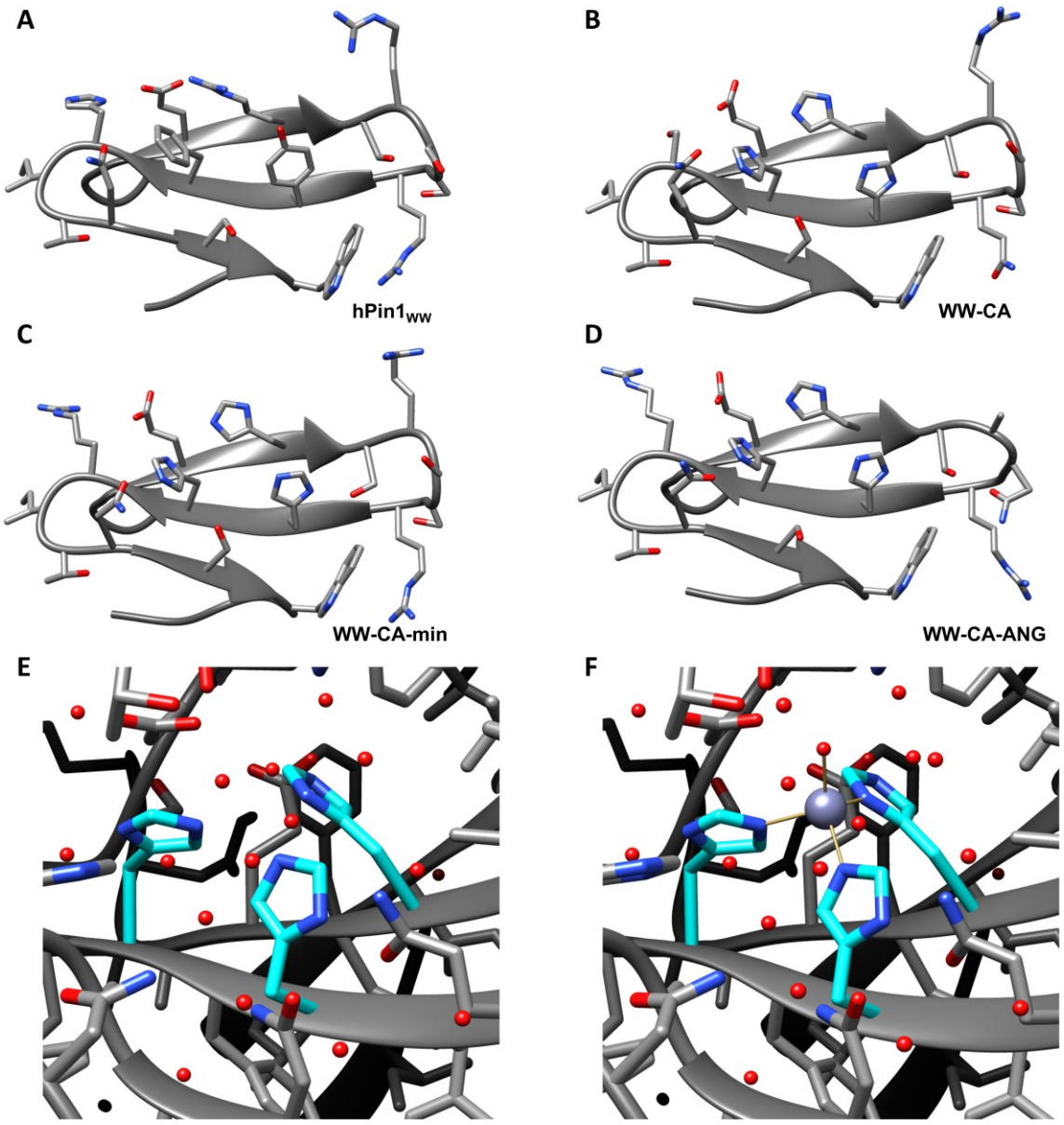

Figure 4-32: A) X-ray crystal structure of hPin1$_{WW}$ (PDB-ID: 4GWT). Three dimensional models generated with AlphaFold2[37, 311] of B) WW-CA, C) WW-CA-min and WW-CA-ANG. The residues on the surface and loop regions of the peptides were explicitly shown. For the calculation, Nle was mutated to Met. X-ray crystal structure of the active site of E) apo hCAII and F) holo hCAII (PDP-ID: 2CBE, 2CBA). The His$_3$ site is highlighted in cyan. Water molecules are shown as red spheres.

Binding at the His$_2$Glu site would also not explain the conformational changes, away from a WW domain structure, observed at high Cu(II) concentration. Binding in the first loop is a more plausible option, because Ni(II) and Zn(II) cannot bind there and loop1 is highly important for WW domain folding.[111] Hence, binding of Cu(II) to loop1 might distort the structure and the extend of distortion is dependent on the stability of the apo peptide. The molten globule WW-CA is therefore mostly effected by Cu(II), while the most stable apo peptide hPin1$_{WW}$-Nle did not denature even at 10 times excess of Cu(II).

While in the titration experiments it was assumed that the peptide coordinated two Cu(II) ions simultaneously, one at the His$_3$ site and the second one in the loop, as there was an excess of

Cu(II) at the end, the major and minor species in the EPR experiment are mononuclear species. This is explained by the fact that regardless of where exactly the second coordination took place, the distance between the two copper atoms had to be small enough (5-8 Å) to allow dipole-dipole coupling, which was not observed in the EPR spectra.

4.3 Metal binding tryptophan zipper

The major part of Chapter 4.3 has been published in *ChemBioChem*.[316]

4.3.1 Design concept of a metal binding tryptophan zipper ($Tz2H_3$)

Following the successful engineering of the WW domain, an even smaller peptide Trpzip2, a β-hairpin peptide of 12 amino acids, was used as a starting point to design a metal-binding peptide. As discussed in Chapter 2.4, the structural stability of Trpzip2 is maintained by the interaction of four tryptophan residues located on one side of the hairpin structure.[70] In addition, a salt bridge between Glu5 and Lys8 is necessary for the structural integrity of the peptide. Similar to WW-CA, a metal-binding site was engineered on the surface of Trpzip2, but instead of replacing a hydrophobic core, the polar residues Thr3, Thr10 and Lys12 were mutated to His, while keeping all the major structural features intact. This metal-binding variant of Trpzip2 is called $Tz2H_3$, as shown in Figure 4-33.

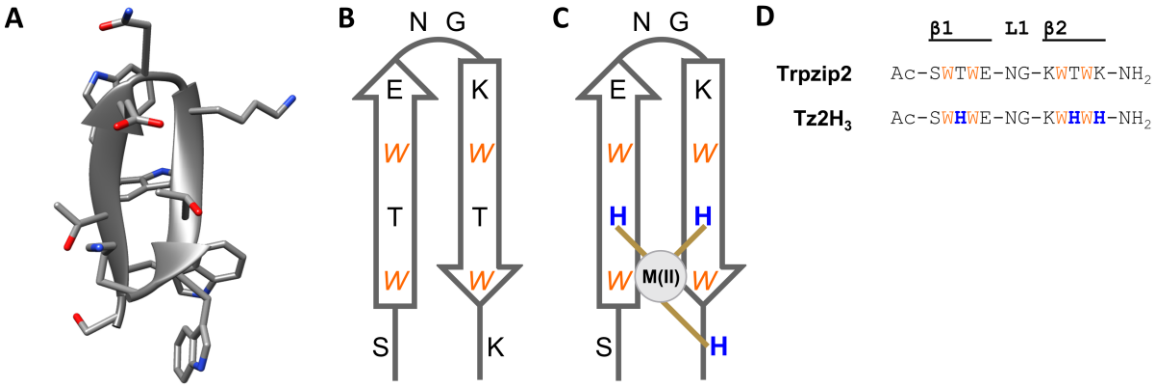

Figure 4-33: Engineering concept. A) NMR structure of Trpzip2 (PDB-ID: 1LE1). B) Two-dimensional schematic representation of the structure of Trpzip2. C) Two-dimensional schematic representation of the supposed structure of $Tz2H_3$. D) Sequences of Trpzip2 and $Tz2H_3$. Italic and orange: Trp residues pointing below the β-sheet forming the hydrophobic core. Blue: His_3 site. Gold-brown lines: coordinative bonds.

4.3.2 Thermal stability of $Tz2H_3$ metal complexes

Trpzip2 and $Tz2H_3$ were synthesised by automated microwave-assisted SPPS, purified by HPLC and identified by MALDI-TOF MS (see Chapter 10.3). CD spectroscopy was performed to analyse the structure (Figure 4-34). The CD spectrum of Trpzip2 was in accordance with the reported spectrum,[70] revealing a characteristic maximum at ~227 nm and a minimum at ~213 nm which resulted from the cross-strand interaction of the tryptophan residues. In the case of $Tz2H_3$ the spectrum is similar except for a slight decrease in the signal intensity of the minimum and a slight increase in the intensity of the maximum, indicating that the engineered peptide adopts a Trpzip-like structure. The thermal denaturation curve of Tripzip2 is sigmoidal with a broad transition and also identical to the one reported in the literature.[70] Although Trpzip2 is a very frequently used model peptide in several biophysical studies, there is no

consistent approach to analyse the thermal denaturation curves for tryptophan zippers. Depending on the method used (mostly two-state model), a T_m value between 72 °C and 79 °C was obtained.[70, 174-175] T_m determined by fitting the two-state model to the data depends strongly on the definition of the pre- and post-transition baseline and a detailed discussion can be found in Chapter 8.2.9. As an alternative, using the 1st derivative $d[\Theta]_{max}/dT$, was reported.[70] The 1st derivative is a bell-shape curve. To determine T_m an empirical Gauss function can be fitted to the 1st derivative, but this has no physical meaning.[317] Alternatively, the data can be fitted with a variant of the van't Hoff equation.[318] For Trpzip2 T_m values of 68±1 °C or 73±3 °C were obtained by fitting using the two-state model setting the pre- and post-transition baselines as temperature independent or dependent, respectively. The second T_m value is in the range of the reported values. Fitting the van't Hoff or Gauss equation to the 1st derivative yielded T_m values of 64±2 °C and 63±1 °C, respectively. The thermal denaturation curve of $Tz2H_3$ is also sigmoidal and the T_m was determined to be 53±1 °C or 60±1 °C (two-state model, constant or linear pre- and post-transition baselines) and when using the 1st derivative T_m values of 53±1 °C or 52±1 °C (van't Hoff or Gauss equation) were determined, respectively. These two examples show that values determined using the 1st derivative were in general more reliable, which is also true for other Trpzip2-derived peptides in this thesis (*vide infra*). Therefore, only the values determined using the van't Hoff equation are reported and discussed in this chapter. As the 1st derivative is very noisy, especially when several curves are superimposed, the plots quickly become unclear. For this reason, only the curve fit is shown. The thermal denaturation curves, the 1st derivatives and the corresponding curve fits are summarized in the Appendix (Chapter 10.8).

Compared to Trpzip2, the T_m value of $Tz2H_3$ is 11 K lower, still, $Tz2H_3$ is a stably folded peptide with a very pronounced exciton signal, an indication of well-interacting Trp residues. The mutations on the hydrophilic side did not disturb the hydrophobic core. The metal binding properties of $Tz2H_3$ were then investigated (Figure 4-34B). Zn(II), Ni(II) and Cu(II) led to changes in the CD spectrum. In all three cases the intensity of the maximum at 227 nm is reduced. Zn(II) did not change the intensity of the minimum, but in the case of Ni(II) and Cu(II) the intensity was also reduced. The thermal denaturation profiles of the $Tz2H_3$ metal complexes were significantly different from those of the apo state. The transition was much broader and although the signal intensity was reduced at low temperatures, at high temperatures the holo states still showed residual signal intensity compared to the apo peptide. The melting curves of the Zn(II) and Ni(II) complexes were not sigmoidal but almost linear. Therefore, no extremum was observed in the 1st derivative of the thermal denaturation curve of Zn(II) complex and the T_m value could not be determined. In case of the Ni(II) complex a flat and very broad minimum was observed and therefore T_m value could not be determined accurately. The thermal denaturation curve of the Cu(II) complex was sigmoidal, but the lower

baseline was missing. Again, the T_m value could not be determined accurately but was estimated to be in a range of 75 °C to 90 °C, which would correspond to a thermostable to hyper thermostable peptide. These CD experiments showed that Tz2H$_3$ is able to bind to Zn(II), Ni(II) and Cu(II).

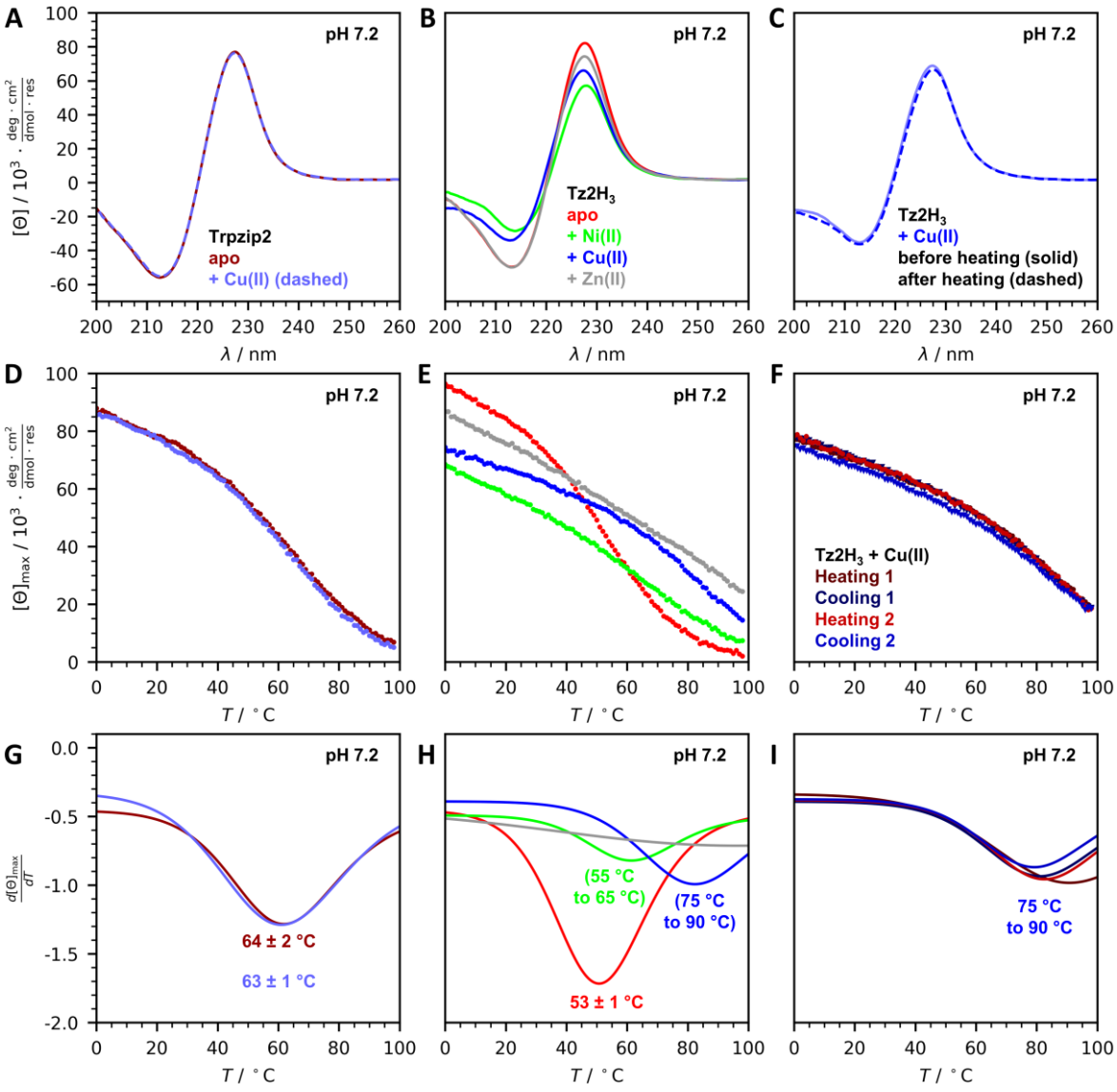

Figure 4-34: Structural analysis of Trpzip2 and Tz2H$_3$. A) CD spectra of Trpzip2 and B) of Tz2H$_3$ in absence and presence of metal ions. C) CD spectra of the Tz2H$_3$-Cu(II) complex before and after heating-cooling cycle. D) Thermal denaturation curves of Trpzip2 and E) of Tz2H$_3$ in absence and presence of metal ions. F) Thermal denaturation and refolding curves of the Tz2H$_3$-Cu(II) complex. G) 1st derivative of thermal denaturation curves of Trpzip2 and E) of Tz2H$_3$ in absence and presence of metal ions. F) 1st derivative of thermal denaturation and refolding curves of the Tz2H$_3$-Cu(II) complex. Conditions: 50 µM peptide, 50 µM metal ions (if present), 10 mM MOPS, pH 7.2, 150 mM NaCl, 1 mm cuvette, 20 °C.

The exciton coupling of the tryptophan residues is very sensitive to changes in the orientation and proximity of the indole moieties and therefore very sensitive to structural changes. As discussed in Chapter 2.4, a T-shape orientation of the two Trp pairs is very characteristic for tryptophan zipper peptides. The binding of metal ions led to individual conformational changes

due to different preferences in coordination geometry, similar to WW-CA as discussed in the previous chapter, and therefore the CD spectra change in a different way for each metal. The orientation of the indole moieties is distorted from the optimal T-shape, which results in a reduction of the signal intensity. At the same time, however, the binding of metal ions leads to an increase in thermal stability.

Beyond thermal stability, it is also important to determine whether the peptide is able to refold after thermal denaturation. Therefore, the peptide unfolding during heating and refolding during cooling were recorded for the thermostable $Tz2H_3$-Cu(II) complex. As shown in Figure 4-34C, the CD spectra before and after the heating-cooling cycle are superimposable. The same was observed for the thermal denaturation and refolding curves, indicating that the folding-unfolding transition is reversible. For the other peptides and peptide-metal complexes, only the CD spectra after the thermal denaturation experiments were measured after the sample is cooled down to 20 °C. The CD spectra before and after thermal denaturation were superimposable, indicating reversibility of the folding-unfolding process for all peptides and peptide metal complexes (Appendix, Chapter 10.8).

To exclude unspecific binding, as observed for $hPin1_{WW}$-Nle, the CD spectra and thermal denaturation curve of Trpzip2 were recorded in the presence of Cu(II) (Figure 4-34A). Both superimpose with the data recorded in the absence of Cu(II), indicating no unspecific Cu(II) binding. Interestingly, the thermal unfolding was not reversible in the presence of Cu(II) (Appendix, Chapter 10.8). This suggests that the denatured state of Trpzip2 interacts non-specifically with Cu(II) and is unable to refold completely. This was not observed for $Tz2H_3$-metal complexes.

4.3.3 Stability of $Tz2H_3$ metal complexes under denaturation conditions

$Tz2H_3$ metal complexes show a high thermal stability, which can correlate with stability under further denaturation conditions, such as chaotropic salts, low pH and organic solvents.[319-321] A well-known chaotropic salt is guanidine hydrochloride (GdnHCl), which is often used to denature proteins.[322]

As was shown for WW-CA, low pH can prevent metal ion binding and structural stability. Therefore, the CD spectrum of $Tz2H_3$ at pH 2 in absence and presence of Cu(II) was recorded (Figure 4-35A). Both spectra were superimposable and still show the characteristic exciton signal with only slight reduction in signal intensities. The two thermal denaturation curves were also superimposable and a T_m value of 35 °C was determined for both. Reducing the pH does not lead to unfolding of $Tz2H_3$ but reduces the stability of the structure. Similar to WW-CA, the His_3 site is responsible for metal ion binding and at low pH the imidazole side chains are protonated. Therefore, Cu(II) did not bind to protonated $Tz2H_3$. The positively charged residues repel each other and weaken the structural stability.

The CD and thermal denaturation curves of Trpzip2 at pH 2 were recorded as a control (Figure 4-35A and D). The CD spectrum is similar to that at pH 7.2 and a sigmoidal thermal denaturation curve with a T_m value of 56 °C was obtained. Both are indicative of a folded peptide. The decrease in stability was only 8 K, in contrast to $Tz2H_3$ with a decrease of 18 °K. Trpzip2 does not suffer from charge repulsion. The decrease of the T_m value could be explained by the protonation of Glu5, which leads to disruption of the salt bridge to Lys8. This effect also occurs in $Tz2H_3$ in addition to the histidine protonation. Lowering the pH has no negative effect on the reversibility of folding for either peptide (Appendix, Chapter 10.8).

Next the effect of the chaotropic salt GdnHCl was tested. Because GdnHCl absorbs UV light below 220 nm,[323] the CD spectrum become noisier with increasing GdnHCl concentration. The CD spectrum of apo $Tz2H_3$ in 6 M GdnHCl (Figure 4-35B) shows a reduced intensity and a red shift of the exciton signal, albeit a folded peptide is still indicated. The thermal denaturation curve lacks the upper baseline and is not sigmoidal, indicating a non-cooperative folding-unfolding behaviour, but from the 1st derivative a T_m value of 19 °C could be determined. In the presence of metal ions, the intensity of the exciton signal increased, and in the case of Zn(II) and Cu(II), a sigmoidal thermal denaturation curve with T_m values of 42 °C and 57 °C were determined, respectively. The thermal denaturation curve of the $Tz2H_3$-Ni(II) complex was again almost linear, but the loss of signal intensity with increasing temperature was much less pronounced than in the case of the apo state, showing that Ni(II) is also able to stabilize the peptide structure under high chaotropic salt concentration. Again, the CD spectra after thermal denaturation experiments were recorded in all cases, but this time thermal unfolding in the presence of GdnHCl was irreversible in each case (Appendix, Chapter 10.8). GdnHCl weakens the structure of $Tz2H_3$, however, binding to metal ions partially restores the structural stability, including the ability to unfold in a cooperative manner. It should be mentioned that most peptides and proteins are fully unfolded at 6 M GdnHCl,[324] therefore the $Tz2H_3$-metal ion complexes can be considered as highly stable towards chaotropic salts.

Up to now, the T_m value of the $Tz2H_3$-Cu(II) complex could not be determined accurately because at 98 °C the peptide metal complex is still partially folded and the lower baseline of the sigmoidal thermal denaturation curve is not reached. This complicates the accurate determination of the T_m value, regardless if the curve is fitted to a two-state-model or the derivative method is used. One method to overcome this drawback includes the use of GdnHCl to reduce the T_m of thermostable proteins and peptides, hence, enabling complete denaturation within the applied measurement window. Thereby, the T_m value decreases linearly with increasing GdnHCl concentration and the T_m value in absence of GdnHCl can be determined by extrapolation.[325] The CD spectra and thermal denaturation curves were recorded at different GdnHCl concentrations (Figure 4-35C and F). With increasing GdnHCl concentration, the exciton maximum was redshifted.

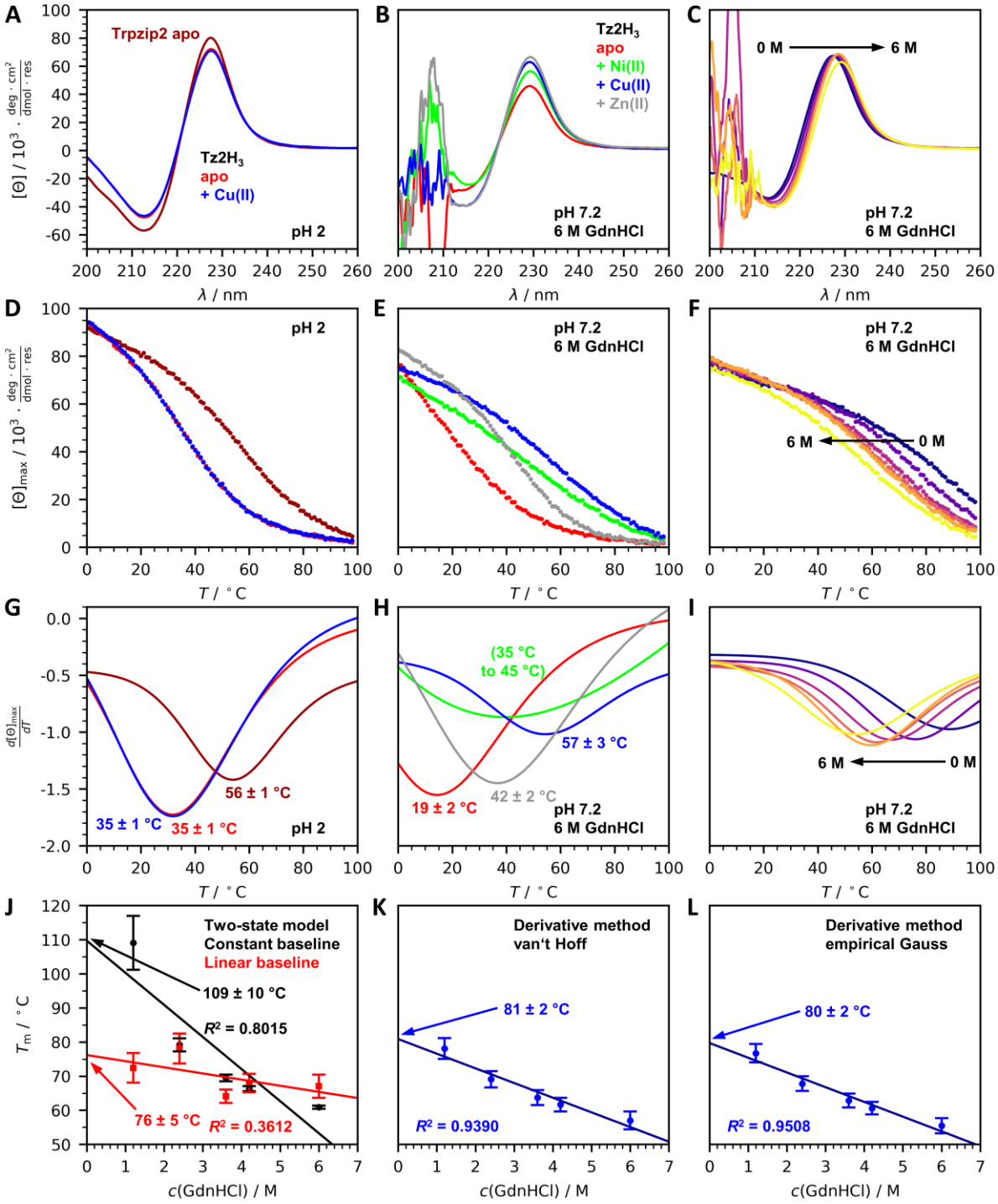

Figure 4-35: CD spectroscopic analysis of Trpzip2 and Tz2H$_3$ under denaturing conditions. A) CD spectra of Trpzip and Tz3H$_3$ in absence and presence of Cu(II) at pH 2, B) Tz2H$_3$ in absence and presence of metal ions and 6 M GdnHCl and C) of the Tz2H$_3$-Cu(II) complex at different GdnHCl concentration. D) Thermal denaturation curves of Trpzip and Tz3H$_3$ in absence and presence of Cu(II) at pH 2, E) Tz2H$_3$ in absence and presence of metal ions and 6 M GdnHCl and F) of the Tz2H$_3$-Cu(II) complex at different GdnHCl concentration. G) 1st Derivatives of thermal denaturation curves of Trpzip and Tz2H$_3$ in absence and presence of Cu(II) at pH 2, H) Tz2H$_3$ in absence and presence of metal ions and 6 M GdnHCl and I) of the Tz2H$_3$-Cu(II) complex at different GdnHCl concentration. J) Plot of T_m, determined by curve fitting using the two-state model, K) 1st derivative and van't Hoff equation or L) 1st derivative and the empirical Gauss equation, *versus* the GdnHCl concentration. Linear regression was used to estimate T_m at 0 M GdnHCl. Conditions: 50 µM peptide, 50 µM metal ions (if present), at pH 2 (150 mM NaCl, 10 mM hydrogensulfate pH 2.0), at 6 M GdnHCl (6 M GdnHCl, 150 mM NaCl, 10 mM

MOPS, pH 7.2) and at different GdnHCl concentration (0, 1.2, 2.4, 3.6, 4.2 and 6 M GdnHCl, 150 mM NaCl, 10 mM MOPS, pH 7.2), 20 °C, 1 mm cuvette.

Interestingly the signal intensity did not decrease until a GdnHCl concentration of 6 M was reached. The midpoints of transition of the thermal denaturation curves were shifted to lower temperatures with increasing GdnHCl concentration (Figure 4-35F), which is very well visible in the 1st derivative plot. In Figure 4-35J to K the resulting T_m values, determined by the four different curve fitting methods, were plotted against the GdnHCl concentration. A linear regression was then performed to extrapolate the T_m value at 0 M GdnHCl. As previously stated, with the two-state model, independent if the baselines were set constant or as linear functions, it was not possible to determine meaningful T_m values. No linear dependency is observed, which is confirmed by the low values for the correlation coefficient R^2. In contrast, both derivative methods, van't Hoff and empirical Gauss (Figure 4-35K and L) yielded T_m values that correlation linearly with the GdnHCl concentration. Therefore, the T_m value of the $Tz2H_3$-Cu(II) complex in the absence of denaturant was determined to be 81 °C, which is regarded at the boundary between thermophilic and hyper thermophilic proteins.[100]

Organic solvents also destabilise the protein structure and limit the use of e.g. enzymes in organic synthesis.[321] To analyse the structure of the designed peptides in organic solvents, the CD spectra of Trpzip2 and $Tz2H_3$ were recorded in MeOH and MeCN/MeOH. Unfortunately, DMF, DMSO and other polar solvents could not be used due to their strong UV absorption in the region of interest below 260 nm.[326] As shown in Figure 4-36A, the exciton signal in MeOH decreased for both peptides and the spectra are very similar. The addition of Cu(II) led to an increase in the intensity of the exciton signal only for $Tz2H_3$, while the spectrum of Trpzip2 remained unchanged. In MeOH/MeCN the exciton signal decreased further and could only partially be restored by the addition of Cu(II) in the case of $Tz2H_3$ (Figure 4-36B). As expected, organic solvents weaken the structure by reducing the hydrophobic effect. MeCN is less polar and non-protic if compared to MeOH, therefore the structure of both peptides was more affected in MeOH/MeCN. Both peptides also behave similarly in organic solvents, but only $Tz2H_3$ is able to bind Cu(II), leading to a partial restoration of the degree of folding. Since organic solvents lead to a significant reduction in peptide folding, the CD spectrum of $Tz2H_3$ was measured in a water/MeCN 1:1 mixture (Figure 4-36C). Interestingly, the exciton signal is much more pronounced than in pure organic solvents, but no change was observed, when Cu(II) was added. It is known from previous experiments, that the Cu(II) binding is pH sensitive. Pure water is slightly acidic due to dissolved atmospheric CO_2. Furthermore, the peptide was purified by HPLC using solvents that contained 0.1% TFA. It is known that lyophilisation alone will not fully remove TFA and the peptide is isolated as TFA salt,[327] therefore, the His residues are protonated under these conditions. To maintain constant pH, MOPS-buffered solution at pH 7.2 was used instead of pure water, while the amount of MeCN concentration unchanged

(Figure 4-36C). In this case, an increase in the exciton signal was observed after the addition of Cu(II), indicating successful Cu(II) binding.

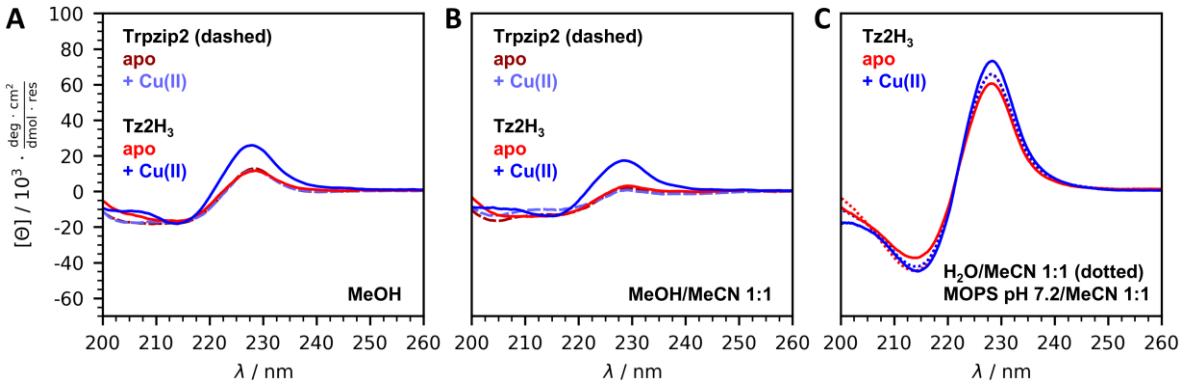

Figure 4-36: CD spectroscopic analysis of Trpzip2 and $Tz2H_3$ in organic solvents. A) CD spectra of Trpzip2 and $Tz2H_3$ at 20 °C in MeOH, B) in MeOH/MeCN, C) water/MeCN or MOPS buffer/MeCN. Conditions: 50 µM peptide, 50 µM $CuSO_4$ (if present) in 100% MeOH, MeOH/MeCN 1:1 *v*/*v*, H_2O/MeCN 1:1 or 10 mM MOPS, pH 7.2, 150 mM NaCl containing 50% *v*/*v* MeCN, 1 mm cuvette, 20 °C.

4.3.4 Metal ion binding affinity of $Tz2H_3$

The binding affinity to the metal ions was further analysed by fluorescence spectroscopy (Figure 4-37A). The tryptophan residues were excited at 295 nm, which resulted in fluorescence emission at 343 nm for apo $Tz2H_3$. In the presence of Zn(II) the fluorescence intensity increased, whereas it was quenched by Ni(II) and Cu(II), with Cu(II) being the stronger quencher. This observation is very similar to the WW-CA peptides. The K_d values were determined by fluorescence titration (Figure 4-37B-D). Saturation binding curves were obtained in all three cases. Zn(II) binds to $Tz2H_3$ with a K_d value of 0.3 µM and Ni(II) with a K_d value of 0.7 µM. The Cu(II) binding curve decreased linearly until the Cu(II) concentration was equal to the peptide concentration, where a plateau was reached. This is typical of a very tight binding event and the K_d value was estimated to be in the sub-nanomolar range. To obtain further information, a competition titration (Figure 4-37E) was performed in the presence of EDTA (K_d ~$10^{-18.8}$ M) or HEDTA (K_d ~$10^{-17.4}$ M).[328] The concentrations of competitor and $Tz2H_3$ were the same, while the concentration of Cu(II) was varied. In both cases the signal intensities remained equal until the Cu(II) concentration was equal to the competitor concentration. Then, the intensity was linearly reduced until the Cu(II) concentration was equal to the sum of the competitor and the peptide concentration. Again, the baseline was reached. It is therefore assumed that Cu(II) is first bound by the competitor, hence, no change in fluorescence was observed, because it binds Cu(II) stronger than $Tz2H_3$. After the competitor was saturated, Cu(II) was bound to $Tz2H_3$. Although an exact K_d value cannot be determined by this method, a lower limit of $10^{-17.4}$ M can be assumed. To overcome this problem, TAMSMB was used as competitor, which has a K_d value for Cu(II) binding of 44 nM[304] and is therefore a weaker Cu(II) binder than HEDTA. After each Cu(II) addition UV/Vis spectra were recorded and the

absorption of the dye at 589 nm was plotted against the Cu(II) concentration. As can be seen in Figure 4-37F, no increase in absorption is visible until the Cu(II) concentration is equal to the peptide concentration. Then, the absorption increases nearly linearly until the Cu(II) concentration is equal to the sum of the $Tz2H_3$ and TAMSMB concentration. Similar to the fluorescence titration experiments, the upper baseline was reached. It can be assumed, that the Cu(II) binding affinity of $Tz2H_3$ is far stronger than the affinity of TAMSMB.

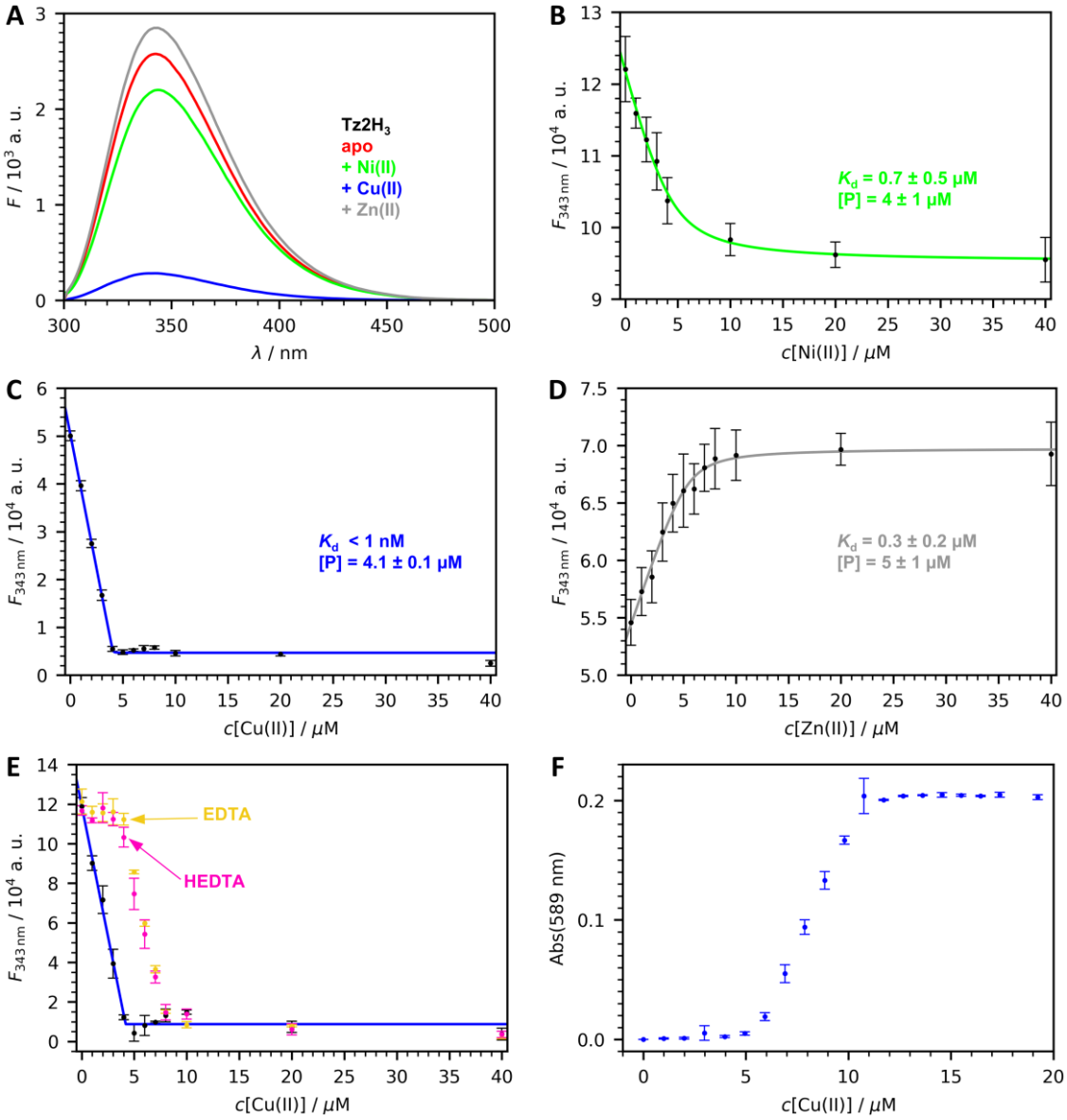

Figure 4-37: Analysis of metal ion binding of $Tz2H_3$. A) Fluorescence spectra of $Tz2H_3$ in absence and presence of metal ions (10 µM peptide, 10 µM metal salts (if present), 10 mM MOPS, pH 7.2, 150 mM NaCl, 10 mm x 2 mm cuvette, excitation at 295 nm, room temperature (20 °C to 25 °C)). B) Fluorescence titration experiments of $Tz2H_3$ with Ni(II), C) Cu(II), D) Zn(II) and Cu(II) with competitive ligands. Measurements were performed in 96-well-plates (4 µM peptide, 4 µM EDTA or HEDTA (if present), 0 µM to 40 µM metal salt, 10 mM MOPS, pH 7.2, 150 mM NaCl, excitation at 295 nm, room temperature (20 °C to 25 °C)). F) Competitive titration experiments of $Tz2H_3$ with Cu(II) in the presence of TAMSMB (5 µM peptide, 5 µM TAMSMB, 10 mM MOPS, pH 7.2, 150 mM NaCl, 1 cm cuvette, titrated with 1 mM $CuSO_4$, 10 mM MOPS, pH 7.2, 150 mM NaCl).

Therefore, no competition was observed and the added Cu(II) is bound to the peptide. If the amount of Cu(II) exceeded the amount of peptide, Cu(II) would only bind to TAMSMB. A typical hyperbolic curve is not observed because the concentration of TAMSMB is much higher than its K_d value for Cu(II) of 44 nM. Therefore, the Cu(II) bound nearly quantitatively to the dye, leading to a linear increase in signal intensity. A second Cu(II) binding site of $Tz2H_3$ cannot be excluded, but its binding affinity would be much weaker than that TAMSMB. Although this second titration also could not give an accurate K_d value, one can conclude that it must be below 1 nM, since in case of WW-CA-ANG (Chapter 4.2.3) a K_d of 0.9 nM could be determined using TAMSMB. Compared to the K_d value for Zn(II) and Ni(II), the K_d value for Cu(II) is at least three orders of magnitude lower. This trend agrees with the Irving-Williams series.

4.3.5 Coordination geometry of the $Tz2H_3$-Cu(II) complex

To obtain further information on the coordination geometry of the Cu(II) site in $Tz2H_3$, EPR spectroscopy was performed in collaboration with the laboratory of Peter Comba (Figure 4-38A). $Tz2H_3$ was added in excess to ensure that all Cu(II) ions were bound. In Figure 4-38 the spin-Hamiltonian parameters obtained by simulating the spectrum are listed. The spectrum is very similar to that of WW-CA-ANG and only one Cu(II) species was determined, which is expected because even if a second binding site were present, the His_3 site binds Cu(II) with such a high affinity that the concentration of the other Cu(II) species would not be detectable. The g values ($g_z > g_{x,y} > 2.0023$) indicate an axial Cu(II) site with a $d_{x^2-y^2}$ ground state. Peisach and Blumberg plotted A_z *versus* g_z values of several Cu(II) complexes with charges from -2 to +2 with N, S and O ligands.[310] The four ligands in the plane play the most important role in the magnetic properties. Therefore, the authors only consider these. The two (or one) axial ligands are only weakly bound and often water molecules. With a g_z value of 2.288, an A_z value of $152 \cdot 10^{-4}$ cm^{-1} and a charge of +2, assuming only neutral ligands, the $Tz2H_3$-Cu(II) complex is in the region of the CuN_3O_1 coordination system (Cu(II) is coordinated by three nitrogen and one oxygen containing ligand). Based on these findings, it can be assumed that Cu(II) is coordinated in the plane by the three imidazole side chains of the histidine residues and the fourth ligand is a water molecule. Comparison of the spectra with published spectra of Cu(II) imidazole/pyridine/amine systems led to the conclusion that the ligands are slightly distorted from the ideal square planar geometry.[329-334] The presence of one or two water molecules as additional axial ligands cannot be excluded.

Insights into the metal ion binding site can also be obtained from a 3D model of $Tz2H_3$, which was generated by AlphaFold2[37, 311] (Figure 4-38B) and as indicated by CD spectroscopy, has the typical structural features of a Trpzip fold. Similar to the WW-CA peptides, the His_3 site in the apo peptide is predicted to be pre-disposed and not pre-organized. Metal binding induces conformational change, which was observed in the CD spectra. Interestingly, Cu(II) stabilizes

the structure of Tz2H$_3$ better than Zn(II), which is different to the experimental observations with the WW-CA peptides.

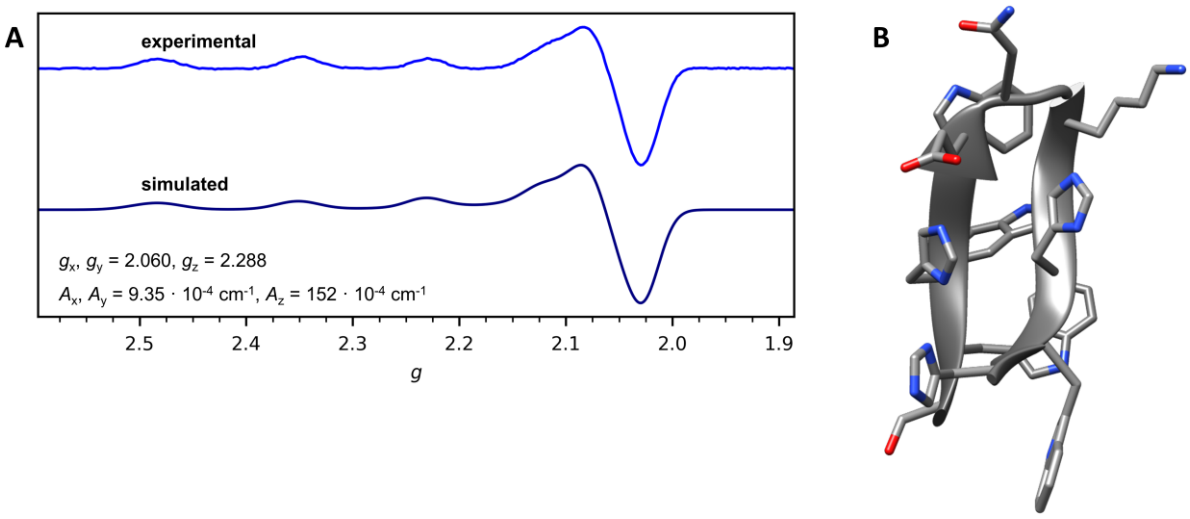

Figure 4-38: A) EPR spectrum of Tz2H$_3$-Cu(II) complex (X-band (9.631500 GHz), 416.67 µM peptide, 400 µM Cu(II), 10 mM MOPS, pH 7.2, 150 mM NaCl, 300 g/L glycerol, temperature below 100 K). B) Three-dimensional model of Tz2H$_3$ generated with AlphaFold2.[37, 311]

It is known from the WW-CA peptides, that a second Cu(II) binding site exists, which is likely to be in the longer Loop 1. Cu(II) binding to this site, which is also present in the parent peptide hPin1$_{WW}$-Nle led to reduction of thermal stability, because Loop 1 is essential for the WW domain folding. From EPR spectroscopy it was known, that even in sub-stoichiometric Cu(II) concentration, the second binding site was partially occupied by Cu(II). In the case of Tz2H$_3$, the loop is even one amino acid shorter than Loop 1 in WW-CA-ANG, making it unlikely to serve as a second Cu(II) binding site. From the 3D model, it cannot be excluded, that His3, Glu5 and His10 form an alternative Cu(II) binding site. Interestingly such a His$_2$Glu site was also present in the three WW-CA peptides and it was proposed as a possible second Cu(II) binding site as well. But in Tz2H$_3$, no additional Cu(II) binding site was detected by titration nor by EPR spectroscopy. Therefore, the His$_2$Glu site can be excluded, also for the WW-CA peptides.

4.4 Test for catalytic activity of metal binding β-sheet peptides

4.4.1 Hydrolysis

The Zn(II) binding sites of the peptides WW-CA-Nle, WW-CA-min, WW-CA-ANG and Tz2H$_3$ were designed using the active centre of carbonic anhydrase II (hCAII) as a natural model (see previous Chapters). The main function of hCAII is to catalyse the hydration of CO_2. In addition, hCAII is known to catalyse several other reactions, the most prominent of which is ester hydrolysis. The mechanism is shown in Scheme 4-1. Coordination to the zinc ion reduces the pK_a of water to 6.8, a significant reduction of 7 orders of magnitude compared to unbound water[245] Deprotonation of the water then leads to a zinc-bound hydroxide, which is the reactive nucleophilic species. In case of carbon dioxide hydration, the hydroxide attacks the carbon and hydrogen carbonate is formed. However, the central active species can also react with other electrophiles, such as esters. The zinc-bound hydroxide attacks the carbonyl group of the ester and a tetrahedral intermediate is formed. The expulsion of the alcohol leads to the free carboxylic acid.[267]

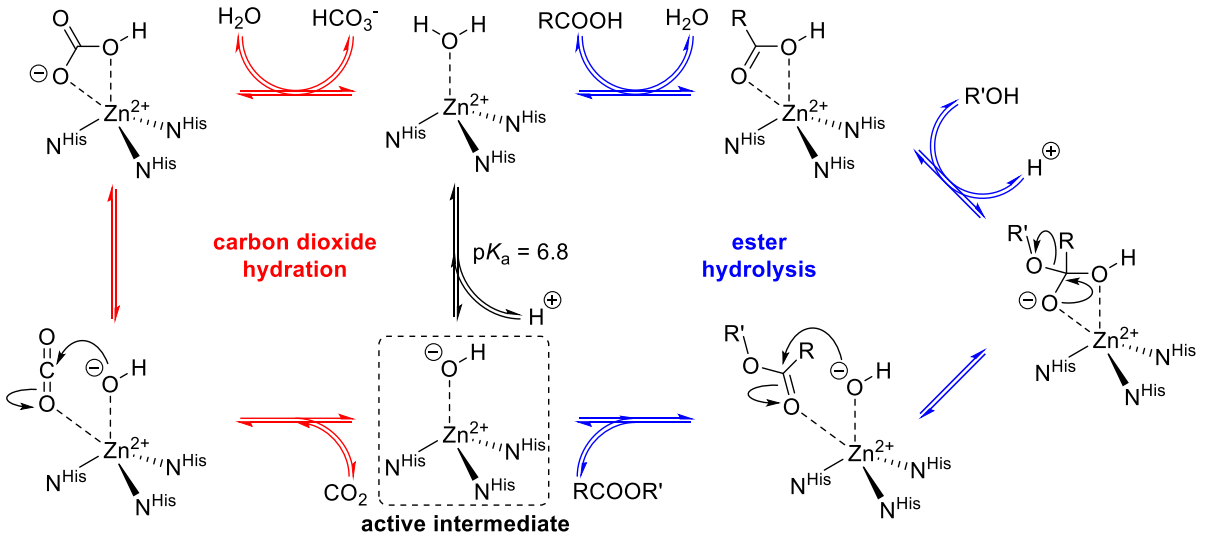

Scheme 4-1: Simplified reaction mechanism of hCAII catalysed CO_2 hydration and ester hydrolysis.

It is therefore interesting to see if the designed peptides are also able to catalyse the hydrolysis of *para*-nitrophenol acetate (*p*NPA). After hydrolysis, the nitrophenol/nitrophenolate is formed, that displays a characteristic isobestic point at 348 nm, which is pH independent and can be detected photometrically.[257] It is known that the side chain of His is also able to catalyse hydrolytic reactions.[335] Therefore, as a control experiment, hydrolysis catalysed by imidazole, imidazole in the presence of Zn(II) and Zn(II) alone was carried out. As an additional control, the hydrolysis was carried out in the presence of hPin1$_{WW}$-Nle and Trpzip2, both in the absence and presence of Zn(II). The hydrolysis in pure buffer was recorded as a background reaction. From the recorded absorbance *versus* time plots the slope *m* was determined using linear regression and the rate or velocity of hydrolysis *v* was calculated according to Equation (1).

$$v = \frac{m_{\text{catalysed reaction}} - m_{\text{background}}}{\varepsilon \cdot d} \left[\frac{\text{M}}{\text{s}}\right] \quad (1)$$

ε is the corrected extinction coefficient at 348 nm of *para*-nitrophenole and *p*NPA (5400 $M^{-1}s^{-1}$- 400 $M^{-1}s^{-1}$ = 5000 $M^{-1}s^{-1}$)[257] and *d* is the pathlength of the cuvette (1 cm).

The results are summarised in Figure 4-39. Zn(II) alone did not significantly accelerate the reaction, but imidazole, as expected, catalysed the hydrolysis of *p*NPA. Addition of Zn(II) to imidazole slowed the reaction down. Tripzip2, which does not contain histidine, showed only slight acceleration of the reaction in the absence of Zn(II). Addition of Zn(II) led to a slight non-significant increase. The other control $hPin1_{WW}$-Nle contains a histidine and thus showed enhanced activity, which was slightly increased by the addition of Zn(II). For WW-CA-Nle, WW-CA-min and WW-CA-ANG, which contain 3 histidines, the hydrolysis rate was only slightly increased compared to $hPin1_{WW}$-Nle. For these three peptides, the addition of Zn(II) decreased the hydrolytic activity. Although also containing three histidines, the hydrolytic activity for $Tz2H_3$ was comparable to that of $hPin1_{WW}$-Nle and was further reduced by the addition of Zn(II).

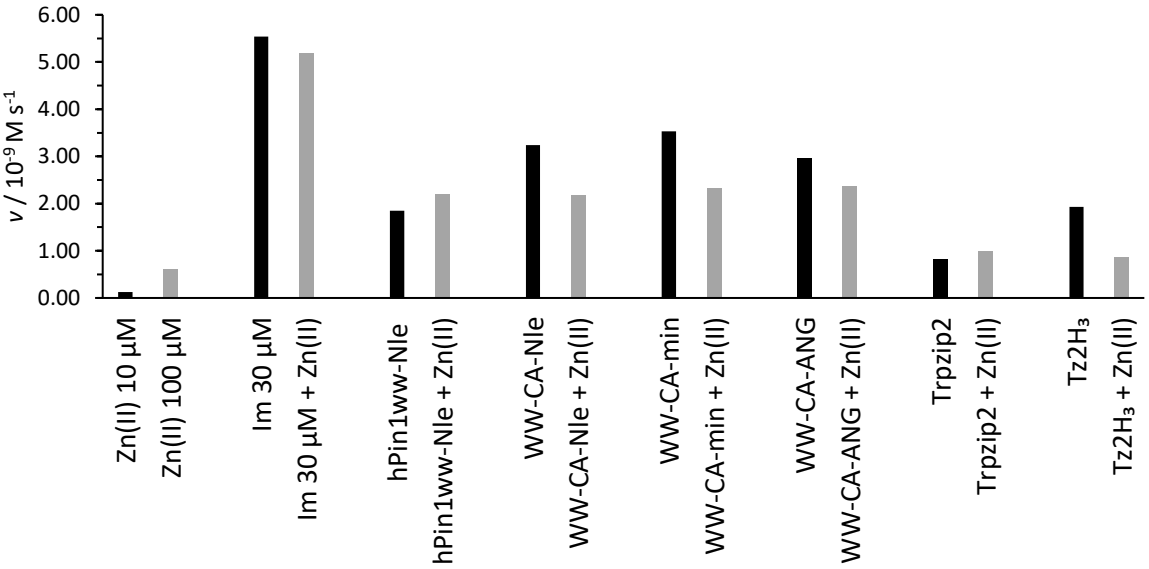

Figure 4-39: *p*NPA hydrolysis rates in the presence of peptides and peptide Zn(II) complexes. Conditions: 1 mM *p*NPA, 10 µM peptide, 10 µM Zn(II), 10 mM MOPS, pH 7.2, 150 mM NaCl, 5% MeCN, rt, 1 cm cuvette. Control: instead of peptide, 30 µM imidazole (Im) was used.

The observation, of Zn(II) complexes being less hydrolytically active than the holo peptides, suggest that the observed catalytic activity is caused by the His residues. Binding of Zn(II) inhibits the activity for the peptides and for free imidazole, which is a nucleophilic catalyst. The mechanism is shown in Scheme 4-2A. The nucleophilic attack of imidazole on the carbonyl carbon of the ester is faster than the comparable reaction with a water molecule. The acyl imidazole formed is highly reactive and easily hydrolysed by water.

As imidazole is the active catalyst, the *p*NPA hydrolysis rate was recorded at different imidazole concentrations. As shown in Figure 4-40A, the reaction rate increased linearly with increasing catalyst concentration. It is therefore expected that this effect is also true for the tested peptides containing one to three His residues. To visualise the dependence of the hydrolysis rate on imidazole-containing residues, k_{obs} is calculated according to Equation (2) and shown in Figure 4-40B.

$$k_{\mathrm{obs}} = \frac{v}{[\mathrm{Catalyst}]} = \frac{v}{[\mathrm{Imidazole}]}\left[\frac{1}{\mathrm{s}}\right] \qquad (2)$$

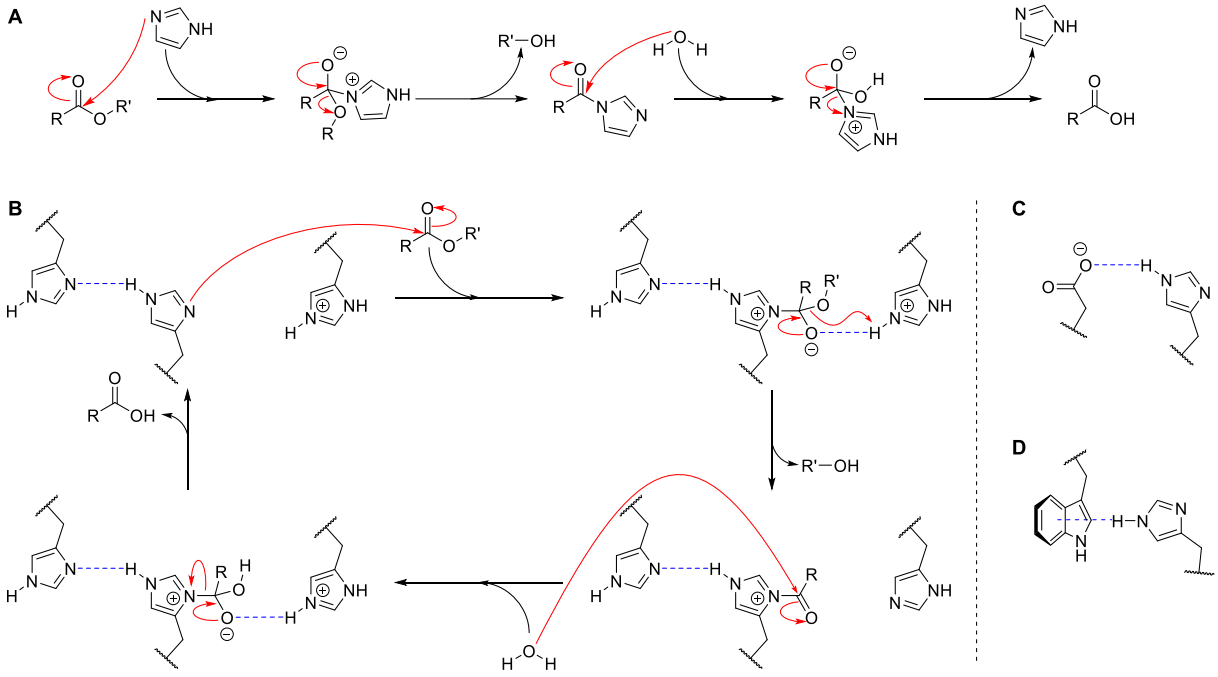

Scheme 4-2: Mechanism of imidazole catalysed ester hydrolysis. A) Hydrolysis catalysed by a single imidazole. B) Cooperativity in catalysis. Increasing of nucleophilicity of imidazole by hydrogen bonding to other imidazole residues. Different protonation states of imidazole enable acid-base catalysis. C) Increase of imidazole nucleophilicity by hydrogen bonding to a carboxylate or D) by aromatic T-shape interaction to an electron rich ring.

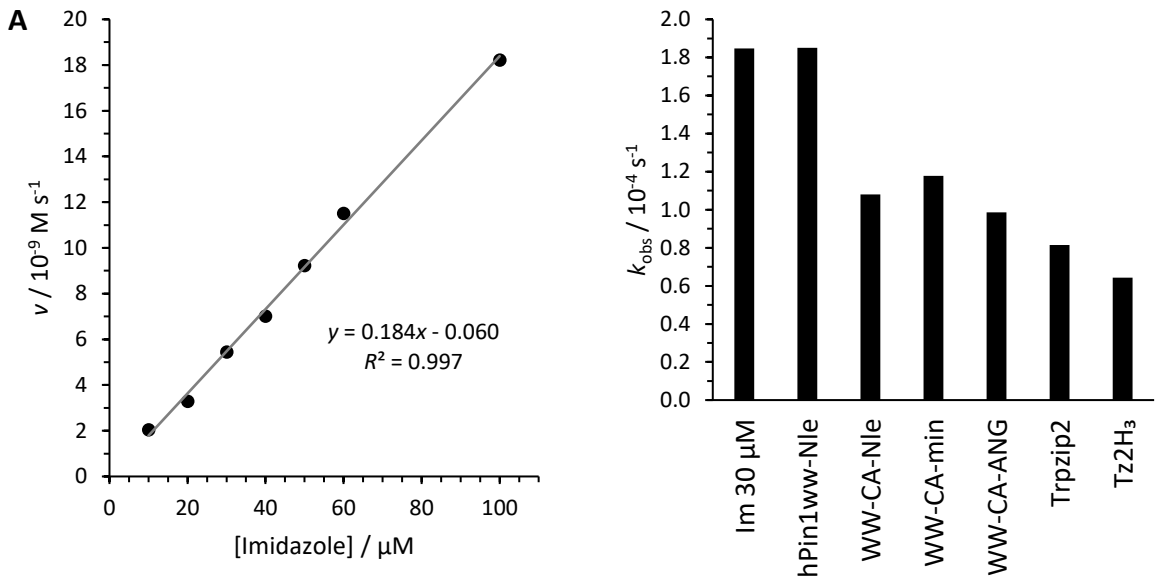

Figure 4-40: A) Rate of *p*NPA hydrolysis as a function of imidazole concentration. The data fits well to a linear model. Conditions: 1 mM *p*NPA, 10 µM to 100 µM imidazole, 10 mM MOPS, pH 7.2, 150 mM NaCl, 5% MeCN, rt, 1 cm cuvette. B) k_{obs} of the different peptides calculated from data in Figure 4-39.

The concentration of imidazole is taken as the concentration of catalytically active species. For peptides containing three His residues, the value is three times the peptide concentration. Surprisingly, hPin1$_{WW}$-Nle showed the same k_{obs} as free imidazole, whereas the k_{obs} of all other peptides were significantly lower. Mutation studies showed that this residue has little influence on structural stability, leading to the assumption that the His side chains behave similar to free imidazole. A closer look at the X-ray crystal structure of hPin1$_{WW}$ revealed that the His residue is located in the second loop and forms a hydrogen bond to Glu12 *via* the Nδ,[66] which, according to Scheme 4-2C, can increase the nucleophilicity of the imidazole residue. The Nε on the other hand, is free and point into the aqueous surrounding. In case of WW-CA-Nle, WW-CA-min or WW-CA-ANG, the three His are located on the β-sheet surface and may not be as accessible as in the loop position.

The hydrolysis reaction is pH dependent and there are hydrolases that only function under acidic or basic conditions.[336-337] Therefore, the catalytic activity of the apo-peptides was measured at pH 4 to 8 and the results are shown in Figure 4-41. At neutral or basic pH, imidazole showed the highest activity but completely lost its activity under acidic conditions. This is expected as imidazolium has a pK_a of 7[338] and therefore at a pH below 7 the protonated unreactive species dominates. For the peptides, the hydrolytic activity also decreases with decreasing pH, but for WW-CA-Nle, WW-CA-min and WW-CA-ANG the activity is not completely lost under acidic conditions. This can be partly explained by the slightly lower pK_a value of the His side chain of 6. However, it would then be expected that no catalytic activity would be observed at pH 4. Another effect might be a lower pK_a of the His side chain due to interaction with other residues. Baltzer *et al*. reported a similar behaviour of the α-helical bundle

KO-42 that contains six His in close proximity. Each His has a different pK_a value ranging from 5.2 to 7.2.[339] The proximity of protonated and deprotonated His residues makes acid-base catalysis possible and may facilitate hydrolysis (Scheme 4-2). Furthermore, the nucleophilicity of imidazole can be enhanced by hydrogen bonding, e.g. to another imidazole or a carboxylic group (Scheme 4-2B and C). Imidazole can also interact with electron-rich aromatic side chains in a T-shaped geometry, which also enhances nucleophilicity (Scheme 4-2D).[228-229]

The position of the His_3 site inhibits the reactivity at neutral pH but enhances it at acidic pH, although the catalytic activity of these peptides is very low compared to other model systems (Table 4-1). For a better comparison, the second order rate constant k_2 is used, calculated according to Equation (3), which also takes into account the substrate concentration.

$$k_2 = \frac{k_{\mathrm{obs}}}{[p\mathrm{NPA}]}\left[\frac{1}{\mathrm{M}\cdot\mathrm{s}}\right] \qquad (3)$$

The main disadvantage of these peptides is the lack of a binding cavity for the predominantly hydrophobic substrate *p*NPA. The active centre is displayed at the surface of the β-sheet. Similar to the peptides in this study, a case was reported for an engineered scorpion toxin that also contained a His_3 site on a β-sheet surface.[340] The k_2 value was comparable to free imidazole and the addition of Zn(II) inhibited the reactivity.

Aza-crown Zn(II) complexes, which also lack a binding cavity and catalyse *p*NPA exclusively *via* the Zn(II)-bound hydroxide, and which are early model systems for studying hCAII functionality, show an order of magnitude lower activity than simple imidazole or 4-methylimidazole.[341] As discussed above, acid-base catalysis, as introduced in KO-42, increases hydrolytic activity under acidic conditions.[339] Placing the His residue in the cleft of thioredoxin yields PZD2, which is by an order of magnitude more active then free imidazole.[342] Similarly, a His_3 site can be placed in a hydrophobic environment as has been done in case of $(TRIL9CL23H)_3$ which is a coiled coil trimer. This model system displays an activity only 100 times lower than the natural hCAII.[232]

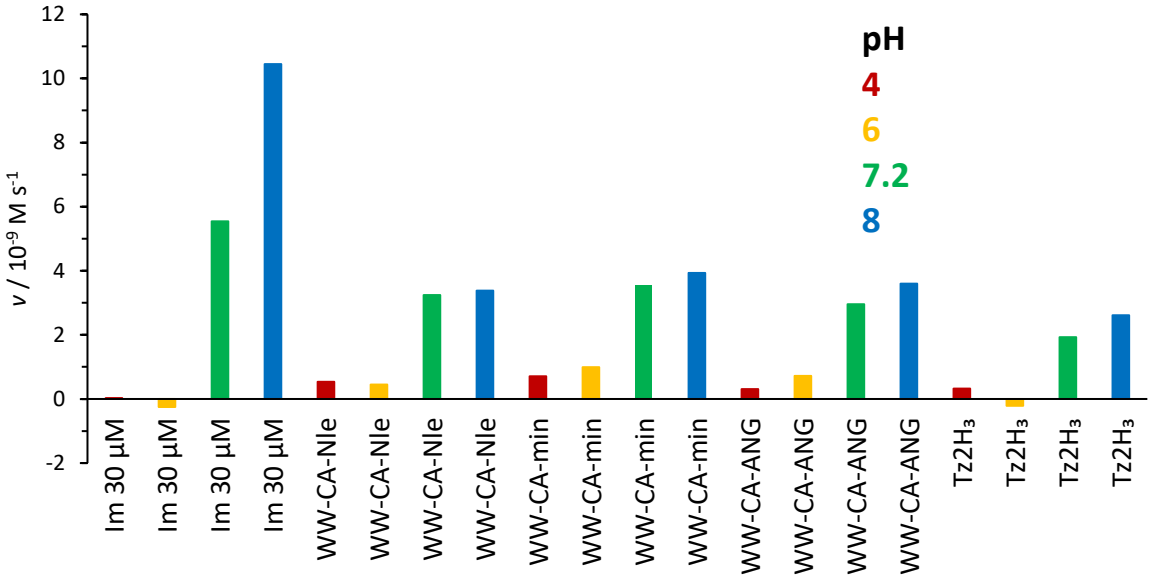

Figure 4-41: *p*NPA hydrolysis rate at different pH values in presence of peptides. Conditions: 1 mM *p*NPA, 10 µM peptide, 10 mM buffer substance (pH 8: HEPES, pH 7.2: MOPS, pH 6: MES, pH 4: formiat), 150 mM NaCl, 5% MeCN, rt, 1 cm cuvette.

From our data and the literature, it is clear that the designed peptides do not show significant activity, due to the lack of a binding cavity and will not show any activity comparable or higher than previously reported systems. It would be interesting to introduce His residues into the hydrophobic core of $hPin1_{WW}$. If this mutation does not disrupt the hydrophobic core too much and the peptide remains folded, this could eventually lead to enhanced hydrolytic activity, also due to a potential aromatic interaction of His with Trp. Another possibility is the swap of His27 and Arg14. From the experiments described above, it is known that His27 behaves like a free imidazole. Changing the position could increase the nucleophilicity due to interaction with Phe25 and Tyr23.

Several *de novo* designed hydrolases exist, but none of them show a *p*NPA hydrolysis efficiency like hCAII (Table 4-1), even though hCAII is not designed for this reaction but for CO_2 hydration. Furthermore, *p*NPA is comparably easy to hydrolyse and decomposes in aqueous solution. Natural hydrolases, such as proteases, are able to hydrolyse the much more stable amide bond, which has not yet been achieved with rationally or computationally designed peptides or proteins, although catalytic amidase antibodies exist.[343] Therefore, the study of artificial hydrolases remains interesting.

Table 4-1: Selected examples of enzymes and enzyme mimics. Given values refers to *p*NPA hydrolysis. In case Zn(II) is present, pK_a refers to Zn(II) bound water, in the other cases to the imidazole.

Enzyme	pK_a	pH	k_2 [$M^{-1}s^{-1}$]	[Lit]
Zn(II)-hCAII	6.8	7 8	1670 2550	[257]
Zn(II)-(TRIL9CL23H)$_3$	8.8	7.5 9	1.38 17.6	[232]
Zn(II)-MID1	8.2	7 8	35 190	[344]
Zn[12]aneN$_4$	7.9	7 8	0.011 0.056	[345-346]
Zn[12]aneN$_4$-ethyl-OH	7.7	7 8	0.077 0.3	[347]
Imidazole	7	6.3 [Lit] 6.9 [Lit] 7.4 [Lit] 7.9 [Lit] 4 6 7.2 8	0.048 0.13 0.17 0.21 0.00093 -0.0083 0.18 0.35	[335]
4-methyl imidazole	7.4	5.1 6.95 8	0.00072 0.11 0.27	[335, 339, 342]
KO-42	5.2 to 7.2	5.1	0.29	[339]
PZD2	-	6.95	2.7	[342]
Charybdotoxin mutant	-	7	0.1	[340]
hPin1$_{WW}$	-	7.2	0.19	-
WW-CA-Nle	6 (average)	4 6 7.2 8	0.018 0.015 0.11 0.11	-
WW-CA-min	-	4 6 7.2 8	0.024 0.033 0.12 0.13	-
WW-CA-ANG	-	4 6 7.2 8	0.010 0.024 0.099 0.12	-
Tripzip2	-	7.2	0.081	-
Tz3H$_3$	-	4 6 7.2 8	0.011 -0.0071 0.064 0.087	-

4.4.2 Phenol oxidation

Phenol oxidation by molecular oxygen is a widespread reaction catalysed by several Cu(II)-containing enzymes, called laccases that play an important role in several metabolism pathways, e.g. in lignin metabolism, which is essential for the formation of wood.[263] The Cu(II) is coordinated by histidine residues in the active centre, similar to the peptides presented here, with the difference that laccases contain four copper ions at the active site. Laccases selectively catalyse the single-electron oxidation of phenols to phenoxy radicals, which then react with each other outside the active centre. *De novo* designed laccases have also been reported, e.g. the Korendovych lab has designed a copper-binding amyloid that is able to activate oxygen and oxidise 2,6-dimethoxyphenol (DMP),[261] a common model substrate that is well studied because one of the possible products (Scheme 4-3),[348] the polymer polyphenylene ether (PPE), is highly thermostable up to 200 °C and therefore widely applicable in e.g. healthcare for the production of heat-sterilisable instruments.[349-350] Other possible products are the C-C coupled dimer 3,3',5,5'-tetramethoxy-4,4'-bisphenol (TMBP), which can further be oxidised to 3,3',5,5'-tetramethoxy-4,4'-diphenoquinone (TMDQ). This is also a good test reaction as the products are easily detectable. DMP is colourless, but TMDQ is orange and its formation can be followed at 477 nm.[351] The polymer is insoluble in water and precipitates.[352]

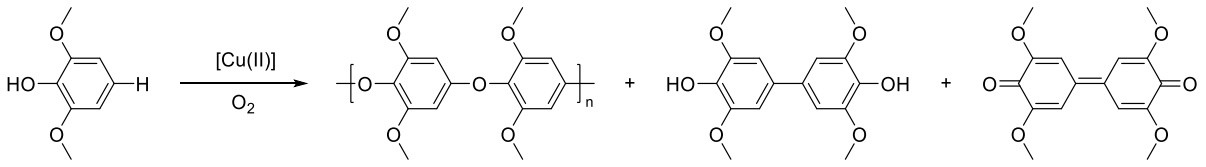

Scheme 4-3: Cu(II) catalysed aerobic oxidation of DMP and possible products.

The product formed depends on the reaction conditions and the catalyst used. There are two possible mechanisms, a radical pathway leading to mostly dimer formation or a cationic pathway leading to polymer formation.

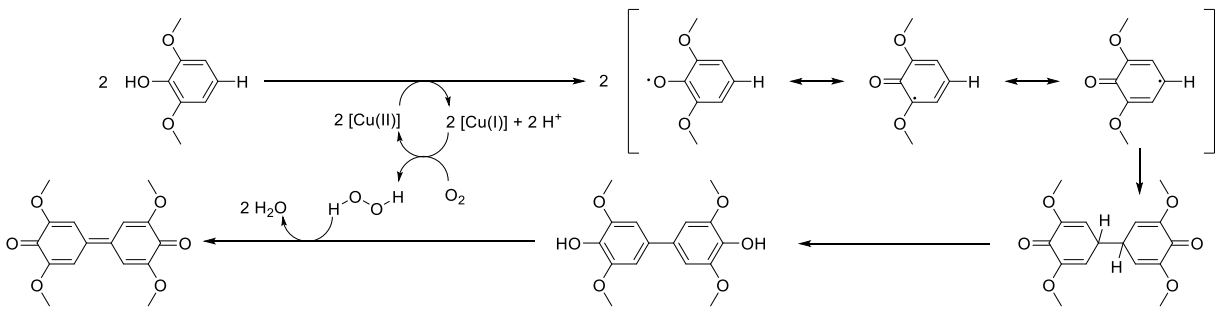

Scheme 4-4: Reaction mechanism of the radical pathway of DMP oxidation.

The phenol radical is formed by one-electron transfer from DMP to Cu(II), which is reduced to Cu(I) (Scheme 4-4). Cu(II) is regenerated by oxidation of Cu(I) by oxygen and hydrogen

peroxide is formed. The radical is resonance stabilised and can react in two ways: the recombination of two *para*-carbon-centred radicals to give a C-C linked dimer, or the reaction of an oxygen-centred and a carbon-centred radical. The first is preferred because the electron density at the *para* position is higher than at the oxygen. After C-C coupling and rearrangement, TMBP is formed. Due to the presence of H_2O_2, TMPB is further oxidised to TMDQ.[353-354]

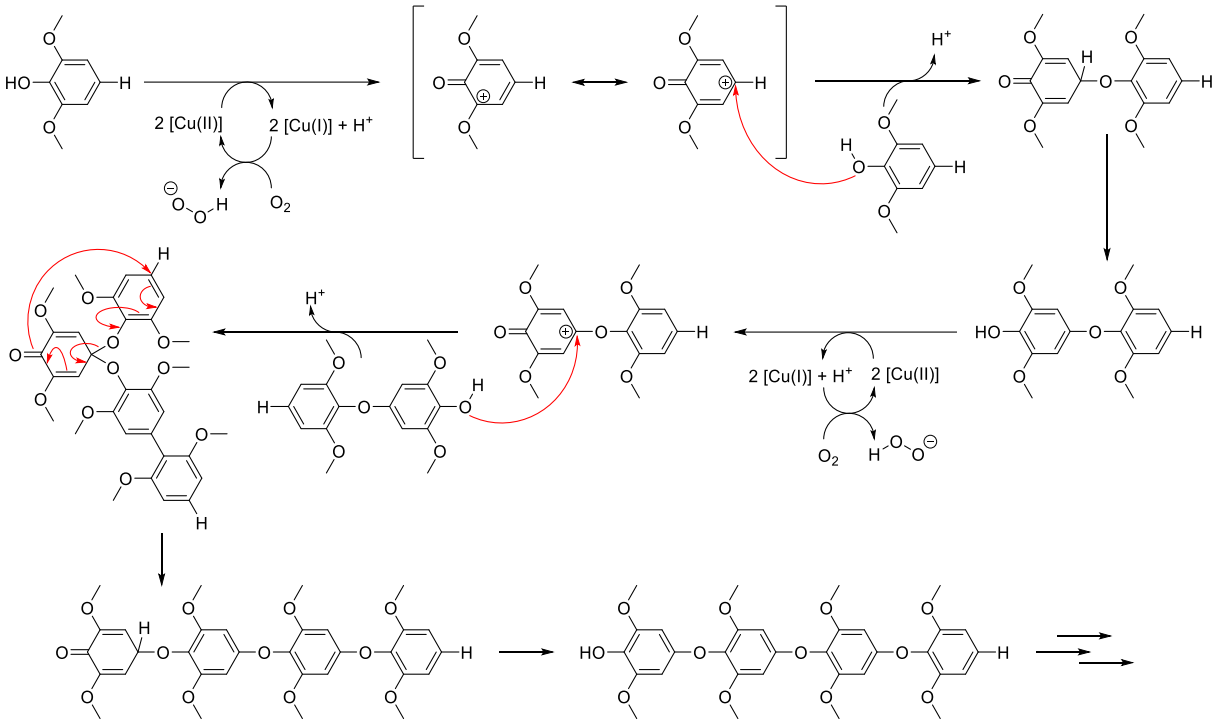

Scheme 4-5: Reaction mechanism of the cationic pathway of DMP oxidation.

In the cationic pathway, two electrons are transferred from DMP to two Cu(II) ions to form the DMP cation. Another DMP molecule nucleophilically attacks the DMP cation. The C-O coupled product is favoured because the hydroxyl group is more nucleophilic than the *para* carbon. Polymerisation can occur by reaction of the dimer with a DMP cation, but there is another mechanism. This is because the dimer is more electron-rich due to the four O-substituents (+M effect) on a phenyl ring compared to only three in DMP. It is therefore more easily oxidised, and the carbocation is better stabilised. At the same time, the dimer is more nucleophilic than DMP due to the same effect. The dimer attacks the oxidised dimer and after two rearrangements a tetramer is formed which can react further.[355-356]

The Cu(II) complexes of the designed peptides WW-CA-Nle, WW-CA-min, WW-CA-ANG and $Tz2H_3$ were tested for their catalytic phenol oxidation activity. It is known that free Cu(II) can also catalyse the reaction and was used as a control. Figure 4-42 shows the absorbance *versus* time plots. In the absence of Cu(II) no reaction was observed and the apo peptides were also unable to catalyse the reaction (Figure 4-42A). In contrast to *p*NPA hydrolysis, there is no background reaction. In the presence of Cu(II) alone, an initial increase in absorbance

was observed, but after approximately 800 s to 1400 s, depending on the Cu(II) concentration, a plateau was reached, followed by a decrease in the absorbance (Figure 4-42B).

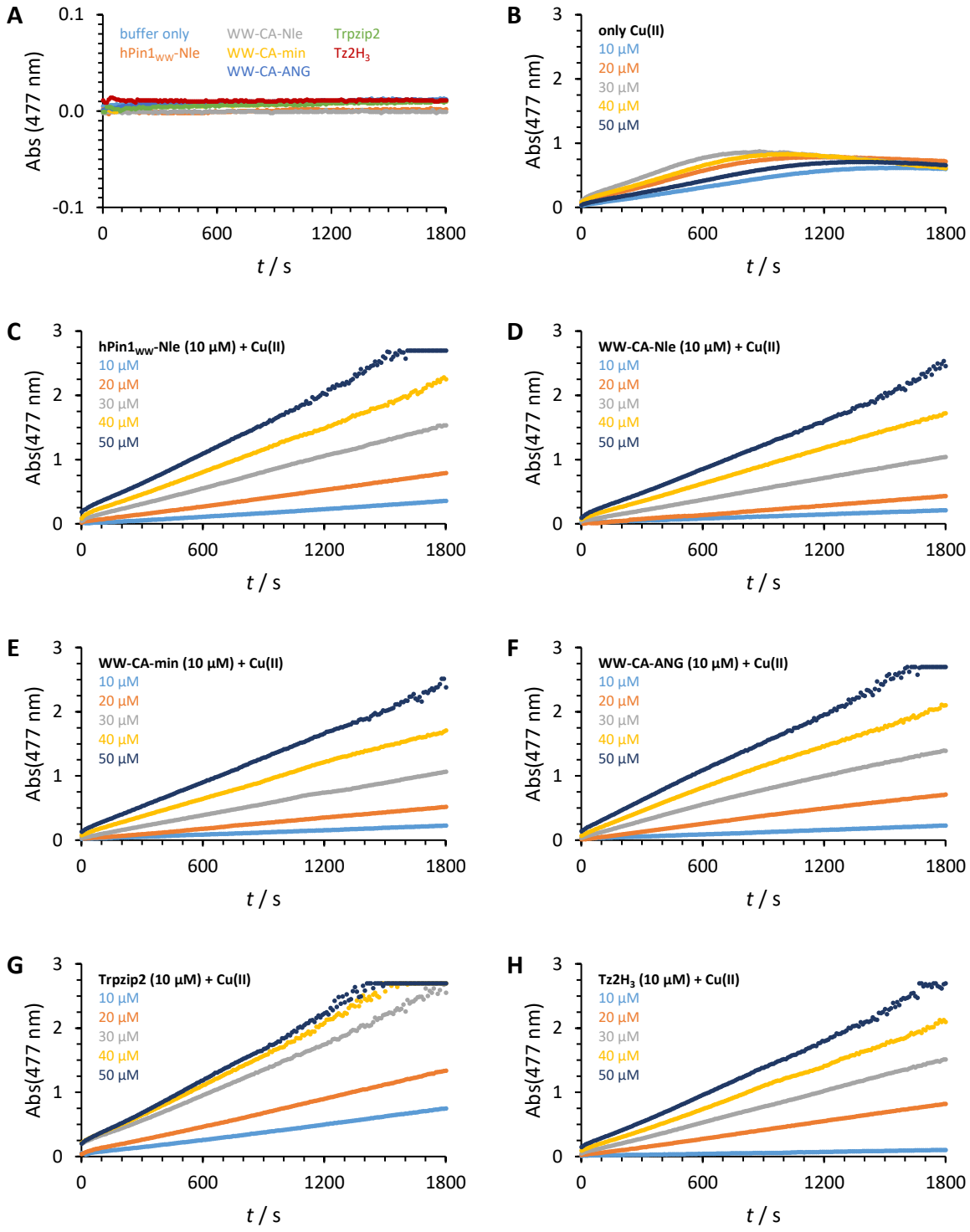

Figure 4-42: Absorbance *versus* time plots of DMP oxidation. A) Blank and apo peptides. In presence of Cu(II) (from 10 mM to 50 µM) and B) no additional peptide, C) hPin1$_{WW}$-Nle, D) WW-CA-Nle, E) WW-CA-min, F) WW-CA-ANG, G) Trpzip2 and H) Tz2H$_3$. Conditions: 10 µM peptide (if present), 0 µM to 50 µM Cu(II), 10 mM MOPS, pH 7.2, 150 mM NaCl, 1% DMSO, rt, 1 cm cuvette.

An orange precipitate formed during this reaction which was accompanied by a decolouration of the reaction solution. This observation indicates that the free Cu(II) catalyses the polymerisation reaction. Initially, soluble di- and oligomers were formed, which then precipitated over time due to chain growth, resulting in decolouration of the solution. Contrary to expectations, the initial rate did not increase linearly with increasing Cu(II) concentration, but increased up to a Cu(II) concentration of 30 µM and then decreased.

A possible explanation is that with increasing Cu(II) concentration, polymer formation is strongly favoured and therefore no increase in absorption is observed due to solid particles in the solution making accurate absorption measurement impossible. This observation is also consistent with the mechanism. In a cationic pathway, two electrons are transferred from DMP to Cu(II) *via* an intermediate in which two Cu(II) bind to one DMP, while the transfer of a single electron results in a radical pathway. As the concentration of Cu(II) increases, the cationic pathway is more likely to occur and therefore polymerisation is observed.

The catalytic activity of the peptide-Cu(II) complexes was then determined. The peptide concentration was kept constant (10 µM) while the Cu(II) concentration was varied from 10 µM to 50 µM. As can be seen in Figure 4-42C to H, all peptides behave very similar. The rate of DMP oxidation increased linearly with increasing Cu(II) concentration. As the absorbance increases above a value of 2, the data become noisier, but a linear dependence is still visible up to a value of 2.7, where the detector was saturated. At low Cu(II) concentrations the rate was lower than the rate of Cu(II)-catalysed oxidation, but at 50 µM the rate was higher. After the measurement the solution was bright orange, but no precipitate was formed. After the cuvettes were left overnight, an orange precipitate formed. These observations suggest a shift in the reaction mechanism. The peptide copper complexes favour the formation of TMDQ, and only after a longer reaction time the formation of polymer is observed. An open question is the influence of the Cu(II):peptide ratio. The peptides have only one or two binding site and one would expect that an increase in Cu(II) concentration would lead to an increase in unbound Cu(II). This unbound Cu(II) should behave similarly to the control experiments and lead to a preferential formation of PPE over TMDP. However, this has not been observed.

For a more quantitative view, the reaction rate v and the second order rate constant k_2 were calculated as described in the previous chapter and presented in Figure 4-43. Linear regression was performed on the linear part of each curve. The values for Cu(II) alone (Figure 4-43A, B) should be taken with caution as polymer formation cannot be measured with this technique and the precipitated polymer affects the accuracy of the photometric measurement. For all peptides, at first sign the rate of DMP oxidation appears to be linear with increasing Cu(II) concentration. This would suggest identical k_2 values for each Cu(II) concentration, which surprisingly is not the case, except for Tripzip2. For hPin1$_{WW}$-Nle, WW-CA-Nle and WW-

CA-min (Figure 4-43D, F, H) a sigmoidal shape is observed, where k_2 values for 30 µM to 50 µM Cu(II) are significantly higher than for 10 µM and 20 µM. In the case of WW-CA-ANG and $Tz2H_3$, saturation is observed.

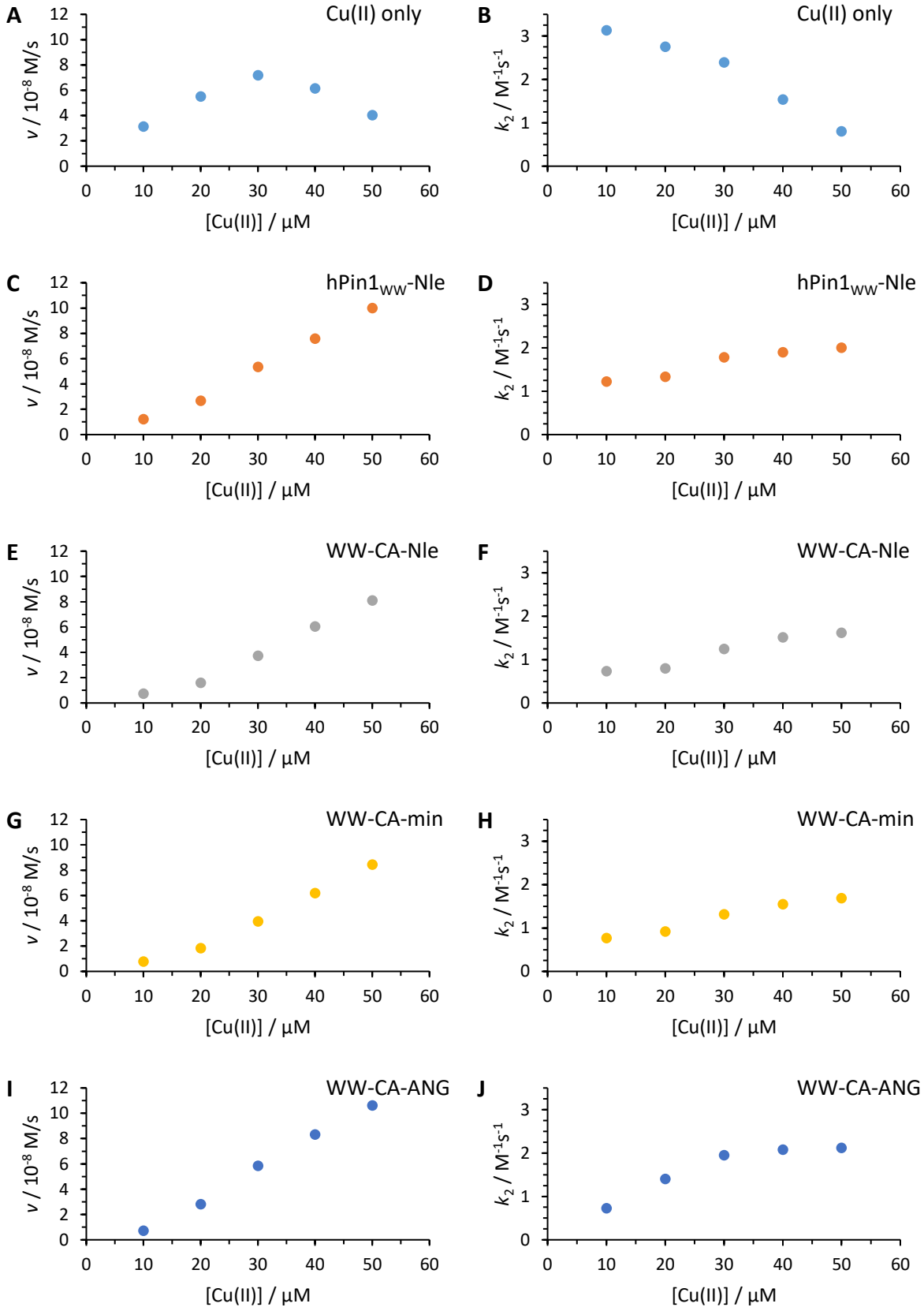

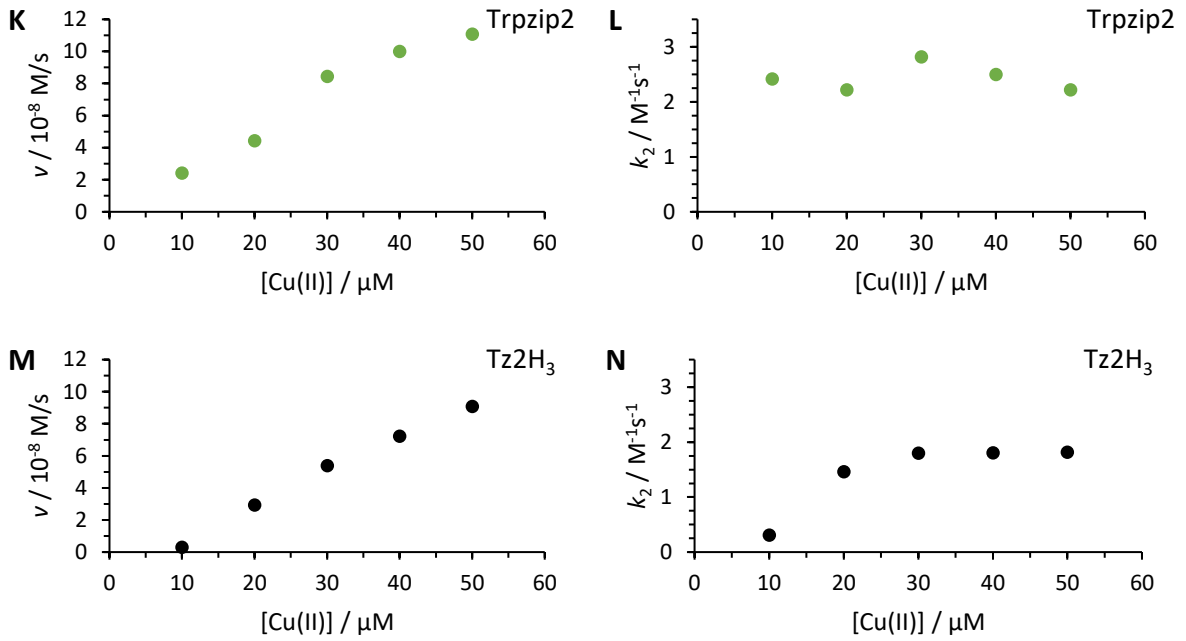

Figure 4-43: DMP oxidation rate and second order rate constant as a function of Cu(II) concentration in A-B) absence of peptide and in presence of C-D) hPin1$_{WW}$-Nle, E-F) WW-CA-Nle, G-H) WW-CA-min, I-J) WW-CA-ANG, K-L), Trpzip2, M-N) Tz2H$_3$. Calculated from data presented in Figure 4-42.

A possible explanation could be a non-specific weak binding of Cu(II) to exposed polar side chains of the peptides. The Cu(II) ions could be bound in a way that prevents the formation of the dinuclear complex with DMP, thus favouring single electron transfer leading to dimerization.

The behaviour of hPin1$_{WW}$-Nle and Trpzip2, which are not designed to bind Cu(II) but are still catalytically active, is unexpected. As described in the previous chapters, hPin1$_{WW}$-Nle binds to Cu(II), but with a much lower affinity than the other peptides. Nevertheless, this weak binding could explain the reactivity. In the case of Trpzip2, no Cu(II) binding has been observed so far. These observations raise even more questions, as it is completely unclear how Trpzip2 could affect the reactivity of Cu(II) without interacting with it. In addition, Trpzip2 + Cu(II) always showed the highest reactivity of all peptides. The reactivity is also different because k_2 did not increase with increasing Cu(II) concentration.

In general, it should be mentioned that the catalytic efficiency of the DMP oxidation is low (around 2 $M^{-1}s^{-1}$) compared to the reported designed Cu(II)-binding amyloid peptides (31 $M^{-1}s^{-1}$),[261] although it should be noted that in this case it was not reported whether polymer formation was observed or not.

It has now been shown that the peptide copper complexes can activate oxygen and selectively catalyse the oxidation of DMP to TMDQ, but oxygen is not the only biological oxidant. Peroxidases use hydrogen peroxide,[262] which was also tested to see if it could increase the reaction rate. Figure 4-44 shows the absorbance *versus* time plots. No reaction was observed

in the absence of Cu(II). Free Cu(II) showed a similar behaviour to O_2, but this time the reaction was much faster and the plateau was reached earlier. The decrease in absorbance and the formation of an orange precipitate were then observed. The part where the absorbance increased could not be fully detected due to manual mixing which takes 30 s. When peptide was added, the reaction was slowed down regardless of which peptide was used. A plateau was observed at an absorbance of around 0.55, but no decrease or increase in intensity was observed thereafter. The mixture was orange at the end of the measurement, and it appears as if the reaction has just stopped. Interestingly, the reaction with Trpzip2 is again the fastest.

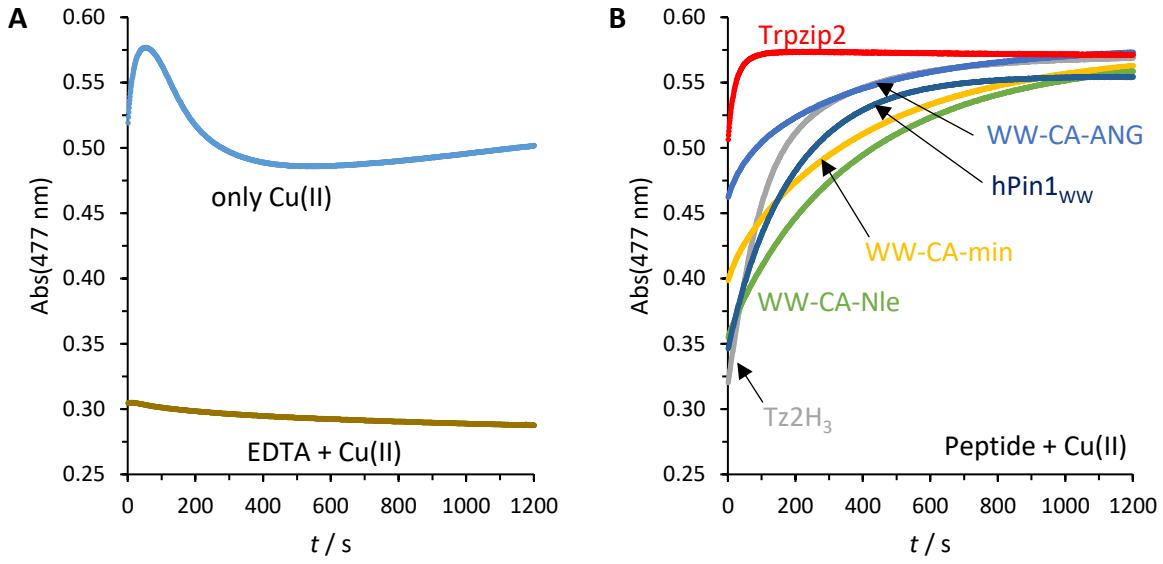

Figure 4-44: DMP oxidation by H_2O_2 A) by free Cu(II) and Cu(II) EDTA complex or B) by peptide Cu(II) complexes. Conditions: 10 µM peptide (if present), 10 µM Cu(II), 10 mM HEPES, pH 8.0, 150 mM NaCl, 1% DMSO, rt, 1 cm cuvette.

The stagnation of the signal increase indicated the decomposition of the catalyst, since it is known from the previous experiments that the absorbance can reach much higher values until the detector is saturated. The reaction was therefore repeated with $Tz2H_3$ and analysed by HPLC (Figure 4-45). First, DMP and $Tz2H_3$ were injected to determine the retention times (Figure 4-45A). DMP was then oxidised in the presence of $Tz2H_3$, Cu(II) and H_2O_2. After selected time points (0, 0.5, 1, 2 and 4 h) aliquots were taken and analysed by HPLC (Figure 4-45B). As expected, the DMP peak decreased over time, but so did the $Tz2H_3$ peak, which was no longer visible after 0.5 h, indicating degradation. On the other hand, other peaks appeared. Interestingly, the degradation of the DMP peak slows down with time.

It was then interesting to see if $Tz2H_3$ was also degraded in the air-mediated DMP oxidation. The reaction was carried out again and analysed by HPLC at different time points (Figure 4-45C). Again, a decrease in the DMP peak was observed, but slower than in the H_2O_2 mediated reaction. Interestingly, in this case a decrease in the $Tz2H_3$ peak was also observed, again much slower. After 0.5 h, which was also the time scale for the reactions monitored by

UV/Vis, most of the peptide was still intact, but after 4 h it was completely degraded. To determine, which reactive compound was responsible for the peptide degradation, the reaction was carried out with only Cu(II), only H_2O_2 or a combination of Cu(II) and H_2O_2. DMP did not react in the presence of the peptide as shown before. Cu(II) is redox active, but as can be seen in Figure 4-45D1, it did not degrade the peptide. Next, H_2O_2 could cause peptide degradation as it is a strong oxidant, but the HPLC trace in Figure 4-45D2 shows no degradation when $Tz2H_3$ was incubated with only H_2O_2. This changes drastically when Cu(II) was also present (Figure 4-45D3). Now the peptide was degraded within 1 h. Although no H_2O_2 is added in the air-mediated DMP oxidation, it is formed during the reaction as shown in Scheme 4-4 due to the reaction of Cu(I) with O_2. However, the concentration is much lower in this case.

The slow degradation of the peptides could also explain the formation of the polymer when the reaction was allowed to continue overnight. Initially, the degraded peptides still bind to Cu(II) and prevent further reaction, leading to a plateau. However, further degradation of the peptides eventually gave rise to peptide fragments that no longer coordinate to Cu(II). The free copper ions catalyse polymer formation.

In conclusion, the designed peptide copper complexes are interesting laccase mimics and are able to activate oxygen but suffer from low stability towards the oxidative environment. Furthermore, the results of O_2 and H_2O_2 mediated oxidation of DMP cannot be fully explained. Apparently, the presence of peptide, whether or not Cu(II) is bound, shifts the mechanism from a cationic to a radical pathway and favours the formation of TMDP, similar to natural laccases which exclusively catalyse TMDP formation, due to the selective formation of phenol radicals. Another interesting point is that natural laccases have a pH optimum at slightly acidic conditions. Therefore, the pH dependence of this reaction should be analysed in more detail. The influence of higher amounts of organic solvents is also interesting, especially for $Tz2H_3$, which is stable under the conditions described in the previous chapter. Organic solvents also open up the possibility of testing more hydrophobic substrates. In general, the substrate range of these peptide-copper complexes should be explored, starting with other typical laccase substrates such as ABTS, *p*-phenylenediamine, guaiacol or syringaldazine.[357] In addition, quantitative analysis of the products formed after DMP oxidation could provide further insight into the reaction mechanism. The selectivity for TMDP formation was maintained even when the Cu(II) concentration was higher than the peptide concentration and free copper should theoretically be present. It is known from CD titrations that the WW domain based peptides change conformation away from a typical WW domain at high Cu(II) concentrations and two copper binding sites where found in competitive titration. ITC can provide additional information on the thermodynamics of conformational change caused by Cu(II) binding. The exact position of the Cu(II) binding and the conformational change of the peptide could be analysed by paramagnetic NMR[358] and the coordination geometry and sphere of Cu(II) by EPR.

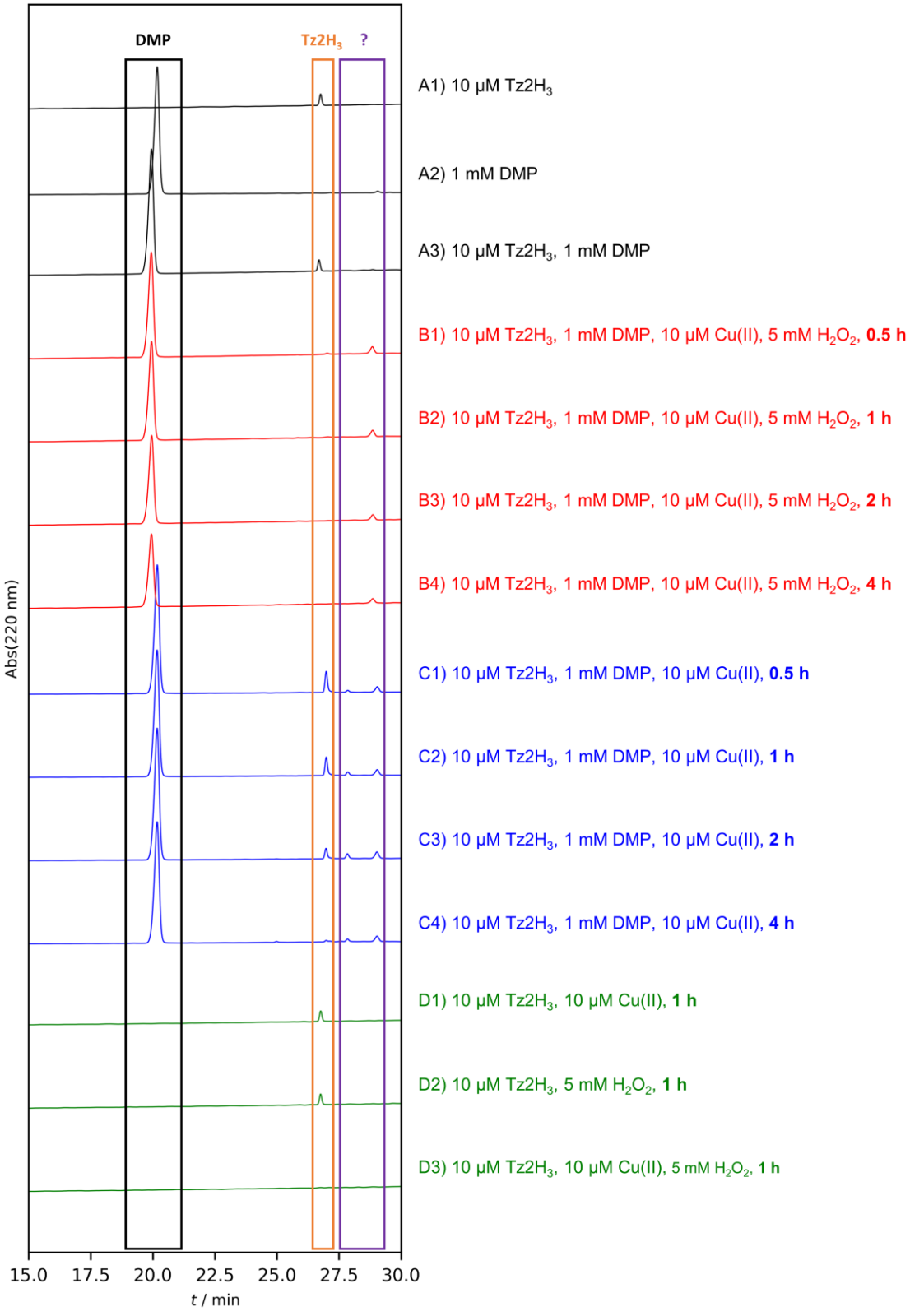

Figure 4-45: HPLC analysis of DMP oxidation. Reaction was performed in 10 mM HEPES, pH 8.0, 150 mM NaCl, 1% DMSO at rt and quenched 1 mM Na_2EDTA prior to injection. Gradient: 10-40% B in A in 30 min. Slight shifts in retention time due to measurements at different days. A) Controls to determine retention time of educts (injected directly). B) DMP oxidation by H_2O_2. C) DMP oxidation by air. D) Oxidative degradation of $Tz2H_3$.

4.4.3 Copper catalysed azide-alkyne cycloaddition

One of the best-known reactions catalysed by Cu(I) is the azide-alkyne cycloaddition (CuAAC), which selectively yields 1,4-disubstituted 1,2,3-triazoles.[359] This type of "click" reaction allows the synthesis of large libraries of organic molecules, which are particularly useful in medicinal chemistry.[360-361] In addition, site-selective bioconjugation can be achieved *in vitro*, as the educts, organic azides and terminal alkynes, as well as the triazole product, do not react with any other functional group in biomolecules and are therefore considered biorthogonal.[362] This reaction can therefore be used *in vivo*. By feeding cells with azide- or alkyne-containing compounds, such as azido sugars, these are incorporated into biomolecules, which can then be selectively labelled.[363] The mechanism of CuAAC is shown in Scheme 4-6A.

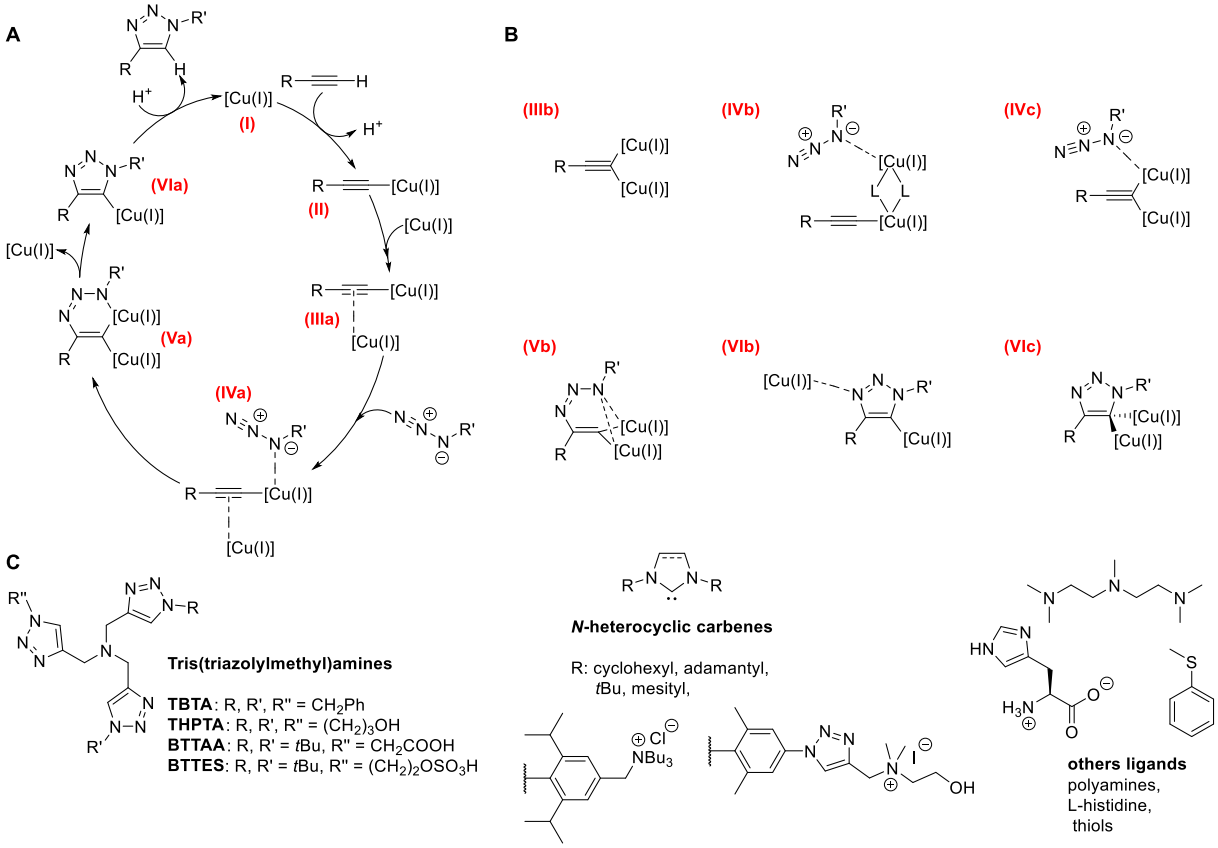

Scheme 4-6: A) Catalytic cycle of CuAAC. B) Alternative structures of intermediates. C) Structure of common ligands for CuAAC. [Cu(I)] symbolize a Cu^+ cation coordinated to ligands (L).

In the early days of CuAAC, a catalytic cycle involving only one Cu(I) was proposed,[359] but further experimental evidence has shown that two Cu(I) ions are involved and that there are six basic steps:[364] Formation of the Cu(I) acetylide and subsequent coordination of a second Cu(I), coordination of the azide to the Cu(I), nucleophilic attack of the triple bond on the N-3 of the azide and formation of the triazole by nucleophilic attack of the N-1 of the azide on the terminal C. Finally, Cu(I) is released by protonation. The structures of intermediates III to VI are highly dependent on the conditions and ligands used.[365] Known structures are shown in

Scheme 4-6B. The use of ligands is necessary to solubilise Cu(I) and to prevent disproportionation to Cu(II) and Cu(0). The most common ligands (Scheme 4-6C) are tris(triazoylmethyl)amines and *N*-heterocyclic carbenes, both aromatic and non-aromatic. In addition, polyamines and thiols also promote CuAAC.[366] The most commonly used ligand for biological CuAAC is THPTA,[367] which is water soluble and coordinates the metal ion *via* the triazoles and the central amine. Histidine is also known to promote CuAAC.[368] It was interesting to see if the Cu(II) and Cu(I) binding peptides are also able to catalyse CuAAC.

The THPTA ligand has two functions.[367] First, it stabilises Cu(I) and keeps it soluble. Second, it is common to use Cu(II) salts which are reduced to Cu(I) with sodium ascorbate (Asc) in air. This reaction produces hydrogen peroxide, which can react with biomolecules. In particular, Trp and His are sensitive to oxidation.[367, 369] THPTA was also found to be a good scavenger of H_2O_2. Therefore, THPTA is used in excess and a Cu(II) concentration of 100 µM and a THPTA concentration of 500 µM is recommended.[367] This high concentration would be a waste of peptide material, therefore the ligand concentration was lowered and another quencher for H_2O_2 was used. As discussed in the previous chapter, the peptides are very sensitive to oxidative damage. It is known from cell culture studies that pyruvate (Pyr) is a good quencher of hydrogen peroxide (mechanisms in Scheme 4-7) and can effectively protect cells from oxidative damage when added to culture media.[370-371]

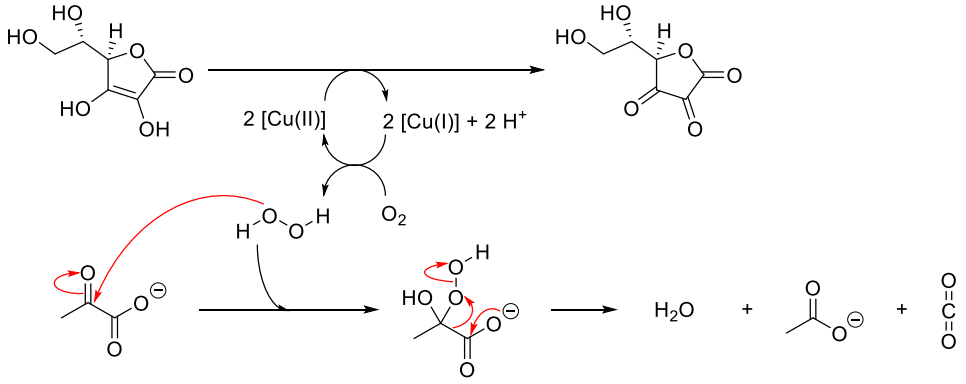

Scheme 4-7: Formation of hydrogen peroxide during Cu(II) reduction by ascorbic acid and quenching of hydrogen peroxide by pyruvate.

To test the ability of pyruvate to prevent peptide oxidation, $Tz2H_3$ was used as a test peptide and incubated with Cu(II) and Asc in the absence and presence of pyruvate. After 1 h, aliquots were taken and analysed by HPLC (Figure 4-46). The peptide without additive (Figure 4-46A) was used as a reference and it was clearly visible that the ascorbate-copper system degraded the peptide (Figure 4-46B). Addition of pyruvate mostly prevented the oxidative damage (Figure 4-46C).

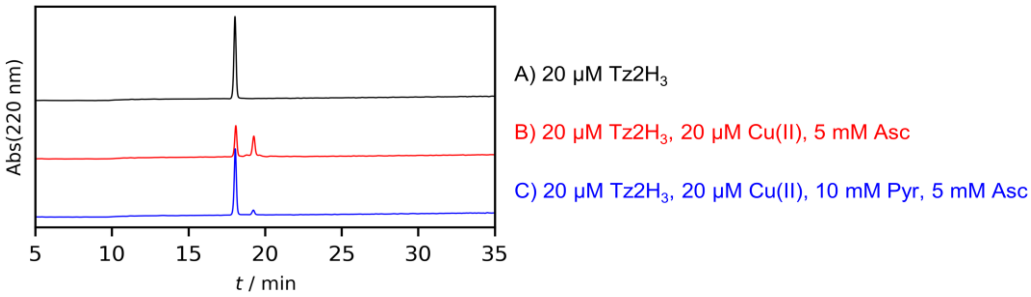

Figure 4-46: HPLC traces of peptide degradation experiment. Reactions were performed in 10 mM MOPS, pH 7.2, 150 mM NaCl at rt and quenched after 1 h with 0.1 M Na_2EDTA prior to injection. Gradient: 20-40% B in A in 30 min.

Based on this positive result, the next step was to test if pyruvate was compatible with CuAAC. Therefore, a CuAAC test reaction between Fmoc-Lys(N_3)-OH and PhCCH (Figure 4-47) was carried out in the absence and presence of pyruvate (10 mM). The concentrations of Asc and Cu(II) were kept constant, while the concentration of THPTA (250 µM or 500 µM) was varied. After allowing the reaction to equilibrate overnight, aliquots were taken and analysed by HPLC (Figure 4-47). The substrates without catalyst did not react (Figure 4-47A). In the presence of THPTA but in the absence of pyruvate (Figure 4-47B and C), no full conversion is observed at either THPTA concentration. In contrast, full conversion was achieved by the addition of pyruvate at both THPTA concentrations (Figure 4-47D and E).

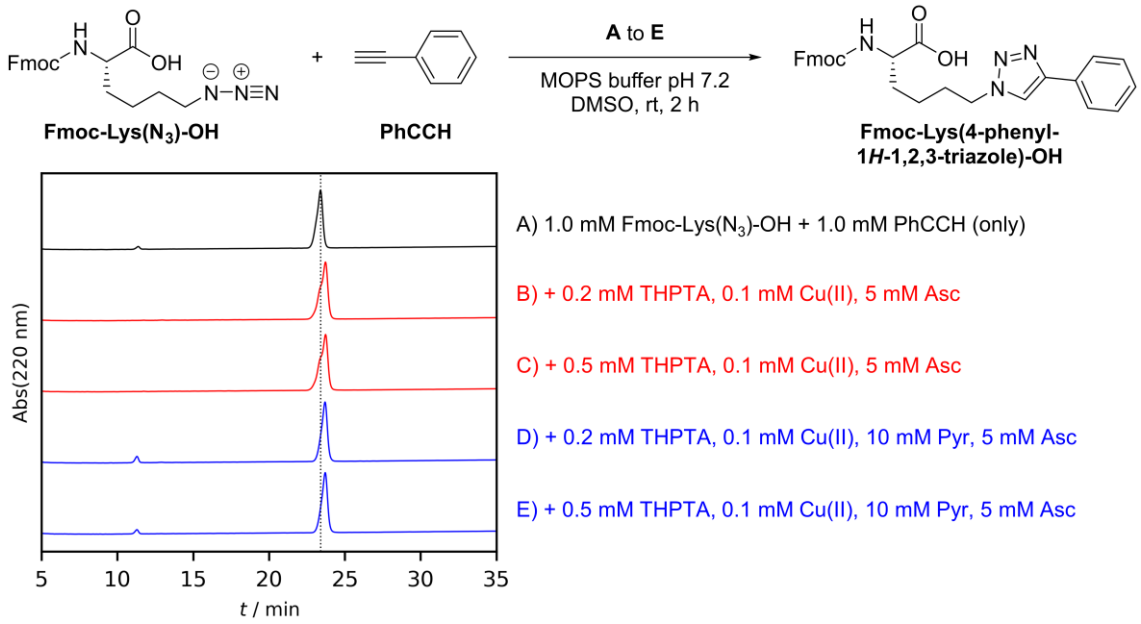

Figure 4-47: HPLC traces of test CuAAC reaction. Reaction was performed in 10 mM MOPS, pH 7.2, 150 mM NaCl, 25% DMSO at rt and quenched after 2 h with 75 mM Na_2EDTA solution containing 25% MeCN prior to injection. Gradient: 40-50% B in A in 30 min. Dotted line indicates t_R of Fmoc-Lys(N_3)-OH.

Encouraged by this result, the reaction was performed with the peptides and the concentration of ligand was reduced further to 125 µM (Figure 4-48). In case of THPTA (Figure 4-48B) conversion was observed, although some substrate was still present. Unfortunately, the

peptides show no to very little conversion (Figure 4-48C to F) and it has to be concluded, that the copper ions are coordinated in a way that prevent them from being catalytically active, which is also known for organic ligands like bipyridine and solvents like MeCN.

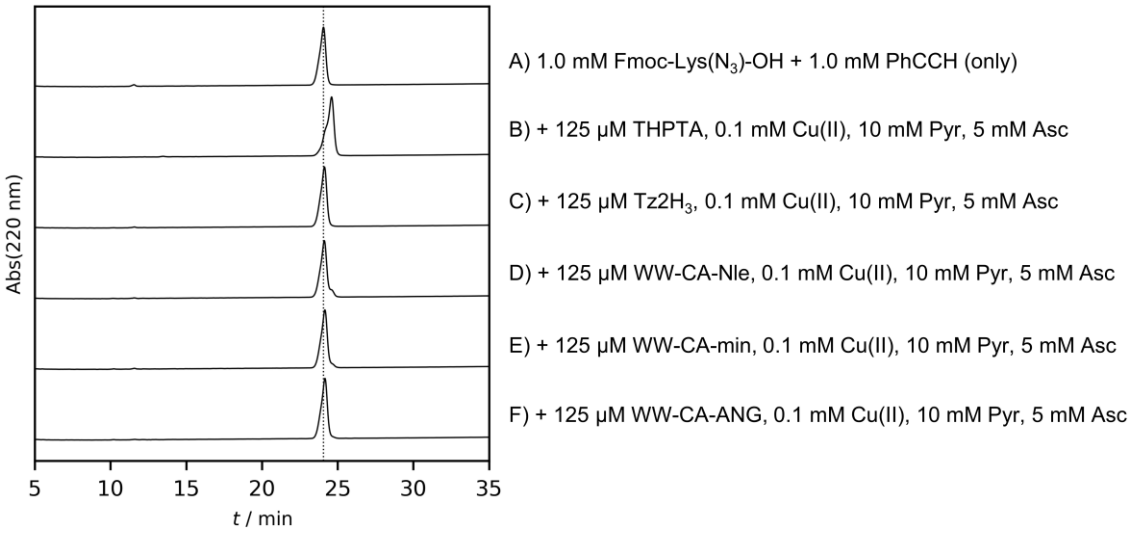

Figure 4-48: HPLC traces of test CuAAC reaction with peptides. Reaction was performed in 10 mM MOPS, pH 7.2, 150 mM NaCl, 25% DMSO at rt and quenched after reacting overnight with 75 mM Na_2EDTA solution containing 25% MeCN prior to injection. Gradient: 40-50% B in A in 30 min. Dotted line indicates t_R of Fmoc-Lys(N_3)-OH.

Although no peptide catalysis was observed, the finding that pyruvate is an efficient scavenger is still interesting and three other alkyne substrates containing electron donating (MeO- and Me_2N-) and withdrawing (F_3C-, O_2N- was unfortunately not soluble in water/DMSO) groups at the *para* position were tested. This time an aliquot was taken after 2 h to gain information about the rate of the reaction. As shown in Figure 4-49A, the reaction with phenylacetylene was not completed after 2 h, but overnight. Phenylacetylenes with electron donating groups react very quickly and almost complete conversion was achieved after 2 hours (Figure 4-49B and C). In the case of electron withdrawing substituents, the conversion was not completed overnight (Figure 4-49D).

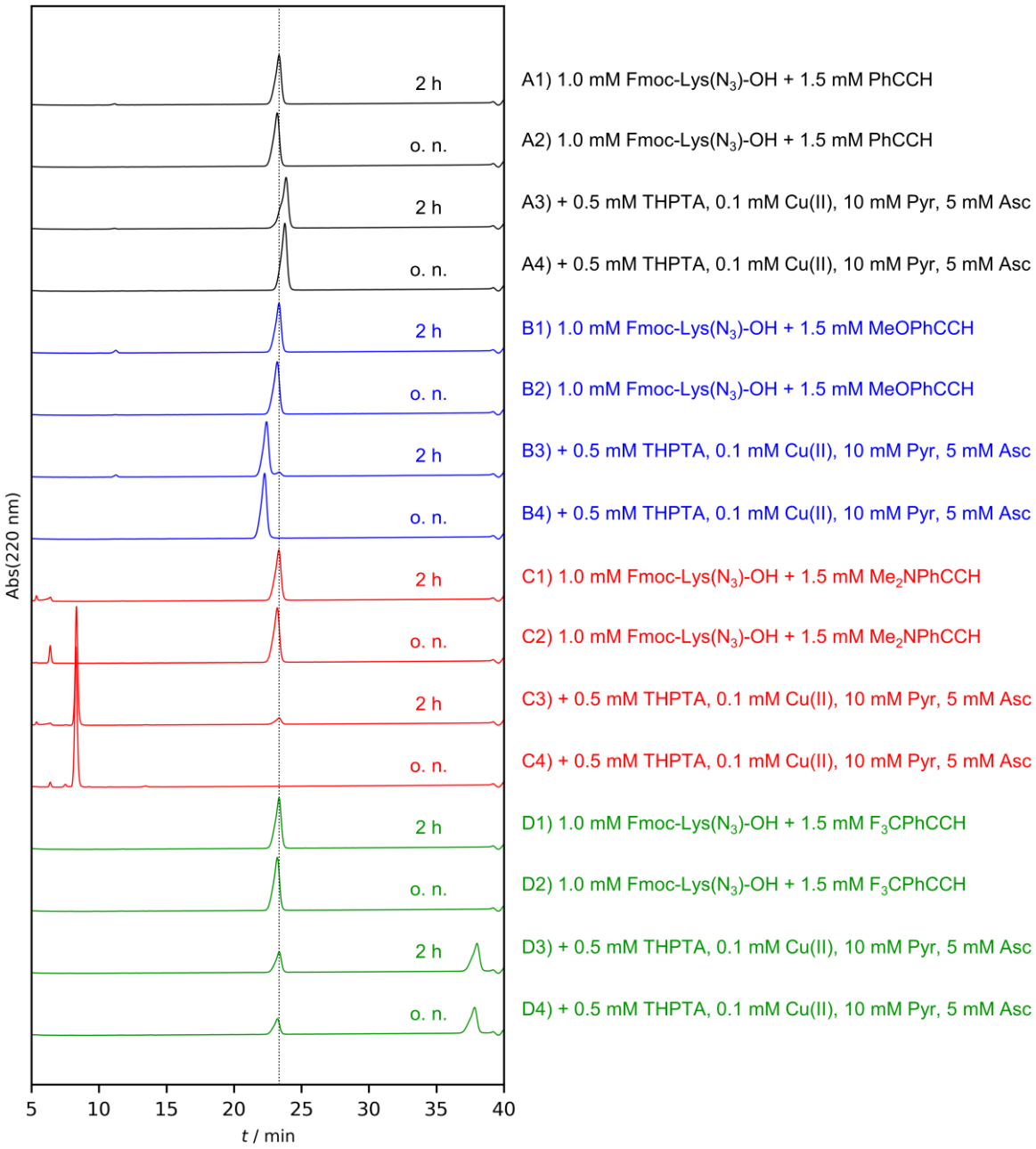

Figure 4-49: HPLC traces of CuAAC scope with peptides. Reaction was performed in 10 mM MOPS, pH 7.2, 150 mM NaCl, 25% DMSO at rt and quenched after reacting 2 h or overnight with 75 mM Na_2EDTA solution containing 25% MeCN prior to injection. Gradient: 40-50% B in A in 30 min. Dotted line indicates t_R of Fmoc-Lys(N_3)-OH.

Further it was tested, whether pyruvate was needed for fast reactions, thus the substrate MeOPhCCH was chosen, and the reaction was performed in presence and absence of pyruvate at different THPTA concentrations (Figure 4-50). In a time scale of 2 h the reaction rate was the same, whether pyruvate was present or not. Interestingly, decreasing the THPTA concentration increased the reaction rate. The use of 0.1 mM THPTA (Figure 4-50B and E) was sufficient for full conversion, but at 0.6 mM (Figure 4-50D and G) the reaction was not complete.

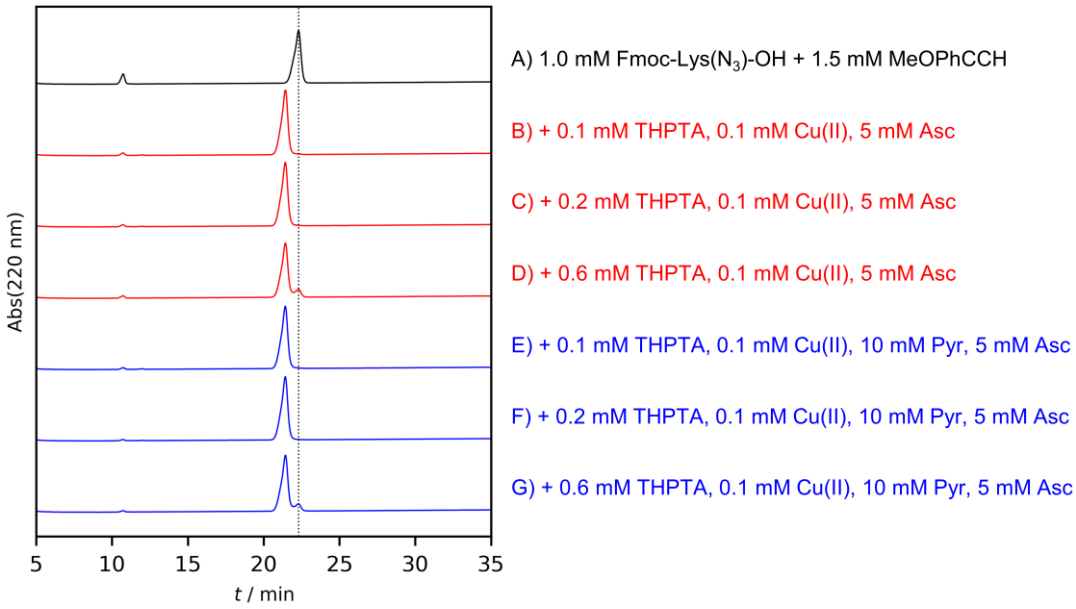

Figure 4-50: HPLC traces of CuAAC reaction dependent on THPTA concentration. Reaction was performed in 10 mM MOPS, pH 7.2, 150 mM NaCl, 25% DMSO at rt and quenched after 2 h with 75 mM Na_2EDTA solution containing 25% MeCN prior to injection. Gradient: 40-50% B in A in 30 min. Dotted line indicates t_R of Fmoc-Lys(N_3)-OH.

From these experiments it can be concluded that pyruvate is a valuable additive in CuAAC. Reactions that take several hours to complete may be incomplete in the absence of pyruvate because the THPTA ligand is oxidised by H_2O_2 before the reaction is completed. In this case, the addition of pyruvate is useful to increase the survival time of THPTA and ensure that the reaction can be completed. Increasing the concentration of THPTA is not an option as this will reduce the reaction rate. For fast reactions the addition of pyruvate is not necessary, but also not harmful. Pyruvate does not slow down the reaction, although the pyruvate concentration is 10 mM, which is 20 times higher than the THPTA concentration, and Cu(II) complexation of pyruvate could be expected. Pyruvate was able to protect peptides from oxidative degradation and is also known to protect cells from oxidative stress. Therefore, this mixture should be further tested for biomolecule labelling and cell surface functionalisation *via* CuAAC.

4.5 Design of sensors for bioactive molecules

4.5.1 Fluorescent labelled WW-CA as sensor for phosphate, pyrophosphate and glyphosate

Parts of Chapter 4.5.1 have been published in *Chemistry – A European Journal*.[372]

It is known from previous experiments that WW-CA changes conformation upon metal binding. The change in conformation is equivalent to a change in the distances between residues. Since WW-CA is weakly folded in the apo state and the folding is induced by metal ions, it can be assumed that the distances between the residues are farther apart in the apo state and come closer together in the folded holo state. Changes in distances can be observed by incorporating a FRET pair into the peptide (Figure 4-51A).[265] The FRET effect is distance dependent. Due to the more compact state of the holo peptide, FRET should be induced in the presence of metal ions if the FRET pair is placed in the correct positions. Therefore, W11 in BS1 was chosen as the FRET donor and as FRET acceptor, W34 was substituted with a homocysteine derivative containing a coumarin residue (Figure 4-51B). These two positions were chosen because the distance between Cα of W11 and W34 is 12 Å in the fully folded state according to NMR and X-ray data and in the hypothetical fully unfolded state, there would be over 20 amino acids between the two residues (Figure 4-51C). For FRET the distance and orientation between the chromophores are an important measure. The Förster radius of coumarin and Trp is about 20 Å,[373] therefore FRET should be clearly observed in the folded state.

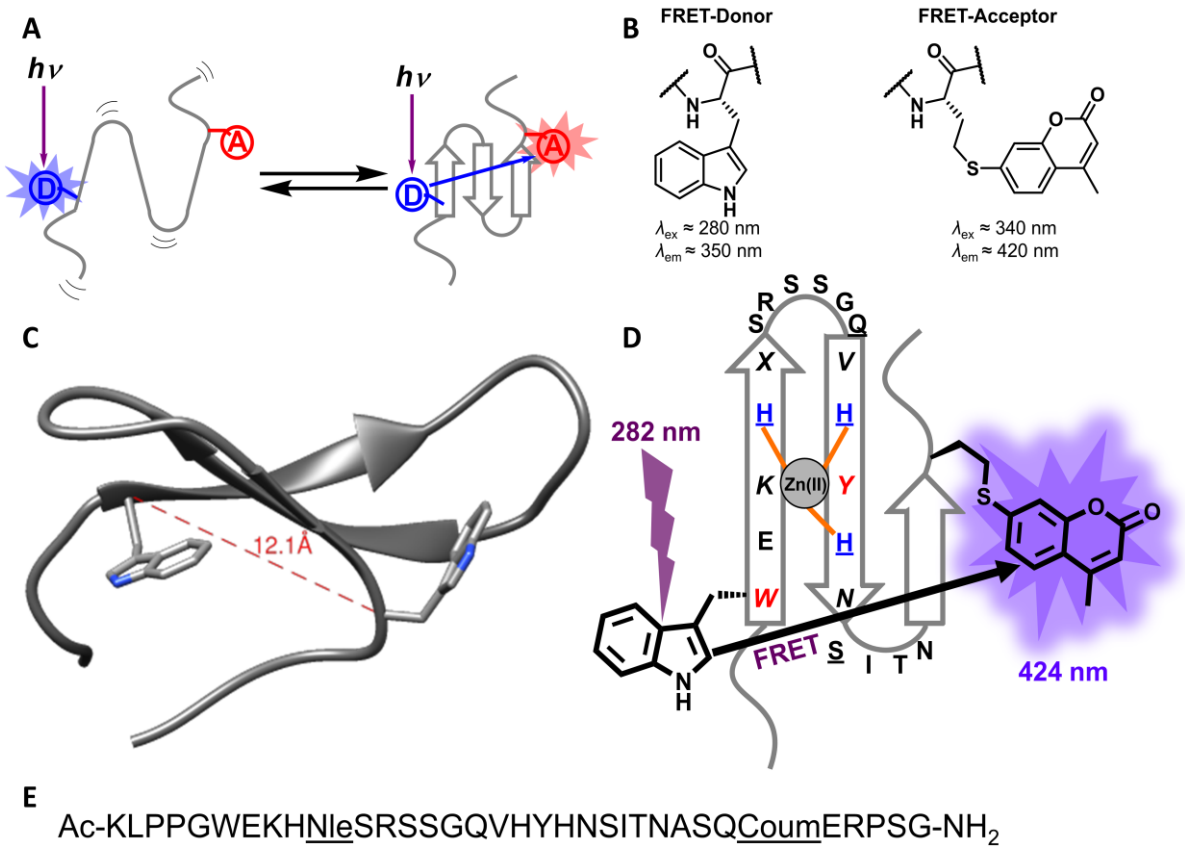

Figure 4-51: Design concept of FRET based metal ion sensor. A) Distance dependence of FRET in a fluorescently labelled switchable peptide. D: FRET Donor, A: FRET Acceptor. B) Chemical structure of tryptophan (donor) and coumarin labelled homocysteine (acceptor). C) X-ray crystal structure of hPin1$_{WW}$ (4GWT). Distance between the α-C atoms of the two Trp residues. D) Schematic representation of WW-CA(W34Coum), X: Nle. E) Sequence of WW-CA(W34Coum).

The synthesis of WW-CA(W34Coum) is shown in Scheme 4-8. First the Fmoc and Dmt protected homoserine (Hse) is synthesised. Treatment of the homoserine with Fmoc-OSu in dioxane/water and $NaHCO_3$ as base followed by recrystallisation from EtOAc gives Fmoc-Hse-OH in 76% yield. The side chain OH group is then protected with Dmt-Cl in pyridine. After purification by column chromatography on SiO_2 and DCM/MeOH with DIPEA as mobile phase, the DIPEA salt of Fmoc-Hse(Dmt)-OH was obtained as a colourless foam in 86% yield. The free acid would be highly unstable due to the acid sensitivity of the Dmt group.[374] Therefore, isolation as a DIPEA salt is mandatory.

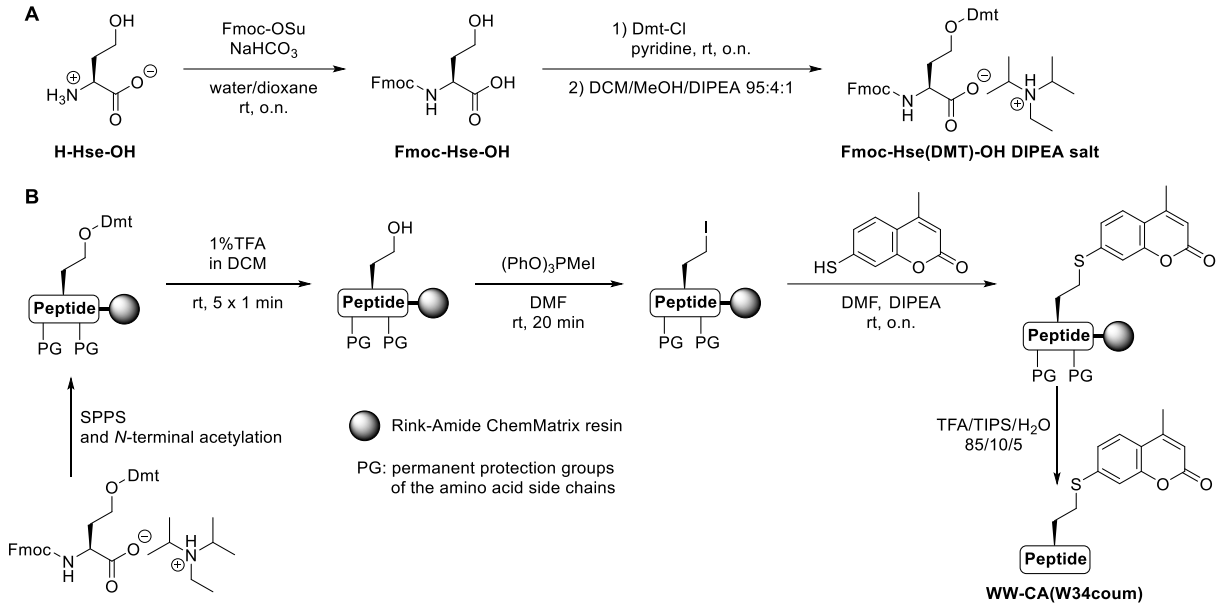

Scheme 4-8: Synthesis of A) Fmoc- and Dmt-protected homoserine building block, B) WW-CA(W34Coum).

The peptide was synthesised on Rink-Amide ChemMatrix resin using standard protected amino acids and the building block. Subsequently, the peptide was acetylated at the *N*-terminus. The Dmt group was then selectively deprotected with 1% TFA in DCM and the OH group was converted to an iodide with MTPI (methyltriphenoxyphosphonium iodide)[375] in DMF. Nucleophilic substitution with 7-mercapto-4-methylcoumarin gave the final peptide (Scheme 4-8B). As can be seen from the HPLC trace of the crude product (Figure 4-52A), the SPPS and nucleophilic substitution proceeded in high yield. After purification by semi-preparative HPLC the peptide was isolated in a yield of 28%. In addition to MALDI-MS (Appendix, Chapter 10.3), the successful introduction of the coumarin was shown by UV/Vis spectroscopy (Figure 4-52B). The maximum at 282 nm is the band of Trp and Tyr absorption. There is also a band with a maximum at 336 nm, which is caused by the absorption of the coumarin.[376] It was then determined whether the addition of Zn(II) affected the absorption spectrum. A slight decrease in coumarin absorption was observed, but in general both spectra were very similar.

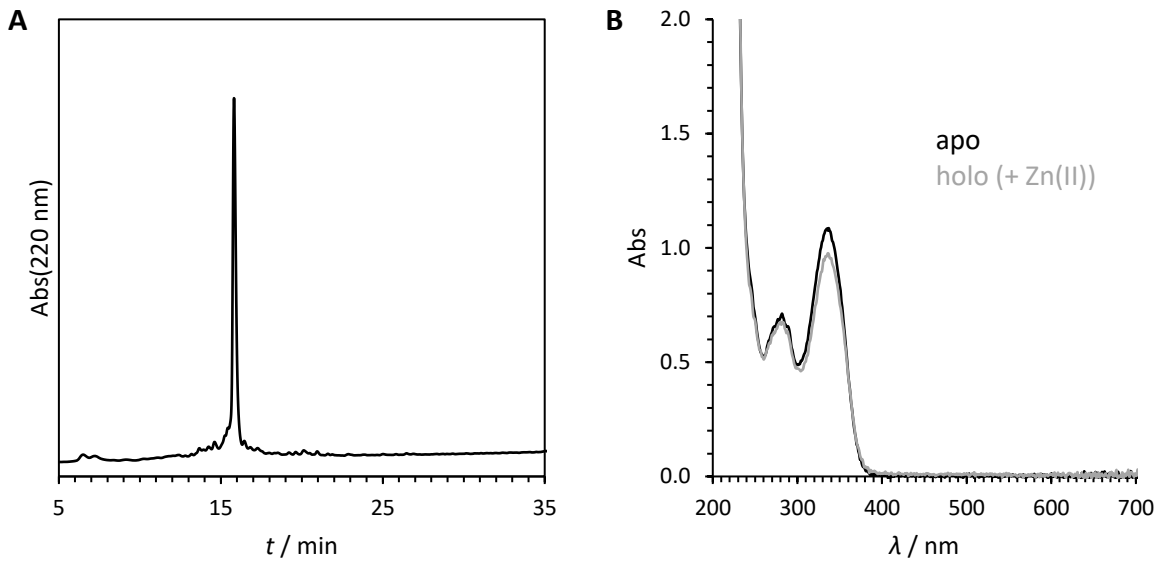

Figure 4-52: A) HPLC trace of crude WW-CA(W34Coum). Gradient: 20- 45% B in A in 30 min. B) UV/Vis spectra of holo and apo WW-CA(W34Coum). Conditions: 100 µM peptide, 100 µM $ZnSO_4$ (if present), 10 mM MOPS, pH 7.2, 150 mM NaCl, rt.

The ability of WW-CA(W34Coum) to adopt a WW domain-like structure was investigated by CD spectroscopy (Figure 4-53). In the apo state a weak exciton signal is present, but stronger than of apo WW-CA. The addition of Zn(II) led to an increase in the exciton signal. Thermal denaturation analysis was then performed. The apo state shows a weak sigmoidal curve with a T_m value of 10 °C, that was increased to 48 °C in the holo state giving clear sigmoidal thermal denaturation curve. This melting behaviour is comparable to that of WW-CA, suggesting that WW-CA(W34Coum) also binds Zn(II) under improved folding. Interestingly, the T_m value increased by more than 10 K compared to WW-CA. It should be mentioned that the N30Q mutation was accidentally not introduced compared to the original WW-CA. As discussed in the previous chapter, these additional mutations destabilise the structure. This was impressively demonstrated with the peptide WW-CA-min, which displays a T_m value of 20 °C in the apo state and a T_m value of 51 °C in the Zn(II) bound state. It contains only the His_3 site and the H27R mutation. Therefore, the increased stability of WW-CA(W34Coum) is not only due to the introduction of the coumarin but also to the lack of N30Q mutation.

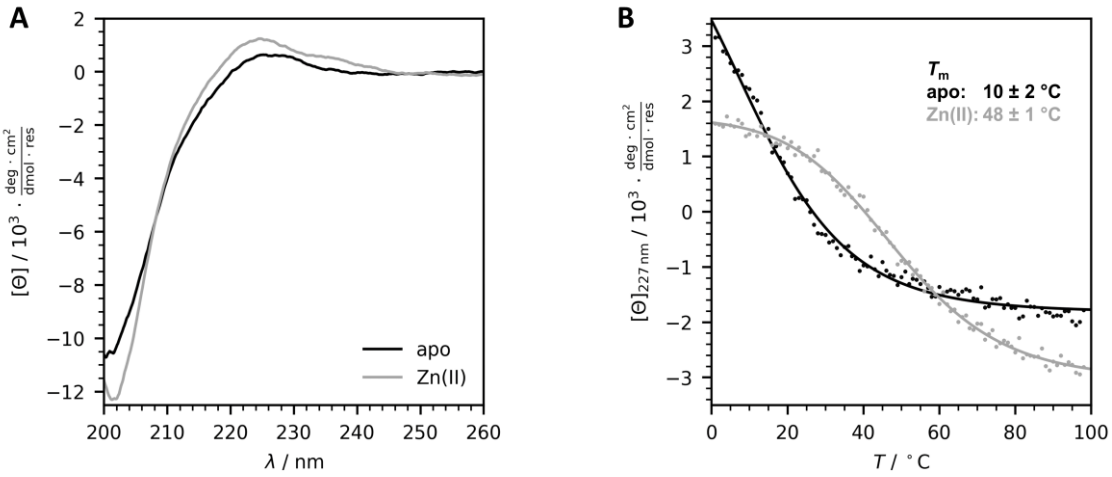

Figure 4-53: A) CD spectra and thermal denaturation profile of WW-CA(W34Coum) in the apo and Zn(II) bound state. Conditions: 50 µM peptide, 50 µM $ZnSO_4$ (if present), 10 mM MOPS, pH 7.2, 150 mM NaCl, 20 °C.

To investigate the FRET, fluorescence spectra were recorded in the absence and presence of Zn(II). Trp was excited at 282 nm. In the apo state, Trp fluorescence was observed at 347 nm and coumarin fluorescence at 424 nm. It is not surprising that the FRET is observed as the peptide is still partially folded as seen in the CD spectrum. An increase in the FRET was observed upon the addition of Zn(II): The Trp fluorescence decreased and the coumarin fluorescence doubled. These findings are very encouraging, showing that the basic idea was successful. Since the change in the FRET is a measure of a change in distance, in this case a shortening of the distance, it is a complementary proof of folding induction which was concluded from CD and NMR spectroscopy.

Various metal ions were then tested. Interestingly, the only other metal ion that caused significant changes in the fluorescence spectrum was Cu(II), which quenched the fluorescence of Trp and coumarin. All other metals, Mg(II), Ca(II), Mn(II), Co(II) and Ni(II), did not interact with WW-CA(W34Coum) in such a way that a change in fluorescence was observed. Therefore, WW-CA(W34Coum) can be considered as a Cu(II) and Zn(II) specific sensor.

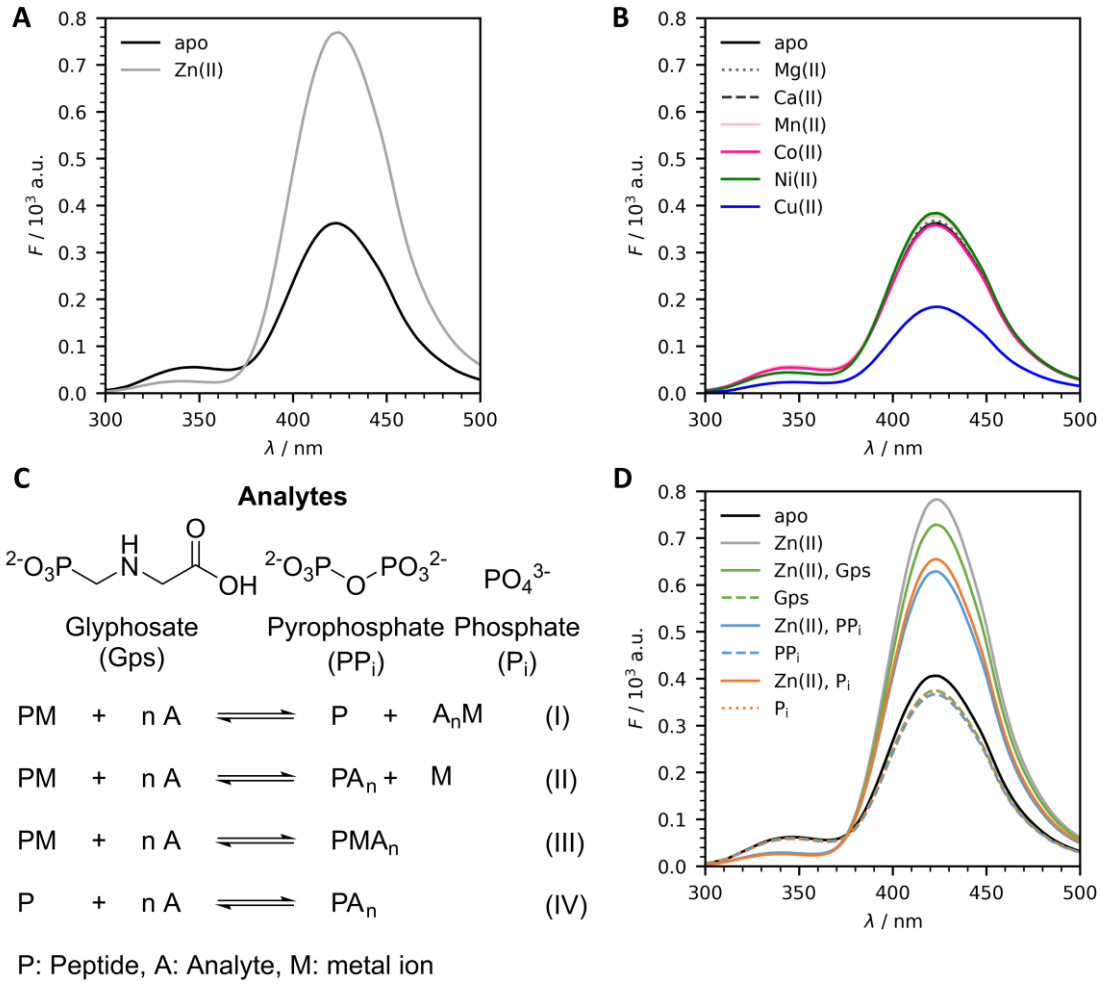

Figure 4-54: A) Fluorescence spectra of WW-CA(W34Coum) in absence and presence of Zn(II) and B) in presence of other divalent metal ions. C) Chemical structure of used analytes and possible complex formation between peptide, metal ions and analytes. D) Fluorescence spectra of WW-CA(W34Coum) in absence and presence of Zn(II) and analytes. Conditions: 10 µM peptide, 10 µM metal ion (if present), 10 µM analyte (if present), 10 mM MOPS, pH 7.2, 150 mM NaCl, rt, λ_{ex} = 282 nm.

Such systems can also be used as receptors for molecules that exhibit competitive binding of metal ions. This effect was exploited for a Cu(II)-binding polymer-wrapped carbon nanotube:[377] Addition of glyphosate (Gps), a widely used herbicide, to the Cu(II)-loaded carbon nanotube removed the Cu(II) from the material, which could be detected by a change in voltage. This principle has now been applied to the system presented here, using the WW-CA-(W34coum)-Zn(II) complex as the receptor. The analytes chosen were pyrophosphate (PP_i), phosphate (P_i) and glyphosate (Gps) (Figure 4-54C), which are all known to form complexes with Zn(II).[378-380] The fluorescence spectra are shown in Figure 4-54D. All analytes quench the fluorescence of the Zn(II) complex, with PP_i being the strongest quencher, followed by P_i and Gps. In addition to sequestering metal ions, the analytes could bind to the receptor and cause a change in fluorescence. Therefore, apo WW-CA(W34Coum) was also measured in the presence of analytes. A slight quenching was observed for all three analytes to a similar extent, indicating possibly non-specific binding to the peptide. The surface of WW-

CA(W34Coum) contains several polar residues that could potentially form hydrogen bonds with the charged substrate. In addition, there are two other possible reactions (Figure 4-54C). One possibility is a displacement type reaction where the analyte binds to the peptide and the metal ion is released. The other possibility is the formation of a complex containing peptide, metal ion and analyte. From the fluorescence experiments it is unclear which of the four possible mechanisms is responsible for the changes in the FRET. Further analysis, e.g. NMR, is required to identify the residues involved.

WW-CA(W34Coum) is a good Zn(II) and Cu(II) receptor due to its specific response, but the changes in FRET for the three analytes PP_i, P_i and Gps are too similar to allow differentiation. Instead of using a single receptor, arrays of non-specific receptors can discriminate even complex mixtures, a concept called differential sensing.

4.5.2 Differential sensing

Several natural proteins use a lock-and-key strategy to bind specifically to a molecule,[381] with antibodies being the prime example.[382] In contrast, the senses of smell and taste relay on unspecific receptors that bind to a range of analytes. Each analyte produces a unique response pattern as each receptor binds it with varying affinities.[383-385]

In analytical chemistry, the conventional approach is to create specific receptors or employ characteristic chemical reactions for the analyte that produce easily detectable products.[386-387] Figure 4-55A illustrates the function of a specific receptor. A receptor that is perfectly specific can only bind to one analyte. When the analyte is present, a binding event occurs and the response, such as fluorescence or a change in absorbance, can be detected. If the receptor is exposed to other analytes, no response can be detected. Therefore, a perfectly specific receptor can be used to detect the analyte of interest in a complex mixture. Beyond this simple "yes-no" answer (qualitative analysis), collecting response intensities at different analyte concentrations with a fixed receptor concentration provides calibration curves that can be used to quantify the analyte.[388] The disadvantage of this high specificity is the need to design a receptor for each analyte.

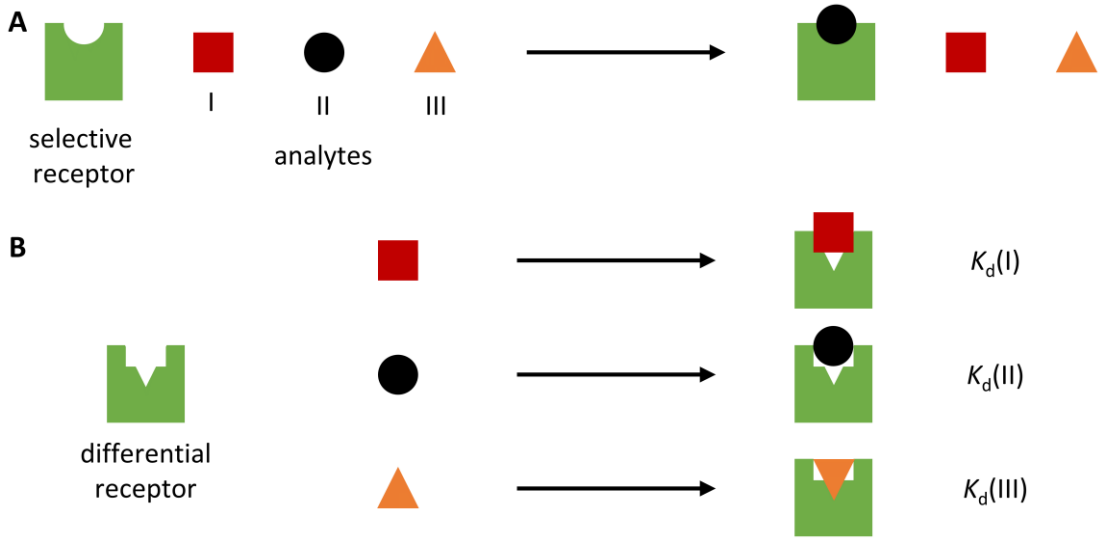

Figure 4-55: Schematic representation of the principle of a) a classical receptor and b) a differential receptor.

Differential sensing, an attempt to mimic the sense of smell and taste, utilises a cross-reactive receptor array in which each receptor can bind multiple analytes (see Figure 4-55B).[389-391] As a result, each analyte binds to each receptor, and a response is always detected. At first glance, this permanent 'yes' response may seem less useful for detection. However, in the optimal case, each receptor has a different affinity for each analyte, resulting in varying response intensities. An analyte is added to each receptor and the response intensity is recorded. The response values are then corrected and normalized (Figure 4-56A). The matrix

can be displayed as a bar graph or heatmap (Figure 4-56C and D), with the height of the bars or greyscale of the heatmap indicating the response intensity.[392] Each analyte produces a unique response intensity for each receptor, resulting in distinct bar plots or heat maps. This is commonly referred to as the analyte's characteristic pattern. Due to natural measurement errors, there may be some variation in this pattern when measurements are repeated (see Figure 4-56E).

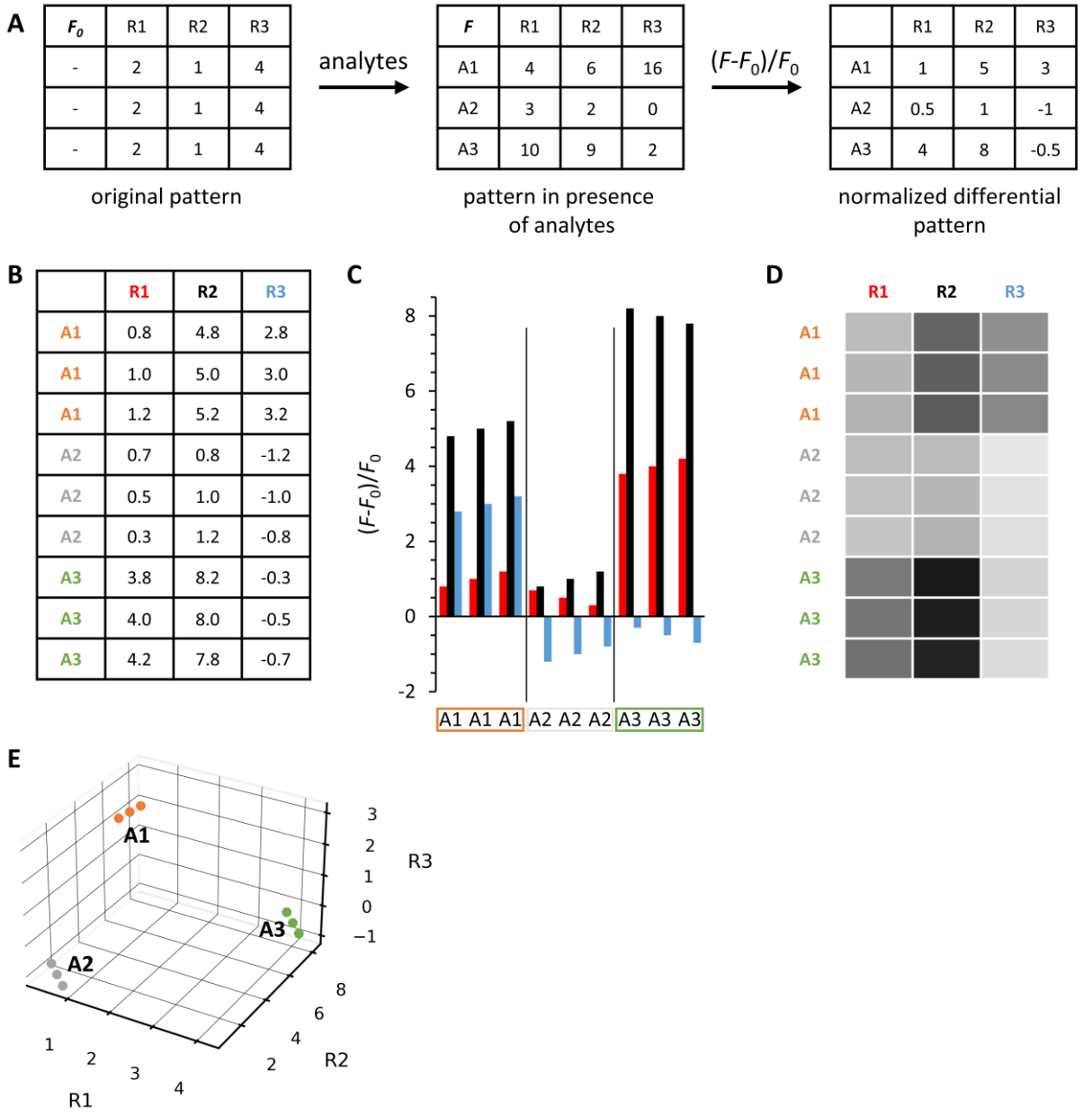

Figure 4-56: Processing and presentation of hypothetical differential sensing data. A) An array based fluorescent sensor consist of three receptors (R1, R2, R3) is confronted with three analytes (A1, A2, A3). After correction and normalization, the data matrix is generated. B) Hypothetical data matrix containing triplicates per analyte with an error set to ±0.2. C) Graphical presentation of the data matrix as bar graph and D) heat map. E) 3D representation of the data matrix. Each analyte is a point in a 3D coordinate system with the receptors as the three axes.

One approach is to view each receptor as an axis that spans an *j*-dimensional space, where *j* represents the number of receptors. In this *j*-D space, each analyte is represented as a point, with its coordinates being the elements of the matrix. The first element corresponds to the coordinate for the first axis, and so on. Since each analyte has distinct coordinates, they occupy different positions in the coordinate system. In a perfect measurement without errors, each measurement will yield the same coordinates. However, due to measurement errors, there is a certain degree of variation in each coordinate. Therefore, the points of the same analyte in repetitive measurements should still be close to each other, an effect called "clustering" (see Figure 4-56G).[392]

In practice, a receptor array can only differentiate a limited number of analytes. There will always be analytes that produce a response pattern that is too similar, making them indistinguishable by the receptor array. Therefore, the first step is to expose the receptor array to a set of analytes and determine which ones can be differentiated. The criteria often include observing clustering and ensuring that the clusters of different analytes are well separated from each other. When an unknown analyte x is measured, its pattern can be compared to the saved patterns to determine its similarity to known analytes. The response pattern of analyte x can be plotted on a coordinate system to identify which cluster it belongs to. It is important to note that if the receptor array is presented with an analyte x not included in the set of analytes, it can only determine that x is different from all others, but it cannot identify analyte x.[390]

For 1D, 2D or 3D plots, visualisation is easy. However, for 4D and higher, this becomes impossible and requires using dimension reducing techniques. The most commonly applied method is principal component analysis (PCA),[393-394] which aims to plot the data in two (or three) dimensions while retaining as much information as possible. Initially, there is a coordinate system with *j* axes, each representing a receptor. After PCA, a new coordinate system with also *j* axes is obtained. The principal components (PC) are the new axes. The mean coordinates of all points serve as the origin of the new coordinate system. PCA can be treated as an Eigenvalue problem. The data matrix *D* is generated where the rows represent the analytes *i* and the columns represent the receptors *j* (example in Figure 4-56B). The matrix element D_{ij} is the measured and corrected response intensity of an analyte *i* with a receptor *j*. Next, matrix *D* is centred to give matrix *C*. The entries of the covariance matrix *V* are calculated using *C*, according to Equation (4). *V* is a *j* x *j* matrix correlating the response of the receptors to each other.

$$\mathrm{cov}(x,y) = \frac{1}{N-1}\sum_{j=1}^{N}\left(x_j - \bar{x_j}\right)\cdot\left(y_j - \bar{y_j}\right) \qquad (4)$$

The Eigenvalue problem is then solved for *V* (Equation (5)), resulting in Eigenvectors that represent the PCs and corresponding Eigenvalues *λ* that represent the variance of each PC.

$$V \cdot \mathrm{PC} = \lambda \cdot \mathrm{PC} \quad (5)$$

The PCs are sorted in descending order of Eigenvalue in the scree plot, with PC1 having the highest Eigenvalue and PC2 having the second highest. All PCs contain all variations of the data, which can be seen as the complete information of the dataset. Each PC represents a fraction of the variance (Eigenvalue of PC/Sum of all Eigenvalues). The cumulative variance is also given, indicating the amount of variance retained depending on the number of PCs used. The objective is to retain as much information as possible in a 2D representation. Therefore, a successful PCA would result in a PC1 and PC2 that capture the majority of the variance. Each Eigenvector (PC) has the same number of entries as receptors. Each entry at position *j* describes the contribution of receptor *j* to this PC. The contribution can be presented in the Loading Plot where the receptors' contributions are shown as vectors with the coordinates PC1 and PC2. The correlation between the receptors can also be analysed. There are three extreme cases to consider: if both vectors show in the same direction, both receptors act equivalently (and are somewhat redundant). In the case of orthogonality, both receptors are independent of each other. If both vectors show in opposite directions, the receptors behave oppositely to each other.[392, 395]

Finally, the data points are transformed into the new coordinate system by taking the dot product of the centred data matrix *C* with a matrix containing the Eigenvectors. To plot the data in the 2D plane, we use the coordinates of PC1 and PC2. This plot is crucial for differential sensing. As previously described, data points from the same analyte in different measurements should ideally cluster together, while clusters from different analytes should be separated. It is important to note that PCA does not alter the data, but rather provides a different representation. If there is insufficient separation observed in the 2D plot, a 3D score plot containing PC1, PC2, and PC3 may help to address this issue.[391]

The prerequisite for differential sensing is a cross-reactive receptor array with an easy-to-detect response. The peptides WW-CA-Nle, WW-CA-min, WW-CA-ANG, and Tz2H$_3$ bind to Zn(II), Ni(II), and Cu(II) with changes in tryptophan fluorescence. In the case of Cu(II) and Ni(II), the Trp fluorescence of the peptides was quenched, as previously shown. By adding an analyte that sequesters Cu(II) or Ni(II), the Trp fluorescence should increase, making these 'turn-on' receptors. The fluorescence of the peptides was enhanced in the presence of Zn(II). Therefore, receptors that sequester Zn(II) would decrease the Trp fluorescence, making them 'turn-off' receptors. The peptides have a broad range of affinities to the metals, with K_d values ranging from sub-nanomolar to lower micromolar. It is also expected that different analytes will have varying affinities to the three metal ions, resulting in a characteristic pattern of fluorescence change. In addition, the combinatorial approach of mixing peptides with metal ions enables the easy preparation of a large number of receptors in a short amount of time.

As analytes, the following bioactive molecules known to form complexes with Ni(II), Cu(II) and Zn(II) were selected as a test system: glyphosate (Gps) pyrophosphate (PP_i), phosphate (P_i), adenosine monophosphate (AMP), cyclic adenosine monophosphate (cAMP), glutamate (Glu) and phytate (Phy).[378, 396-397] The chemical structures are depicted in Scheme 4-9.

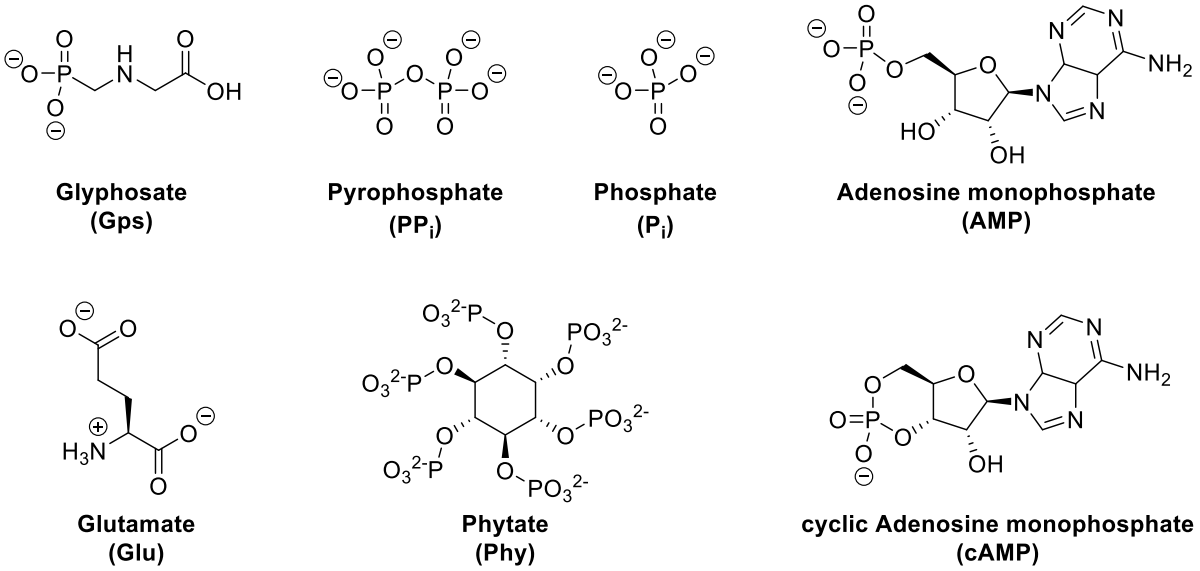

Scheme 4-9: Chemical structures of the analytes used in differential sensing.

Experiments were performed in 96-well plates. As there are a total of 12 receptors (4 peptides times 3 metal ions), each column (1 to 12) contains one complex as shown in Table 4-2 and each row (A to H) contains one analyte. The experiment was repeated four times. The plate with the highest error was excluded.

Table 4-2: Overview of the filling of the 96-well plate for differential sensing.

		$Tz2H_3$			WW-CA-Nle			WW-CA-ANG			WW-CA-min		
		1	2	3	4	5	6	7	8	9	10	11	12
Blank	A	Cu(II)	Ni(II)	Zn(II)	Cu(II)	Ni(II)	Zn(II)	Cu(II)	Ni(II)	Zn(II)	Cu(II)	Ni(II)	Zn(II)
Gps	B	Cu(II)	Ni(II)	Zn(II)	Cu(II)	Ni(II)	Zn(II)	Cu(II)	Ni(II)	Zn(II)	Cu(II)	Ni(II)	Zn(II)
PP_i	C	Cu(II)	Ni(II)	Zn(II)	Cu(II)	Ni(II)	Zn(II)	Cu(II)	Ni(II)	Zn(II)	Cu(II)	Ni(II)	Zn(II)
P_i	D	Cu(II)	Ni(II)	Zn(II)	Cu(II)	Ni(II)	Zn(II)	Cu(II)	Ni(II)	Zn(II)	Cu(II)	Ni(II)	Zn(II)
AMP	E	Cu(II)	Ni(II)	Zn(II)	Cu(II)	Ni(II)	Zn(II)	Cu(II)	Ni(II)	Zn(II)	Cu(II)	Ni(II)	Zn(II)
cAMP	F	Cu(II)	Ni(II)	Zn(II)	Cu(II)	Ni(II)	Zn(II)	Cu(II)	Ni(II)	Zn(II)	Cu(II)	Ni(II)	Zn(II)
Glu	G	Cu(II)	Ni(II)	Zn(II)	Cu(II)	Ni(II)	Zn(II)	Cu(II)	Ni(II)	Zn(II)	Cu(II)	Ni(II)	Zn(II)
Phy	H	Cu(II)	Ni(II)	Zn(II)	Cu(II)	Ni(II)	Zn(II)	Cu(II)	Ni(II)	Zn(II)	Cu(II)	Ni(II)	Zn(II)

The Trp was excited at 295 nm and the intensity *F* was recorded at 345 nm, corrected and normalized The results are presented in Figure 4-57A as a heatmap. Values > 0 indicate fluorescence enhancement, values < 0 fluorescence quenching and values = 0 no change in

fluorescence. Upon visual analysis of the heatmap, it is evident that the receptors containing Cu(II) produce the strongest responses. Additionally, Gps exhibits the most distinct pattern among the analytes, followed by pyrophosphate. However, the patterns of the remaining analytes are not easily distinguishable. As anticipated, the addition of Gps and PP_i to Cu(II)-containing peptides led to an increase in fluorescence intensity due to the sequestration of Cu(II) by the analytes. For peptides containing Ni(II) and Zn(II), the changes observed were minimal, suggesting that the analyte was unable to effectively compete with the peptides in binding to the metal ions.

PCA was then performed to project the data onto a two-dimensional plane. The scree plot (Figure 4-57B) shows that most of the information is retained in the first two principal components (PCs), which account for 80% of the variance, with PC1 dominating.

The loading plot (Figure 4-57C) shows the contributions of the receptors to PC1 and PC2. All receptors contribute significantly to PC1 and PC2, except for WW-CA-min+Zn(II), which only contributes to PC1. By comparing the angle between the vectors, one can determine the similarity of the receptors. Three groups of similar receptors can be observed: 1) WW-CA-min+Cu(II) and WW-CA-ANG+Cu(II) 2) WW-CA-Nle+Zn(II), WW-CA-Nle+Cu(II), $Tz2H_3$+Cu(II) and WW-CA-min+Ni(II), 3) WW-CA-Nle+Ni(II), $Tz2H_3$+Zn(II), $Tz2H_3$+Ni(II) and WW-CA-ANG+Ni(II). WW-CA-ANG+Zn(II) and WW-CA-min+Zn(II) are not similar to other receptors. Interestingly, the groups are very heterogeneous. Neither similar peptides, nor metal ions dominate a group.

The score plot (Figure 4-57D) demonstrates the receptor array's ability to distinguish between analytes. Only the data points for Gps and PP_i are sufficiently separated from the other analytes, although clustering is not optimal for the repeats. It is not possible to distinguish between all other analytes as there is no clustering observed. Upon comparing the directions of the vectors in the loading plot with the position of the analytes in the score plot, it is evident that all receptors point more towards Gps and PP_i. This observation is not surprising, as these two analytes are most effectively discriminated.

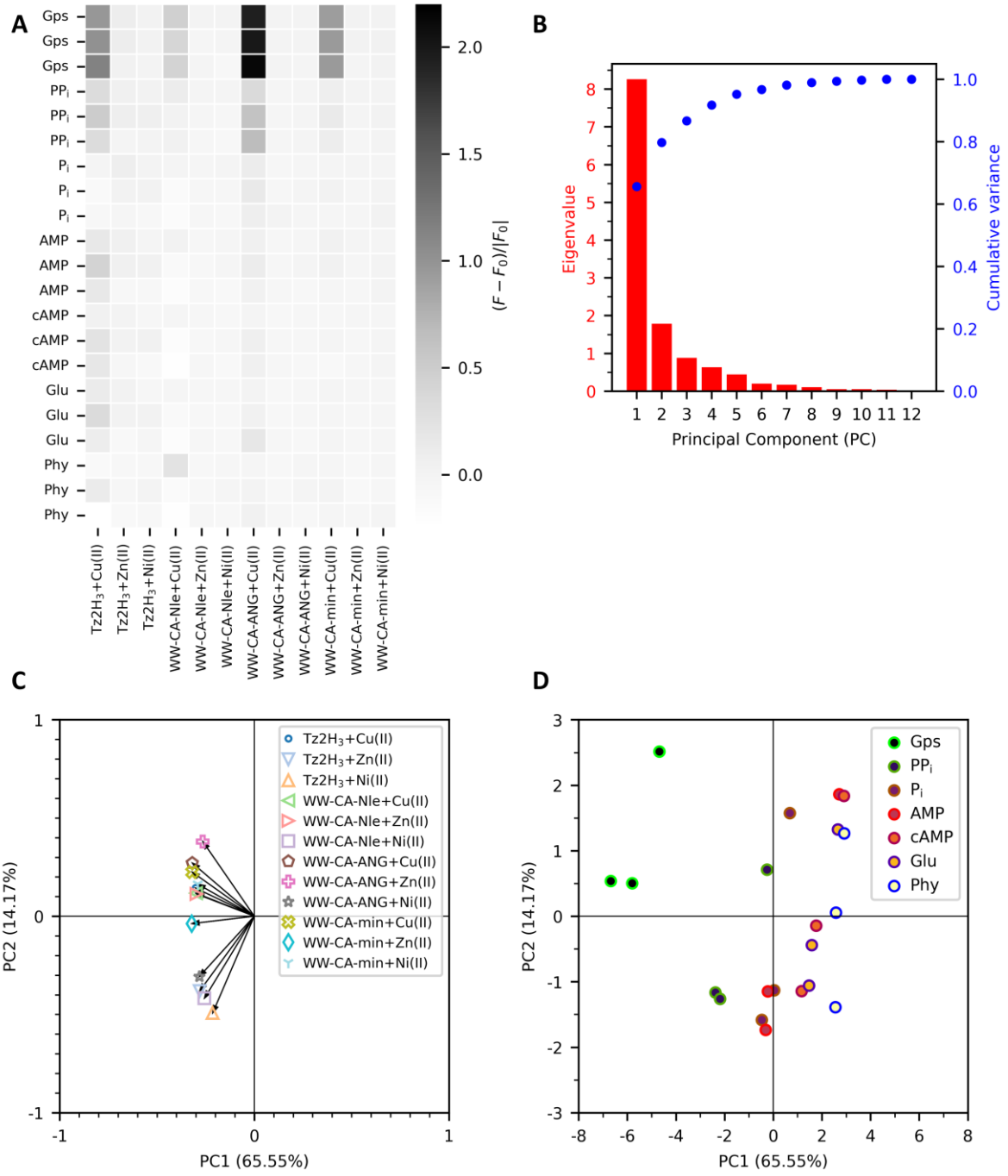

Figure 4-57: Results of differential sensing experiment. A) Heat map of normalized fluorescence response for each receptor-analyte mixture. Measurements were performed in triplicates. B) Scree plot, C) Loading plot and D) Score plot of principal component analysis. Conditions: 4 µM peptide, 4 µM metal ion, 4 µM analyte, 10 mM MOPS, pH 7.2, 150 mM NaCl, 20 °C – 25 °C, λ_{ex} = 295 nm, λ_{em} = 345 nm, experiments were performed in 96-well plates as triplicates.

As the Cu(II) containing receptors exhibited the strongest response, PCA was repeated solely with these receptors. From the heatmap of the Cu(II) containing receptors (Figure 4-58A), the characteristic pattern of Gps and PP_i is easily detected by eye. The scree plot (Figure 4-58B) shows that almost all information (91%) is preserved in PC1. The loading plot (Figure 4-58C) once again demonstrates a high similarity between WW-CA-min+Cu(II) and WW-CA-ANG+Cu(II), while $Tz2H_3$+Cu(II) and WW-CA-Nle+Cu(II), which were previously very similar,

are now independent. In Figure 4-58D, the score plot shows that the GPS data points are clustered together and are well separated from those of the other analytes, which are clustered around the origin, making differentiation impossible. The data points for PP_i are also separated enough from the other data to differentiate it, although the distance is not very high. A comparison of the loading and score plot again shows a correlation between the direction of the vectors and the position of GPS and PP_i.

In conclusion, the receptor array used here can discriminate Gps and partially PP_i from the set of analytes. The other analytes could not be distinguished from each other. One observation is the small change in fluorescence intensity for the other analytes. It should be noted that the analyte concentration (4 µM) is equivalent to the receptor concentration (equivalent peptide and metal ions), which is very low compared to other systems reported in the literature, where analyte concentrations in the mM range are common.[398-400] Plate reader assays always suffer from high noise, therefore small changes in signal intensity may not be accurately detected. For an initial test, triplicates are sufficient, but it was shown, that for better results, more replicates should be measured. After more reliable data is collected, further data analysis methods beyond PCA should be considered. Very prominent examples are linear discriminant analysis (LDA) and hierarchical clustering analysis (HCA).[392, 395]

The loading plot suggests that there may be some redundancy among certain receptors. Therefore, future experiments should concentrate on selecting the most reliable receptors to form the final receptor array.

Nevertheless, this initial experiment demonstrates that the receptor array has potential for differential sensing. To broaden the scope of this array, further optimization and testing with additional substrates is necessary.

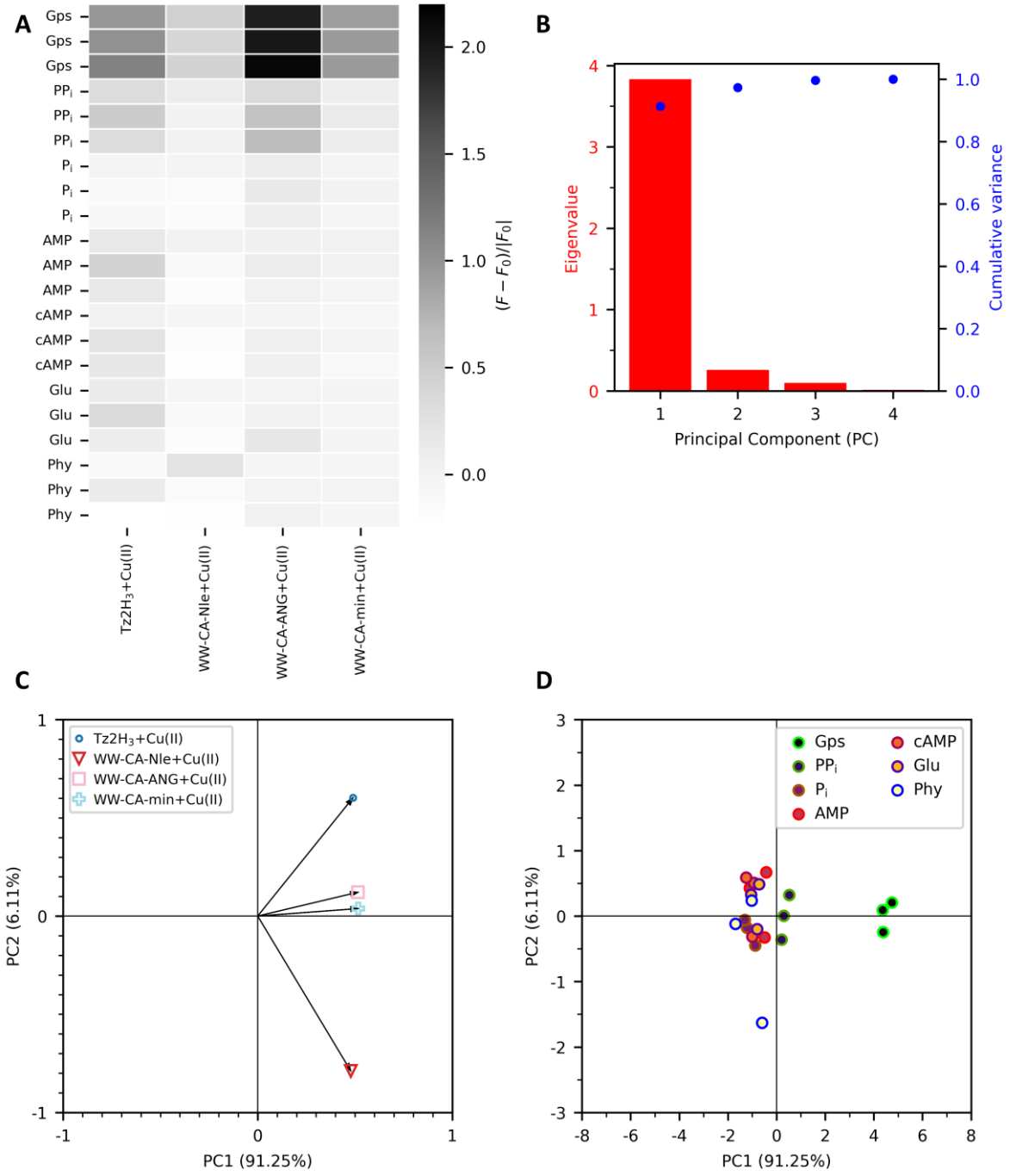

Figure 4-58: Re-analysis of differential sensing experiment. Reduced set of receptors (only Cu(II) containing ones) were used. A) Heat map of normalized fluorescence response for receptor-analyte mixture. B) Scree plot, C) Loading plot and D) Score plot of principal component analysis. Conditions: see Figure 4-57.

4.6 Aspartimide formation

The major part of Chapter 4.6 has been published in *RSC Chemical Biology*.[401]

4.6.1 Mechanism of aspartimide formation and prevention strategies

It is clear from this report that some amino acids can cause problems. One of these is methionine, which can oxidise to Met(O), which could lead to an altered peptide structure, and was therefore replaced by norleucine in our studies to avoid this problem. Another amino acid that could cause problems during chemical synthesis is aspartate (Asp). Asp acts as ligand in metal binding sites,[402-403] is crucial for the activity of proteases[404-405] and, when placed in loop positions, is known to increase peptide thermostability, particularly in β-sheet peptides.[111, 406] Unfortunately, during SPPS, Asp residues are prone to aspartimide formation (mechanism in Scheme 4-10A).[74] The coupling of the side-chain protected Asp is not problematic, but during Fmoc deprotection with piperidine in DMF, the backbone amide can be deprotonated and attack the carbonyl carbon of the protected Asp side chain. The formed aspartimide is highly prone to epimerization and can be attacked by nucleophiles, often piperidine, at two positions, leading to in total four different piperidine adducts. The degree of aspartimide formation is highly dependent on the sequence. In certain circumstances, aspartimide may be formed at higher levels than the desired peptide. This would be the case for Asp-Gly sequences, while Asp-Val or Asp-Leu are less sensitive and Asp-Pro is insensitive to this side reaction.[302]

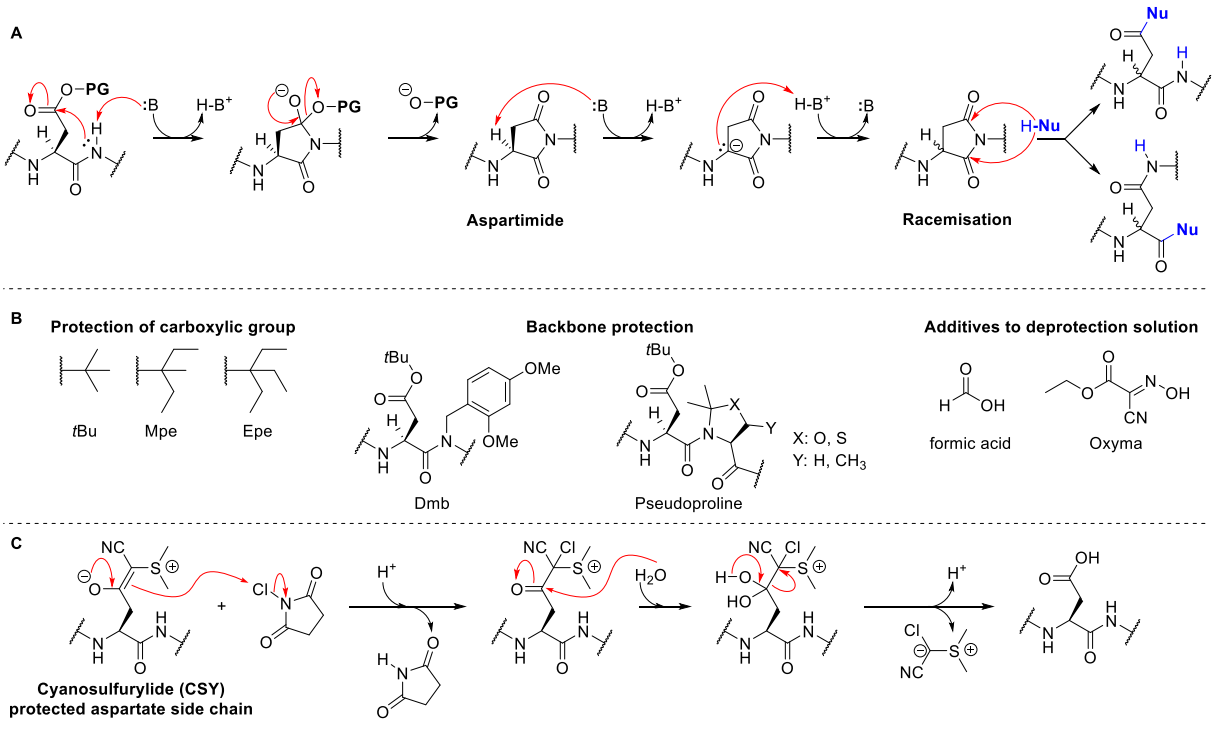

Scheme 4-10: A) Mechanism of aspartimide formation. B) Strategies to prevent aspartimide formation. C) Mechanism of the oxidative deprotection of the CSY protecting group under mild acidic conditions.

Several strategies have been developed to reduce aspartimide formation (Scheme 4-10B). The first important strategy includes optimization of the protection group for the Asp carboxylic side chain. For instance, bulky protecting groups in part suppress this undesired side reaction.[407] It was observed that the commonly used *t*Bu group is better in this regard than sterically less hindered groups like benzyl. Increasing the steric bulk by using methylpentyl (Mpe) or ethylpentyl (Epe) groups further reduces aspartimide formation, but with the drawback of lower coupling efficiency.[408] Beside the side chain, the amide backbone can also be protected using benzylic groups or pseudoprolines which fully suppresses aspartimide formation during SPPS.[409-410] Because in both cases low coupling efficiency is problematic, dipeptide fragments (Fmoc-Asp(O*t*Bu)-Xxx-OH) are employed in SPPS.[411] The backbone protecting groups are removed during the final acidic cleavage and deprotection with concentrated TFA, which is convenient on the one hand, but promotes aspartimide formation on the other, albeit less than the basic conditions e.g. during Fmoc removal.[74] It has been demonstrated, that the use of bases with a lower pK_a than piperidine, e.g. piperazine, can reduce the amount of aspartimide formation.[412] More efficient is the addition of acids to the deprotection mixture, with formic acid and Oxyma showing the best results.[413-414] However, the discussed methods reduce, but not fully prevent aspartimide formation. The latter was reported to be possible with the cyanosulfur ylide (CSY) protecting group, which was developed by Neumann *et al*. (Scheme 4-10C).[415] The carboxylic group is protected by a carbon-carbon double bond instead of an easier to cleave ester bond and was shown to be stable under strong basic and acidic conditions. As a positive side effect, CSY decreases the aggregation tendency of the protected peptides on the resin due to its zwitterionic nature, and thus improves the yield of SPPS especially for difficult sequences. After SPPS and cleavage, the CSY group is removed by *N*-chlorosuccinimide in mild acidic aqueous buffer (pH 4.5) containing acetonitrile.

Table 4-3: Overview of Asp containing peptides. X = Nle.

Peptide	Description	Sequence
WW-ADG	hPin1 WW domain (6-39), Met15Nle, Arg17_Ser19delinAlaAsp	H-KLPPGWEKRXS-ADGRVYYFNHITNASQWERPSG-OH
WW-PQBP1	PQBP1 WW domain (47-80), Cys60Ser	Ac-GLPPSWYKVFDPSSGLPYYWNADTDLVSWLSPHD-NH_2
SH3-NC	*N*-terminal *c*-Crk SH3 domain (134-190), Met181Nle	Ac-AEYVRALFDFNGNDEEDLPFKKGDILRIRDKPEEQWWNAEDSEGKRG XIPVPYVEKY-NH_2
TP	Test peptide	Ac-FDGLA-NH_2

Inspired by these results, a literature-known thermostable mutant of the hPin1 WW domain[111] (WW-ADG) was synthesised to test the potential of the CSY protecting group in the suppression of aspartimide formation (sequence in Table 4-3). Additionally, the WW domain of PQBP1 (WW-PQBP1) was synthesized, which plays a role in neuronal signal transduction, and WW-PQBP1 mutants can cause the Golabi-Ito-Hall syndrome.[416] WW-PQBP1 contains

four aspartates and, similar to WW-ADG, chemical synthesis of this peptide has not been reported before, only expression.[111, 416] Another challenging β-sheet peptide is the *N*-terminal *c*-Crk SH3 domain (SH3-NC), a part of a proto-oncogenic protein, which contains 57 amino acids from which 6 are aspartates.[417] Similar to WW domains, SH3 domains are protein interaction modules and bind to polyproline sequences. SH3-NC was synthesized using native chemical ligation of two fragments obtained by SPPS.[418] Due to the de-aggregating effect of the CSY group, a full-length linear synthesis of SH3-NC by SPPS was anticipated.

4.6.2 Synthesis of Fmoc-Asp(CSY)-OH

First, the synthesis of the building block Fmoc-Asp(CSY)-OH was optimised (Scheme 4-11). In principle, the synthesis includes the formation of the C-H acid salt (cyanomethyl) dimethylsulfonium bromide by reaction of bromoacenonitrile and dimethylsulfide, which is reacted with the activated side chain carboxylic acid of Fmoc-Asp-O*t*Bu. In the final step, the *tert*-butyl group is removed under mild acidic conditions using formic acid. In contrast to Neumann *et al*.[415] the reagent for the activation of the carboxylic acid was changed to the cheaper HBTU. The reaction was carried out on a multi-gram scale and synthesis costs were reduced from 17.69 €/g to 9.73 €/g (detailed calculation of cost see Appendix, Chapter 10.4).

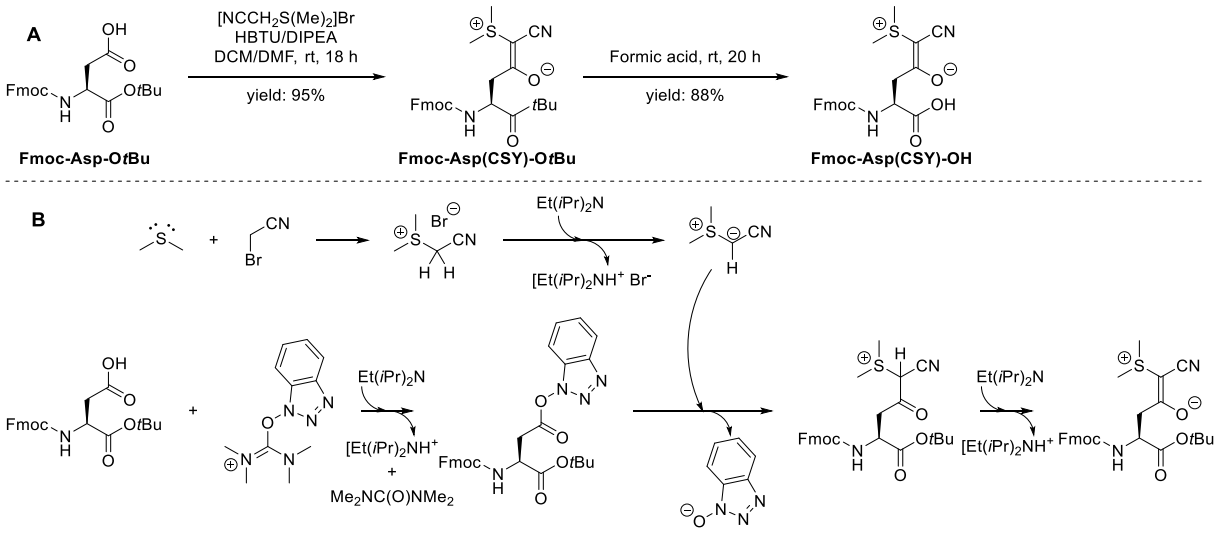

Scheme 4-11: Synthesis of Fmoc-Asp(CSY)-OH. A) Overview of the synthesis. B) Reaction mechanism.

4.6.3 Microwave assisted synthesis of CSY-protected peptides

With the building block in hand, WW-ADG(CSY) was synthesised using microwave-assisted SPPS and a standard synthesis protocol, starting with a Fmoc deprotection step using 20% piperidine in DMF and microwave heating at 90 °C, followed by a DMF wash and coupling step using Fmoc-protected amino acid building blocks, DIC and Oxyma in DMF at 90 °C and a final DMF wash (details are listed in the Appendix Chapter 10.2). After standard acidic cleavage, the crude peptide was analysed by MALDI-TOF-MS and HPLC (Figure 4-59). Interestingly, the formation of aspartimide and piperidine adducts was observed. In HPLC purification, the main

peak of the crude peptide was isolated, and MS analysis revealed a mixture of CSY-protected and aspartimide-containing peptide species, but no peptide species without a CSY group.

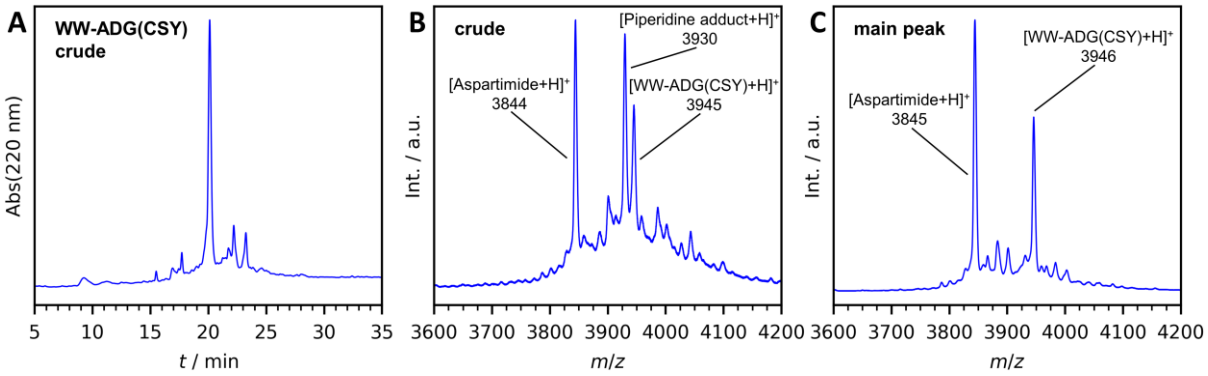

Figure 4-59: A: HPLC of crude WW-ADG(CSY) synthesized with standard procedure (coupling and deprotection at 90 °C). Gradient: 20-40% B in A in 30 min. B: MALDI-TOF-MS of crude and C: of main HPLC peak. Calculated average mass (g/mol) of possible species: $[WW\text{-}ADG(CSY)+H]^+$ 3945, $[WW\text{-}ADG(CSY)+Na]^+$ 3967, $[WW\text{-}ADG(CSY)+K]^+$ 3984, $[WW\text{-}ADG+H]^+$ 3862, $[WW\text{-}ADG+Na]^+$ 3884, $[WW\text{-}ADG+K]^+$ 3900, $[Aspartimide+H]^+$ 3844, $[Aspartimide+Na]^+$ 3866, $[Aspartimide+K]^+$ 3882, $[Piperidine\ adduct+H]^+$ 3929, $[Piperidine\ adduct+Na]^+$ 3951, $[Piperidine\ adduct+K]^+$ 3968.

In Neumann *et al.*[415] the CSY group was described to be stable to all common SPPS conditions, but the peptides were synthesised at room temperature. It can be assumed that the CSY group is not stable under microwave heating. To test this hypothesis, a short test peptide (TP) was synthesised at room temperature. As can be seen in Figure 4-60Aa, only the CSY protected peptide is present after cleavage from the resin, hence the reported results are reproducible. To test the stability of the CSY group, the resin-bound peptide was then equilibrated under different conditions. Heating the peptide in pure DMF (Figure 4-60Ab) did not lead to any degradation, showing that the CSY protecting group is in principle stable at high temperature.

The formation of by-products was observed when the peptide was heated in the Fmoc-deprotection mixture, 20% piperidine in DMF (Figure 4-60Ac). Different by-products were observed depending on the incubation time. A short incubation time resulted in the formation of aspartimide (Figure 4-60Ac). If the incubation was prolonged, the aspartimide was nucleophilically attacked by piperidine and the formation of piperidine amide could be observed (Figure 4-60Ad-e). To determine, which property of piperidine, basicity or nucleophilicity, was responsible for the degradation of CSY, the peptide was heated in a solution of 2% DBU in DMF (Figure 4-60Af). DBU is a stronger base than piperidine and can be used to remove Fmoc. It is not nucleophilic, but induces aspartimide formation to a greater extent than piperidine when the traditional *t*Bu protecting group is used.[74] In this case, no by-product formation was observed, suggesting that the nucleophilicity of piperidine is responsible for the degradation of CSY. A proposed mechanism is shown in Scheme 4-12.

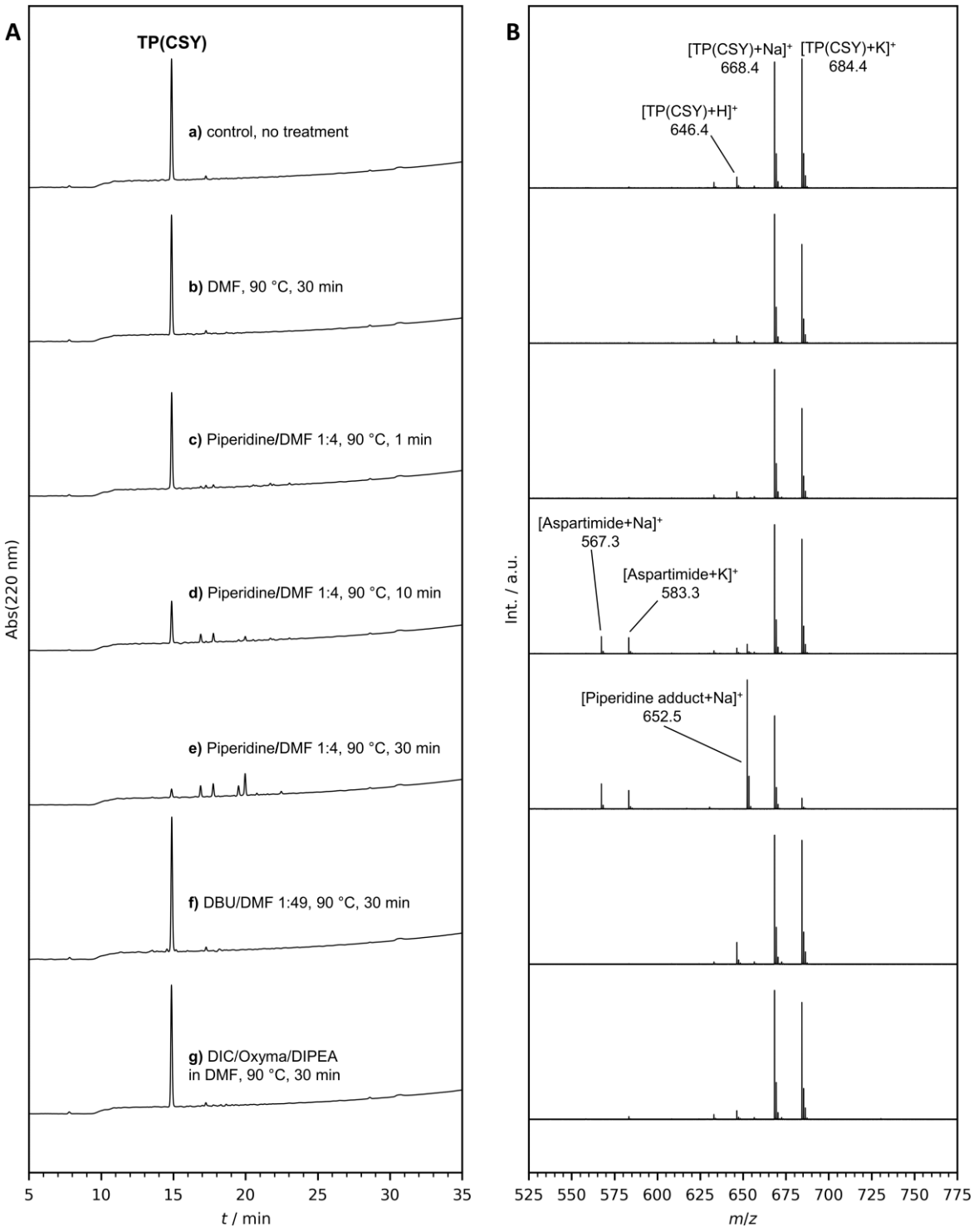

Figure 4-60: Treatment of resin-bound and CSY protected TP under different conditions of microwave-assisted solid-phase peptide synthesis. A: HPLC traces of crude peptide mixtures after acidic cleavage from the resin. Gradient: 20-70% B in A in 30 min. B: MALDI-TOF-MS of crude peptide mixtures after acidic cleavage from the resin. Calculated exact mass (Da) of possible species: $[TP(CSY)+H]^+$ 646.3, $[TP(CSY)+Na]^+$ 668.3, $[TP(CSY)+K]^+$ 684.3, $[TP+H]^+$ 563.3, $[TP+Na]^+$ 585.3, $[TP+K]^+$ 601.2, $[Aspartimide+H]^+$ 545.3, $[Aspartimide+Na]^+$ 567.25, $[Aspartimide+K]^+$ 583.2, $[Piperidine\ adduct+H]^+$ 630.4, $[Piperidine\ adduct+Na]^+$ 652.3, $[Piperidine\ adduct+K]^+$ 668.3.

The first two steps are similar to classical aspartimide formation. The backbone amide is deprotonated by piperidine and the carbonyl carbon of the side chain is attacked to form a five-

membered ring. Dimethylsulfide is then replaced by piperidine in a nucleophilic substitution, which cannot occur with DBU. Finally, the C-C bond is cleaved to give aspartimide and piperidylacetonitril.

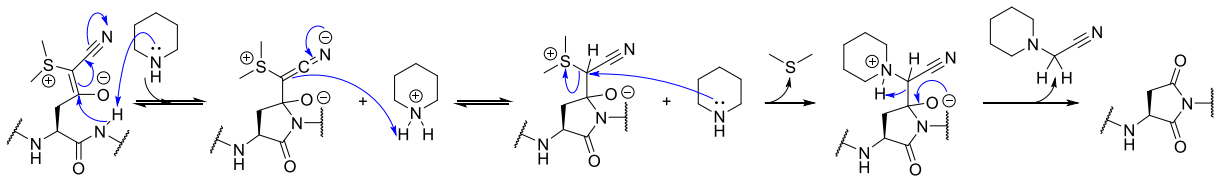

Scheme 4-12: Postulated mechanism of aspartimide formation during microwave heated Fmoc deprotection using CSY protected aspartates.

The direct attack of piperidine on the carbonyl C can be excluded because aspartimide is always observed as the first product and not a CSY-deprotected peptide with a free aspartate side chain or a piperidine adduct.

Finally, the peptide was heated in a mixture containing DIC, Oxyma and DIPEA in DMF (Figure 4-60Ag). The CSY group was stable under standard coupling conditions. The new automated SPPS protocol includes an Fmoc deprotection step at room temperature and a coupling step at elevated temperatures. Additional washing steps with DMF were added to cool the resin after the coupling step. The details of the standard coupling cycle and the new cycle are shown in the Appendix, Chapter 10.2.

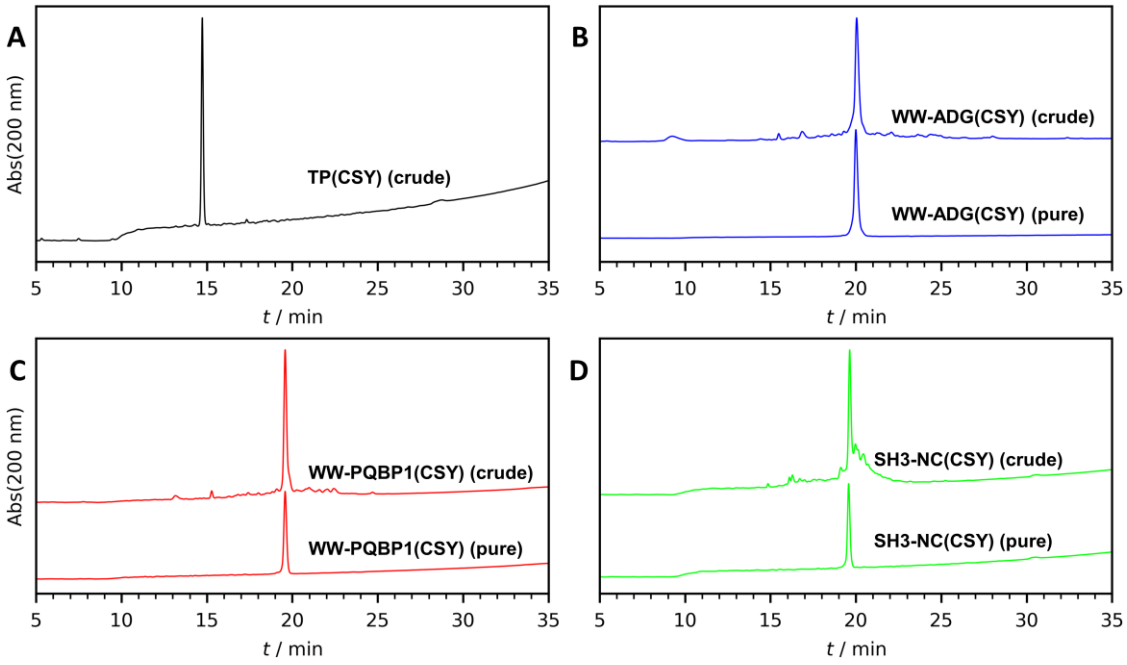

Figure 4-61: HPLC traces of crude and purified peptides obtained by microwave-assisted SPPS using the optimized synthesis protocol with Fmoc removal at rt. Gradients: A) 20-70%, B) 20-40%, C), 30-70% and D) 20-70% B in A in 30 min.

Using this new method, TP(CSY) was synthesised in excellent quality (HPLC trace in Figure 4-61A). Next, the synthesis of WW-ADG(CSY) was conducted, and in contrast to the first

synthesis, proceeded smoothly (HPLC trace in Figure 4-61B). To further test the strength of the new synthesis protocol, the peptide WW-PQBP1, containing four aspartates, and SH3-NC, a 57 amino acid peptide with six aspartates, were synthesised. Both CSY-protected peptides were obtained in very good quality of the crude product (HPLC trace in Figure 4-61C, D) and all three peptides were easily purified by semi-preparative HPLC (Figure 4-61).

4.6.4 Oxidative CSY deprotection

To obtain the native peptides, the CSY group has to be removed under oxidative conditions. Neumann *et al*.[415] reported NCS as superior deprotection reagent to *N*-chlorosaccharine, *N*-bromo-succinimide and *N*-iodo-succinimide. However, it was of interest if other oxidants were also suitable for CSY deprotection. Therefore, the deprotection of Fmoc-Asp(CSY)-OH as a test substrate was carried out using different oxidants, including iodine, sodium periodate, oxone and *m*CPBA, in different solvent systems. The conditions are summarised in Figure 4-62. NCS in acetate buffer pH 4.5 with MeCN, as reported by Neumann *et al*., was found to be the most efficient deprotecting reaction mixture, while in all other cases, no to low conversion was observed.

Therefore, all three CSY-protected peptides were treated with the literature-known conditions, NCS in MeCN and acetate buffer pH 4.5.[415] Surprisingly, incomplete deprotection of the CSY group and formation of by-products were observed (Figure 4-63, condition a). It is evident, that for these peptides the deprotection conditions had to be optimized. Thus, the CSY-protected peptides were deprotected with NCS in different solvent systems, which are summarised in Figure 4-63. It was hypothesized, that β-sheet peptides might aggregate, resulting in the burial of the CSY protected aspartates, making them inaccessible to NCS. Instead of reacting with the CSY group, the NCS reacted with other oxidation sensitive residues and caused peptide degradation. Therefore, solvents and additives were tested that prevent aggregation. The most well-known additive is GdnHCl, a strong chaotropic salt, that should initiate unfolding of the pepitdes.[322] Furthermore, the fluorinated alcohols trifluoroethanole (TFE) and hexafluoroisopropanole (HFIP), which are known to dissolve aggregated β-amyloid fibrils, were tested.[419-421]

For WW-ADG(CSY) or SH3-NC(CSY) the optimal condition (Figure 4-63Ab and Cb) was to dissolve the peptides in buffer A and 10% HFIP. A solution of NCS in buffer B was added over 20 min (total 2.2 equiv. NCS/CSY). After quenching with sodium ascorbate and diluting with buffer A, the mixture was lyophilised and successfully purified by HPLC (Figure 4-64A and C). In case of WW-PQBP1(CSY), the procedure had to be modified due to partial aggregation and insufficient deprotection (Figure 4-63Bb). MeCN was replaced by DMF, which was able to dissolve all aggregates and led to full deprotection with only low amount of by-products formed (Figure 4-63Bc). However, lyophilisation was not possible in this case, since DMF is not

volatile. Instead, the mixture was injected directly in the HPLC. On analytical HPLC the separation was unproblematic, but on semi-preparative HPLC two purifications were necessary due to a decrease in separation efficiency caused by the high DMF content. Finally, native WW-PQBP1 was obtained in high purity (Figure 4-64B). This modified procedure was also successfully tested with the other two peptides on an analytical scale (Figure 4-63Ac and Cc). All other conditions (Figure 4-63d to h) led to incomplete deprotection, peptide aggregation and the formation of significant amounts of side-products.

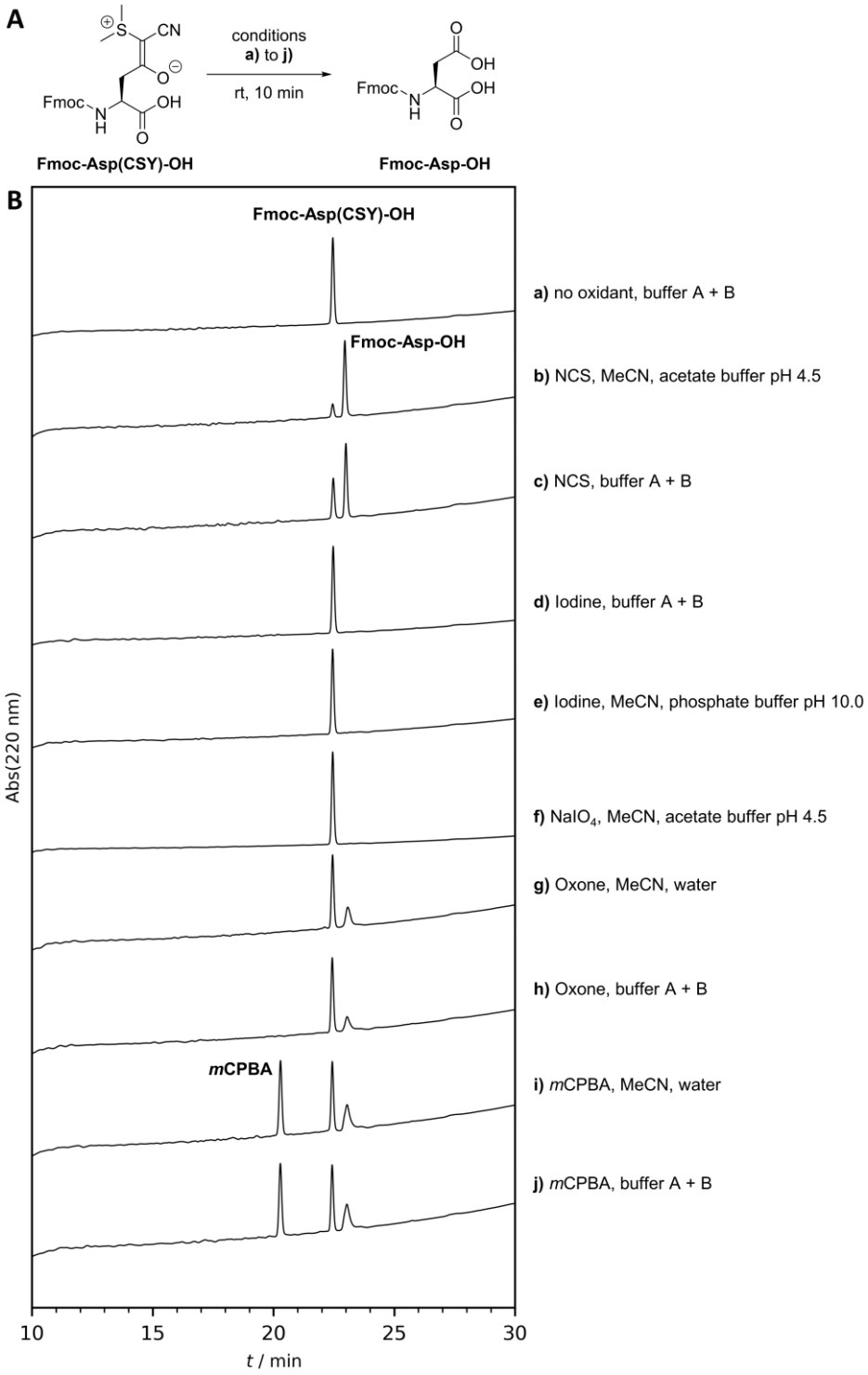

Figure 4-62: Screening of different cleavage conditions for the CSY protecting group from Fmoc-Asp(CSY)-OH with different oxidants (2.0 equiv.). Before injecting to HPLC excess NCS was quenched with sodium ascorbate.

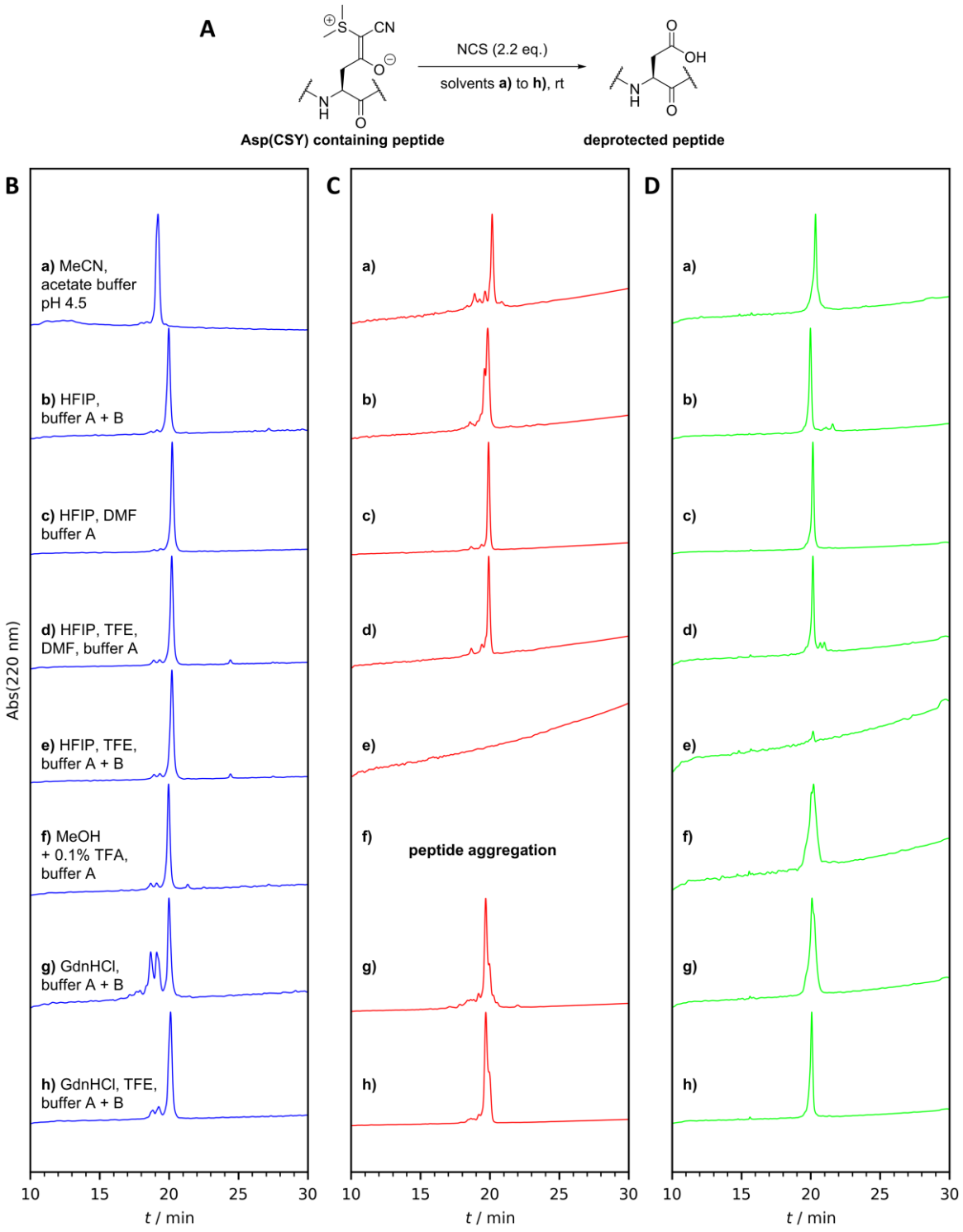

Figure 4-63: A) Screening of conditions for the removal of the CSY protecting group from B) WW-ADG(CSY), C) WW-PQBP1(CSY) and D) SH3-NC using NCS (2.2 equiv. regarding amount of CSY) and different solvent systems containing additives. Before injecting to HPLC excess NCS was quenched with sodium ascorbate. HPLC gradients: B) 20-40%, C) 30-70% and D) 20-70% B in A in 30 min.

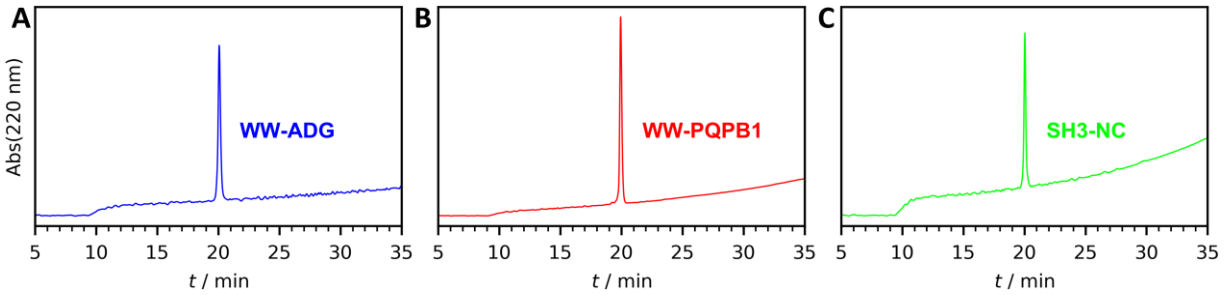

Figure 4-64: HPLC traces of CSY deprotected and purified peptides. Gradient: A) 20-40%, B) 30-70% and C) 20-70% B in A in 30 min.

4.6.5 Structural analysis of CSY protected and native peptides

It is of high interest to analyse the influence of the CSY protecting group on peptide folding and the structural integrity of the peptides after oxidative deprotection. Therefore, CD spectra and thermal denaturation curves of native and CSY protected peptides were recorded (Figure 4-65). The CD spectra of WW-ADG in the unprotected and CSY protected form, show the typical features of a well-folded WW domain with the characteristic maximum at 227 nm (details see Chapter 2.1).[111] The signal intensity is slightly reduced in the presence of the CSY group. The thermal denaturation curves of both peptides were sigmoidal with a T_m value of 70 °C for WW-ADG(CSY) and 79 °C for unprotected WW-ADG, which is in the range of the reported value by Jäger *et al.*: 77.5 °C.[111] These results are a clear indication of a WW domain-like folding, while the presence of the CSY group slightly weakens the folding and reduced thermal stability. In case of WW-PQBP1, the CD spectra of WW-PQBP1(CSY) show much weaker signal intensities than the CD spectra of the native peptide. Both spectra are characteristic of a WW domain-like structure. Again, the presence of CSY lowers the T_m value by 11 K, from 36 °C for unprotected WW-PQBP1 to 25 °C for the CSY protected peptide. These observations are very similar to WW-ADG. The stronger effect of the CSY group can be explained by the higher amount of CSY protected aspartates. Also, the CD spectrum of unprotected SH3-NC is typical of an SH3 domain with a maximum at 220 nm,[422] and similar to the other two peptides, the signal intensities are reduced for the CSY protected peptide. The thermal denaturation curve of SH3-NC(CSY) is not sigmoidal, and no meaningful T_m value could be extracted, while native SH3-NC gives a sigmoidal curve with a T_m of 44 °C. Also, in the case of SH3-NC it is evident that CSY weakens the structure and thermal stability. The CD spectra finally confirmed that the synthesis of all three peptides were successful, and the peptides were able to indecently fold into their expected native conformation.

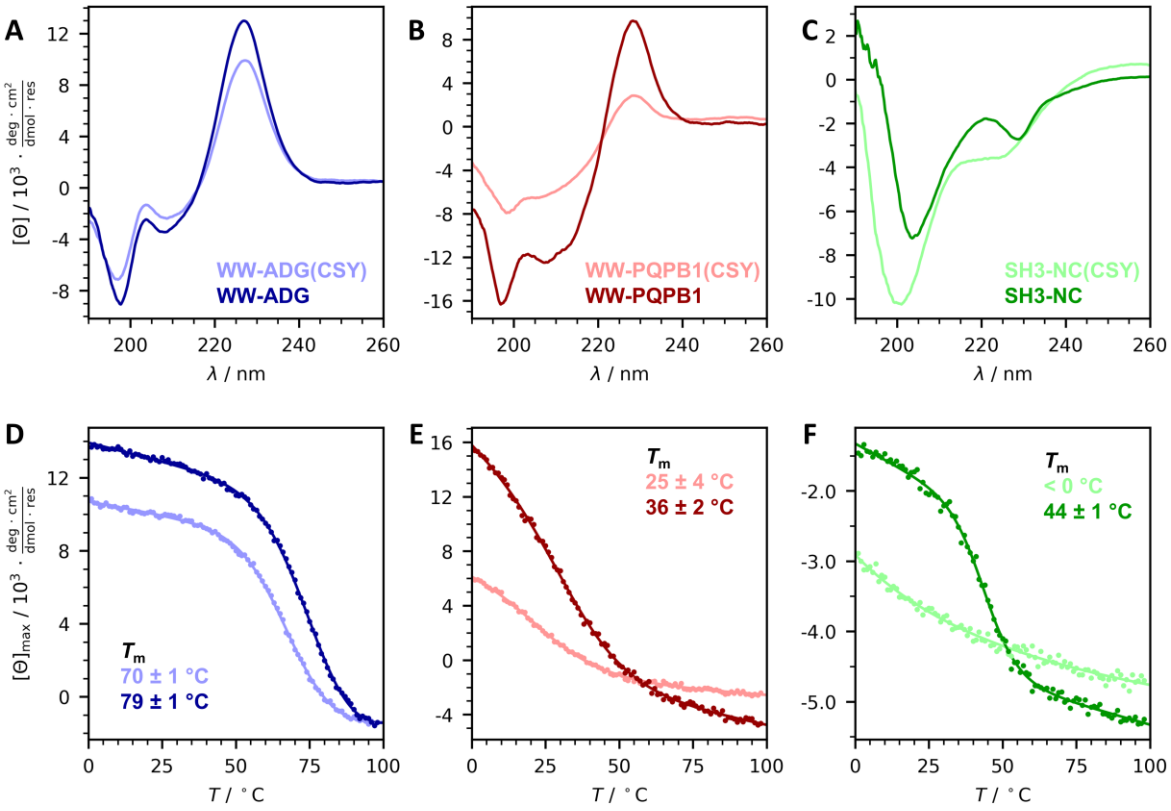

Figure 4-65: CD-spectra and thermal denaturation curves of native and CSY protected peptides. Conditions: 50 µM peptide or 20 µM for WW-PQBP1 due to solubility issues in 10 mM sodium phosphate buffer pH 7.0, 20 °C. Thermal denaturation was recorded from 1 °C to 98 °C. The fit of CD thermal denaturation curves was performed with Eq. (17) assuming linear pre- and post-transition baselines (for details see Chapter 8.2.9).

The question remains why deprotection of the CSY group in the peptides under study was not successful under the conditions used by Neumann *et al*.[415] CD spectroscopy revealed the CSY-protected peptides were at least partially folded in phosphate buffer, which could already indicate the problem. To analyse the structure of the peptides under the different deprotection conditions, CD spectra of WW-ADG(CSY) and SH3-NC(CSY) were recorded in acetate buffer pH 4.5 and 10% HFIP/buffer A (Figure 4-66). WW-PQBP1(CSY) could not be used due to solubility problems. DMF could also not be used to dissolve WW-PQBP1(CSY) because it strongly absorbs UV light below 260 nm, the region of interest in CD spectroscopy.[326] The spectra in acetate buffer of WW-ADG(CSY) and SH3-NC(CSY) are almost superimposable on the spectra recorded in phosphate buffer, showing that the peptides are folded under the deprotection conditions of Neumann *et al*..[415] The spectra of WW-ADG(CSY) and SH3-NC(CSY) in HFIP/buffer A show two minima (208 nm and 222 nm) and one maximum (215 nm), which is typical for an α-helical conformation. It is known that fluorinated solvents, especially HFIP, force peptides into an α-helical conformation, which also explains its ability to de-aggregate β-sheet peptides.[423] As long as the CSY-protected peptides are folded in their native-like state, the Asp(CSY) side chains are most likely buried and hence less accessible

to NCS. The addition of HFIP forces the peptides into an α-helical conformation, in which all side chains, including Asp(CSY), point outwards thus enabling complete CSY deprotection.

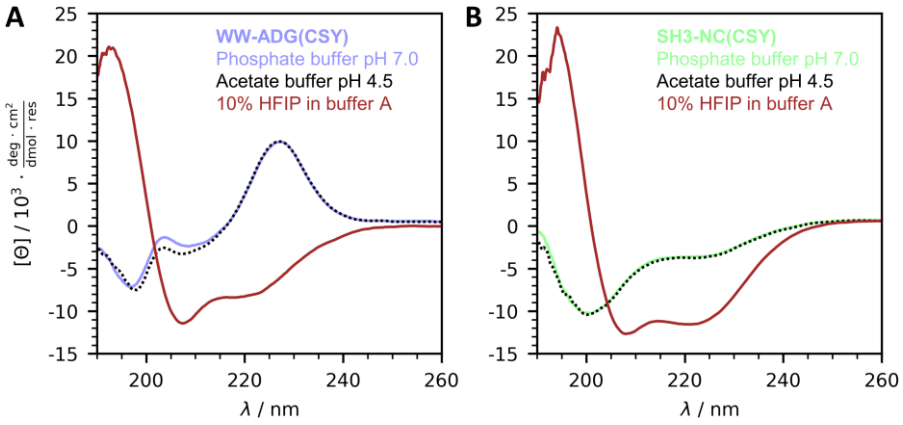

Figure 4-66: CD spectra of peptides A) WW-ADG(CSY) and B) SH3-NC(CSY) in different buffers. Conditions: 50 µM peptide dissolved in 10 mM sodium phosphate buffer pH 7.0, 10 mM sodium acetate buffer pH 4.5 or 10% HFIP in buffer A, 20 °C.

5 Conclusion

The initial aim of this thesis was threefold: designing, synthesising, and characterising metal ion binding β-sheet miniproteins based on the WW domain and tryptophan zipper scaffold, testing these miniproteins for catalytic activity, and investigating possibilities for using them in biosensing.

The first part of the study involved the successful design of three WW domains and a tryptophan zipper that bind to Ni(II), Cu(II), and Zn(II). This was achieved by mutating the smaller solvent exposed hydrophobic core to a His_3 site, inspired by the active site of hCAII, while leaving the main hydrophobic core intact. The initial WW domain, called WW-CA, is a molten globule that lacks thermostability and is prone to aggregation. However, it is reversibly switchable between an uncooperative and cooperative folded state upon metal ion binding or a change in pH. Two additional variants, WW-CA-min and WW-CA-ANG, were rationally designed by introducing mutations based on structural assumptions. These variants exhibit cooperatively folded apo states, increased thermostabilities, and higher metal ion binding affinities. The WW-CA-ANG-Zn(II) complex exhibited a T_m value of 70 °C, which is 36 K higher than that of the WW-CA-Zn(II) complex. Additionally, it was found that all three WW-CA variants bind two Cu(II) ions, and the parent peptide $hPin1_{WW}$-Nle also binds to Cu(II), albeit with lower affinity and under destabilization of the WW-domain structure.

Using the tryptophan zipper as a scaffold, a highly stable peptide, $Tz2H_3$, was designed. The Cu(II) complex of $Tz2H_3$ showed the highest thermostability (T_m value of 80 °C) and binding affinity (far below 1 nM for Cu(II)) of all peptides under study. In contrast to the WW domains, three polar residues on the surface of Trpzip2 were mutated to His. Since all essential stabilizing residues were left untouched, apo $Tz2H_3$ adopted a stable structure.

Generally, an increase in T_m resulted in a decrease in K_d, but not in a linear way. At a certain point, K_d decreased only marginally. The reason for this is the lack of preorganization of the His_3 site in all four designed miniproteins, but a predisposition for metal ion binding, causing a conformational change. To achieve a higher binding affinity, the design of a preorganized site, similar to hCAII, is required. Interestingly, this protein exhibits a T_m value of 51 °C and 59 °C in the apo and holo state, respectively,[312] but binds Zn(II) with a much lower K_d in the pM range.[245] Still, a such high affinity for Zn(II) is not required for function: several hydrolytically active Zn(II) containing peptides and proteins only have a K_d in the µM range.[226, 232, 258, 276, 344]

The WW-CA variants are the first designed WW domain that binds Ni(II), Cu(II), and Zn(II). Although WW domains have been extensively studied, only a few designed WW domains are known to bind to molecules other than their natural peptide ligands.[133-134] In addition to WW-CA, only two other switchable WW domains are known: one is pH switchable,[122] and the other

folds upon binding to its natural ligand.[120] While there are many designed and functional β-hairpins, metal ion binding has rarely been included. Instead, thermostability and resistance to chemical denaturation have typically been achieved through the use of disulphide bonds or other covalent cross-linking.[208-209] However, it is known that introduction of a metal binding site is an effective strategy.[203] The incorporation of a His_3 site into a protein or peptide scaffold for metal ion binding is not a new concept. However, it is worth noting that initially globular β-sheet containing peptides and proteins were used as scaffolds,[424-427] but lack of catalytic activity and low solubility, a common problem in the early days of β-sheet design, shifted the interest to α-helical peptides.[41] These early designs were never used for other applications. Although a simple concept, placing the His_3 site in the wrong position, such as the main hydrophobic core, loops, or flexible termini, can result in a complete loss of folding, even in the presence of metal ions, or lead to aggregation.[428-429] Understanding the relationship between sequence and structure is crucial, and identifying a metal ion binding site is not a trivial task.

The inherent flexibility of WW-CA and its molten globule nature make it ideal for biosensing applications. Additionally, the binding of Zn(II), Ni(II), and Cu(II) to the peptide causes detectable conformational changes in both CD and fluorescence spectroscopy. A FRET-based receptor, WW-CA(Coum), was designed by mutating Trp34 to a coumarin-labelled homocysteine, which can selectively differentiate Zn(II) and Cu(II) from other divalent metal ions. The Zn(II) complex was sensitive to phosphate, pyrophosphate, and glyphosate. However, the change in FRET was not sufficient for unambiguous differentiation since each analyte caused a reduction in FRET, albeit to a varying degree.

At first glance, the lack of specificity may appear to be a disadvantage, but it can be utilised in differential sensing. Four peptides are available that bind to three different metal ions with significantly different affinities, ranging from sub-nM to lower mM, and cause changes in tryptophan fluorescence. This allows for the formation of an array containing twelve cross-reactive receptors. Testing this array with seven bioactive molecules demonstrated its capability to differentiate glyphosate from the other analytes. Further optimization is required to improve the signal-to-noise ratio and differentiate a wider range of analytes. Differential sensing currently employs various types of receptors, including natural proteins such as serum albumin or GFP, as well as unstructured short peptides.[391] Only one other receptor array based on *de novo* designed proteins is reported so far, which uses α-helical barrels.[430] Therefore, the receptor array used in this work is the first biochemical tongue using designed β-sheet miniproteins.

The complexes of peptides and metal ions were also tested for enzymatic activity, including hydrolysis of activated esters, phenol oxidation, and Cu(I)-catalysed azide-alkyne cycloaddition. In the case of ester hydrolysis, it was found that the His residues act as

nucleophilic catalysts. Although the activity was less than that of free imidazole at neutral pH, the peptides were still active under acidic conditions. This is a hint for acid-base catalysis mediated by the three His residues in proximity, which was also observed for a designed α-helical bundle containing six His residues.[339] It has been demonstrated that peptide-Cu(II) complexes can activate oxygen and catalyse DMP oxidation, favouring the C-C coupling over polymerization, but it has to be mentioned, that the rate enhancement was low to moderate and that Cu complexes of small organic ligands are already reported to performing the same task.[348] During DMP oxidation, Cu(II) is reduced and it can be assumed that the peptides are able to bind to Cu(I). Cu(I) is known to catalyse the CuAAC reaction, but unfortunately, the designed miniproteins turned out to be unsuitable ligands. By chance, it was discovered that pyruvate can be a valuable additive in CuAAC, protecting the Cu(I) stabilizing ligand and the substrates from oxidative degradation caused by hydrogen peroxide, which is formed as a side product during ascorbate-mediated reduction of Cu(II). The THPTA ligand used so far also acts as an H_2O_2 scavenger,[367] but high concentrations of THPTA slowed down the reaction. Recently, it was reported that pyruvate can be used as a reductant in photoinduced CuAAC using UV light at 365 nm.[431] Although the authors demonstrate that the cells survived and proliferated after CuAAC, it is important to note that UV light can cause DNA damage and mutations,[432] which may affect the behaviour of the cells. This was not tested in the study. Therefore, CuAAC protocols that use ascorbate as a reductant, including pyruvate, may improve applicability *in vivo*.

Compared to enzymatically active designed α-helical coiled coils and barrels,[230, 232, 344] the WW domain and Trpzip lack a cavity necessary for substrate binding. All three reactions used substrates with hydrophobic aromatic groups, which are known to bind into hydrophobic cavities.[433] Placing the catalytic active site inside such a cavity increases the likelihood of a reaction taking place. This approach is frequently employed and involves the insertion of artificial metal-containing cofactors into the binding cleft of streptavidin, a predominantly β-sheet protein. This enables several catalytic reactions, including hydrogenation, alcohol oxidation, and Suzuki-Miyaura cross-coupling.[434]

WW domains are not catalytically active by nature, and no design was made towards this direction until this work. Therefore, the initial step, has been accomplished, although the rate enhancement of the designed peptides is not outstanding or useful in organic synthesis, these are the first catalytically active WW domains so far. Regarding β-hairpins, previous studies have reported on the hydrolytic activity of His-containing sequences[228-229] and the electrochemical production of H_2 through the incorporation of a Ni-phosphine cofactor.[241, 243] Short β-turns, consisting of only four residues and with organocatalysts as side chains, have been found to perform stereoselective reactions in organic solvents,[435-436] however, these molecules cannot be considered as miniproteins.

In the design of the peptides used in this work, aspartates were substituted with asparagines to avoid aspartimide formation. However, this substitution can be a drawback as the two amino acids are not always interchangeable. Aspartic acid often provides greater structural stability than asparagine,[111, 406] can also act as a coordinative ligand to metal ions[402-403] and are essential in hydrolytic enzymes.[404-405] The CSY group was tested following the literature protocol to access Asp-containing peptides.[415] However, this proved to be challenging, and the protocol had to be adapted for β-sheet peptides. Optimization was performed for microwave-assisted automated synthesis and CSY removal conditions. It was found that coupling under microwave heating and Fmoc deprotection at room temperature resulted in excellent crude synthesis quality. According to the literature, NCS was found to be the best oxidant for removing the CSY group. However, the solvent system of the CSY removal cocktail must contain HFIP to disaggregate the peptides. By using the optimized method, it was possible to synthesize peptides up to 57 amino acids without aspartimide formation and in high purity.

This unplanned side project, in conjunction with the insights gained from peptide design and the possibilities of late-stage functionalisation, has opened the door for the design of new WW domain and Trpzip variants that could further expand the scope of functional β-sheet miniproteins.

6 Summary

Proteins with structure and function beyond the natural scope have been designed, which includes an impressive variety of artificial enzymes, receptors and biomaterials.[29, 32, 41, 75, 78] While the sequence-structure-function relationship of α-helical coiled-coils is well understood and has led to a plethora of *de novo* designed scaffolds with diverse functions,[40, 42] globular β-sheet proteins have been less explored for design purposes.

This work uses the well-characterised WW domain of hPin1, a triple-stranded antiparallel β-sheet miniprotein, and the β-hairpin Trpzip2 (Figure 6-1) as scaffolds to design catalytically active and receptor-like β-sheet miniproteins by incorporating a metal ion binding site. WW domains are polyproline binding peptides with no catalytic activity and have served as a model system in many biophysical studies,[68] but have seldom been used to design new functional miniproteins.

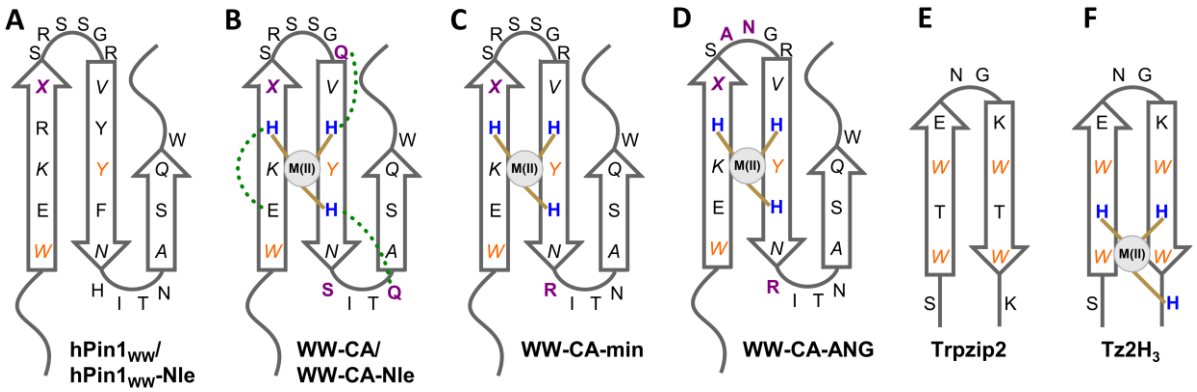

Figure 6-1: Overview of the peptides used in this work. A) to F) 2D Schematic representation of the peptide structure. Italic residues point below the β-sheet, orange: conserved amino acids of the inner hydrophobic core, blue: His_3 site, violet: additional mutations. Dotted green lines represent hydrogen bonds, golden lines represent coordinative bonds. X: Met (only in $hPin1_{WW}$ and WW-CA) or Nle (in all other cases).

The top-down design strategy consists of grafting the active site of human carbonic anhydrase II,[244] specifically the His_3 site, onto the solvent-exposed surface of $hPin1_{WW}$ and Trpzip2. This involves additional mutations to prevent a second metal ion binding site and alter the stability of the peptides. In case of $hPin1_{WW}$ the smaller solvent exposed hydrophobic core was mutated, while in case of Trpzip2 only polar residues were exchanged to His. In both peptides, the main hydrophobic core was left intact. The result is four designs in total (see Figure 6-1). The first designed peptide, WW-CA (or WW-CA-Nle), aims to mimic the second coordination sphere of hCAII. The second design, WW-CA-min, includes only the necessary minimum number of mutations. The third peptide, WW-CA-ANG, replaces the first loop with a sequence known to increase stability. The β-hairpin $Tz2H_3$ incorporates only the His_3 site without further mutations. The peptides were synthesized using solid-phase peptide synthesis (SPPS), purified *via* high-performance liquid chromatography (HPLC), and their identity was confirmed

using matrix-assisted laser desorption/ionization time-of-flight mass spectrometry (MALDI-TOF-MS). WW-CA/WW-CA-Nle specifically binds Ni(II), Cu(II), and Zn(II) compared to other divalent metal ions. This binding event induces a characteristic conformational change, as observed in the CD spectrum (Figure 6-2). The peptide can be switched between the apo and holo state, indicating a reversible binding event. Furthermore, WW-CA/WW-CA-Nle is fully pH-switchable with a pK_a of 6. When analysed using CD and NMR spectroscopy, it was found that apo WW-CA/WW-CA-Nle is an uncooperatively folded molten globule. However, Zn(II) binding stabilises the peptide structure, leading to a cooperative folding-unfolding process with a T_m value of 33 °C. Regrettably, WW-CA/WW-CA-Nle aggregates upon unfolding in the presence of Zn(II) and its low thermostability makes it unsuitable for *in vivo* applications.

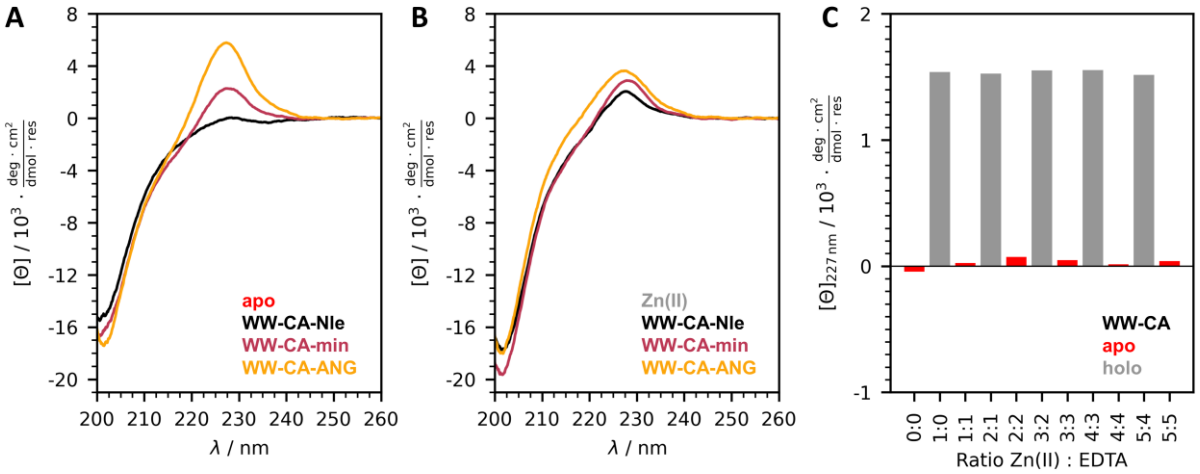

Figure 6-2: CD spectroscopic analysis of WW-CA variants in A) absence and B) presence of Zn(II). Conditions: 50 µM peptide, 50 µM $ZnSO_4$ (if present), 10 mM MOPS, 150 mM NaCl, pH 7.2, 1 mm cuvette. CD spectra were recorded at 20 °C. C) Conformational switch of WW-CA by alternate addition of Zn(II) and EDTA, corresponding [Θ] values at 227 nm *versus* the molar ratio of added Zn(II) and EDTA. Conditions: 10 µM WW-CA, 10 mM MOPS, 150 mM NaCl, pH 7.2, 1 cm cuvette, 20 °C, titrated with 2 mM $ZnSO_4$ or 2 mM Na_2H_2EDTA in 10 mM MOPS, 150 mM NaCl, pH 7.2.

Therefore, WW-CA/WW-CA-Nle was redesigned, and the resulting WW-CA variants, WW-CA-min and WW-CA-ANG, exhibit cooperative folding in the apo states and bind to Ni(II), Cu(II), and Zn(II) with characteristic conformational changes (see Figure 6-2). Additionally, the Zn(II) complex of WW-CA-ANG is thermostable, with a T_m value of 70 °C. As shown in Table 6-1, the improved thermal stabilities have led to enhanced metal ion binding affinities. The K_d values were at least one order of magnitude lower compared to WW-CA/WW-CA-Nle. CD and ITC measurements, combined with computational structure prediction using AlphaFold2, indicate that the His_3 site is predisposed but not preorganized for metal ion binding. This explains the saturation-like correlation between thermostability and binding affinity. Competitive titration and EPR measurements revealed an additional Cu(II) binding site, which was not originally intended. The parent peptide hPin1$_{WW}$-Nle was analysed and found to selectively bind Cu(II), but not Ni(II) or Zn(II). Binding of Cu(II) reduced the thermal stability of hPin1$_{WW}$-Nle by 10 K.

It is likely that the flexible loop1 serves as the second binding site. Further studies are required to confirm this hypothesis.

The designed tryptophan zipper $Tz2H_3$ is a stable and cooperative folded peptide with a T_m value of 53°C. In the presence of Cu(II), the T_m value increased to 80 °C, making it thermostable to hyperthermostable. $Tz2H_3$ binds Ni(II) and Zn(II) with comparable affinities to WW domain-based peptides. However, the Cu(II) binding was improved, and in all cases, only one metal ion is bound. Unlike $hPin1_{WW}$-Nle, the parent peptide Trpzip2 did not bind Cu(II). The $Tz2H_3$-Cu(II) complex remained stable even in the presence of high concentrations of chaotropic salts (6 M GdnHCl) and organic solvents (MeOH, MeCN) (Figure 6-3). Similar to the WW-CA variants, the His_3 site in $Tz2H_3$ is also predisposed to metal ion binding.

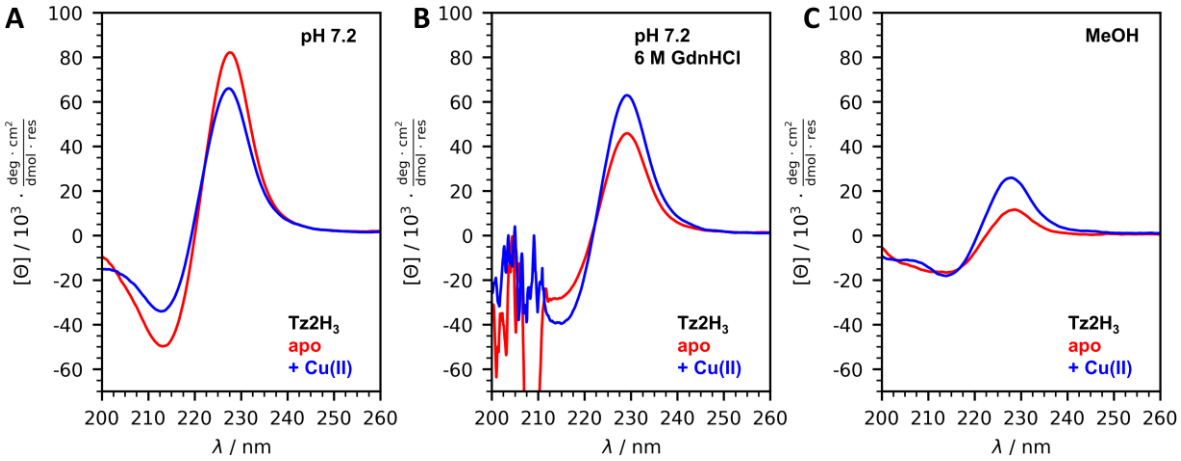

Figure 6-3: Structural analysis of $Tz2H_3$. A) CD spectra of $Tz2H_3$ in absence and presence of $CuSO_4$, B) with addition of 6 M GdnHCl (noisy spectra due to UV absorption of GdnHCl). C) $Tz2H_3$ in absence and presence of Cu(II) in MeOH. Conditions: 50 µM peptide, 50 µM metal ions (if present), 6 M GdnHCl (if present), aqueous buffer (10 mM MOPS, pH 7.2, 150 mM NaCl) or MeOH, 1 mm cuvette. CD spectra were recorded at 20 °C.

Table 6-1: Melting temperature and dissociation constants of peptide metal ion complexes.

T_m / °C K_d / µM	WW-CA-Nle	WW-CA-min	WW-CA-ANG	$Tz2H_3$
apo	< 0	20 ± 1	36 ± 1	53 ± 1
Ni(II)	26 ± 2	38 ± 1	52 ± 1	---[#]
	5 ± 1[a*]	0.6 ± 0.3[a]	0.5 ± 0.1[b]	0.7 ± 0.5
Zn(II)	33 ± 1	51 ± 1	70 ± 1	---[#]
	1.4 ± 0.4[b]	0.7 ± 0.1[b]	0.5 ± 0.2[b]	0.3 ± 0.2
Cu(II)	31 ± 1	38 ± 1	51 ± 2	81 ± 2
	$(2.7 \pm 0.4)\cdot10^{-3}$ (0.6 ± 0.1)[c]	$(1.6 \pm 0.5)\cdot10^{-3}$ (0.9 ± 0.3)[c]	$(0.9 \pm 0.2)\cdot10^{-3}$ (1.7 ± 0.2)[c]	$<< 1\cdot10^{-3}$

K_d determined with [a]CD, [b]fluorescence and [c]competitive titration. *WW-CA, #linear thermal denaturation curve, T_m could not be determined

The conformational change upon metal ion binding and the molten globule nature of WW-CA/WW-CA-Nle should correlate with changes in distances between residues in the apo and holo state. These changes can be monitored by FRET.[265] Trp11 in the first β-strand is already present and serve as the FRET donor. As the FRET acceptor, Trp34 is substituted with a coumarin-labelled homocysteine *via* an on-resin late-stage iodination-substitution approach (Figure 6-4A). The resulting peptide WW-CA(Coum) binds to Zn(II), which causes a two-fold increase in FRET intensity. This indicates that Zn(II) binding indeed induces folding, which shortens the distance between the residues and leads to FRET enhancement. Cu(II) also binds, causing fluorescence quenching, while all other tested divalent metal ions did not cause any changes (Figure 6-4B). Therefore, WW-CA(Coum) can be considered a selective receptor for Zn(II) and Cu(II). Furthermore, the WW-CA(Coum)-Zn(II) complex was utilized to detect glyphosate, phosphate, and pyrophosphate through competition of metal binding or direct interaction with the peptide, resulting in analyte-specific changes in FRET (Figure 6-4C). It is worth noting that the changes observed were minor in absence of Zn(II).

Differential sensing can expand the range of detectable molecules by using an array of cross-reactive receptors.[391] The combination of the four designed peptides with Ni(II), Cu(II), and Zn(II) results in a total of twelve receptors. These peptides are ideal for differential sensing due to their wide range of metal ion binding affinity, resulting in characteristic tryptophan fluorescence changes for each metal ion. The array was challenged with seven bioactive molecules, and tryptophan fluorescence was recorded. Principal component analysis[394] was used for dimension reduction, resulting in a score plot that showed clustering of replicate measurements for each analyte (Figure 6-4D). The biochemical tongue was able to differentiate glyphosate from the other analytes. However, the other analytes could not be discriminated from each other, indicating the need for further optimization. To date, receptors for differential sensing have included unstructured peptides,[437] natural proteins,[438] and *de novo* designed α-helical barrels.[430] Therefore, the receptor array presented here is the first which used designed globular β-sheet miniproteins.

After the structural studies, the catalytic activity of the four miniproteins was tested. To test for hydrolytic activity, *p*NPA was used as a model substrate since the natural model, hCAII, catalyses hydrolysis beside CO_2 hydration.[257] It was found that the activity was higher in the absence of Zn(II) and that the ester hydrolysis was due to the imidazole moieties in the His side chain. The activity was not fully quenched under acidic conditions, which was not observed in presence of free imidazole. This suggests the possibility of acid-base catalysis. The His residues are in close proximity, which can cause individual pK_a values to differ from the mean pK_a value of around 6. However, the catalytic efficiency was lower than that of other *de novo* designed hydrolases[226] and similar to that of free imidazole.[335]

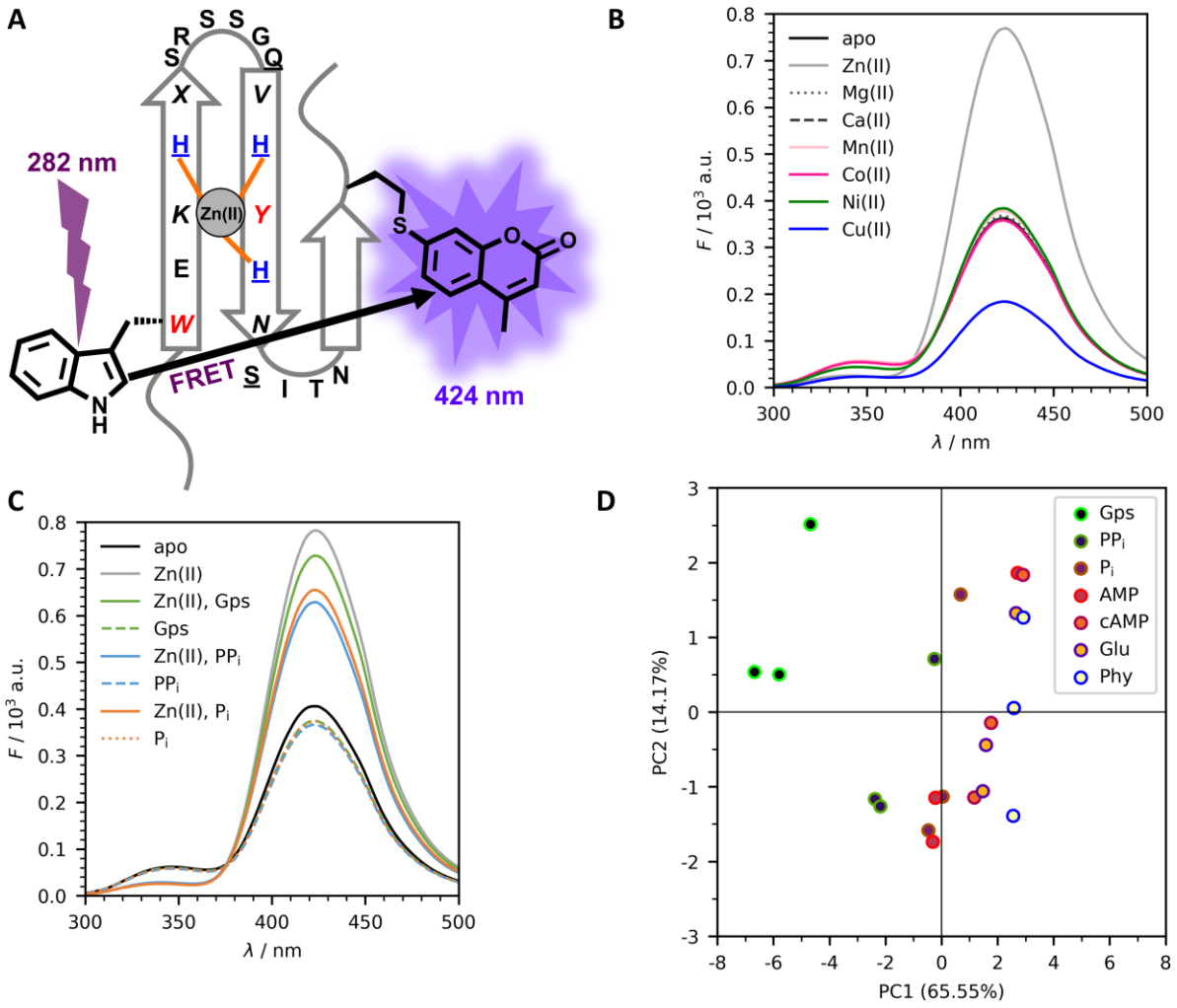

Figure 6-4: Sensors based on globular β-sheet peptides. A) Schematic representation of WW-CA(W34Coum), X: Nle. B) Fluorescence spectra of WW-CA(W34Coum) in absence and presence of divalent metal ions. C) Fluorescence spectra of WW-CA(W34Coum) in absence and presence of Zn(II) and analytes (Gps: glyphosate, PP_i: pyrophosphate, P_i: phosphate). Conditions: 10 µM peptide, 10 µM metal ion (if present), 10 µM analyte (if present), 10 mM MOPS, pH 7.2, 150 mM NaCl, rt, λ_{ex} = 282 nm. D) Differential sensing using a receptor array based on β-sheet peptide-metal complexes using WW-CA-Nle, WW-CA-min, WW-CA-ANG and $Tz2H_3$ combined with Ni(II), Cu(II) and Zn(II). Score plot of principal component analysis. Conditions: 4 µM peptide, 4 µM metal ion, 4 µM analyte (Gps: glyphosate, PP_i: pyrophosphate, P_i: phosphate, AMP: adenosine monophosphate, cAMP: cyclic AMP, Glu: glutamate, Phy: phytate), 10 mM MOPS, pH 7.2, 150 mM NaCl, 20 °C – 25 °C, λ_{ex} = 295 nm, λ_{em} = 345 nm, experiments were performed in 96-well plates as triplicates.

The phenol oxidation activity was tested using the model substrate DMP[357] due to the peptides ability to bind redox active Cu(I)/(II). Although the rate enhancement was not outstanding compared to natural laccases and designed Cu(II) binding β-sheet amyloids,[261, 351] a shift in selectivity was observed. Free Cu(II) ions catalysed polymerization by a cationic mechanism and C-C coupling by a radical mechanism with low selectivity. However, Cu(II) peptide complexes shift the selectivity towards C-C coupling. Increasing the ratio of Cu(II) to peptide up to 5:1 enhances the reaction rate, but the selectivity for the radical mechanism persists. This finding is highly interesting and warrants further investigation. Cu(I) complexes can catalyse CuAAC reactions,[359] but the designed peptides were not suitable ligands and instead

suppress the reaction. However, a side discovery was made that pyruvate is a useful antioxidative additive in CuAAC. It protects the Cu(I) stabilizing ligand and the substrates from degradation caused by H_2O_2 formation during ascorbate-mediated Cu(I) formation. The four peptides exhibited similar and interesting catalytic activity, despite differences in thermostability and binding affinity. The low to moderate catalytic efficiency may be attributed to the lack of a substrate binding cavity. While catalytically active species have been observed in β-hairpins, this is not the case for WW domains. Therefore, this work presents the first catalytically active WW domains.

None of the designed peptides in this work contain aspartates due to the severe side reaction of aspartimide formation during SPPS.[74] Although the CSY protection group was initially planned to be used to suppress this side reaction,[415] the reported protocol was found to be unsuitable for β-sheet peptides. The optimization of the synthesis of the building block Fmoc-Asp(CSY)-OH, the conditions for automated microwave-assisted SPPS, and the deprotection of the CSY group were achieved (Figure 6-5). The reported procedure for building block synthesis was successfully upscaled, and cheaper reagents were used to reduce costs. It was discovered that microwave heating can be used for coupling steps during SPPS, but Fmoc-deprotection must be carried out at room temperature to yield crude CSY-protected peptides in excellent quality. Additionally, it was found that solvent mixtures containing water/MeCN/HFIP/TFA or water/DMF/HFIP/TFA are superior to the reported acetate buffer/MeCN mixture due to better disaggregation of the β-sheet peptides, which allows the deprotection agent NCS to access the CSY group. Using the optimized method two WW domains and a SH3 domain, which contain 33, 34, and 57 amino acids, respectively, were successfully synthesized in excellent quality. From now on, designed β-sheet miniproteins containing Asp should be easily accessible.

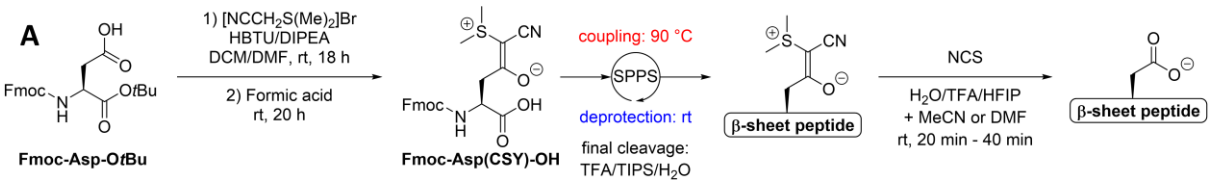

B

Peptide	Sequence
WW-ADG	H-KLPPGWEKRXS-ADGRVYYFNHITNASQWERPSG-OH
WW-PQBP1	Ac-GLPPSWYKVFDPSSGLPYYWNADTDLVSWLSPHD-NH_2
SH3-NC	Ac-AEYVRALFDFNGNDEEDLPFKKGDILRIRDKPEEQWWNAEDSEGKRGXIPVPYVEKY-NH_2

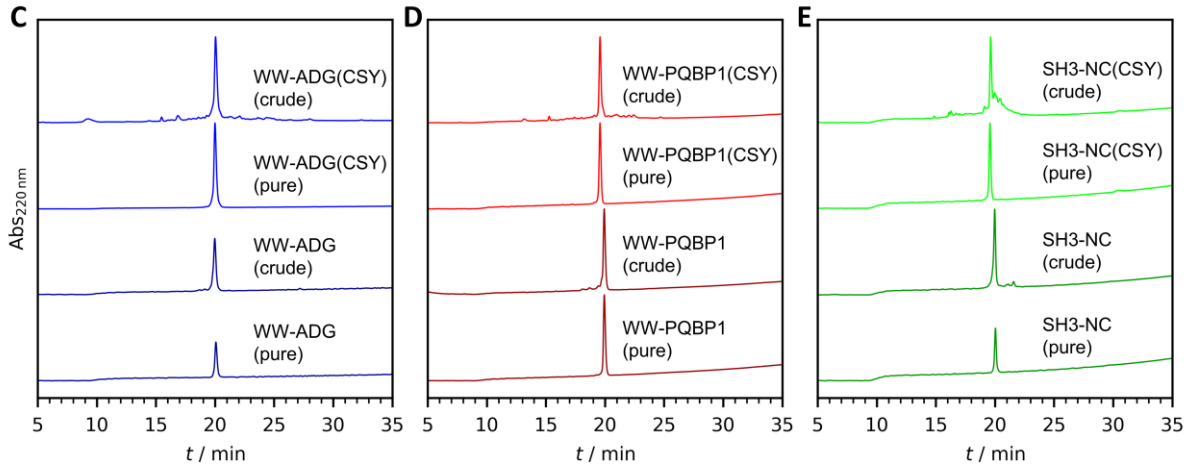

Figure 6-5: A) Overview of the optimized conditions to synthesize aspartate containing β-sheet peptides using the CSY protecting group. B) Sequences of synthesized peptides. C) to E) HPLC traces of crude and purified CSY-protected and deprotected peptides. MeCN was used in the CSY removal cocktail for WW-ADG(CSY) and SH3-NC(CSY), while DMF was used in case of WW-PQBP1(CSY).

7 Outlook

The design approach was successful in yielding four metal ion binding β-sheet miniproteins with a wide range of stability and metal ion binding affinity, both of which are sufficient for function. Further increase in thermostability is not necessary for increasing binding affinity or catalytic activity, but it is an interesting task, given that there are organisms living in biotopes over 100°C.[319] Increasing thermostability is also positively correlated with stability towards organic solvents, which weaken the hydrophobic effect that is essential for folding in the WW domains and tryptophan zippers. Additional stabilization can be achieved by introducing more salt bridges, hydrogen bonds, and cation-π interactions. In addition to non-covalent interactions, disulphide bonds, cross-linking of the *N*- and *C*-termini, and stapling can further increase stability. Replacing the hydrophobic core with a lipophobic core could be of great interest. This could result in the β-hairpin or WW domain only folding in organic solvents, while remaining unfolded in an aqueous buffer. It is known, that β-hairpins containing only hydrophobic residues are folded in organic solvents.[151, 439] While the hydrophobic effect was missing, cross-strand hydrogen bonds of the amide backbone and aromatic interaction in T-shape conformation were still present and stabilize the structure, but the folding-unfolding transition was not cooperative.[439]

The affinity towards 3d metals follows the prediction of the Irving-Williams series. Each designed peptide binds to the metal ions with the following relative affinity: Ni(II)<Cu(II)>Zn(II). The K_d values for Ni(II) and Zn(II) are in the lower μM to upper nM range, and for Cu(II), they are in the lower nM to upper fM range. It would be interesting to shift the affinity range further in both directions, generating peptides with much lower and much higher affinity. Inverting the Irving-Williams series is a challenging task that was recently achieved using a designed α-helical scaffold.[440-441] Intuitively, the design of a highly rigid scaffold would be obvious, that dictates the coordination geometry and therefore favouring certain metal ions over others. Surprisingly, the reported α-helical proteins were flexible, and each 3d metal ion forced the protein into a different conformation, similar to the miniproteins in this work. The key was, that the conformation induced by Cu(II) was energetically unfavourable and therefore the binding affinity of Ni(II) or Zn(II) was higher. To move towards this goal, a first step would be the elucidation of the 3D structure of the designed metallopeptides, including the finding of the second Cu(II) binding site. There are still more possible places for coordination sites and beside His, other amino acids, like Glu or Cys, are also metal coordinating. However, the inversion of the Irving-Williams series is a challenging task, and most natural metalloproteins are incapable of achieving it.[442]

The strategy used in this work involved investigating the structural consequences of introduced mutations and their influence on stability and metal ion binding affinity of each designed peptide

before testing for catalytic activity. This process was very time consuming. To improve the search for catalytic active peptides, a reverse strategy should be employed. This involves synthesising a library of peptides or using display techniques to test for catalytic activity. Successful candidates can then be analysed in more detail. The results of this work provide a necessary basis for the targeted insertion of mutations. For a selection process to be successful, the initial activity of a protein is necessary.[443] This activity is then subsequently enhanced and optimized with every selection round.

Biocatalysis offers benefits beyond rate enhancement, including selectivity as demonstrated in the oxidation of DMP. The presence of a peptide-Cu(II) complex favoured C-C coupling and suppressed polymerization. To clearly identify the structures, the products must be isolated and characterized using NMR spectroscopy. Additionally, it is important to analyse the influence of different solvents, temperatures, and pH values. Further analysis of the peptides at excess of Cu(II) is necessary to fully understand their structure. CD titration has suggested the possibility of more than two binding sites and a significant change in peptide conformation at high Cu(II) concentrations. It has been proposed that the selectivity is due to a preference for a radical-mediated mechanism. To investigate this further, EPR spectroscopy could be employed to observe the radicals. Furthermore, using ABTS as a substrate could provide valuable insights, as it undergoes oxidation through a radical pathway.[444]

The designed peptides did not enhance the rate of *p*NPA hydrolysis beyond that of free imidazole. However, there may be a shift in selectivity similar to that observed in DMP oxidation, which was not tested. Therefore, it is necessary to record the hydrolysis rate of chiral esters, such as *p*-nitrophenyl esters of D- and L- amino acids, in the presence of apo- and holo-peptides. Hydrolytic β-hairpins utilize the interaction of His with Trp and Tyr to enhance the nucleophilicity of the imidazole moiety,[228-229] which can also be applied in WW domains. However, it is questionable whether the WW domains would be more reactive than the smaller β-hairpins. Additionally, small β-turns containing nucleophilic organocatalysts as side chains, such as *N*-methyl imidazole or pyridine, are known to catalyse stereoselective acyl transfer reactions, often in organic solvents.[435-436, 445-446] This approach could be applied to WW domains. It is important to note that while an increase in reaction rate is unlikely, the stereoselectivity may be enhanced.

Regarding CuAAC, the peptides designed cannot be used further. However, it is important to analyse in more detail the influence of pyruvate. It is recommended to test click reactions involving biomacromolecules such as proteins or nucleic acids, as well as *in vivo* labelling of cells, in order to develop a user-friendly CuAAC protocol.

The receptor array was successful in sensing glyphosate, but further optimization is required to determine the detection range. The analyte concentration of 4 μM used in the initial design

is already very low, and it is not uncommon for reported systems to work with analyte concentrations in the mM range. [398-400] This is due to the observation that some receptors only give a weak response with all tested analytes. To improve the array's detectable molecules, it is recommended to reduce the number of receptors to only the ones with significant change in fluorescence. Additionally, receptors that contain additional Ca(II) or Mg(II) can be added to the array. It is important to note that earth-alkali metal ions do not influence the peptide complex with Ni(II), Cu(II) or Zn(II), but they may interact with some analytes. If two different analytes interact with the receptor in the same way, they cannot be discriminated. However, if only one of the analytes interacts with Ca(II) or Mg(II), discrimination would be possible.

Due to the competition between the analyte and the receptor for the metal ion, it is important to have a wide range of peptides with varying metal ion affinities. This is because analytes can also have a diverse range of metal binding affinities. Peptides are advantageous over small organic dyes like TAMSMB, which require several days to weeks for synthesis using classic in-solution organic synthesis.[447] Peptide libraries can be quickly synthesized in a modular approach *via* SPPS. The analysis in this work examines the relationship between binding affinity and introduced mutations, providing a foundation for future designs.

In addition to pure substances, the biochemical tongue should also be challenged with complex mixtures. Serum samples from healthy and ill patients,[430] lysates of different bacteria[448] or cancer cell types[449] are of medicinal relevance. Foods and beverages are also popular analytes.[450-452] Due to its high sensitivity towards glyphosate, this method could be a useful detection method, which may be faster than approaches based on chromatography and mass spectrometry.[453] One significant limitation of these receptors is that they use tryptophan fluorescence, which is excited at 295 nm and measured at 345 nm. Both wavelengths are in the UV range, and almost all complex biological samples absorb in this region.[454] WW-CA(Coum) demonstrated that FRET-based receptors can be designed. However, WW-CA(Coum) also needs to be excited in the UV region. Therefore, a FRET pair with excitation and readout in the visible or near-infrared region should be introduced.[455] Although any fluorescent amino acid derivative can replace W34 without causing structural disturbance, W11 is crucial for the hydrophobic core. To attach the dye to the indole ring of W11, late-stage functionalization can be used, and several C-H activation methods are known for this purpose.[456]

This study focuses on the WW domain and the tryptophan zipper as scaffolds for peptide design. However, there are numerous other all β-sheet miniproteins,[49, 105] such as the SH3 domains[457] or the cold shock domains,[458] that can be used as a starting point for designing even more functional β-sheet miniproteins and expanding the toolbox of synthetic biology.

8 Material and Methods

The major part of Chapter 8 and the Appendix (Chapter 10) has been published in *ACS Synthetic Biology*,[266] *ChemBioChem*,[301, 316] *Chemistry – A European Journal*,[372] and *RSC Chemical Biology*,[401] mostly in the Supporting Information.

8.1 General

8.1.1 Reagents and solvents

Standard Fmoc-protected amino acids and *N,N*-diisopropylcarbodiimide (DIC) were acquired from *Iris Biotech GmbH* (Marktredwitz, Germany). Oxyma®, *N,N*-diisopropylethylamine (DIPEA), piperidine, H-Rink amide ChemMatrix® resin, MeCN (HPLC grade), trifluoroacetic acid (TFA, HPLC grade) and triisopropylsilane (TIPS) were acquired from *Merck KGaA* (Darmstadt, Germany). DMF (peptide synthesis grade) was purchased from *Fisher Scientific* (Loughborough, United Kingdom). All other solvents and reagents were at least *pro analysis* grade quality and were acquired from *Carbolution Chemicals GmbH* (St. Ingebert, Germany), *Carl Roth GmbH + Co. KG* (Karlsruhe, Germany), *Fisher Scientific* (Loughborough, United Kingdom), *Grüssing GmbH* (Filsum, Germany), *Honeywell* (Seelze, Germany), *Merck KGaA* (Darmstadt, Germany), *neoFroxx GmbH* (Einhausen, Germany), *SERVA Electrophoresis GmbH* (Heidelberg, Germany), *Th. Geyer GmbH & Co. KG* (Renningen, Germany) and *VWR International* (Fontenay-sous-Bois, France). Reagents and solvents were used as received.

8.1.2 Preparation of buffers and stock solutions, pH measurement

Ultrapure water was used for all analytical and biochemical experiments. It was provided by a *Sartorius arium® mini* lab water system. The pH was measured with a *Hanna instruments HI 2210* pH-meter equipped with a *HI 1330* pH electrode and adjusted using a NaOH-solution (1 M) or a HCl-solution (1 M), respectively. Buffer substances, including liquids, were weighed. For dilution to the final volume the solutions were transferred quantitatively into graduated flask. All aqueous solutions were filtered through a *CHROMAFIL Xtra* H-PTFE syringe filter with 0.2 µM pore size from *Machery-Nagel*. Buffers were prepared as 5 x stock solution containing 750 mM NaCl and 50 mM buffer substance (HEPES: pH 8.0; MOPS: pH 7.2, 6.6; MES: pH 6.4, 6.2, 6.0, 5.6; formate: pH 4.0; hydrogen sulfate: pH 2.5, 2.0).

8.1.3 Cleaning of glassware for analytical and biochemical experiments

For the cleaning ultrapure water and p. a. grade solvents were used. Beakers, graduated flask and measuring cylinders were rinsed with water (3 x) and isopropanol (3 x) and dried in a stream of N_2. Cuvettes were rinsed with water (3 x), 2% hellmanex (3 x), water (3 x), 60% nitric acid (1 x), water (10 x) and isopropanol (3 x) and dried in a stream of N_2. Thereafter, the

polished windows were cleaned outside by a lint free tissue soaked in isopropanol, rinsed with water and isopropanol and blow dry in a stream of N_2.

8.1.4 Lyophilisation

For freeze drying three different methods were used. Samples were generally frozen in liquid N_2 and placed under reduced pressure. To avoid contamination, the opening of the vessels was covered with lint free tissue fixed with rubber band. For larger amounts of aqueous solutions (>1.5 mL) polypropylene centrifugation tubes with a volume of 15 mL or 50 mL were used and after freezing the samples were lyophilized on *Christ Alpha 2-4-LSCbasic* connected to a *VACUUBRAND RZ 6* pump. For smaller amounts of aqueous solutions (<1.5 mL) polypropylene reaction tubes with a volume of 1.5 mL or 2 mL were used. After freezing, the samples were lyophilised on a *Savant Speedvac Concentrator* connected to a *Savant Refrigiated Condensation Trap* and a *VACUUBRAND RZ 6* pump. The volume of solutions containing volatile organic solvents like DCM was first evaporated under reduced pressure at 40 °C on a rotary evaporator using round bottom flask, until an oily residue is formed. After freezing, the samples were lyophilized in an evacuated desiccator connected with a *VACCUBRAND PC 520 NT* pump.

8.1.5 High performance liquid chromatography

Semi-preparative HPLC was performed on a *Jasco* chromatography system with a *PU-4180* pump, a *CO-4060* column oven, a *UV-4070* detector and a *LC-NetII/ADC Interface Box* or a *Shimadzu* chromatography system with a *CBM-40* system controller, a *DGU-405* degassing unit, a *LC-40D* solvent delivery module, an *SPD-M40* photo diode array detector and a *CTO-40S* column oven was used. A *VDS optilab VDSpher® PUR 100 C18-SE* (250 mm x 10 mm, 100 Å, 5 µm) or *Marcherey-Nagel Nucleodur® C18 ec* (250 mm x 10 mm, 100 Å, 5 µm) or *Marcherey-Nagel Nucleodur® C18 ec* (250 mm x 10 mm, 300 Å, 5 µm) column at a flow rate of 3 mL/min at 50 °C was used. Semi-preparative chromatograms were monitored at 220 nm and 280 nm. Analytical HPLC was performed using a *Hitachi Primaide* chromatography system containing a *Primaide Organizer*, a *1110* pump, a *1210* auto sampler, *1310* column oven and a *1430* diode array detector. A *VDS optilab VDSpher® PUR 100 C18-SE* (250 mm x 4.6 mm, 100 Å, 5 µm) column and a flow rate of 1 mL/min at 50 °C were used. Analytical chromatograms were monitored from 190 nm to 400 nm. As solvent system, water + 0.1% TFA (Buffer A) and MeCN + 0.1% TFA (Buffer B) was used. The general setup of gradients is described in Table 8-1. The exact composition is given in the description of the chromatograms.

Table 8-1: General setup of HPLC gradients. The percentages of Buffer B in Buffer A (*v*/*v*) are given. The specific values for x and y are given in the description of the chromatograms as following: (Gradient: x-y% B in A in 30 min).

Preparative	Isocratic 1	linear gradient	Isocratic 2	Isocratic 3
time / min	0 → 8	8 → 38	39 → 44	45 → 50
Composition	x%	x – y%	100%	x%
Analytical				
time / min	0 → 5	5 → 35	36 → 41	42 → 50
Composition	x%	x – y%	95%	x%

8.1.6 Mass spectrometry

Matrix-assisted laser desorption ionisation time-of-flight mass spectrometry (MALDI-TOF MS) was performed on a *Bruker Autoflex Speed*. 1 µl of the matrix 2,5-dihydroxybenzoic acid or Super-DHB, a 9:1 (*w*/*w*) mixture of 2,5-dihydroxybenzoic acid and 2-hydroxy-5-methoxybenzoic acid (20 mg/mL in 3:7 buffer A/buffer B) was mixed with 1 µl of the sample, pipetted onto the target plate and air dried. The mass spectra were processed with *mMass*.[459]

Electrospray ionisation (ESI) was performed on an ion cyclotron resonance Bruker Apex-Qe.

8.1.7 UV/Vis spectroscopy (general settings)

UV/Vis spectra were recorded at room temperature (20 °C to 25 °C) on an *IMPLEN NP80* nanophotometer using a cuvette or the drop function. Settings for cuvette: pathlength: 10 mm, wavelength range: 200 nm to 900 nm, baseline correction at 750 nm, smoothing: off, manual dilution: 1. Setting for drop function: pathlength: 0.67 mm, wavelength range: 200 nm to 900 nm, baseline correction at 750 nm, smoothing: off, manual dilution: 1. In the spectra measurement mode, specific wavelengths can be selected. In the kinetic measurement mode, a wavelength has to be selected, which is used for monitoring. Furthermore, the total time and the time interval, at which datapoints are collected, can be set. Details on the assays based on UV/Vis spectroscopy are given in the following Chapters.

8.1.8 Circular dichroism spectroscopy (general settings)

CD measurements were performed on a *Jasco J-1500* (or *J-810*) CD spectrometer, equipped with *Jasco PTC-510* (or *PTC-423S*) Peltier thermostatted rectangular cell holder. The measuring chamber was flushed constantly with N_2.

Settings (*J-1500*): data interval: 0.1 nm, scanning speed: 100 nm/min, CD scale: 2000 mdeg/1.0 dOD, D.I.T: 2 s, bandwidth: 1 nm.

Settings (*J-810*): data pitch: 0.1 nm, scanning speed: 100 nm/min, sensitivity: low, response: 2 s, bandwidth: 1 nm. Details on the assays based on CD spectroscopy are given in the following chapters.

8.1.9 Fluorescence spectroscopy (general settings)

Fluorescence measurements were performed on a *Jasco FP8500* spectrofluorometer or *BMG LABTECH CLARIOstar Plus* at room temperature (20 °C to 25 °C).

Settings (*FP8500*): measurement range: 300 – 500 nm, data interval: 0.5 nm, ex. Wavelength: 295 nm, ex. bandwidth: 1 nm, em. bandwidth: 2.5 nm or 5 nm, response: 1 s, sensitivity: high, scan speed: 200 nm/s, auto gain: on, filters: not used.

Settings (*CLARIOstar Plus*): endpoint mode, excitation wavelength: 295 nm, excitation bandwidth: 10 nm, dichroic filter: 320 nm, emission wavelength, bandwidth and gain: depend on assay, settings are given in the following chapters, focal height: 4.4 mm, scan mode: orbital averaging, scan diameter: 4 mm, No. of flashes per well: 64, top optic was used, settling time: 0.5 s, reading direction: bidirectional, horizontal left to right, top to bottom.

Details on the assays based on UV/Vis spectroscopy are given in the following chapters.

8.1.10 NMR spectroscopy of small organic molecules

Products of organic synthesis were prepared for NMR spectroscopy by dissolving them in DMSO-d_6 (^{1}H-NMR spectra referenced at 2.50 ppm, ^{13}C-NMR spectra at 39.52 ppm). Borosilicate NMR tubes with a diameter of 5 mm were used. ^{1}H-NMR, ^{13}C-NMR, ^{1}H-^{1}H-COSY and ^{1}H-^{13}C-HSQC spectra were recorded using a *Bruker Avance III 600* spectrometer or a *Bruker Avance III 400* spectrometer. A *Bruker Avance III 300* spectrometer was used to obtain ^{1}H-NMR spectra of already known compounds to confirm purity and identity.

Spectra processing and analysis was performed using *TopSpin 3.6.1* and *MestReNova 14.1.2*. Signal multiplicities were abbreviated with s (singlet), d (doublet), t (triplet), q (quartet) and m (multiplet).

8.1.11 IR spectroscopy

ATR-IR spectroscopy was performed on the *FT/IR-4600* Fourier transformation infrared spectrometer from *Jasco*. Spectra were recorded in a range from 500 to 4000 cm^{-1} with a resolution of 4 cm^{-1}.

8.1.12 Melting point measurement

The melting point of solid substances was determined using a melting point meter *M5000* by *Krüss* in a 1 mm capillary tube.

8.1.13 Thin layer and column chromatography

Thin layer chromatography (TLC) was performed to monitor the reaction. *Merck TLC Silica gel 60 F_{254}* on aluminium foil was used. The spots were visualized with UV-light (254 nm). Staining was performed with diluted sulfuric acid to detect Dmt protected compounds.

Column chromatography was performed with *Merck Silica gel 60* (0.040 to 0.063 mm). The collected fractions were analysed with TLC.

8.1.14 Software for data analysis and visualization

Data were analysed with *Anaconda 2022.05 (Python 3.9)*, *OriginPro® b9.5.1.195* and *Microsoft Excel Version 2202* if not stated otherwise. Peptide structures were visualized with *UCSF Chimera 1.14*.[460] Chemical structures were drawn with ChemDraw 19.0.

8.2 Peptide synthesis and characterization

8.2.1 Automated solid phase peptide synthesis

Peptides were synthesized on a microwave-assisted peptide synthesizer (*CEM Liberty Blue*, see Appendix, Chapter 10.2 for detailed settings and conditions for each individual peptide). Preloaded H-Gly-HMPB ChemMatrix® resin, H-Rink-Amide ChemMatrix® resin or Fmoc-Rink-Amide MBHA polystyrene resin was used as solid support. Prior to synthesis, the resin was swollen in DMF for at least 10 min. Fmoc protected amino acids were used as 0.2 M solution in DMF. Diisopropyl carbodiimide (DIC) dissolved in DMF (0.5 M) was used as activator, and Oxyma® solution in DMF (1.0 M) plus 0.1 M DIPEA was used as the activator base. A solution of piperidine/DMF 1:4 *v*/*v* was used to remove the Fmoc protecting group. After synthesis the resin was transferred to *BD* syringes equipped with a PE frit. For *N*-terminal acetylation the peptide resin was treated with acetic anhydride (0.5 mL) in DMF (4.5 mL) for 10 min, then washed with DMF (3 x 5 mL), MeOH (3 x 5 mL) and DCM (6 x 5 mL) and finally dried under reduced pressure. In case the peptide is not acetylated, it was directly washed and dried.

8.2.2 Cleavage and deprotection

Cleavage of the peptide from the resin and final deprotection were carried out in *BD* syringes equipped with a PE frit using a cleavage cocktail containing trifluoroacetic acid (TFA) containing triisopropylsilane (TIPS) and water at room temperature. The final volume of the cleavage cocktail was 10 mL for 0.1 mmol scale and 1 mL for a 5 µmol scale deprotection. The detailed composition and incubation time is summarized in the Appendix, Chapter 10.3 for each peptide. The resin was filtered off and washed with TFA (2 x 5 mL for a 0.1 mmol scale, 2 x 1 mL for 5 µmol scale). The TFA was removed in a stream of nitrogen and the peptide was precipitated from ice-cold Et_2O (25 mL for a 0.1 mmol scale, 10 mL for a 5 µmol scale). The peptide was isolated by centrifugation. The pellet was washed with Et_2O (2 x 25 mL for a 0.1 mmol scale, 2 x 10 mL for a 5 µmol scale) and dissolved in 20% *v*/*v* acetonitrile/water + 0.1% TFA (20 mL per 0.1 mmol batch) and freeze-dried.

8.2.3 Peptide purification

Lyophilized peptides were dissolved in a mixture of A and B that is equal or lower the concentration of B in A of the used gradient and filtered through a *CHROMAFIL Xtra* H-PTFE syringe filter with 0.2 µM pore size from *Machery-Nagel* prior to injection (0.5 mL to 1.5 mL) into the semi-preparative HPLC. Fractions containing peptide were identified by MALDI-TOF MS. Analytical HPLC (5 µL of sample diluted with 45 µL of A, injection volume: 10 µL if not otherwise stated) was used to check purity. Fractions with a purity of at least 95% were pooled and lyophilized.

8.2.4 General handling of peptides

The used β-sheet peptides in this study are potentially prone to aggregation.

Lyophilized peptides are stored at - 20 °C. Crude peptides, dissolved in buffer A and B can be stored for several months at 4 °C. For HPLC purification the sample is vortexed, centrifuged and an aliquot is taken and filtered with a syringe filter prior to injection. The purified fractions should be lyophilized as fast as possible on the same day. If not, the fractions can be stored overnight at 4 °C. For concentration determination the lyophilised peptides are dissolved in ultra-pure water. Neutralisation or pH adjustment should be avoided and massively increase the chance of aggregation. Aliquotation and lyophilisation should be performed as fast as possible, storage should be avoided. In case the peptide solution is not fully used for aliquotation, buffer B should be added (at least 20%) before the sample is lyophilized. Repeated lyophilisation and re-dissolving in water of the same peptide sample cause aggregation. Peptide solution should not be frozen for storage and repeated freezing-thawing cycles have to be avoided.

Lyophilized peptide aliquots in polypropylene reaction tubes with defined quantity are dissolved first in ultra-pure water, vortexed and spun down. Then 5 x concentrated buffer stock is added and after vortexing and down-spinning other substances can be added. It is not recommended to dissolve lyophilized peptides directly in buffer solution, which can cause immediate aggregation. For assays, where peptide solution in water is required, the solution is prepared freshly and used immediately (in less than 1 h for WW domain variants, Trpzip2 variants are stable for several days if stored at 4 °C). Buffered peptide solution (up to 1 mM) can stand at room temperature for several days without changes. After addition of metal solution to buffered peptide solution an equilibration time of at least 15 min is required. Equilibration overnight is also possible.

Aggregated peptides and buffered solution containing peptides can be pooled and lyophilized. After dissolving in an appropriate amount of buffer A/B and filtration through a syringe filter it can be recycled by HPLC purification.

8.2.5 Peptide concentration determination using UV/Vis spectroscopy

Lyophilized peptides were dissolved in water and the concentration was determined by measuring the absorbance *A* at 280 nm. The extinction coefficient of the peptides were calculated from the weighted sum of the extinction coefficients $\varepsilon_{280\,nm}$ of Trp residues (5500 $M^{-1}cm^{-1}$) and Tyr residues (1490 $M^{-1}cm^{-1}$) using the Lambert-Beer-law Eq. (6), where *d* is the pathlength.[461]

$$c = \frac{A}{\varepsilon \cdot d} \tag{6}$$

In case the extinction coefficient of the peptide is unknown (CSY protected peptides, peptides containing chromophores), the amount was determined by weighing. The drop function of the spectrometer was used and 1 µL of peptide solution was pipetted on the pedestal.

8.2.6 Competitive titration using UV/Vis spectroscopy

Measurements were performed in a 1 cm quartz cuvette with a magnetic stirring bar containing a solution (2 mL) of 5 µM peptide, 5 µM TAMSMB ((2-(2-thiazolylazo)-4-methyl-5-(sulfomethylamino) benzoic acid)), 10 mM MOPS, pH 7.2, 150 mM NaCl. Each titration step consists of addition of, 2 µL of Titrant 1 (1 mM $CuSO_4$ in water) and 2 µL of Titrant 2 (20 mM MOPS, pH 7.2, 300 mM NaCl). The mixture was stirred for 4 min and equilibrated for 1 min. At the beginning and after each titration step a spectrum is recorded. The titration was repeated, until saturation was observed in the UV/Vis spectra. Three independent measurements were performed. The absorbance at 589 nm was plotted *versus* the Cu(II) concentration. For TAMSMB a K_d of 44 nM was assumed.[304] The dilution of peptide and TAMSMB concentration due to titration was taken into account. Therefore, the concentration of Cu(II), peptide and TAMSMB were calculated explicitly for each titration point. K_d values were determined by curve fitting using the DynaFit software[462] using Eq. (7) to (9).

$$\mathrm{P} + \mathrm{M} <==> \mathrm{PM} : \mathrm{Kd1\ dissoc} \tag{7}$$

$$\mathrm{PM} + \mathrm{M} <==> \mathrm{PMM} : \mathrm{Kd2\ dissoc} \tag{8}$$

$$\mathrm{M} + \mathrm{L} <==> \mathrm{ML} : \mathrm{Kd^*\ dissoc} \tag{9}$$

8.2.7 CD spectra measurement

CD spectra were recorded from 190 to 260 nm in 1 mm quarz cuvettes (*Starna*), which can be sealed with a PTFE stopper, at 20 °C. After placing the cuvette into the holder, the sample was left to equilibrate for 5 min prior to measurement. Ten spectra were recorded, and the data were accumulated. The measured ellipticity Θ (in mdeg) was converted to mean residue ellipticity [Θ] (in deg cm^2/(dmol res)) using Eq. (10),[250] where Θ_{Blank} is the blank signal, *c* is the peptide concentration in mol/L, *l* is the pathlength in mm, and *n* is the number of backbone

peptide bonds. Details on peptide and metal ion concentration as well as the used buffer are given in the Figure legends. Samples are in general prepared in polypropylene reaction tubes and transferred to the cuvette for measurement if not otherwise stated.

$$[\Theta] = \frac{\Theta - \Theta_{\mathrm{Blank}}}{c \cdot l \cdot n} \tag{10}$$

8.2.8 CD titration

General: In a 10 mm quarz cuvette (*Starna*), which can be sealed with a PTFE stopper, equipped with a magnetic stirrer, MOPS buffered titrant solution was added to MOPS buffered peptide solution (volume: 2 mL). For titration experiments the peptide solution is prepared in the cuvette by addition of water (800 µL), 25 µM peptide stock in water (800 µM) and 5x buffer stock (400 µL). Before the spectra were recorded from 220 to 240 nm, the solution was stirred for 10 min and paused for 1 min. The measured Θ was converted into [Θ] according to Eq. (10). The total peptide and titrant concentrations were corrected for dilution for each titration point and curve fitting was performed with the quadratic equation (11).[303]

$$Y(c) = Y_0 + S \cdot \frac{(c + [\mathrm{P}] + K_\mathrm{d}) - \sqrt{(c + [\mathrm{P}] + K_\mathrm{d})^2 - 4 \cdot [\mathrm{P}] \cdot c}}{2 \cdot [\mathrm{P}]} \tag{11}$$

In this case Y is the ellipticity at the wavelength of the maximum $[\Theta]_{max}$, c is the total metal ion concentration, K_d the dissociation constant, Y_0 the y-axis intercept, S the scaling factor and [P], the total peptide concentration. It should be noted that the often-used hyperbolic equation (12)

$$Y(c) = Y_0 + S \cdot \frac{c}{K_\mathrm{d} + c} \tag{12}$$

is only valid if the total peptide concentration is much lower than the K_d value. This is not the case for the peptides studied in this thesis. The peptide concentration used was in the µM range and the K_d values in the µM to fM range. Therefore, this equation was not used for fitting.[303]

Zn(II)/Ni(II)-Titration: Titrant: (2 mM $ZnSO_4$ or $NiSO_4$,10 mM MOPS, 150 mM NaCl, pH 7.2), titration steps (total volume of added titrant): 0, 2, 4, 6, 8, 10, 12, 14, 16, 20, 25, 30, 40, 60, and 100 µL, peptide solution: (10 µM peptide, 10 mM MOPS, 150 mM NaCl, pH 7.2).

Cu(II)-Titration: Two separate titrants had to be used because $CuSO_4$ was not stable in MOPS buffer and aggregated. Titrant 1: (20 mM MOPS, 300 mM NaCl, pH 7.2). Titrant 2: (4 mM $CuSO_4$). Titrant 1 and 2 were added consecutively to the peptide solution (10 µM peptide, 10 mM MOPS, 150 mM NaCl, pH 7.2) in the following steps, respectively (total volume of added titrant): 0, 1, 2, 3, 4, 5, 6, 7, 8, 9, 10, 12.5, 15, 20, 50 µL.

Zn(II)-Switch: Titrant 1: (2 mM $ZnSO_4$, 10 mM MOPS, 150 mM NaCl, pH 7.2). Titrant 2: (2 mM Na_2EDTA, 10 mM MOPS, 150 mM NaCl, pH 7.2). Titrants 1 and 2 (each 10 µL) were added

alternately to the peptide solution (10 µM peptide, 10 mM MOPS, 150 mM NaCl, pH 7.2). The $[\Theta]_{227\ nm}$ values were plotted against the ratio of [Zn(II)]/[EDTA].

pH-Switch: Titrant 1 (2 M $HCl_{(aq)}$). Titrant 2 (2 M $NaOH_{(aq)}$). Titrants 1 and 2 (each 10 µL) were added alternately to the peptide solution (10 µM peptide, 10 µM $ZnSO_4$, 10 mM MOPS, 150 mM NaCl, pH 7.2 or 10 µM peptide, 10 mM MOPS, 150 mM NaCl, pH 7.2). The $[\Theta]_{227\ nm}$ values were plotted against the ratio of [HCl]/[NaOH].

NaCl-Titration. Titrant: (3 M NaCl, 10 mM MOPS, pH 7.2), titration steps: 0, 25, 50, 100, 150, 200 µL. Peptide solution: (10 µM peptide, 10 µM $ZnSO_4$, 10 mM MOPS, pH 7.2). The experiment was repeated with a peptide solution without $ZnSO_4$. In this case, 10 µL of $ZnSO_4$ solution (2 mM) was added after the last titration point to prove the folding capability of the peptide. The $[\Theta]_{227\ nm}$ values were plotted against the NaCl concentration.

8.2.9 CD Thermal denaturation

Melting curves were recorded from 0 to 98 °C in 1 mm cuvettes using [Θ] at the maximum at 20 °C, with a temperature gradient of 1 °C/min. Data points were collected every 0.5 or 1 °C.

Several procedures how to fit thermal denaturation curves were reported and give slightly different results.[463] Most common is the two-state-model assuming that the folding-unfolding transition can be described as a temperature dependent equilibrium between a folded (F) and unfolded state (U) with an equilibrium constant *K* (Eq. (13)).[251]

$$\mathrm{F} \rightleftharpoons \mathrm{U} \quad \text{and} \quad K = \frac{[\mathrm{U}]}{[\mathrm{F}]} \tag{13}$$

The fraction of folded peptide α_F, which can adopt values between 1 (fully folded) and 0 (completely unfolded), can be described with a sigmoidal function (Eq. (14)):

$$\alpha_{\mathrm{F}}(T) = \frac{1}{1+K} = \frac{1}{1+\exp\left(-\frac{\Delta G}{R \cdot T}\right)} \tag{14}$$

with *T* the temperature in Kelvin, *R* the universal gas constant and Δ*G* the free enthalpy, which can be expressed as (Eq. (15)):

$$\Delta G = \Delta H \cdot \left(1 - \frac{T}{T_{\mathrm{m}}}\right) - \Delta C_p \cdot \left((T_{\mathrm{m}} - T) + T \cdot \ln\left(\frac{T_{\mathrm{m}}}{T}\right)\right) \tag{15}$$

with Δ*H* the enthalpy, T_m the melting temperature (temperature at which Δ*G* is zero) and ΔC_p the change in heat capacity between the folded and unfolded state by constant pressure.

Under experimental conditions, a signal, in this case the ellipticity at the maximum $[\Theta]_{max}$ is recorded which is assumed to be proportional to α_F. Also, the signal often does not start at 1 and end with 0. It is therefore necessary to add a term to consider the pre- and post-transition baseline (*A* and *B*):

$$[\Theta]_{\max} = A + (B - A) \cdot \alpha_{\mathrm{F}} \tag{16}$$

The two baselines can be assumed as a constant value, but depending on the protein, the baselines are temperature dependent and then it is appropriate to describe the baselines as linear function in the form of $A = a \cdot T + b$, $B = c \cdot T + d$, or in some cases as quadratic functions,[268] which did not yield meaningful values for the peptides in this study. Finally, it is known, that ΔC_p cannot be determined by CD thermal unfolding accurately, but only by differential scanning calorimetry (DSC).[251] In case ΔC_p is known, it can be fixed to this value, but this is not the case here, therefore it was set to zero. Taking these considerations into account yields Eq. (17), which was used for curve fitting.

$$[\Theta]_{\max}(T) = A + \frac{B - A}{1 + \exp\left(\left. -\Delta H \cdot \left(1 - \frac{T}{T_{\mathrm{m}}}\right) \right/ R \cdot T \right)} \tag{17}$$

This equation yields T in K, but in biological context the Celsius scale is more convenient. Therefore T [K] = (t [°C] +273.15) K was introduced into the fitting function, which is common practice.[251]

Furthermore, this model is only valid for a two-state folding-unfolding mechanism, which is valid for monomeric apo peptides, but not valid anymore in case of peptide-metal or peptide ligand complexes, since the peptide and metal ion concentration and the temperature dependent binding affinity of the metal ion to the folded as well as unfolded state has to be taken into account. The resulted equations are reported, but contain several parameters, which have to be determined by other methods or guessed before the function can be fitted to the data or can be used to simulate curves.[307, 464-466] This is beyond the scope of this thesis and the use of Eq. (17) therefore only lead to approximate values for T_{m} and ΔH. Therefore, T_{m} should be seen as the midpoint of transition and a measure to estimate the thermostability of a peptide or peptide metal-ion complex. ΔH is a measure for the steepness of the transition. High values led to a steep transition and low values to a broad transition.

The results of Eq. (17) strongly depend on the choice of baseline, which is a known problem.[318] As an alternative, it was proposed to obtain the first derivative of the melting curve, which gives a bell-shape curve. Unfortunately, the fitting function based on the van't Hoff equation, which was presented in the paper of John and Weeks[318] contains a small mistake. Therefore, the equation will be derived explicitly here.

Similar to the case discussed before, it is assumed, that ΔC_p is zero. Therefore, the equilibrium constant K can be expressed with Eq. (18):

$$K = \exp\left(-\frac{\Delta G}{R \cdot T}\right) = \exp\left(-\frac{\Delta H \cdot \left(1 - \frac{T}{T_\mathrm{m}}\right)}{R \cdot T}\right) = \exp\left(\frac{\Delta H}{R} \cdot \left(\frac{1}{T_\mathrm{m}} - \frac{1}{T}\right)\right) \quad (18)$$

Then the derivative of the fraction folded is formed (Eq. (19)):

$$\frac{d\alpha_\mathrm{F}(T)}{dT} = \frac{d}{dT}\frac{1}{1+K} = -\frac{\Delta H}{R \cdot T^2} \cdot \frac{K}{(1+K)^2} \quad (19)$$

It is further assumed, that the derivative of the measured signal $[\Theta]_{max}$ is proportional to the derivative of the fraction folded. Therefore, *A* is introduced as a scaling factor and *B* is introduced as the *y*-axis offset of the bell-shaped curve yielding Eq. (20), which was used for fitting the data.

$$\frac{d[\Theta]_\mathrm{max}(T)}{dT} = B + A \cdot \frac{d\alpha_\mathrm{F}(T)}{dT} \quad (20)$$

Bell-shaped curved data can also be fitted with an empirical Gaussian function without physical meaning (Eq. (21)).[317]

$$\frac{d[\Theta]_\mathrm{max}(T)}{dT} = B + A \cdot \exp\left(-\frac{(T - T_\mathrm{m})^2}{2 \cdot w^2}\right) \quad (21)$$

B is the offset, *A* the amplitude, *w* the width and T_m is melting temperature, which in this model is defined as the extremum of the curve.

The derivative approach was criticized, because the extremum of the bell-shaped curve does not have to corresponds to the true T_m value, which is defined as the temperature, at which the concentration of folded and unfolded state is equal. Additionally, the claim that this method eliminates the pre- and post-transitional baselines is only valid, if those are perfectly linear. Furthermore, the disadvantage of numerical derivatives is the increases in noise.[467] The modified van't Hoff equation (20), which is also based on the two-state assumption, therefore exhibits all of the drawbacks discussed for Eq. (17).

A comparison of the published papers cited in Chapter 2.3.2 and 2.5.2, in which T_m values for WW domains and β-hairpins are reported, reveals that there is no standard approach, with each laboratory employing its own fitting protocol. Consequently, in this thesis the thermal denaturation data was fitted using all four approaches and the resulting plots are shown in the Appendix, Chapter 10.8, with the exception of WW domains, where the numerical 1st derivative of the thermal denaturation data was found to be too noisy to be useful. In the Results and Discussions (Chapter 4), the best fits were presented. For all WW-CA variants, the best results were obtained using Eq. (17) and assuming constant pre- and post-transition baselines. In case of hPin1$_{WW}$-Nle, very pronounced linear pre- and post-transition baselines were observed, and Eq. (17) gave the best results. In contrast, Eq. (17) was not optimal for fitting

the thermal denaturation curves of the tryptophan zipper peptides. Consequently, the 1st derivative was fitted with Eq. (20) and Eq. (21), which yielded comparable results.

8.2.10 Determination of the acidity constant using CD spectroscopy

Spectra measurement and thermal denaturation experiments were conducted under the following conditions: 100 µM peptide, 100 µM $ZnSO_4$,10 mM buffer substance, 150 mM NaCl. Buffer substances for pH 2, 2.5: hydrogen sulfate, pH 4: formate, pH 5.6, 6.0, 6.2, and 6.4: MES, pH 6.6, 7.2: MOPS, pH 8.0: HEPES. To determine the pK_a value, the $[\Theta]_{227\,nm}$ values were plotted against the corresponding pH values and fitted using a modified Henderson-Hasselbalch equation (22).[122]

$$[\Theta]_{227\,nm}(\mathrm{pH}) = A + \frac{B - A}{1 + 10^{(\mathrm{pH} - \mathrm{p}K_a)\cdot C}} \tag{22}$$

A and *B* are the pre- and post-transition baselines and *C* the steepness of transition.

8.2.11 Fluorescence spectra measurement

Measurements were performed with 10 µM peptide, 10 µM metal salts (if present), 10 mM MOPS, pH 7.2, 150 mM NaCl. Pure buffer was used as blank. The samples were prepared in polypropylene tubes and incubated for at least 12 h at room temperature (20 °C to 25 °C). For measurement an aliquot (200 µL) was transferred in *Hellma* ultra-micro quartz cuvettes (10 mm x 2 mm).

8.2.12 Fluorescence titration

The WW domain and Trpzip derived peptides were sensitive to photobleaching. Therefore, titrations cannot be performed by continuous addition of metal salt solution to the peptide solution in the cuvette and repeated spectra measurement. Therefore, fluorescence titration was performed either by recording single spectra as described in the previous section with varying metal ion concentrations in cuvettes or in 96 well-plates (*Greiner Bio-One*, black, non-binding, flat bottom) on a *BMG LABTECH CLARIOstar Plus* at room temperature (20 °C to 25 °C). Samples were prepared in polypropylene reaction tubes und equilibrated for at least 12 h at room temperature (20 °C to 25 °C) before measurement. Every well was filled with 100 µL solution containing 4 µM peptide, 4 µM EDTA or HEDTA (if present) 0 to 40 µM metal ions, 10 mM MOPS, pH 7.2, 150 mM NaCl. A plate containing only buffer was used as blank. The intrinsic tryptophan fluorescence was measured at an emission wavelength of 348 nm (WW-CA-Nle), 342 nm (WW-CA-min), 340 nm (WW-CA-ANG) and 343 nm ($Tz2H_3$). The emission bandwidth was set to 10 nm. A gain of 2000 (WW-CA-Nle + Ni(II) or Cu(II)), 1800 (WW-CA-Nle + Zn(II), WW-CA-min or WW-CA-ANG + Ni(II) or Cu(II)) and 1600 (WW-CA-min or WW-CA-ANG + Zn(II)) was used. For $Tz2H_3$ the gain was set to 1800 (Zn(II)), 2022 (Ni(II))

and 1800 or 2022 (Cu(II)). The data was then fitted to Eq. (11), in which *Y* is the blank-corrected fluorescence intensity (F_{max}).

8.2.13 Isothermal titration calorimetry

Titrations were performed with a *Malvern MicroCal PEAQ-ITC* instrument. In the cell, a solution containing 10 µM peptide, 10 mM MOPS, pH 7.2, 150 mM NaCl was placed and titrated with 200 µM $ZnSO_4$, 10 mM MOPS, pH 7.2, 150 mM NaCl using following parameter: 1st injection: 0.2 µL (data discarded), followed by 12 injections with a volume of 2 µL each, stirring speed: 750 rpm, initial delay: 60 s, injection spacing: 150 s, injection duration: 4 s, reference power: 10 µcal/s, feedback: high, temperature: 20 °C. Titrant to buffer titration was performed to determine the background reaction. Two independent experiments were performed. Data processing and analysis was performed with the provided software by Malvern. The data was background and baseline corrected and then fitted using a model for a single set of identical binding sites.

8.2.14 NMR spectroscopy of peptides

These NMR experiments were performed in collaboration with the Kovermann laboratory (University of Konstanz). One-dimensional ^{1}H as well as two-dimensional ^{1}H-^{13}C HSQC spectra were conducted on a *Bruker Avance III* 600 MHz setup equipped with a CP-TCI cryo probe. Two-dimensional ^{1}H-^{15}N HSQC spectra have been acquired on a *Bruker Neo* 800 MHz setup equipped with a *CP-QCI* cryo probe. Temperature calibration has been done according to the known dependence of chemical shifts of methanol (275 K ≤ *T* ≤ 300 K) as well as ethylene glycol (*T* ≥ 300 K). Direct referencing of the proton dimension of all spectra acquired in this study has been achieved by using the resonance signal of sodium 3-(trimethylsilyl)proprionate (TMSP). NMR spectra were analysed with the software *MestReNova 14.1.2*. The following buffers have been used: 10 mM buffer substance (pH 7.2: MOPS, pH 2.0: hydrogen sulfate), 150 mM NaCl, 5% *v/v* D_2O. A peptide concentration of 1 mM was used. In case Zn(II) was present, a concentration of 1 mM $ZnSO_4$ was used. Due to the usage of MOPS buffer additional signals are visible at 3.90, 3.03 and 2.11 ppm.

Diffusion experiments of WW-CA-Nle were performed with pulse-field gradient NMR spectroscopy. NMR data were recorded for 21 different gradient strengths ranging between 0.06 – 0.6 $Tm^{-1}(2\pi)^{-1}$ at 298 K. The diffusion time was set to 80 ms and a gradient length of 3 ms was used. The diffusion coefficients were determined with the Stejskal-Tanner equation Eq. (23).[468]

$$f(G) = A \cdot \exp[-\gamma^2 G^2 \delta^2 (2\pi^{-1})^2 D(\Delta - \delta/3)] \quad (23)$$

where *γ* is the gyromagnetic ratio for protons, *G* is the gradient strength, *d* is the length of the gradient, Δ is the diffusion time and *D* is the diffusion coefficient. For thermal unfolding

monitored by NMR spectroscopy two methods were used. First, the ratio of the integral of the backbone amide region (A_{NH}, 9.75 to 7.70 ppm) and the aliphatic region (A_{CH}, 1.92 to -1.00 ppm) were plotted against the temperature. Second, the native fraction f_n was calculated by Eq. (24).[273]

$$f_n = \frac{F_n}{F_n + F_{n+u}} \tag{24}$$

F_n is the integral of the high field shifted aliphatic signals which are typical for the native conformation and F_{n+u} is the integral of the aliphatic region which represents the folded as well as unfolded conformation and can be taken as an estimation of the increase of unfolded conformation. Four combinations of F_n and F_{n+u} were tested to prove that the trend is not an artefact of choosing the integration limits (see Chapter 4.1.4.2).

8.2.15 Electron paramagnetic resonance spectroscopy

These EPR experiments were performed in collaboration with the Comba Laboratory (Heidelberg University). X-band electron paramagnetic resonance (EPR) spectra were recorded on a *Bruker ElexSys e500* equipped with a *F-70 Sumitomo* cryogenics helium cryostat, *Bruker ER4116-DM* resonator, *Oxford LLT 650* low loss transfer tube, and an *Oxford ITC503* temperature controller. EPR tubes (3 mm, quartz) were filled with 120 µL of sample (416.67 µM peptide, 400 µM $CuSO_4$, 300 g/L glycerol, 10 mM MOPS, pH 7.2, 150 mM NaCl). The samples were frozen in liquid nitrogen and measured below 100 K. The magnetic field *B* was recorded and converted to *g* using Eq. (25)

$$g = \frac{h}{\mu_B} \cdot \frac{v}{B} = 7.144775 \cdot 10^{-7}\,\mathrm{G{\cdot}s} \cdot 10^{9} \cdot \frac{v\,[\mathrm{GHz}]}{B[\mathrm{G}]} \tag{25}$$

with *h* the Planck constant, μ_B the Bohr magneton and *v* the microwave frequency (WW-CA-Nle: 9.630070 GHz, WW-CA-min: 9.630025 GHz, WW-CA-ANG: 9.630462 GHz, $Tz2H_3$: 9.631500 GHz). The spin Hamiltonian parameters were obtained by simulation of the experimental data with the *XSophe/XEPR* (version 1.1.4 and 2.6b.86) software package and *EasySpin 5.2.35* included as an add-on in *MATLAB R2022b*.[309]

8.2.16 Structure prediction

The predicted structures were obtained in the *ColabFold 1.5.3* version of *AlphaFold2* with MMseqs2.[311] No template was passed to the protocol and all predicted structures were minimized with Amber before output. All other parameters were left on the default recommended values.

8.3 Assays to determine enzymatic activity

8.3.1 Hydrolysis assay

Measurements were performed in disposable cuvettes (UV-cuvette micro, centre height 8.5 mm, *d* = 1 cm from *Brand*). Following stock solution were used: buffer stock 5x containing 50 mM buffer substance (pH 8.0: HEPES, pH 7.2: MOPS, pH 6.0: MES, pH 4.0: formate) and 750 mM NaCl, catalyst in water: 100 µM peptide or 300 µM imidazole, Zn(II)-stock: 100 µM or 1 mM $ZnSO_4$, substrate stock: 20 mM *p*NPA in MeCN (prepared freshly every day). Solutions were added in the following order): water, catalyst stock (if present), buffer stock, Zn(II) stock (if present) and mixed by pipetting up and down. Finally, *p*NPA stock was added, mixed for 30 s and the absorbance at 348 nm, the isobestic point of the product *para*-nitrophenole ($\varepsilon_{348\,nm}$ = 5000 M^{-1} cm^{-1}),[257] was recorded every 5 s for 10 min. The final volume was 200 µL. In case no or a lower amount of substrate stock was added, e.g. the blank sample, pure MeCN has to be added, to keep the MeCN concentration at 5% *v*/*v*. Details on final concentration are given in the description of the Figures in Chapter 4.4.1, respectively. The slopes *m* were determined by linear regression of the linear region of the curve. Calculation of the *v*, k_{obs} and k_2 was discussed previously in Chapter 4.4.1.

8.3.2 Phenol oxidase assay

Measurements were performed in disposable cuvettes (UV-cuvette micro, centre height 8.5 mm, *d* = 1 cm from *Brand*) or polypropylene reaction tubes (for HPLC monitoring). Following stock solution were used: buffer stock 5x containing 50 mM buffer substance (pH 8.0: HEPES, pH 7.2: MOPS) and 750 mM NaCl, 50 µM peptide in water, Cu(II)-stock: 100 µM $CuSO_4$, substrate stock: 10 mM DMP in water containing 10% DMSO, 50 mM H_2O_2 in water. Solutions were added in the following order): water, peptide stock (if present), buffer stock, Cu(II) stock (if present) and mixed by pipetting up and down. Finally, DMP stock and H_2O_2 stock (if present) was added, mixed for 30 s and the absorbance of the oxidation product 3,3',5,5'-tetramethoxydiphenylquinone at 477 nm ($\varepsilon_{477\,nm}$ = 14800 M^{-1} cm^{-1}),[351] was used to calculate the kinetic parameters. [Catalyst] corresponds to the concentration of Cu(II) and [Substrate] is the DMP concentration. The final volume was 100 µL. In case no or a lower amount of substrate stock was added, e.g. the blank sample, pure DMSO had to be added, to keep the DMSO concentration at 1% *v*/*v*. Details on final concentration are given in the description of the Figures in Chapter 4.4.2, respectively. Data analysis was performed similar to the hydrolysis assay. For HPLC analysis, after an amount of time (specified in the Figures in Chapter 4.4.2) an aliquot (20 µL) was taken and quenched with 1 mM Na_2EDTA solution (20 µL) prior to injection (10 µL).

8.3.3 Cu(I)-catalysed azide-alkyne cycloaddition reaction

Samples were prepared in polypropylene reaction tubes. Following stock solutions were prepared: MOPS buffer pH 7.2 stock 5x (50 mM MOPS, 750 mM NaCl), peptides in water (100 mM), THPTA in water (2 mM and 5 mM), $CuSO_4$ in water (2 mM), pyruvate in water (100 mM), sodium ascorbate in water (100 mM, freshly prepared), Fmoc-Lys(N_3)-OH in DMSO (8 mM) and alkyne in DMSO (8 mM and 12 mM). The solutions were added in the following order: water, buffer stock, peptide or THPTA, $CuSO_4$. The tube was vortexed, spun down and incubated for 15 min to ensure formation of the THPTA- or peptide-Cu(II) complex. In case of higher peptides concentration (125 µM) in the final mixture is required, the appropriated amount of peptide stock equivalent to 25 nmol was added, then the water was completely removed by lyophilisation and other solutions were added on top. After incubation, the substrate stocks in DMSO were added and mixed well. To start the reaction, sodium ascorbate stock was added and again the sample was vortexed and spun down. The final volume was 200 µL and the DMSO concentration 25% *v*/*v*. Details on final concentration are given in the description of the Figures in Chapter 4.4.3, respectively. To follow the course of reaction, 20 µL aliquots were taken after an amount of time (specified in the Figures in Chapter 4.4.3), quenched with 20 µL of a solution of Na_2EDTA in water containing 25% *v*/*v* MeCN (75 mM) and 10 µL was injected into analytical HPLC. Gradients are given in the Figure legends. As a control, solutions contain substrates, but no catalyst were used.

8.4 Sensor design

8.4.1 Synthesis of Fmoc-Hse-OH

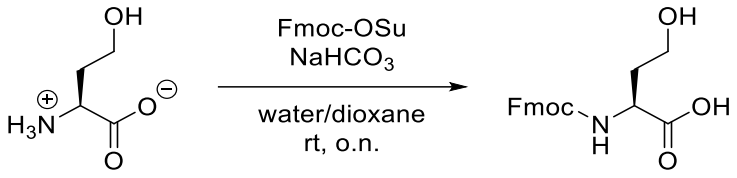

H-Hse-OH **Fmoc-Hse-OH**

Homoserine (2.00 g, 16.8 mmol, 1.00 equiv.), Fmoc-OSu (5.66 g, 16.8 mmol, 1.00 equiv.) and $NaHCO_3$ (2.75 g, 32.7 mmol, 1.95 equiv.) were dissolved in water (55 mL) and dioxane (65 mL). The solution was stirred overnight at rt. Dioxane was removed under reduced pressure. The mixture was transferred into a separating funnel with water (200 mL), 5% $NaHCO_3$ in water (150 mL) and DCM (150 mL). The DCM phase was separated. The aqueous phase was washed with chloroform (50 mL). Since the chloroform phase could not be separated, diethyl ether (600 mL) was added, and the phases were separated. The aqueous phase was washed one additional time with diethyl ether (200 mL). Citric acid (50 g) was added to the aqueous phase. The aqueous phase was extracted with EtOAc (3 x 150 mL). The combined organic phases were washed with brine (100 mL), dried over Na_2SO_4 and filtered.

The solvent was removed under reduced pressure to give an oil, which was dissolved in EtOAc (25 mL). Crystallisation occurred overnight at −21 °C. The colourless solid was filtered and washed with ice-cold EtOAc. The product was dried in a desiccator under reduced pressure. The mother liquor was evaporated under reduced pressure and recrystallization was performed as stated. The crystal fractions were combined (4.34 g, 12.7 mmol, 76%).

TLC: R_f (DCM/MeOH/HCOOH 10:1:0.1) = 0.44.

ESI-MS: $[M-H]^-$ calc. 340.1190, found 340.1179.

^{1}H NMR (400 MHz, DMSO-d$_6$) δ = 12.50 (s, 1H, COOH), 7.89 (d, 2H, J = 7.5 Hz, H_{ar}), 7.73 (dd, 2H, J = 7.4, 1.1 Hz, H_{ar}), 7.57 (d, 1H, J = 8.0 Hz, NH), 7.42 (td, J = 7.5, 1.2 Hz, 2H, H_{ar}), 7.33 (t, 2H, J = 7.5 Hz, H_{ar}), 4.56 (s, 1H, OH), 4.33 - 4.16 (m, 3H, CH-CH_2 Fmoc), 4.15 - 4.05 (m, 1H, α-CH), 3.54 - 3.39 (m, 2H, γ-CH_2), 1.94 - 1.67 (m, 2H, β-CH_2) ppm.

^{13}C NMR (101 MHz, DMSO-d$_6$) δ = 174.23 (COOH), 156.11 (NH-COO Fmoc), 143.81 (C_{ar}), 140.69 (C_{ar}), 127.61 (HC_{ar}), 127.05 (HC_{ar}), 125.25 (HC_{ar}), 120.08 (HC_{ar}), 65.60 (CH-**C**H_2 Fmoc), 57.23 (γ-CH_2), 50.83 (α-CH), 46.62 (**C**H-CH_2 Fmoc), 33.82 (β-CH_2) ppm.

The analytical data are identical to the literature.[469]

8.4.2 Synthesis of Fmoc-Hse(Dmt)-OH

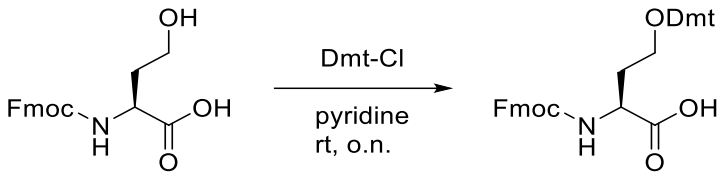

Fmoc-Hse-OH **Fmoc-Hse(Dmt)-OH**

Fmoc-Hse-OH (1.00 g, 2.93 mmol, 1.00 equiv.) was dissolved in anhydrous pyridine (15 mL) in a N_2 atmosphere. Dmt-Cl (2.02 g, 5.96 mmol, 2.03 equiv.) was added in four portions in 30 min intervals and the mixture was stirred overnight at rt. The reaction mixture was transferred with MeOH (3 x 25 mL) into a round bottom flask and the solvent was evaporated under reduced pressure. The residue was dissolved in EtOAc (200 mL), filtered and washed with water (3 x 100 mL) and brine (100 mL) and dried over Na_2SO_4. After filtering, the solvent was evaporated under reduced pressure. The viscous yellow oil was kept at −21 °C. The crude product was purified by column chromatography (silica gel, DCM:MeOH:DIPEA (95:4:1)). Product fractions were identified by TLC and the solvent evaporated under reduced pressure. The remaining oil was frozen in liquid nitrogen and freeze-dried in vacuum to yield a colourless foam (1.94 g, 2.51 mmol, 86% as DIPEA salt).

TLC: R_f (DCM/MeOH/DIPEA 95:4:1) = 0.20.

ESI-MS: $[M+Na]^+$ calc.: 666.2462, found 666.2462.

IR (ATR): $\tilde{\nu}$ = 3398, 2964, 1712 (*v* CO), 1607 (*v* CO), 1507, 1443, 1386, 1245, 1174, 1057, 1030, 826, 759, 738, 701, 580 cm^{-1}.

^{1}H NMR (400 MHz, DMSO-d_6) δ = 7.88 (d, 2H, *J* = 7.6 Hz, H_{ar}), 7.67 (t, 2H, *J* = 7.6 Hz, H_{ar}), 7.45-7.13 (m, 14H, NH DIPEA, H_{ar}), 7.09 (s, 1H, α-NH), 6.86-6.79 (m, 4H, H_{ar}), 4.24 (d, 2H, *J* = 7.8 Hz, CH-C**H**$_2$ Fmoc), 4.21-4.14 (m, 1H, C**H**-CH_2 Fmoc), 4.09-4.00 (m, 1H, α-CH), 3.68 (d, 6H, *J* = 4.1 Hz, OCH_3), 3.17-3.04 (m, 5H, C**H**-CH_3 DIPEA, γ-CH_2), 3.03-2.93 (m, 1H, γ-CH_2), 2.58 (q, 4H, *J* = 7.1 Hz, C**H**$_2$-CH_3 DIPEA), 2.11-1.98 (m, 1H, β-CH_2 Hse), 1.90-1.73 (m, 1H, β-CH_2), 1.05-0.95 (m, 30H, CH_3 DIPEA) ppm.

^{13}C NMR (101 MHz, DMSO-d_6) δ = 173.76 (COO^-), 157.91 (C_{ar}OMe), 155.73 (O-C(O)-NH), 145.15 (C_{ar}), 143.82 (C_{ar}), 140.66 (C_{ar}), 135.97 (C_{ar}), 129.56 (C_{ar}), 127.60 (C_{ar}), 127.01 (C_{ar}), 126.46 (C_{ar}), 125.19 (C_{ar}), 120.04 (C_{ar}), 113.01 (C_{ar}), 85.24 ($C(Ph)_3$), 65.54 (CH-**C**H_2 Fmoc), 59.76 (γ-CH_2), 54.90 (O-CH_3), 51.98 (α-CH), 48.91 (**C**H-CH_3 DIPEA), 46.66 (**C**H-CH_2 Fmoc), 31.87 (β-CH_2), 19.79 (CH-**C**H_3 DIPEA), 15.65 (CH_2-**C**H_3 DIPEA) ppm.

8.4.3 Late-stage functionalisation

The WW-CA variant containing Hse was synthesized by SPPS. Details are summarised in the Appendix, Chapter 10.3. Dry resin loaded with 5 µmol peptide was placed in a 2 mL syringe reactor with a PE frit. To remove the Dmt protecting group, the resin was washed with 1% TFA in DCM (5 x 1 mL) and DCM (10 x 1 mL). The peptide was directly iodinated afterwards to prevent depsipeptide formation. The resin was not dried and used directly in the next step.

For iodination, methyltriphenoxyphosphonium iodide (115 mg, 0.25 mmol, 50 equiv.) was dissolved in dry DMF (0.5 mL) under N_2 atmosphere. The resin was incubated with the iodination reagent for 20 min under shaking. The solution was removed, and the resin was washed with DMF (5 x 1 mL) and DCM (10 x 1 mL) and dried under reduced pressure. The iodinated peptide is stable for several days in an evacuated desiccator, but it is recommended to continue with the next step as soon as possible.

For nucleophilic substitution, 7-mercapto-4-methylcoumarin (48.1 mg, 0.25 mmol, 50 equiv.) and DIPEA (42.5 µL, 0.25 mmol, 50 equiv.) was dissolved in dry DMF (1 mL) in an N_2 atmosphere and added to the iodinated peptide on resin. The mixture was shaken overnight at room temperature (20 °C to 25 °C). After reaction, the solution was removed, the resin was washed with DMF (5 x 1 mL) and DCM (10 x 1 mL) and dried under reduced pressure.

Cleavage and final deprotection was performed as described above.

8.4.4 Differential sensing

Experiments were performed in 96 well-plates (*Greiner Bio-One*, black, non-binding, flat bottom) on a *BMG LABTECH CLARIOstar Plus* at room temperature (20 °C to 25 °C). The

emission wavelength was set to 345 nm and the emission bandwidth to 30 nm. A gain of 1500 was used.

Receptor stock solutions contain 8 µM peptide (WW-CA-Nle, WW-CA-min, WW-CA-ANG or $Tz2H_3$), 8 µM metal salt ($NiSO_4$, $CuSO_4$ or $ZnSO_4$), 10 mM MOPS, pH 7.2, 150 mM NaCl and were prepared 16 h to 24 h before the start of the experiments. Analyte stock solution (8 µM in aqueous buffer containing 10 mM MOPS, pH 7.2, 150 mM NaCl) were prepared according to two different procedures. Shelf stable substance with known molecular mass were weighed into a graduate flask and were dissolved subsequently (glyphosate, sodium pyrophosphate decahydrate, disodium hydrogen phosphate dihydrate, monosodium glutamate and phytic acid 50% *w*/*w* in water). Substances containing an unknown amount of waters of crystallisation were weighed in approximately assuming the molecular weight of the dry substance and dissolved in buffer solution. The concentration was determined by photometry and subsequent dilution was performed (adenosine monophosphate sodium salt hydrate and cyclic adenosine monophosphate sodium salt hydrate, $\varepsilon_{260\,nm}$ = 15400 M^{-1} cm^{-1}).[470]

First, the plate was filled with receptor solution (50 µL each well), then analyte solution (50 µL each well) was added and mixed by pipetting up and down. The plate was incubated for 2 h in an equilibrium chamber (Figure 8-1) with high humidity to prevent evaporation prior to measurement. A plate containing only buffer was used as blank, which was also incubated as described.

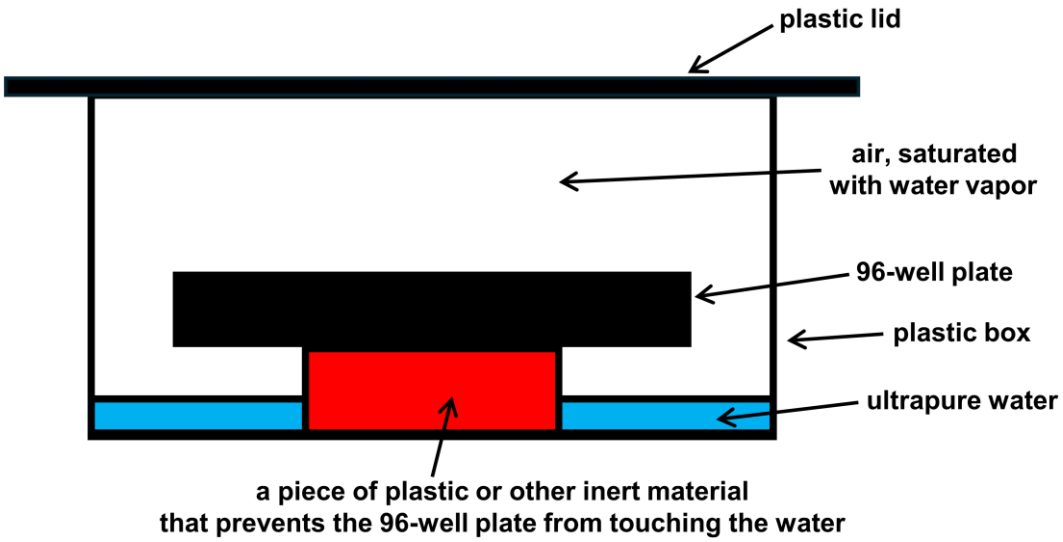

Figure 8-1: Schematic 2D representation of a 96-well plate in the equilibration chamber.

8.5 Synthesis of aspartate containing peptides

8.5.1 Synthesis of Fmoc-Asp(CSY)-O*t*Bu

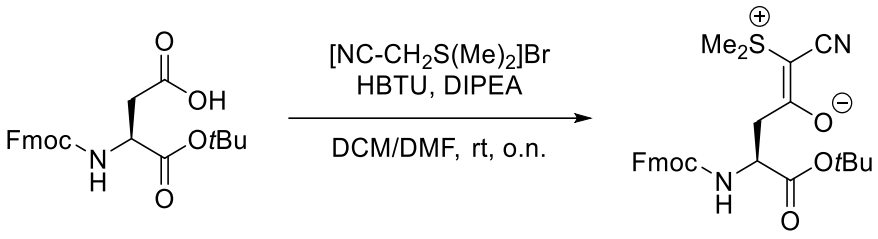

Fmoc-Asp-O*t*Bu **Fmoc-Asp(CSY)-O*t*Bu**

All reactions were performed in a nitrogen atmosphere. A mixture of dimethyl sulfide (2.27 g, 2.66 mL, 36.46 mmol,1.50 equiv.) and 1-bromoacetonitrile (4.37 g, 2.54 mL, 36.46 mmol, 1.50 equiv.) was stirred for 18 h at room temperature.

The resulting (cyanomethyl)-di-methyl sulfonium bromide was suspended in dry DCM (40 mL) using ultrasonication for 15 min and stirred for another 10 min. For better solvation DMF (20 mL) was added to the suspension.

Separately, Fmoc-Asp-O*t*Bu (10.00 g, 24.30 mmol, 1.00 equiv.) was dissolved in DMF (60 mL). HBTU (13.83 g, 36.46 mmol, 1.50 equiv.) was added and the suspension was stirred for 15 min. Then DIPEA (9.42 g, 12.40 mL, 72.90 mmol, 3.00 equiv.) was added and stirring continued for 10 min. The solution was transferred to the suspension of (cyanomethyl)-di-methyl sulfonium bromide and the flask was washed with DMF (30 mL), which also was transferred to the suspension. The reaction mixture was stirred at room temperature overnight.

The reaction mixture was washed with 10% citric acid (200 mL) and the aqueous phase was then extracted with DCM (3 x 20 mL). The combined organic phases were concentrated *in vacuo*, then dissolved in ethyl acetate (200 mL) and washed with a saturated $NaHCO_3$ solution (100 mL), deionized H_2O (3 x 100 mL) and brine (100 mL), respectively. The organic phase was dried over Na_2SO_4, filtered and the solvent was removed under reduced pressure.

The crude product was purified by column chromatography (SiO_2, DCM/MeOH 100:0 → 30:1). The product-containing fractions were combined and the solvent was removed under reduced pressure to give an oily residue which was lyophilised to give Fmoc-Asp(CSY)-O*t*Bu as a yellowish foam (11.46 g, 23.17 mmol, 95%).

TLC: R_f = 0.12 (SiO_2, DCM:MeOH, 40:1).

ESI-MS: *m*/*z* $[M+H]^+$ calc. 495.1948, found 495.1950; $[M+Na]^+$ calc. 517.1768, found 517.1769.

IR (ATR): $\tilde{\nu}$ = 3324.7, 2975.6, 2930.3, 2171.5 (*v* CN), 1714.4 (*v* CO), 1580.9 (*v* CO), 1499.8 (*v* CO), 1447.8, 1367.3, 1308.5, 1247.7, 1222.6, 1148.5, 1040.4, 988.3, 841.8, 759.8, 738.6, 619.2, 532.3 cm^{-1}.

^{1}H-NMR (600 MHz, DMSO-d$_6$): δ = 7.89 (d, J = 7.5 Hz, 2H, H_{ar}), 7.71 (d, J = 7.4 Hz, 2H, H_{ar}), 7.56 (d, J = 8.4 Hz, 1H, NH), 7.42 (t, J = 7.5 Hz, 2H, H_{ar}), 7.34-7.31 (m, 2H, H_{ar}), 4.40-4.37 (m, 1H, $C_\alpha H$), 4.35-4.15 (m, 3H, CH_2, CH), 2.78 (s, 6H, $S(CH_3)_2$), 2.72 (t, J = 6.4 Hz, 2H, $C_\beta H_2$), 1.37 (s, 9H, $C(CH_3)_3$) ppm.

^{13}C-NMR (151 MHz, DMSO-d$_6$): δ = 185.65 (COON), 170.91 (COOC), 155.94 (CO), 143.93 (2 x C_{ar}), 140.73 (2 x C_{ar}), 127.66 (2 x CH_{ar}), 127.09 (2 x CH_{ar}), 125.27 (2 x CH_{ar}), 120.14 (2 x CH_{ar}), 119.37 (CN), 80.58 (C), 65.65 (CH_2), 55.19 (C), 50.84 ($C_\alpha H$), 46.62 (CH), 27.60 (5 x CH_3) ppm.

8.5.2 Synthesis of Fmoc-Asp(CSY)-OH

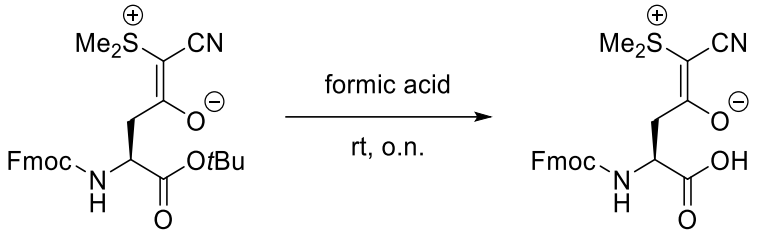

Fmoc-Asp(CSY)-O*t*Bu **Fmoc-Asp(CSY)-OH**

Fmoc-Asp(CSY)-O*t*Bu (5.00 g, 10.11 mmol, 1.00 equiv.) was dissolved in formic acid (150 mL) and stirred at room temperature for 20 h. The organic acid was removed under reduced pressure. The oily residue was coevaporated with methanol (150 mL) and DCM (10 mL) yielding a yellow foam, which was again coevaporated with petrol ether (3 x 50 mL). The substance was dried *in vacuo* over $NaHCO_3$ overnight.

The yellow foam was dissolved in ethyl acetate (80 mL). Immediately a colourless precipitate was formed. The suspension stirred at room temperature for 3 h giving a thick slurry mixture. It was diluted with ethyl acetate (30 mL) and heated under reflux for 30 min. After cooling to room temperature, the colourless precipitate was filtered off, washed with ethyl acetate and dried under reduced pressure. The mother liquor was concentrated *in vacuo* to give a yellow foam again and was recrystallised from ethyl acetate (20 mL). Fmoc-Asp(CSY)-OH was yielded as a colourless powder (3.90 g, 8.89 mmol, 88%).

Melting point: 145 to 146 °C.

TLC: R_f = 0.55 (SiO_2, DCM:MeOH:HCOOH, 10:1:0.1).

ESI-MS: m/z $[M+H]^+$ calc. 439.1322 found 439.1325.

IR (ATR): $\tilde{\nu}$ = 3520.5, 3475.7, 3377.3, 3025.4, 2930.0, 2181.4 (ν CN), 1701.3 (ν_{as} CO), 1522.4 (ν CO), 1444.8 (ν CO), 1325.5, 1259.9, 1221.2 1149.6, 1045.2, 997.5, 917.0, 779.8, 735.1, 633.7, 618.8, 583.0, 535.3 cm^{-1}.

^{1}H-NMR (400 MHz, DMSO-d_6): δ = 12.61 (s, 1H, COOH), 7.89 (d, J = 7.6 Hz, 2H, H_{ar}), 7.71 (d, J = 7.3 Hz, 2H, H_{ar}), 7.51 (d, J = 8.4 Hz, NH), 7.42 (t, J = 7.5 Hz, 2H, H_{ar}), 7.35-7.30 (m, 2H, H_{ar}), 4.50-4.40 (m, 1H, $C_\alpha H$), 4.32-4.16 (m, 3H, CH, CH_2), 2.84-2.69 (m, 8H, $S(CH_3)_2$, $C_\beta H_2$) ppm.

^{13}C-NMR (101 MHz, DMSO-d_6): δ = 185.81 (COON), 173.27 (COOH), 155.78 (CO), 143.81 (2 x C_{ar}), 140.68 (2 x C_{ar}), 127.61 (2 x CH_{ar}), 127.06 (2 x CH_{ar}), 125.27 (2 x CH_{ar}), 120.08 (2 x CH_{ar}), 119.27 (CN), 65.65 (CH_2), 55.05 (C), 50.06 ($C_\alpha H$), 46.60 (CH), 39.67 ($C_\beta H_2$), 27.54 ($S(CH_3)_2$) ppm.

8.5.3 Deprotection of Fmoc-Asp(CSY)-OH

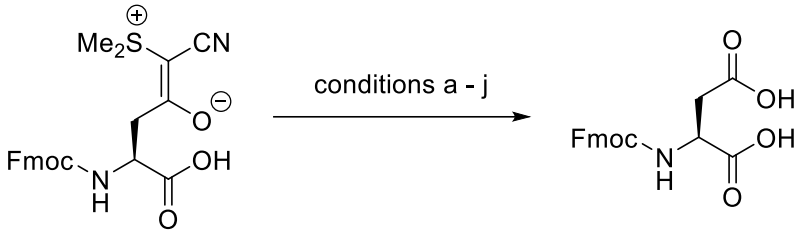

Fmoc-Asp(CSY)-OH **Fmoc-Asp-OH**

The reactions were performed in polypropylene reaction tubes. After each addition of reagent, the mixture was vortexed and spun down with a small tabletop centrifuge. A solution of Fmoc-Asp(CSY)-OH in MeCN or buffer B (2 mM, 10 µL, 1 equiv.) was mixed with the solvent system summarized in Table 8-2. The oxidant solution (4 mM, 2 x 5 µL, 2 equiv.) (Table 8-2) was then added. Between the additions, the mixture was equilibrated for 5 min. The reaction was quenched by addition of sodium ascorbate in water containing 10% *v*/*v* MeCN (20 mM, 10 µL, 10 equiv.). An aliquot (10 µL) was taken, diluted with buffer A (10 µL) and analysed with analytical HPLC.

Table 8-2: Conditions for the deprotection of Fmoc-Asp(CSY)-OH.

	Fmoc-Asp(CSY)-OH (2 mM) dissolved in	**solvent system**	**oxidant solution (4 mM)**
a	buffer B	buffer B (10 µL), buffer A (180 µL)	buffer B, no oxidant
b	buffer B	buffer B (10 µL), buffer A (180 µL)	NCS in buffer B
c	MeCN	MeCN (10 µL), acetate buffer pH 4.5 (50 mM, 40 µL), H_2O (140 µL)	NCS in MeCN
d	buffer B	buffer B (10 µL), buffer A (180 µL)	Iodine in buffer B
e	MeCN	MeCN (10 µL), phosphate buffer pH 10.0 (50 mM, 40 µL), H_2O (140 µL)	Iodine in MeCN
f	MeCN	MeCN (10 µL), acetate buffer pH 4.5 (50 mM, 40 µL), H_2O (140 µL)	$NaIO_4$ in water
g	MeCN	MeCN (10 µL), water (180 µL)	Oxone in water
h	buffer B	buffer B (10 µL), buffer A (180 µL)	Oxone in buffer A
i	MeCN	MeCN (10 µL), water (180 µL)	*m*CPBA in water
j	buffer B	buffer B (10 µL), buffer A (180 µL)	*m*CPBA in buffer A

8.5.4 Deprotection of CSY group containing peptides

The reactions were performed in polypropylene reaction tubes. After each addition of reagent, the mixture was vortexed and spun down with a small table-top centrifuge. After completion of the reaction, an aliquot (10 µL) was taken, diluted with buffer A (10 µL) and analysed with analytical HPLC.

(a) Conditions according to Neuman *et al*.[415] CSY protected peptide (25 nmol) was dissolved in acetate buffer 10 mM (200 µL). NCS in MeCN (the concentration of NCS depends on the number of CSY groups per peptide molecule: *c*(NCS) = *N*(CSY) · 1.25 mM, 4 x 11 µL, in total 2.2 equiv. per CSY group) was added. Between each addition, the mixture was equilibrated for 10 min. The reaction was quenched with sodium ascorbate in water containing 10% *v*/*v* MeCN (*c*(NaAsc) = *N*(CSY) · 7.5 mM) was added (44 µL, 6.0 equiv. regarding to NCS).

(b) CSY protected peptide (250 nmol) was dissolved in buffer A (1800 µL) and HFIP (200 µL). NCS dissolved in buffer B (*c*(NCS) = *N*(CSY) · 1.25 mM, 4 x 110 µL, in total 2.2 equiv. per CSY group) was added. Between each addition, the mixture was equilibrated for 10 min. The reaction was quenched with sodium ascorbate in 10% B in A (*c*(NaAsc) = *N*(CSY) · 7.5 mM) was added (440 µL, 6.0 equiv. regarding to NCS). The samples were frozen in liquid nitrogen and freeze-dried to obtain a colourless foam, which was further purified by HPLC.

(c) Preparative scale. CSY protected peptide (250 nmol) was dissolved in buffer A (1 mL), DMF (800 µL) and HFIP (200 µL). NCS in DMF (*c*(NCS) = *N*(CSY) · 1.25 mM, 4 x 110 µL, in total 2.2 equiv. per CSY group) was added. Between each addition, the mixture was equilibrated for 5 min. The reaction was quenched with sodium ascorbate in buffer A (*c*(NaAsc) = *c*(NCS) · 20, 110 µL, 5.0 equiv. regarding to NCS) and buffer A:DMF 1:1 (1450 µL) was added. The mixture was directly injected into the semipreparative HPLC. Due to high content of DMF several peaks can occur, which all contain peptide. These were collected, pooled and re-purified after freeze drying.

(c) Analytical scale. CSY protected peptide (25 nmol) was dissolved in buffer A (100 µL), HFIP (20 µL) and DMF (80 µL). NCS in DMF (5 mM, 4 x *V*, *V* = *N*(CSY) · 2.75 µL, in total 2.2 equiv. per CSY group) was added. Between each addition, the mixture was equilibrated for 5 min. The reaction was quenched with sodium ascorbate in buffer A (100 mM, *V* = *N*(CSY) · 2.75 µL, 5.0 equiv. regarding to NCS) and buffer A (*V* = 190 µL - *N*(CSY) · 2.75 µL) was added.

(d) CSY protected peptide (25 nmol) was dissolved in buffer A (100 µL), HFIP (20 µL) and TFE (80 µL). NCS in DMF (5 mM, 4 x *V*, *V* = *N*(CSY) · 2.75 µL, in total 2.2 equiv. per CSY group) was added. Between each addition, the mixture was equilibrated for 5 min. The reaction was quenched with sodium ascorbate in buffer A (100 mM, *V* = *N*(CSY) · 2.75 µL, 5.0 equiv. regarding to NCS) and buffer A (*V* = 190 µL - *N*(CSY) · 2.75 µL) was added.

(e) CSY protected peptide (25 nmol) was dissolved in buffer A (100 µL), HFIP (20 µL) and TFE (80 µL). NCS in MeCN (5 mM, 4 x *V*, *V* = *N*(CSY) · 2.75 µL, in total 2.2 equiv. per CSY group) was added. Between each addition, the mixture was equilibrated for 5 min. The reaction was quenched with sodium ascorbate in buffer A (100 mM, *V* = *N*(CSY) · 2.75 µL, 5.0 equiv. regarding to NCS) and buffer A (*V* = 190 µL - *N*(CSY) · 2.75 µL) was added.

(f) CSY protected peptide (250 nmol) was dissolved in buffer A (1800 µL) and HFIP (200 µL). NCS in MeOH + 0.1% TFA (5 mM, 4 x *V*, *V* = *N*(CSY) · 27.5 µL, in total 2.2 equiv. per CSY group) was added. Between each addition, the mixture was equilibrated for 10 min. The reaction was quenched with sodium ascorbate in buffer A (100 mM, *V* = *N*(CSY) · 27.5 µL, 5.0 equiv. regarding to NCS) and buffer A (*V* = 1900 µL - *N*(CSY) · 27.5 µL) was added.

(g) CSY protected peptide (250 nmol) was dissolved in buffer A (500 µL) and guanidine hydrochloride in buffer A (6.0 M, 1500 µL). NCS in buffer B (5 mM, 4 x *V*, *V* = *N*(CSY) · 27.5 µL, in total 2.2 equiv. per CSY group) was added. Between each addition, the mixture was equilibrated for 10 min. The reaction was quenched with sodium ascorbate in buffer A (100 mM, *V* = *N*(CSY) · 27.5 µL, 5.0 equiv. regarding to NCS) and buffer A (*V* = 1900 µL - *N*(CSY) · 27.5 µL) was added.

(h) CSY protected peptide (250 nmol) was dissolved in buffer A (1050 µL), guanidine hydrochloride in buffer A (6.0 M, 750 µL) and TFE (200 µL). NCS in buffer B (5 mM, 4 x *V*, *V* = *N*(CSY) · 27.5 µL, in total 2.2 equiv. per CSY group) was added. Between each addition, the mixture was equilibrated for 10 min. The reaction was quenched with sodium ascorbate in buffer A (100 mM, *V* = *N*(CSY) · 27.5 µL, 5.0 equiv. regarding to NCS) and buffer A (*V* = 1900 µL - *N*(CSY) · 27.5 µL) was added.

9 Literature

[1] F. H. Crick, **On protein synthesis**, *Symp. Soc. Exp. Biol.* **1958**, *12*, 138-163.

[2] F. Crick, **Central Dogma of Molecular Biology**, *Nature* **1970**, *227*, 561-563.

[3] M. Cobb, **60 years ago, Francis Crick changed the logic of biology**, *PLoS Biol.* **2017**, *15*, e2003243.

[4] T. D. Pollard, R. D. Goldman, **Overview of the Cytoskeleton from an Evolutionary Perspective**, *Cold Spring Harbor Perspect. Biol.* **2018**, *10*.

[5] S. Ricard-Blum, **The Collagen Family**, *Cold Spring Harbor Perspect. Biol.* **2011**, *3*.

[6] M. J. Lee, M. B. Yaffe, **Protein Regulation in Signal Transduction**, *Cold Spring Harbor Perspect. Biol.* **2016**, *8*.

[7] T. Pawson, P. Nash, **Protein–protein interactions define specificity in signal transduction**, *Genes Dev.* **2000**, *14*, 1027-1047.

[8] K. W. Kelley, D. A. Weigent, R. Kooijman, **Protein hormones and immunity**, *Brain Behav. Immun.* **2007**, *21*, 384-392.

[9] J. Parkin, B. Cohen, **An overview of the immune system**, *Lancet* **2001**, *357*, 1777-1789.

[10] D. R. Goulet, W. M. Atkins, **Considerations for the Design of Antibody-Based Therapeutics**, *J. Pharm. Sci.* **2020**, *109*, 74-103.

[11] S. Wu, R. Snajdrova, J. C. Moore, K. Baldenius, U. T. Bornscheuer, **Biocatalysis: Enzymatic Synthesis for Industrial Applications**, *Angew. Chem. Int. Ed.* **2021**, *60*, 88-119.

[12] T. J. Erb, P. R. Jones, A. Bar-Even, **Synthetic metabolism: metabolic engineering meets enzyme design**, *Curr. Opin. Chem. Biol.* **2017**, *37*, 56-62.

[13] E. J. Milner-White, **Protein three-dimensional structures at the origin of life**, *Interface Focus* **2019**, *9*, 20190057.

[14] G. Caetano-Anollés, M. Wang, D. Caetano-Anollés, Jay E. Mittenthal, **The origin, evolution and structure of the protein world**, *Biochem. J.* **2009**, *417*, 621-637.

[15] K. A. Dill, S. B. Ozkan, M. S. Shell, T. R. Weikl, **The Protein Folding Problem**, *Annu. Rev. Biophys.* **2008**, *37*, 289-316.

[16] K. A. Dill, J. L. MacCallum, **The Protein-Folding Problem, 50 Years On**, *Science* **2012**, *338*, 1042-1046.

[17] R. Renneberg, D. Süßbier, V. Berkling, V. Loroch, *Biotechnologie für Einsteiger*, 5 ed., Springer Spektrum, Berlin, Heidelberg, **2018**.

[18] K. Buchholz, J. Collins, **The roots—a short history of industrial microbiology and biotechnology**, *Appl. Microbiol. Biotechnol.* **2013**, *97*, 3747-3762.

[19] J. Y. Nehete, R. S. Bhambar, M. R. Narkhede, S. R. Gawali, **Natural proteins: Sources, isolation, characterization and applications**, *Pharmacogn. Rev.* **2013**, *7*, 107-116.

[20] W. H. Brondyk, in *Methods in Enzymology, Vol. 463* (Eds.: R. R. Burgess, M. P. Deutscher), Academic Press, **2009**, pp. 131-147.

[21] M. Ohuchi, H. Murakami, H. Suga, **The flexizyme system: a highly flexible tRNA aminoacylation tool for the translation apparatus**, *Curr. Opin. Chem. Biol.* **2007**, *11*, 537-542.

[22] J. Tian, K. Ma, I. Saaem, **Advancing high-throughput gene synthesis technology**, *Mol. BioSyst.* **2009**, *5*, 714-722.

[23] B. Leader, Q. J. Baca, D. E. Golan, **Protein therapeutics: a summary and pharmacological classification**, *Nat. Rev. Drug Discovery* **2008**, *7*, 21-39.

[24] X. Hu, P. Cebe, A. S. Weiss, F. Omenetto, D. L. Kaplan, **Protein-based composite materials**, *Mater. Today* **2012**, *15*, 208-215.

[25] K. B. Otte, B. Hauer, **Enzyme engineering in the context of novel pathways and products**, *Curr. Opin. Biotechnol.* **2015**, *35*, 16-22.

[26] C. Jackson, A. Anderson, K. Alexandrov, **The present and the future of protein biosensor engineering**, *Curr. Opin. Struct. Biol.* **2022**, *75*, 102424.

[27] E. H. C. Bromley, K. Channon, E. Moutevelis, D. N. Woolfson, **Peptide and Protein Building Blocks for Synthetic Biology: From Programming Biomolecules to Self-Organized Biomolecular Systems**, *ACS Chem. Biol.* **2008**, *3*, 38-50.

[28] L. Olivi, M. Berger, R. N. P. Creyghton, N. De Franceschi, C. Dekker, B. M. Mulder, N. J. Claassens, P. R. ten Wolde, J. van der Oost, **Towards a synthetic cell cycle**, *Nat. Commun.* **2021**, *12*, 4531.

[29] D. N. Woolfson, **A Brief History of De Novo Protein Design: Minimal, Rational, and Computational**, *J. Mol. Biol.* **2021**, *433*, 167160.

[30] S. Lutz, S. M. Iamurri, in *Protein Engineering: Methods and Protocols* (Eds.: U. T. Bornscheuer, M. Höhne), Springer New York, New York, NY, **2018**, pp. 1-12.

[31] F. H. Arnold, **Directed Evolution: Bringing New Chemistry to Life**, *Angew. Chem. Int. Ed.* **2018**, *57*, 4143-4148.

[32] W. M. Dawson, G. G. Rhys, D. N. Woolfson, **Towards functional de novo designed proteins**, *Curr. Opin. Chem. Biol.* **2019**, *52*, 102-111.

[33] G. A. Khoury, J. Smadbeck, C. A. Kieslich, C. A. Floudas, **Protein folding and de novo protein design for biotechnological applications**, *Trends Biotechnol.* **2014**, *32*, 99-109.

[34] P.-S. Huang, S. E. Boyken, D. Baker, **The coming of age of de novo protein design**, *Nature* **2016**, *537*, 320-327.

[35] G. M. Süel, S. W. Lockless, M. A. Wall, R. Ranganathan, **Evolutionarily conserved networks of residues mediate allosteric communication in proteins**, *Nat. Struct. Biol.* **2003**, *10*, 59-69.

[36] F. Richter, A. Leaver-Fay, S. D. Khare, S. Bjelic, D. Baker, **De Novo Enzyme Design Using Rosetta3**, *PLoS One* **2011**, *6*, e19230.

[37] J. Jumper, R. Evans, A. Pritzel, T. Green, M. Figurnov, O. Ronneberger, K. Tunyasuvunakool, R. Bates, A. Žídek, A. Potapenko, A. Bridgland, C. Meyer, S. A. A. Kohl, A. J. Ballard, A. Cowie, B. Romera-Paredes, S. Nikolov, R. Jain, J. Adler, T. Back, S. Petersen, D. Reiman, E. Clancy, M. Zielinski, M. Steinegger, M. Pacholska, T. Berghammer, S. Bodenstein, D. Silver, O. Vinyals, A. W. Senior, K. Kavukcuoglu, P. Kohli, D. Hassabis, **Highly accurate protein structure prediction with AlphaFold**, *Nature* **2021**, *596*, 583-589.

[38] M. Baek, F. DiMaio, I. Anishchenko, J. Dauparas, S. Ovchinnikov, G. R. Lee, J. Wang, Q. Cong, L. N. Kinch, R. D. Schaeffer, C. Millán, H. Park, C. Adams, C. R. Glassman, A. DeGiovanni, J. H. Pereira, A. V. Rodrigues, A. A. van Dijk, A. C. Ebrecht, D. J. Opperman, T. Sagmeister, C. Buhlheller, T. Pavkov-Keller, M. K. Rathinaswamy, U. Dalwadi, C. K. Yip, J. E. Burke, K. C. Garcia, N. V. Grishin, P. D. Adams, R. J. Read, D. Baker, **Accurate prediction of protein structures and interactions using a three-track neural network**, *Science* **2021**, *373*, 871-876.

[39] N. Anand, R. Eguchi, I. I. Mathews, C. P. Perez, A. Derry, R. B. Altman, P.-S. Huang, **Protein sequence design with a learned potential**, *Nat. Commun.* **2022**, *13*, 746.

[40] D. N. Woolfson, **Understanding a protein fold: The physics, chemistry, and biology of alpha-helical coiled coils**, *J. Biol. Chem.* **2023**, *299*, 104579.

[41] I. V. Korendovych, W. F. DeGrado, **De novo protein design, a retrospective**, *Q. Rev. Biophys.* **2020**, *53*, e3.

[42] W. M. Rink, F. Thomas, **De Novo Designed α-Helical Coiled-Coil Peptides as Scaffolds for Chemical Reactions**, *Chem. Eur. J.* **2019**, *25*, 1665-1677.

[43] I. Ghosh, J. Chmielewski, **Peptide self-assembly as a model of proteins in the pre-genomic world**, *Curr. Opin. Chem. Biol.* **2004**, *8*, 640-644.

[44] E. Arad, R. Jelinek, **Catalytic amyloids**, *Trends Chem.* **2022**, *4*, 907-917.

[45] K. E. Marshall, R. Marchante, W.-F. Xue, L. C. Serpell, **The relationship between amyloid structure and cytotoxicity**, *Prion* **2014**, *8*, 192-196.

[46] J. Dou, A. A. Vorobieva, W. Sheffler, L. A. Doyle, H. Park, M. J. Bick, B. Mao, G. W. Foight, M. Y. Lee, L. A. Gagnon, L. Carter, B. Sankaran, S. Ovchinnikov, E. Marcos, P.-S. Huang, J. C. Vaughan, B. L. Stoddard, D. Baker, **De novo design of a fluorescence-activating β-barrel**, *Nature* **2018**, *561*, 485-491.

[47] Y. Kipnis, A. O. Chaib, A. A. Vorobieva, G. Cai, G. Reggiano, B. Basanta, E. Kumar, P. R. E. Mittl, D. Hilvert, D. Baker, **Design and optimization of enzymatic activity in a de novo β-barrel scaffold**, *Protein Sci.* **2022**, *31*, e4405.

[48] E. G. Baker, G. J. Bartlett, K. L. Porter Goff, D. N. Woolfson, **Miniprotein Design: Past, Present, and Prospects**, *Acc. Chem. Res.* **2017**, *50*, 2085-2092.

[49] A. Ciesiołkiewicz, J. Lizandra Perez, Ł. Berlicki, **Miniproteins in medicinal chemistry**, *Bioorg. Med. Chem. Lett.* **2022**, *71*, 128806.

[50] J. M. Collins, K. A. Porter, S. K. Singh, G. S. Vanier, **High-Efficiency Solid Phase Peptide Synthesis (HE-SPPS)**, *Org. Lett.* **2014**, *16*, 940-943.

[51] Z. P. Gates, N. Hartrampf, **Flow-based SPPS for protein synthesis: A perspective**, *Pept. Sci.* **2020**, *112*, e24198.

[52] J. M. Palomo, **Solid-phase peptide synthesis: an overview focused on the preparation of biologically relevant peptides**, *RSC Adv.* **2014**, *4*, 32658-32672.

[53] M. Erak, K. Bellmann-Sickert, S. Els-Heindl, A. G. Beck-Sickinger, **Peptide chemistry toolbox–Transforming natural peptides into peptide therapeutics**, *Bioorg. Med. Chem.* **2018**, *26*, 2759-2765.

[54] V. Mäde, S. Els-Heindl, A. G. Beck-Sickinger, **Automated solid-phase peptide synthesis to obtain therapeutic peptides**, *Beilstein J. Org. Chem.* **2014**, *10*, 1197-1212.

[55] J. L. Ilsley, M. Sudol, S. J. Winder, **The WW domain: Linking cell signalling to the membrane cytoskeleton**, *Cell. Signalling* **2002**, *14*, 183-189.

[56] Z. Salah, A. Alian, R. I. Aqeilan, **WW domain-containing proteins: Retrospectives and the future**, *Front. Biosci. Landmark* **2012**, *17*, 331-348.

[57] P. Tian, R. B. Best, **How Many Protein Sequences Fold to a Given Structure? A Coevolutionary Analysis**, *Biophys. J.* **2017**, *113*, 1719-1730.

[58] M. J. Macias, V. Gervais, C. Civera, H. Oschkinat, **Structural analysis of WW domains and design of a WW prototype**, *Nat. Struct. Biol.* **2000**, *7*, 375-379.

[59] W. P. Russ, D. M. Lowery, P. Mishra, M. B. Yaffe, R. Ranganathan, **Natural-like function in artificial WW domains**, *Nature* **2005**, *437*, 579-583.

[60] M. Socolich, S. W. Lockless, W. P. Russ, H. Lee, K. H. Gardner, R. Ranganathan, **Evolutionary information for specifying a protein fold**, *Nature* **2005**, *437*, 512-518.

[61] K. P. Lu, X. Z. Zhou, **The prolyl isomerase PIN1: a pivotal new twist in phosphorylation signalling and disease**, *Nat. Rev. Mol. Cell Biol.* **2007**, *8*, 904-916.

[62] R. Ranganathan, K. P. Lu, T. Hunter, J. P. Noel, **Structural and functional analysis of the mitotic rotamase Pin1 suggests substrate recognition is phosphorylation dependent**, *Cell* **1997**, *89*, 875-886.

[63] M. A. Verdecia, M. E. Bowman, K. P. Lu, T. Hunter, J. P. Noel, **Structural basis for phosphoserine-proline recognition by group IV WW domains**, *Nat. Struct. Biol.* **2000**, *7*, 639-643.

[64] E. Bayer, S. Goettsch, J. W. Mueller, B. Griewel, E. Guiberman, L. M. Mayr, P. Bayer, **Structural analysis of the mitotic regulator hPin1 in solution: insights into domain architecture and substrate binding**, *J. Biol. Chem.* **2003**, *278*, 26183-26193.

[65] J. A. Kowalski, K. Liu, J. W. Kelly, **NMR solution structure of the isolated Apo Pin1 WW domain: comparison to the x-ray crystal structures of Pin1**, *Biopolymers* **2002**, *63*, 111-121.

[66] D. E. Mortenson, D. F. Kreitler, H. G. Yun, S. H. Gellman, K. T. Forest, **Evidence for small-molecule-mediated loop stabilization in the structure of the isolated Pin1 WW domain**, *Acta Crystallogr. Sect. D Biol. Crystallogr.* **2013**, *69*, 2506-2512.

[67] R. Wintjens, J. M. Wieruszeski, H. Drobecq, P. Rousselot-Pailley, L. Buee, G. Lippens, I. Landrieu, **1H NMR study on the binding of Pin1 Trp-Trp domain with phosphothreonine peptides**, *J. Biol. Chem.* **2001**, *276*, 25150-25156.

[68] M. S. Ardejani, E. T. Powers, J. W. Kelly, **Using Cooperatively Folded Peptides To Measure Interaction Energies and Conformational Propensities**, *Acc. Chem. Res.* **2017**, *50*, 1875-1882.

[69] M. Jager, S. Deechongkit, E. K. Koepf, H. Nguyen, J. Gao, E. T. Powers, M. Gruebele, J. W. Kelly, **Understanding the mechanism of β-sheet folding from a chemical and biological perspective**, *Pept. Sci.* **2008**, *90*, 751-758.

[70] A. G. Cochran, N. J. Skelton, M. A. Starovasnik, **Tryptophan zippers: Stable, monomeric β-hairpins**, *Proc. Natl. Acad. Sci. U. S. A.* **2001**, *98*, 5578-5583.

[71] R. M. Hughes, M. L. Waters, **Model systems for beta-hairpins and beta-sheets**, *Curr. Opin. Struct. Biol.* **2006**, *16*, 514-524.

[72] D. Pantoja-Uceda, C. M. Santiveri, M. A. Jimenez, **De novo design of monomeric beta-hairpin and beta-sheet peptides**, *Methods Mol. Biol.* **2006**, *340*, 27-51.

[73] M. A. Jimenez, **Design of monomeric water-soluble beta-hairpin and beta-sheet peptides**, *Methods Mol. Biol.* **2014**, *1216*, 15-52.

[74] R. Subirós-Funosas, A. El-Faham, F. Albericio, **Aspartimide formation in peptide chemistry: occurrence, prevention strategies and the role of N-hydroxylamines**, *Tetrahedron* **2011**, *67*, 8595-8606.

[75] M. J. Chalkley, S. I. Mann, W. F. DeGrado, **De novo metalloprotein design**, *Nat. Rev. Chem.* **2022**, *6*, 31-50.

[76] M. L. Zastrow, V. L. Pecoraro, **Designing functional metalloproteins: from structural to catalytic metal sites**, *Coord. Chem. Rev.* **2013**, *257*, 2565-2588.

[77] G. Liu, N. Xia, L. Tian, Z. Sun, L. Liu, **Progress in the Development of Biosensors Based on Peptide–Copper Coordination Interaction**, *Biosensors* **2022**, *12*, 809.

[78] O. Zozulia, M. A. Dolan, I. V. Korendovych, **Catalytic peptide assemblies**, *Chem. Soc. Rev.* **2018**, *47*, 3621-3639.

[79] T. L. Pham, F. Thomas, **Design of Functional Globular β-Sheet Miniproteins**, *ChemBioChem* **2024**, *25*, e202300745.

[80] M. Sudol, T. Hunter, **NeW wrinkles for an old domain**, *Cell* **2000**, *103*, 1001-1004.

[81] Y. Kato, M. Ito, K. Kawai, K. Nagata, M. Tanokura, **Determinants of ligand specificity in groups I and IV WW domains as studied by surface plasmon resonance and model building**, *J. Biol. Chem.* **2002**, *277*, 10173-10177.

[82] Y. Kato, K. Nagata, M. Takahashi, L. Lian, J. J. Herrero, M. Sudol, M. Tanokura, **Common mechanism of ligand recognition by group II/III WW domains: redefining their functional classification**, *J. Biol. Chem.* **2004**, *279*, 31833-31841.

[83] M. Meiyappan, G. Birrane, J. A. A. Ladias, **Structural basis for polyproline recognition by the FE65 WW domain**, *J. Mol. Biol.* **2007**, *372*, 970-980.

[84] J. R. Pires, F. Taha-Nejad, F. Toepert, T. Ast, U. Hoffmuller, J. Schneider-Mergener, R. Kuhne, M. J. Macias, H. Oschkinat, **Solution structures of the YAP65 WW domain and the variant L30 K in complex with the peptides GTPPPPYTVG, N-(n-octyl)-GPPPY and PLPPY and the application of peptide libraries reveal a minimal binding epitope**, *J. Mol. Biol.* **2001**, *314*, 1147-1156.

[85] M. Jäger, H. Nguyen, J. C. Crane, J. W. Kelly, M. Gruebele, **The folding mechanism of a β-sheet: the WW domain1**, *J. Mol. Biol.* **2001**, *311*, 373-393.

[86] A. Zarrinpar, W. A. Lim, **Converging on proline: the mechanism of WW domain peptide recognition**, *Nat. Struct. Biol.* **2000**, *7*, 611-613.

[87] A. J. Potter, S. Ray, L. Gueritz, C. L. Nunns, C. J. Bryant, S. F. Scrace, N. Matassova, L. Baker, P. Dokurno, D. A. Robinson, A. E. Surgenor, B. Davis, J. B. Murray, C. M. Richardson, J. D. Moore, **Structure-guided design of α-amino acid-derived Pin1 inhibitors**, *Bioorg. Med. Chem. Lett.* **2010**, *20*, 586-590.

[88] B. J. Pinch, Z. M. Doctor, B. Nabet, C. M. Browne, H.-S. Seo, M. L. Mohardt, S. Kozono, X. Lian, T. D. Manz, Y. Chun, S. Kibe, D. Zaidman, D. Daitchman, Z. C. Yeoh, N. E. Vangos, E. A. Geffken, L. Tan, S. B. Ficarro, N. London, J. A. Marto, S. Buratowski, S. Dhe-Paganon, X. Z. Zhou, K. P. Lu, N. S. Gray, **Identification of a potent and selective covalent Pin1 inhibitor**, *Nat. Chem. Biol.* **2020**, *16*, 979-987.

[89] G. Poli, M. Di Stefano, J. A. Estevez, F. Minutolo, C. Granchi, A. Giordano, S. Parisi, M. Mauceri, V. Canzonieri, M. Macchia, I. Caligiuri, T. Tuccinardi, F. Rizzolio, **New PIN1 inhibitors identified through a pharmacophore-driven, hierarchical consensus docking strategy**, *J. Enzyme Inhib. Med. Chem.* **2022**, *37*, 145-150.

[90] J. Zhang, W. Zhou, Y. Chen, Y. Wang, Z. Guo, W. Hu, Y. Li, X. Han, S. Si, **Small molecules targeting Pin1 as potent anticancer drugs**, *Front. Pharmacol.* **2023**, *14*.

[91] E. Aragon, N. Goerner, A. I. Zaromytidou, Q. Xi, A. Escobedo, J. Massague, M. J. Macias, **A Smad action turnover switch operated by WW domain readers of a phosphoserine code**, *Genes Dev.* **2011**, *25*, 1275-1288.

[92] L. M. Luh, R. Hansel, F. Lohr, D. K. Kirchner, K. Krauskopf, S. Pitzius, B. Schafer, P. Tufar, I. Corbeski, P. Guntert, V. Dotsch, **Molecular crowding drives active Pin1 into nonspecific complexes with endogenous proteins prior to substrate recognition**, *J. Am. Chem. Soc.* **2013**, *135*, 13796-13803.

[93] C. Schelhorn, P. Martin-Malpartida, D. Sunol, M. J. Macias, **Structural Analysis of the Pin1-CPEB1 interaction and its potential role in CPEB1 degradation**, *Sci. Rep.* **2015**, *5*, 14990.

[94] M. Jäger, M. Dendle, J. W. Kelly, **Sequence determinants of thermodynamic stability in a WW domain—An all-β-sheet protein**, *Protein Sci.* **2009**, *18*, 1806-1813.

[95] S. Deechongkit, P. E. Dawson, J. W. Kelly, **Toward Assessing the Position-Dependent Contributions of Backbone Hydrogen Bonding to β-Sheet Folding Thermodynamics Employing Amide-to-Ester Perturbations**, *J. Am. Chem. Soc.* **2004**, *126*, 16762-16771.

[96] S. Deechongkit, H. Nguyen, E. T. Powers, P. E. Dawson, M. Gruebele, J. W. Kelly, **Context-dependent contributions of backbone hydrogen bonding to β-sheet folding energetics**, *Nature* **2004**, *430*, 101-105.

[97] A. A. Fuller, D. Du, F. Liu, J. E. Davoren, G. Bhabha, G. Kroon, D. A. Case, H. J. Dyson, E. T. Powers, P. Wipf, M. Gruebele, J. W. Kelly, **Evaluating β-turn mimics as β-sheet folding nucleators**, *Proc. Natl. Acad. Sci. U. S. A.* **2009**, *106*, 11067-11072.

[98] W. Chen, S. Enck, J. L. Price, D. L. Powers, E. T. Powers, C. H. Wong, H. J. Dyson, J. W. Kelly, **Structural and energetic basis of carbohydrate-aromatic packing interactions in proteins**, *J. Am. Chem. Soc.* **2013**, *135*, 9877-9884.

[99] C.-H. Hsu, S. Park, D. E. Mortenson, B. L. Foley, X. Wang, R. J. Woods, D. A. Case, E. T. Powers, C.-H. Wong, H. J. Dyson, J. W. Kelly, **The Dependence of Carbohydrate–Aromatic Interaction Strengths on the Structure of the Carbohydrate**, *J. Am. Chem. Soc.* **2016**, *138*, 7636-7648.

[100] L. J. Rothschild, R. L. Mancinelli, **Life in extreme environments**, *Nature* **2001**, *409*, 1092-1101.

[101] K. Richter, M. Haslbeck, J. Buchner, **The Heat Shock Response: Life on the Verge of Death**, *Mol. Cell* **2010**, *40*, 253-266.

[102] W. Martin, J. Baross, D. Kelley, M. J. Russell, **Hydrothermal vents and the origin of life**, *Nat. Rev. Microbiol.* **2008**, *6*, 805-814.

[103] F. Rigoldi, S. Donini, A. Redaelli, E. Parisini, A. Gautieri, **Review: Engineering of thermostable enzymes for industrial applications**, *APL Bioeng.* **2018**, *2*.

[104] S. Ishino, Y. Ishino, **DNA polymerases as useful reagents for biotechnology – the history of developmental research in the field**, *Front. Microbiol.* **2014**, *5*, 465.

[105] M. Teufl, C. U. Zajc, M. W. Traxlmayr, **Engineering Strategies to Overcome the Stability–Function Trade-Off in Proteins**, *ACS Synth. Biol.* **2022**, *11*, 1030-1039.

[106] M. Iglesias-Bexiga, F. Castillo, E. S. Cobos, T. Oka, M. Sudol, I. Luque, **WW domains of the yes-kinase-associated-protein (YAP) transcriptional regulator behave as independent units with different binding preferences for PPxY motif-containing ligands**, *PLoS One* **2015**, *10*, e0113828.

[107] J. K. Myers, D. P. Morris, A. L. Greenleaf, T. G. Oas, **Phosphorylation of RNA polymerase II CTD fragments results in tight binding to the WW domain from the yeast prolyl isomerase Ess1**, *Biochemistry* **2001**, *40*, 8479-8486.

[108] S. Deechongkit, J. W. Kelly, **The Effect of Backbone Cyclization on the Thermodynamics of β-Sheet Unfolding: Stability Optimization of the PIN WW Domain**, *J. Am. Chem. Soc.* **2002**, *124*, 4980-4986.

[109] M. Jäger, M. Dendle, A. A. Fuller, J. W. Kelly, **A cross-strand Trp–Trp pair stabilizes the hPin1 WW domain at the expense of function**, *Protein Sci.* **2007**, *16*, 2306-2313.

[110] D. E. Mortenson, D. F. Kreitler, N. C. Thomas, I. A. Guzei, S. H. Gellman, K. T. Forest, **Evaluation of β-Amino Acid Replacements in Protein Loops: Effects on Conformational Stability and Structure**, *ChemBioChem* **2018**, *19*, 604-612.

[111] M. Jäger, Y. Zhang, J. Bieschke, H. Nguyen, M. Dendle, M. E. Bowman, J. P. Noel, M. Gruebele, J. W. Kelly, **Structure–function–folding relationship in a WW domain**, *Proc. Natl. Acad. Sci. U. S. A.* **2006**, *103*, 10648-10653.

[112] B. L. Kier, J. M. Anderson, N. H. Andersen, **Circular Permutation of a WW Domain: Folding Still Occurs after Excising the Turn of the Folding-Nucleating Hairpin**, *J. Am. Chem. Soc.* **2014**, *136*, 741-749.

[113] X. I. Ambroggio, B. Kuhlman, **Design of protein conformational switches**, *Curr. Opin. Struct. Biol.* **2006**, *16*, 525-530.

[114] T. Christensen, W. Hassouneh, D. J. Callahan, A. Chilkoti, in *Comprehensive Biophysics* (Ed.: E. H. Egelman), Elsevier, Amsterdam, **2012**, pp. 238-266.

[115] J.-H. Ha, S. N. Loh, **Protein Conformational Switches: From Nature to Design**, *Chem. Eur. J.* **2012**, *18*, 7984-7999.

[116] J. Volarić, W. Szymanski, N. A. Simeth, B. L. Feringa, **Molecular photoswitches in aqueous environments**, *Chem. Soc. Rev.* **2021**, *50*, 12377-12449.

[117] K. Montrose, R. M. López Cabezas, J. Paukštytė, J. Saarikangas, **Winter is coming: Regulation of cellular metabolism by enzyme polymerization in dormancy and disease**, *Exp. Cell Res.* **2020**, *397*, 112383.

[118] Victoria E. Abraira, David D. Ginty, **The Sensory Neurons of Touch**, *Neuron* **2013**, *79*, 618-639.

[119] F. Bezanilla, **Voltage-gated ion channels**, *IEEE Trans. NanoBiosci.* **2005**, *4*, 34-48.

[120] E. K. Koepf, H. M. Petrassi, G. Ratnaswamy, M. E. Huff, M. Sudol, J. W. Kelly, **Characterization of the Structure and Function of W → F WW Domain Variants: Identification of a Natively Unfolded Protein That Folds upon Ligand Binding**, *Biochemistry* **1999**, *38*, 14338-14351.

[121] C. M. Santiveri, M. A. Jiménez, **Tryptophan residues: Scarce in proteins but strong stabilizers of β-hairpin peptides**, *Pept. Sci.* **2010**, *94*, 779-790.

[122] J. M. Anderson, N. H. Andersen, **A pH Switch for β-Sheet Protein Folding**, *Angew. Chem. Int. Ed.* **2017**, *56*, 7074-7077.

[123] J. Fantini, **Fundamental Mechanisms in Membrane Receptology: Old Paradigms, New Concepts and Perspectives**, *Receptors* **2024**, *3*, 107-121.

[124] W. M. Oldham, H. E. Hamm, **Heterotrimeric G protein activation by G-protein-coupled receptors**, *Nat. Rev. Mol. Cell Biol.* **2008**, *9*, 60-71.

[125] E. Pazos, O. Vázquez, J. L. Mascareñas, M. Eugenio Vázquez, **Peptide-based fluorescent biosensors**, *Chem. Soc. Rev.* **2009**, *38*, 3348-3359.

[126] T. Phumlani, S. Poslet Morgan, N.-T. Zikhona, in *Nanopores* (Eds.: A. Sadia, M. S. Akhtar, S. Hyung-Shik), IntechOpen, Rijeka, **2021**, p. Ch. 3.

[127] P. A. Dalby, R. H. Hoess, W. F. Degrado, **Evolution of binding affinity in a WW domain probed by phage display**, *Protein Sci.* **2000**, *9*, 2366-2376.

[128] J. Kasanov, G. Pirozzi, A. J. Uveges, B. K. Kay, **Characterizing Class I WW domains defines key specificity determinants and generates mutant domains with novel specificities**, *Chem. Biol.* **2001**, *8*, 231-241.

[129] S. Patel, P. Mathonet, A. M. Jaulent, C. G. Ullman, **Selection of a high-affinity WW domain against the extracellular region of VEGF receptor isoform-2 from a combinatorial library using CIS display**, *Protein Eng. Des. Sel.* **2013**, *26*, 307-315.

[130] H. Yanagida, T. Matsuura, T. Yomo, **Compensatory Evolution of a WW Domain Variant Lacking the Strictly Conserved Trp Residue**, *J. Mol. Evol.* **2008**, *66*, 61-71.

[131] M. Kohlberger, G. Gadermaier, **SELEX: Critical factors and optimization strategies for successful aptamer selection**, *Biotechnol. Appl. Biochem.* **2022**, *69*, 1771-1792.

[132] R. Micura, C. Höbartner, **Fundamental studies of functional nucleic acids: aptamers, riboswitches, ribozymes and DNAzymes**, *Chem. Soc. Rev.* **2020**, *49*, 7331-7353.

[133] A. L. Stewart, J. H. Park, M. L. Waters, **Redesign of a WW domain peptide for selective recognition of single-stranded DNA**, *Biochemistry* **2011**, *50*, 2575-2584.

[134] H. Neitz, N. B. Paul, F. R. Häge, C. Lindner, R. Graebner, M. Kovermann, F. Thomas, **Identification of novel functional mini-receptors by combinatorial screening of split-WW domains**, *Chem. Sci.* **2022**, *13*, 9079-9090.

[135] P. Morales, M. A. Jiménez, **Design and structural characterisation of monomeric water-soluble α-helix and β-hairpin peptides: State-of-the-art**, *Arch. Biochem. Biophys.* **2019**, *661*, 149-167.

[136] C. D. DuPai, B. W. Davies, C. O. Wilke, **A systematic analysis of the beta hairpin motif in the Protein Data Bank**, *Protein Sci.* **2021**, *30*, 613-623.

[137] P. V. Panteleev, I. A. Bolosov, S. V. Balandin, T. V. Ovchinnikova, **Structure and Biological Functions of β-Hairpin Antimicrobial Peptides**, *Acta Naturae* **2015**, *7*, 37-47.

[138] **IUPAC-IUB Commission on Biochemical Nomenclature: Abbreviations and symbols for the description of the conformation of polypeptide chains**, *J. Mol. Biol.* **1970**, *52*, 1-17.

[139] W. Kabsch, C. Sander, **Dictionary of protein secondary structure: Pattern recognition of hydrogen-bonded and geometrical features**, *Biopolymers* **1983**, *22*, 2577-2637.

[140] B. L. Sibanda, T. L. Blundell, J. M. Thornton, **Conformation of β-hairpins in protein structures: A systematic classification with applications to modelling by homology, electron density fitting and protein engineering**, *J. Mol. Biol.* **1989**, *206*, 759-777.

[141] O. Koch, G. Klebe, **Turns revisited: A uniform and comprehensive classification of normal, open, and reverse turn families minimizing unassigned random chain portions**, *Proteins Struct. Funct. Bioinf.* **2009**, *74*, 353-367.

[142] M. Shapovalov, S. Vucetic, R. L. Dunbrack, Jr., **A new clustering and nomenclature for beta turns derived from high-resolution protein structures**, *PLoS Comput. Biol.* **2019**, *15*, e1006844.

[143] M. Pelay-Gimeno, A. Glas, O. Koch, T. N. Grossmann, **Structure-Based Design of Inhibitors of Protein–Protein Interactions: Mimicking Peptide Binding Epitopes**, *Angew. Chem. Int. Ed.* **2015**, *54*, 8896-8927.

[144] J. A. Robinson, **β-Hairpin Peptidomimetics: Design, Structures and Biological Activities**, *Acc. Chem. Res.* **2008**, *41*, 1278-1288.

[145] E. Lenci, A. Trabocchi, **Peptidomimetic toolbox for drug discovery**, *Chem. Soc. Rev.* **2020**, *49*, 3262-3277.

[146] M. Aumailley, M. Gurrath, G. Müller, J. Calvete, R. Timpl, H. Kessler, **Arg-Gly-Asp constrained within cyclic pentapoptides Strong and selective inhibitors of cell adhesion to vitronectin and laminin fragment P1**, *FEBS Lett.* **1991**, *291*, 50-54.

[147] D. F. Veber, R. M. Freidinger, D. S. Perlow, W. J. Paleveda, F. W. Holly, R. G. Strachan, R. F. Nutt, B. H. Arison, C. Homnick, W. C. Randall, M. S. Glitzer, R. Saperstein, R. Hirschmann, **A potent cyclic hexapeptide analogue of somatostatin**, *Nature* **1981**, *292*, 55-58.

[148] G. Weckbecker, I. Lewis, R. Albert, H. A. Schmid, D. Hoyer, C. Bruns, **Opportunities in somatostatin research: biological, chemical and therapeutic aspects**, *Nat. Rev. Drug Discovery* **2003**, *2*, 999-1017.

[149] B. Laufer, J. Chatterjee, A. O. Frank, H. Kessler, **Can N-methylated amino acids serve as substitutes for prolines in conformational design of cyclic pentapeptides?**, *J. Pept. Sci.* **2009**, *15*, 141-146.

[150] T. S. Haque, J. C. Little, S. H. Gellman, **Stereochemical Requirements for β-Hairpin Formation: Model Studies with Four-Residue Peptides and Depsipeptides**, *J. Am. Chem. Soc.* **1996**, *118*, 6975-6985.

[151] I. L. Karle, S. K. Awasthi, P. Balaram, **A designed beta-hairpin peptide in crystals**, *Proc. Natl. Acad. Sci. U. S. A.* **1996**, *93*, 8189-8193.

[152] D. Núñez-Villanueva, A. Plata-Ruiz, I. Romero-Muñiz, I. Martín-Pérez, L. Infantes, R. González-Muñiz, M. Martín-Martínez, **β-Turn Induction by a Diastereopure Azepane-Derived Quaternary Amino Acid**, *J. Org. Chem.* **2023**, *88*, 14688-14696.

[153] E. Benedetti, A. Bavoso, B. Di Blasio, V. Pavone, C. Pedone, C. Toniolo, G. M. Bonora, **Peptaibol antibiotics: a study on the helical structure of the 2-9 sequence of emerimicins III and IV**, *Proc. Natl. Acad. Sci. U. S. A.* **1982**, *79*, 7951-7954.

[154] J. S. Nowick, J. O. Brower, **A New Turn Structure for the Formation of β-Hairpins in Peptides**, *J. Am. Chem. Soc.* **2003**, *125*, 876-877.

[155] X. Li, A. L. Sabol, M. Wierzbicki, P. J. Salveson, J. S. Nowick, **An Improved Turn Structure for Inducing β-Hairpin Formation in Peptides**, *Angew. Chem. Int. Ed.* **2021**, *60*, 22776-22782.

[156] M. Körling, A. Geyer, **Beyond Natural Limitations: Long-Range Influence of Non-Natural Flexible and Rigid β-Turn Mimetics in a Native β-Hairpin Motif**, *Eur. J. Org. Chem.* **2015**, *2015*, 6448-6457.

[157] U. Nagai, K. Sato, **Synthesis of a bicyclic dipeptide with the shape of β-turn central part**, *Tetrahedron Lett.* **1985**, *26*, 647-650.

[158] M. Hata, G. R. Marshall, **Do benzodiazepines mimic reverse-turn structures?**, *J. Comput. Aided Mol. Des.* **2006**, *20*, 321-331.

[159] W. C. Ripka, G. V. De Lucca, A. C. Bach, R. S. Pottorf, J. M. Blaney, **Protein β-turn mimetics I. Design, synthesis, and evaluation in model cyclic peptides**, *Tetrahedron* **1993**, *49*, 3593-3608.

[160] L. Lomlim, J. Einsiedel, F. W. Heinemann, K. Meyer, P. Gmeiner, **Proline Derived Spirobarbiturates as Highly Effective β-Turn Mimetics Incorporating Polar and Functionalizable Constraint Elements**, *J. Org. Chem.* **2008**, *73*, 3608-3611.

[161] E. Graf von Roedern, E. Lohof, G. Hessler, M. Hoffmann, H. Kessler, **Synthesis and Conformational Analysis of Linear and Cyclic Peptides Containing Sugar Amino Acids**, *J. Am. Chem. Soc.* **1996**, *118*, 10156-10167.

[162] S. A. W. Gruner, E. Locardi, E. Lohof, H. Kessler, **Carbohydrate-Based Mimetics in Drug Design: Sugar Amino Acids and Carbohydrate Scaffolds**, *Chem. Rev.* **2002**, *102*, 491-514.

[163] S. Crecente-Garcia, A. Neckebroeck, J. S. Clark, B. O. Smith, A. R. Thomson, **β-Turn Mimics by Chemical Ligation**, *Org. Lett.* **2020**, *22*, 4424-4428.

[164] B. Ciani, M. Jourdan, M. S. Searle, **Stabilization of β-Hairpin Peptides by Salt Bridges: Role of Preorganization in the Energetic Contribution of Weak Interactions**, *J. Am. Chem. Soc.* **2003**, *125*, 9038-9047.

[165] E. de Alba, F. J. Blanco, M. A. Jiménez, M. Rico, J. L. Nieto, **Interactions Responsible for the pH Dependence of the β-Hairpin Conformational Population Formed by a Designed Linear Peptide**, *Eur. J. Biochem.* **1995**, *233*, 283-292.

[166] A. J. Riemen, M. L. Waters, **Design of Highly Stabilized β-Hairpin Peptides through Cation−π Interactions of Lysine and N-Methyllysine with an Aromatic Pocket**, *Biochemistry* **2009**, *48*, 1525-1531.

[167] C. D. Tatko, M. L. Waters, **The geometry and efficacy of cation–π interactions in a diagonal position of a designed β-hairpin**, *Protein Sci.* **2003**, *12*, 2443-2452.

[168] C. M. Santiveri, E. León, M. Rico, M. A. Jiménez, **Context-Dependence of the Contribution of Disulfide Bonds to β-Hairpin Stability**, *Chem. Eur. J.* **2008**, *14*, 488-499.

[169] J. M. Anderson, B. L. Kier, B. Jurban, A. Byrne, I. Shu, L. A. Eidenschink, A. A. Shcherbakov, M. Hudson, R. M. Fesinmeyer, N. H. Andersen, **Aryl–aryl interactions in designed peptide folds: Spectroscopic characteristics and optimal placement for structure stabilization**, *Biopolymers* **2016**, *105*, 337-356.

[170] A. Lewandowska, S. Ołdziej, A. Liwo, H. A. Scheraga, **β-hairpin-forming peptides; models of early stages of protein folding**, *Biophys. Chem.* **2010**, *151*, 1-9.

[171] C. M. Santiveri, J. Santoro, M. Rico, M. A. Jiménez, **Factors involved in the stability of isolated β-sheets: Turn sequence, β-sheet twisting, and hydrophobic surface burial**, *Protein Sci.* **2004**, *13*, 1134-1147.

[172] Y. Xiao, C. Chen, Y. He, **Folding Mechanism of Beta-Hairpin Trpzip2: Heterogeneity, Transition State and Folding Pathways**, *Int. J. Mol. Sci.* **2009**, *10*, 2838-2848.

[173] T. Takekiyo, L. Wu, Y. Yoshimura, A. Shimizu, T. A. Keiderling, **Relationship between hydrophobic interactions and secondary structure stability for Trpzip beta-hairpin peptides**, *Biochemistry* **2009**, *48*, 1543-1552.

[174] L. Wu, D. McElheny, R. Huang, T. A. Keiderling, **Role of Tryptophan−Tryptophan Interactions in Trpzip β-Hairpin Formation, Structure, and Stability**, *Biochemistry* **2009**, *48*, 10362-10371.

[175] L. Wu, D. McElheny, T. Takekiyo, T. A. Keiderling, **Geometry and Efficacy of Cross-Strand Trp/Trp, Trp/Tyr, and Tyr/Tyr Aromatic Interaction in a β-Hairpin Peptide**, *Biochemistry* **2010**, *49*, 4705-4714.

[176] J. S. Richardson, D. C. Richardson, **Natural β-sheet proteins use negative design to avoid edge-to-edge aggregation**, *Proc. Natl. Acad. Sci. U. S. A.* **2002**, *99*, 2754-2759.

[177] M. Ramírez-Alvarado, F. J. Blanco, L. Serrano, **De novo design and structural analysis of a model β-hairpin peptide system**, *Nat. Struct. Biol.* **1996**, *3*, 604-612.

[178] V. Stanojlovic, A. Müller, A. Moazzam, A. Hinterholzer, K. Ożga, Ł. Berlicki, M. Schubert, C. Cabrele, **A Conformationally Stable Acyclic β-Hairpin Scaffold Tolerating the Incorporation of Poorly β-Sheet-Prone Amino Acids**, *ChemBioChem* **2022**, *23*, e202100604.

[179] H.-W. Siu, B. Heck, M. Kovermann, K. Hauser, **Template-assisted design of monomeric polyQ models to unravel the unique role of glutamine side chains in disease-related aggregation**, *Chem. Sci.* **2021**, *12*, 412-426.

[180] M. D'Hondt, N. Bracke, L. Taevernier, B. Gevaert, F. Verbeke, E. Wynendaele, B. De Spiegeleer, **Related impurities in peptide medicines**, *J. Pharm. Biomed. Anal.* **2014**, *101*, 2-30.

[181] W. A. Loughlin, J. D. A. Tyndall, M. P. Glenn, D. P. Fairlie, **Beta-Strand Mimetics**, *Chem. Rev.* **2004**, *104*, 6085-6118.

[182] W. A. Loughlin, J. D. A. Tyndall, M. P. Glenn, T. A. Hill, D. P. Fairlie, **Update 1 of: Beta-Strand Mimetics**, *Chem. Rev.* **2010**, *110*, PR32-PR69.

[183] M. Muttenthaler, G. F. King, D. J. Adams, P. F. Alewood, **Trends in peptide drug discovery**, *Nat. Rev. Drug. Discov.* **2021**, *20*, 309-325.

[184] D. Obrecht, E. Chevalier, K. Moehle, J. A. Robinson, **β-Hairpin protein epitope mimetic technology in drug discovery**, *Drug Discovery Today Technol.* **2012**, *9*, e63-e69.

[185] F. M. Paulussen, T. N. Grossmann, **Peptide-based covalent inhibitors of protein–protein interactions**, *J. Pept. Sci.* **2023**, *29*, e3457.

[186] L. Wang, N. Wang, W. Zhang, X. Cheng, Z. Yan, G. Shao, X. Wang, R. Wang, C. Fu, **Therapeutic peptides: current applications and future directions**, *Signal Transduct. Target. Ther.* **2022**, *7*, 48.

[187] S. M. Butterfield, M. M. Sweeney, M. L. Waters, **The Recognition of Nucleotides with Model β-Hairpin Receptors: Investigation of Critical Contacts and Nucleotide Selectivity**, *J. Org. Chem.* **2005**, *70*, 1105-1114.

[188] S. M. Butterfield, M. L. Waters, **A Designed β-Hairpin Peptide for Molecular Recognition of ATP in Water**, *J. Am. Chem. Soc.* **2003**, *125*, 9580-9581.

[189] F. Diez-García, D. Pantoja-Uceda, M. Á. Jiménez, A. Chakrabartty, D. V. Laurents, **Structure of a simplified β-hairpin and its ATP complex**, *Arch. Biochem. Biophys.* **2013**, *537*, 62-71.

[190] J. H. Park, M. L. Waters, **Positional effects of click cyclization on β-hairpin structure, stability, and function**, *Org. Biomol. Chem.* **2013**, *11*, 69-77.

[191] L. L. Cline, M. L. Waters, **Design of a β-hairpin peptide-intercalator conjugate for simultaneous recognition of single stranded and double stranded regions of RNA**, *Org. Biomol. Chem.* **2009**, *7*, 4622-4630.

[192] S. M. Butterfield, C. M. Goodman, V. M. Rotello, M. L. Waters, **A Peptide Flavoprotein Mimic: Flavin Recognition and Redox Potential Modulation in Water by a Designed β Hairpin**, *Angew. Chem. Int. Ed.* **2004**, *43*, 724-727.

[193] D. J. Wilger, J. H. Park, R. M. Hughes, M. E. Cuellar, M. L. Waters, **Induced-Fit Binding of a Polyproline Helix by a β-Hairpin Peptide**, *Angew. Chem. Int. Ed.* **2011**, *50*, 12201-12204.

[194] S. M. Butterfield, W. J. Cooper, M. L. Waters, **Minimalist Protein Design: A β-Hairpin Peptide That Binds ssDNA**, *J. Am. Chem. Soc.* **2005**, *127*, 24-25.

[195] A. L. Stewart, M. L. Waters, **Structural Effects on ss- and dsDNA Recognition by a β-Hairpin Peptide**, *ChemBioChem* **2009**, *10*, 539-544.

[196] Z. Athanassiou, R. L. A. Dias, K. Moehle, N. Dobson, G. Varani, J. A. Robinson, **Structural Mimicry of Retroviral Tat Proteins by Constrained β-Hairpin Peptidomimetics: Ligands with High Affinity and Selectivity for Viral TAR RNA Regulatory Elements**, *J. Am. Chem. Soc.* **2004**, *126*, 6906-6913.

[197] Z. Athanassiou, K. Patora, R. L. A. Dias, K. Moehle, J. A. Robinson, G. Varani, **Structure-Guided Peptidomimetic Design Leads to Nanomolar β-Hairpin Inhibitors of the Tat−TAR Interaction of Bovine Immunodeficiency Virus**, *Biochemistry* **2007**, *46*, 741-751.

[198] T. C. Leeper, Z. Athanassiou, R. L. A. Dias, J. A. Robinson, G. Varani, **TAR RNA Recognition by a Cyclic Peptidomimetic of Tat Protein**, *Biochemistry* **2005**, *44*, 12362-12372.

[199] S. Pal, P. t Hart, **RNA-Binding Macrocyclic Peptides**, *Front. Mol. Biosci.* **2022**, *9*, 883060.

[200] M. J. Walker, G. Varani, in *Methods in Enzymology, Vol. 623* (Ed.: A. E. Hargrove), Academic Press, **2019**, pp. 339-372.

[201] R. Jackstadt, M. C. Hodder, O. J. Sansom, **WNT and β-Catenin in Cancer: Genes and Therapy**, *Annu. Rev. Cancer Biol.* **2020**, *4*, 177-196.

[202] M. Wendt, R. Bellavita, A. Gerber, N.-L. Efrém, T. van Ramshorst, N. M. Pearce, P. R. J. Davey, I. Everard, M. Vazquez-Chantada, E. Chiarparin, P. Grieco, S. Hennig, T. N. Grossmann, **Bicyclic β-Sheet Mimetics that Target the Transcriptional Coactivator β-Catenin and Inhibit Wnt Signaling**, *Angew. Chem. Int. Ed.* **2021**, *60*, 13937-13944.

[203] F. H. Arnold, J.-H. Zhang, **Metal-mediated protein stabilization**, *Trends Biotechnol.* **1994**, *12*, 189-192.

[204] A. Muheim, R. J. Todd, D. R. Casimiro, H. B. Gray, F. H. Arnold, **Ruthenium-mediated protein cross-linking and stabilization**, *J. Am. Chem. Soc.* **1993**, *115*, 5312-5313.

[205] J. T. Kellis, R. J. Todd, F. H. Arnold, **Protein Stabilization by Engineered Metal Chelation**, *Bio/Technology* **1991**, *9*, 994-995.

[206] M. Lella, R. Mahalakshmi, **De novo design of metal-binding cleft in a Trp-Trp stapled thermostable β-hairpin peptide**, *Pept. Sci.* **2021**, *113*, e24240.

[207] B. Biggs, A. L. Presley, D. L. Van Vranken, **The retro-mannich cleavage of δ1,δ1′-tryptophan dimers**, *Bioorg. Med. Chem.* **1998**, *6*, 975-981.

[208] K. M. Makwana, R. Mahalakshmi, **Trp-Trp Cross-Linking: A Structure–Reactivity Relationship in the Formation and Design of Hyperstable Peptide β-Hairpin and α-Helix Scaffolds**, *Org. Lett.* **2015**, *17*, 2498-2501.

[209] G. Bhardwaj, V. K. Mulligan, C. D. Bahl, J. M. Gilmore, P. J. Harvey, O. Cheneval, G. W. Buchko, S. V. S. R. K. Pulavarti, Q. Kaas, A. Eletsky, P.-S. Huang, W. A. Johnsen, P. Greisen, Jr., G. J. Rocklin, Y. Song, T. W. Linsky, A. Watkins, S. A. Rettie, X. Xu, L. P. Carter, R. Bonneau, J. M. Olson, E. Coutsias, C. E. Correnti, T. Szyperski, D. J. Craik, D. Baker, **Accurate de novo design of hyperstable constrained peptides**, *Nature* **2016**, *538*, 329-335.

[210] B. L. Kier, J. M. Anderson, N. H. Andersen, **Disulfide-Mediated β-Strand Dimers: Hyperstable β-Sheets Lacking Tertiary Interactions and Turns**, *J. Am. Chem. Soc.* **2015**, *137*, 5363-5371.

[211] W. Szymański, J. M. Beierle, H. A. V. Kistemaker, W. A. Velema, B. L. Feringa, **Reversible Photocontrol of Biological Systems by the Incorporation of Molecular Photoswitches**, *Chem. Rev.* **2013**, *113*, 6114-6178.

[212] M. M. Lerch, M. J. Hansen, G. M. van Dam, W. Szymanski, B. L. Feringa, **Emerging Targets in Photopharmacology**, *Angew. Chem. Int. Ed.* **2016**, *55*, 10978-10999.

[213] S. Pearson, J. Feng, A. del Campo, **Lighting the Path: Light Delivery Strategies to Activate Photoresponsive Biomaterials In Vivo**, *Adv. Funct. Mater.* **2021**, *31*, 2105989.

[214] S. Afonin, O. Babii, A. Reuter, V. Middel, M. Takamiya, U. Strähle, I. V. Komarov, A. S. Ulrich, **Light-controllable dithienylethene-modified cyclic peptides: photoswitching the in vivo toxicity in zebrafish embryos**, *Beilstein J. Org. Chem.* **2020**, *16*, 39-49.

[215] O. Babii, S. Afonin, M. Berditsch, S. Reiβer, P. K. Mykhailiuk, V. S. Kubyshkin, T. Steinbrecher, A. S. Ulrich, I. V. Komarov, **Controlling Biological Activity with Light: Diarylethene-Containing Cyclic Peptidomimetics**, *Angew. Chem. Int. Ed.* **2014**, *53*, 3392-3395.

[216] O. Babii, S. Afonin, L. V. Garmanchuk, V. V. Nikulina, T. V. Nikolaienko, O. V. Storozhuk, D. V. Shelest, O. I. Dasyukevich, L. I. Ostapchenko, V. Iurchenko, S. Zozulya, A. S. Ulrich, I. V. Komarov, **Direct Photocontrol of Peptidomimetics: An Alternative to Oxygen-Dependent Photodynamic Cancer Therapy**, *Angew. Chem. Int. Ed.* **2016**, *55*, 5493-5496.

[217] O. Babii, S. Afonin, A. Y. Ishchenko, T. Schober, A. O. Negelia, G. M. Tolstanova, L. V. Garmanchuk, L. I. Ostapchenko, I. V. Komarov, A. S. Ulrich, **Structure–Activity Relationships of Photoswitchable Diarylethene-Based β-Hairpin Peptides as Membranolytic Antimicrobial and Anticancer Agents**, *J. Med. Chem.* **2018**, *61*, 10793-10813.

[218] S. Ramazi, J. Zahiri, **Post-translational modifications in proteins: resources, tools and prediction methods**, *Database* **2021**, *2021*.

[219] A. J. Riemen, M. L. Waters, **Controlling Peptide Folding with Repulsive Interactions between Phosphorylated Amino Acids and Tryptophan**, *J. Am. Chem. Soc.* **2009**, *131*, 14081-14087.

[220] A. J. Riemen, M. L. Waters, **Dueling Post-Translational Modifications Trigger Folding and Unfolding of a β-Hairpin Peptide**, *J. Am. Chem. Soc.* **2010**, *132*, 9007-9013.

[221] H. Zamora-Carreras, B. Maestro, E. Strandberg, A. S. Ulrich, J. M. Sanz, M. Á. Jiménez, **Micelle-Triggered β-Hairpin to α-Helix Transition in a 14-Residue**

Peptide from a Choline-Binding Repeat of the Pneumococcal Autolysin LytA, *Chem. Eur. J.* **2015**, *21*, 8076-8089.

[222] H. Zamora-Carreras, B. Maestro, E. Strandberg, A. S. Ulrich, J. M. Sanz, M. Á. Jiménez, **Roles of Amphipathicity and Hydrophobicity in the Micelle-Driven Structural Switch of a 14-mer Peptide Core from a Choline-Binding Repeat**, *Chem. Eur. J.* **2018**, *24*, 5825-5839.

[223] S. Ko, J.-Y. Kim, J. Y. Park, Y.-j. Jung, M.-J. Choi, K. S. Jin, Y. Kim, Y.-b. Lim, W.-j. Jeong, **Modulating the folding and binding of peptides using a stimuli-responsive molecular tweezer**, *Chem. Sci.* **2023**, *14*, 9600-9607.

[224] R. Singh, M. Kumar, A. Mittal, P. K. Mehta, **Microbial enzymes: industrial progress in 21st century**, *3 Biotech* **2016**, *6*, 174.

[225] N. M. Mesbah, **Industrial Biotechnology Based on Enzymes From Extreme Environments**, *Front. Bioeng. Biotechnol.* **2022**, *10*.

[226] M. L. Zastrow, V. L. Pecoraro, **Designing Hydrolytic Zinc Metalloenzymes**, *Biochemistry* **2014**, *53*, 957-978.

[227] X. Liu, R. Waters, H. E. Gilbert, G. T. Barroso, K. M. Boyle, L. S. Witus, **The role of β-hairpin conformation in ester hydrolysis peptide catalysts based on a TrpZip scaffold**, *RSC Adv.* **2021**, *11*, 23714-23718.

[228] M. Matsumoto, S. J. Lee, M. R. Gagné, M. L. Waters, **Cross-strand histidine–aromatic interactions enhance acyl-transfer rates in beta-hairpin peptide catalysts**, *Org. Biomol. Chem.* **2014**, *12*, 8711-8718.

[229] M. Matsumoto, S. J. Lee, M. L. Waters, M. R. Gagné, **A Catalyst Selection Protocol That Identifies Biomimetic Motifs from β-Hairpin Libraries**, *J. Am. Chem. Soc.* **2014**, *136*, 15817-15820.

[230] A. J. Burton, A. R. Thomson, W. M. Dawson, R. L. Brady, D. N. Woolfson, **Installing hydrolytic activity into a completely de novo protein framework**, *Nat. Chem.* **2016**, *8*, 837-844.

[231] C. M. Rufo, Y. S. Moroz, O. V. Moroz, J. Stöhr, T. A. Smith, X. Hu, W. F. DeGrado, I. V. Korendovych, **Short peptides self-assemble to produce catalytic amyloids**, *Nat. Chem.* **2014**, *6*, 303-309.

[232] M. L. Zastrow, A. F. A. Peacock, J. A. Stuckey, V. L. Pecoraro, **Hydrolytic catalysis and structural stabilization in a designed metalloprotein**, *Nat. Chem.* **2012**, *4*, 118-123.

[233] O. H. Hashim, N. A. Adnan, **Coenzyme, cofactor and prosthetic group — Ambiguous biochemical jargon**, *Biochem. Educ.* **1994**, *22*, 93-94.

[234] J. D. Fischer, G. L. Holliday, S. A. Rahman, J. M. Thornton, **The Structures and Physicochemical Properties of Organic Cofactors in Biocatalysis**, *J. Mol. Biol.* **2010**, *403*, 803-824.

[235] C. J. Reedy, M. M. Elvekrog, B. R. Gibney, **Development of a heme protein structure–electrochemical function database**, *Nucleic Acids Res.* **2007**, *36*, D307-D313.

[236] M. Mahajan, S. Bhattacharjya, **β-Hairpin Peptides: Heme Binding, Catalysis, and Structure in Detergent Micelles**, *Angew. Chem. Int. Ed.* **2013**, *52*, 6430-6434.

[237] A. D'Souza, M. Mahajan, S. Bhattacharjya, **Designed multi-stranded heme binding β-sheet peptides in membrane**, *Chem. Sci.* **2016**, *7*, 2563-2571.

[238] A. D'Souza, X. Wu, E. K. L. Yeow, S. Bhattacharjya, **Designed Heme-Cage β-Sheet Miniproteins**, *Angew. Chem. Int. Ed.* **2017**, *56*, 5904-5908.

[239] A. D'Souza, S. Bhattacharjya, **De Novo-Designed β-Sheet Heme Proteins**, *Biochemistry* **2021**, *60*, 431-439.

[240] A. D'Souza, J. Torres, S. Bhattacharjya, **Expanding heme-protein folding space using designed multi-heme β-sheet mini-proteins**, *Commun. Chem.* **2018**, *1*, 78.

[241] M. L. Reback, G. W. Buchko, B. L. Kier, B. Ginovska-Pangovska, Y. Xiong, S. Lense, J. Hou, J. A. S. Roberts, C. M. Sorensen, S. Raugei, T. C. Squier, W. J. Shaw, **Enzyme Design from the Bottom Up: An Active Nickel Electrocatalyst with a Structured Peptide Outer Coordination Sphere**, *Chem. Eur. J.* **2014**, *20*, 1510-1514.

[242] E. S. Wiedner, A. M. Appel, S. Raugei, W. J. Shaw, R. M. Bullock, **Molecular Catalysts with Diphosphine Ligands Containing Pendant Amines**, *Chem. Rev.* **2022**, *122*, 12427-12474.

[243] M. L. Reback, B. Ginovska, G. W. Buchko, A. Dutta, N. Priyadarshani, B. L. Kier, M. L. Helm, S. Raugei, W. J. Shaw, **Investigating the role of chain and linker length on the catalytic activity of an H(2) production catalyst containing a beta-hairpin peptide**, *J. Coord. Chem.* **2016**, *69*, 1730-1747.

[244] A. E. Eriksson, T. A. Jones, A. Liljas, **Refined structure of human carbonic anhydrase II at 2.0 Å resolution**, *Proteins Struct. Funct. Bioinf.* **1988**, *4*, 274-282.

[245] V. M. Krishnamurthy, G. K. Kaufman, A. R. Urbach, I. Gitlin, K. L. Gudiksen, D. B. Weibel, G. M. Whitesides, **Carbonic Anhydrase as a Model for Biophysical and Physical-Organic Studies of Proteins and Protein−Ligand Binding**, *Chem. Rev.* **2008**, *108*, 946-1051.

[246] S. L. Pedersen, A. P. Tofteng, L. Malik, K. J. Jensen, **Microwave heating in solid-phase peptide synthesis**, *Chem. Soc. Rev.* **2012**, *41*, 1826-1844.

[247] C. T. Mant, Y. Chen, Z. Yan, T. V. Popa, J. M. Kovacs, J. B. Mills, B. P. Tripet, R. S. Hodges, in *Peptide Characterization and Application Protocols* (Ed.: G. B. Fields), Humana Press, Totowa, NJ, **2007**, pp. 3-55.

[248] W. J. Henzel, J. T. Stults, **Reversed-Phase Isolation of Peptides**, *Curr. Protoc. Protein Sci.* **2001**, *24*, 11.16.11-11.16.16.

[249] W. Sandoval, **Matrix-Assisted Laser Desorption/Ionization Time-of-Flight Mass Analysis of Peptides**, *Curr. Protoc. Protein Sci.* **2014**, *77*, 16.12.11-16.12.11.

[250] N. J. Greenfield, **Using circular dichroism spectra to estimate protein secondary structure**, *Nat. Protoc.* **2006**, *1*, 2876-2890.

[251] N. J. Greenfield, **Using circular dichroism collected as a function of temperature to determine the thermodynamics of protein unfolding and binding interactions**, *Nat. Protoc.* **2006**, *1*, 2527-2535.

[252] N. J. Greenfield, **Determination of the folding of proteins as a function of denaturants, osmolytes or ligands using circular dichroism**, *Nat. Protoc.* **2006**, *1*, 2733-2741.

[253] N. Hellmann, D. Schneider, in *Protein Supersecondary Structures: Methods and Protocols* (Ed.: A. E. Kister), Springer New York, New York, NY, **2019**, pp. 379-401.

[254] in *Principles of Fluorescence Spectroscopy* (Ed.: J. R. Lakowicz), Springer US, Boston, MA, **2006**, pp. 529-575.

[255] A. H. Kwan, M. Mobli, P. R. Gooley, G. F. King, J. P. Mackay, **Macromolecular NMR spectroscopy for the non-spectroscopist**, *FEBS J.* **2011**, *278*, 687-703.

[256] K. Wüthrich, **Protein structure determination in solution by NMR spectroscopy**, *J. Biol. Chem.* **1990**, *265*, 22059-22062.

[257] J. A. Verpoorte, S. Mehta, J. T. Edsall, **Esterase Activities of Human Carbonic Anhydrases B and C**, *J. Biol. Chem.* **1967**, *242*, 4221-4229.

[258] S. Studer, D. A. Hansen, Z. L. Pianowski, P. R. E. Mittl, A. Debon, S. L. Guffy, B. S. Der, B. Kuhlman, D. Hilvert, **Evolution of a highly active and enantiospecific metalloenzyme from short peptides**, *Science* **2018**, *362*, 1285-1288.

[259] Y. Cen, W. Singh, M. Arkin, T. S. Moody, M. Huang, J. Zhou, Q. Wu, M. T. Reetz, **Artificial cysteine-lipases with high activity and altered catalytic mechanism created by laboratory evolution**, *Nat. Commun.* **2019**, *10*, 3198.

[260] W. J. Song, F. A. Tezcan, **A designed supramolecular protein assembly with in vivo enzymatic activity**, *Science* **2014**, *346*, 1525-1528.

[261] O. V. Makhlynets, P. M. Gosavi, I. V. Korendovych, **Short Self-Assembling Peptides Are Able to Bind to Copper and Activate Oxygen**, *Angew. Chem. Int. Ed.* **2016**, *55*, 9017-9020.

[262] L. T. Nguyen, W. F. Ho, K.-L. Yang, **Copper–tripeptides (cuzymes) with peroxidase-mimetic activity**, *RSC Adv.* **2020**, *10*, 17408-17415.

[263] L. Arregui, M. Ayala, X. Gómez-Gil, G. Gutiérrez-Soto, C. E. Hernández-Luna, M. Herrera de los Santos, L. Levin, A. Rojo-Domínguez, D. Romero-Martínez, M. C. N. Saparrat, M. A. Trujillo-Roldán, N. A. Valdez-Cruz, **Laccases: structure, function, and potential application in water bioremediation**, *Microb. Cell Fact.* **2019**, *18*, 200.

[264] X. Zhang, Y. Hu, X. Yang, Y. Tang, S. Han, A. Kang, H. Deng, Y. Chi, D. Zhu, Y. Lu, **FÖrster resonance energy transfer (FRET)-based biosensors for biological applications**, *Biosens. Bioelectron.* **2019**, *138*, 111314.

[265] T. Heyduk, **Measuring protein conformational changes by FRET/LRET**, *Curr. Opin. Biotechnol.* **2002**, *13*, 292-296.

[266] T. L. Pham, M. Kovermann, F. Thomas, **Switchable Zinc(II)-Responsive Globular β-Sheet Peptide**, *ACS Synth. Biol.* **2022**, *11*, 254-264.

[267] M. Lopez, H. Vu, C. K. Wang, M. G. Wolf, G. Groenhof, A. Innocenti, C. T. Supuran, S.-A. Poulsen, **Promiscuity of Carbonic Anhydrase II. Unexpected Ester Hydrolysis of Carbohydrate-Based Sulfamate Inhibitors**, *J. Am. Chem. Soc.* **2011**, *133*, 18452-18462.

[268] S. Yadav, F. Ahmad, **A New Method for the Determination of Stability Parameters of Proteins from Their Heat-Induced Denaturation Curves**, *Anal. Biochem.* **2000**, *283*, 207-213.

[269] G. R. Grimsley, J. M. Scholtz, C. N. Pace, **A summary of the measured p*K* values of the ionizable groups in folded proteins**, *Protein Sci.* **2009**, *18*, 247-251.

[270] E. K. Koepf, H. M. Petrassi1, M. Sudol, J. W. Kelly, **WW: An isolated three-stranded antiparallel β-sheet domain that unfolds and refolds reversibly; evidence for a structured hydrophobic cluster in urea and GdnHCl and a disordered thermal unfolded state**, *Protein Sci.* **1999**, *8*, 841-853.

[271] V. Reusche, F. Thomas, **Effect of Methionine Sulfoxide on the Synthesis and Purification of Aggregation-Prone Peptides**, *ChemBioChem* **2021**, *22*, 1779-1783.

[272] V. Reusche, **Untersuchungen zur Aggregation des ALS-relevanten TDP-43(307-347)**, Doctoral Thesis, Georg-August-Universtät Göttingen (Göttingen), **2022**.

[273] T. Szyperski, J. L. Mills, D. Perl, J. Balbach, **Combined NMR-observation of cold denaturation in supercooled water and heat denaturation enables accurate measurement of ΔC_p of protein unfolding**, *Eur. Biophys. J.* **2006**, *35*, 363-366.

[274] D. S. Wishart, C. G. Bigam, A. Holm, R. S. Hodges, B. D. Sykes, **1H, 13C and 15N random coil NMR chemical shifts of the common amino acids. I. Investigations of nearest-neighbor effects**, *J. Biomol. NMR* **1995**, *5*, 67-81.

[275] K. Kluska, J. Adamczyk, A. Krężel, **Metal binding properties, stability and reactivity of zinc fingers**, *Coord. Chem. Rev.* **2018**, *367*, 18-64.

[276] M. L. Zastrow, V. L. Pecoraro, **Influence of Active Site Location on Catalytic Activity in de Novo-Designed Zinc Metalloenzymes**, *J. Am. Chem. Soc.* **2013**, *135*, 5895-5903.

[277] P. Comba, **Coordination compounds in the entatic state**, *Coord. Chem. Rev.* **2000**, *200-202*, 217-245.

[278] J. Stanek, A. Hoffmann, S. Herres-Pawlis, **Renaissance of the entatic state principle**, *Coord. Chem. Rev.* **2018**, *365*, 103-121.

[279] B. L. Vallee, R. J. Williams, **Metalloenzymes: the entatic nature of their active sites**, *Proc. Natl. Acad. Sci. U. S. A.* **1968**, *59*, 498-505.

[280] K. Hakansson, A. Wehnert, A. Liljas, **X-ray analysis of metal-substituted human carbonic anhydrase II derivatives**, *Acta Crystallogr. Sect. D Biol. Crystallogr.* **1994**, *50*, 93-100.

[281] K. Håkansson, M. Carlsson, L. A. Svensson, A. Liljas, **Structure of native and apo carbonic anhydrase II and structure of some of its anion-ligand complexes**, *J. Mol. Biol.* **1992**, *227*, 1192-1204.

[282] M. V. Golynskiy, M. S. Koay, J. L. Vinkenborg, M. Merkx, **Engineering Protein Switches: Sensors, Regulators, and Spare Parts for Biology and Biotechnology**, *ChemBioChem* **2011**, *12*, 353-361.

[283] P. A. Evans, K. D. Topping, D. N. Woolfson, C. M. Dobson, **Hydrophobic clustering in nonnative states of a protein: Interpretation of chemical shifts in NMR spectra of denatured states of lysozyme**, *Proteins Struct. Funct. Bioinf.* **1991**, *9*, 248-266.

[284] R. Page, W. Peti, I. A. Wilson, R. C. Stevens, K. Wüthrich, **NMR screening and crystal quality of bacterially expressed prokaryotic and eukaryotic proteins in a structural genomics pipeline**, *Proc. Natl. Acad. Sci. U. S. A.* **2005**, *102*, 1901-1905.

[285] E. Judy, N. Kishore, **A look back at the molten globule state of proteins: thermodynamic aspects**, *Biophys. Rev. (Springer)* **2019**, *11*, 365-375.

[286] V. N. Uversky, A. V. Finkelstein, **Life in Phases: Intra- and Inter- Molecular Phase Transitions in Protein Solutions**, *Biomolecules* **2019**, *9*, 842.

[287] A. Pastore, S. R. Martin, P. A. Temussi, **Generalized View of Protein Folding: In Medio Stat Virtus**, *J. Am. Chem. Soc.* **2019**, *141*, 2194-2200.

[288] C. M. Davis, R. B. Dyer, **WW domain folding complexity revealed by infrared spectroscopy**, *Biochemistry* **2014**, *53*, 5476-5484.

[289] T. Handel, S. Williams, W. DeGrado, **Metal ion-dependent modulation of the dynamics of a designed protein**, *Science* **1993**, *261*, 879-885.

[290] T. Brandt, J. L. Kaar, A. R. Fersht, D. B. Veprintsev, **Stability of p53 Homologs**, *PLoS One* **2012**, *7*, e47889.

[291] C. Alfano, Y. Fichou, K. Huber, M. Weiss, E. Spruijt, S. Ebbinghaus, G. De Luca, M. A. Morando, V. Vetri, P. A. Temussi, A. Pastore, **Molecular Crowding: The History and Development of a Scientific Paradigm**, *Chem. Rev.* **2024**, *124*, 3186-3219.

[292] B. Köhn, M. Kovermann, **Macromolecular Crowding Tunes Protein Stability by Manipulating Solvent Accessibility**, *ChemBioChem* **2019**, *20*, 759-763.

[293] B. Köhn, M. Kovermann, **All atom insights into the impact of crowded environments on protein stability by NMR spectroscopy**, *Nat. Commun.* **2020**, *11*, 5760.

[294] L. A. Munishkina, A. Ahmad, A. L. Fink, V. N. Uversky, **Guiding Protein Aggregation with Macromolecular Crowding**, *Biochemistry* **2008**, *47*, 8993-9006.

[295] R. Kumar, R. Kumar, D. Sharma, M. Garg, V. Kumar, M. C. Agarwal, **Macromolecular crowding-induced molten globule states of the alkali pH-denatured proteins**, *Biochim. Biophys. Acta Proteins Proteomics* **2018**, *1866*, 1102-1114.

[296] B. Kumari, Shabnam, M. Yadav, M. Kumar, P. Kushwaha, N. Prakash Prabhu, R. Kumar, **Determinants for macromolecular crowding-induced thermodynamic stabilization of acid-denatured cytochrome c to molten globules**, *J. Mol. Liq.* **2023**, *387*, 122608.

[297] P. McPhie, Y.-s. Ni, A. P. Minton, **Macromolecular Crowding Stabilizes the Molten Globule Form of Apomyoglobin with Respect to Both Cold and Heat Unfolding**, *J. Mol. Biol.* **2006**, *361*, 7-10.

[298] M. Hirai, S. Ajito, M. Sugiyama, H. Iwase, S.-i. Takata, N. Shimizu, N. Igarashi, A. Martel, L. Porcar, **Direct Evidence for the Effect of Glycerol on Protein Hydration and Thermal Structural Transition**, *Biophys. J.* **2018**, *115*, 313-327.

[299] V. Vagenende, M. G. S. Yap, B. L. Trout, **Mechanisms of Protein Stabilization and Prevention of Protein Aggregation by Glycerol**, *Biochemistry* **2009**, *48*, 11084-11096.

[300] T. Arakawa, S. Timasheff, **The stabilization of proteins by osmolytes**, *Biophys. J.* **1985**, *47*, 411-414.

[301] T. L. Pham, M. R. Conde González, S. Fazliev, A. Kishore, P. Comba, F. Thomas, **Relationship of Thermostability and Binding Affinity in Metal-binding WW-Domain Minireceptors**, *ChemBioChem* **2024**, *25*, e202300715.

[302] J. L. Lauer, C. G. Fields, G. B. Fields, **Sequence dependence of aspartimide formation during 9-fluorenylmethoxycarbonyl solid-phase peptide synthesis**, *Lett. Pept. Sci.* **1995**, *1*, 197-205.

[303] T. R. Young, Z. Xiao, **Principles and practice of determining metal–protein affinities**, *Biochem. J.* **2021**, *478*, 1085-1116.

[304] H. Wada, T. Ishizuki, G. Nakagawa, **Synthesis of 2-(2-thiazolylazo)-4-methyl-5-(sulfopropyl-amino) benzoic acid and the application to the flow-injection analysis of copper(II)**, *Microchim. Acta* **1983**, *81*, 235-244.

[305] F. Rose, **Ueber die Verbindungen des Eiweiss mit Metalloxyden**, *Ann. Phys.* **1833**, *104*, 132-142.

[306] H. Irving, R. J. P. Williams, **637. The stability of transition-metal complexes**, *J. Chem. Soc.* **1953**, 3192-3210.

[307] P. Cimmperman, L. Baranauskienė, S. Jachimovičiūtė, J. Jachno, J. Torresan, V. Michailovienė, J. Matulienė, J. Sereikaitė, V. Bumelis, D. Matulis, **A Quantitative Model of Thermal Stabilization and Destabilization of Proteins by Ligands**, *Biophys. J.* **2008**, *95*, 3222-3231.

[308] L. Ruckthong, M. L. Zastrow, J. A. Stuckey, V. L. Pecoraro, **A Crystallographic Examination of Predisposition versus Preorganization in de Novo Designed Metalloproteins**, *J. Am. Chem. Soc.* **2016**, *138*, 11979-11988.

[309] S. Stoll, A. Schweiger, **EasySpin, a comprehensive software package for spectral simulation and analysis in EPR**, *J. Magn. Reson.* **2006**, *178*, 42-55.

[310] J. Peisach, W. E. Blumberg, **Structural implications derived from the analysis of electron paramagnetic resonance spectra of natural and artificial copper proteins**, *Arch. Biochem. Biophys.* **1974**, *165*, 691-708.

[311] M. Mirdita, K. Schütze, Y. Moriwaki, L. Heo, S. Ovchinnikov, M. Steinegger, **ColabFold: making protein folding accessible to all**, *Nat. Methods* **2022**, *19*, 679-682.

[312] B. S. Avvaru, S. A. Busby, M. J. Chalmers, P. R. Griffin, B. Venkatakrishnan, M. Agbandje-McKenna, D. N. Silverman, R. McKenna, **Apo-Human Carbonic Anhydrase II Revisited: Implications of the Loss of a Metal in Protein Structure, Stability, and Solvent Network**, *Biochemistry* **2009**, *48*, 7365-7372.

[313] J. A. Hunt, M. Ahmed, C. A. Fierke, **Metal Binding Specificity in Carbonic Anhydrase Is Influenced by Conserved Hydrophobic Core Residues**, *Biochemistry* **1999**, *38*, 9054-9062.

[314] L. L. Kiefer, J. A. Ippolito, C. A. Fierke, D. W. Christianson, **Redesigning the zinc binding site of human carbonic anhydrase II: structure of a His2Asp-Zn2+ metal coordination polyhedron**, *J. Am. Chem. Soc.* **1993**, *115*, 12581-12582.

[315] M. A. Holmes, B. W. Matthews, **Structure of thermolysin refined at 1.6 Å resolution**, *J. Mol. Biol.* **1982**, *160*, 623-639.

[316] T. L. Pham, S. Fazliev, P. Baur, P. Comba, F. Thomas, **An Engineered β-Hairpin Peptide Forming Thermostable Complexes with ZnII, NiII, and CuII through a His3 Site**, *ChemBioChem* **2023**, *24*, e202200588.

[317] M. Zaboikin, C. Freter, N. Srinivasakumar, **Gaussian decomposition of high-resolution melt curve derivatives for measuring genome-editing efficiency**, *PLoS One* **2018**, *13*, e0190192.

[318] D. M. John, K. M. Weeks, **Van't Hoff enthalpies without baselines**, *Protein Sci.* **2000**, *9*, 1416-1419.

[319] N. Merino, H. S. Aronson, D. P. Bojanova, J. Feyhl-Buska, M. L. Wong, S. Zhang, D. Giovannelli, **Living at the Extremes: Extremophiles and the Limits of Life in a Planetary Context**, *Front. Microbiol.* **2019**, *10*.

[320] F. H. Arnold, **Engineering proteins for nonnatural environments**, *FASEB J.* **1993**, *7*, 744-749.

[321] F. H. Arnold, **Engineering enzymes for non-aqueous solvents**, *Trends Biotechnol.* **1990**, *8*, 244-249.

[322] O. D. Monera, C. M. Kay, R. S. Hodges, **Protein denaturation with guanidine hydrochloride or urea provides a different estimate of stability depending on the contributions of electrostatic interactions**, *Protein Sci.* **1994**, *3*, 1984-1991.

[323] Y. Wei, A. A. Thyparambil, R. A. Latour, **Protein helical structure determination using CD spectroscopy for solutions with strong background absorbance from 190 to 230nm**, *Biochim. Biophys. Acta Proteins Proteomics* **2014**, *1844*, 2331-2337.

[324] C. Tanford, K. Kawahara, S. Lapanje, **Proteins in 6 m Guanidine Hydrochloride: DEMONSTRATION OF RANDOM COIL BEHAVIOR**, *J. Biol. Chem.* **1966**, *241*, 1921-1923.

[325] J. Hiblot, G. Gotthard, E. Chabriere, M. Elias, **Structural and enzymatic characterization of the lactonase SisLac from Sulfolobus islandicus**, *PLoS One* **2012**, *7*, e47028.

[326] L. R. Snyder, J. J. Kirkland, J. W. Dolan, in *Introduction to Modern Liquid Chromatography*, **2009**, pp. 879-886.

[327] L. E. Valenti, M. B. Paci, C. P. De Pauli, C. E. Giacomelli, **Infrared study of trifluoroacetic acid unpurified synthetic peptides in aqueous solution: Trifluoroacetic acid removal and band assignment**, *Anal. Biochem.* **2011**, *410*, 118-123.

[328] Z. Xiao, A. G. Wedd, **The challenges of determining metal–protein affinities**, *Nat. Prod. Rep.* **2010**, *27*, 768-789.

[329] E. Mathieu, A. E. Tolbert, K. J. Koebke, C. Tard, O. Iranzo, J. E. Penner-Hahn, C. Policar, V. Pecoraro, **Rational De Novo Design of a Cu Metalloenzyme for Superoxide Dismutation**, *Chem. Eur. J.* **2020**, *26*, 249-258.

[330] R. P. Bonomo, F. Riggi, A. J. Di Bilio, **EPR reinvestigation of the copper(II)-imidazole system**, *Inorg. Chem.* **1988**, *27*, 2510-2512.

[331] P. Comba, L. R. Gahan, G. Haberhauer, G. R. Hanson, C. J. Noble, B. Seibold, A. L. van den Brenk, **Copper(II) Coordination Chemistry of Westiellamide and Its Imidazole, Oxazole, and Thiazole Analogues**, *Chem. Eur. J.* **2008**, *14*, 4393-4403.

[332] P. Comba, T. W. Hambley, M. A. Hitchman, H. Stratemeier, **Interpretation of Electronic and EPR Spectra of Copper(II) Amine Complexes: A Test of the MM-AOM Method**, *Inorg. Chem.* **1995**, *34*, 3903-3911.

[333] S. Godlewska, J. Jezierska, K. Baranowska, E. Augustin, A. Dołęga, **Copper(II) complexes with substituted imidazole and chlorido ligands: X-ray, UV–Vis, magnetic and EPR studies and chemotherapeutic potential**, *Polyhedron* **2013**, *65*, 288-297.

[334] S. Mitra, D. Prakash, K. Rajabimoghadam, Z. Wawrzak, P. Prasad, T. Wu, S. K. Misra, J. S. Sharp, I. Garcia-Bosch, S. Chakraborty, **De Novo Design of a Self-Assembled Artificial Copper Peptide that Activates and Reduces Peroxide**, *ACS Catal.* **2021**, *11*, 10267-10278.

[335] T. C. Bruice, G. L. Schmir, **The catalysis of the hydrolysis of p-nitrophenyl acetate by imidazole and its derivatives**, *Arch. Biochem. Biophys.* **1956**, *63*, 484-486.

[336] K. Sayali, P. Sadichha, S. Surekha, **Microbial esterases: an overview**, *Int. J. Curr. Microbiol. Appl. Sci.* **2013**, *2*, 135-146.

[337] M. B. Rao, A. M. Tanksale, M. S. Ghatge, V. V. Deshpande, **Molecular and Biotechnological Aspects of Microbial Proteases**, *Microbiol. Mol. Biol. Rev.* **1998**, *62*, 597-635.

[338] R. J. Sundberg, R. B. Martin, **Interactions of histidine and other imidazole derivatives with transition metal ions in chemical and biological systems**, *Chem. Rev.* **1974**, *74*, 471-517.

[339] K. S. Broo, L. Brive, P. Ahlberg, L. Baltzer, **Catalysis of Hydrolysis and Transesterification Reactions of p-Nitrophenyl Esters by a Designed Helix−Loop−Helix Dimer**, *J. Am. Chem. Soc.* **1997**, *119*, 11362-11372.

[340] C. Vita, C. Roumestand, F. Toma, A. Ménez, **Scorpion toxins as natural scaffolds for protein engineering**, *Proc. Natl. Acad. Sci. U. S. A.* **1995**, *92*, 6404-6408.

[341] M. Subat, K. Woinaroschy, S. Anthofer, B. Malterer, B. König, **1,4,7,10-Tetraazacyclododecane Metal Complexes as Potent Promoters of Carboxyester Hydrolysis under Physiological Conditions**, *Inorg. Chem.* **2007**, *46*, 4336-4356.

[342] D. N. Bolon, S. L. Mayo, **Enzyme-like proteins by computational design**, *Proc. Natl. Acad. Sci. U. S. A.* **2001**, *98*, 14274-14279.

[343] D. Zhao, J. Chen, X. Hu, S. Zhang, **Catalytic Antibodies: Design, Expression, and Their Applications in Medicine**, *Appl. Biochem. Biotechnol.* **2023**, *195*, 1514-1540.

[344] B. S. Der, D. R. Edwards, B. Kuhlman, **Catalysis by a De Novo Zinc-Mediated Protein Interface: Implications for Natural Enzyme Evolution and Rational Enzyme Engineering**, *Biochemistry* **2012**, *51*, 3933-3940.

[345] T. Koike, E. Kimura, **Roles of zinc(II) ion in phosphatases. A model study with zinc(II)-macrocyclic polyamine complexes**, *J. Am. Chem. Soc.* **1991**, *113*, 8935-8941.

[346] T. Koike, M. Takamura, E. Kimura, **Role of Zinc(II) in .beta.-Lactamase II: A Model Study with a Zinc(II)-Macrocyclic Tetraamine (1,4,7,10-Tetraazacyclododecane, Cyclen) Complex**, *J. Am. Chem. Soc.* **1994**, *116*, 8443-8449.

[347] T. Koike, S. Kajitani, I. Nakamura, E. Kimura, M. Shiro, **The catalytic carboxyester hydrolysis by a new zinc(II) complex with an alcohol-pendant cyclen (1-(2-hydroxyethyl)-1,4,7,10-tetraazacyclododecane): A novel model for indirect activation of the serine nucleophile by zinc(II) in zinc enzymes**, *J. Am. Chem. Soc.* **1995**, *117*, 1210-1219.

[348] B.-S. Liao, Y.-H. Liu, S.-M. Peng, S.-T. Liu, **Efficient oxidative coupling of 2,6-disubstituted phenol catalyzed by a dicopper(ii) complex**, *Dalton Trans.* **2012**, *41*, 1158-1164.

[349] R. I. Warren, **Polyphenylene ethers and their alloys**, *Polym. Eng. Sci.* **1985**, *25*, 477-482.

[350] E. N. Peters, **Poly(phenylene ether) Based Amphiphilic Block Copolymers**, *Polymers* **2017**, *9*, 433.

[351] D. Slomczynski, J. P. Nakas, S. W. Tanenbaum, **Production and Characterization of Laccase from Botrytis cinerea 61-34**, *Appl. Environ. Microbiol.* **1995**, *61*, 907-912.

[352] Q. Liu, B. Shentu, J. Zhu, Z. Weng, **Mechanism of the particle formation during the oxidative polymerization of 2,6-dimethylphenol in an aqueous medium**, *J. Appl. Polym. Sci.* **2007**, *104*, 3649-3653.

[353] W. B. Betts, J. E. King, **Oxidative coupling of 2,6-dimethoxyphenol by fungi and bacteria**, *Mycol. Res.* **1991**, *95*, 526-530.

[354] M. Grzybowski, B. Sadowski, H. Butenschön, D. T. Gryko, **Synthetic Applications of Oxidative Aromatic Coupling—From Biphenols to Nanographenes**, *Angew. Chem. Int. Ed.* **2020**, *59*, 2998-3027.

[355] S. Gupta, J. A. P. P. van Dijk, P. Gamez, G. Challa, J. Reedijk, **Mechanistic studies for the polymerization of 2,6-dimethylphenol to poly(2,6-dimethyl-1,4-phenylene**

ether): LC–MS analyses showing rearrangement and redistribution products, *Appl. Catal. A* **2007**, *319*, 163-170.

[356] P. Gamez, S. Gupta, J. Reedijk, **Copper-catalyzed oxidative coupling of 2,6-dimethylphenol: A radicalar or an ionic polymerization?**, *C. R. Chim.* **2007**, *10*, 295-304.

[357] K. Kataoka, H. Komori, Y. Ueki, Y. Konno, Y. Kamitaka, S. Kurose, S. Tsujimura, Y. Higuchi, K. Kano, D. Seo, T. Sakurai, **Structure and Function of the Engineered Multicopper Oxidase CueO from Escherichia coli—Deletion of the Methionine-Rich Helical Region Covering the Substrate-Binding Site**, *J. Mol. Biol.* **2007**, *373*, 141-152.

[358] I. B. Trindade, A. Coelho, F. Cantini, M. Piccioli, R. O. Louro, **NMR of paramagnetic metalloproteins in solution: Ubi venire, quo vadis?**, *J. Inorg. Biochem.* **2022**, *234*, 111871.

[359] R. Berg, B. F. Straub, **Advancements in the mechanistic understanding of the copper-catalyzed azide–alkyne cycloaddition**, *Beilstein J. Org. Chem.* **2013**, *9*, 2715-2750.

[360] H. C. Kolb, M. G. Finn, K. B. Sharpless, **Click Chemistry: Diverse Chemical Function from a Few Good Reactions**, *Angew. Chem. Int. Ed.* **2001**, *40*, 2004-2021.

[361] P. Thirumurugan, D. Matosiuk, K. Jozwiak, **Click Chemistry for Drug Development and Diverse Chemical–Biology Applications**, *Chem. Rev.* **2013**, *113*, 4905-4979.

[362] S. I. Presolski, V. P. Hong, M. G. Finn, **Copper-Catalyzed Azide–Alkyne Click Chemistry for Bioconjugation**, *Curr. Protoc. Chem. Biol.* **2011**, *3*, 153-162.

[363] V. Hong, N. F. Steinmetz, M. Manchester, M. G. Finn, **Labeling Live Cells by Copper-Catalyzed Alkyne−Azide Click Chemistry**, *Bioconjugate Chem.* **2010**, *21*, 1912-1916.

[364] M. Meldal, C. W. Tornøe, **Cu-Catalyzed Azide−Alkyne Cycloaddition**, *Chem. Rev.* **2008**, *108*, 2952-3015.

[365] M. S. Ziegler, K. V. Lakshmi, T. D. Tilley, **Dicopper Cu(I)Cu(I) and Cu(I)Cu(II) Complexes in Copper-Catalyzed Azide–Alkyne Cycloaddition**, *J. Am. Chem. Soc.* **2017**, *139*, 5378-5386.

[366] S. Neumann, M. Biewend, S. Rana, W. H. Binder, **The CuAAC: Principles, Homogeneous and Heterogeneous Catalysts, and Novel Developments and Applications**, *Macromol. Rapid Commun.* **2020**, *41*, 1900359.

[367] V. Hong, S. I. Presolski, C. Ma, M. G. Finn, **Analysis and Optimization of Copper-Catalyzed Azide–Alkyne Cycloaddition for Bioconjugation**, *Angew. Chem. Int. Ed.* **2009**, *48*, 9879-9883.

[368] D. C. Kennedy, C. S. McKay, M. C. B. Legault, D. C. Danielson, J. A. Blake, A. F. Pegoraro, A. Stolow, Z. Mester, J. P. Pezacki, **Cellular Consequences of Copper Complexes Used To Catalyze Bioorthogonal Click Reactions**, *J. Am. Chem. Soc.* **2011**, *133*, 17993-18001.

[369] X. M. Lam, W. G. Lai, E. K. Chan, V. Ling, C. C. Hsu, **Site-Specific Tryptophan Oxidation Induced by Autocatalytic Reaction of Polysorbate 20 in Protein Formulation**, *Pharm. Res.* **2011**, *28*, 2543-2555.

[370] A. R. Giandomenico, G. E. Cerniglia, J. E. Biaglow, C. W. Stevens, C. J. Koch, **The Importance of Sodium Pyruvate in Assessing Damage Produced by Hydrogen Peroxide**, *Free Radical Biol. Med.* **1997**, *23*, 426-434.

[371] V. A. Guarino, W. M. Oldham, J. Loscalzo, Y.-Y. Zhang, **Reaction rate of pyruvate and hydrogen peroxide: assessing antioxidant capacity of pyruvate under biological conditions**, *Sci. Rep.* **2019**, *9*, 19568.

[372] M. Werner, J. Pampel, T. L. Pham, F. Thomas, **Late-Stage Functionalisation of Peptides on the Solid Phase by an Iodination-Substitution Approach**, *Chem. Eur. J.* **2022**, *28*, e202201339.

[373] A. B. T. Ghisaidoobe, S. J. Chung, **Intrinsic Tryptophan Fluorescence in the Detection and Analysis of Proteins: A Focus on Förster Resonance Energy Transfer Techniques**, *Int. J. Mol. Sci.* **2014**, *15*, 22518-22538.

[374] J. Nielsen, S. Brenner, K. D. Janda, **Synthetic methods for the implementation of encoded combinatorial chemistry**, *J. Am. Chem. Soc.* **1993**, *115*, 9812-9813.

[375] G. P. Miller, E. T. Kool, **A simple method for electrophilic functionalization of DNA**, *Org. Lett.* **2002**, *4*, 3599-3601.

[376] A. E. Lanterna, M. González-Béjar, M. Frenette, J. C. Scaiano, **Photophysics of 7-mercapto-4-methylcoumarin and derivatives: complementary fluorescence behaviour to 7-hydroxycoumarins**, *Photochem. Photobiol. Sci.* **2017**, *16*, 1284-1289.

[377] M. Balcı Leinen, S. Lindenthal, D. Heimfarth, J. Zaumseil, **Networks of as-dispersed, polymer-wrapped (6,5) single-walled carbon nanotubes for selective Cu2+ and glyphosate sensing**, *Nanoscale* **2022**, *14*, 13542-13550.

[378] M. Mertens, S. Höss, G. Neumann, J. Afzal, W. Reichenbecher, **Glyphosate, a chelating agent—relevant for ecological risk assessment?**, *Environ. Sci. Pollut. Res.* **2018**, *25*, 5298-5317.

[379] S. J. Archibald, in *Comprehensive Coordination Chemistry II* (Eds.: J. A. McCleverty, T. J. Meyer), Pergamon, Oxford, **2003**, pp. 1147-1251.

[380] O. A. Moe, S. A. Wiest, **Determination of stability constants for zinc-pyrophosphate complexes**, *Anal. Biochem.* **1977**, *77*, 73-78.

[381] A. E. Fenster, D. N. Harpp, J. A. Schwarcz, **A useful model for the" lock and key" analogy**, *J. Chem. Educ.* **1984**, *61*, 967.

[382] B. Byrne, E. Stack, N. Gilmartin, R. O'Kennedy, **Antibody-Based Sensors: Principles, Problems and Potential for Detection of Pathogens and Associated Toxins**, *Sensors* **2009**, *9*, 4407-4445.

[383] A. Kato, K. Touhara, **Mammalian olfactory receptors: pharmacology, G protein coupling and desensitization**, *Cell. Mol. Life Sci.* **2009**, *66*, 3743-3753.

[384] S. D. Roper, **The Cell Biology of Vertebrate Taste Receptors**, *Annu. Rev. Neurosci.* **1989**, *12*, 329-353.

[385] H. Saito, Q. Chi, H. Zhuang, H. Matsunami, J. D. Mainland, **Odor Coding by a Mammalian Receptor Repertoire**, *Sci. Signaling* **2009**, *2*, ra9-ra9.

[386] W. J. Peveler, M. Yazdani, V. M. Rotello, **Selectivity and Specificity: Pros and Cons in Sensing**, *ACS Sens.* **2016**, *1*, 1282-1285.

[387] J. Krämer, R. Kang, L. M. Grimm, L. De Cola, P. Picchetti, F. Biedermann, **Molecular Probes, Chemosensors, and Nanosensors for Optical Detection of Biorelevant Molecules and Ions in Aqueous Media and Biofluids**, *Chem. Rev.* **2022**, *122*, 3459-3636.

[388] M. Azadeh, B. Gorovits, J. Kamerud, S. MacMannis, A. Safavi, J. Sailstad, P. Sondag, **Calibration Curves in Quantitative Ligand Binding Assays: Recommendations and Best Practices for Preparation, Design, and Editing of Calibration Curves**, *AAPS J.* **2017**, *20*, 22.

[389] J. J. Lavigne, E. V. Anslyn, **Sensing A Paradigm Shift in the Field of Molecular Recognition: From Selective to Differential Receptors**, *Angew. Chem. Int. Ed.* **2001**, *40*, 3118-3130.

[390] J. P. Anzenbacher, P. Lubal, P. Buček, M. A. Palacios, M. E. Kozelkova, **A practical approach to optical cross-reactive sensor arrays**, *Chem. Soc. Rev.* **2010**, *39*, 3954-3979.

[391] S.-F. Wong, S. M. Khor, **State-of-the-art of differential sensing techniques in analytical sciences**, *TrAC Trends Anal. Chem.* **2019**, *114*, 108-125.

[392] S. M. Scott, D. James, Z. Ali, **Data analysis for electronic nose systems**, *Microchim. Acta* **2006**, *156*, 183-207.

[393] J. Lever, M. Krzywinski, N. Altman, **Principal component analysis**, *Nat. Methods* **2017**, *14*, 641-642.

[394] S. Stewart, M. A. Ivy, E. V. Anslyn, **The use of principal component analysis and discriminant analysis in differential sensing routines**, *Chem. Soc. Rev.* **2014**, *43*, 70-84.

[395] P. C. Jurs, G. A. Bakken, H. E. McClelland, **Computational Methods for the Analysis of Chemical Sensor Array Data from Volatile Analytes**, *Chem. Rev.* **2000**, *100*, 2649-2678.

[396] R. Jastrzab, M. Nowak, M. Zabiszak, A. Odani, M. T. Kaczmarek, **Significance and properties of the complex formation of phosphate and polyphosphate groups in particles present in living cells**, *Coord. Chem. Rev.* **2021**, *435*, 213810.

[397] F. Bahfie, M. R. Supriadi, S. Oediyani, F. Nurjaman, W. Astuti, E. Prasetyo, D. Susanti, **Use of monosodium glutamate (MSG) for green leaching process: An overview**, *Period. Mineral.* **2022**, *91*.

[398] B. Wang, J. Han, N. M. Bojanowski, M. Bender, C. Ma, K. Seehafer, A. Herrmann, U. H. F. Bunz, **An Optimized Sensor Array Identifies All Natural Amino Acids**, *ACS Sens.* **2018**, *3*, 1562-1568.

[399] N. M. Bojanowski, M. Bender, K. Seehafer, U. H. F. Bunz, **Discrimination of Saccharides by a Simple Array**, *Chem. Eur. J.* **2017**, *23*, 12253-12258.

[400] J. Han, B. Wang, M. Bender, J. Pfisterer, W. Huang, K. Seehafer, M. Yazdani, V. M. Rotello, C. M. Rotello, U. H. F. Bunz, **Fingerprinting antibiotics with PAE-based fluorescent sensor arrays**, *Polym. Chem.* **2017**, *8*, 2723-2732.

[401] T. L. Pham, J. Zilke, C. C. Müller, F. Thomas, **The CSY-protecting group in the microwave-assisted synthesis of aggregation-prone peptides**, *RSC Chem. Biol.* **2022**, *3*, 426-430.

[402] S. Nakayama, R. H. Kretsinger, **Evolution of the EF-Hand Family of Proteins**, *Annu. Rev. Biophys.* **1994**, *23*, 473-507.

[403] E. A. Permyakov, **Metal Binding Proteins**, *Encyclopedia* **2021**, *1*, 261-292.

[404] P. B. Szecsi, **The aspartic proteases**, *Scand. J. Clin. Lab. Invest.* **1992**, *52*, 5-22.

[405] L. Hedstrom, **Serine Protease Mechanism and Specificity**, *Chem. Rev.* **2002**, *102*, 4501-4524.

[406] W. J. Duddy, J. W. M. Nissink, F. H. Allen, E. J. Milner-White, **Mimicry by asx- and ST-turns of the four main types of β-turn in proteins**, *Protein Sci.* **2004**, *13*, 3051-3055.

[407] R. Behrendt, P. White, J. Offer, **Advances in Fmoc solid-phase peptide synthesis**, *J. Pept. Sci.* **2016**, *22*, 4-27.

[408] R. Behrendt, S. Huber, R. Martí, P. White, **New t-butyl based aspartate protecting groups preventing aspartimide formation in Fmoc SPPS**, *J. Pept. Sci.* **2015**, *21*, 680-687.

[409] A.-B. M. Abdel-Aal, G. Papageorgiou, R. Raz, M. Quibell, F. Burlina, J. Offer, **A backbone amide protecting group for overcoming difficult sequences and suppressing aspartimide formation**, *J. Pept. Sci.* **2016**, *22*, 360-367.

[410] P. Dumy, M. Keller, D. E. Ryan, B. Rohwedder, T. Wöhr, M. Mutter, **Pseudo-Prolines as a Molecular Hinge: Reversible Induction of cis Amide Bonds into Peptide Backbones**, *J. Am. Chem. Soc.* **1997**, *119*, 918-925.

[411] V. Cardona, I. Eberle, S. Barthélémy, J. Beythien, B. Doerner, P. Schneeberger, J. Keyte, P. D. White, **Application of Dmb-Dipeptides in the Fmoc SPPS of Difficult and Aspartimide-Prone Sequences**, *Int. J. Pept. Res. Ther.* **2008**, *14*, 285-292.

[412] J. D. Wade, M. N. Mathieu, M. Macris, G. W. Tregear, **Base-induced side reactions in Fmoc-solid phase peptide synthesis:Minimization by use of piperazine as Nα-deprotectionreagent**, *Lett. Pept. Sci.* **2000**, *7*, 107-112.

[413] T. Michels, R. Dölling, U. Haberkorn, W. Mier, **Acid-Mediated Prevention of Aspartimide Formation in Solid Phase Peptide Synthesis**, *Org. Lett.* **2012**, *14*, 5218-5221.

[414] R. Subirós-Funosas, A. El-Faham, F. Albericio, **Use of Oxyma as pH modulatory agent to be used in the prevention of base-driven side reactions and its effect on 2-chlorotrityl chloride resin**, *Pept. Sci.* **2012**, *98*, 89-97.

[415] K. Neumann, J. Farnung, S. Baldauf, J. W. Bode, **Prevention of aspartimide formation during peptide synthesis using cyanosulfurylides as carboxylic acid-protecting groups**, *Nat. Commun.* **2020**, *11*, 982.

[416] E. Pucheta-Martinez, N. D'Amelio, M. Lelli, J. L. Martinez-Torrecuadrada, M. Sudol, G. Saladino, F. L. Gervasio, **Changes in the folding landscape of the WW domain provide a molecular mechanism for an inherited genetic syndrome**, *Sci. Rep.* **2016**, *6*, 30293.

[417] R. B. Birge, C. Kalodimos, F. Inagaki, S. Tanaka, **Crk and CrkL adaptor proteins: networks for physiological and pathological signaling**, *Cell Commun. Signaling* **2009**, *7*, 13.

[418] F. Mende, M. Beisswenger, O. Seitz, **Automated Fmoc-Based Solid-Phase Synthesis of Peptide Thioesters with Self-Purification Effect and Application in the Construction of Immobilized SH3 Domains**, *J. Am. Chem. Soc.* **2010**, *132*, 11110-11118.

[419] M. Buck, **Trifluoroethanol and colleagues: cosolvents come of age. Recent studies with peptides and proteins**, *Q. Rev. Biophys.* **1998**, *31*, 297-355.

[420] N. Chaudhary, S. Singh, R. Nagaraj, **Morphology of self-assembled structures formed by short peptides from the amyloidogenic protein tau depends on the solvent in which the peptides are dissolved**, *J. Pept. Sci.* **2009**, *15*, 675-684.

[421] S. Chen, R. Wetzel, **Solubilization and disaggregation of polyglutamine peptides**, *Protein Sci.* **2001**, *10*, 887-891.

[422] J. A. Camarero, D. Fushman, S. Sato, I. Giriat, D. Cowburn, D. P. Raleigh, T. W. Muir, **Rescuing a destabilized protein fold through backbone cyclization**, *J. Mol. Biol.* **2001**, *308*, 1045-1062.

[423] N. Hirota, Y. Goto, K. Mizuno, **Cooperative α-helix formation of β-lactoglobulin and melittin induced by hexafluoroisopropanol**, *Protein Sci.* **1997**, *6*, 416-421.

[424] A. Pessi, E. Bianchi, A. Crameri, S. Venturini, A. Tramontano, M. Sollazzo, **A designed metal-binding protein with a novel fold**, *Nature* **1993**, *362*, 367-369.

[425] H. N. Mueller, A. Skerra, **Grafting of a High-Affinity Zn(II)-Binding Site on the .beta.-Barrel of Retinol-Binding Protein Results in Enhanced Folding Stability and Enables Simplified Purification**, *Biochemistry* **1994**, *33*, 14126-14135.

[426] A. Schmidt, H. N. Müller, A. Skerra, **A Zn(II)-binding site engineered into retinol-binding protein exhibits metal-ion specificity and allows highly efficient affinity purification with a newly designed metal ligand**, *Chem. Biol.* **1996**, *3*, 645-653.

[427] M. Klemba, K. H. Gardner, S. Marino, N. D. Clarke, L. Regan, **Novel metal-binding proteins by design**, *Nat. Struct. Biol.* **1995**, *2*, 368-373.

[428] M. S. Wisz, C. Z. Garrett, H. W. Hellinga, **Construction of a Family of Cys2His2 Zinc Binding Sites in the Hydrophobic Core of Thioredoxin by Structure-Based Design**, *Biochemistry* **1998**, *37*, 8269-8277.

[429] C. Zhu, C. Zhang, H. Liang, L. Lai, **Engineering a zinc binding site into the de novo designed protein DS119 with a βαβ structure**, *Protein Cell* **2011**, *2*, 1006-1013.

[430] W. M. Dawson, K. L. Shelley, J. M. Fletcher, D. A. Scott, L. Lombardi, G. G. Rhys, T. J. LaGambina, U. Obst, A. J. Burton, J. A. Cross, G. Davies, F. J. O. Martin, F. J. Wiseman, R. L. Brady, D. Tew, C. W. Wood, D. N. Woolfson, **Differential sensing with arrays of de novo designed peptide assemblies**, *Nat. Commun.* **2023**, *14*, 383.

[431] J. Jeong, G. Szczepaniak, S. S. Yerneni, F. Lorandi, H. Jafari, S. Lathwal, S. R. Das, K. Matyjaszewski, **Biocompatible photoinduced CuAAC using sodium pyruvate**, *Chem. Commun.* **2021**, *57*, 12844-12847.

[432] M. Ichihashi, M. Ueda, A. Budiyanto, T. Bito, M. Oka, M. Fukunaga, K. Tsuru, T. Horikawa, **UV-induced skin damage**, *Toxicology* **2003**, *189*, 21-39.

[433] F. Thomas, W. M. Dawson, E. J. M. Lang, A. J. Burton, G. J. Bartlett, G. G. Rhys, A. J. Mulholland, D. N. Woolfson, **De Novo-Designed α-Helical Barrels as Receptors for Small Molecules**, *ACS Synth. Biol.* **2018**, *7*, 1808-1816.

[434] T. Heinisch, T. R. Ward, **Artificial Metalloenzymes Based on the Biotin–Streptavidin Technology: Challenges and Opportunities**, *Acc. Chem. Res.* **2016**, *49*, 1711-1721.

[435] K. Akagawa, in *Peptide Applications in Biomedicine, Biotechnology and Bioengineering* (Ed.: S. Koutsopoulos), Woodhead Publishing, **2018**, pp. 513-564.

[436] E. R. Jarvo, S. J. Miller, **Amino acids and peptides as asymmetric organocatalysts**, *Tetrahedron* **2002**, *58*, 2481-2495.

[437] A. P. Umali, S. E. LeBoeuf, R. W. Newberry, S. Kim, L. Tran, W. A. Rome, T. Tian, D. Taing, J. Hong, M. Kwan, H. Heymann, E. V. Anslyn, **Discrimination of flavonoids and red wine varietals by arrays of differential peptidic sensors**, *Chem. Sci.* **2011**, *2*, 439-445.

[438] M. De, S. Rana, H. Akpinar, O. R. Miranda, R. R. Arvizo, U. H. F. Bunz, V. M. Rotello, **Sensing of proteins in human serum using conjugates of nanoparticles and green fluorescent protein**, *Nat. Chem.* **2009**, *1*, 461-465.

[439] R. Mahalakshmi, S. Raghothama, P. Balaram, **NMR Analysis of Aromatic Interactions in Designed Peptide β-Hairpins**, *J. Am. Chem. Soc.* **2006**, *128*, 1125-1138.

[440] T. S. Choi, F. A. Tezcan, **Overcoming universal restrictions on metal selectivity by protein design**, *Nature* **2022**, *603*, 522-527.

[441] T. S. Choi, F. A. Tezcan, **Design of a Flexible, Zn-Selective Protein Scaffold that Displays Anti-Irving–Williams Behavior**, *J. Am. Chem. Soc.* **2022**, *144*, 18090-18100.

[442] A. W. Foster, T. R. Young, P. T. Chivers, N. J. Robinson, **Protein metalation in biology**, *Curr. Opin. Chem. Biol.* **2022**, *66*, 102095.

[443] S. M. Gould, D. S. Tawfik, **Directed Evolution of the Promiscuous Esterase Activity of Carbonic Anhydrase II**, *Biochemistry* **2005**, *44*, 5444-5452.

[444] I. R. Ilyasov, V. L. Beloborodov, I. A. Selivanova, R. P. Terekhov, **ABTS/PP Decolorization Assay of Antioxidant Capacity Reaction Pathways**, *Int. J. Mol. Sci.* **2020**, *21*, 1131.

[445] A. J. Metrano, N. C. Abascal, B. Q. Mercado, E. K. Paulson, A. E. Hurtley, S. J. Miller, **Diversity of Secondary Structure in Catalytic Peptides with β-Turn-Biased Sequences**, *J. Am. Chem. Soc.* **2017**, *139*, 492-516.

[446] E. A. C. Davie, S. M. Mennen, Y. Xu, S. J. Miller, **Asymmetric Catalysis Mediated by Synthetic Peptides**, *Chem. Rev.* **2007**, *107*, 5759-5812.

[447] H. Wada, T. Ishizuki, G. Nakagawa, **2-(2-thiazolylazo)-4-methyl-5-(sulfomethylamino)benzoic acid as a reagent for the spectrophotometric determination of cobalt**, *Anal. Chim. Acta* **1982**, *135*, 333-341.

[448] J. Han, H. Cheng, B. Wang, M. S. Braun, X. Fan, M. Bender, W. Huang, C. Domhan, W. Mier, T. Lindner, K. Seehafer, M. Wink, U. H. F. Bunz, **A Polymer/Peptide Complex-Based Sensor Array That Discriminates Bacteria in Urine**, *Angew. Chem. Int. Ed.* **2017**, *56*, 15246-15251.

[449] A. Bajaj, O. R. Miranda, R. Phillips, I.-B. Kim, D. J. Jerry, U. H. F. Bunz, V. M. Rotello, **Array-Based Sensing of Normal, Cancerous, and Metastatic Cells Using Conjugated Fluorescent Polymers**, *J. Am. Chem. Soc.* **2010**, *132*, 1018-1022.

[450] Z. Li, K. S. Suslick, **Portable Optoelectronic Nose for Monitoring Meat Freshness**, *ACS Sens.* **2016**, *1*, 1330-1335.

[451] N. M. Bojanowski, F. Hainer, M. Bender, K. Seehafer, U. H. F. Bunz, **An Optical Sensor Array Discriminates Syrups and Honeys**, *Chem. Eur. J.* **2018**, *24*, 4255-4258.

[452] J. Han, B. Wang, M. Bender, K. Seehafer, U. H. F. Bunz, **Poly(p-phenyleneethynylene)-based tongues discriminate fruit juices**, *Analyst* **2017**, *142*, 537-543.

[453] A. L. Valle, F. C. C. Mello, R. P. Alves-Balvedi, L. P. Rodrigues, L. R. Goulart, **Glyphosate detection: methods, needs and challenges**, *Environ. Chem. Lett.* **2019**, *17*, 291-317.

[454] A. M. Smith, M. C. Mancini, S. Nie, **Second window for in vivo imaging**, *Nat. Nanotechnol.* **2009**, *4*, 710-711.

[455] M. Zhao, B. Li, H. Zhang, F. Zhang, **Activatable fluorescence sensors for in vivo bio-detection in the second near-infrared window**, *Chem. Sci.* **2021**, *12*, 3448-3459.

[456] W. Wang, M. M. Lorion, J. Shah, A. R. Kapdi, L. Ackermann, **Late-stage peptide diversification by position-selective C− H activation**, *Angew. Chem. Int. Ed.* **2018**, *57*, 14700-14717.

[457] N. Kurochkina, U. Guha, **SH3 domains: modules of protein–protein interactions**, *Biophys. Rev. (Springer)* **2013**, *5*, 29-39.

[458] U. Heinemann, Y. Roske, **Cold-Shock Domains—Abundance, Structure, Properties, and Nucleic-Acid Binding**, *Cancers* **2021**, *13*, 190.

[459] M. Strohalm, D. Kavan, P. Novák, M. Volný, V. Havlíček, **mMass 3: A Cross-Platform Software Environment for Precise Analysis of Mass Spectrometric Data**, *Anal. Chem.* **2010**, *82*, 4648-4651.

[460] E. F. Pettersen, T. D. Goddard, C. C. Huang, G. S. Couch, D. M. Greenblatt, E. C. Meng, T. E. Ferrin, **UCSF Chimera—A visualization system for exploratory research and analysis**, *J. Comput. Chem.* **2004**, *25*, 1605-1612.

[461] C. N. Pace, F. Vajdos, L. Fee, G. Grimsley, T. Gray, **How to measure and predict the molar absorption coefficient of a protein**, *Protein Sci.* **1995**, *4*, 2411-2423.

[462] P. Kuzmič, **Program DYNAFIT for the Analysis of Enzyme Kinetic Data: Application to HIV Proteinase**, *Anal. Biochem.* **1996**, *237*, 260-273.

[463] J.-L. Mergny, L. Lacroix, **Analysis of Thermal Melting Curves**, *Oligonucleotides* **2003**, *13*, 515-537.

[464] J. F. Brandts, L. N. Lin, **Study of strong to ultratight protein interactions using differential scanning calorimetry**, *Biochemistry* **1990**, *29*, 6927-6940.

[465] A. Shrake, P. D. Ross, **Origins and consequences of ligand-induced multiphasic thermal protein denaturation**, *Biopolymers* **1992**, *32*, 925-940.

[466] D. Matulis, J. K. Kranz, F. R. Salemme, M. J. Todd, **Thermodynamic Stability of Carbonic Anhydrase: Measurements of Binding Affinity and Stoichiometry Using ThermoFluor**, *Biochemistry* **2005**, *44*, 5258-5266.

[467] J. M. Majikes, M. Zwolak, J. A. Liddle, **Best practice for improved accuracy: A critical reassessment of van't Hoff analysis of melt curves**, *Biophys. J.* **2022**, *121*, 1986-2001.

[468] D. Sinnaeve, **The Stejskal–Tanner equation generalized for any gradient shape—an overview of most pulse sequences measuring free diffusion**, *Concepts Magn. Reson. Part A* **2012**, *40A*, 39-65.

[469] F. Filira, B. Biondi, L. Biondi, E. Giannini, M. Gobbo, L. Negri, R. Rocchi, **Opioid peptides: synthesis and biological properties of [(Nγ-glucosyl,Nγ-methoxy)-α,γ-diamino-(S)-butanoyl]4-deltorphin-1-neoglycopeptide and related analogues**, *Org. Biomol. Chem.* **2003**, *1*, 3059-3063.

[470] R. M. Bock, N.-S. Ling, S. A. Morell, S. H. Lipton, **Ultraviolet absorption spectra of adenosine-5′-triphosphate and related 5′-ribonucleotides**, *Arch. Biochem. Biophys.* **1956**, *62*, 253-264.

10 Appendix

10.1 Abbreviations

[Θ]	mean residue ellipticity
°C	Degree Celsius
1/2/3D	one/two/three dimensional
a. u.	Arbitrary units
Abs	Absorbance
ABTS	2,2'-Azino-bis(3-ethylbenzothiazoline)-6-sulfonic acid
A_{CH}	Integral of the CH region
AMP	Adenosine monophosphate
A_{NH}	Integral of the NH region
ATP	Adenosine triphosphate
cAMP	Cyclic adenosine monophosphate
CD	Circular dichroism
CSY	Cyanosulfurylide protection group
CT	*C*-Terminal region
CTP	Cytidin triphosphate
D	Diffusion coefficient
DBU	1,8-Diazabicyclo[5.4.0]undec-7-ene
DCM	Dichloromethane
DIC	*N*,*N'*-Di(propan-2-yl)methanediimine
DIPEA	*N,N*-Diisopropylethylamine
DMF	*N*,*N*-Dimethylformamide
DMP	2,6-Dimethoxyphenol
DMSO	Dimethyl sulfoxide
Dmt	Dimethoxytrityl
DNA	Desoxyribonucleic acid
Ds	Double strand
dTTP	Desoxy thymidine triphosphate
EDTA	Ethylenediaminetetraacetate
EPR	Electron paramagnetic resonance
Eq.	Equation
Equiv.	Equivalents
EtOAc	Ethyl acetate
f_n	Fraction of native peptide
F_n	Integral of the native signals
F_{n+u}	Integral of the native and unfolded signal
FRET	Förster resonance energy transfer
FT	Fourier-Transform
GdnHCl	Guanidine hydrochloride
Gps	Glyphosate
GTP	Guanosine triphosphate
HBP	Hydrogen bonding position
hCAII	human carbonic anhydrase II
HEDTA	Hydroxyethylethylenediaminetriacetate
HEPES	4-(2-hydroxyethyl)-1-piperazineethanesulfonic acid
HFIP	1,1,1,3,3,3-Hexafluoroisopropanol
hPin1	Human protein interacting with never in mitosis A 1
$hPin1_{WW}$	WW domain of hPin1
HPLC	High performance liquid chromatography
HSQC	Heteronuclear single quantum coherence
IC_{50}	Half maximal inhibitory concentration
Im	Imidazole
Int.	Intensity
IR	Infrared
ITC	Isothermal titration calorimetry
K	Kelvin
K	Equilibrium constant
k_{cat}	Turnover number

K_d	Dissociation constant
K_m	Michaelis-Menten constant
k_{obs}	Observed kinetic constant
LP	Loop
M	Molar
MALDI	Matrix-assisted laser desorption/ionization
*m*CPBA	*meta*-Chloroperoxybenzoic acid
MeCN	Acetonitrile
MeOH	Methanol
MES	2-(*N*-Morpholino)ethanesulfonic acid
MG	Molten globule
MOPS	3-(*N*-Morpholino)propanesulfonic acid
MS	Mass spectrometry
MSP	Marginaly stable protein
NCS	*N*-Chlorosuccinimide
nHBp	Non-hydrogen bonding position
NMR	Nuclear magnetic resonance
NT	*N*-terminal region
o.n.	Overnight
Oxone	Potassium peroxymonosulfate
Oxyma	Ethyl cyanohydroxyiminoacetate
PC	Principal component
PCA	Principal component analysis
Phy	Phytate
P_i	Phosphate
pK_a	Acidity constant
*p*NPA	*para*-Nitrophenyl acetate
PPE	Polyphenylene ether
PP_i	Pyrophosphate
Ppm	Parts per million
PTFE	Polytetrafluoroethylene
RNA	Ribonucleic acid
Rt	Room temperature
SPPS	Solid-phase peptide synthesis
Ss	Single strand
T	Temperature
TAMSMB	(2-(2-thiazolylazo)-4-methyl-5-(sulfomethylamino) benzoic acid)
TCEP	Tris(2-carboxyethyl)phosphine
TFA	Trifluoroacetic acid
TFE	2,2,2-Trifluoroethanol
THPTA	Tris(3-hydroxypropyltriazolylmethyl)amine
TIPS	Triisopropyl silane
TLC	Thin layer chromatography
T_m	Melting temperature
TMBP	3,3',5,5'-Tetramethoxy-4,4'-bisphenol
TMDQ	3,3',5,5'-Tetramethoxy-4,4'-diphenoquinone
TOF	time-of-flight
Trpzip	Tryptophan zipper
UV/Vis	Ultra violet/visible
V	Reaction rate
α_F	Fraction folded
ΔC_p	Change in heat capacity at constant pressure
ΔG	Change in Gibbs free energy
ΔH	Change in enthalpy
ΔS	Change in entropy
λ	Wavelenght

10.2 Settings of the peptide synthesizer

The following Tables (Table 10-1 - Table 10-15) contain the detailed settings for the microwave-assisted peptide syntheses performed in this study using the *CEM LibertyBlue* peptide synthesizer.

Most peptides were synthesized according to the **standard procedure**, which includes:

- **Resin swelling**
- **First Single Coupling** for the first amino acid, except those listed below
- **Single Coupling** for further amino acids, except those listed below
- **Single 50 °C 10 min Coupling** for Fmoc-His(Trt)-OH
- **Double Coupling** for Fmoc-Arg(Pbf)-OH
- **Double Coupling Gly** for Fmoc-Gly-OH
- **Final Deprotection** to remove the last Fmoc group

If the peptides were synthesised using different settings, this is indicated in Chapter 10.3.

Table 10-1: Settings for Microwave Methods. Mixing of the reaction mixture was performed by bubbling nitrogen through the reaction vessel frit (bubble for 2 s, off for 3 s).

Microwave Method	Temperature / °C	Power / W	Hold Time / s	DeltaT / °C
Standard deprotection	75	155	15	2
	90	30	50	1
Conventional deprotection	25	0	300	2
Standard coupling	75	170	15	2
	90	30	110	1
Conventional coupling	25	0	3600	2
50 °C 10 min Coupling	25	0	120	2
	50	35	480	1

Table 10-2: Settings for **Resin Swelling**.

	Cycle Steps	Parameter values
1	Swell Resin	Main solvent volume: 15 mL, Time: 300 s

Table 10-3: Settings for **First Single Coupling**.

	Cycle Steps	Parameter values
1	Deprotection	Reaction Method: Standard Deprotection, Deprotection Volume: 4 mL
2	Deprotection	Reaction Method: Standard Deprotection, Deprotection Volume: 4 mL
3	Wash	Volume: 4 mL, Drain Time: 10 s
4	Wash	Volume: 4 mL, Drain Time: 5 s
5	Wash	Volume: 4 mL, Drain Time: 5 s
6	Wash	Volume: 4 mL, Drain Time: 5 s
7	Coupling	Reaction Method: Standard coupling, Amino Acid: from method, Amino Acid Volume: 2.5 mL, Activator Bottle Position: PositionACT, Activator Volume: 2 mL, Activator Base Position: PositionACTB, Activator Base Volume: 1 mL, Delayed Reagent Time: 0 s, Delayed Reagent Bottle Position: PositionACTB, Delayed Reagent Volume: 0 mL, Manifold Wash Volume: 2 mL
8	Wash	Volume: 4 mL, Drain Time: 10 s
9	Wash	Volume: 4 mL, Drain Time: 5 s

Table 10-4: Settings for **Single Coupling**.

	Cycle Steps	Parameter values
1	Deprotection	Reaction Method: Standard Deprotection, Deprotection Volume: 4 mL
2	Wash	Volume: 4 mL, Drain Time: 10 s
3	Wash	Volume: 4 mL, Drain Time: 5 s
4	Wash	Volume: 4 mL, Drain Time: 5 s
5	Wash	Volume: 4 mL, Drain Time: 5 s
6	Coupling	Reaction Method: Standard coupling, Amino Acid: from method, Amino Acid Volume: 2.5 mL, Activator Bottle Position: PositionACT, Activator Volume: 2 mL, Activator Base Position: PositionACTB, Activator Base Volume: 1 mL, Delayed Reagent Time: 0 s, Delayed Reagent Bottle Position: PositionACTB, Delayed Reagent Volume: 0 mL, Manifold Wash Volume: 2 mL
7	Wash	Volume: 4 mL, Drain Time: 10 s
8	Wash	Volume: 4 mL, Drain Time: 5 s

Table 10-5. Settings for **Single 50 °C 10 min Coupling**.

	Cycle Steps	Parameter values
1	Deprotection	Reaction Method: Standard Deprotection, Deprotection Volume: 4 mL
2	Wash	Volume: 4 mL, Drain Time: 10 s
3	Wash	Volume: 4 mL, Drain Time: 5 s
4	Wash	Volume: 4 mL, Drain Time: 5 s
5	Wash	Volume: 4 mL, Drain Time: 5 s
6	Coupling	Reaction Method: 50 °C 10 min coupling, Amino Acid: from method, Amino Acid Volume: 2.5 mL, Activator Bottle Position: PositionACT, Activator Volume: 2 mL, Activator Base Position: PositionACTB, Activator Base Volume: 1 mL, Delayed Reagent Time: 0 s, Delayed Reagent Bottle Position: PositionACTB, Delayed Reagent Volume: 0 mL, Manifold Wash Volume: 2 mL
7	Wash	Volume: 4 mL, Drain Time: 10 s
8	Wash	Volume: 4 mL, Drain Time: 5 s

Table 10-6: Settings for **Single RT Coupling**.

	Cycle Steps	Parameter values
1	Deprotection	Reaction Method: Conventional Deprotection, Deprotection Volume: 4 mL
2	Deprotection	Reaction Method: Conventional Deprotection, Deprotection Volume: 4 mL
3	Wash	Volume: 4 mL, Drain Time: 10 s
4	Wash	Volume: 4 mL, Drain Time: 5 s
5	Wash	Volume: 4 mL, Drain Time: 5 s
6	Wash	Volume: 4 mL, Drain Time: 5 s
7	Coupling	Reaction Method: Conventional coupling, Amino Acid: from method, Amino Acid Volume: 2.5 mL, Activator Bottle Position: PositionACT, Activator Volume: 2 mL, Activator Base Position: PositionACTB, Activator Base Volume: 1 mL, Delayed Reagent Time: 0 s, Delayed Reagent Bottle Position: PositionACTB, Delayed Reagent Volume: 0 mL, Manifold Wash Volume: 2 mL
8	Wash	Volume: 4 mL, Drain Time: 10 s
9	Wash	Volume: 4 mL, Drain Time: 5 s

Table 10-7: Settings for **Single Coupling Cool Down**.

	Cycle Steps	Parameter values
1	Deprotection	Reaction Method: Standard Deprotection, Deprotection Volume: 4 mL
2	Wash	Volume: 4 mL, Drain Time: 10 s
3	Wash	Volume: 4 mL, Drain Time: 5 s
4	Wash	Volume: 4 mL, Drain Time: 5 s
5	Wash	Volume: 4 mL, Drain Time: 5 s
6	Coupling	Reaction Method: Standard coupling, Amino Acid: from method, Amino Acid Volume: 2.5 mL, Activator Bottle Position: PositionACT, Activator Volume: 2 mL, Activator Base Position: PositionACTB, Activator Base Volume: 1 mL, Delayed Reagent Time: 0 s, Delayed Reagent Bottle Position: PositionACTB, Delayed Reagent Volume: 0 mL, Manifold Wash Volume: 2 mL
7	Wash	Volume: 4 mL, Drain Time: 10 s

8	Wash	Volume: 4 mL, Drain Time: 10 s
9	Wash	Volume: 4 mL, Drain Time: 10 s
10	Wash	Volume: 4 mL, Drain Time: 10 s

Table 10-8. Settings for **Single Coupling CSY**.

	Cycle Steps	**Parameter values**
1	Deprotection	Reaction Method: Conventional Deprotection, Deprotection Volume: 4 mL
2	Deprotection	Reaction Method: Conventional Deprotection, Deprotection Volume: 4 mL
3	Wash	Volume: 4 mL, Drain Time: 10 s
4	Wash	Volume: 4 mL, Drain Time: 5 s
5	Wash	Volume: 4 mL, Drain Time: 5 s
6	Wash	Volume: 4 mL, Drain Time: 5 s
7	Coupling	Reaction Method: Standard coupling, Amino Acid: from method, Amino Acid Volume: 2.5 mL, Activator Bottle Position: PositionACT, Activator Volume: 2 mL, Activator Base Position: PositionACTB, Activator Base Volume: 1 mL, Delayed Reagent Time: 0 s, Delayed Reagent Bottle Position: PositionACTB, Delayed Reagent Volume: 0 mL, Manifold Wash Volume: 2 mL
8	Wash	Volume: 4 mL, Drain Time: 10 s
9	Wash	Volume: 4 mL, Drain Time: 10 s
10	Wash	Volume: 4 mL, Drain Time: 10 s
11	Wash	Volume: 4 mL, Drain Time: 10 s

Table 10-9: Settings for **Single 50 °C 10 min Coupling CSY**.

	Cycle Steps	**Parameter values**
1	Deprotection	Reaction Method: Conventional Deprotection, Deprotection Volume: 4 mL
2	Deprotection	Reaction Method: Conventional Deprotection, Deprotection Volume: 4 mL
3	Wash	Volume: 4 mL, Drain Time: 10 s
4	Wash	Volume: 4 mL, Drain Time: 5 s
5	Wash	Volume: 4 mL, Drain Time: 5 s
6	Wash	Volume: 4 mL, Drain Time: 5 s
7	Coupling	Reaction Method: 50 °C 10 min coupling, Amino Acid: from method, Amino Acid Volume: 2.5 mL, Activator Bottle Position: PositionACT, Activator Volume: 2 mL, Activator Base Position: PositionACTB, Activator Base Volume: 1 mL, Delayed Reagent Time: 0 s, Delayed Reagent Bottle Position: PositionACTB, Delayed Reagent Volume: 0 mL, Manifold Wash Volume: 2 mL
8	Wash	Volume: 4 mL, Drain Time: 10 s
9	Wash	Volume: 4 mL, Drain Time: 10 s
10	Wash	Volume: 4 mL, Drain Time: 10 s
11	Wash	Volume: 4 mL, Drain Time: 10 s

Table 10-10: Settings for **Double Coupling**.

	Cycle Steps	**Parameter values**
1	Deprotection	Reaction Method: Standard Deprotection, Deprotection Volume: 4 mL
2	Wash	Volume: 4 mL, Drain Time: 10 s
3	Wash	Volume: 4 mL, Drain Time: 5 s
4	Wash	Volume: 4 mL, Drain Time: 5 s
5	Wash	Volume: 4 mL, Drain Time: 5 s
6	Coupling	Reaction Method: Standard coupling, Amino Acid: from method, Amino Acid Volume: 2.5 mL, Activator Bottle Position: Position ACT, Activator Volume: 2 mL, Activator Base Position: Position ACTB, Activator Base Volume: 1 mL, Delayed Reagent Time: 0 s, Delayed Reagent Bottle Position: PositionACTB, Delayed Reagent Volume: 0 mL, Manifold Wash Volume: 2 mL
7	Wash	Volume: 4 mL, Drain Time: 5 s
8	Coupling	see step 6
9	Wash	Volume: 4 mL, Drain Time: 10 s
10	Wash	Volume: 4 mL, Drain Time: 5 s

Table 10-11: Settings for **Double Coupling Gly**.

	Cycle Steps	Parameter values
1	Deprotection	Reaction Method: Standard Deprotection, Deprotection Volume: 4 mL
2	Wash	Volume: 4 mL, Drain Time: 10 s
3	Wash	Volume: 4 mL, Drain Time: 5 s
4	Wash	Volume: 4 mL, Drain Time: 5 s
5	Wash	Volume: 4 mL, Drain Time: 5 s
6	Wash	Volume: 4 mL, Drain Time: 5 s
7	Wash	Volume: 4 mL, Drain Time: 10 s
8	Coupling	Reaction Method: Standard coupling, Amino Acid: from method, Amino Acid Volume: 2.5 mL, Activator Bottle Position: Position ACT, Activator Volume: 2 mL, Activator Base Position: Position ACTB, Activator Base Volume: 1 mL, Delayed Reagent Time: 0 s, Delayed Reagent Bottle Position: PositionACTB, Delayed Reagent Volume: 0 mL, Manifold Wash Volume: 2 mL
9	Wash	Volume: 4 mL, Drain Time: 10 s
10	Wash	Volume: 4 mL, Drain Time: 10 s
11	Coupling	see step 8
12	Wash	Volume: 4 mL, Drain Time: 10 s
13	Wash	Volume: 4 mL, Drain Time: 5 s
14	Wash	Volume: 4 mL, Drain Time: 5 s
15	Wash	Volume: 4 mL, Drain Time: 5 s

Table 10-12: Settings for **Double Coupling Cool Down**.

	Cycle Steps	Parameter values
1	Deprotection	Reaction Method: Standard Deprotection, Deprotection Volume: 4 mL
2	Wash	Volume: 4 mL, Drain Time: 10 s
3	Wash	Volume: 4 mL, Drain Time: 5 s
4	Wash	Volume: 4 mL, Drain Time: 5 s
5	Wash	Volume: 4 mL, Drain Time: 5 s
6	Wash	Volume: 4 mL, Drain Time: 5 s
7	Wash	Volume: 4 mL, Drain Time: 10 s
8	Coupling	Reaction Method: Standard coupling, Amino Acid: from method, Amino Acid Volume: 2.5 mL, Activator Bottle Position: Position ACT, Activator Volume: 2 mL, Activator Base Position: Position ACTB, Activator Base Volume: 1 mL, Delayed Reagent Time: 0 s, Delayed Reagent Bottle Position: PositionACTB, Delayed Reagent Volume: 0 mL, Manifold Wash Volume: 2 mL
9	Wash	Volume: 4 mL, Drain Time: 10 s
10	Wash	Volume: 4 mL, Drain Time: 10 s
11	Coupling	see step 8
12	Wash	Volume: 4 mL, Drain Time: 10 s
13	Wash	Volume: 4 mL, Drain Time: 10 s
14	Wash	Volume: 4 mL, Drain Time: 10 s
15	Wash	Volume: 4 mL, Drain Time: 10 s

Table 10-13: Settings for **Double Coupling CSY**.

	Cycle Steps	Parameter values
1	Deprotection	Reaction Method: Conventional Deprotection, Deprotection Volume: 4 mL
2	Deprotection	Reaction Method: Conventional Deprotection, Deprotection Volume: 4 mL
3	Wash	Volume: 4 mL, Drain Time: 10 s
4	Wash	Volume: 4 mL, Drain Time: 5 s
5	Wash	Volume: 4 mL, Drain Time: 5 s
6	Wash	Volume: 4 mL, Drain Time: 5 s
7	Wash	Volume: 4 mL, Drain Time: 5 s
8	Wash	Volume: 4 mL, Drain Time: 10 s
9	Coupling	Reaction Method: Standard coupling, Amino Acid: from method, Amino Acid Volume: 2.5 mL, Activator Bottle Position: Position ACT, Activator Volume: 2 mL, Activator Base Position: Position ACTB, Activator Base Volume: 1 mL, Delayed Reagent Time: 0 s, Delayed Reagent Bottle Position: PositionACTB, Delayed Reagent Volume: 0 mL, Manifold Wash Volume: 2 mL
10	Wash	Volume: 4 mL, Drain Time: 10 s

11	Wash	Volume: 4 mL, Drain Time: 10 s
12	Coupling	see step 9
13	Wash	Volume: 4 mL, Drain Time: 10 s
14	Wash	Volume: 4 mL, Drain Time: 10 s
15	Wash	Volume: 4 mL, Drain Time: 10 s
16	Wash	Volume: 4 mL, Drain Time: 10 s

Table 10-14: Settings for **Final Deprotection**.

	Cycle Steps	Parameter values
1	Deprotection	Reaction Method: Standard Deprotection, Deprotection Volume: 4 mL
2	Wash	Volume: 4 mL, Drain Time: 5 s
3	Wash	Volume: 4 mL, Drain Time: 5 s
4	Wash	Volume: 4 mL, Drain Time: 5 s
5	Wash	Volume: 4 mL, Drain Time: 5 s

Table 10-15: Settings for **RT Final Deprotection**.

	Cycle Steps	Parameter values
1	Deprotection	Reaction Method: Conventional Deprotection, Deprotection Volume: 4 mL
2	Deprotection	Reaction Method: Conventional Deprotection, Deprotection Volume: 4 mL
3	Wash	Volume: 4 mL, Drain Time: 10 s
4	Wash	Volume: 4 mL, Drain Time: 5 s
5	Wash	Volume: 4 mL, Drain Time: 5 s
6	Wash	Volume: 4 mL, Drain Time: 5 s

10.3 Details on synthesis and characterisation of peptides

10.3.1 WW-CA

H-KLPPGWEKHMSRSSGQVHYHNSITQASQWERPSG-OH

$C_{170}H_{256}N_{54}O_{51}S$, Monoisotopic mass: 3901.9 Da, Molar mass: 3904.3 g/mol

$\varepsilon_{280\ nm}$ = 12490 $M^{-1}cm^{-1}$

Synthesis. Resin: H-Gly-HMPB-ChemMatrix® 200 mg, 0.5 mmol/g, 0.1 mmol scale. The peptide was synthesized according to the standard procedure (Chapter 10.2) and was not acetylated. Cleavage cocktail: TFA (8.5 mL), TIPS (1 mL), water (0.5 mL), incubation time: 4 to 5 h.

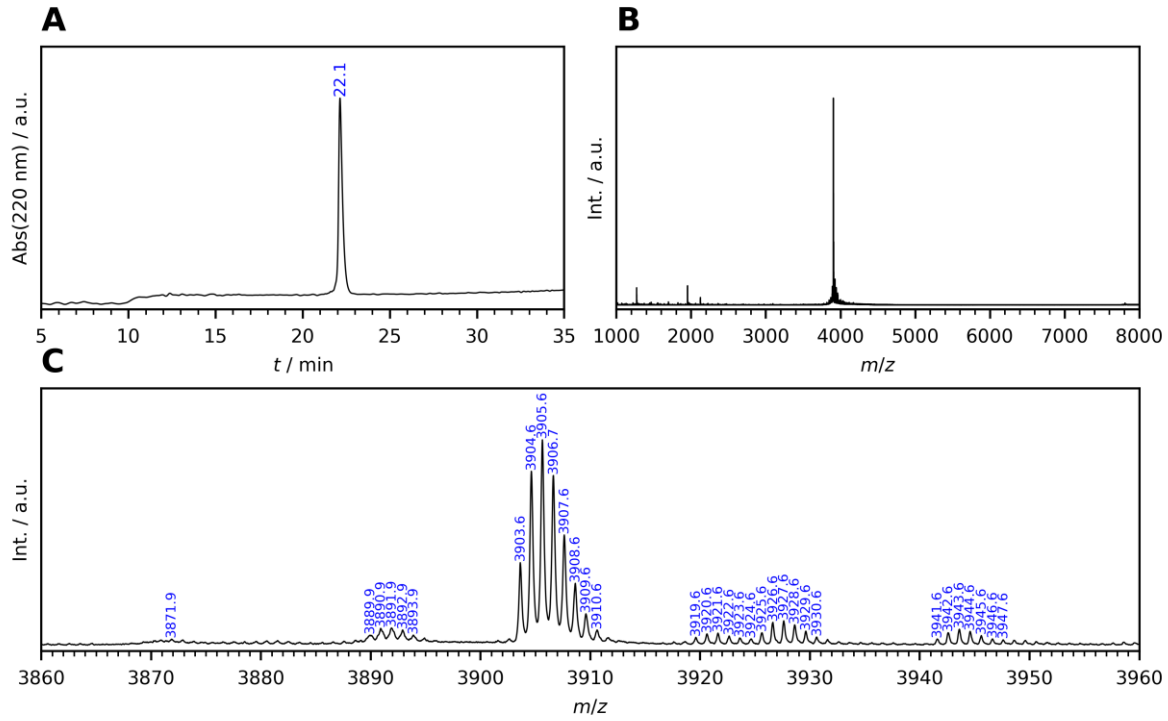

Figure 10-1: Analytical data for WW-CA. A) Analytical HPLC trace (Gradient: 10-40% B in A in 30 min). B) MALDI-TOF-MS (complete spectrum) and C) zoom. $[M+H]^+$ calc. 3902.9, $[M+Na]^+$ calc. 3924.9, $[M+K]^+$ calc. 3940.8, $[M+O+H]^+$ calc. 3918.9, $[M+O+Na]^+$ calc. 3940.9, $[M+O+K]^+$ calc. 3956.8.

10.3.2 WW-CA-Nle

H-KLPPGWEKH*Nle*SRSSGQVHYHNSITQASQWERPSG-OH

$C_{171}H_{258}N_{54}O_{51}$, Monoisotopic mass: 3883.9 Da, Molar mass: 3886.2 g/mol

$\varepsilon_{280\ nm}$ = 12490 $M^{-1}cm^{-1}$

Synthesis. Resin: H-Gly-HMPB-ChemMatrix® 200 mg, 0.5 mmol/g, 0.1 mmol scale. The peptide was synthesized according to the standard procedure (Chapter 10.2) and was not acetylated. Cleavage cocktail: TFA (8.5 mL), TIPS (1 mL), water (0.5 mL), incubation time: 4 to 5 h.

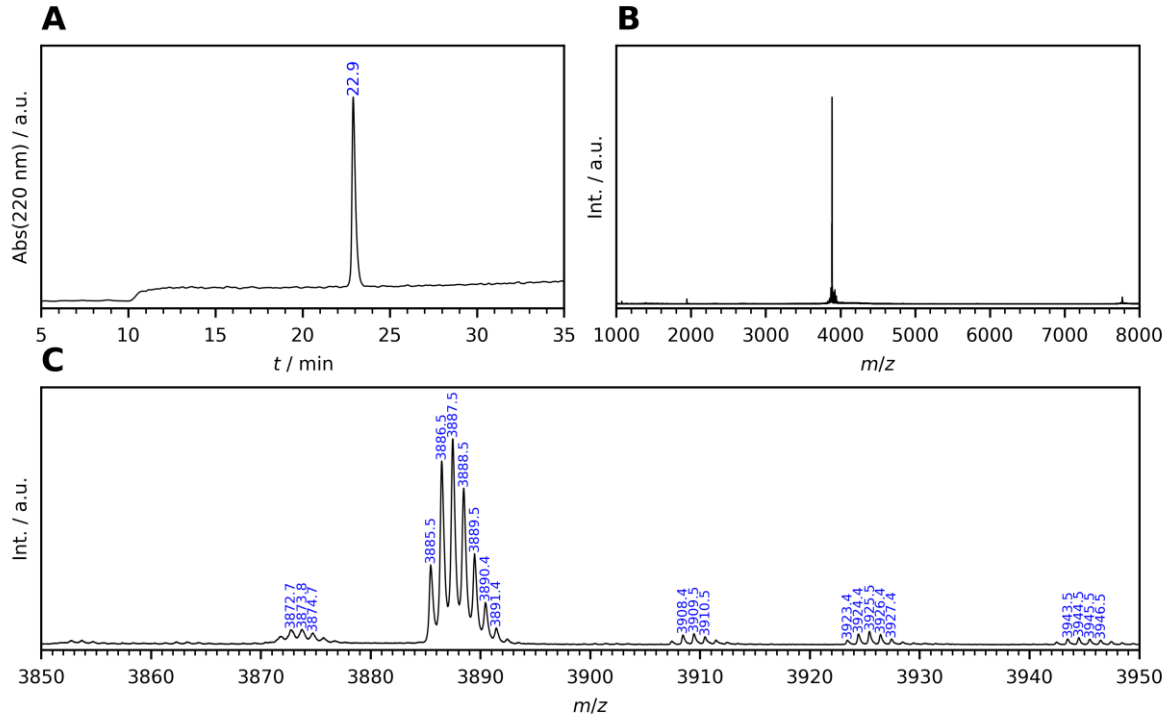

Figure 10-2: Analytical data for WW-CA-Nle. A) Analytical HPLC trace (Gradient: 10-40% B in A in 30 min). B) MALDI-TOF-MS (complete spectrum) and C) zoom. $[M+H]^+$ calc. 3884.9, $[M+Na]^+$ calc. 3906.9, $[M+K]^+$ calc. 3922.9.

10.3.3 hPin1$_{WW}$-Nle

H-KLPPGWEKR*Nle*SRSSGRVYYFNHITNASQWERPSG-OH

$C_{180}H_{271}N_{55}O_{50}$, Monoisotopic mass: 4003.0 Da, Molar mass: 4005.5 g/mol

$\varepsilon_{280\ nm}$ = 13980 $M^{-1}cm^{-1}$

Synthesis. Resin: H-Gly-HMPB-ChemMatrix® 200 mg, 0.5 mmol/g, 0.1 mmol scale. The peptide was synthesized according to the standard procedure (Chapter 10.2) and was not acetylated. Cleavage cocktail: TFA (8.5 mL), TIPS (1 mL), water (0.5 mL), incubation time: 4 to 5 h.

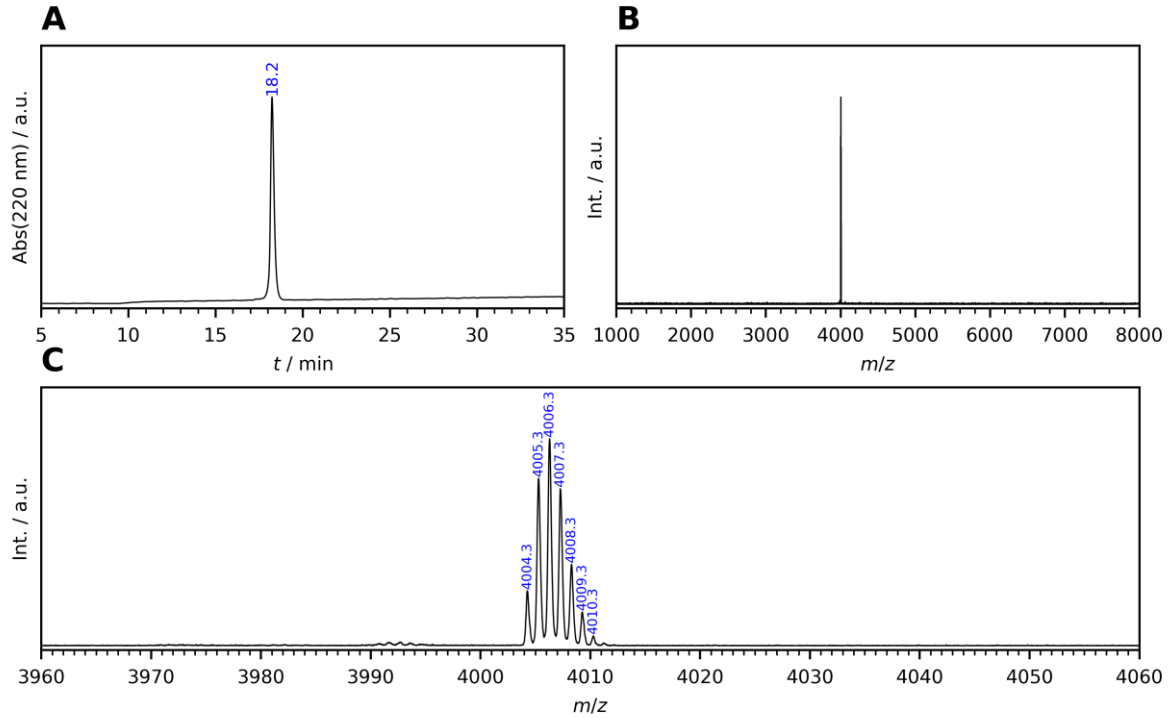

Figure 10-3: Analytical data for hPin1$_{WW}$-Nle. A) Analytical HPLC trace (Gradient: 20-40% B in A in 30 min). B) MALDI-TOF-MS (complete spectrum) and C) zoom. $[M+H]^+$ calc. 4004.0.

10.3.4 WW-CA-min

H-KLPPGWEKH*Nle*SRSSGRVHYHNRITNASQWERPSG-H

$C_{174}H_{267}N_{59}O_{49}$, Monoisotopic mass: 3967.0 Da, Molar mass: 3969.4 g/mol

$\varepsilon_{280\ nm}$ = 12490 $M^{-1}cm^{-1}$

Synthesis. Resin: H-Gly-HMPB-ChemMatrix® 200 mg, 0.5 mmol/g, 0.1 mmol scale. The peptide was synthesized according to the standard procedure (Chapter 10.2) and was not acetylated. Cleavage cocktail: TFA (8.5 mL), TIPS (1 mL), water (0.5 mL), incubation time: 4 to 5 h.

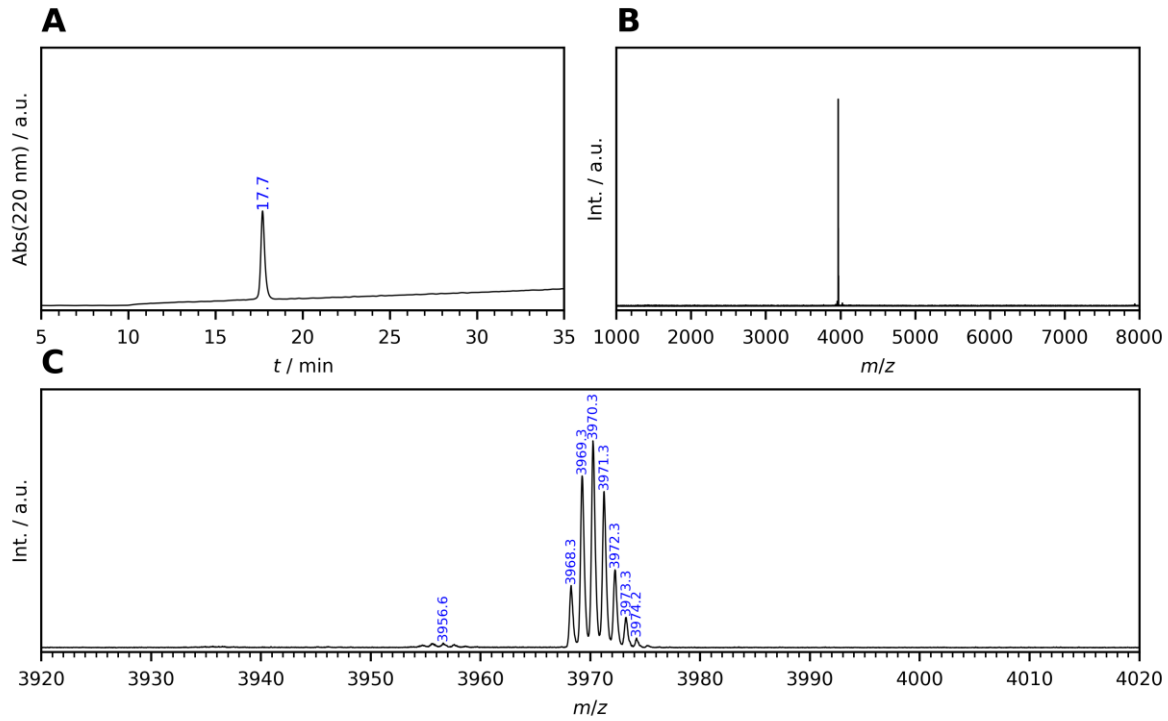

Figure 10-4: Analytical data for WW-CA-min. A) Analytical HPLC trace (Gradient: 15-35% B in A in 30 min). B) MALDI-TOF-MS (complete spectrum) and C) zoom. $[M+H]^+$ calc. 3968.0.

10.3.1 WW-CA-ANG

H-KLPPGWEKH*Nle*SANGRVHYHNRITNASQWERPSG-OH

$C_{169}H_{256}N_{56}O_{47}$, Monoisotopic mass: 3821.9 Da, Molar mass: 3824.3 g/mol

$\varepsilon_{280\ nm}$ = 12490 $M^{-1}cm^{-1}$

Synthesis. Resin: H-Gly-HMPB-ChemMatrix® 200 mg, 0.5 mmol/g, 0.1 mmol scale. The peptide was synthesized according to the standard procedure (Chapter 10.2) and was not acetylated. Cleavage cocktail: TFA (8.5 mL), TIPS (1 mL), water (0.5 mL), incubation time: 4 to 5 h.

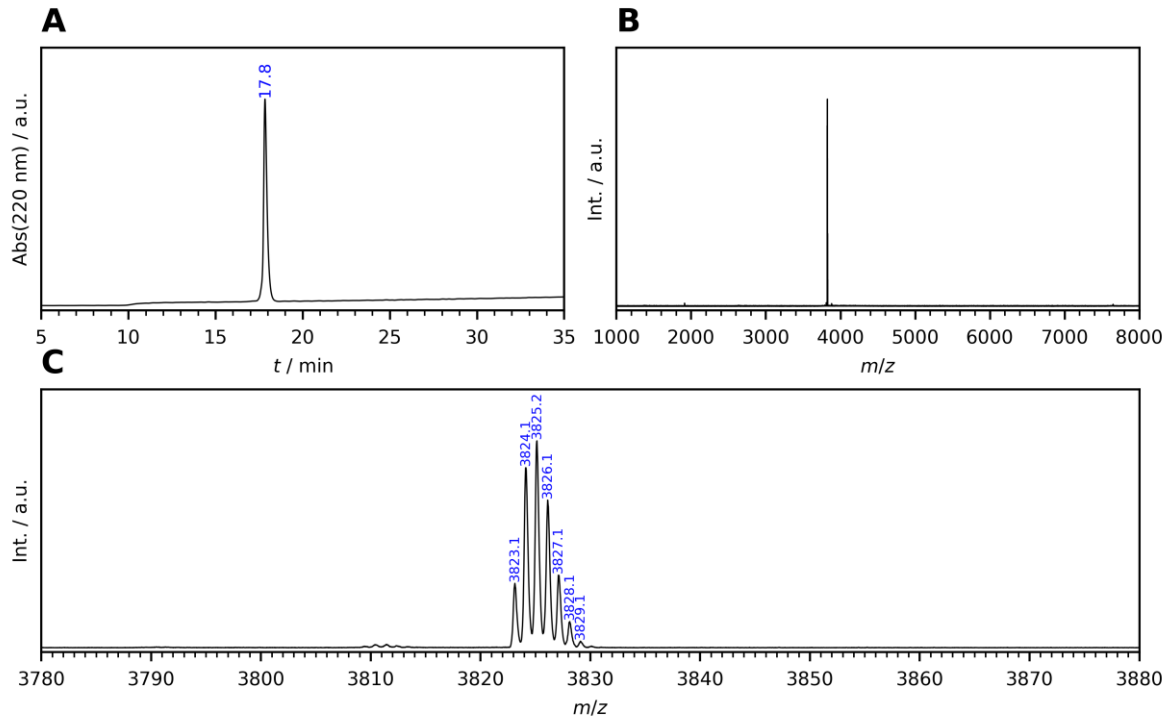

Figure 10-5: Analytical data for WW-CA-ANG. A) Analytical HPLC trace (Gradient: 15-45% B in A in 30 min). B) MALDI-TOF-MS (complete spectrum) and C) zoom. $[M+H]^+$ calc. 3822.9.

10.3.2 Trpzip2

Ac-SWTWENGKWTWK-NH_2

Chemical Formula: $C_{80}H_{104}N_{20}O_{19}$, Monoisotopic mass: 1648.8 Da, Molar mass: 1649.8 g/mol

$\varepsilon_{280\ nm}$ = 22000 $M^{-1}cm^{-1}$

Synthesis. Resin: H-Rink-Amide-ChemMatrix® 200 mg, 0.5 mmol/g, 0.1 mmol scale. The peptide was synthesized according to the standard procedure (Chapter 10.2) and was acetylated. Cleavage cocktail: TFA (8.5 mL), TIPS (1.0 mL), water (0.5 mL), incubation time: 4 to 5 h.

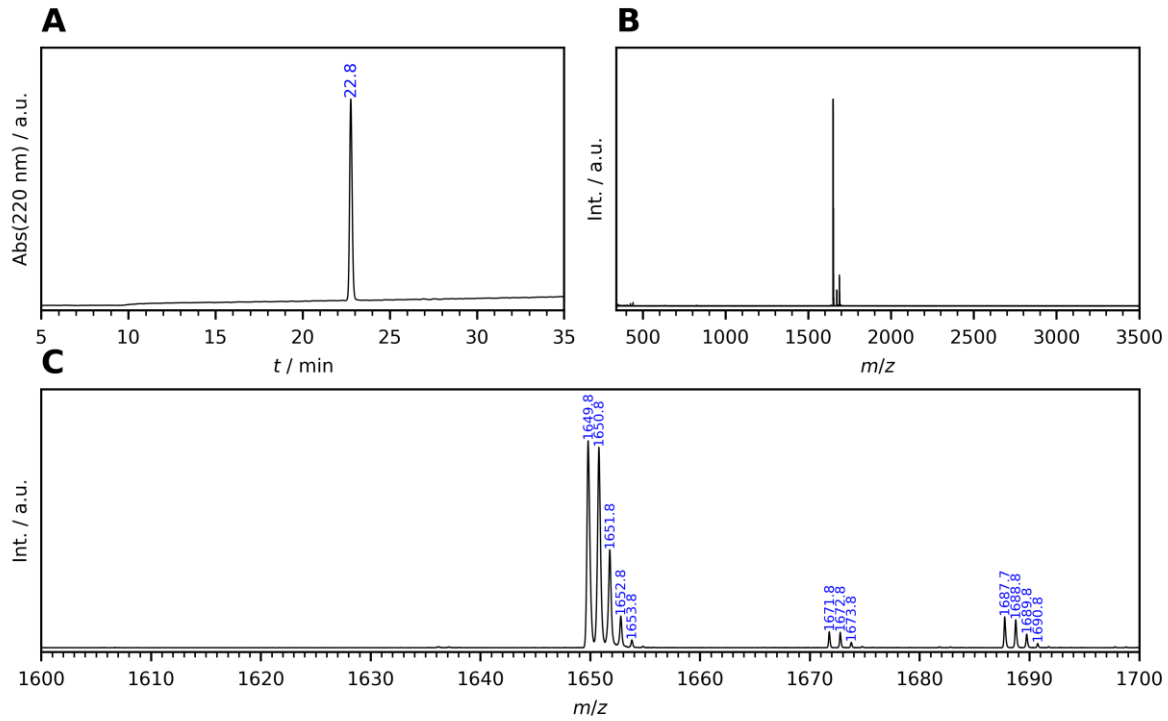

Figure 10-6: Analytical data for Trpzip2. A) Analytical HPLC trace (Gradient: 20-40% B in A in 30 min). B) MALDI-TOF-MS (complete spectrum) and C) zoom. $[M+H]^+$ calc. 1649.8, $[M+Na]^+$ calc. 1671.8, $[M+K]^+$ calc. 1687.7.

10.3.3 $Tz2H_3$

Ac-SWHWENGKWHWH-NH_2

Chemical Formula: $C_{84}H_{99}N_{25}O_{17}$, Monoisotopic mass: 1729.8 Da, Molar mass: 1730.9 g/mol

$\varepsilon_{280\ nm}$ = 22000 $M^{-1}cm^{-1}$

Synthesis. Resin: H-Rink-Amide-ChemMatrix® 200 mg, 0.5 mmol/g, 0.1 mmol scale. The peptide was synthesized according to the standard procedure (Chapter 10.2) and was acetylated. Cleavage cocktail: TFA (8.5 mL), TIPS (1.0 mL), water (0.5 mL), incubation time: 4 to 5 h.

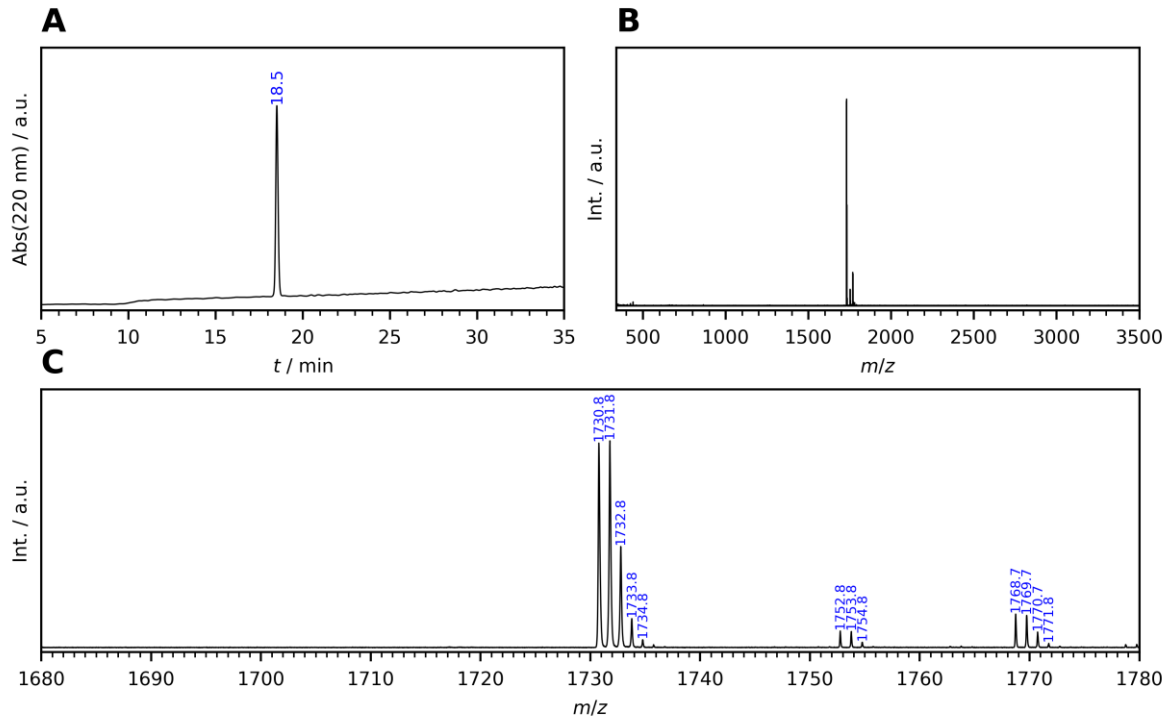

Figure 10-7: Analytical data for $Tz2H_3$. A) Analytical HPLC trace (Gradient: 20-40% B in A in 30 min). B) MALDI-TOF-MS (complete spectrum) and C) zoom. $[M+H]^+$ calc. 1730.8, $[M+Na]^+$ calc. 1752.8, $[M+K]^+$ calc. 1768.7.

10.3.4 WW-CA(W34Coum)

Ac- KLPPGWEKH*Nle*SRSSGQVHYHNSITNASQCoumERPSG-NH_2

Chemical Formula: $C_{175}H_{262}N_{54}O_{53}S$, Monoisotopic mass: 3999.9 Da, Molar mass: 4002.4 g/mol

Synthesis. Resin: H-Rink-Amide-ChemMatrix® 200 mg, 0.5 mmol/g, 0.1 mmol scale. The peptide was synthesized according to the standard procedure (Chapter 10.2) and was acetylated. On-resin late-stage functionalization is described in Chapter 8.4.3. Cleavage cocktail for resin containing 5 µmol peptide: TFA (850 µL), TIPS (100 µL), water (50 µL), incubation time: 5 h.

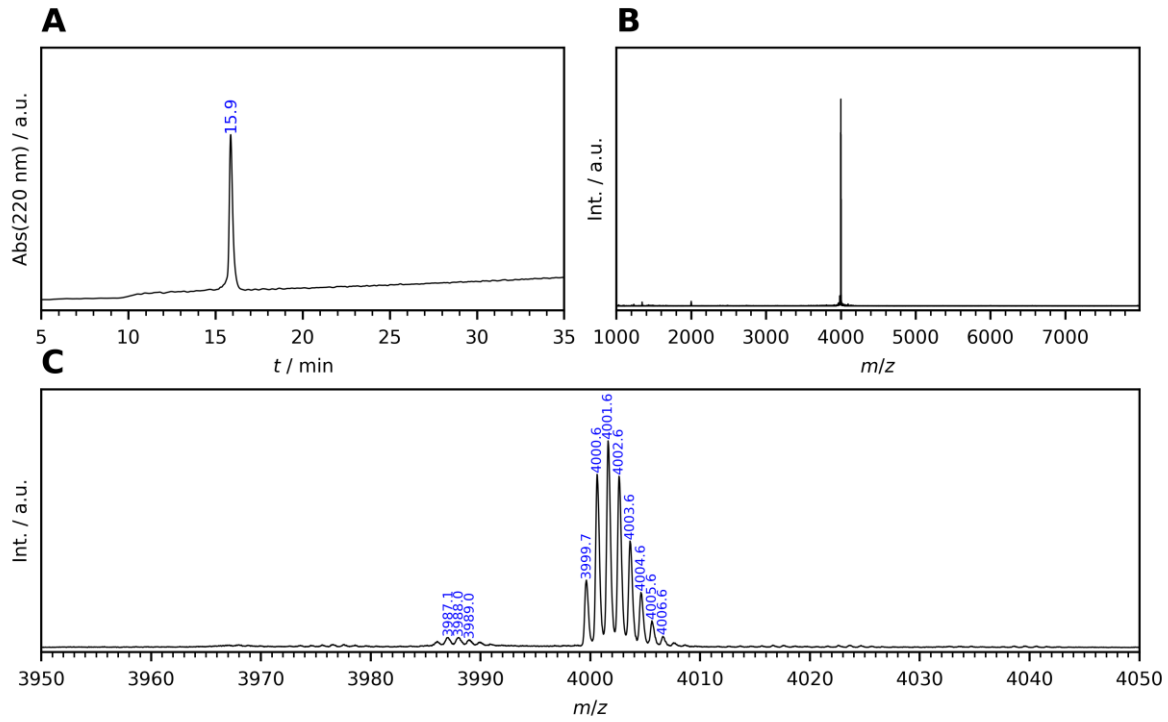

Figure 10-8: Analytical data for WW-CA(W34Coum). A) Analytical HPLC trace (Gradient: 20-45% B in A in 30 min). B) MALDI-TOF-MS (complete spectrum) and C) zoom. $[M+H]^+$ calc. 4000.9.

10.3.5 Test peptide

CSY protected

Ac-F<u>D(CSY)</u>GLA-NH_2

$C_{30}H_{43}N_7O_7S$, Monoisotopic mass: 645.3 Da, Molar mass: 645.8 g/mol

Synthesis. Resin: H-Rink-Amide-ChemMatrix® 200 mg, 0.5 mmol/g, 0.1 mmol scale. The peptide was synthesized according to the settings summarized in Table 10-16 and was acetylated. Cleavage cocktail: TFA (9.5 mL), TIPS (0.25 mL), water (0.25 mL), incubation time: 3 to 4 h.

Table 10-16: Settings for the synthesis of test peptide.

	Step	Used Cycles (synthesis at room temperature)	Used Cycles (optimized method)
1	Resin swelling	Resin swelling	Resin swelling
2	A	First Single Coupling	First Single Coupling
3	L	Single Coupling	Single Coupling
4	G	Double Coupling	Double Coupling Cool Down
5	D(CSY)	Single RT Coupling	Single Coupling CSY
6	F	Single RT Coupling	Single Coupling CSY
7	Final Deprotection	RT Final Deprotection	RT Final Deprotection

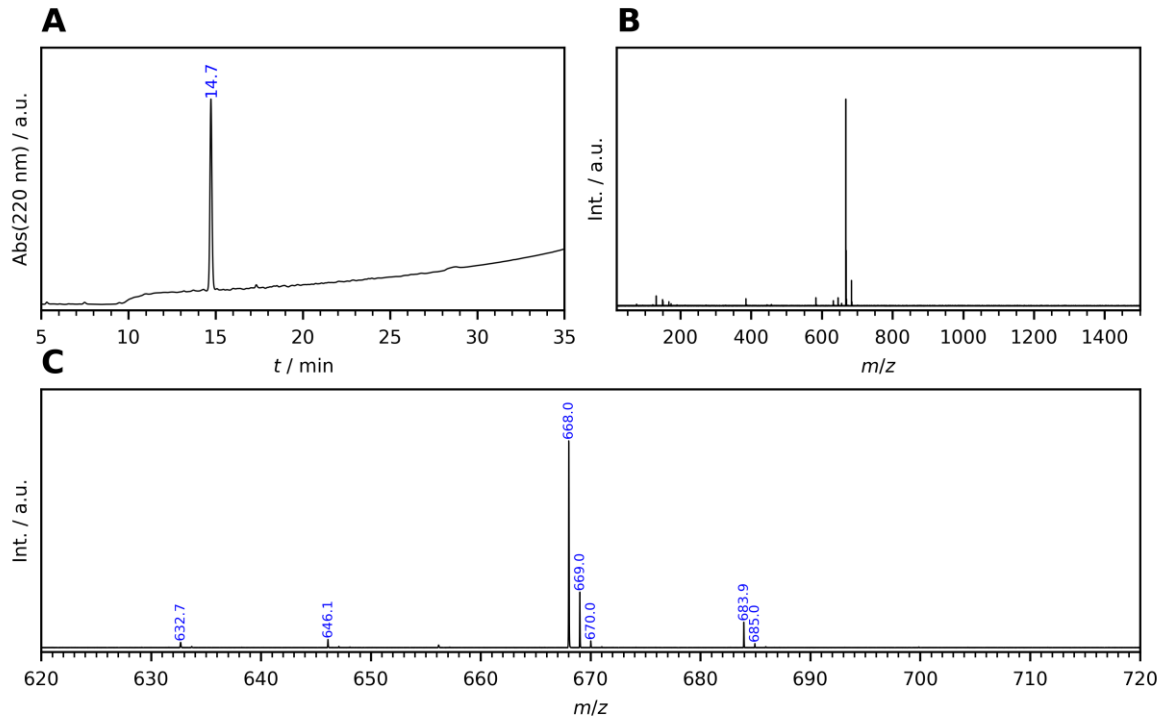

Figure 10-9: Analytical data for Test peptide(CSY). A) Analytical HPLC trace (Gradient: 20-70% B in A in 30 min). B) MALDI-TOF-MS (complete spectrum) and C) zoom. $[M+H]^+$ calc. 646.3, $[M+Na]^+$ calc. 668.3, $[M+K]^+$ calc. 684.3.

10.3.6 WW-ADG

CSY-Protected WW-ADG:

H-KLPPGWEKR*Nle*SAD(CSY)GRVYYFNHITNASQWERPSG-OH

$C_{179}H_{264}N_{52}O_{48}S$, Monoisotopic mass: 3942.0 Da, Molar mass: 3944.5 g/mol

Synthesis. Resin: H-Gly-HMPB-ChemMatrix® 200 mg, 0.5 mmol/g, 0.1 mmol scale. The peptide was synthesized according to the settings summarized in Table 10-17 was not acetylated. Cleavage cocktail: TFA (8.5 mL), TIPS (1 mL), water (0.5 mL), incubation time: 4 to 5 h. After final cleavage the crude product was obtained as a yellowish powder (143.5 mg). A part of it (42.6 mg) was purified by HPLC and after freeze-drying a colourless powder (12.1 mg, 3.07 µmol, 28%) was obtained.

Table 10-17: Settings for the synthesis of WW-ADG(CSY).

	Step	Used Cycles (Standard conditions)	Used Cycles (optimized conditions)
1	Resin swelling	Resin swelling	Resin swelling
2	G	already loaded	already loaded
3	S	First Single Coupling	First Single Coupling
4	P	Single Coupling	Single Coupling
5	R	Double Coupling	Double Coupling
6	E	Single Coupling	Single Coupling
7	W	Single Coupling	Single Coupling
8	Q	Single Coupling	Single Coupling
9	S	Single Coupling	Single Coupling
10	A	Single Coupling	Single Coupling
11	N	Single Coupling	Single Coupling
12	T	Single Coupling	Single Coupling
13	I	Single Coupling	Single Coupling
14	H	Single Coupling 50 °C	Single Coupling 50 °C
15	N	Single Coupling	Single Coupling
16	F	Single Coupling	Single Coupling
17	Y	Single Coupling	Single Coupling
18	Y	Single Coupling	Single Coupling
19	V	Single Coupling	Single Coupling
20	R	Double Coupling	Double Coupling
21	G	Double Coupling	Double Coupling Cool Down
22	D(CSY)	Single Coupling	Single Coupling CSY
23	A	Single Coupling	Single Coupling CSY
24	S	Single Coupling	Single Coupling CSY
25	Nle	Single Coupling	Single Coupling CSY
26	R	Double Coupling	Double Coupling CSY
27	K	Single Coupling	Single Coupling CSY
28	E	Single Coupling	Single Coupling CSY
29	W	Single Coupling	Single Coupling CSY
30	G	Double Coupling	Double Coupling CSY
31	P	Single Coupling	Single Coupling CSY
32	P	Single Coupling	Single Coupling CSY
33	L	Single Coupling	Single Coupling CSY
34	K	Single Coupling	Single Coupling CSY
35	Final deprotection	Final Deprotection	RT Final Deprotection

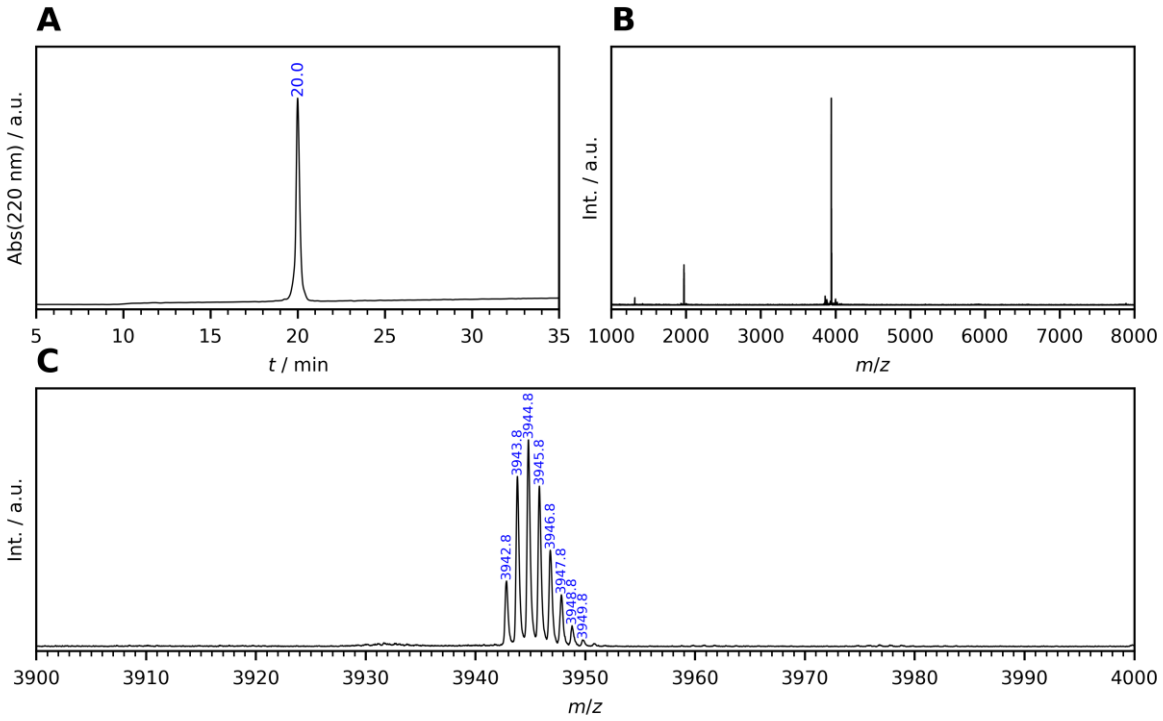

Figure 10-10: Analytical data for WW-ADG(CSY). A) Analytical HPLC trace (Gradient: 20-40% B in A in 30 min). B) MALDI-TOF-MS (complete spectrum) and C) zoom. $[M+H]^+$ calc. 3943.0.

Native WW ADG:

H-KLPPGWEKR*Nle*SADGRVYYFNHITNASQWERPSG-OH

$C_{175}H_{259}N_{51}O_{49}$, Monoisotopic mass: 3858.9 Da, Molar mass: 3861.3 g/mol

$\varepsilon_{280\ nm}$ = 13980 $M^{-1}cm^{-1}$

Synthesis. WW-ADG(CSY) was CSY-deprotected with method (b) (Chapter 8.5.4). Unprotected peptide was obtained as a colourless powder (112.2 nmol, 45%).

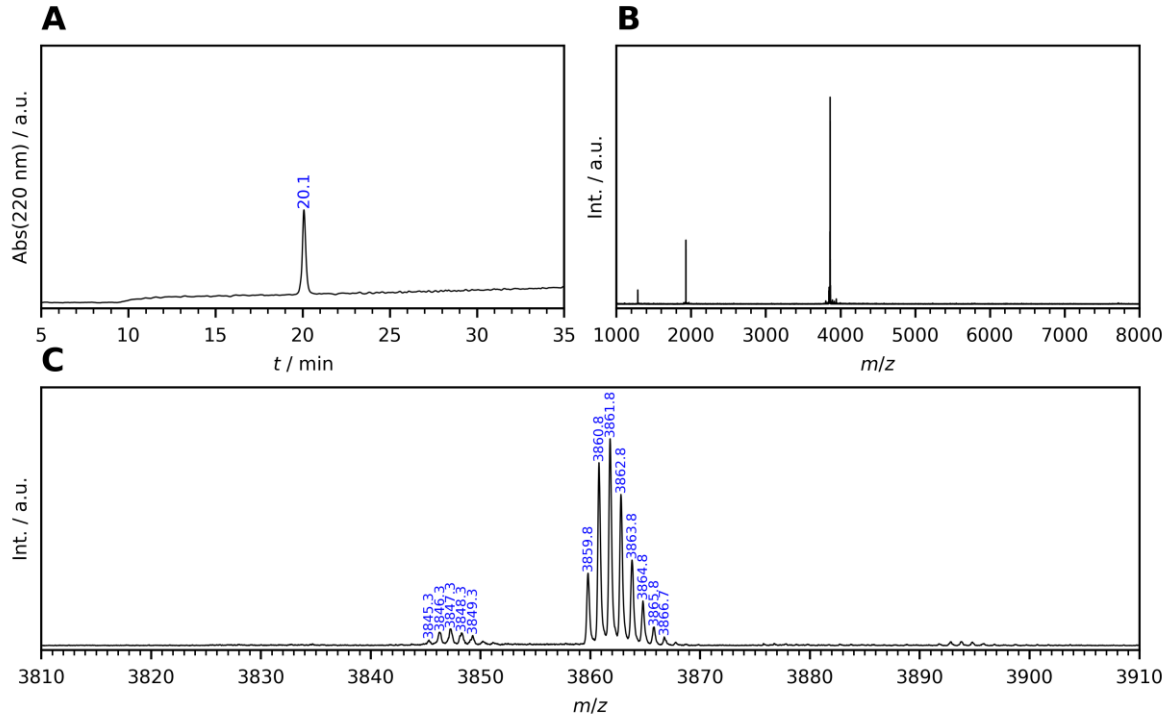

Figure 10-11: Analytical data for WW-ADG. A) Analytical HPLC trace (Gradient: 20-40% B in A in 30 min). B) MALDI-TOF-MS (complete spectrum) and C) zoom. $[M+H]^+$ calc. 3859.9.

10.3.7 WW-PQBP1

CSY-protected WW-PQBP1:

Ac-GLPPSWYKVFD(CSY)PSSGLPYYWNAD(CSY)TD(CSY)LVSWLSPHD(CSY)-NH_2

$C_{204}H_{276}N_{46}O_{49}S_4$, Monoisotopic mass: 4281.9 Da, Molar mass: 4285.0 g/mol

Synthesis. Resin: H-Rink-Amide-ChemMatrix® 200 mg, 0.5 mmol/g, 0.1 mmol scale. The peptide was synthesized according to the settings summarized in Table 10-18 and was acetylated. Cleavage cocktail: TFA (9.0 mL), TIPS (0.5 mL), water (0.5 mL), incubation time: 4 to 5 h. After final cleavage the crude product was obtained as a yellowish powder (157.1 mg). A part of it (41.0 mg) was purified by HPLC and after freeze-drying a colourless powder (11.2 mg, 2.61 µmol, 27%) was obtained.

Table 10-18: Settings for the synthesis of $PQBP1_{WW}$(CSY).

	Step	Used Cycles (optimized conditions)
1	Resin swelling	Resin swelling
2	D(CSY)	Double Coupling CSY
3	H	Single 50 °C 10 min Coupling CSY
4	P	Single Coupling CSY
5	S	Single Coupling CSY
6	L	Single Coupling CSY
7	W	Single Coupling CSY
8	S	Single Coupling CSY
9	V	Single Coupling CSY
10	L	Single Coupling CSY
11	D(CSY)	Single Coupling CSY
12	T	Single Coupling CSY
13	D(CSY)	Single Coupling CSY
14	A	Single Coupling CSY
15	N	Single Coupling CSY
16	W	Single Coupling CSY
17	Y	Single Coupling CSY
18	Y	Single Coupling CSY
19	P	Single Coupling CSY
20	L	Single Coupling CSY
21	G	Double Coupling CSY
22	S	Single Coupling CSY
23	S	Single Coupling CSY
24	P	Single Coupling CSY
25	D(CSY)	Single Coupling CSY
26	F	Single Coupling CSY
27	V	Single Coupling CSY
28	K	Single Coupling CSY
29	Y	Single Coupling CSY
30	W	Single Coupling CSY
31	S	Single Coupling CSY
32	P	Single Coupling CSY
33	P	Single Coupling CSY
34	L	Single Coupling CSY
35	G	Double Coupling CSY
36	Final deprotection	RT Final Deprotection

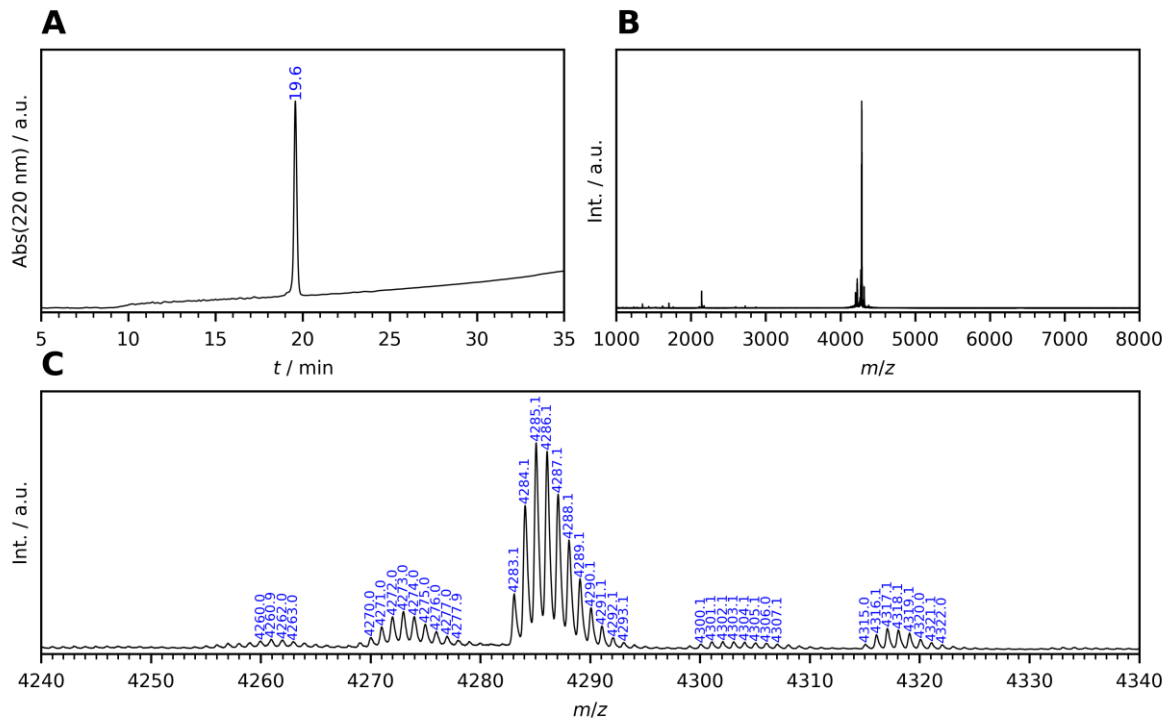

Figure 10-12: Analytical data for WW-PQPB1(CSY). A) Analytical HPLC trace (Gradient: 30-70% B in A in 30 min). B) MALDI-TOF-MS (complete spectrum) and C) zoom. $[M+H]^+$ calc. 4282.9, $[M+Na]^+$ calc. 4304.9, $[M+K]^+$ calc. 4320.9.

Native WW-PQBP1:

Ac-GLPPSWYKVFDPSSGLPYYWNADTDLVSWLSPHD-NH_2

$C_{188}H_{256}N_{42}O_{53}$, Monoisotopic mass: 3949.9 Da, Molar mass: 3952.4 g/mol

$\varepsilon_{280\ nm}$ = 20970 $M^{-1}cm^{-1}$

Synthesis. WW-PQBP1(CSY) (250 nmol) was CSY-deprotected with method (c) (Chapter 8.5.4). The unprotected peptide was obtained as a colourless powder (41.5 nmol, 17%).

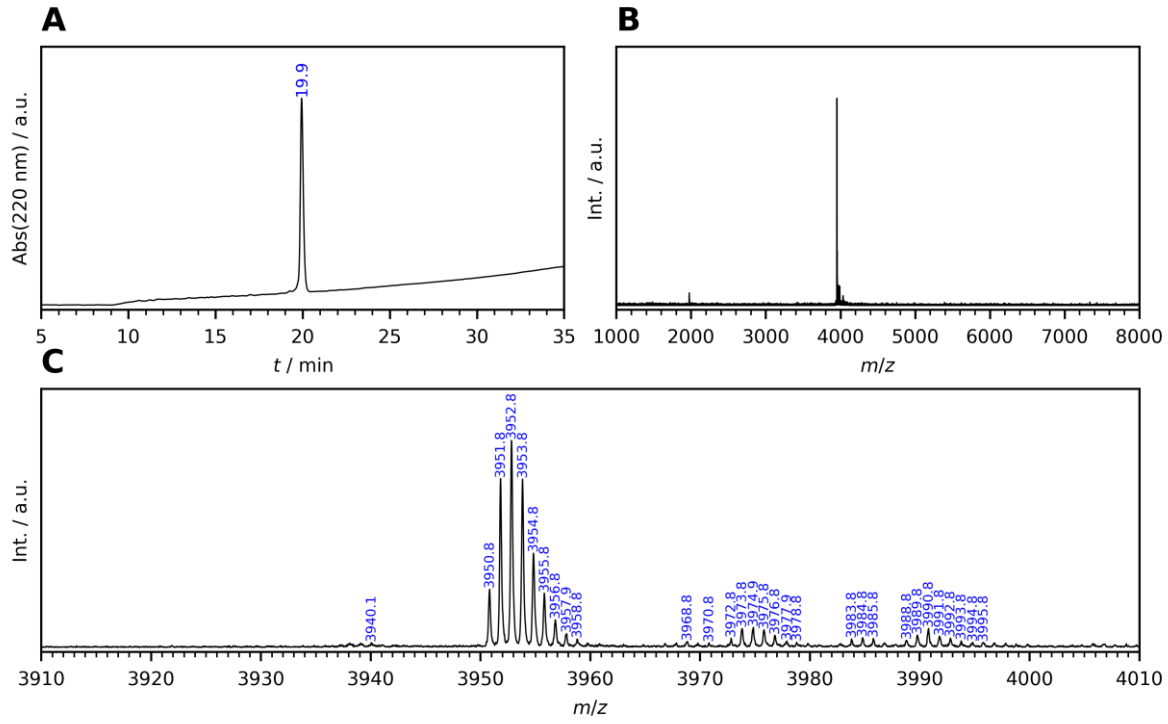

Figure 10-13: Analytical data for PQBP1. A) Analytical HPLC trace (Gradient: 30-70% B in A in 30 min). B) MALDI-TOF-MS (complete spectrum) and C) zoom. $[M+H]^+$ calc. 3950.9, $[M+Na]^+$ calc. 3972.9, $[M+K]^+$ calc. 3988.8.

10.3.8 SH3-NC

CSY-protected SH3-NC:

Ac-AEYVRALFD(CSY)FNGND(CSY)EED(CSY)LPFKKGD(CSY)ILRIRD(CSY)KPEEQWWN AED(CSY)SEGKRG*Nle*IPVPYVEKY-NH_2

$C_{334}H_{493}N_{87}O_{88}S_6$, Monoisotopic mass: 7322.5 Da, Molar mass: 7327.5 g/mol

Synthesis. Resin: H-Rink-Amide-ChemMatrix® 100 mg, 0.5 mmol/g, 0.05 mmol scale (still the amount of reagents was set for 0.1 mmol scale to drive reactions to completion). The peptide was synthesized according to the settings summarized in Table 10-19 and was acetylated. Cleavage cocktail: TFA (8.5 mL), TIPS (1 mL), water (0.5 mL), incubation time: 4 to 5 h. After final cleavage the crude product was obtained as a yellowish powder (155.3 mg). A part of it (76.2 mg) was purified by HPLC and after freeze-drying a colourless powder (14.2 mg, 1.94 µmol, 19%) was obtained.

Table 10-19: Settings for the synthesis of SH3-NC(CSY).

	Step	Used Cycles (optimized conditions)
1	Resin swelling	Resin swelling
2	Y	First Single Coupling
3	K	Single Coupling
4	E	Single Coupling
5	V	Single Coupling
6	Y	Single Coupling
7	P	Single Coupling
8	V	Single Coupling
9	P	Single Coupling
10	I	Single Coupling
11	Nle	Single Coupling
12	G	Double Coupling Gly
13	R	Double Coupling
14	K	Single Coupling
15	G	Double Coupling Gly
16	E	Single Coupling
17	S	Single Coupling Cool Down
18	D(CSY)	Single Coupling CSY
19	E	Single Coupling CSY
20	A	Single Coupling CSY
21	N	Single Coupling CSY
22	W	Single Coupling CSY
23	W	Single Coupling CSY
24	Q	Single Coupling CSY
25	E	Single Coupling CSY
26	E	Single Coupling CSY
27	P	Single Coupling CSY
28	K	Single Coupling CSY
29	D(CSY)	Single Coupling CSY
30	R	Double Coupling CSY
31	I	Single Coupling CSY
32	R	Double Coupling CSY
33	L	Single Coupling CSY
34	I	Single Coupling CSY
35	D(CSY)	Single Coupling CSY

36	G	Double Coupling CSY
37	K	Single Coupling CSY
38	K	Single Coupling CSY
39	F	Single Coupling CSY
40	P	Single Coupling CSY
41	L	Single Coupling CSY
42	D(CSY)	Single Coupling CSY
43	E	Single Coupling CSY
44	E	Single Coupling CSY
45	D(CSY)	Single Coupling CSY
46	N	Single Coupling CSY
47	G	Double Coupling CSY
48	N	Single Coupling CSY
49	F	Single Coupling CSY
50	D(CSY)	Single Coupling CSY
51	F	Single Coupling CSY
52	L	Single Coupling CSY
53	A	Single Coupling CSY
54	R	Double Coupling CSY
55	V	Single Coupling CSY
56	Y	Single Coupling CSY
57	E	Single Coupling CSY
58	A	Single Coupling CSY
59	Final deprotection	RT Final Deprotection

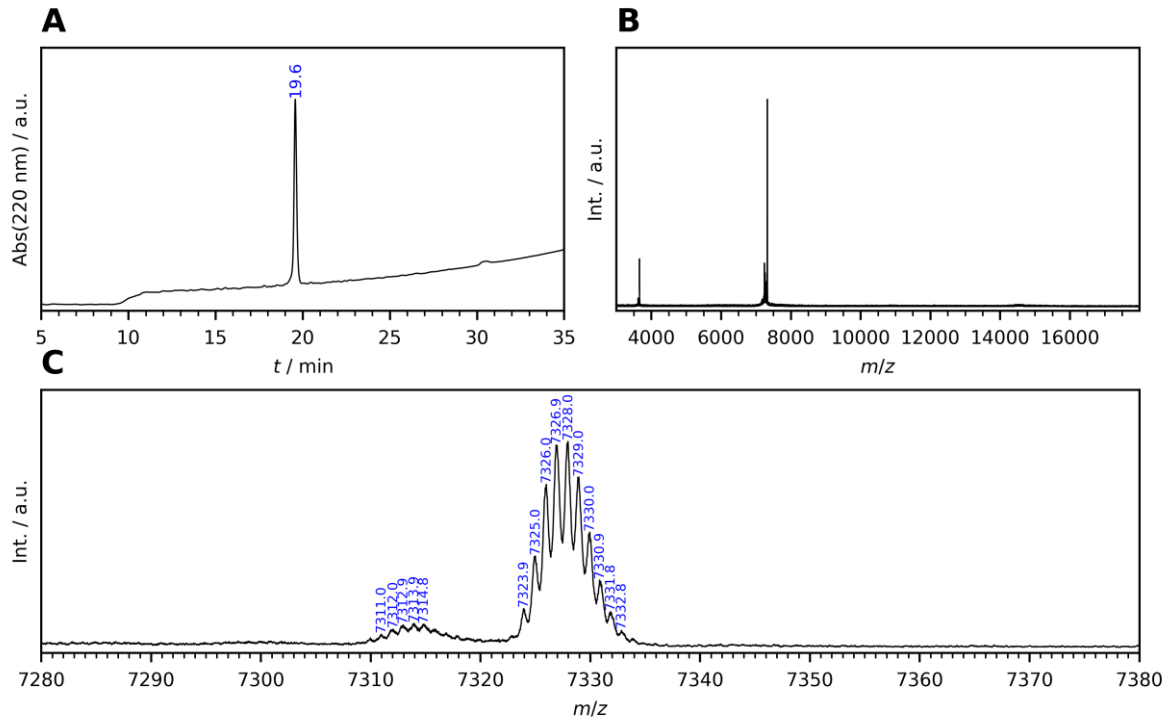

Figure 10-14: Analytical data for SH3-NC(CSY). A) Analytical HPLC trace (Gradient: 20-70% B in A in 30 min). B) MALDI-TOF-MS (complete spectrum) and C) zoom. $[M+H]^+$ calc. 7323.5.

Native SH3-NC:

Ac-AEYVRALFDFNGNDEEDLPFKKGDILRIRDKPEEQWWNAEDSEGKRG*Nle*IPVPYVEKY-NH_2

$C_{310}H_{463}N_{81}O_{94}$, Monoisotopic mass: 6824.4 Da, Molar mass: 6828.6 g/mol

$\varepsilon_{280\ nm}$ = 15470 $M^{-1}cm^{-1}$

Synthesis. SH3-NC(CSY) (250 nmol) was CSY-deprotected with method (b) (Chapter 8.5.4). Unprotected peptide was obtained as a colourless powder (101.4 nmol, 41%).

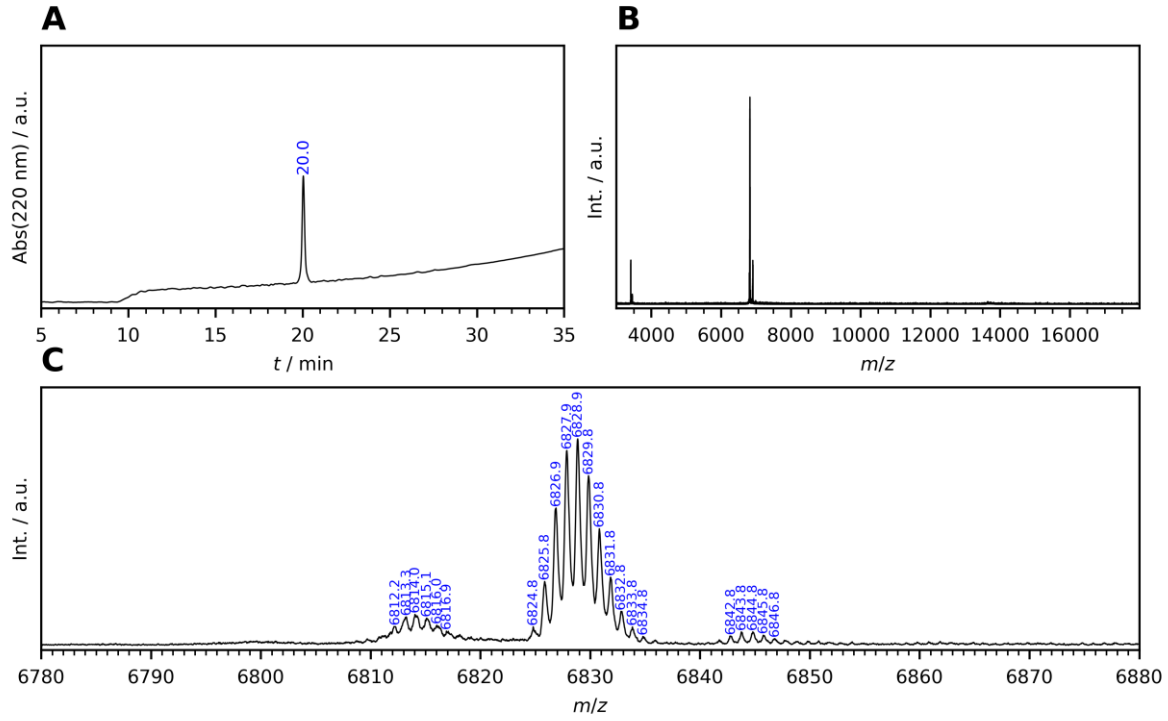

Figure 10-15: Analytical data for SH3-NC. A) Analytical HPLC trace (Gradient: 20-70% B in A in 30 min). B) MALDI-TOF-MS (complete spectrum) and C) zoom. $[M+H]^+$ calc. 6825.4.

10.4 Calculation of the cost of the synthesis of Fmoc-Asp(CSY)-OH

The cost of the synthesis of Fmoc-Asp(CSY)-OH is calculated for the here presented procedure and is compared to the synthesis reported by Neumann *et al*. (*Nat. Commun.* **2020**, *11*, 982). Taxes were not included into the given price (Table S24). Solvents and silica gel were not included, since both procedures used similar amounts.

Table 10-20: Prices of the used reagents.

Reagent	Supplier	Package	Price / €	Price/g or mL
dimethyl sulfide	Merck (Sigma-Aldrich)	250 mL	35.77	0.14308 €/mL
bromo acetonitrile	Merck (Sigma-Aldrich)	25 g	70.20	2.80800 €/g
Fmoc-Asp-O*t*Bu	Carbolution	25 g	152.50	6.10000 €/g
T3P in EtOAC	Merck (Sigma-Aldrich)	10 mL	33.60	3.36000 €/mL
HBTU	Carbolution	100 g	49.50	0.49500 €/g
DIPEA	Merck (Sigma-Aldrich)	500 mL	103.6	0.20720 €/mL
TFA	Merck (Sigma-Aldrich)	500 mL	86.02	0.17204 €/mL
formic acid	VWR	1000 mL	11.34	0.01134 €/mL

Cost of the synthesis reported in this work:

1.) Fmoc-Asp(CSY)-O*t*Bu

Used Reagents: dimethyl sulfide (2.66 mL), bromo acetonitrile (4.37 g), Fmoc-Asp-O*t*Bu (10 g), HBTU (13.83 g) and DIPEA (12.4 mL).

Total cost: 83.07 €

Yield: Fmoc-Asp(CSY)-O*t*Bu (11.46 g)

price per g: 7.25 €/g

2.) Fmoc-Asp(CSY)-OH

Used Reagents: Fmoc-Asp(CSY)-O*t*Bu (5 g) and formic acid (150 mL).

Total cost: 37.94 €

Yield: Fmoc-Asp(CSY)-OH (3.90 g)

price per g: 9.73 €

Cost of the synthesis reported by Neumann *et al.*:

1.) [NC-CH_2-SMe_2]Br

Used reagents: dimethyl sulfide (7.53 mL) and bromo acetonitrile (12.35 g)

Total cost: 35.76 €

Yield: [NC-CH_2-SMe_2]Br 16.8 g

Price per g: 2.13 €/g

2.) Fmoc-Asp(CSY)-O*t*Bu

Used Reagents: [NC-CH2-SMe_2]Br (0.53 g), Fmoc-Asp-O*t*Bu (1 g), T3P(2.01 mL) and DIPEA 1.29 mL).

Total cost: 14.25 €

Yield: Fmoc-Asp(CSY)-O*t*Bu (1.07 g)

price per g: 13.32 €/g

3.) Fmoc-Asp(CSY)-OH

Used Reagents: Fmoc-Asp(CSY)-O*t*Bu (1 g) and TFA (10 mL).

Total cost: 15.04 €

Yield: Fmoc-Asp(CSY)-OH (0.85 g)

price per g: 17.69 €

10.5 Additional NMR spectra

10.5.1 Fmoc-Hse-OH

^{1}H NMR (400 MHz, DMSO-d_6)

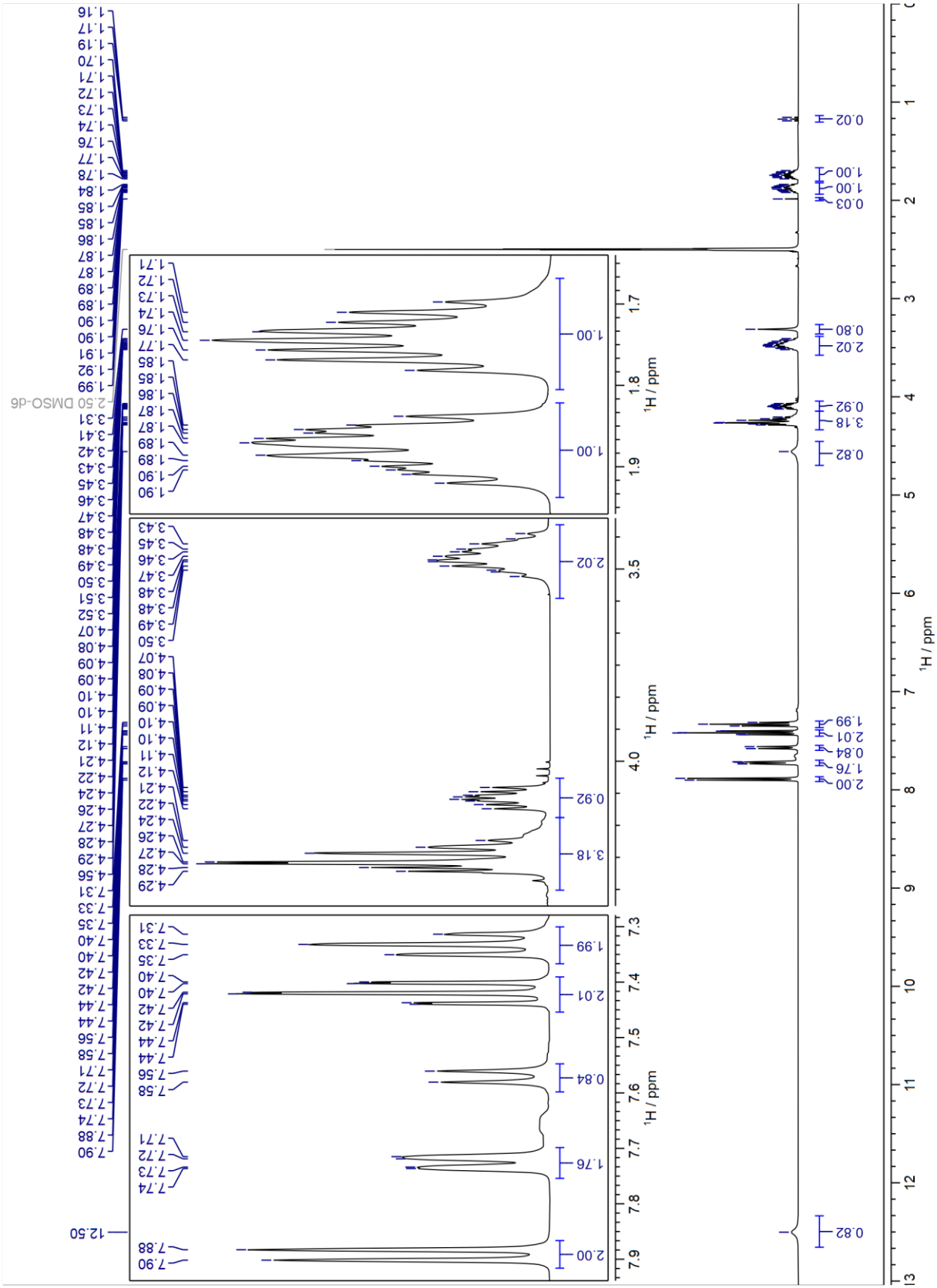

^{13}C-NMR (101 MHz, DMSO-d_6)

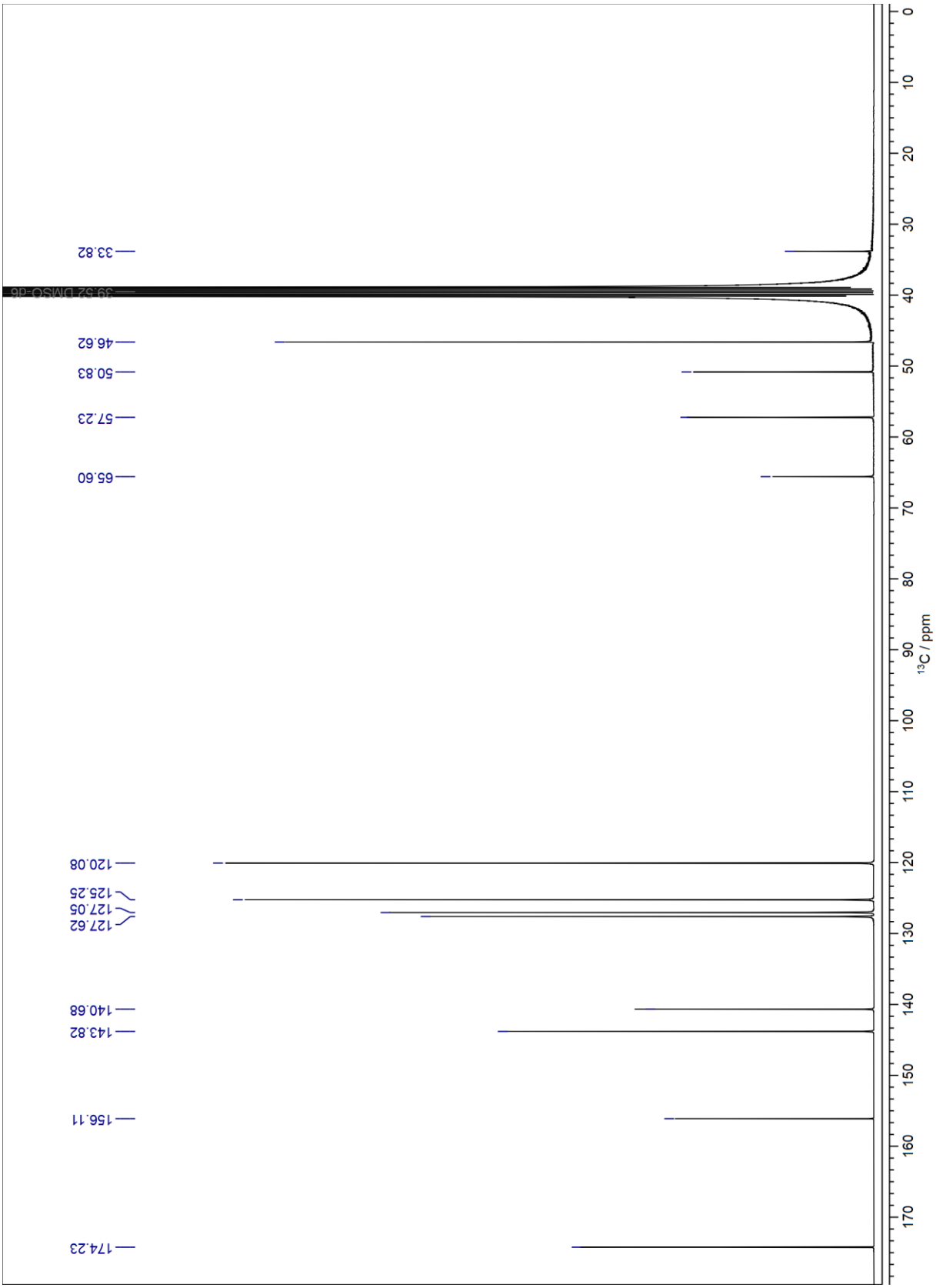

10.5.2 Fmoc-Hse(Dmt)-OH DIPEA salt

^{1}H NMR (400 MHz, DMSO-d_6)

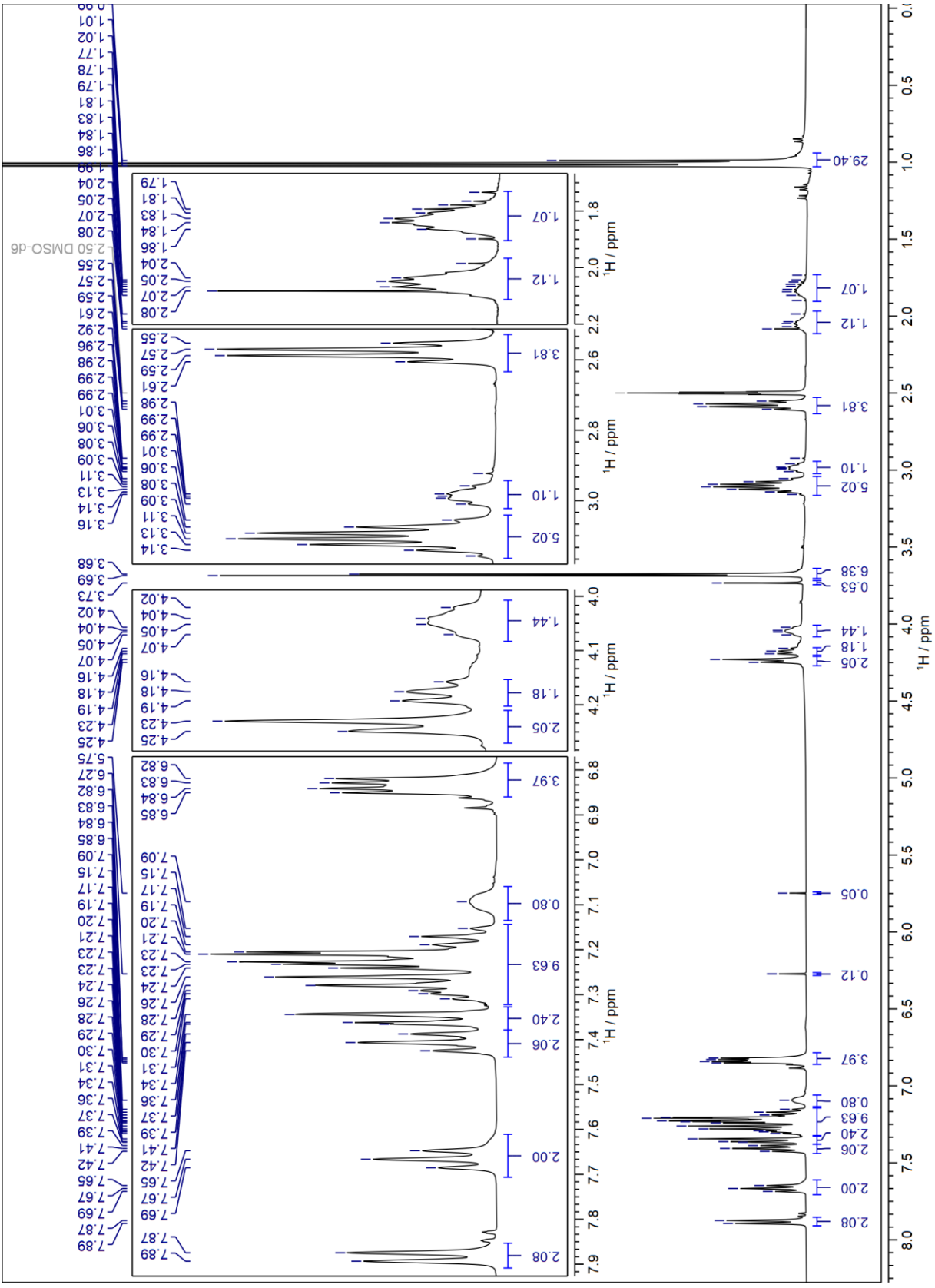

^{13}C NMR (101 MHz, DMSO-d_6)

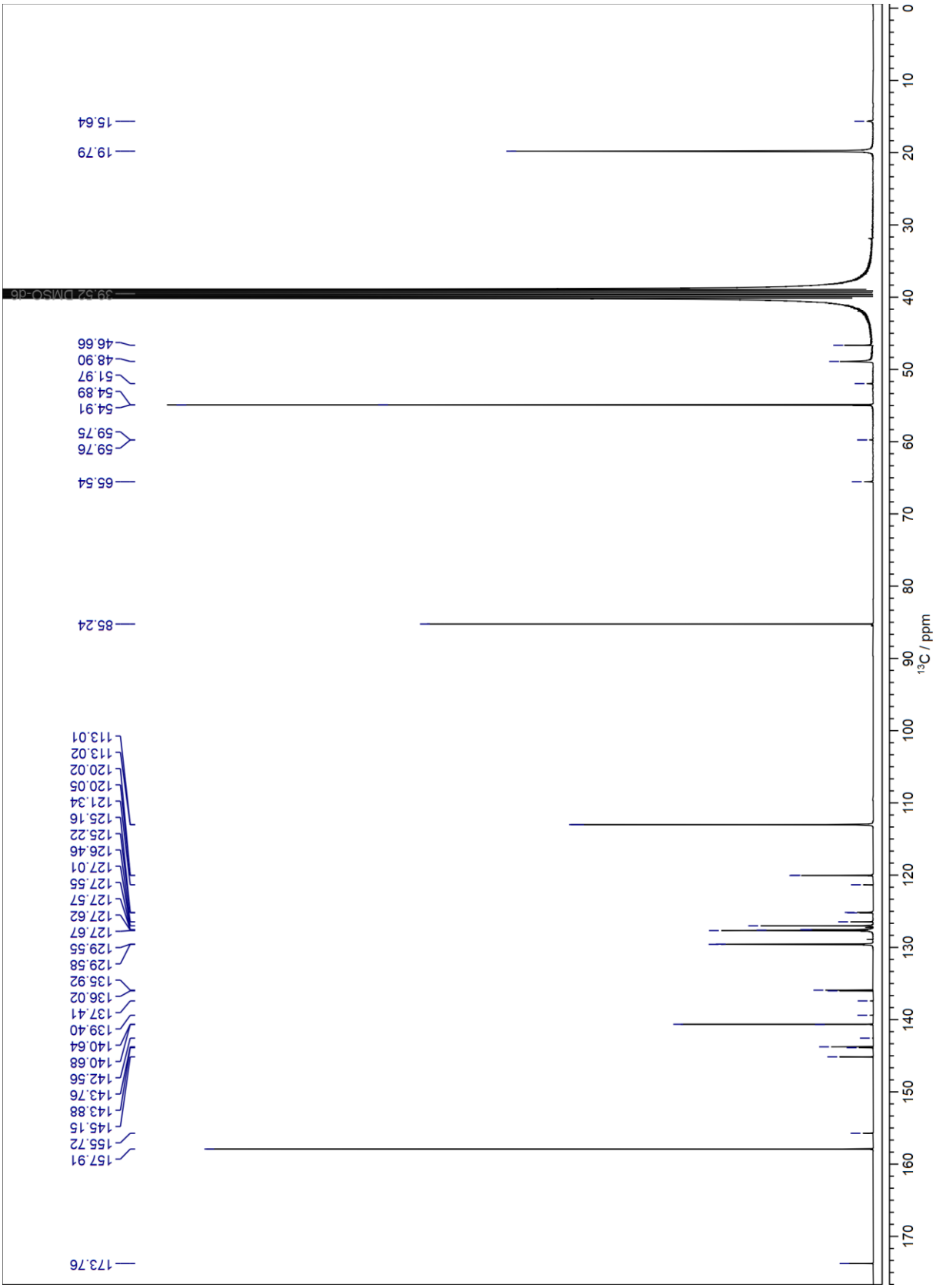

^{1}H-^{1}H COSY (400 MHz, 400 MHz, DMSO-d_6)

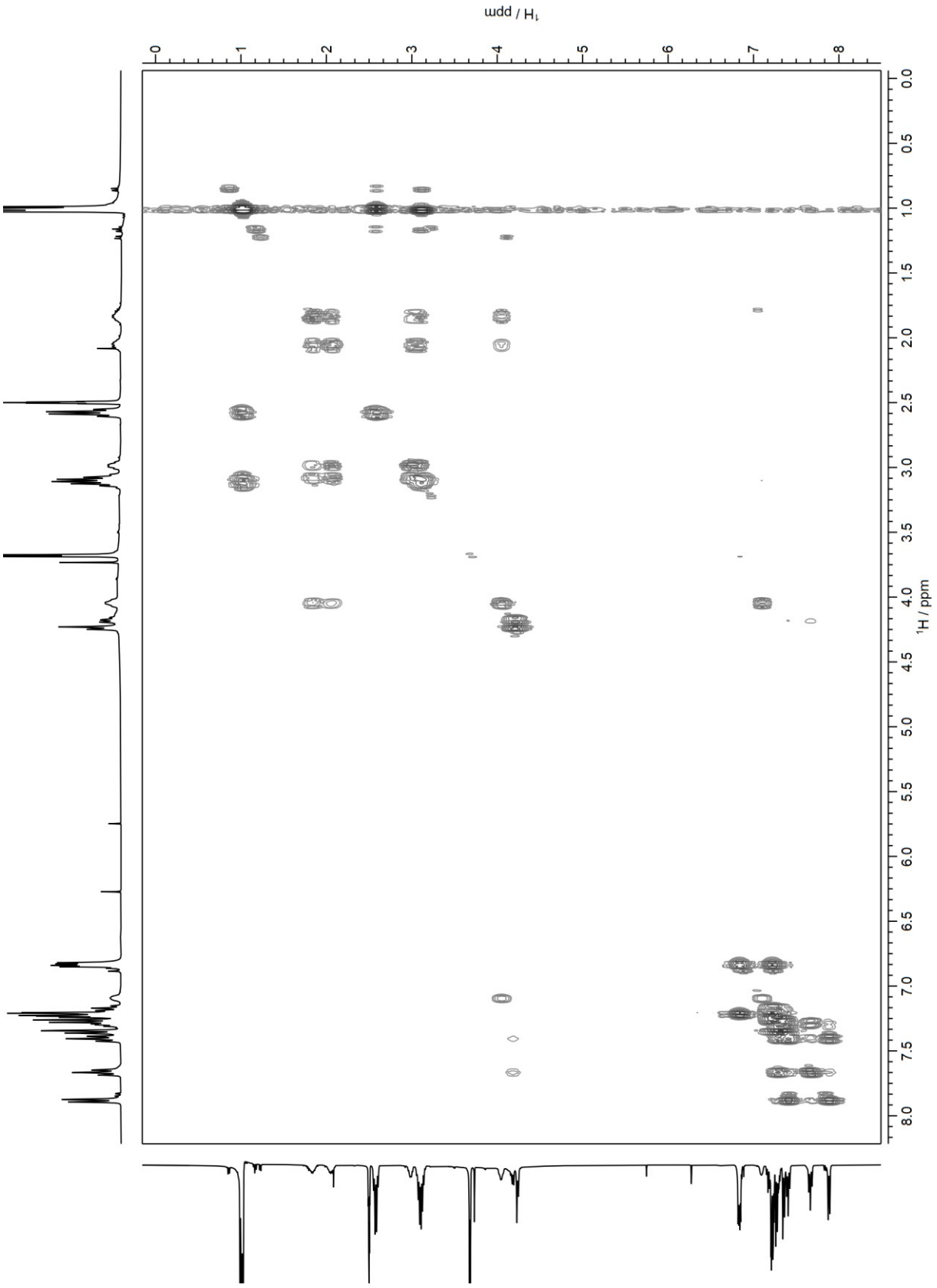

^{1}H-^{13}C HSQC (400 MHz, 101 MHz, DMSO-d_6)

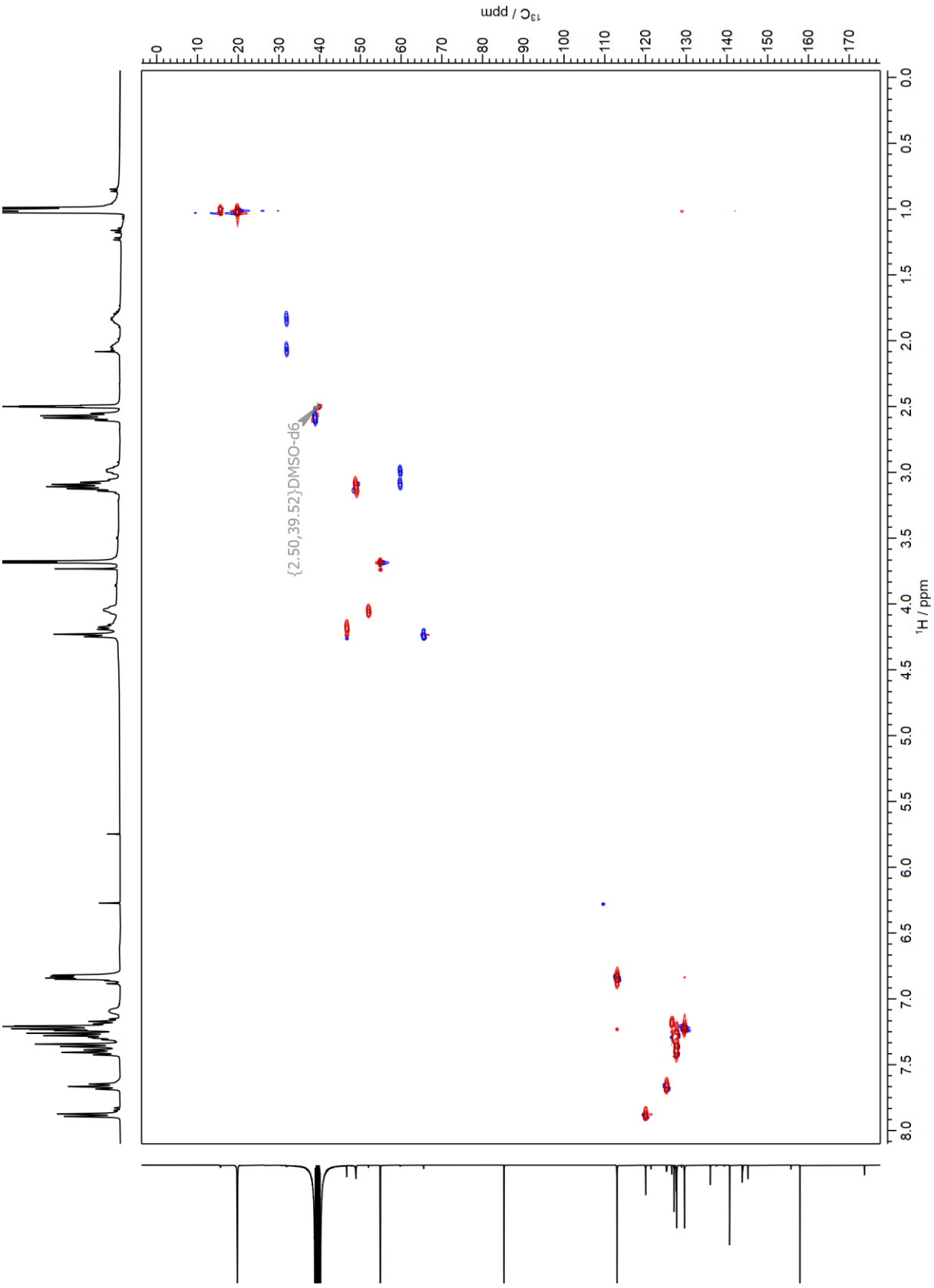

10.5.3 Fmoc-Asp(CSY)-O*t*Bu

^{1}H-NMR (600 MHz, DMSO-d_6)

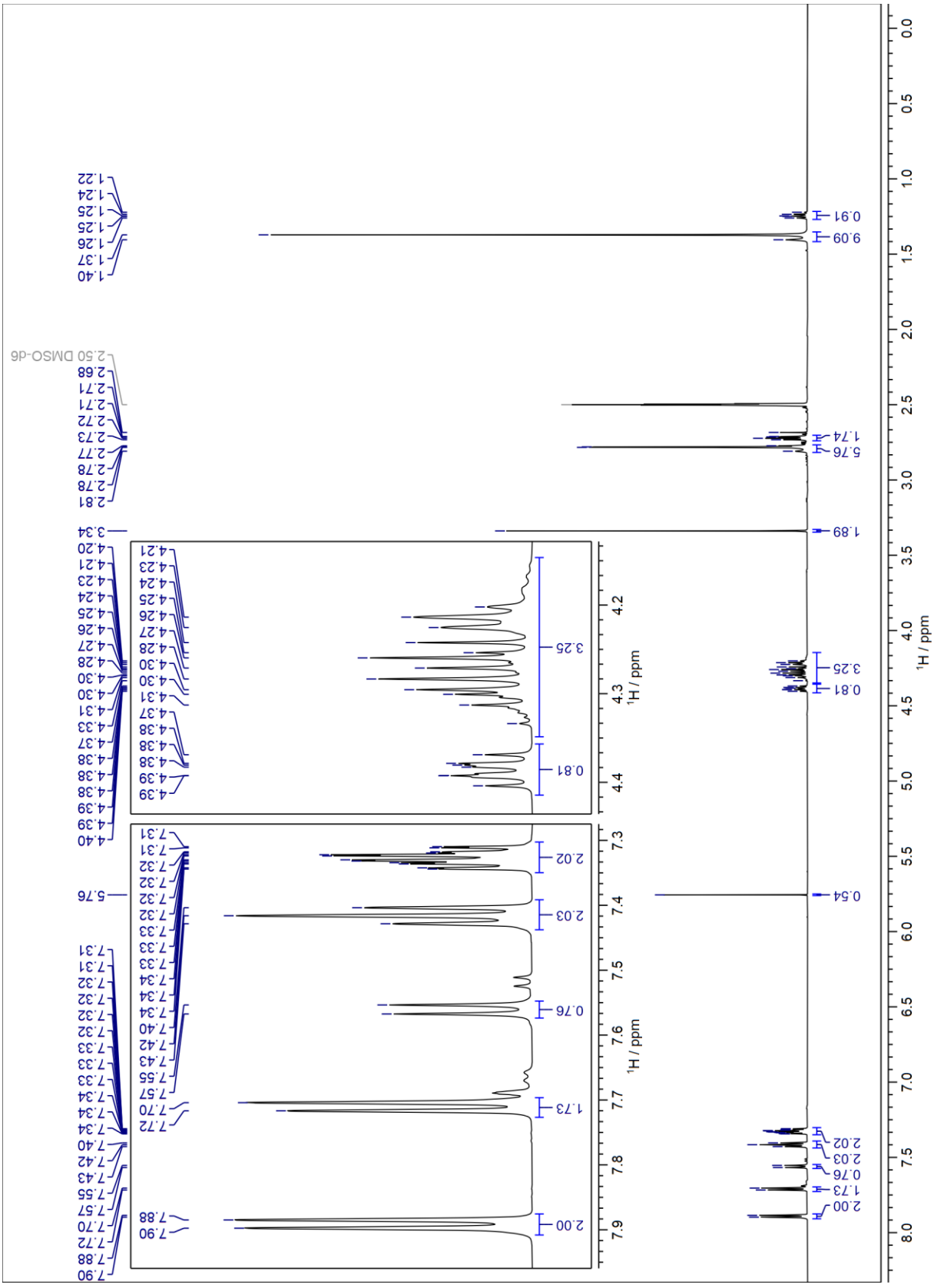

^{13}C-NMR (151 MHz, DMSO-d6)

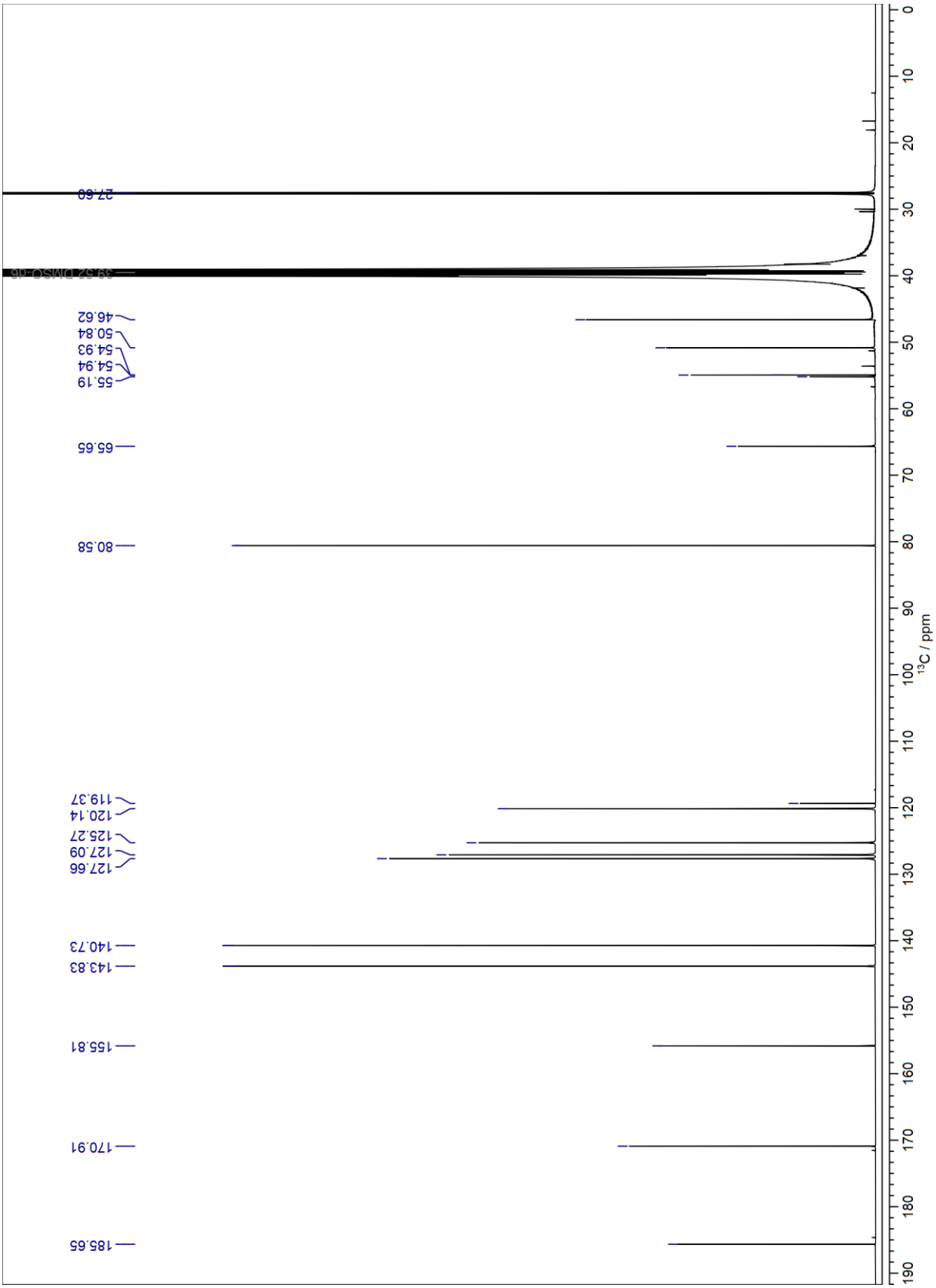

^{1}H-^{1}H COSY (600 MHz, 600 MHz, DMSO-d_6)

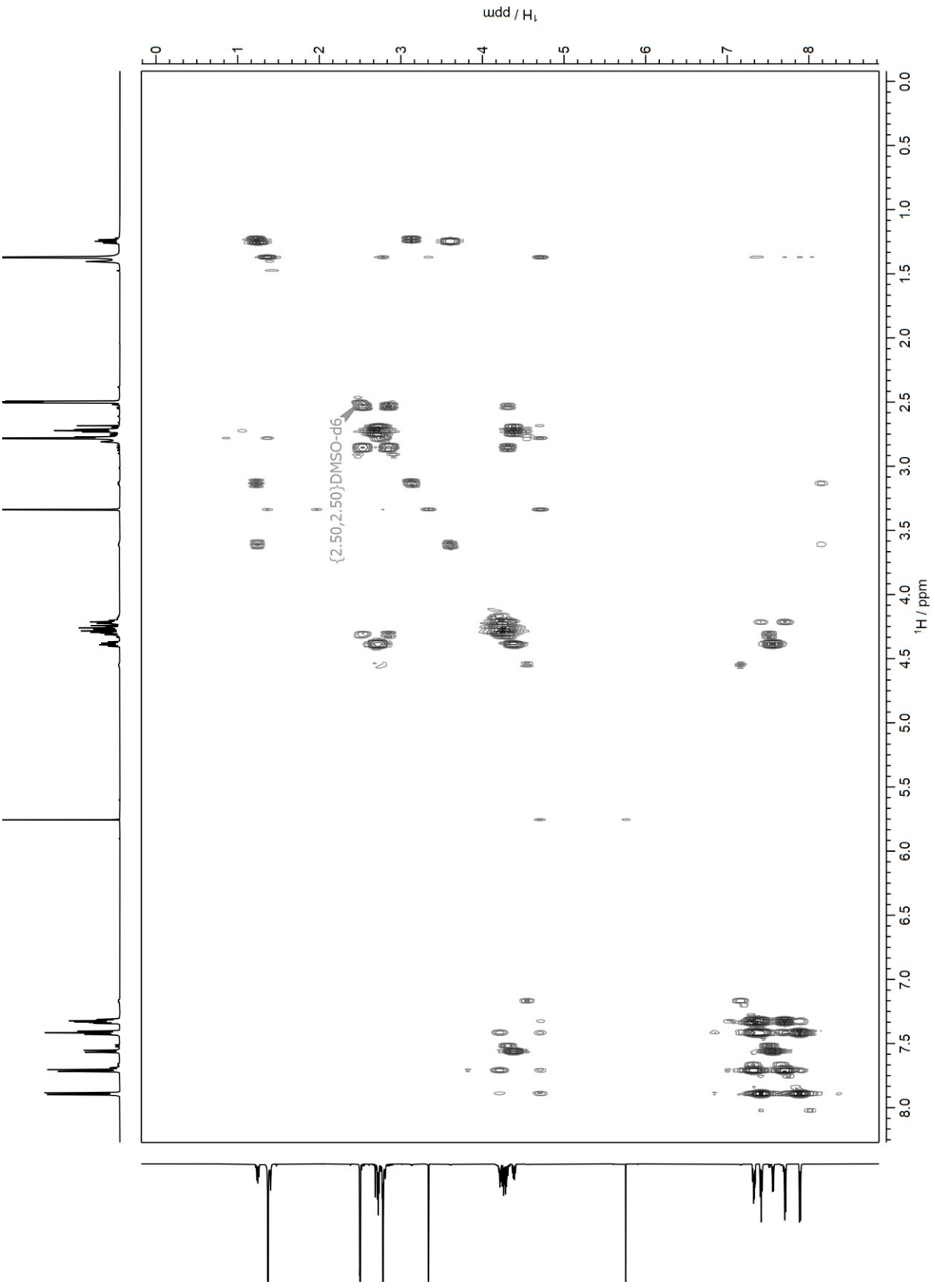

^{1}H-^{13}C HSQC (600 MHz, 151 MHz, DMSO-d_6)

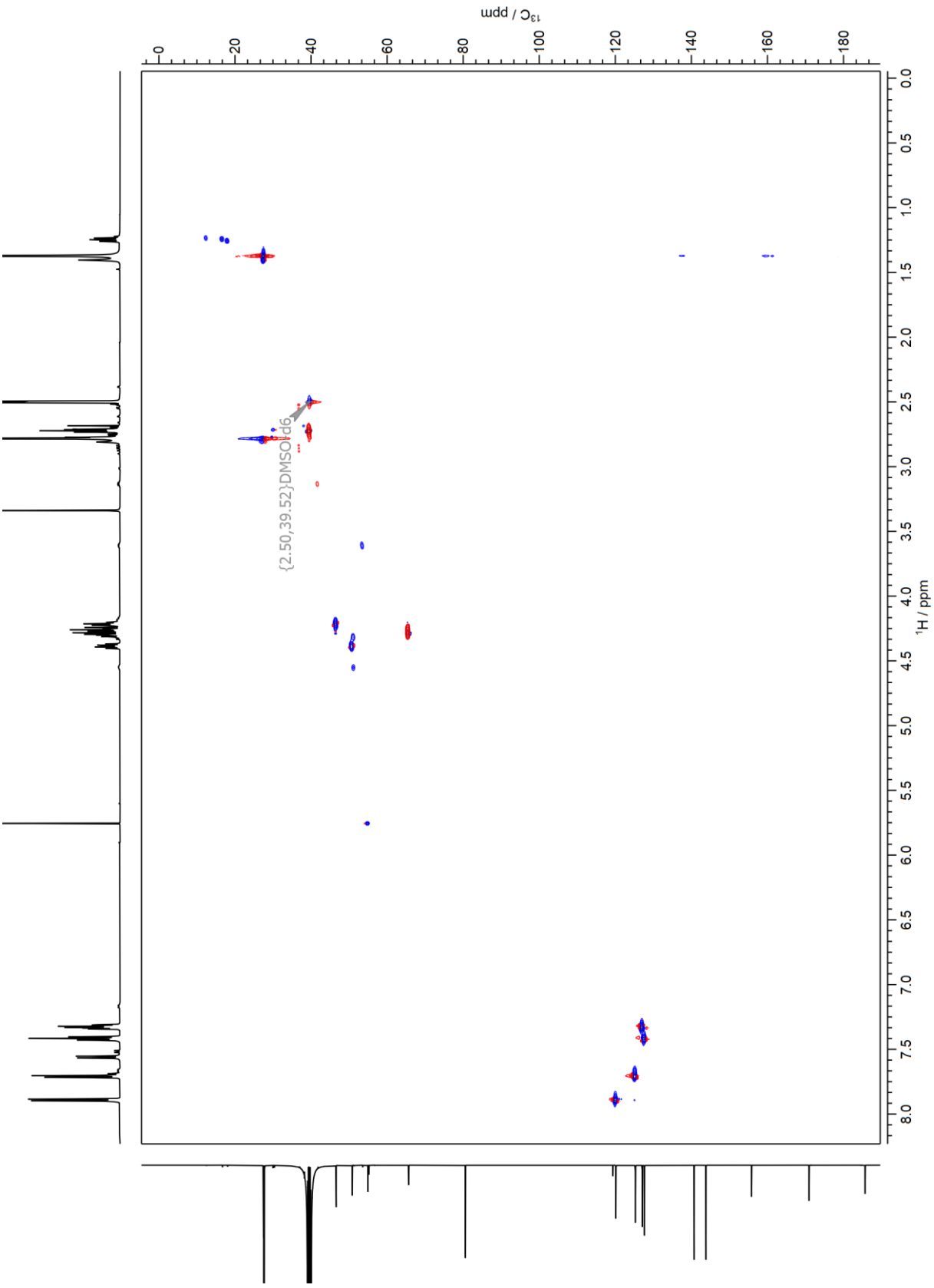

10.5.4 Fmoc-Asp(CSY)-OH

^{1}H-NMR (400 MHz, DMSO-d_6)

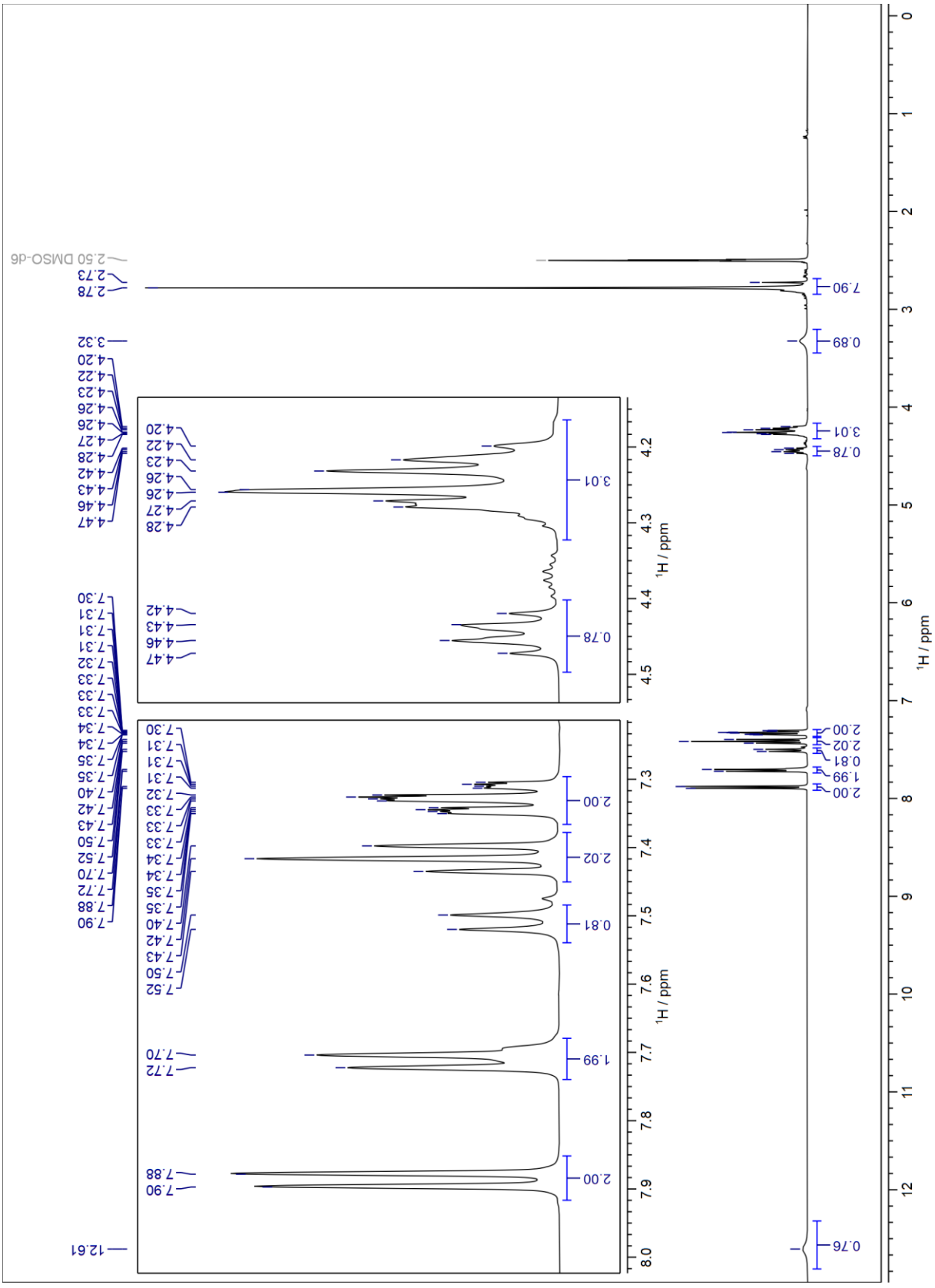

^{13}C-NMR (101 MHz, DMSO-d_6)

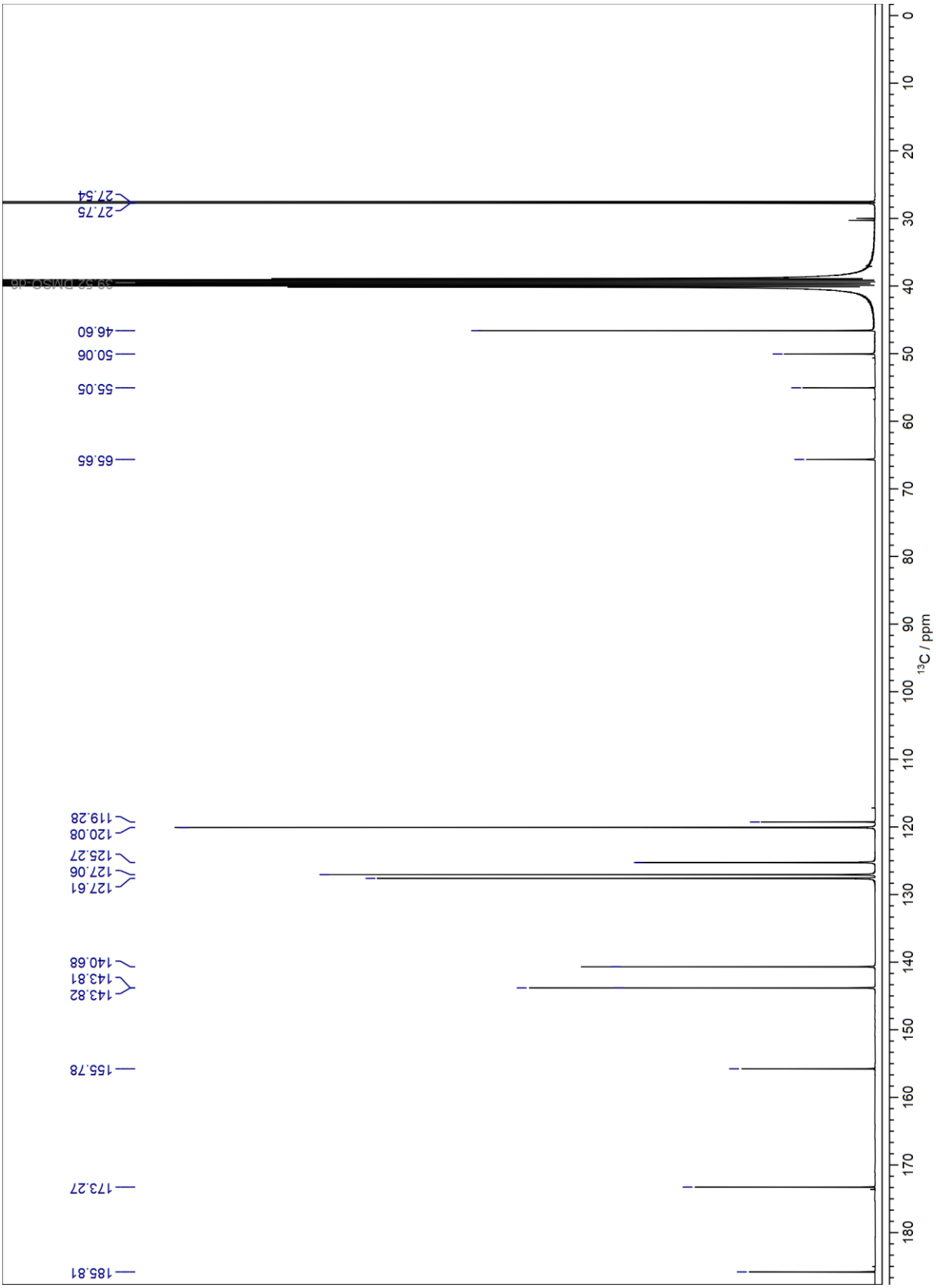

$^{1}H,^{1}H$ COSY (400 MHz, 400 MHz, DMSO-d_6)

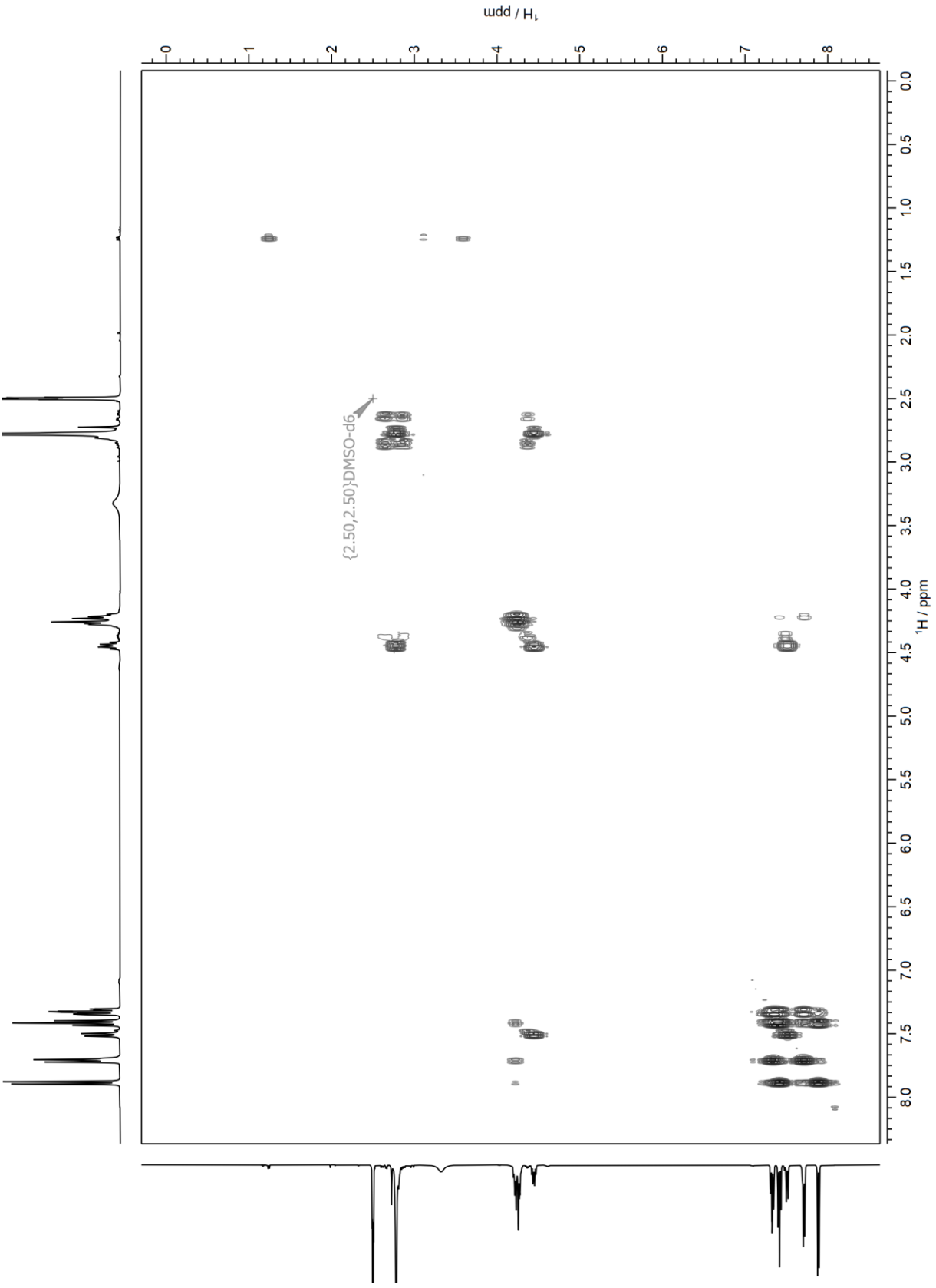

$^{1}H,^{13}C$ HSQC (400 MHz, 101 MHz, DMSO-d_6)

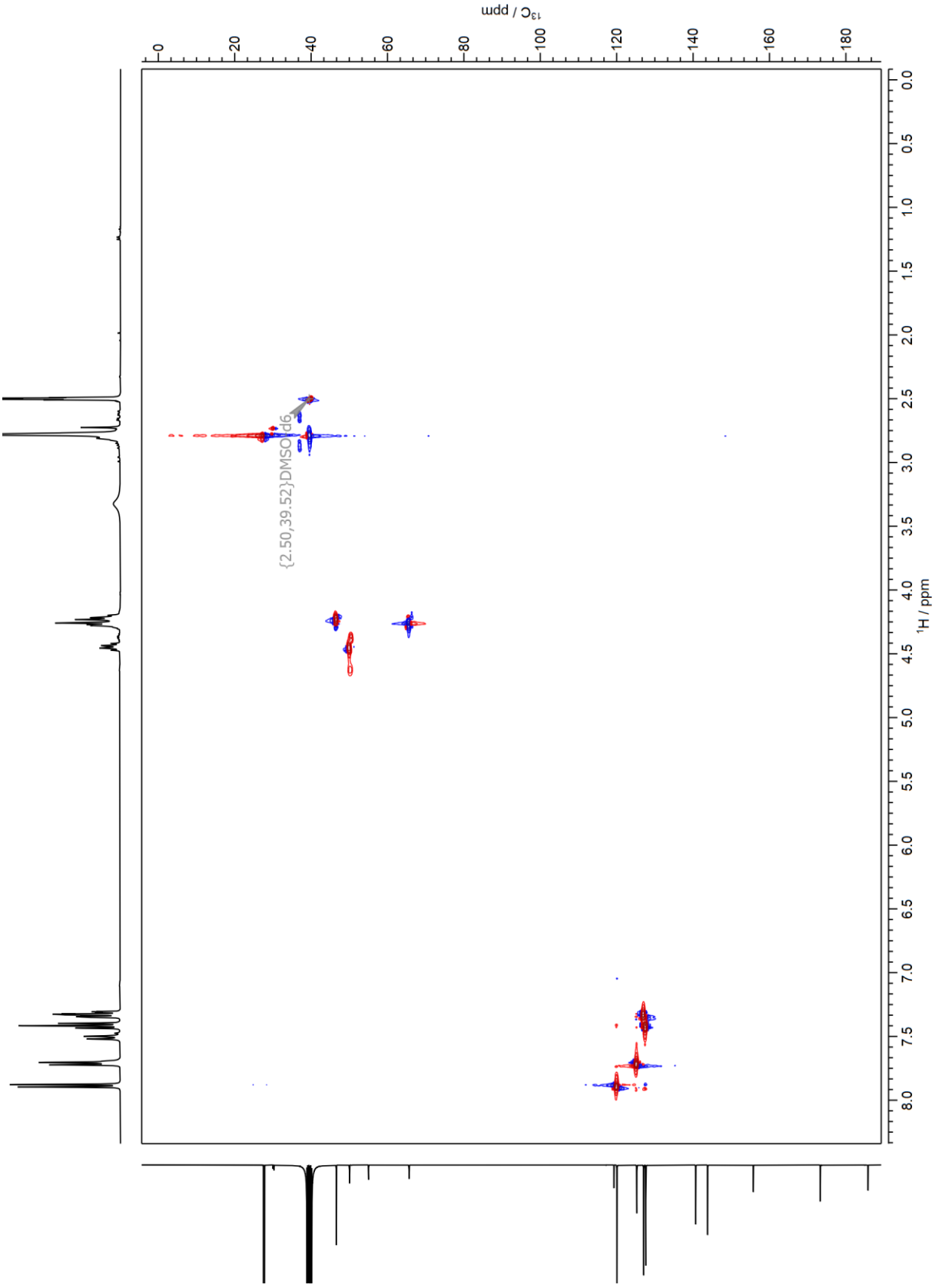

10.5.5 WW-CA-Nle in absence and presence of Zn(II)

^{1}H-^{15}N HSQC (800 MHz, 5% *v*/*v* D_2O in MOPS-buffered saline). Alternative dispersion of chemical shifts Δδ. For more details see Figure 4-15.

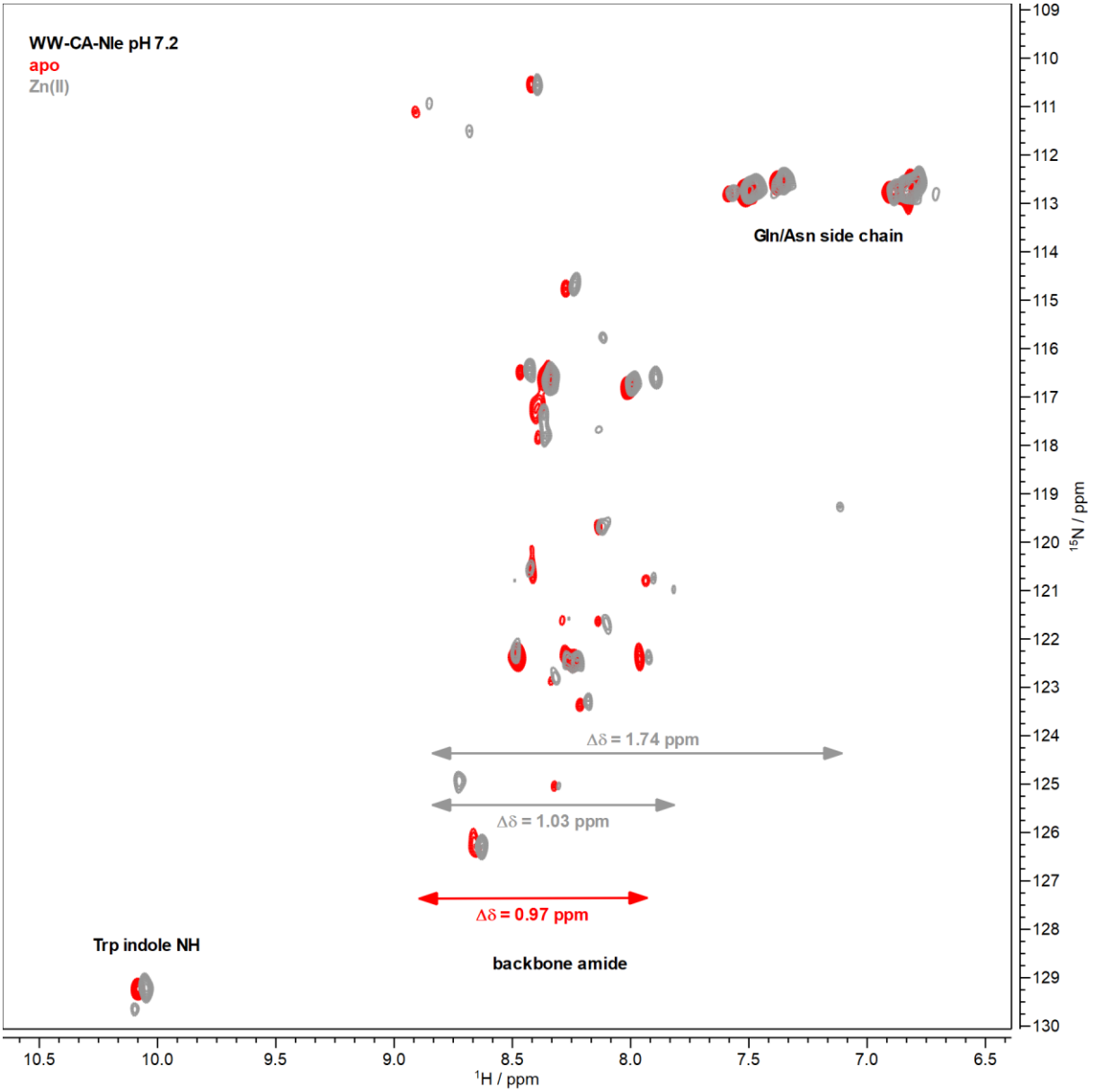

10.6 Additional FT-IR spectra

10.6.1 Fmoc-Hse(Dmt)-OH DIPEA salt

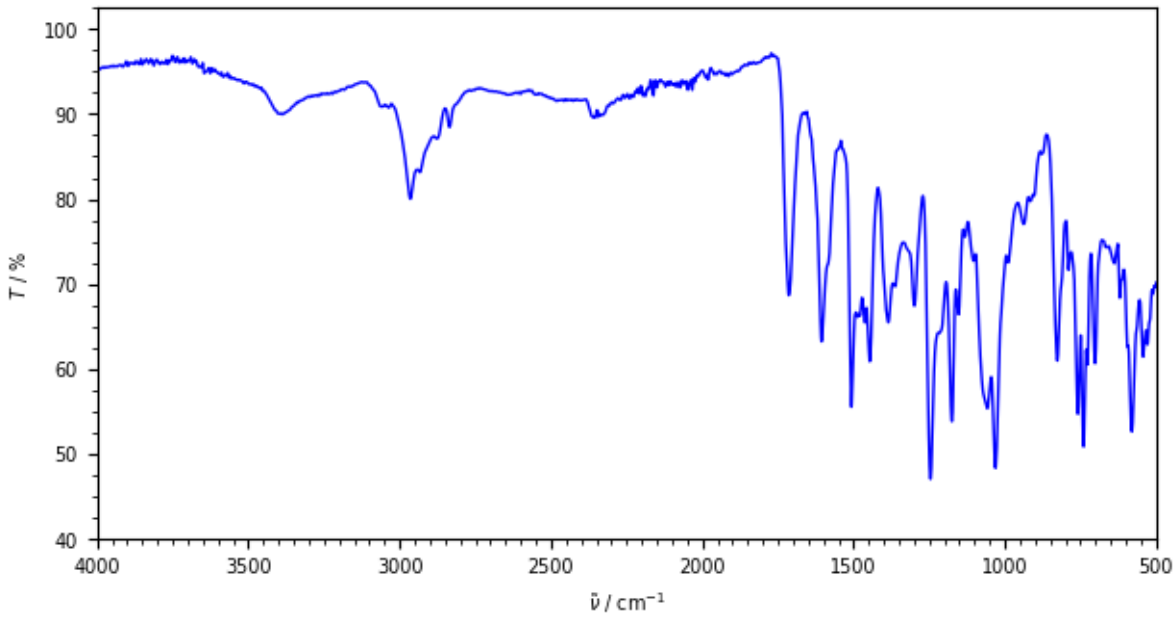

10.6.2 Fmoc-Asp(CSY)-O*t*Bu

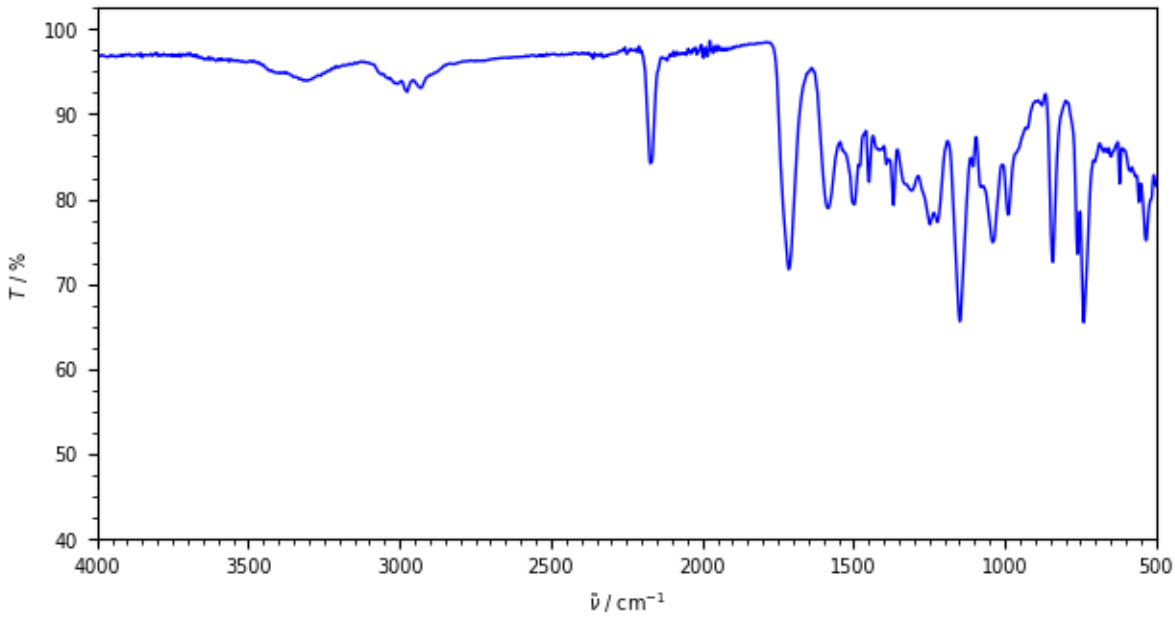

10.6.3 Fmoc-Asp(CSY)-OH

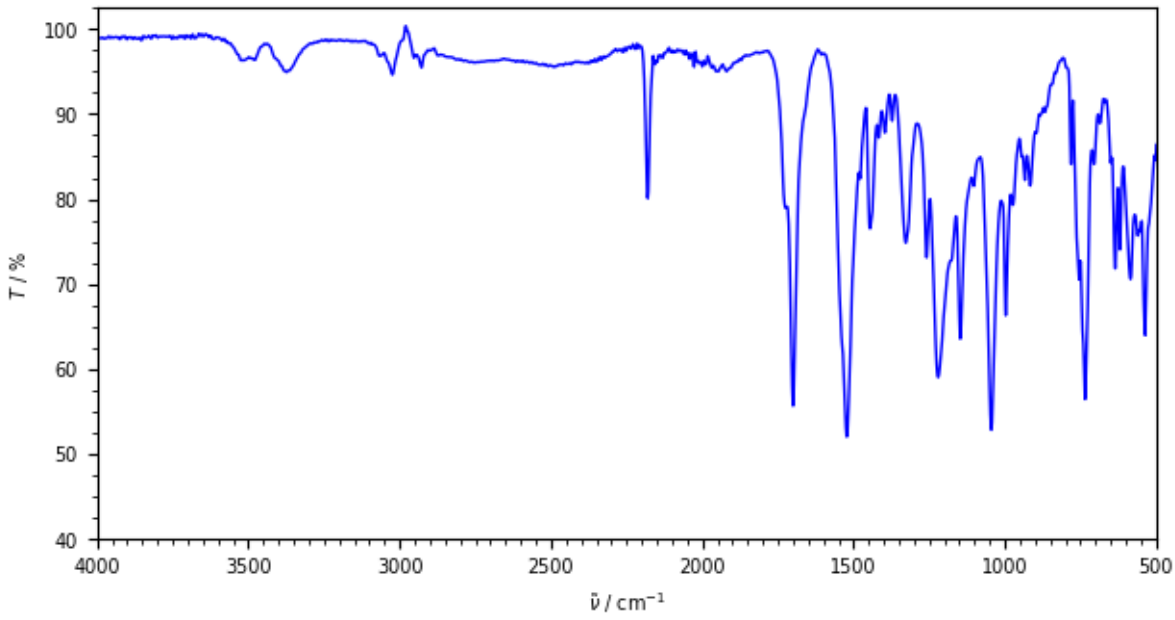

10.7 Additional ESI-MS spectra

10.7.1 Fmoc-Hse-OH

Mass Spectrum Formula Report

Analysis Info Acquisition Date 12/2/2020 8 56 52 AM

Analysis Name D \Data\Thomas\icr40886_000002 d

Comment Pham, AK Thomas LSF004 in DCM/MeOH

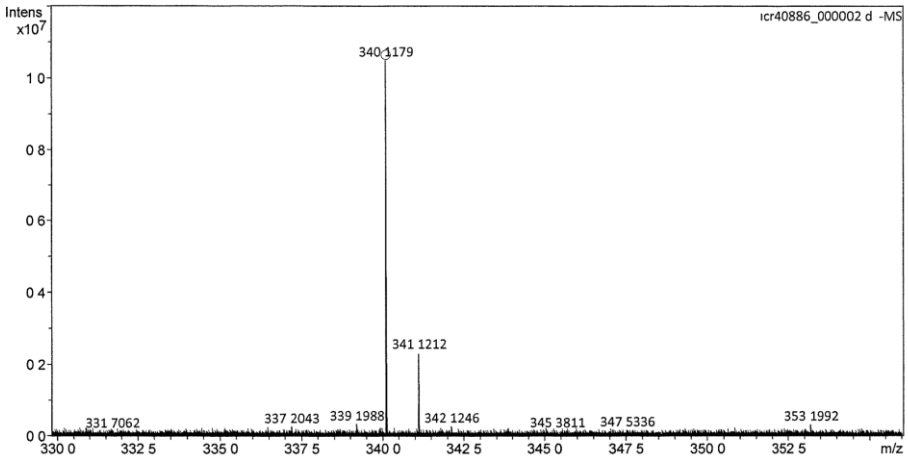

Meas m/z	Ion Formula	m/z	err [ppm]	mSigma	rdb	e⁻ Conf	N-Rule
340 1179	C19H18NO5	340 1190	3 5	9 8	11 5	even	ok
	C17H16N4O4	340 1177	-0 5	19 0	12 0	odd	ok
	C18H12N8	340 1190	3 4	20 8	17 0	odd	ok

Bruker Compass DataAnalysis 4 3 printed 12/2/2020 8 59 29 AM Page 1 of 1

10.7.2 Fmoc-Hse(Dmt)-OH DIPEA salt

Mass Spectrum Formula Report

Analysis Info Acquisition Date 12/2/2020 8 56 52 AM

Analysis Name D \Data\Thomas\icr40886_000002 d

Comment Pham, AK Thomas LSF004 in DCM/MeOH

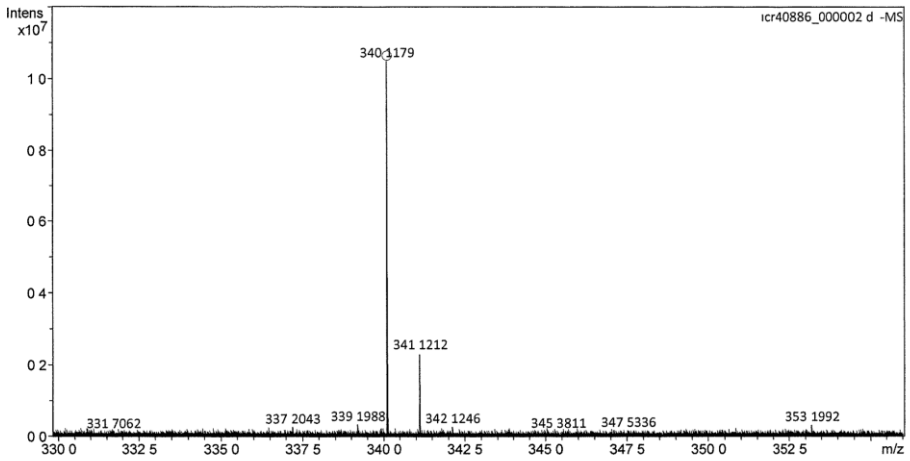

Meas m/z	Ion Formula	m/z	err [ppm]	mSigma	rdb	e⁻ Conf	N-Rule
340 1179	C19H18NO5	340 1190	3 5	9 8	11 5	even	ok
	C17H16N4O4	340 1177	-0 5	19 0	12 0	odd	ok
	C18H12N8	340 1190	3 4	20 8	17 0	odd	ok

10.7.3 Fmoc-Asp(CSY)-O*t*Bu

Mass Spectrum Formula Report

Analysis Info

Analysis Name D:\Data\Thomas\icr42367_000002.d

Comment Pham, AK Thomas: D(CSg)1 in DCM/MeOH

Acquisition Date 4/23/2021 8:37:47 AM

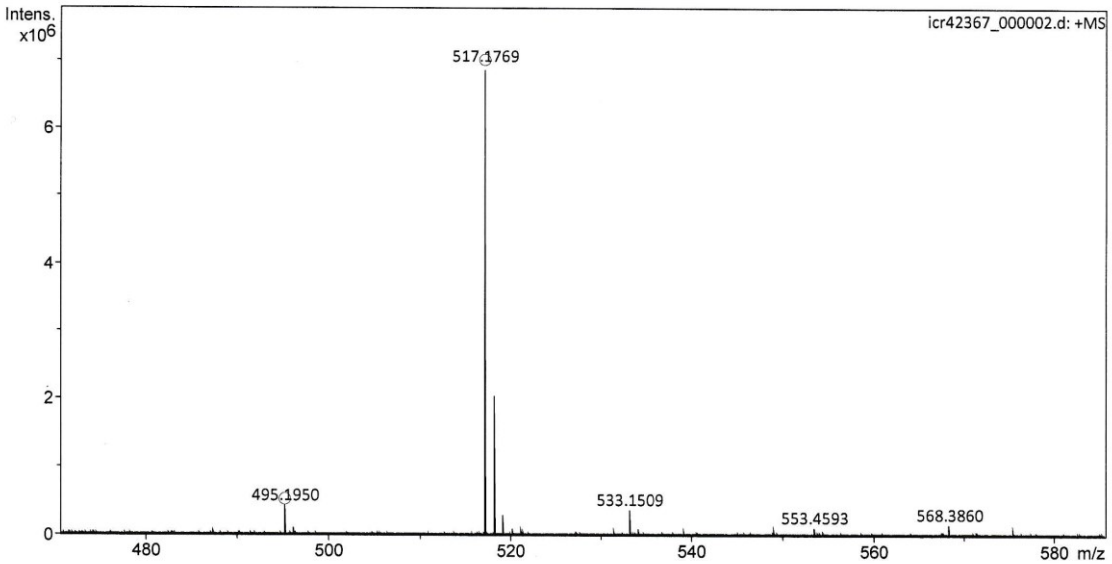

Meas. m/z	Ion Formula	m/z	err [ppm]	mSigma	rdb	e⁻ Conf	N-Rule
495.1950	C21H29N5O9	495.1960	2.0	19.2	10.0	odd	ok
	C20H33NO13	495.1946	-0.7	23.7	5.0	odd	ok
	C19H27N8O8	495.1946	-0.7	26.6	10.5	even	ok
	C20H23N12O4	495.1960	2.0	27.0	15.5	even	ok
	C26H25N9S	495.1948	-0.3	29.1	19.0	odd	ok
	C27H31N2O5S	495.1948	-0.3	29.9	13.5	even	ok
	C18H21N15O3	495.1946	-0.7	38.9	16.0	odd	ok
	C33H25N3O2	495.1941	-1.7	52.1	23.0	odd	ok
	C35H27O3	495.1955	1.0	71.1	22.5	even	ok
517.1769	C27H30N2NaO5S	517.1768	-0.3	7.1	13.5	even	ok
	C26H31NO8S	517.1765	-0.9	8.9	12.0	odd	ok
	C27H27N5O4S	517.1778	1.7	10.5	17.0	odd	ok
	C26H24N9NaS	517.1768	-0.3	16.4	19.0	odd	ok
	C25H25N8O3S	517.1765	-0.9	16.6	17.5	even	ok
	C21H28N5NaO9	517.1779	1.9	28.3	10.0	odd	ok
	C33H24N3NaO2	517.1761	-1.7	30.4	23.0	odd	ok
	C33H21N6O	517.1771	0.4	31.4	26.5	even	ok
	C20H29N4O12	517.1776	1.4	32.4	8.5	even	ok
	C20H32NNaO13	517.1766	-0.7	35.0	5.0	odd	ok
	C20H22N12NaO4	517.1779	1.9	39.5	15.5	even	ok
	C35H26NaO3	517.1774	0.9	46.4	22.5	even	ok

10.7.4 Fmoc-Asp(CSY)-OH

Mass Spectrum Formula Report

Analysis Info Acquisition Date 4/28/2021 8:15:38 AM

Analysis Name D:\Data\Thomas\icr42414_000001.d

Comment Zilke, AK Thomas: N-Fmoc-Asp(CSY)-OH in DCM/MeOH

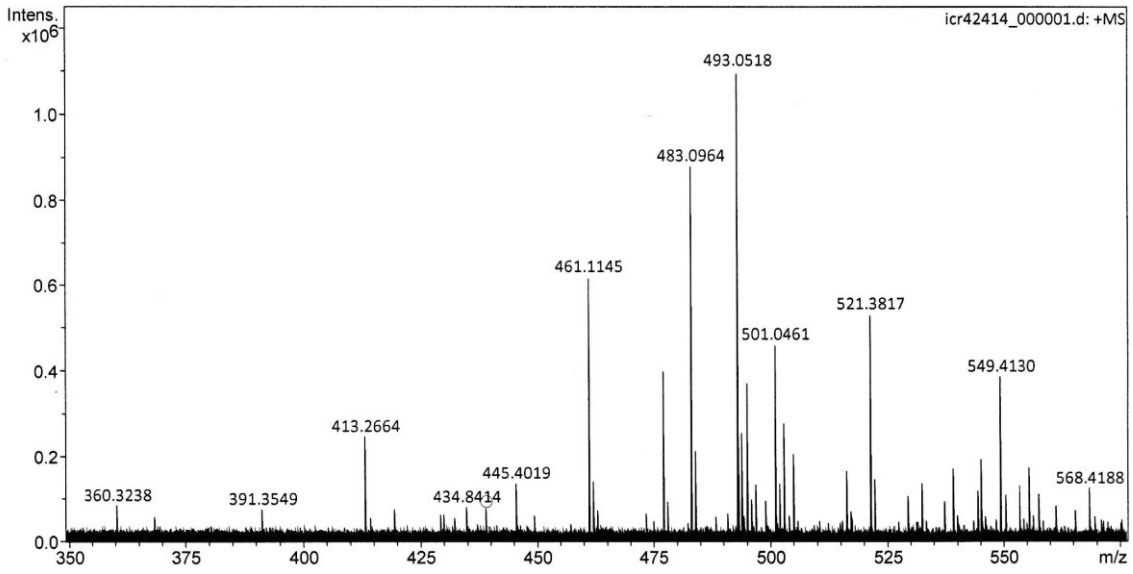

Meas. m/z	Ion Formula	m/z	err [ppm]	mSigma	rdb	e⁻ Conf	N-Rule
439.1325	C23H23N2O5S	439.1322	-0.6	n.a.	13.5	even	ok
	C31H19O3	439.1329	0.9	n.a.	22.5	even	ok

10.8 Additional CD spectra and CD thermal denaturation profiles

10.8.1 WW domains

WW-CA apo (100 µM peptide in MOPS buffered saline)

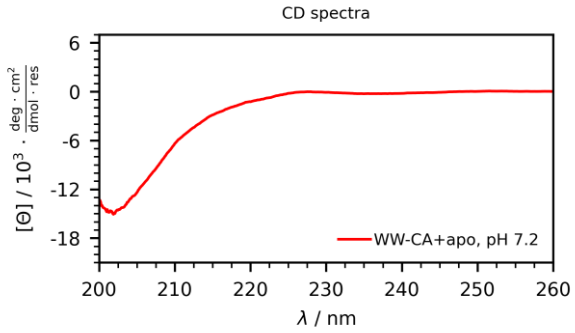

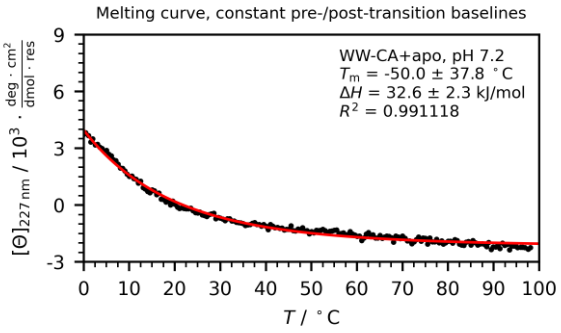

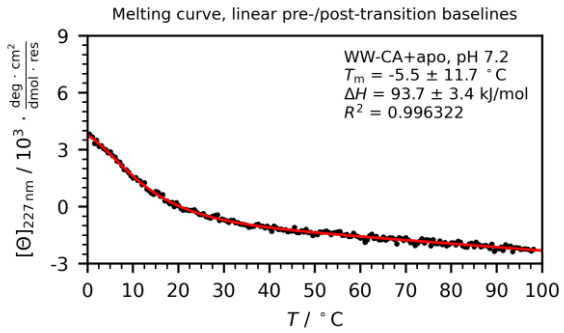

WW-CA + Zn(II) (100 µM peptide + 100 µM metal ions in MOPS/HEPES/MES buffered saline)

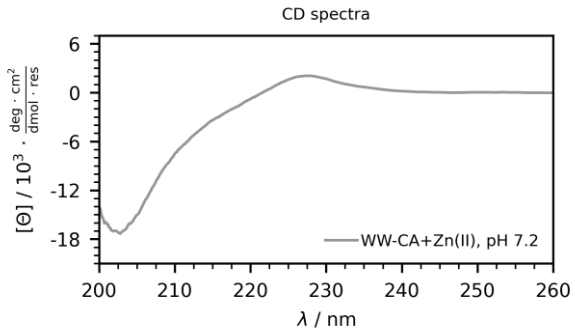

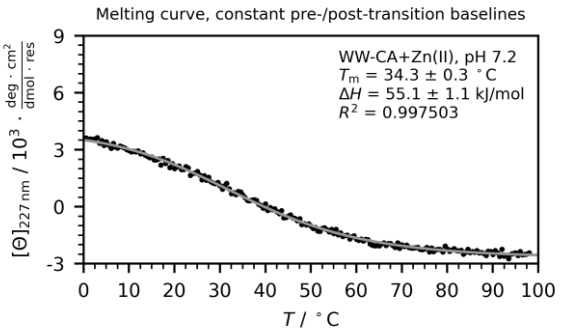

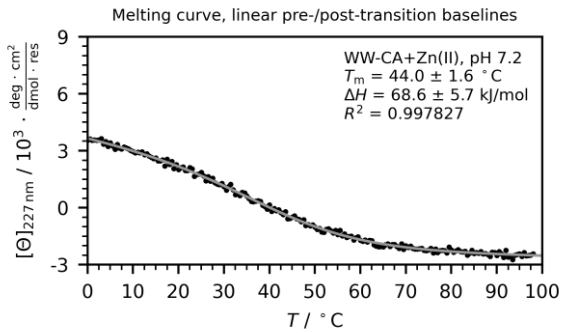

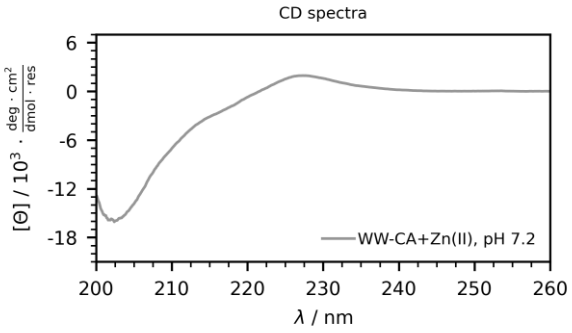
CD spectra
WW-CA+Zn(II), pH 7.2
λ / nm

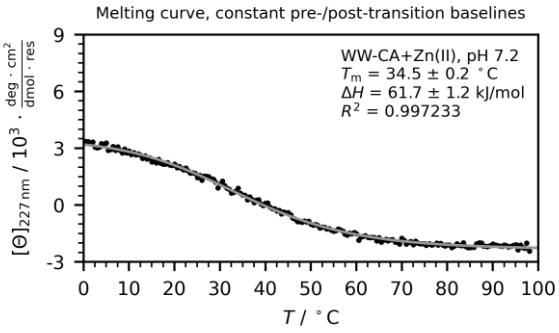
Melting curve, constant pre-/post-transition baselines
WW-CA+Zn(II), pH 7.2
T_m = 34.5 ± 0.2 °C
ΔH = 61.7 ± 1.2 kJ/mol
R^2 = 0.997233
T / °C

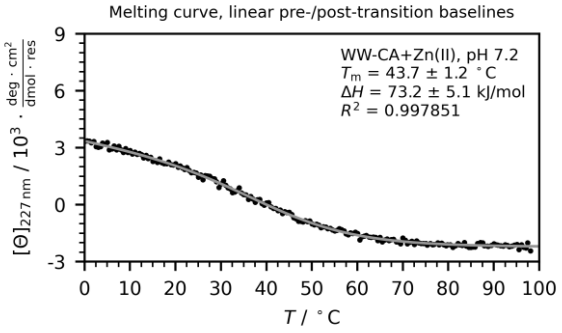
Melting curve, linear pre-/post-transition baselines
WW-CA+Zn(II), pH 7.2
T_m = 43.7 ± 1.2 °C
ΔH = 73.2 ± 5.1 kJ/mol
R^2 = 0.997851
T / °C

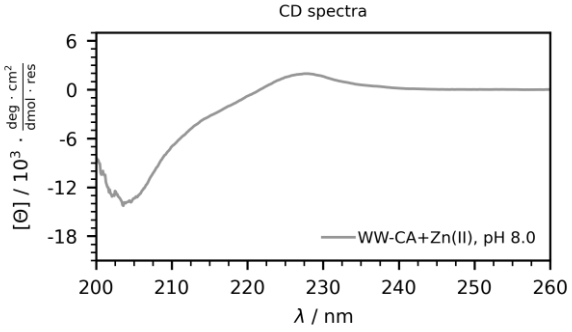
CD spectra
WW-CA+Zn(II), pH 8.0
λ / nm

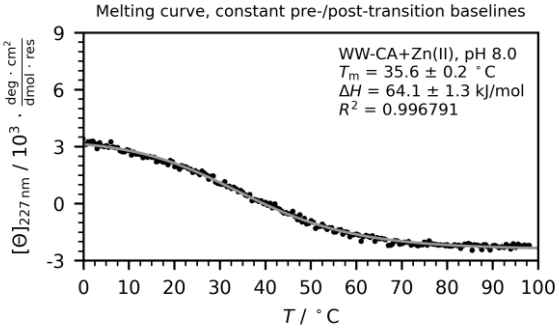
Melting curve, constant pre-/post-transition baselines
WW-CA+Zn(II), pH 8.0
T_m = 35.6 ± 0.2 °C
ΔH = 64.1 ± 1.3 kJ/mol
R^2 = 0.996791
T / °C

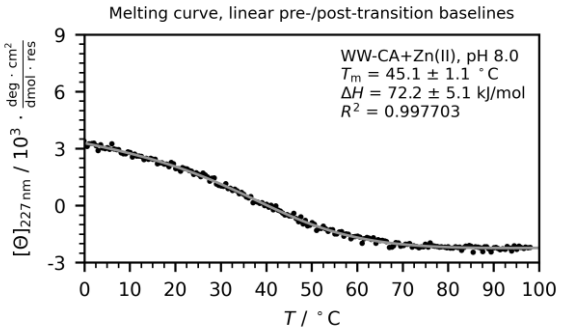
Melting curve, linear pre-/post-transition baselines
WW-CA+Zn(II), pH 8.0
T_m = 45.1 ± 1.1 °C
ΔH = 72.2 ± 5.1 kJ/mol
R^2 = 0.997703
T / °C

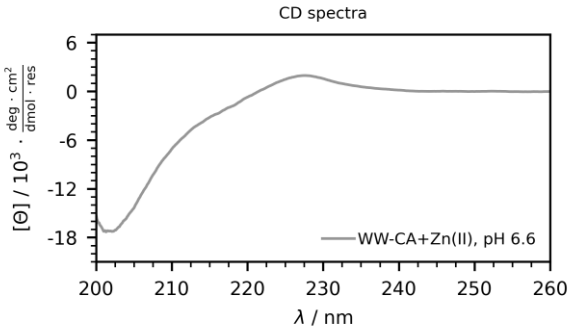
CD spectra
WW-CA+Zn(II), pH 6.6
λ / nm

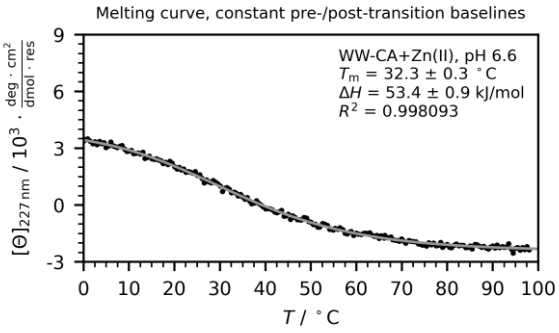
Melting curve, constant pre-/post-transition baselines
WW-CA+Zn(II), pH 6.6
T_m = 32.3 ± 0.3 °C
ΔH = 53.4 ± 0.9 kJ/mol
R^2 = 0.998093
T / °C

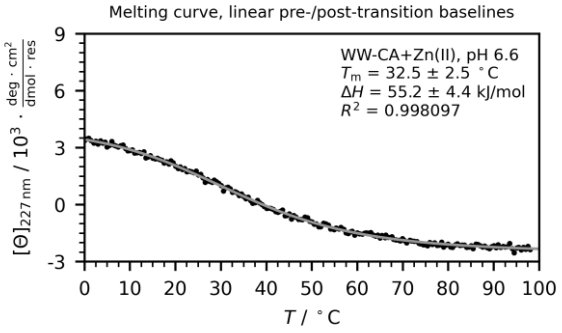
Melting curve, linear pre-/post-transition baselines
WW-CA+Zn(II), pH 6.6
T_m = 32.5 ± 2.5 °C
ΔH = 55.2 ± 4.4 kJ/mol
R^2 = 0.998097
T / °C

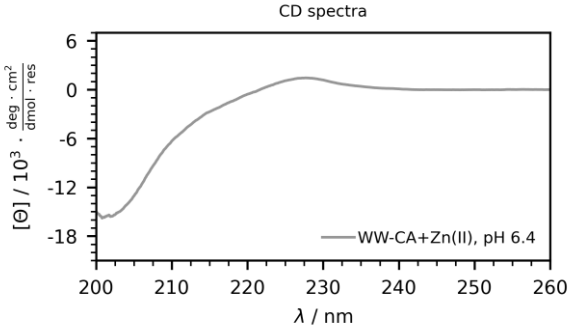
CD spectra
WW-CA+Zn(II), pH 6.4
λ / nm

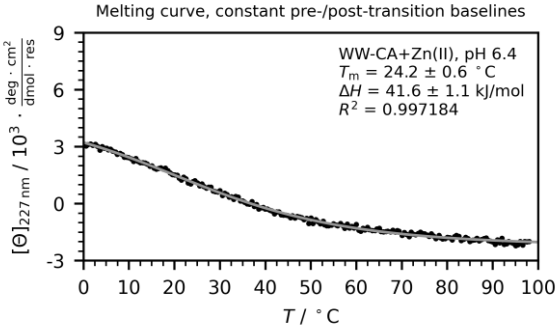
Melting curve, constant pre-/post-transition baselines
WW-CA+Zn(II), pH 6.4
T_m = 24.2 ± 0.6 °C
ΔH = 41.6 ± 1.1 kJ/mol
R^2 = 0.997184
T / °C

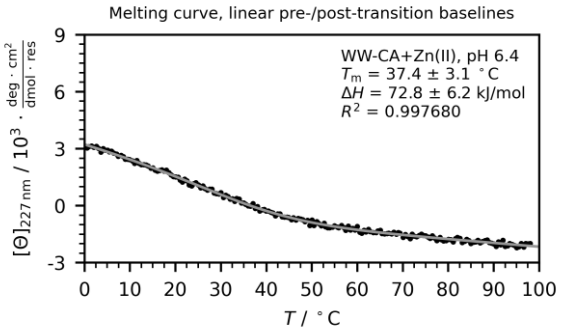
Melting curve, linear pre-/post-transition baselines
WW-CA+Zn(II), pH 6.4
T_m = 37.4 ± 3.1 °C
ΔH = 72.8 ± 6.2 kJ/mol
R^2 = 0.997680
T / °C

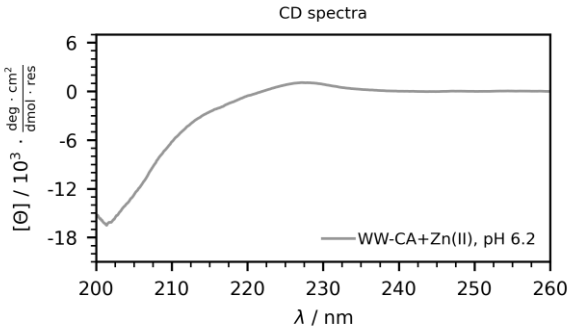

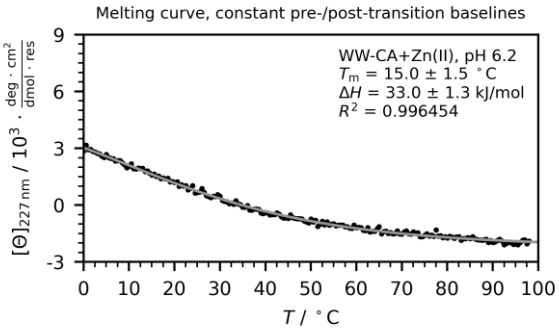

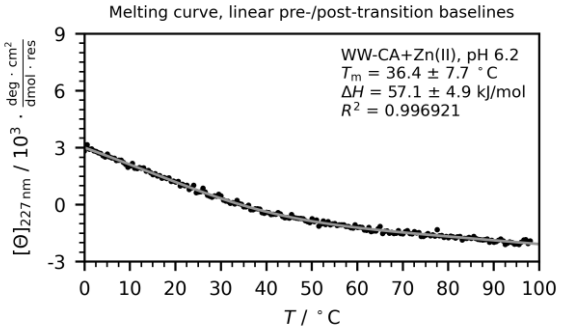

WW-CA + Cu(II) (100 μM peptide + 100 μM metal ions in MOPS buffered saline)

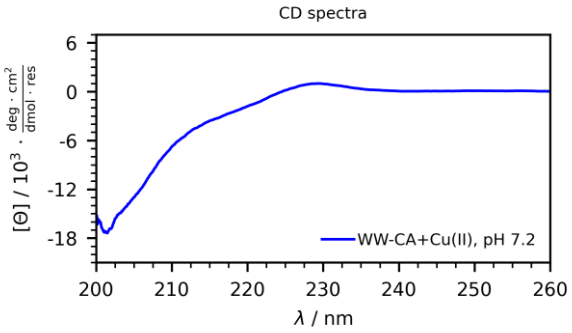

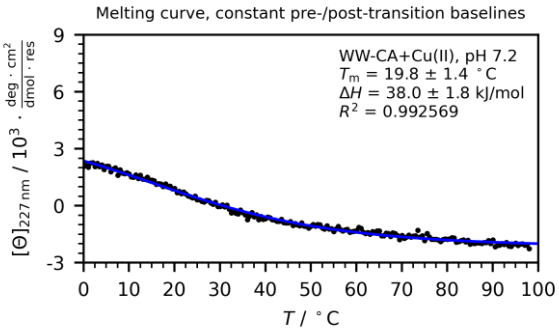

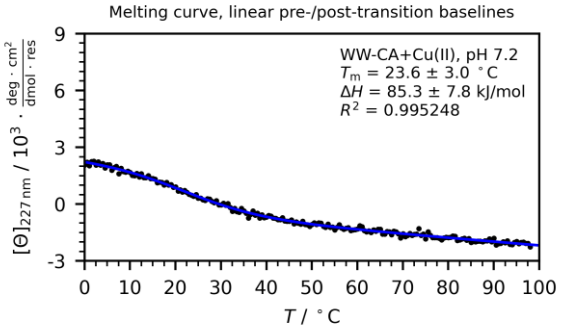

WW-CA + Ni(II) (100 µM peptide + 100 µM metal ions in MOPS buffered saline)

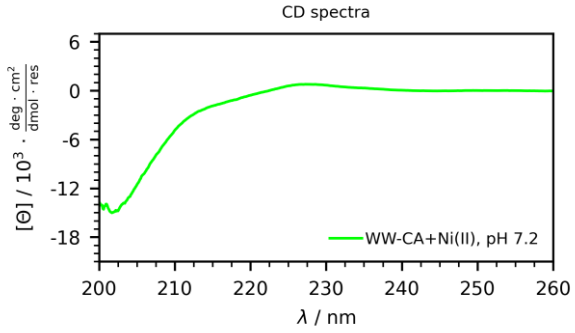

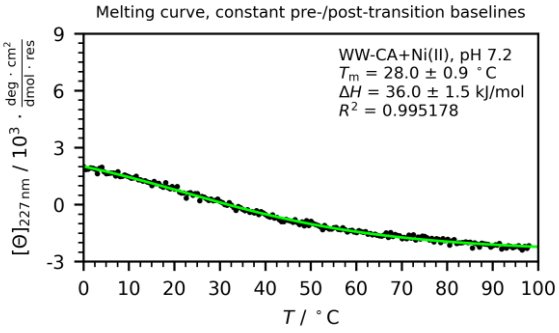

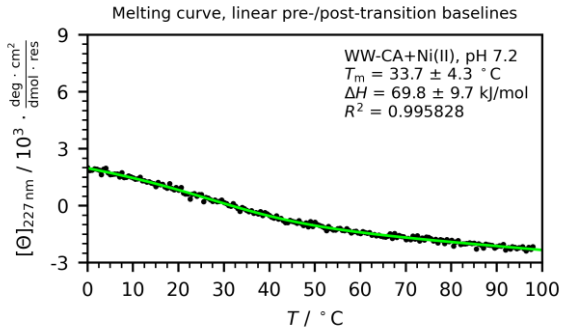

WW-CA-Nle apo (100 µM peptide in MOPS buffered saline)

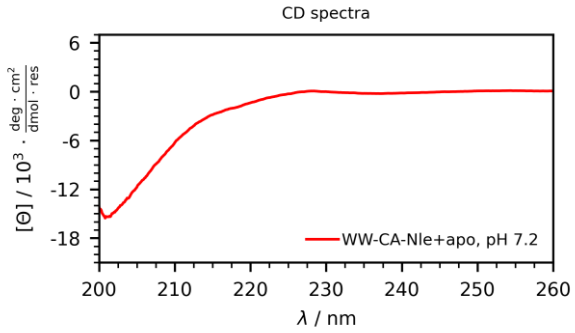

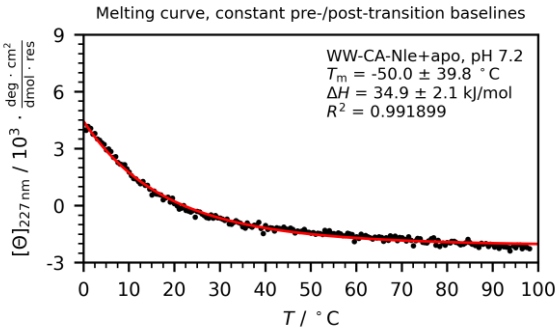

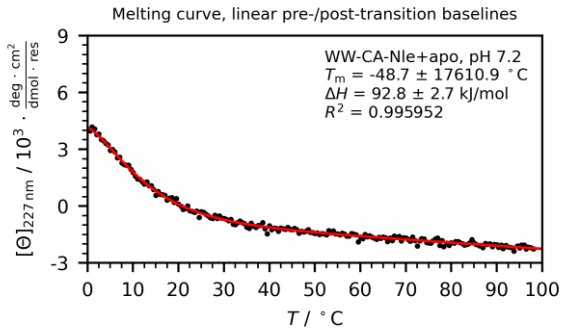

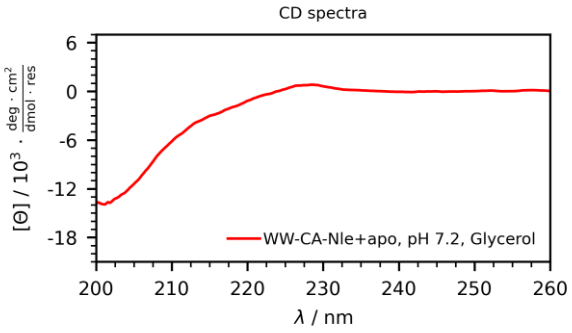

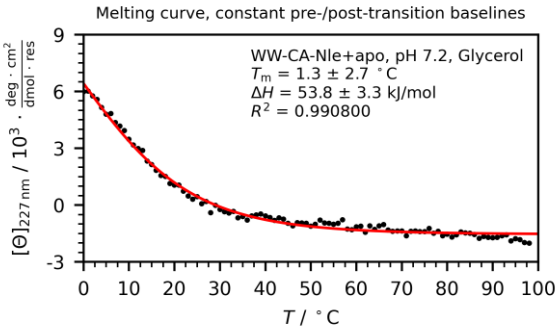

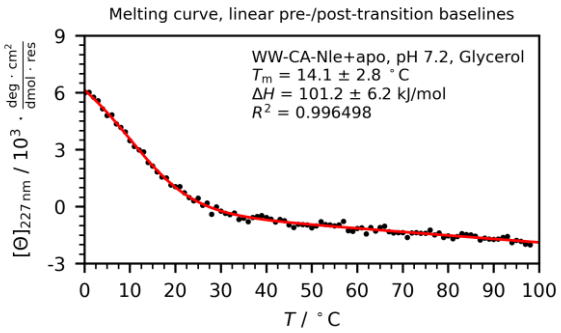

(50 µM peptide in MOPS buffered saline)

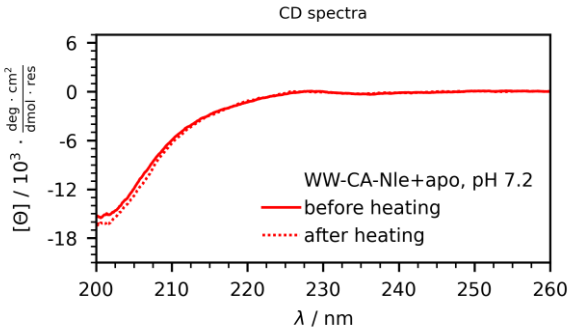

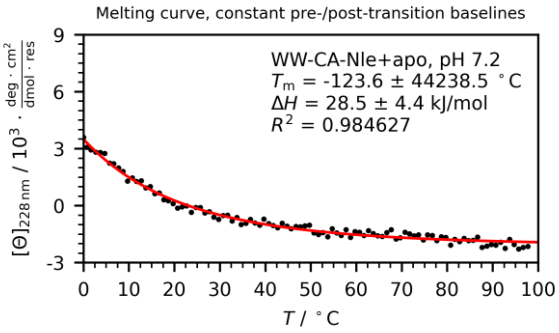

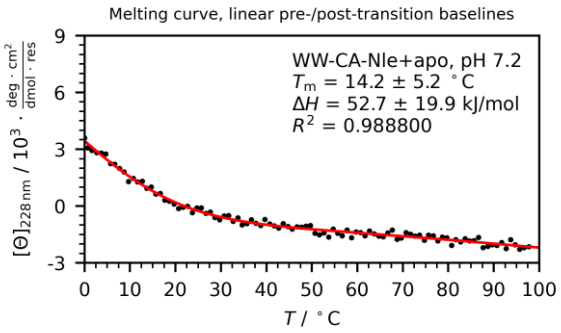

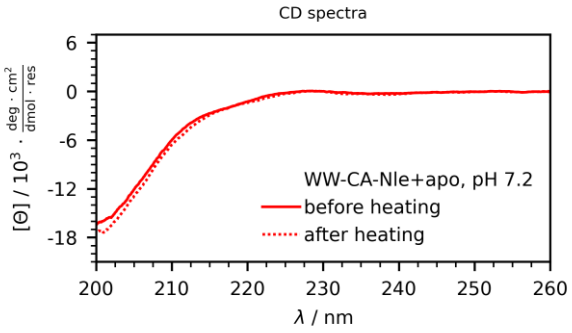

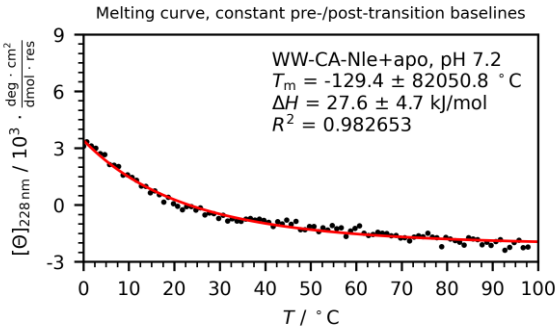

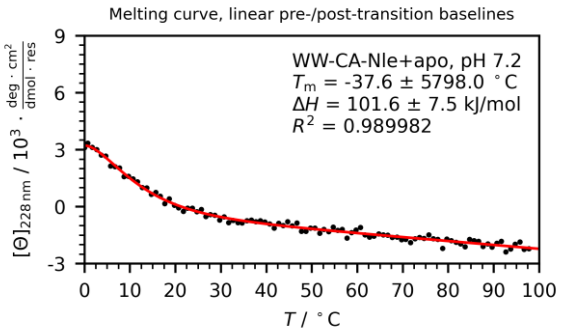

WW-CA-Nle + Zn(II) (100 µM peptide + 100 µM metal ions in MOPS buffered saline)

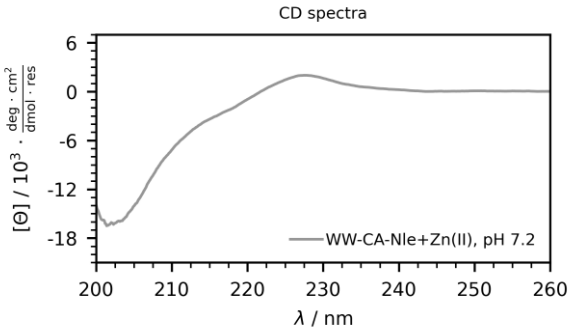

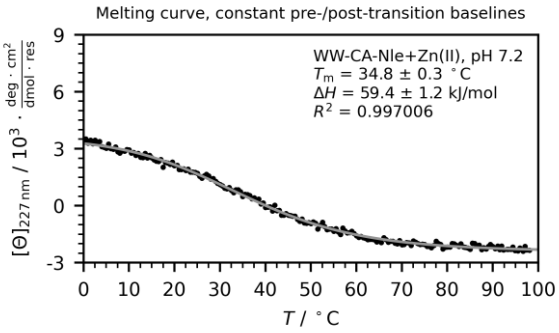

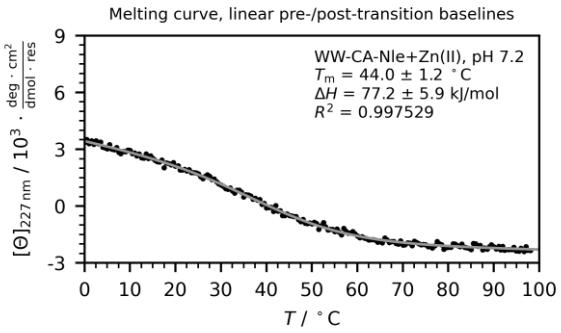

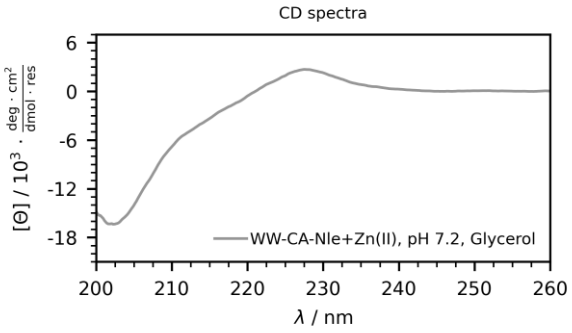

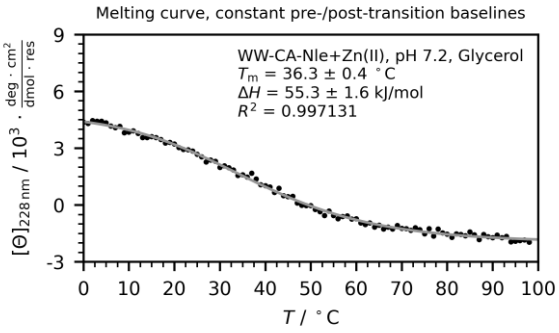

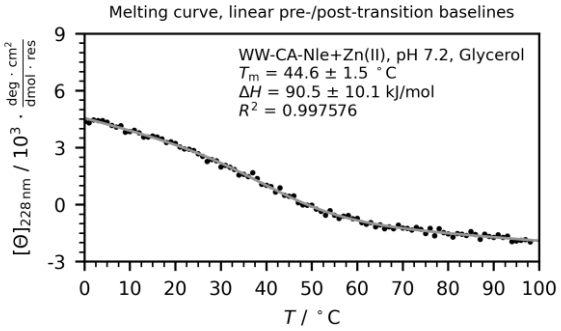

(50 μM peptide + 50 μM metal ions in MOPS buffered saline)

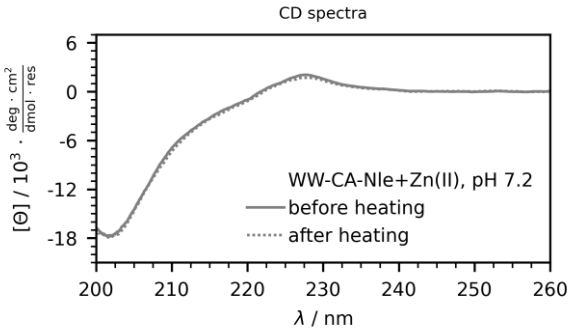

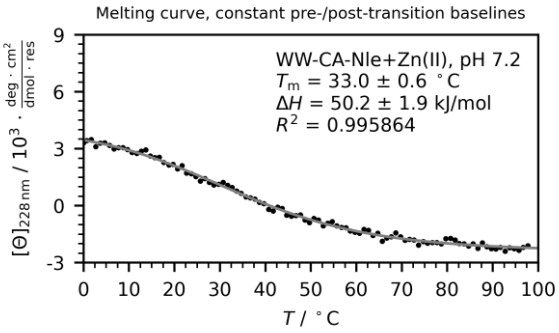

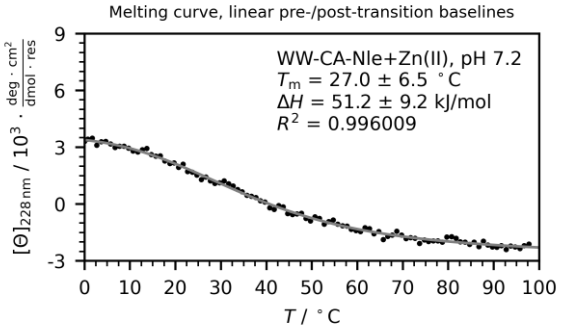

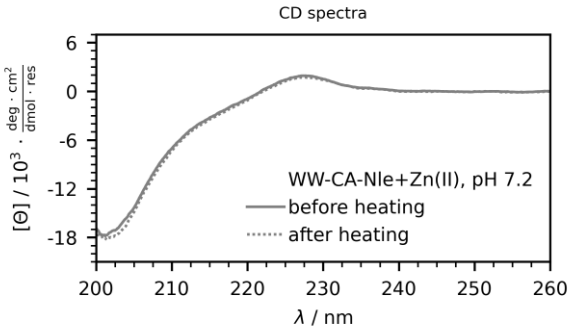

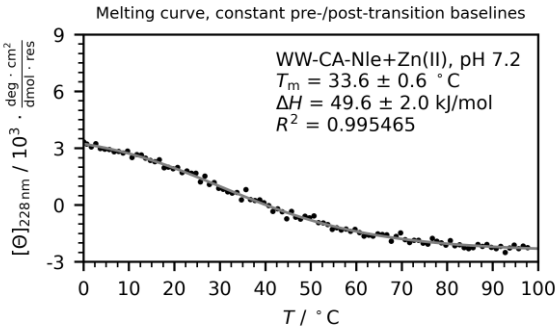

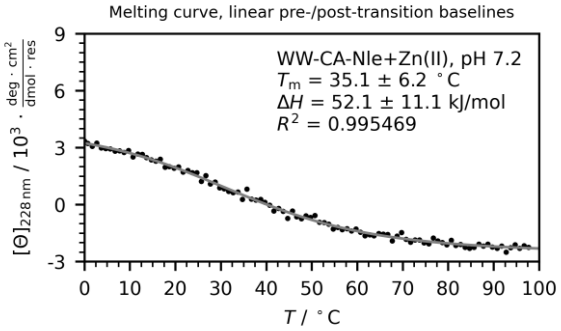

WW-CA-Nle + Cu(II) (50 µM peptide + 50 µM metal ions in MOPS buffered saline)

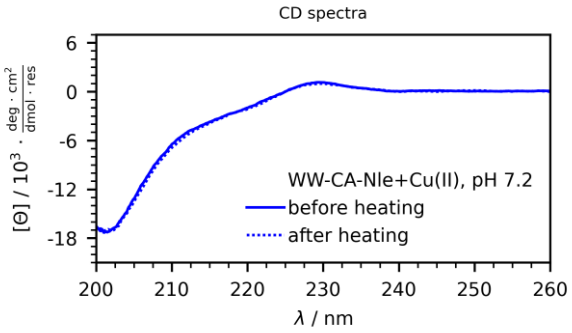

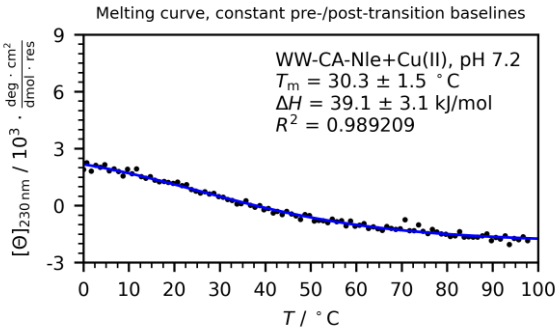

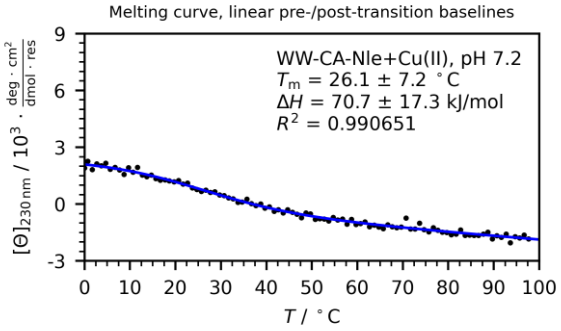

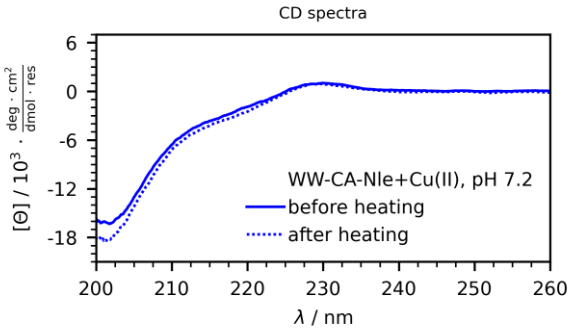

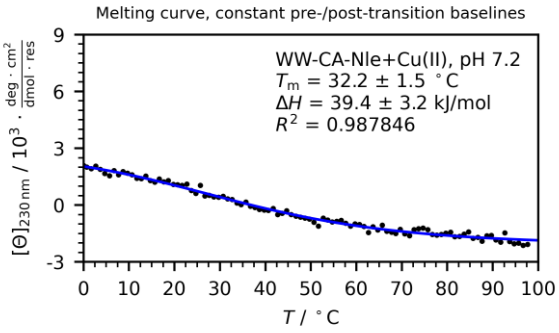

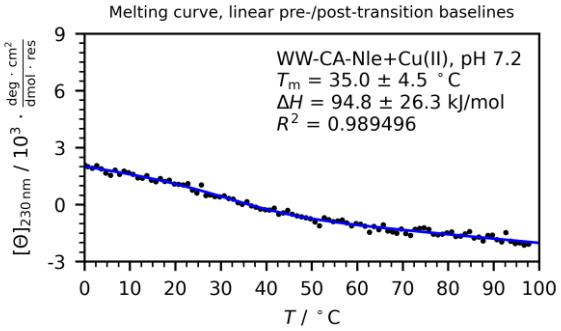

WW-CA-Nle + Ni(II) (50 µM peptide + 50 µM metal ions in MOPS buffered saline)

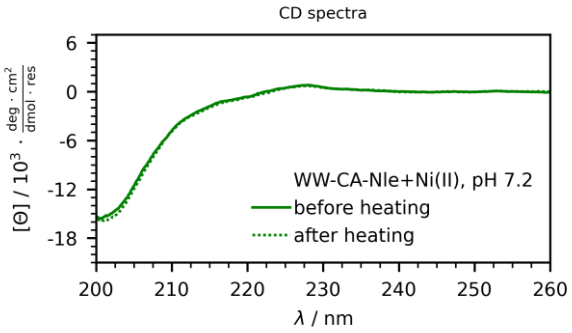

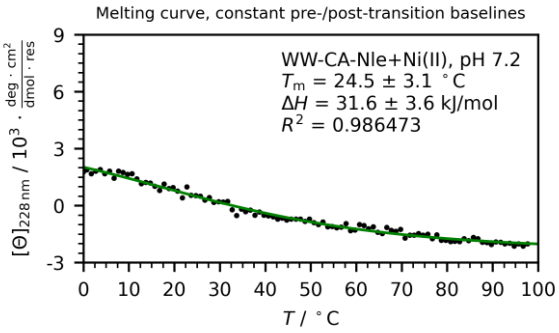

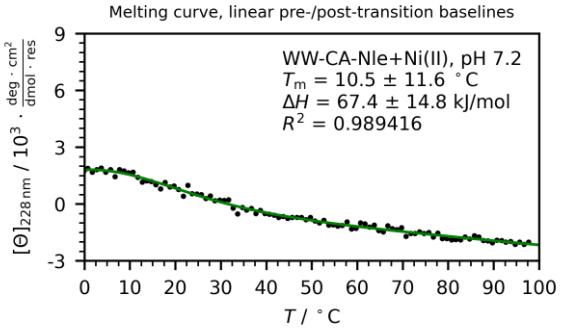

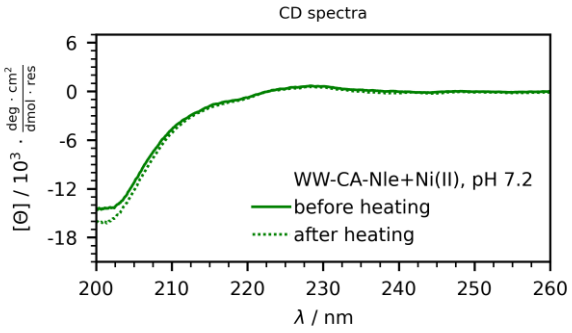

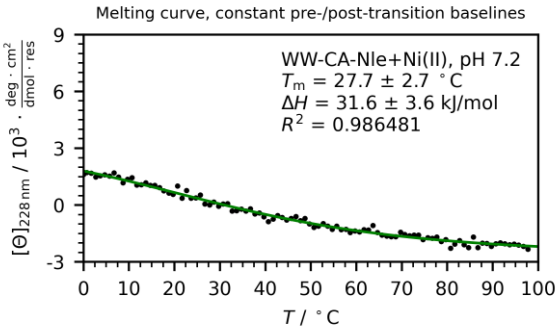

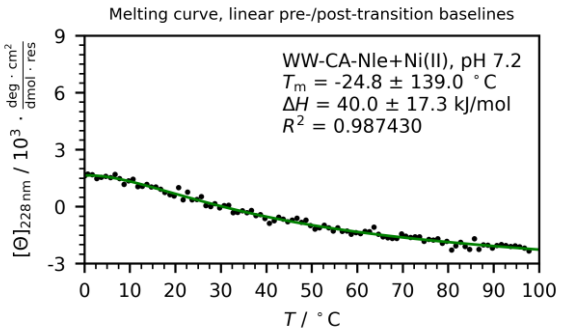

WW-CA-min apo (50 µM peptide in MOPS buffered saline)

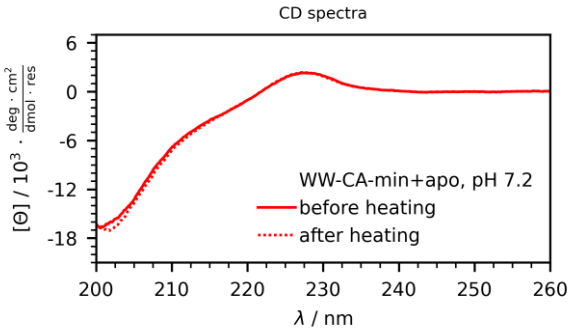

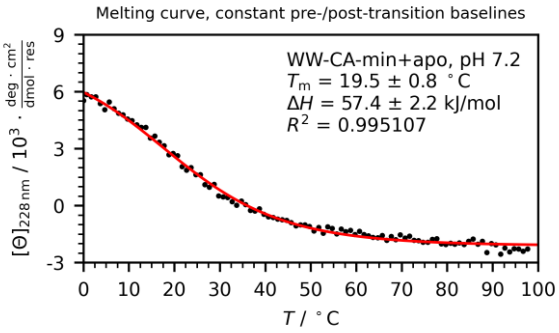

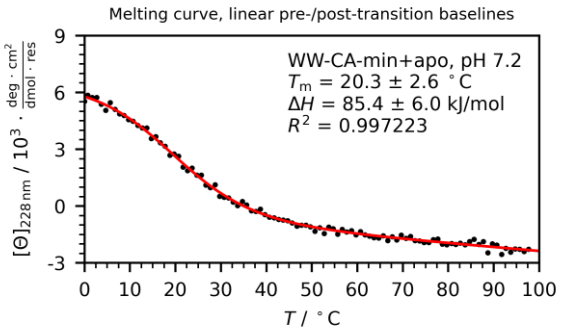

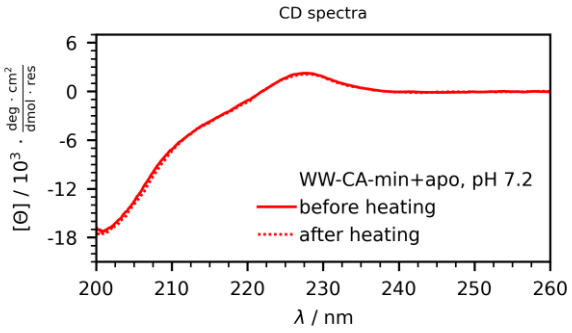

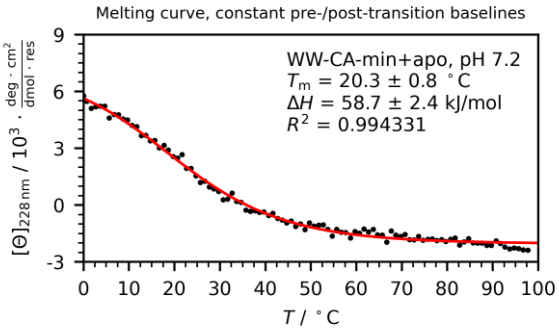

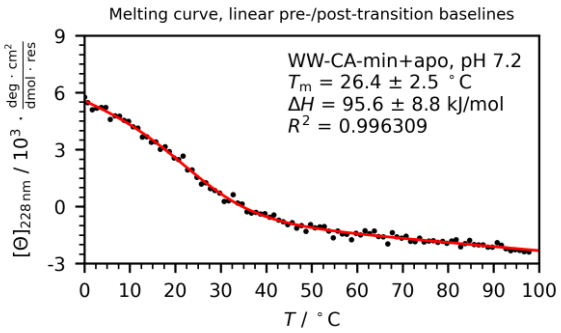

WW-CA-min + Zn(II) (50 µM peptide + 50 µM metal ions in MOPS buffered saline)

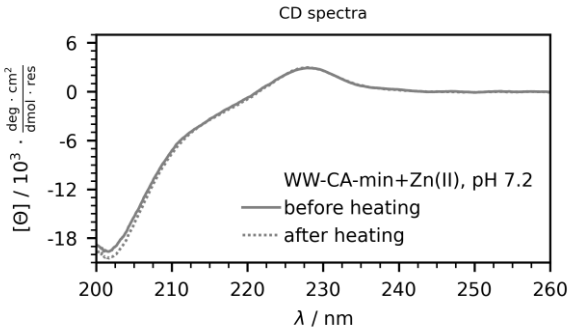

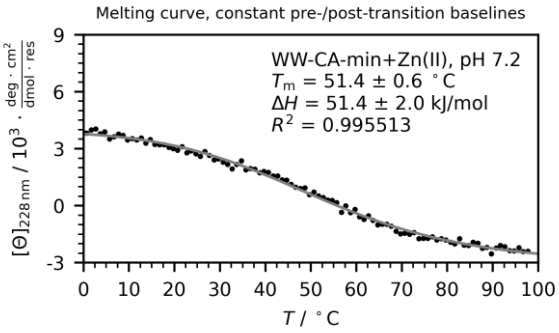

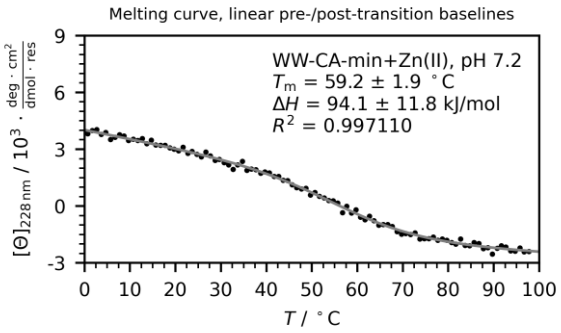

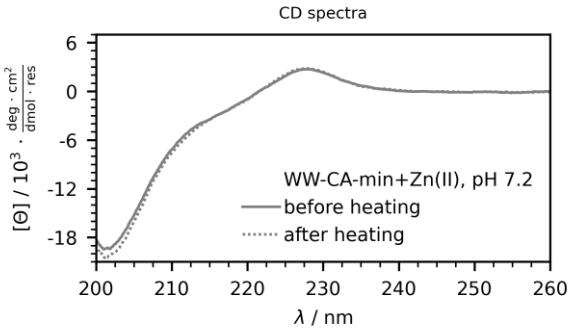

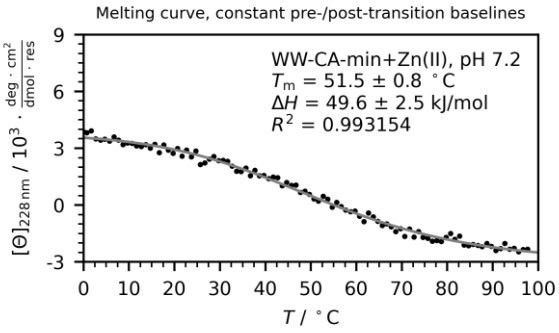

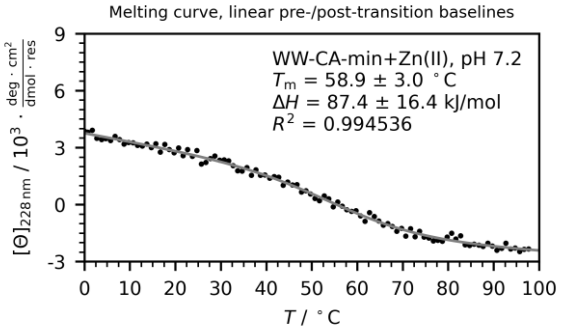

WW-CA-min + Cu(II) (50 µM peptide + 50 µM metal ions in MOPS buffered saline)

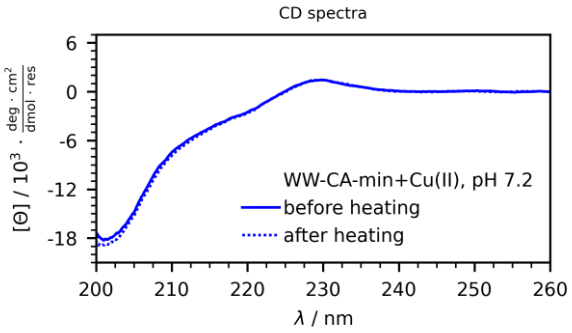

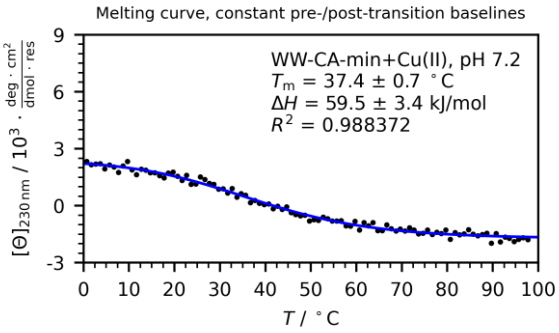

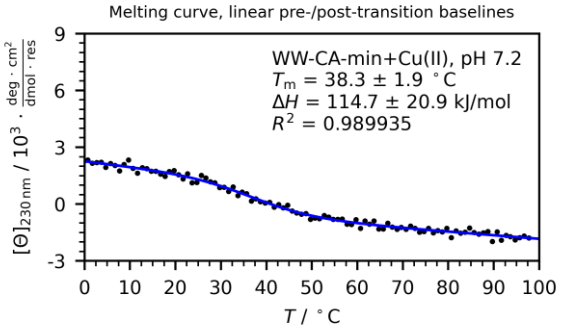

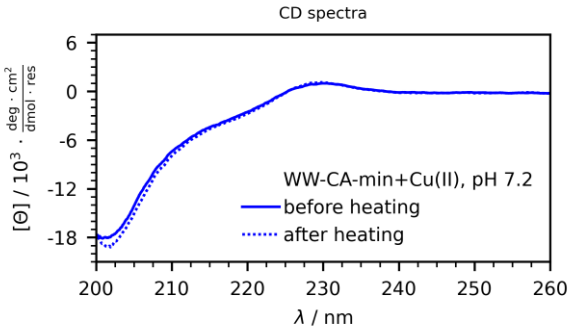

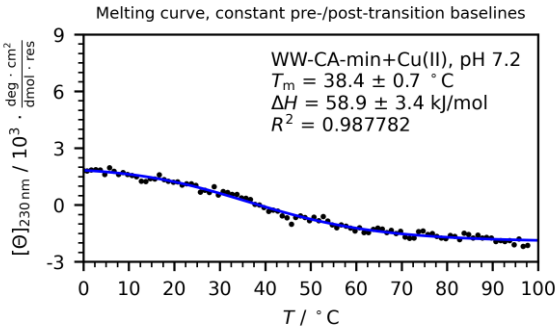

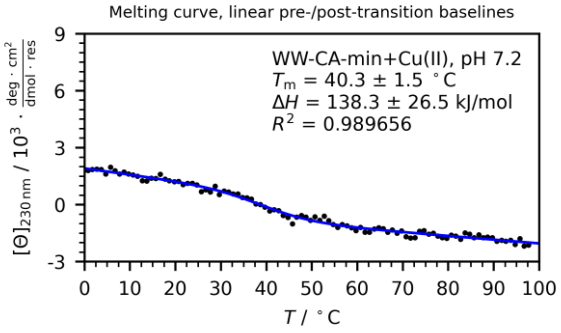

WW-CA-min + Ni(II) (50 μM peptide + 50 μM metal ions in MOPS buffered saline)

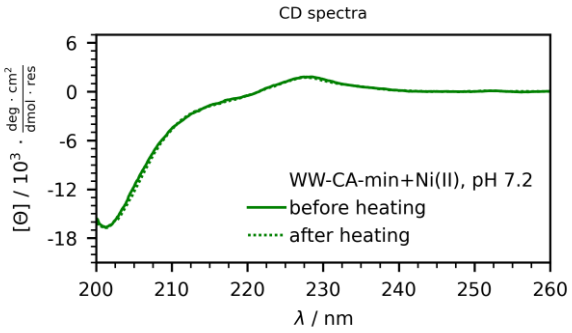

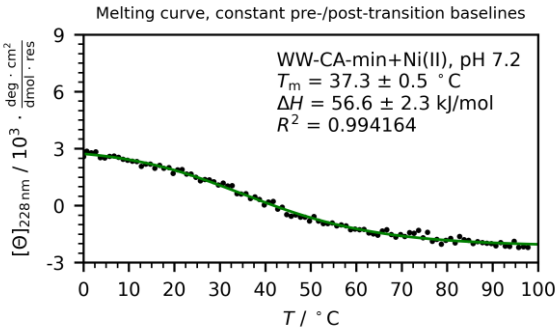

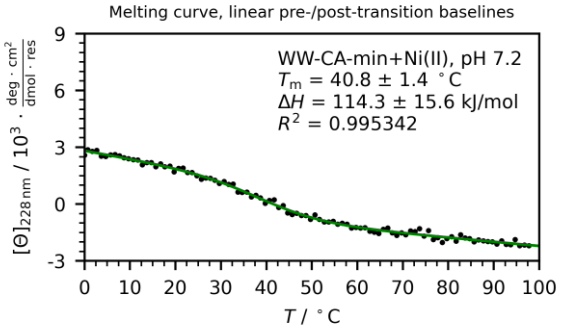

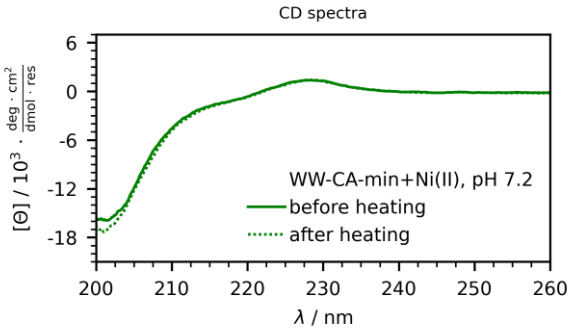

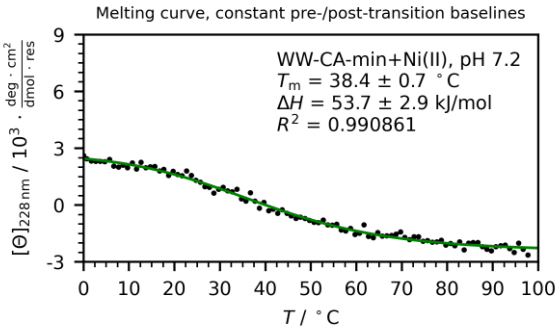

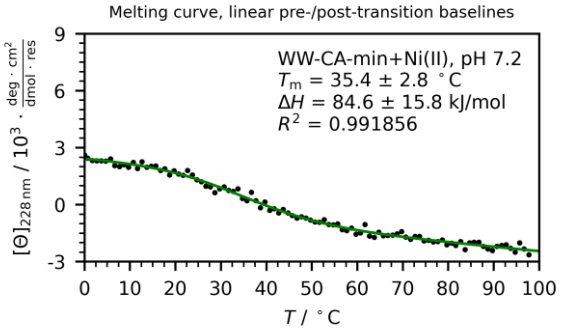

WW-CA-ANG apo (50 µM peptide in MOPS buffered saline)

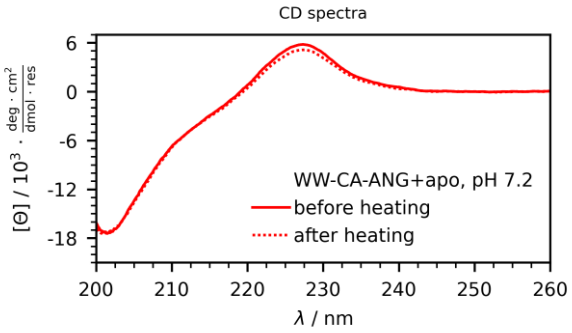

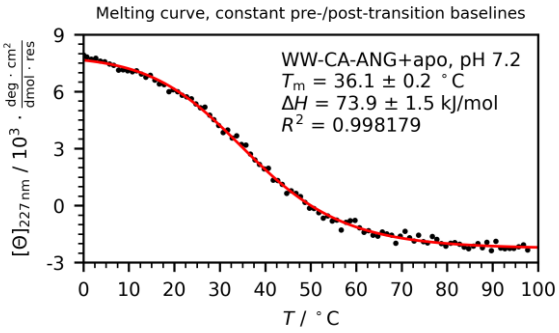

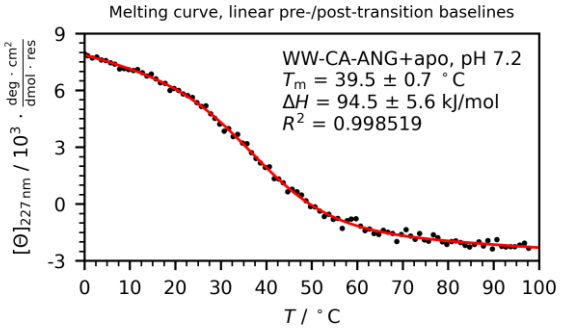

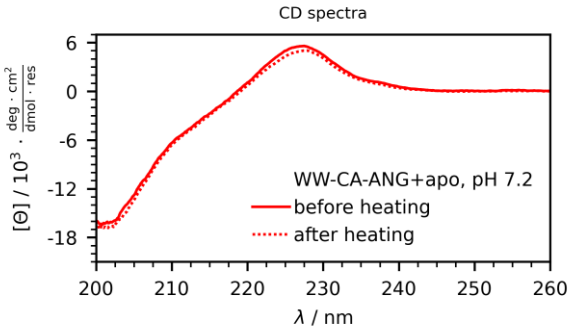

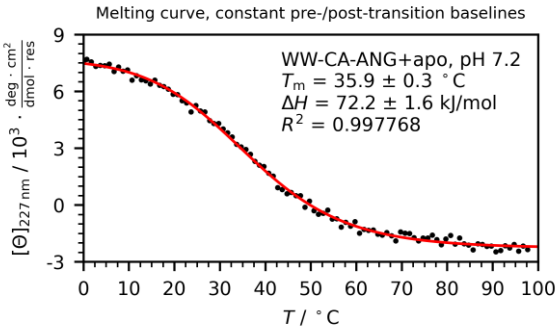

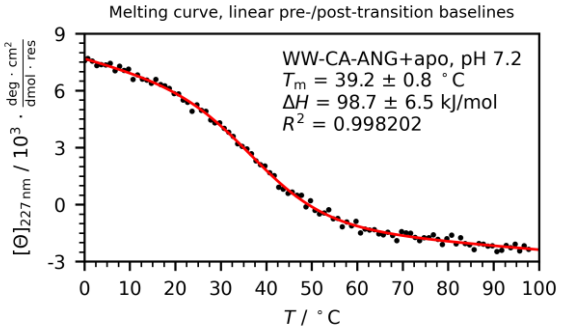

WW-CA-ANG + Zn(II) (50 μM peptide + 50 μM metal ions in MOPS buffered saline)

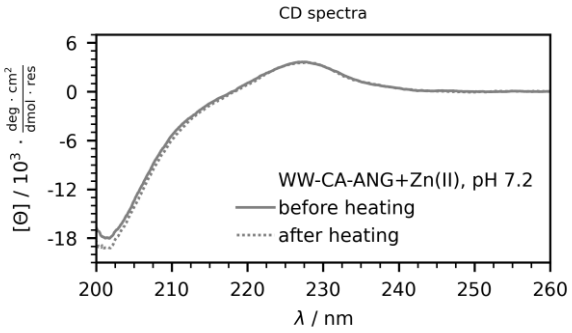

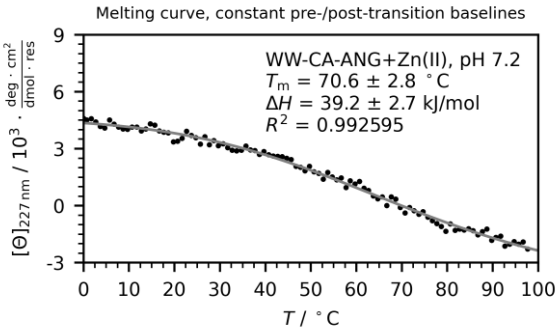

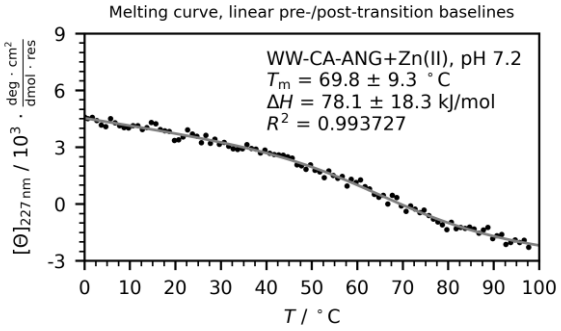

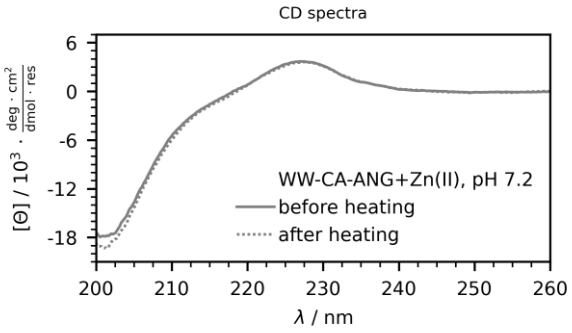

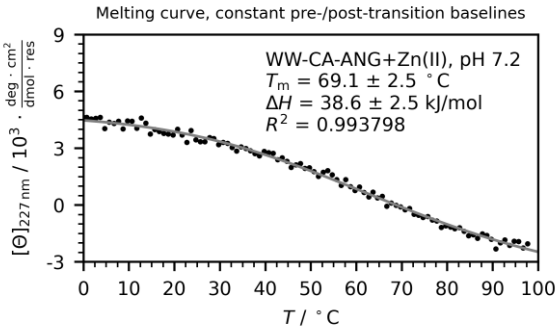

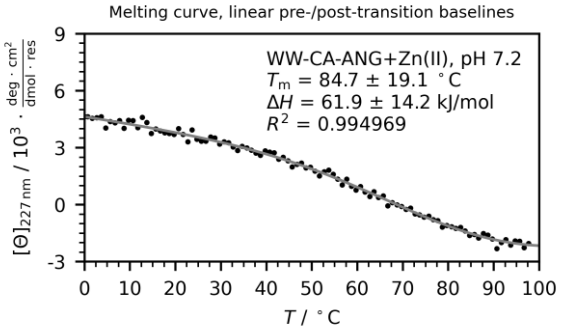

WW-CA-ANG + Cu(II) (50 μM peptide + 50 μM metal ions in MOPS buffered saline)

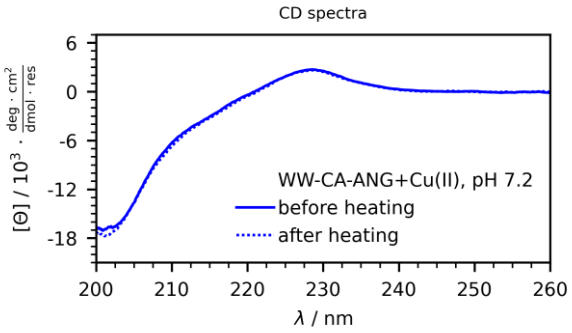

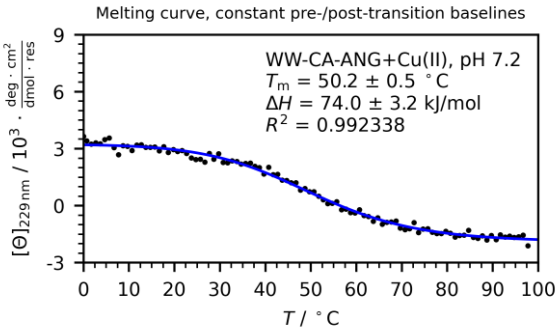

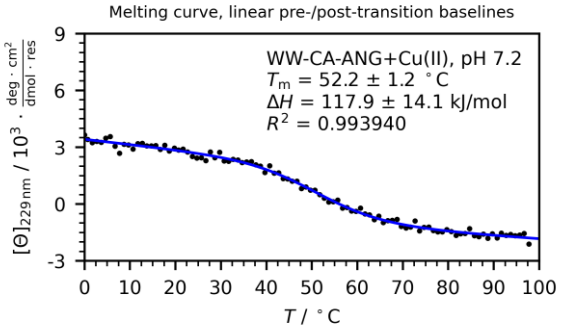

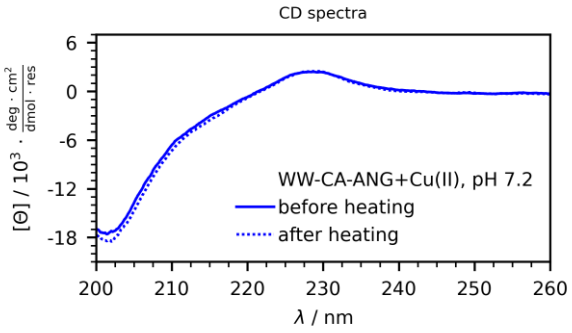

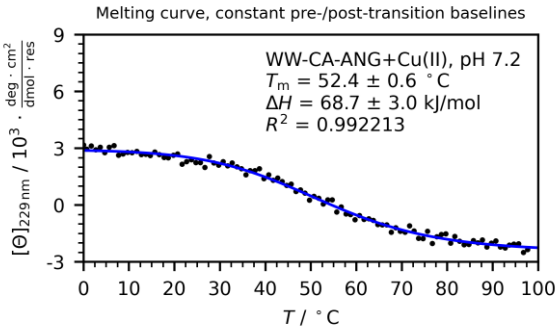

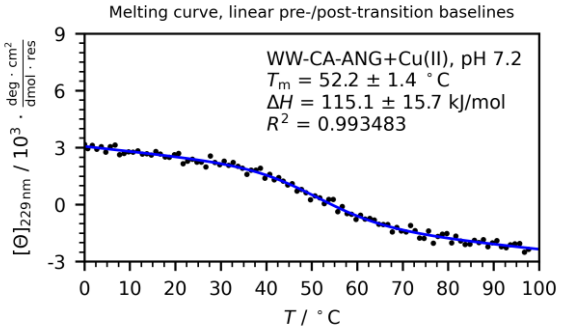

WW-CA-ANG + Ni(II) (50 μM peptide + 50 μM metal ions in MOPS buffered saline)

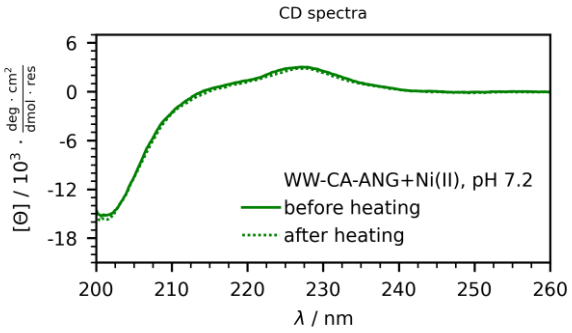

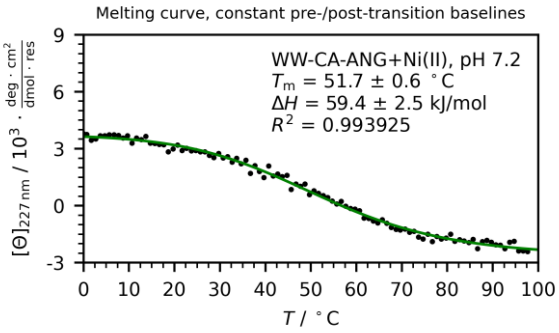

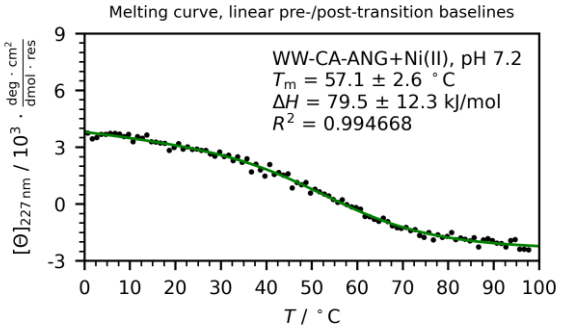

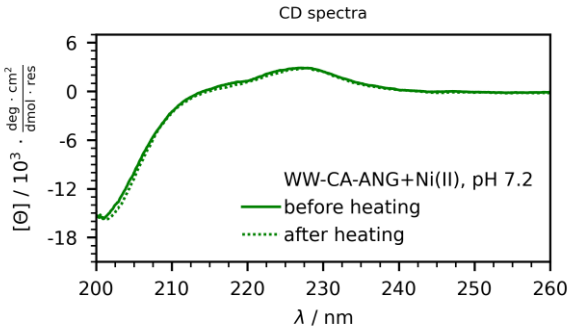

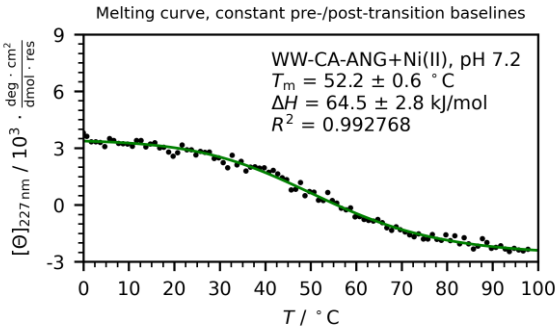

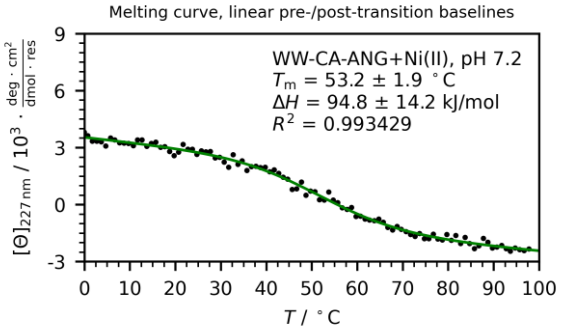

hPin1$_{WW}$-Nle apo (50 µM peptide in MOPS buffered saline)

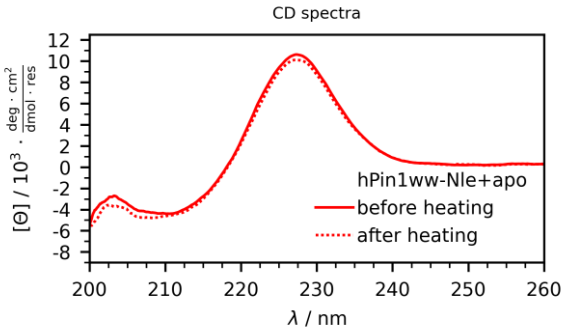

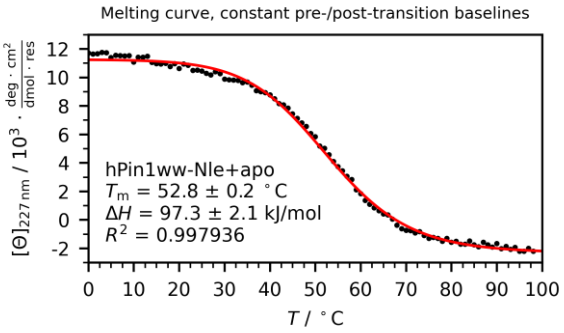

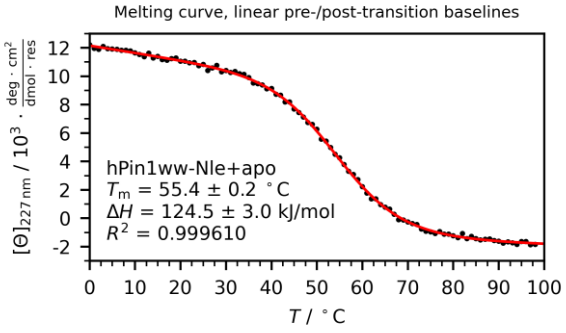

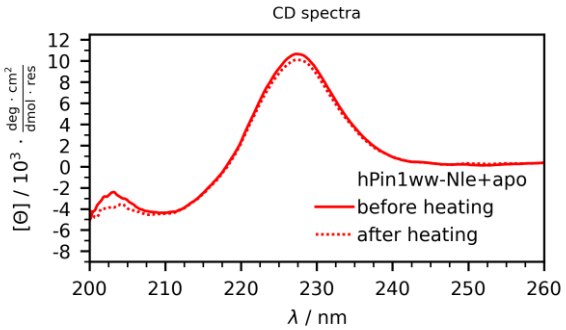

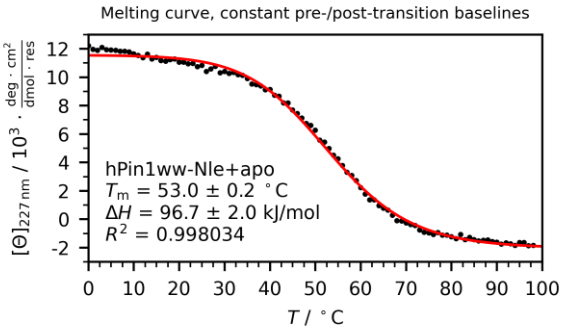

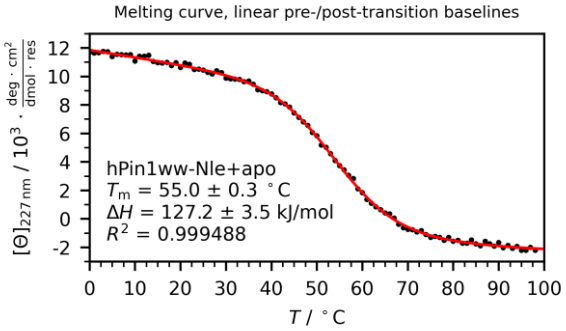

hPin1$_{WW}$-Nle + Zn(II) (50 µM peptide + 50 µM metal ions in MOPS buffered saline)

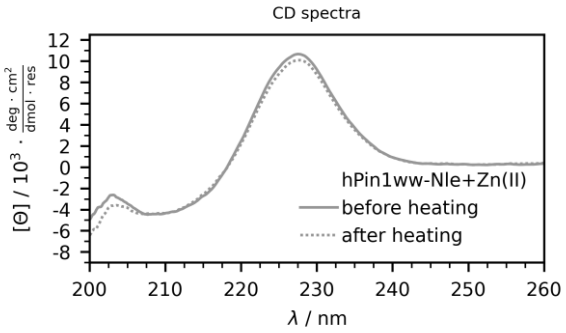

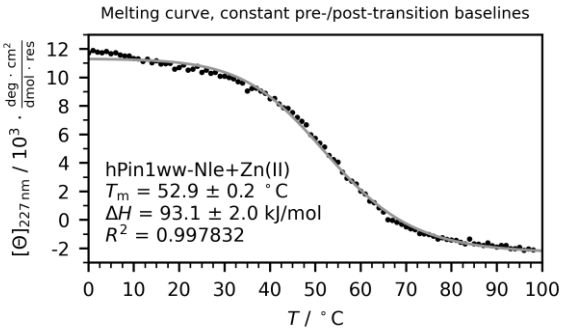

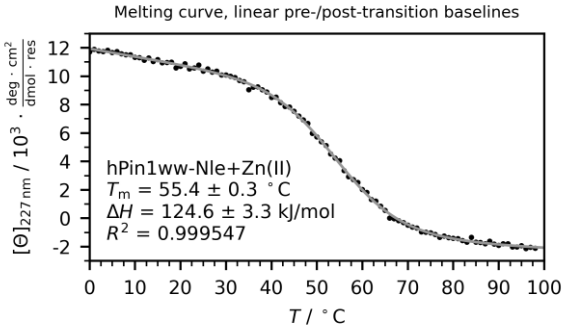

hPin1$_{WW}$-Nle + Cu(II) (50 µM peptide + 50 µM metal ions in MOPS buffered saline)

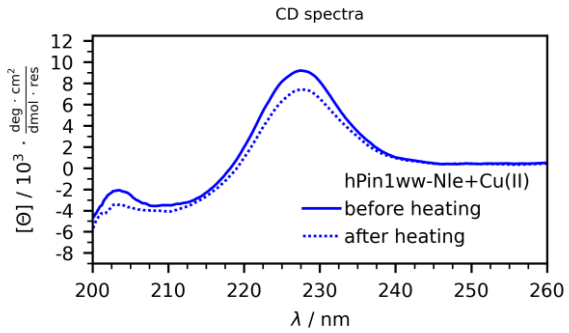

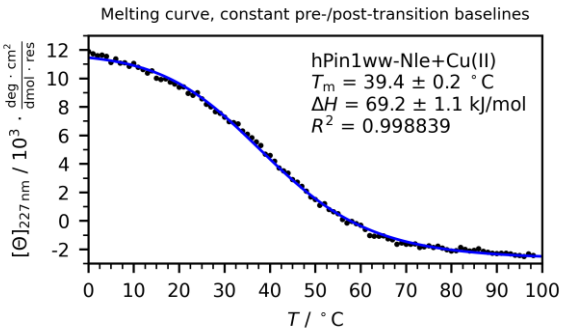

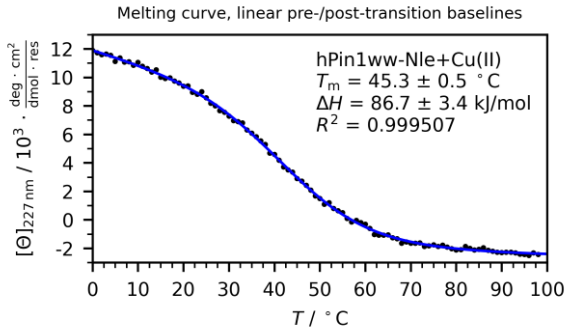

hPin1$_{WW}$-Nle + Ni(II) (50 µM peptide + 50 µM metal ions in MOPS buffered saline)

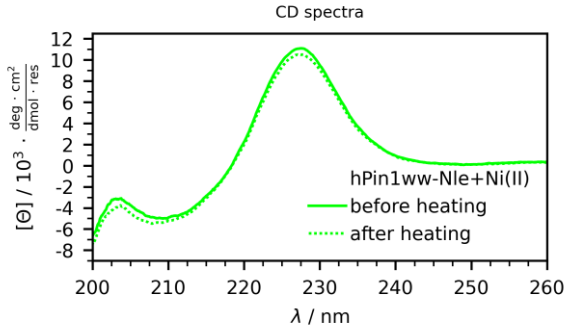

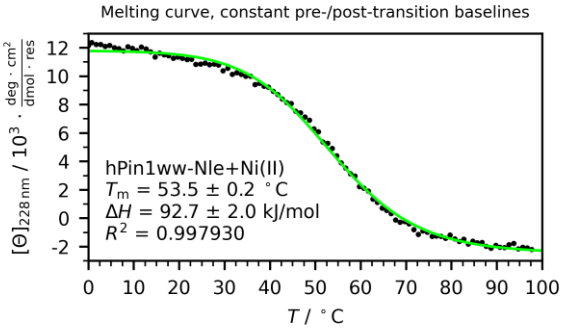

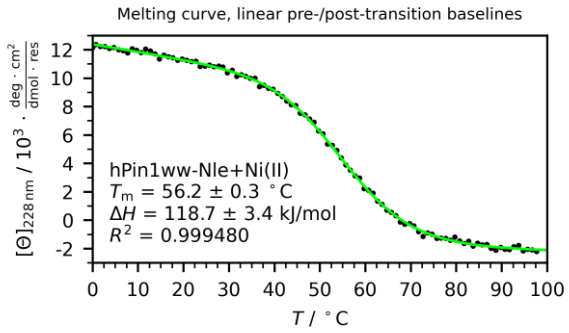

10.8.2 Tryptophan zippers

(The black line in the derivative plot is the smoothed data (moving average, window size: 9) to guide the eye)

Tripzip2 (50 µM peptide + 50 µM metal ions (if present) in MOPS/hydrogen sulfate buffered saline)

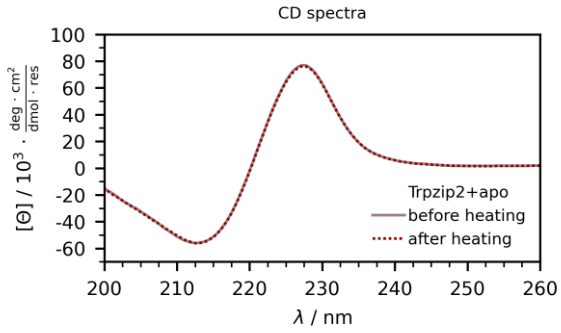

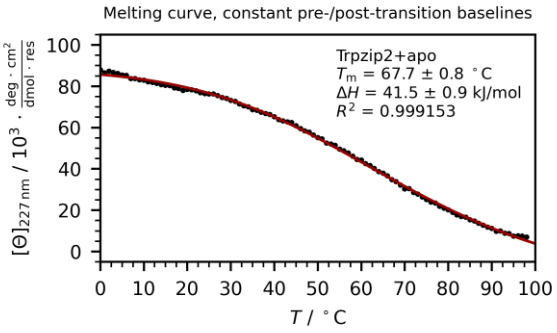

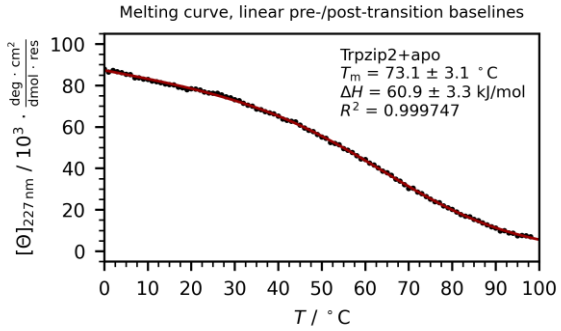

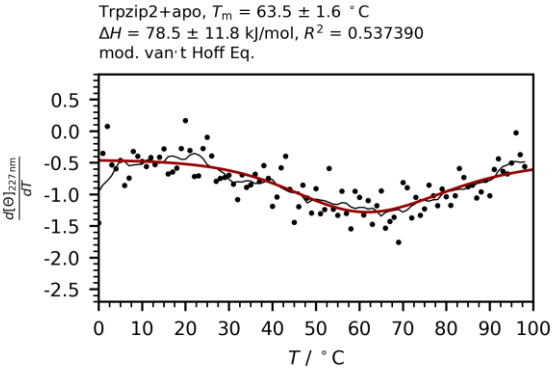

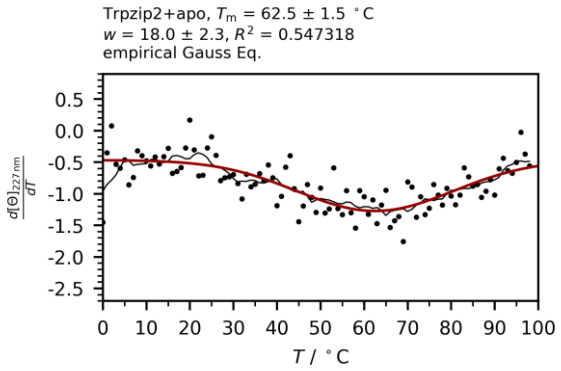

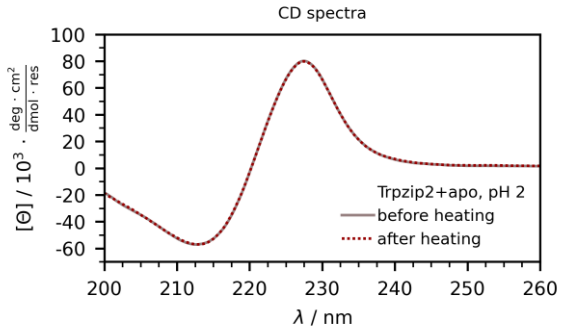
CD spectra
Trpzip2+apo, pH 2
before heating
after heating
λ / nm

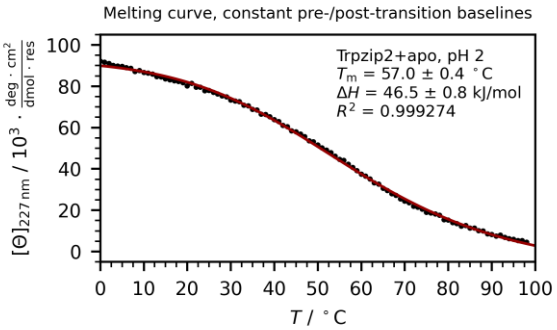
Melting curve, constant pre-/post-transition baselines
Trpzip2+apo, pH 2
T_m = 57.0 ± 0.4 °C
ΔH = 46.5 ± 0.8 kJ/mol
R^2 = 0.999274
T / °C

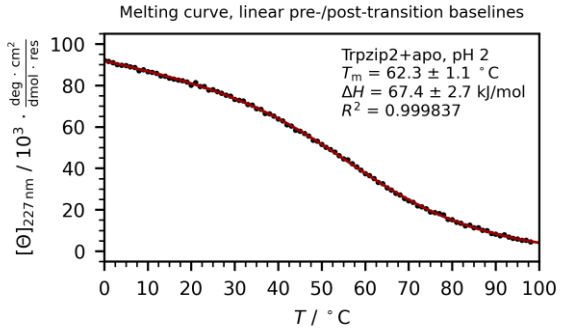
Melting curve, linear pre-/post-transition baselines
Trpzip2+apo, pH 2
T_m = 62.3 ± 1.1 °C
ΔH = 67.4 ± 2.7 kJ/mol
R^2 = 0.999837
T / °C

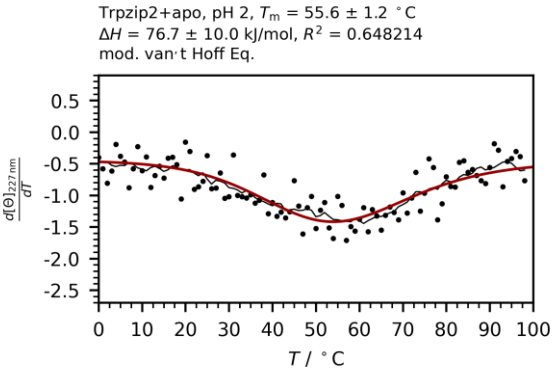
Trpzip2+apo, pH 2, T_m = 55.6 ± 1.2 °C
ΔH = 76.7 ± 10.0 kJ/mol, R^2 = 0.648214
mod. van't Hoff Eq.
T / °C

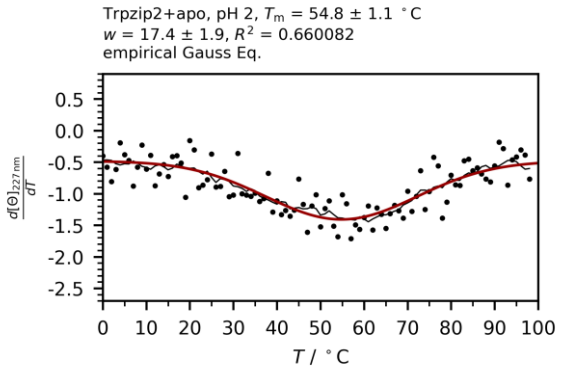
Trpzip2+apo, pH 2, T_m = 54.8 ± 1.1 °C
w = 17.4 ± 1.9, R^2 = 0.660082
empirical Gauss Eq.
T / °C

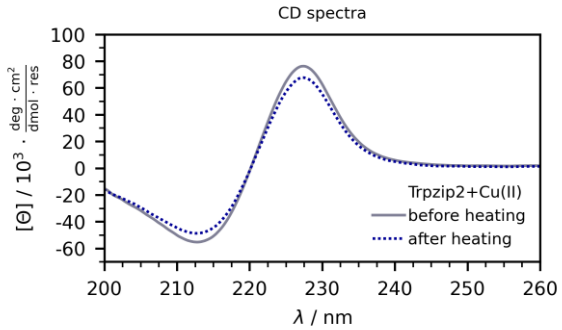
CD spectra
Trpzip2+Cu(II)
before heating
after heating
λ / nm

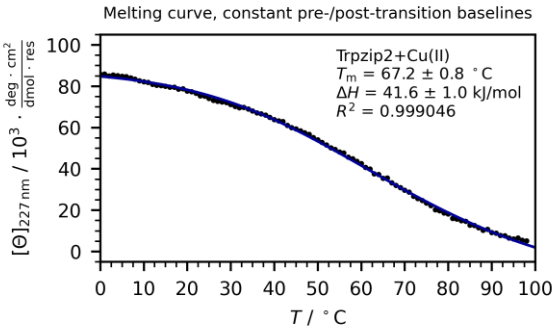
Melting curve, constant pre-/post-transition baselines
Trpzip2+Cu(II)
T_m = 67.2 ± 0.8 °C
ΔH = 41.6 ± 1.0 kJ/mol
R^2 = 0.999046
T / °C

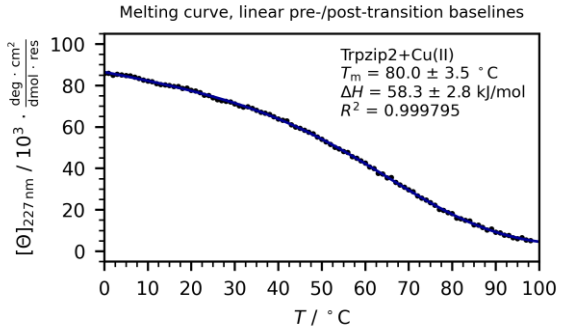
Melting curve, linear pre-/post-transition baselines
Trpzip2+Cu(II)
T_m = 80.0 ± 3.5 °C
ΔH = 58.3 ± 2.8 kJ/mol
R^2 = 0.999795
T / °C

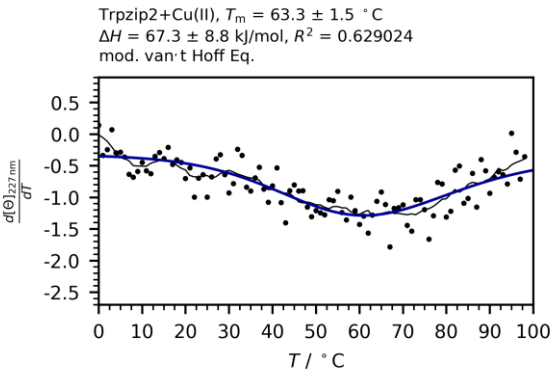
Trpzip2+Cu(II), T_m = 63.3 ± 1.5 °C
ΔH = 67.3 ± 8.8 kJ/mol, R^2 = 0.629024
mod. van't Hoff Eq.
T / °C

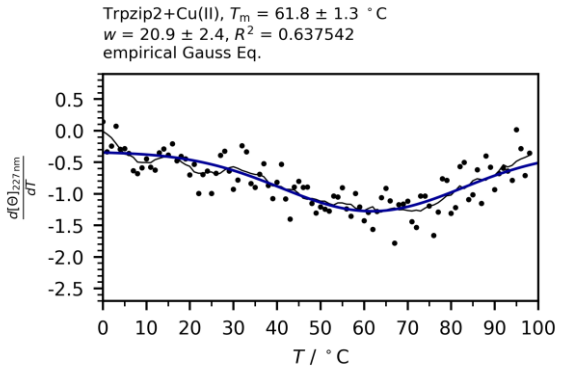
Trpzip2+Cu(II), T_m = 61.8 ± 1.3 °C
w = 20.9 ± 2.4, R^2 = 0.637542
empirical Gauss Eq.
T / °C

Tz2H$_3$ apo (50 µM peptide in MOPS buffered saline)

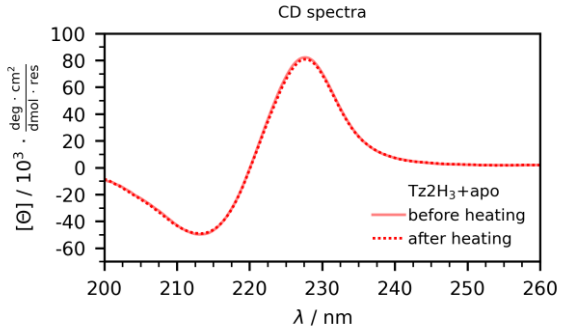

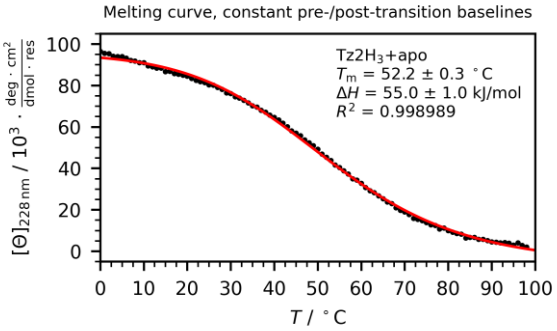

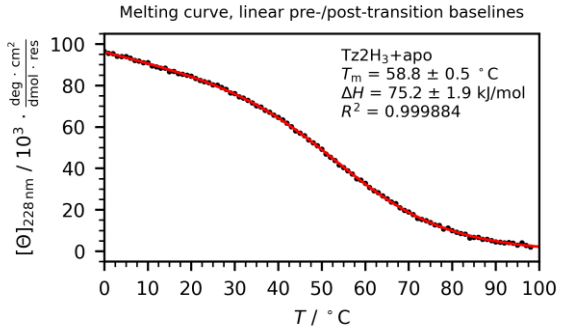

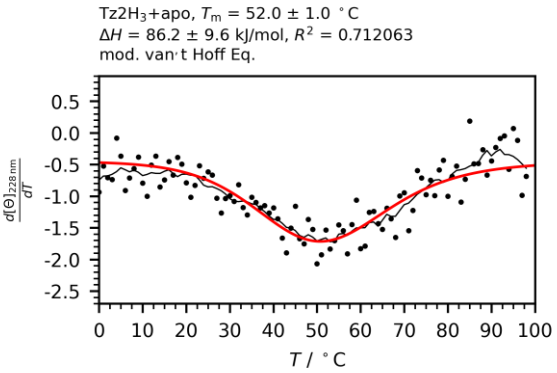

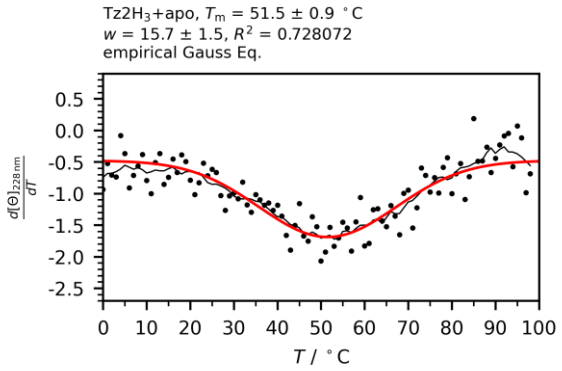

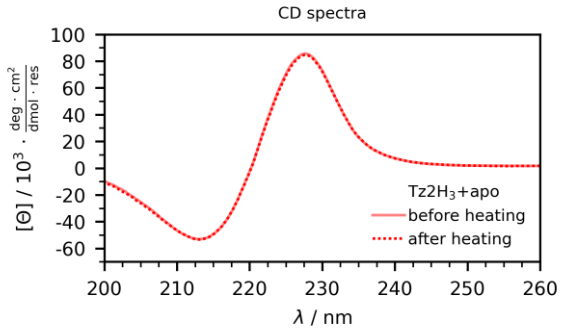
CD spectra
Tz2H3+apo
before heating
after heating
λ / nm

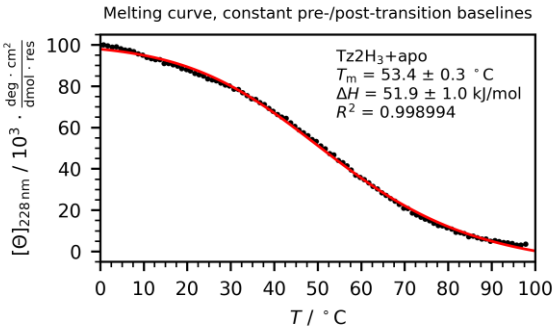
Melting curve, constant pre-/post-transition baselines
Tz2H3+apo
Tm = 53.4 ± 0.3 °C
ΔH = 51.9 ± 1.0 kJ/mol
R2 = 0.998994
T / °C

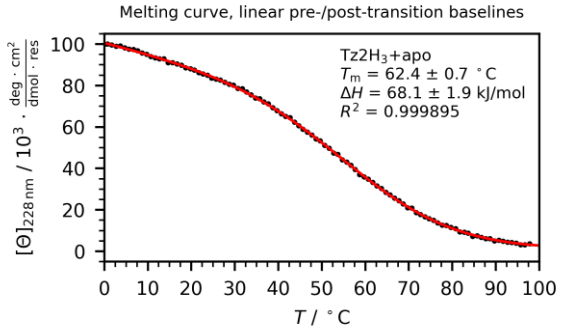
Melting curve, linear pre-/post-transition baselines
Tz2H3+apo
Tm = 62.4 ± 0.7 °C
ΔH = 68.1 ± 1.9 kJ/mol
R2 = 0.999895
T / °C

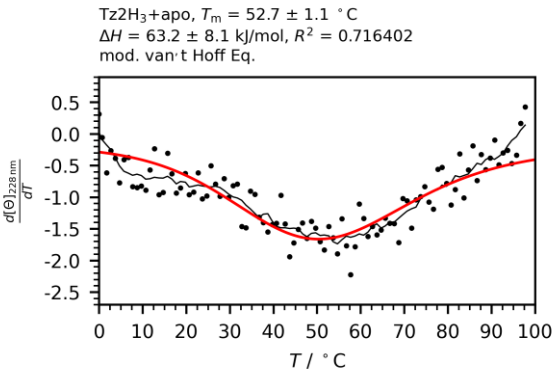
Tz2H3+apo, Tm = 52.7 ± 1.1 °C
ΔH = 63.2 ± 8.1 kJ/mol, R2 = 0.716402
mod. van't Hoff Eq.
T / °C

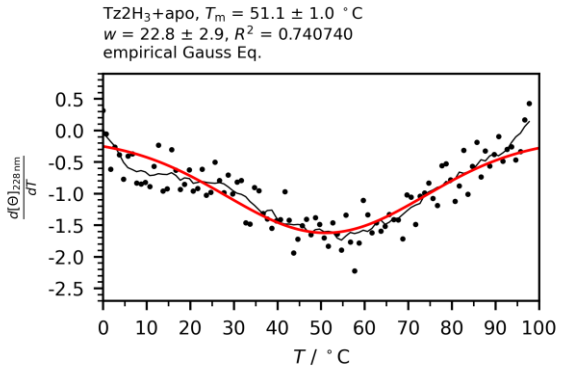
Tz2H3+apo, Tm = 51.1 ± 1.0 °C
w = 22.8 ± 2.9, R2 = 0.740740
empirical Gauss Eq.
T / °C

Tz2H$_3$ + Zn(II) (50 µM peptide in hydrogen sulfate buffered saline)

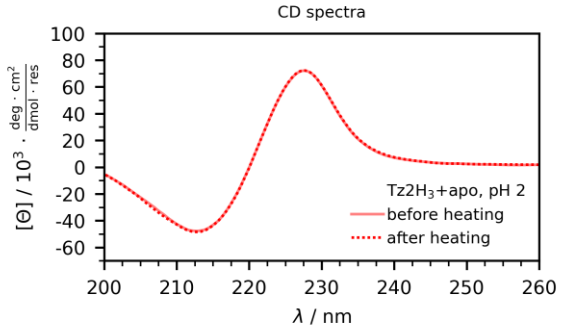

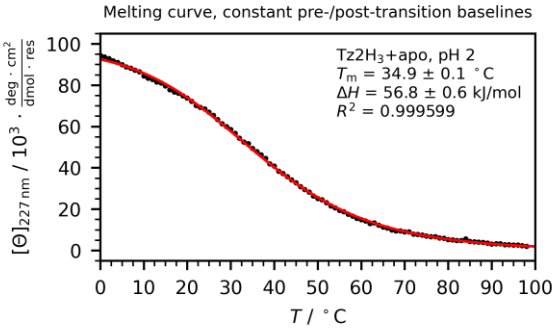

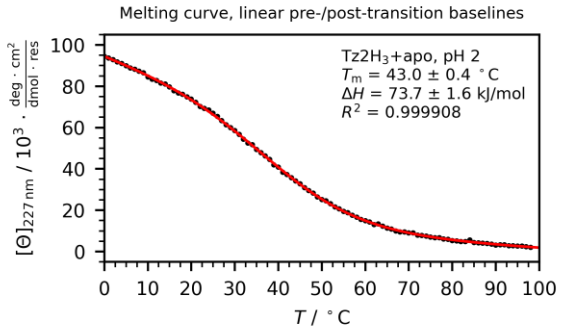

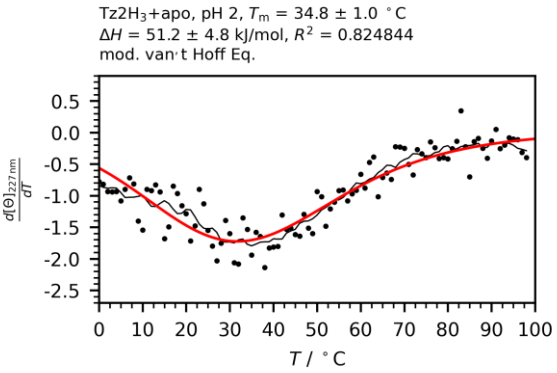

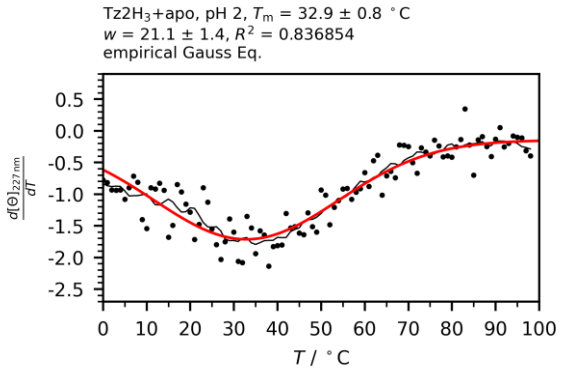

Tz2H$_3$ + Zn(II) (50 µM peptide + 50 µM metal ions in MOPS buffered saline)

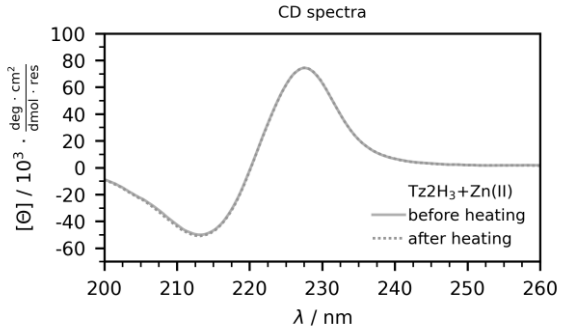

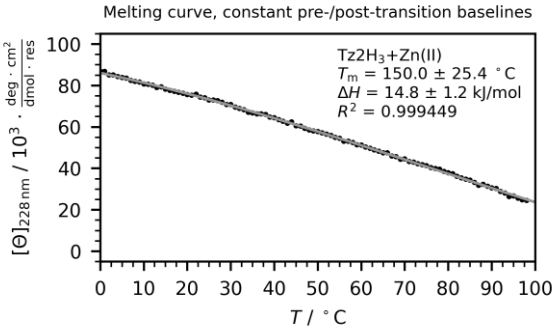

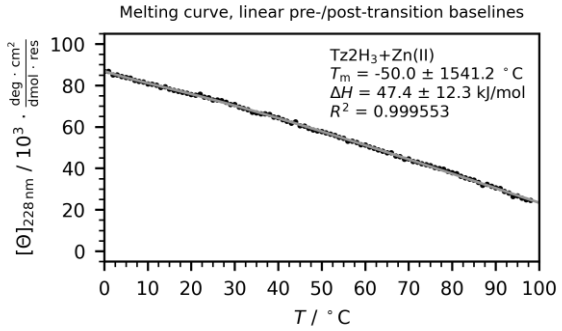

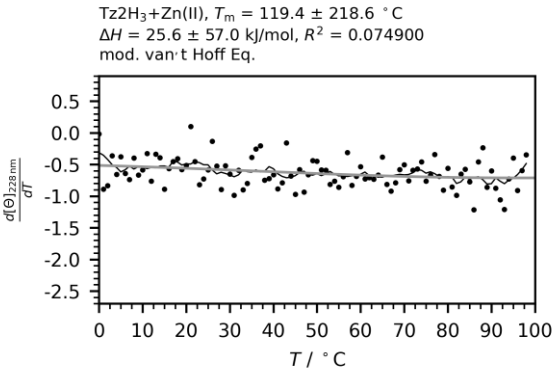

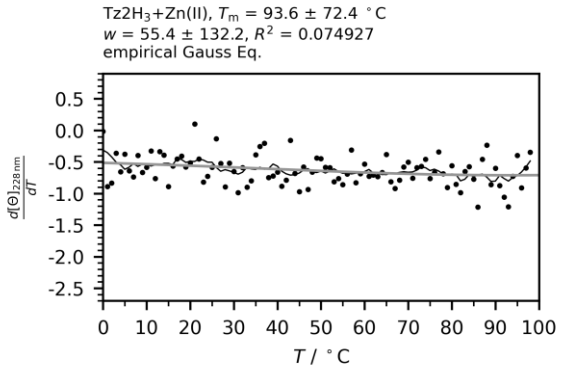

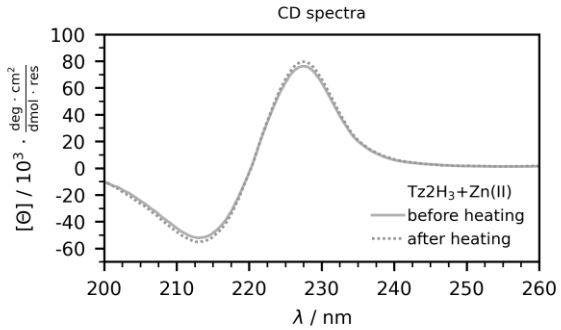
CD spectra
Tz2H3+Zn(II)
before heating
after heating
λ / nm

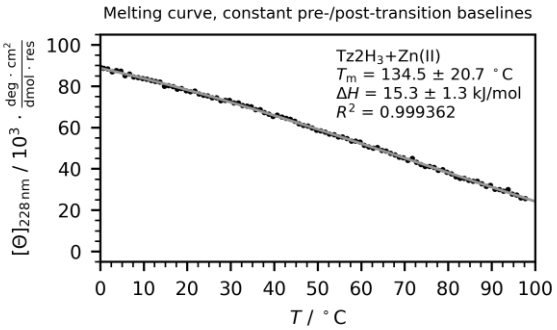
Melting curve, constant pre-/post-transition baselines
Tz2H3+Zn(II)
Tm = 134.5 ± 20.7 °C
ΔH = 15.3 ± 1.3 kJ/mol
R2 = 0.999362
T / °C

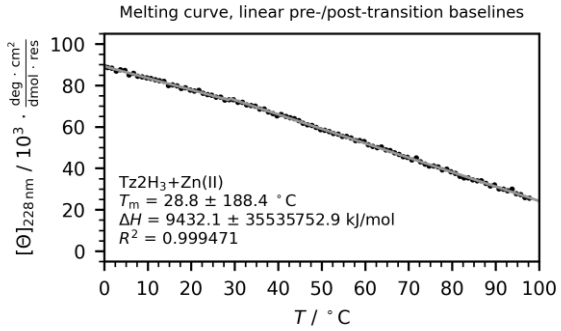
Melting curve, linear pre-/post-transition baselines
Tz2H3+Zn(II)
Tm = 28.8 ± 188.4 °C
ΔH = 9432.1 ± 35535752.9 kJ/mol
R2 = 0.999471
T / °C

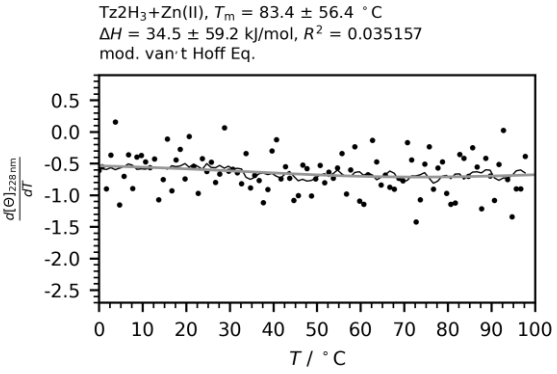
Tz2H3+Zn(II), Tm = 83.4 ± 56.4 °C
ΔH = 34.5 ± 59.2 kJ/mol, R2 = 0.035157
mod. van't Hoff Eq.
T / °C

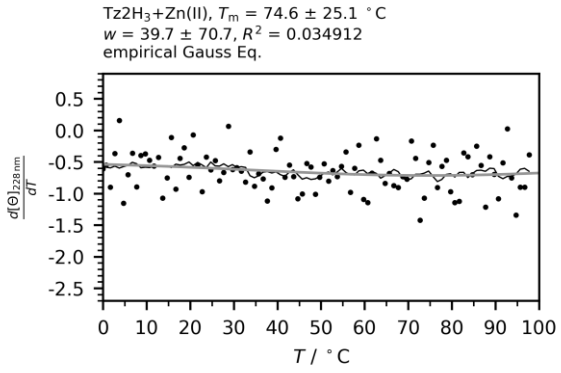
Tz2H3+Zn(II), Tm = 74.6 ± 25.1 °C
w = 39.7 ± 70.7, R2 = 0.034912
empirical Gauss Eq.
T / °C

Tz2H$_3$ + Cu(II) (50 µM peptide + 50 µM metal ions in MOPS buffered saline)

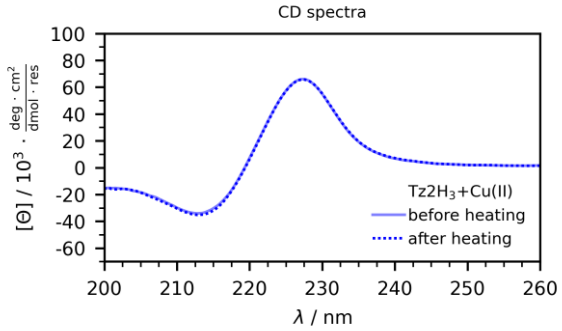

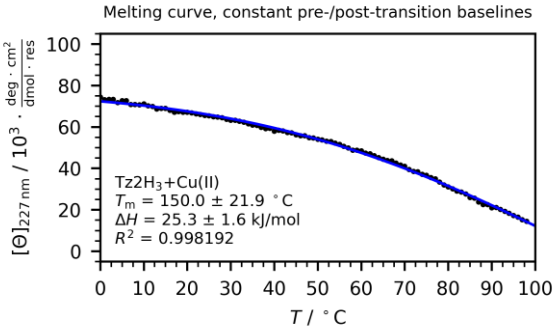

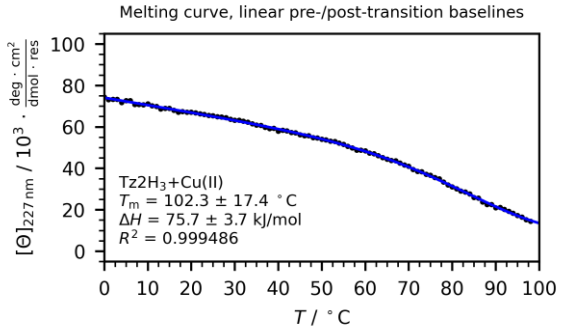

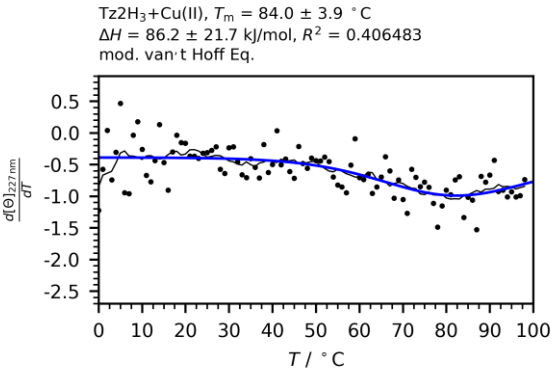

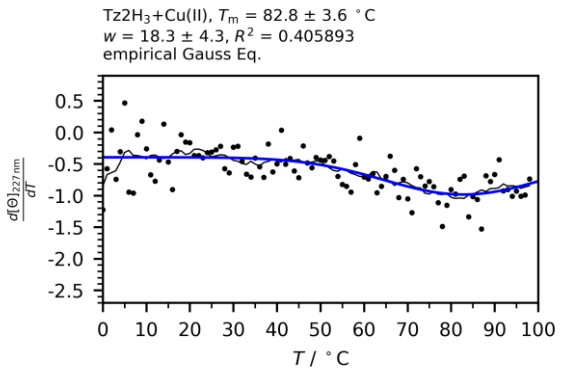

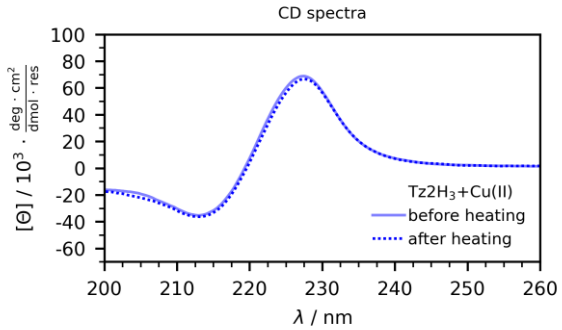
CD spectra
Tz2H3+Cu(II)
before heating
after heating
λ / nm

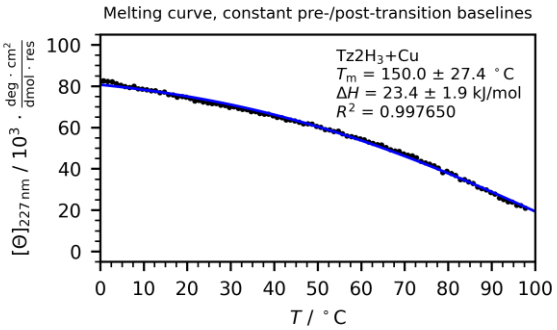
Melting curve, constant pre-/post-transition baselines
Tz2H3+Cu
Tm = 150.0 ± 27.4 °C
ΔH = 23.4 ± 1.9 kJ/mol
R2 = 0.997650
T / °C

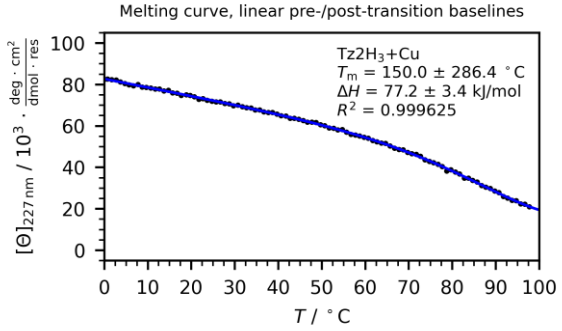
Melting curve, linear pre-/post-transition baselines
Tz2H3+Cu
Tm = 150.0 ± 286.4 °C
ΔH = 77.2 ± 3.4 kJ/mol
R2 = 0.999625
T / °C

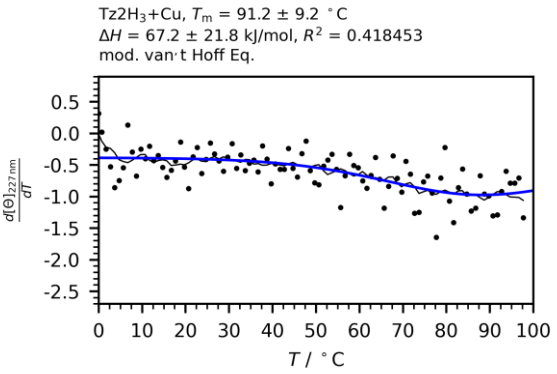
Tz2H3+Cu, Tm = 91.2 ± 9.2 °C
ΔH = 67.2 ± 21.8 kJ/mol, R2 = 0.418453
mod. van't Hoff Eq.
T / °C

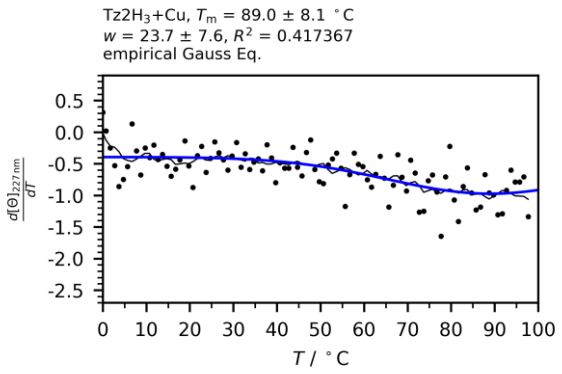
Tz2H3+Cu, Tm = 89.0 ± 8.1 °C
w = 23.7 ± 7.6, R2 = 0.417367
empirical Gauss Eq.
T / °C

(50 μM peptide + 50 μM metal ions in hydrogen sulfate buffered saline)

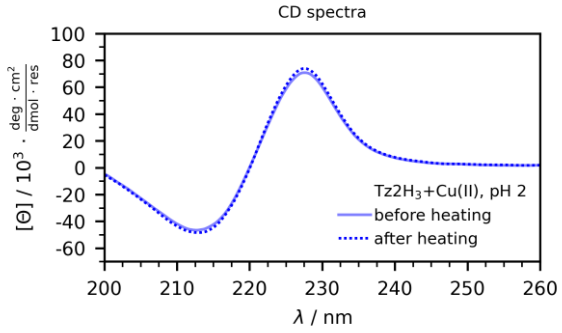

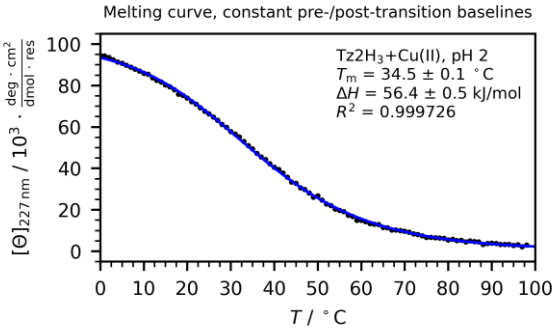

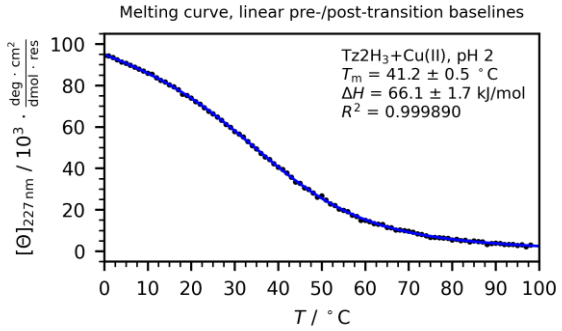

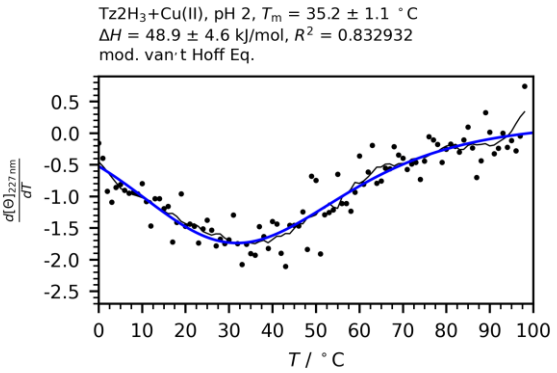

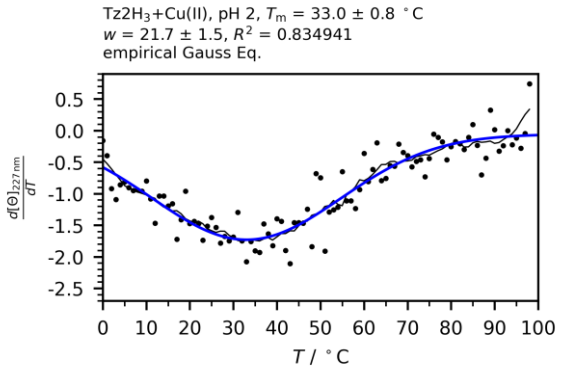

(50 μM peptide + 50 μM metal ions in MOPS buffered saline and GdnHCl)

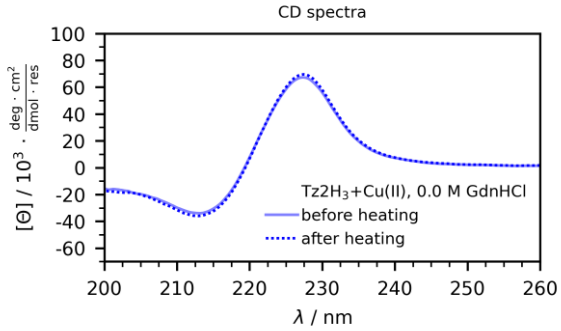

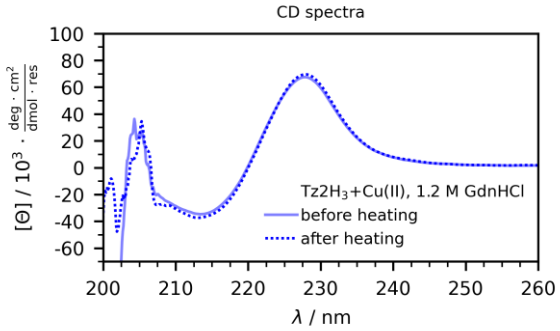

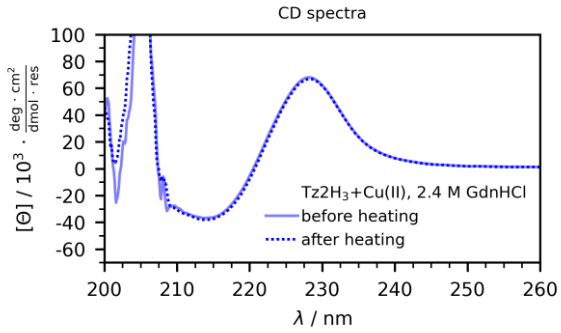

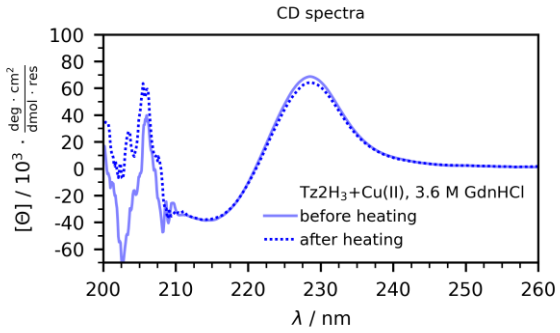

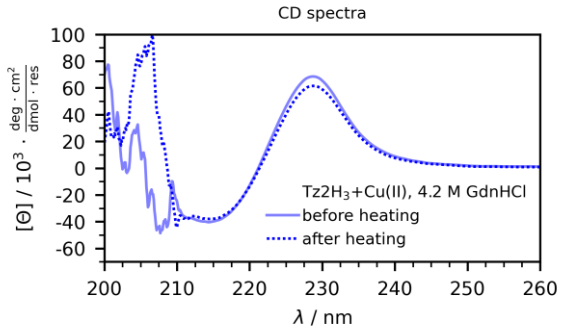

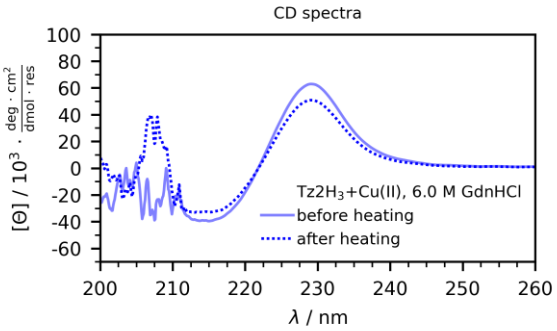

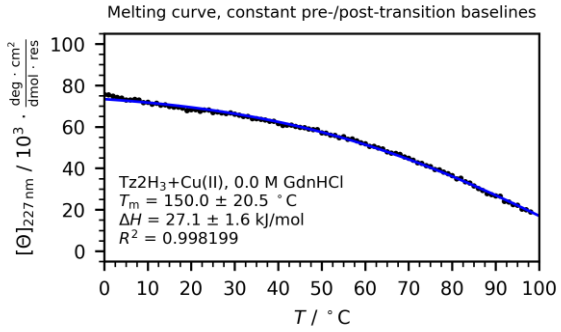

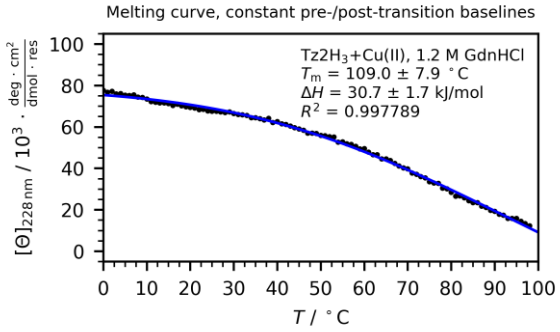

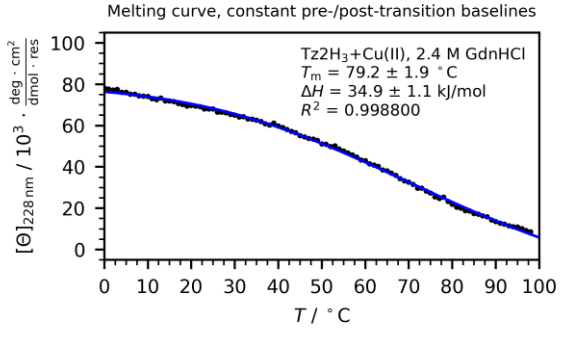

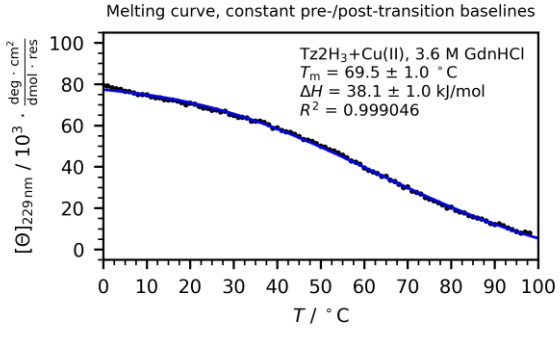

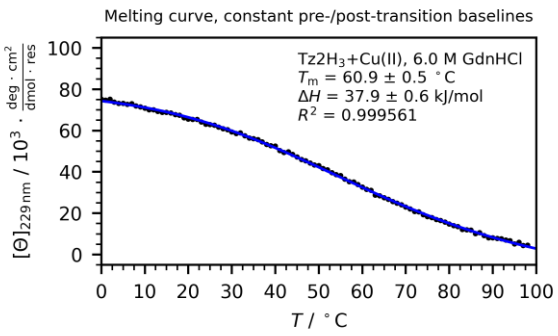
Melting curve, constant pre-/post-transition baselines
Tz2H3+Cu(II), 6.0 M GdnHCl
Tm = 60.9 ± 0.5 °C
ΔH = 37.9 ± 0.6 kJ/mol
R2 = 0.999561
[Θ]229 nm / 10³ · deg · cm² / dmol · res
T / °C

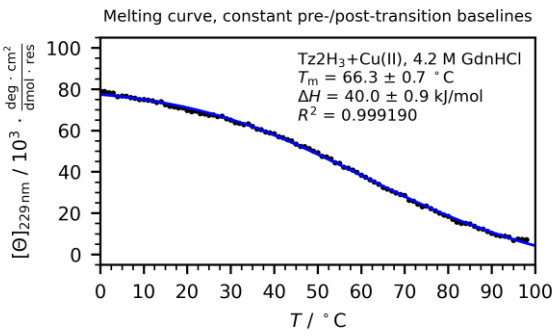
Melting curve, constant pre-/post-transition baselines
Tz2H3+Cu(II), 4.2 M GdnHCl
Tm = 66.3 ± 0.7 °C
ΔH = 40.0 ± 0.9 kJ/mol
R2 = 0.999190
[Θ]229 nm / 10³ · deg · cm² / dmol · res
T / °C

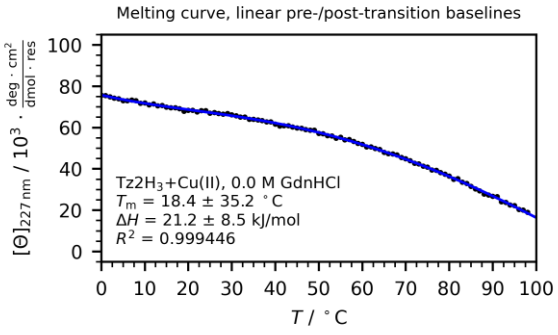
Melting curve, linear pre-/post-transition baselines
Tz2H3+Cu(II), 0.0 M GdnHCl
Tm = 18.4 ± 35.2 °C
ΔH = 21.2 ± 8.5 kJ/mol
R2 = 0.999446
[Θ]227 nm / 10³ · deg · cm² / dmol · res
T / °C

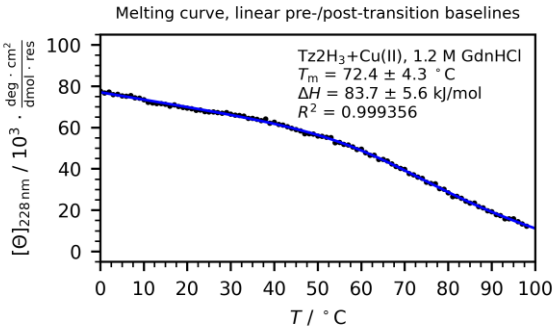
Melting curve, linear pre-/post-transition baselines
Tz2H3+Cu(II), 1.2 M GdnHCl
Tm = 72.4 ± 4.3 °C
ΔH = 83.7 ± 5.6 kJ/mol
R2 = 0.999356
[Θ]228 nm / 10³ · deg · cm² / dmol · res
T / °C

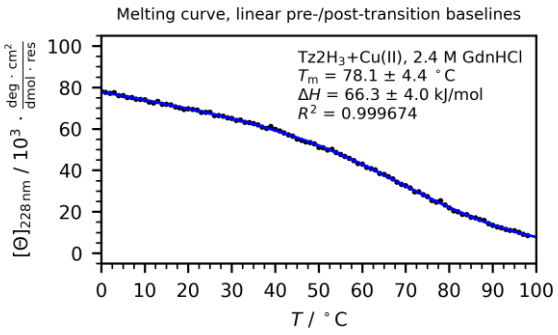
Melting curve, linear pre-/post-transition baselines
Tz2H3+Cu(II), 2.4 M GdnHCl
Tm = 78.1 ± 4.4 °C
ΔH = 66.3 ± 4.0 kJ/mol
R2 = 0.999674
[Θ]228 nm / 10³ · deg · cm² / dmol · res
T / °C

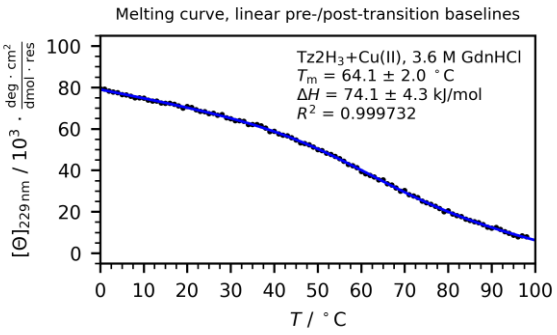
Melting curve, linear pre-/post-transition baselines
Tz2H3+Cu(II), 3.6 M GdnHCl
Tm = 64.1 ± 2.0 °C
ΔH = 74.1 ± 4.3 kJ/mol
R2 = 0.999732
[Θ]229 nm / 10³ · deg · cm² / dmol · res
T / °C

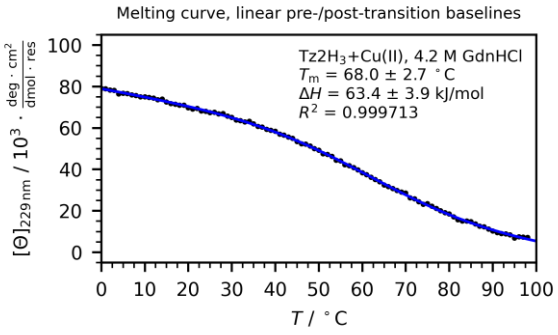
Melting curve, linear pre-/post-transition baselines
Tz2H3+Cu(II), 4.2 M GdnHCl
Tm = 68.0 ± 2.7 °C
ΔH = 63.4 ± 3.9 kJ/mol
R2 = 0.999713
[Θ]229 nm / 10³ · deg · cm² / dmol · res
T / °C

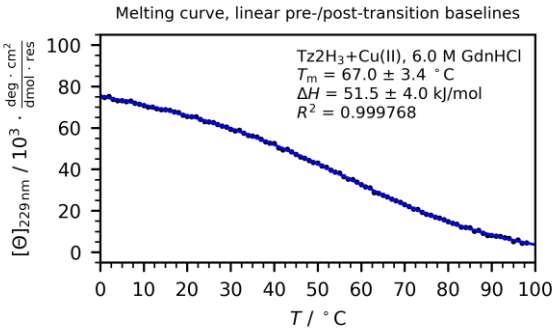
Melting curve, linear pre-/post-transition baselines
Tz2H3+Cu(II), 6.0 M GdnHCl
Tm = 67.0 ± 3.4 °C
ΔH = 51.5 ± 4.0 kJ/mol
R2 = 0.999768
[Θ]229 nm / 10³ · deg · cm² / dmol · res
T / °C

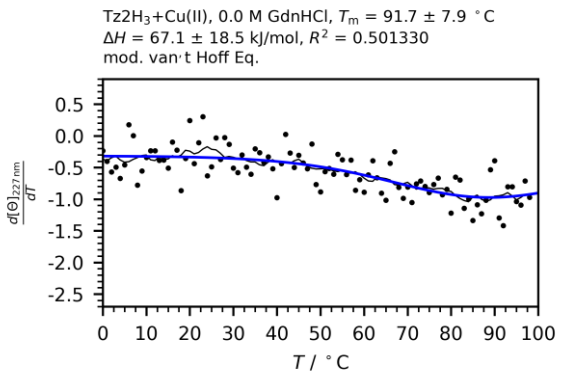
Tz2H3+Cu(II), 0.0 M GdnHCl, Tm = 91.7 ± 7.9 °C
ΔH = 67.1 ± 18.5 kJ/mol, R2 = 0.501330
mod. van't Hoff Eq.
d[Θ]227nm/dT
T / °C

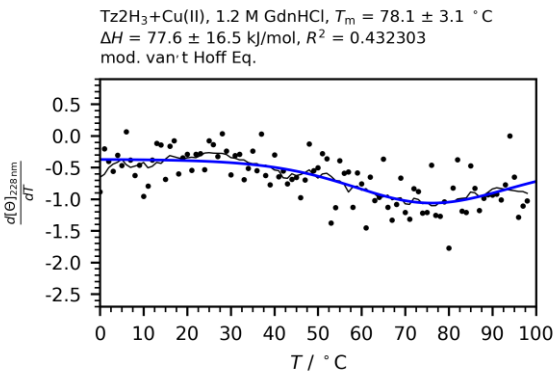
Tz2H3+Cu(II), 1.2 M GdnHCl, Tm = 78.1 ± 3.1 °C
ΔH = 77.6 ± 16.5 kJ/mol, R2 = 0.432303
mod. van't Hoff Eq.
d[Θ]228nm/dT
T / °C

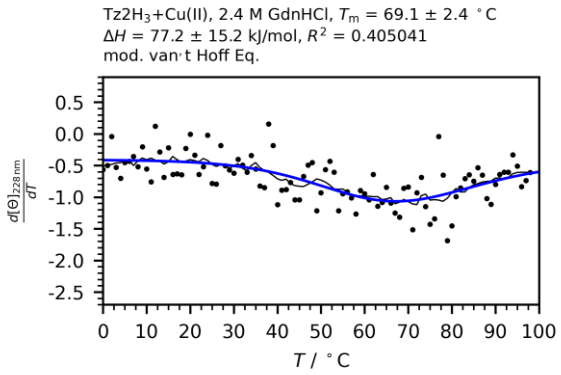
Tz2H3+Cu(II), 2.4 M GdnHCl, Tm = 69.1 ± 2.4 °C
ΔH = 77.2 ± 15.2 kJ/mol, R2 = 0.405041
mod. van't Hoff Eq.
d[Θ]228nm/dT
T / °C

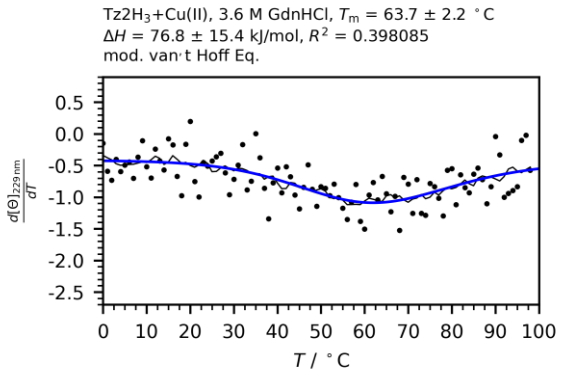
Tz2H3+Cu(II), 3.6 M GdnHCl, Tm = 63.7 ± 2.2 °C
ΔH = 76.8 ± 15.4 kJ/mol, R2 = 0.398085
mod. van't Hoff Eq.
d[Θ]229nm/dT
T / °C

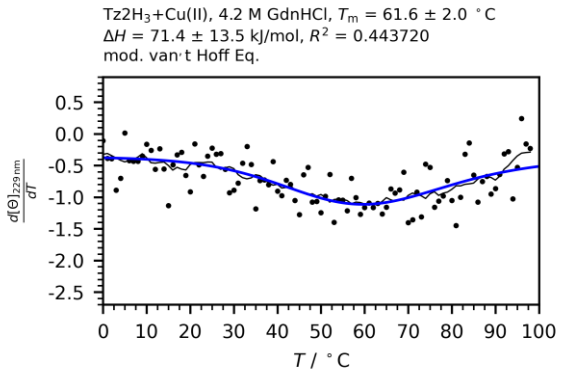
Tz2H3+Cu(II), 4.2 M GdnHCl, Tm = 61.6 ± 2.0 °C
ΔH = 71.4 ± 13.5 kJ/mol, R2 = 0.443720
mod. van't Hoff Eq.
d[Θ]229nm/dT
T / °C

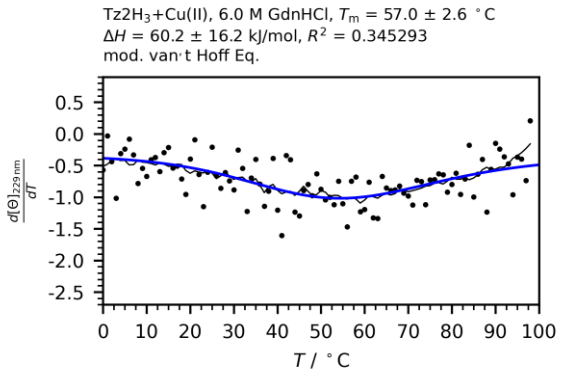
Tz2H3+Cu(II), 6.0 M GdnHCl, Tm = 57.0 ± 2.6 °C
ΔH = 60.2 ± 16.2 kJ/mol, R2 = 0.345293
mod. van't Hoff Eq.
d[Θ]229nm/dT
T / °C

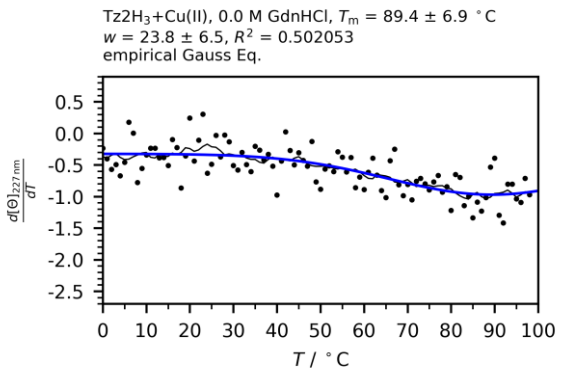
Tz2H3+Cu(II), 0.0 M GdnHCl, Tm = 89.4 ± 6.9 °C
w = 23.8 ± 6.5, R2 = 0.502053
empirical Gauss Eq.
d[Θ]227 nm / dT
T / °C

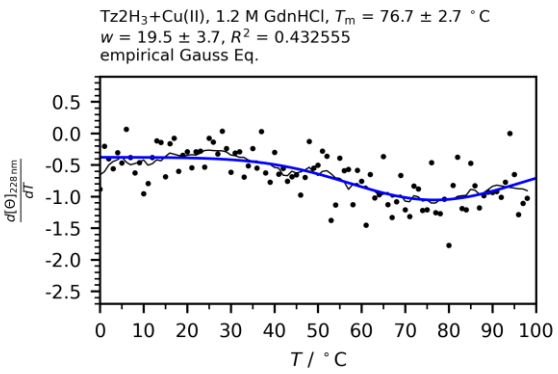
Tz2H3+Cu(II), 1.2 M GdnHCl, Tm = 76.7 ± 2.7 °C
w = 19.5 ± 3.7, R2 = 0.432555
empirical Gauss Eq.
d[Θ]228 nm / dT
T / °C

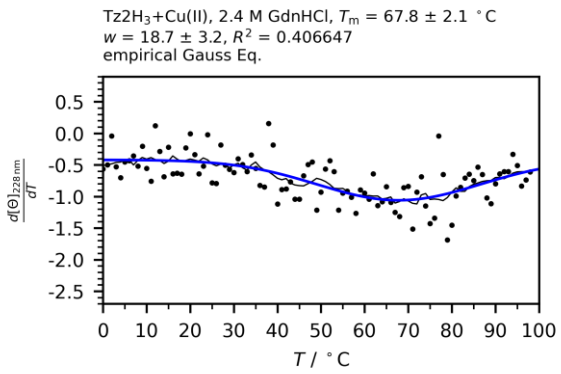
Tz2H3+Cu(II), 2.4 M GdnHCl, Tm = 67.8 ± 2.1 °C
w = 18.7 ± 3.2, R2 = 0.406647
empirical Gauss Eq.
d[Θ]228 nm / dT
T / °C

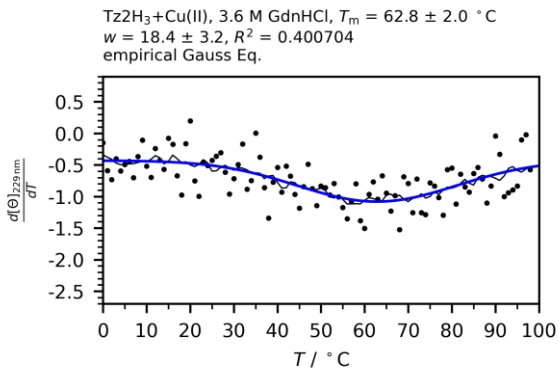
Tz2H3+Cu(II), 3.6 M GdnHCl, Tm = 62.8 ± 2.0 °C
w = 18.4 ± 3.2, R2 = 0.400704
empirical Gauss Eq.
d[Θ]229 nm / dT
T / °C

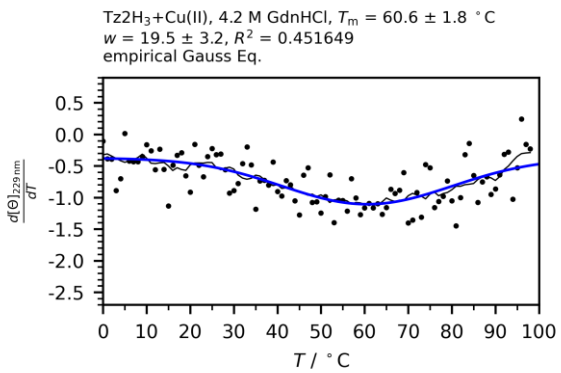
Tz2H3+Cu(II), 4.2 M GdnHCl, Tm = 60.6 ± 1.8 °C
w = 19.5 ± 3.2, R2 = 0.451649
empirical Gauss Eq.
d[Θ]229 nm / dT
T / °C

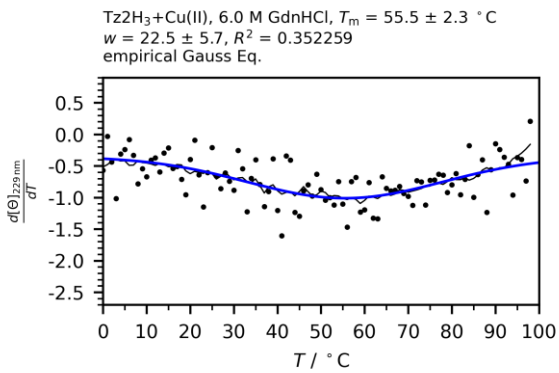
Tz2H3+Cu(II), 6.0 M GdnHCl, Tm = 55.5 ± 2.3 °C
w = 22.5 ± 5.7, R2 = 0.352259
empirical Gauss Eq.
d[Θ]229 nm / dT
T / °C

Tz2H$_3$ + Ni(II) (50 µM peptide + 50 µM metal ions in MOPS buffered saline)

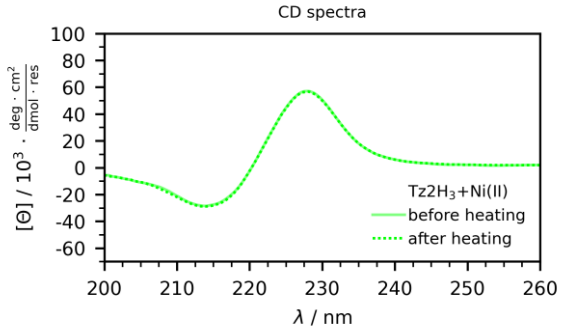

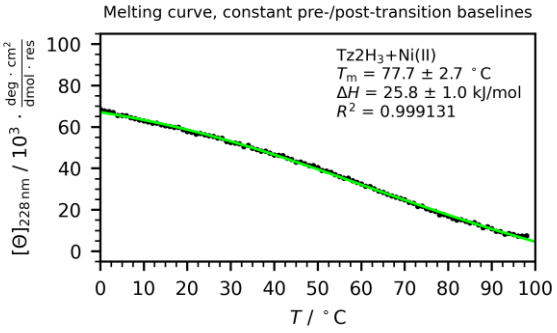

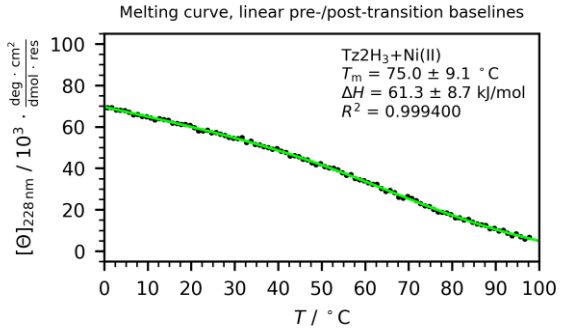

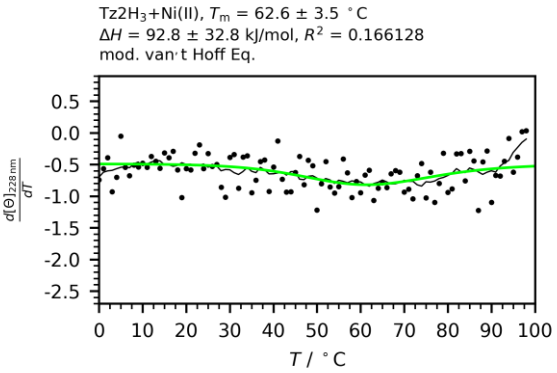

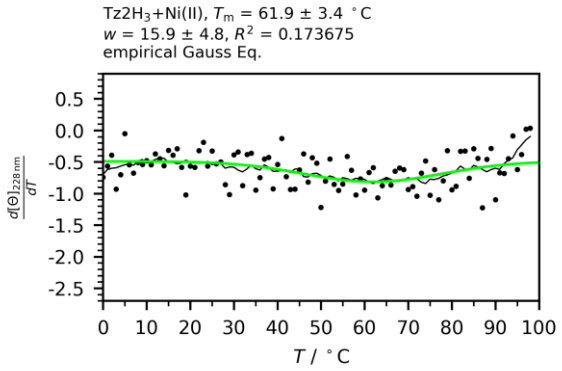

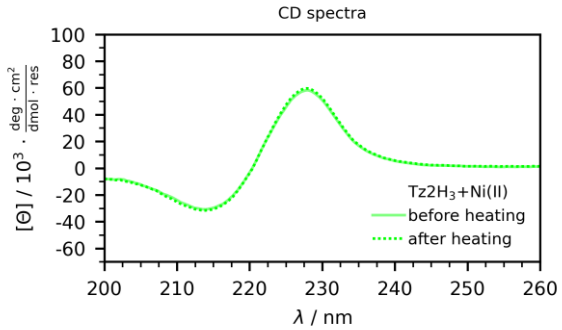
CD spectra
[Θ] / 10³ · deg · cm² / dmol · res
λ / nm
Tz2H3+Ni(II)
before heating
after heating

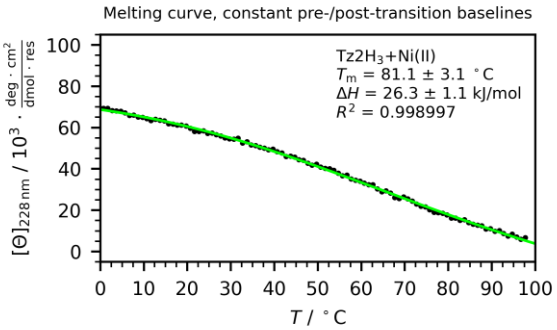
Melting curve, constant pre-/post-transition baselines
[Θ]228 nm / 10³ · deg · cm² / dmol · res
T / °C
Tz2H3+Ni(II)
Tm = 81.1 ± 3.1 °C
ΔH = 26.3 ± 1.1 kJ/mol
R² = 0.998997

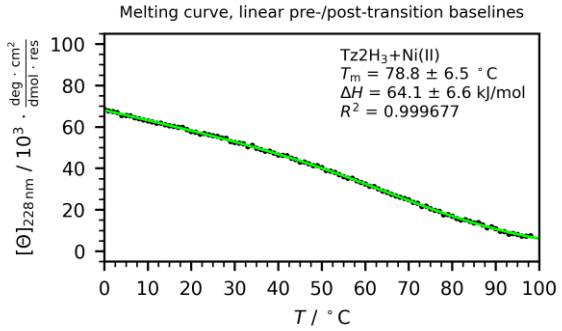
Melting curve, linear pre-/post-transition baselines
[Θ]228 nm / 10³ · deg · cm² / dmol · res
T / °C
Tz2H3+Ni(II)
Tm = 78.8 ± 6.5 °C
ΔH = 64.1 ± 6.6 kJ/mol
R² = 0.999677

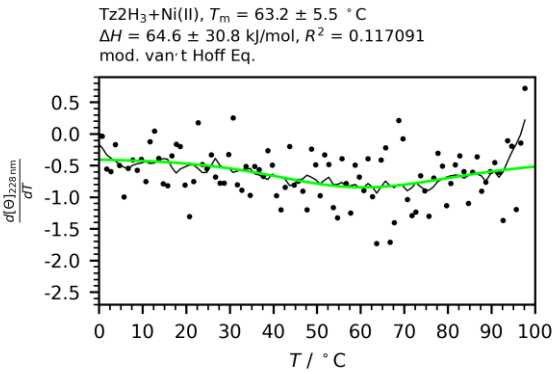
Tz2H3+Ni(II), Tm = 63.2 ± 5.5 °C
ΔH = 64.6 ± 30.8 kJ/mol, R² = 0.117091
mod. van't Hoff Eq.
d[Θ]228 nm / dT
T / °C

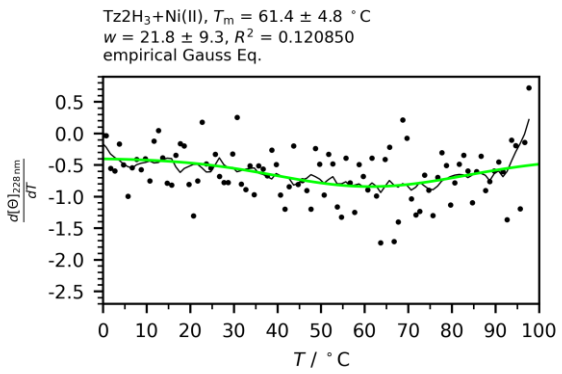
Tz2H3+Ni(II), Tm = 61.4 ± 4.8 °C
w = 21.8 ± 9.3, R² = 0.120850
empirical Gauss Eq.
d[Θ]228 nm / dT
T / °C

(50 μM peptide + 50 μM metal ions in MOPS buffered saline)

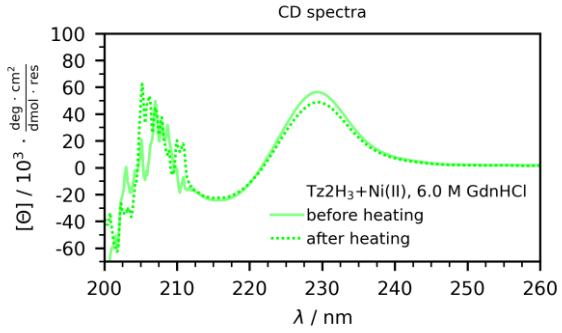

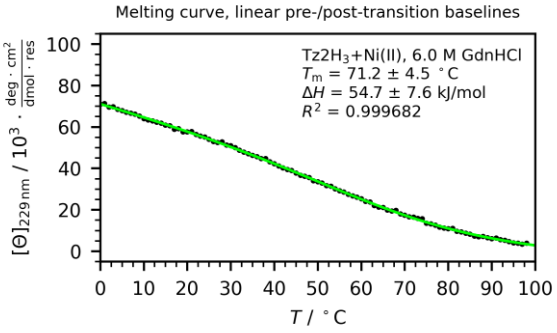

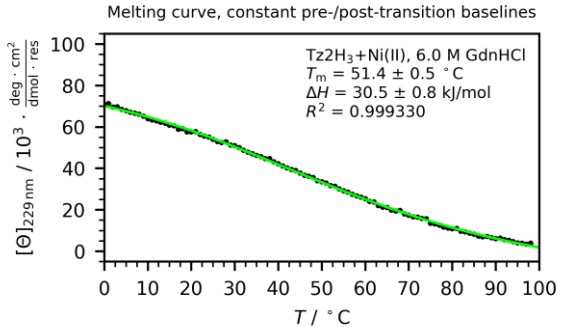

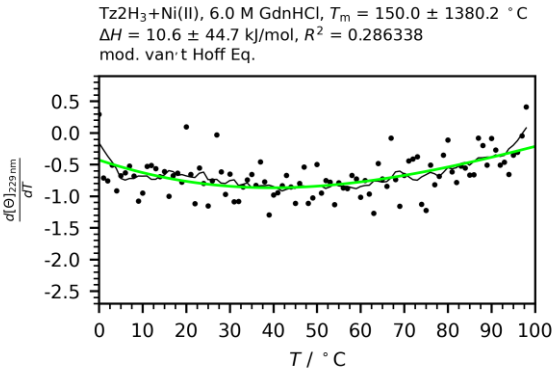

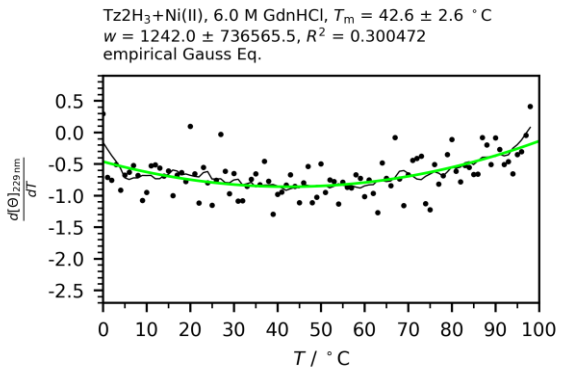

10.9 Additional AlphaFold2 output plots

WW-CA

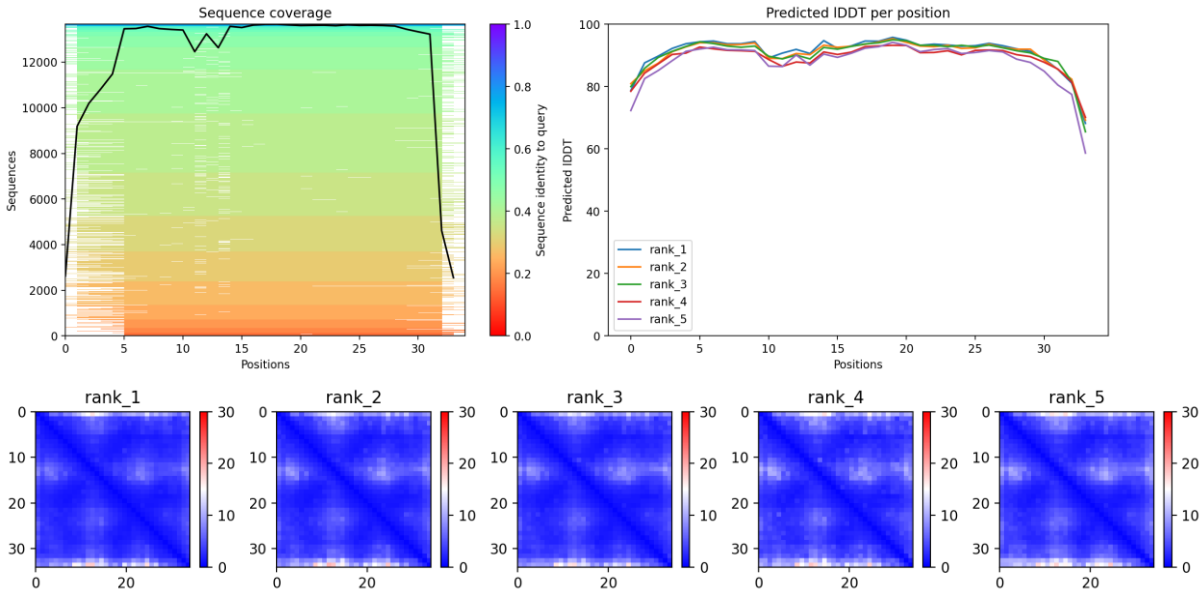

WW-CA-min (Nle to Met Mutant)

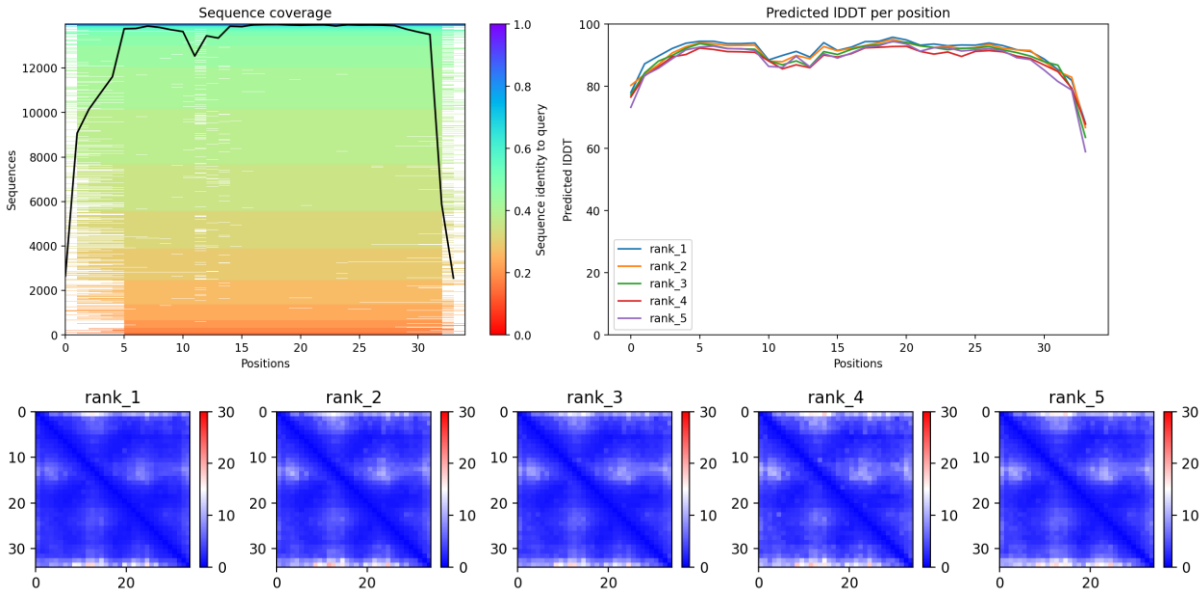

WW-CA-ANG (Nle to Met Mutant)

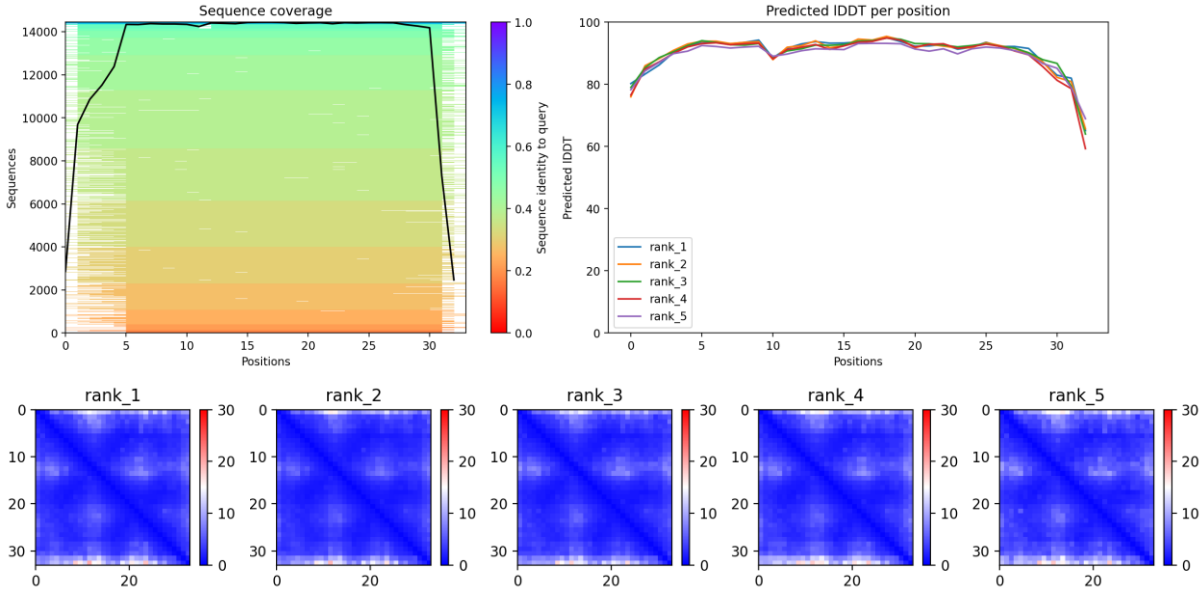

$Tz2H_3$

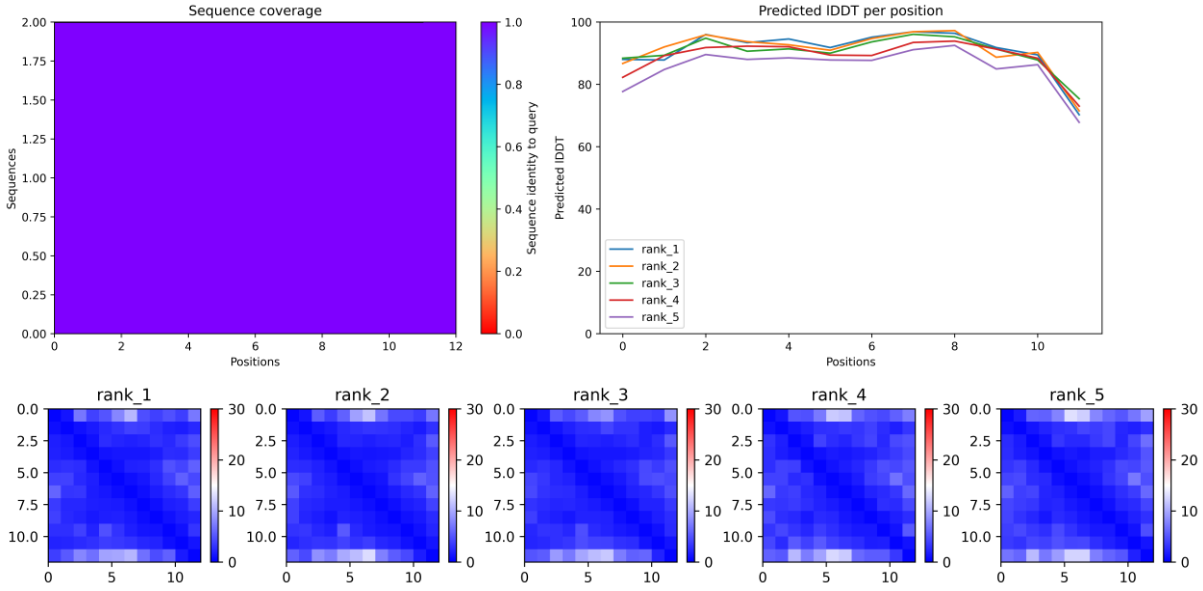

11 Danksagung

Zuerst bedanke ich mich sehr herzlich bei Prof. Dr. Franziska Thomas für die Möglichkeit, auf diesem spannenden Thema arbeiten zu können, für die exzellente Betreuung, die vielen Anregungen, fachlichen Diskussionen, das entgegengebrachte Vertrauen und die Freiheit, eigene Ideen ausprobieren zu dürfen.

Prof. Dr. Peter Comba danke ich für die erfolgreiche Kollaboration auf dem Gebiet der EPR-Spektroskopie, für die Mitnutzung von Equipment und für die Übernahme des Zweitgutachtens.

Prof. Dr. Michael Kovermann danke ich für die erfolgreiche Kollaboration auf dem Gebiet der Peptid-NMR.

Prof. Dr. Christian Klein und Prof. Dr. Michael Mastalerz danke ich für den Zugang zu CD-Spektrometern.

Dr. Jürgen Gross und den Mitarbeiterinnen und Mitarbeitern der Massenabteilung danke ich für die aufgenommenen Massenspektren und den Zugang zum MALDI-TOF Gerät.

Dr. Jürgen Graf und den Mitarbeiterinnen und Mitarbeitern der NMR-Abteilung danke ich für die aufgenommenen NMR-Spektren.

Dr. Marion Kerscher danke ich für die Wartung des EPR-Geräts.

Dr. Fania Geiger danke ich für die Organisation der sehr schönen FI-EMS Young Scientist Retreats und das kreative Rahmenprogramm.

Bei den Werkstätten und der Verwaltung am CAM/IMSEAM und am OCI bedanke ich mich für die vielen Reparaturen und die nicht-fachliche Organisation drumherum.

Martin Dörner und den Mitarbeiterinnen und Mitarbeitern der Chemikalienausgabe sowie Peter Helm danke ich für die Entgegennahme von Unmengen an Bestellungen.

Beim Fonds der Chemischen Industrie bedanke ich mich für die ideelle und finanzielle Förderung durch das Kekulé-Stipendium.

Dr. Philipp Baur (AK Comba) danke ich für die erfolgreiche Kollaboration in der EPR-Spektroskopie. Vielen Dank für die Stunden, die du in diesem Kellerraum verbracht hattest, um das Gerät vorzubereiten. Ebenso danke ich dir, dass du mich mit zu den XAS-Messungen am PSI mitgenommen hast. Das war eine spannende Erfahrung, an einer Großforschungseinrichtung zu arbeiten.

Ein großer Dank geht an den ganzen AK Thomas für die schöne Zeit innerhalb und außerhalb des Labors, für die vielen guten Ratschläge, wenn mal was nicht funktioniert hat, für die angenehmen Mittagspausen mit anregenden Gesprächen, für die vielen gemeinsam

bestrittenen Konferenzen, für die Wanderungen und Fahrten in der realen und virtuellen Welt, bei strahlendem Sonnenschein und strömenden Regen, für die Grillabende, die vielen Kuchen, Desserts und anderen Spezialitäten aus der ganzen Welt.

Bei Dr. Vanessa Reusche und Dr. Mathis Rink bedanke ich mich für die gute Aufnahme in den AK Thomas noch zu Göttinger Zeiten. Für die Organisation und Durchführung des Laborumzugs von Göttingen nach Heidelberg ist Vanessa ein großer Dank auszusprechen. Ich habe mich auch sehr gefreut, dass du noch eine Weile in Heidelberg geblieben und mich in die Geheimnisse des manchmal durchaus launigen Peptid-Synthesizers eingewiesen hast, sowie in die Verwendungsweise der „magischen“ Flüssigkeit HFIP, die so einige Probleme zu lösen vermag. Mathis danke ich für die Zusendung unerwarteter wissenschaftlicher Literatur.

Während des Umzugs und in der Corona-Hochphase sind Florian Häge, Christina Lindner und Roman Gräbner hinzugekommen und gemeinsam haben wir einiges Auf- und Umgebaut. Dafür möchte ich euch danken. Christina danke ich darüber hinaus für die erfolgreiche Zusammenarbeit. Wer spontan irgendein Peptid oder ein offenes Ohr brauchte, war bei dir immer gut aufgehoben. Bei Florian und Roman bedanke ich mich für die gemeinsame Bewältigung der OC2-Praktikumsbetreuung. Roman danke ich darüber hinaus für den regen fachlichen Austausch, die vielen Gespräche über die virtuelle Welt, Python und Tidyverse.

Marius Werner danke ich für die hervorragende Zusammenarbeit. Ich habe mich sehr gefreut, dass du bei mir dein Forschungspraktikum gemacht hast und zur Master- und Doktorarbeit in den AK Thomas zurückgekehrt bist. Vielen Dank für die schöne und produktive Zeit im Labor und Büro und für die vielen Gespräche. Du hast das Late-Stage Projekt auf ein anderes Level gehoben und bist in allen Bezugssystemen, real und virtuell, atemberaubend schnell und uneinholbar.

Einen großen Dank geht an meinen Banknachbarn, HPLC- und Mikroskop-Flüsterer Thomas Heim für die erfolgreiche Zusammenarbeit, die vielen tiefgründigen fachlichen, kulturellen und nichtfachlichen Gespräche, die abendlichen Einkaufstouren, das Schließen von Bildungslücken in der Social-Media-Kompetenz, dem Römischen Reich und Motorsport sowie das geteilte Snacklager. Ebenso danke ich dir, dass du die Bürde auf dich genommen hast, den Schatz des AK Thomas sicher zu verwahren.

Niklas Schwegler danke ich für die erfolgreiche Zusammenarbeit, den zahlreichen fachlichen und philosophischen Austausch über reale und fiktive Welten, auf Erden und weit entfernter Galaxien, über die geraden und krummen Wege. Ebenso danke ich dir, dass du, zusammen mit Marius, den Peptidsynthesizer pflegst, ihn bei Laune hältst und die Geheimnisse, denen auch ihr zuteilwurdet, weitergibst.

Laura Brüchle danke ich für die fachlichen Gespräche, ihr Organisationstalent und die Koordination zwischen AK Thomas und AK Kivala, ohne dass einige Grillabende nicht zustande gekommen wären. An dieser Stelle ist auch dem ganzen AK Kivala zu danken. Als ich neu nach Heidelberg und ins CAM/IMSEAM gekommen bin, habt ihr mich gleich aufgenommen, sodass ich nicht ganz allein war. Für die Organisation der Getränkekasse und die immerwährende Verfügbarkeit von Getränken, insbesondere Eistee, danke ich Dr. Sabine Frisch und Leon Martins.

Ich habe mich sehr über das rege Interesse von unerwartet vielen Studierenden gefreut und bedanke mich für die tatkräftige und erfolgreiche Mitarbeit bei folgenden Forschis: Guillermo Lozano, Christine Müller, Rebeka Papp, Dennis Drescher und Simon Lilje. Bei Kim Ziebner, Miguel Oliveira Singh und Jennifer Zielke, bedanke ich mich, dass ihr eure Bachelorarbeit bei mir angefertigt habt. Und zwei, Julius Pampel und Agon Kokollari, haben ihr Forschungspraktikum und ihre Bachelorarbeit bei mir geschrieben. Ihr habt alle viel dazu beigetragen, dass am Ende alles eine Runde Geschichte wird.

Several students of the Matter to Life (MtL) program joined our lab and performed great research. Three of them also choose to work with me on peptide design, for which I am very grateful: Sunnatullo Fazliev, Agi Kishore and Marcos Rafael Conde Gonzáles. You generated a lot of high-quality data and contributed significantly to the success of my thesis.

Furthermore, I thank Sunnatullo and Jennifer for joining me during the synchrotron trip and for your work during the intensive night shifts.

I am very happy that Agi and Marcos decided to stay for the PhD in AKT and further expand the scope of designed β-sheet peptides. I really appreciate having both of you as colleagues.

Ein großer Dank geht an die vielen HiWis, die bei uns waren und uns immer wieder die eine oder andere Arbeit abgenommen haben. Insbesondere danke ich Chiara Keil und Jennifer, die nach ihrer Bachelorarbeit im AKT immer noch nicht genug hatten, und Timo Färber für die gelungene Zusammenarbeit. Und ich habe mich auch sehr darüber gefreut, dass Chiara und Jonas Huber nach ihrer Masterarbeit auch zur Doktorarbeit zurückgekehrt sind.

Zuletzt bedanke ich mich bei meiner Familie, die mich auf diesem langen Weg immer unterstützt hat.

12 Selbstständigkeitserklärung

GESAMTFAKULTÄT FÜR MATHEMATIK, INGENIEUR- UND NATURWISSENSCHAFTEN

COMBINED FACULTY OF MATHEMATICS, ENGINEERING AND NATURAL SCIENCES

Eidesstattliche Versicherung gemäß § 8 der Promotionsordnung für die Gesamtfakultät für Mathematik, Ingenieur- und Naturwissenschaften der Universität Heidelberg / Sworn Affidavit according to § 8 of the doctoral degree regulations of the Combined Faculty of Mathematics, Engineering and Natural Sciences at Heidelberg University

1. Bei der eingereichten Dissertation zu dem Thema / The thesis I have submitted entitled

Design of metal-binding globular β-sheet miniproteins as biosensors and artificial enzymes

handelt es sich um meine eigenständig erbrachte Leistung / is my own work.

2. Ich habe nur die angegebenen Quellen und Hilfsmittel benutzt und mich keiner unzulässigen Hilfe Dritter bedient. Insbesondere habe ich wörtlich oder sinngemäß aus anderen Werken übernommene Inhalte als solche kenntlich gemacht. / I have only used the sources indicated and have not made unauthorised use of services of a third party. Where the work of others has been quoted or reproduced, the source is always given.

3. Die Arbeit oder Teile davon habe ich ~~wie folgt/~~bislang nicht[1)] an einer Hochschule des In- oder Auslands als Bestandteil einer Prüfungs- oder Qualifikationsleistung vorgelegt. / I have not yet / have already[1)] presented this thesis or parts thereof to a university as part of an examination or degree.

4. Die Richtigkeit der vorstehenden Erklärungen bestätige ich. / I confirm that the declarations made above are correct.

5. Die Bedeutung der eidesstattlichen Versicherung und die strafrechtlichen Folgen einer unrichtigen oder unvollständigen eidesstattlichen Versicherung sind mir bekannt. / I am aware of the importance of a sworn affidavit and the criminal prosecution in case of a false or incomplete affidavit.

Ich versichere an Eides statt, dass ich nach bestem Wissen die reine Wahrheit erklärt und nichts verschwiegen habe. / I affirm that the above is the absolute truth to the best of my knowledge and that I have not concealed anything.

…….. ……..……..

Ort und Datum / Place and date Unterschrift / Signature

[1)] Nicht Zutreffendes streichen. Bei Bejahung sind anzugeben: der Titel der andernorts vorgelegten Arbeit, die Hochschule, das Jahr der Vorlage und die Art der Prüfungs- oder Qualifikationsleistung. / Please cross out what is not applicable. If applicable, please provide: the title of the thesis that was presented elsewhere, the name of the university, the year of presentation and the type of examination or degree.

The German text is legally binding.

13 Curriculum Vitae

Truc Lam Pham

ORCID-iD: https://orcid.org/0000-0003-3808-2083

Education/Academic

Ruprecht-Karls-Universität Heidelberg
PhD studies Chemistry 12/2019 – 06/2024
Supervisor: Prof. Dr. Franziska Thomas
Topic: *Design of metal-binding globular β-sheet miniproteins as biosensors and artificial enzymes*

Georg-August-Universität Göttingen
Chemistry, Master of Science 10/2017 – 09/2019
Master thesis with Prof. Dr. Franziska Thomas
Topic: *Transformation of a protein-binding domain into an artificial enzyme*

Georg-August-Universität Göttingen
Biochemistry, Bachelor of Science 10/2014 – 07/2017
Bachelor thesis with Prof. Dr. Claudia Höbartner
Topic: *Synthesis und characterization of long modified RNA*

Ziehenschule (High School) Frankfurt am Main 09/2005 – 06/2014
Abitur (equivalent to A levels)

Awards

Poster Prize Award, Top 3 (16th German Peptide Symposium) 08/2023

Registration Fee Waivers - 36th European Peptide Symposium GRANTS 08/2022

Kekulé Fellowship of "Fonds der Chemischen Industrie" 08/2020 – 07/2022

Scholarship of "Studienstiftung des deutschen Volkes" 01/2015 – 09/2019